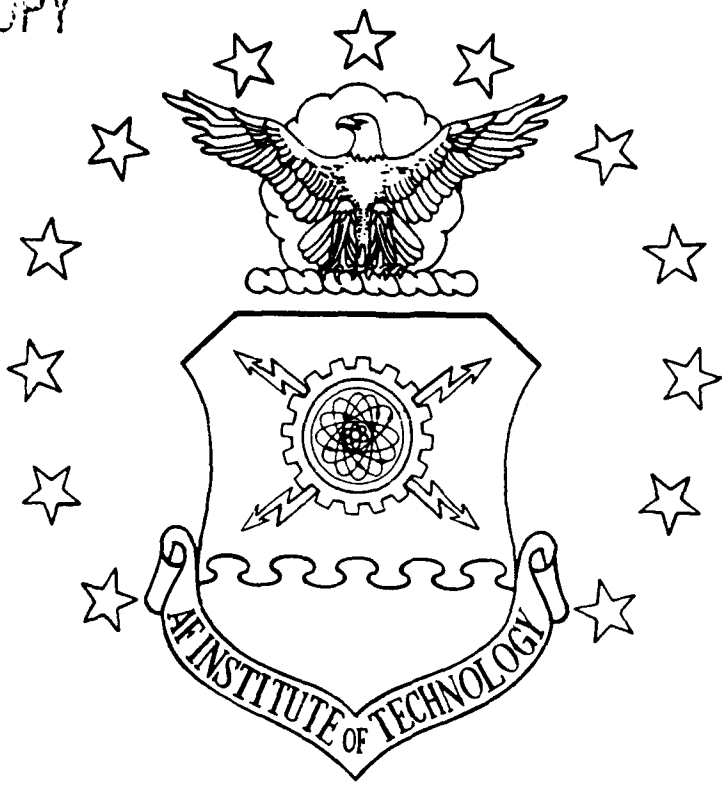


1

NOT THE COPY

AD-A231 196



KALMAN FILTER TRACKING OF A  
 REFLECTIVE TARGET USING FORWARD  
 LOOKING INFRARED MEASUREMENTS  
 AND LASER ILLUMINATION

THESIS

Roger J. Evans, Captain, USAF

AFIT/GE ENG. 90D-20

**DISTRIBUTION STATEMENT A**  
 Approved for public release;  
 Distribution Unlimited

**DTIC**  
**SELECTED**  
**JAN 22 1991**

DEPARTMENT OF THE AIR FORCE  
 AIR UNIVERSITY

**AIR FORCE INSTITUTE OF TECHNOLOGY**

Wright-Patterson Air Force Base, Ohio

01 1 99 174



AFIT/GE/ENG/90D-20

KALMAN FILTER TRACKING OF A  
REFLECTIVE TARGET USING FORWARD  
LOOKING INFRARED MEASUREMENTS  
AND LASER ILLUMINATION

THESIS

Roger J. Evans, Captain, USAF

AFIT/GE/ENG/90D-20

DTIC  
ELECTE  
JAN 22 1991  
S E D

Approved for public release; distribution unlimited

KALMAN FILTER TRACKING OF A REFLECTIVE TARGET USING  
FORWARD LOOKING INFRARED MEASUREMENTS  
AND LASER ILLUMINATION

THESIS

Presented to the Faculty of the School of Engineering  
of the Air Force Institute of Technology  
Air University

In Partial Fulfillment of the  
Requirements for the Degree of  
Master of Science in Electrical Engineering

Roger J. Evans, B.S.A.E.  
Captain, USAF

December 1990

Accession For	
NTIS GRA&I	
DTIC TAB	
Unannounced	
Justification	
By _____	
Distribution/	
Availability Codes	
Dist	Avail and/or Special
A-1	



## *Acknowledgments*

This thesis, in support of the the Air Force Weapons Laboratory, investigates the use of a linear Kalman filter in tracking the center-of-mass of a missile hardbody at a distance of 2,000 kilometers. The research, accomplished in nine months of an eighteen-month Electrical Engineering Masters Degree program, represents the efforts, assistance, and sacrifices of many people.

The research would not have been possible, if it were not for the efforts of the students who went before me. You all impressed me with your work, and this helped me to try harder when the solutions didn't come so easily. The many discussions with my advisor, Dr. Peter Maybeck, provided the knowledge and motivation to look beyond the obvious, and to seek perfection in my work. I will always be grateful for the help he gave me both "on and off the field".

Friendships are a gift in life. I thank my classmate Capt Rick Stacey for his comments and suggestions during the course of this research. His critiques were always held in the highest regard, and I value his friendship.

The accomplishment of this thesis and the AFIT program is shared with my family. My children, Natalie and Ryan, have continually inspired me. Their young understanding of the situation was always an amazement to me. I love you both. If it were not for my wife, Karen, none of this would have been completed. She performed the functions of two parents, and provided the family atmosphere. Her strength gave me the confidence and determination to succeed. This document, and all the effort that went into making it happen is dedicated to her. All my love...We did it!

Roger J. Evans

# Table of Contents

	Page
Acknowledgments .....	ii
Table of Contents .....	iii
List of Figures .....	ix
List of Tables .....	xx
List of Symbols .....	xxi
Abstract .....	xxix
I. Introduction .....	1-1
1.1 Background .....	1-4
1.2 Summary of AFIT Research .....	1-7
1.3 Thesis Objectives .....	1-21
1.3.1 Separation of Error Statistics on the FLIR Plane .....	1-23
1.3.2 Development of Eight-State Kalman Filter .....	1-24
1.3.3 Missile Reflectivity Model .....	1-25
1.3.4 Laser Sweeping Technique Investigation .....	1-26
1.3.5 Filter Performance Evaluation .....	1-26
1.3.6 Trajectory Analysis .....	1-27
1.3.7 Doppler Shift Analysis .....	1-27
1.3.8 Improved Atmospheric Modeling .....	1-27
1.4 Thesis Overview .....	1-28
II. Kalman Filter Theory .....	2-1
2.1 Introduction .....	2-1
2.2 Linear Kalman Filter .....	2-2
2.3 Extended Kalman Filter .....	2-5
2.4 Summary .....	2-9

	Page
III. Simulation Space .....	3-1
3.1 Introduction .....	3-1
3.2 Coordinate Frames .....	3-1
3.2.1 Inertial Reference Frame .....	3-2
3.2.2 Target Reference Frame .....	3-3
3.2.3 $\alpha$ - $\beta$ - $r$ Reference Frame .....	3-3
3.2.4 $\alpha$ - $\beta$ (FLIR Image) Plane .....	3-3
3.2.5 Absolute $\alpha$ - $\beta$ - $r$ Reference Frame .....	3-5
3.2.6 Trans-FLIR Plane .....	3-5
3.2.7 ALT-ACT Plane .....	3-5
3.3 FLIR Image Plane .....	3-6
3.3.1 FLIR Field-Of-View Geometry .....	3-7
3.3.2 Target Model on FLIR Image Plane .....	3-8
3.3.3 Target Velocity Projection onto FLIR Image Plane .....	3-11
3.3.4 Target Image Projection onto FLIR Image Plane .....	3-15
3.4 FLIR Sensor Pointing Controller .....	3-17
3.5 Target Trajectory .....	3-18
3.6 Summary .....	3-21
IV. Truth Model .....	4-1
4.1 Introduction .....	4-1
4.2 State Description .....	4-7
4.3 Dynamics Model .....	4-8
4.3.1 Target Model State Description .....	4-12
4.3.2 Atmospheric Jitter Model .....	4-15
4.3.3 Bending/Vibration Model .....	4-19
4.3.4 Plume Pogo Model .....	4-23

	Page
4.4 Measurement Models .....	4-27
4.4.1 FLIR Model .....	4-28
4.4.1.1 Spatially Correlated Background Noise .....	4-30
4.4.2 Low-Energy Laser Reflection Models .....	4-32
4.4.2.1 Hardbody Binary Model .....	4-35
4.4.2.2 Hardbody Reflectivity Model .....	4-41
4.4.3 Low-Energy Laser Sweeping .....	4-47
4.4.3.1 Center-of-Mass Computation with Binary Model .....	4-48
4.4.3.2 Center-of-Mass Computation with Reflectivity Model .....	4-50
4.5 Truth Model Parameters .....	4-50
4.5.1 Target Trajectory Initial Conditions .....	4-51
4.5.2 Target Model, Dimensions, and Orientation .....	4-52
4.5.3 Intensity Functions .....	4-52
4.5.4 Atmospheric Jitter .....	4-52
4.5.5 Bending/Vibration .....	4-52
4.5.6 Plume Pogo Characteristics .....	4-52
4.5.7 Spatially Correlated Background Noise .....	4-53
4.5.8 Low-Energy Laser Measurement Dimensions .....	4-53
4.5.9 Reflectivity Measurement Model .....	4-53
4.6 Summary .....	4-53
V. Filter Models .....	5-1
5.1 Introduction .....	5-1
5.2 Six-State Filter .....	5-3
5.2.1 Dynamics Model .....	5-3
5.2.2 FLIR Measurement Model .....	5-9

	Page
5.2.2.1 Enhanced Correlation Algorithm .....	5-11
5.2.2.2 Data Processing in the Fourier Domain .....	5-13
5.2.2.3 Template Generation .....	5-13
5.2.2.4 "Pseudo-Measurements" .....	5-16
5.2.2.5 FLIR Field-of-View Rotation .....	5-18
5.2.3 Filter Parameters .....	5-25
5.2.3.1 Modeling Values .....	5-25
5.2.3.2 Initial Conditions .....	5-25
5.2.3.3 Tuning Values .....	5-26
5.3 One-State Filter .....	5-26
5.3.1 Dynamics Model .....	5-28
5.3.2 Measurement Model .....	5-29
5.3.3 Filter Parameters .....	5-30
5.3.3.1 Modeling Values .....	5-30
5.3.3.2 Initial Conditions .....	5-31
5.3.3.3 Tuning Values .....	5-31
5.4 Eight-State Filter .....	5-31
5.4.1 Dynamics Model .....	5-31
5.4.2 Measurement Models .....	5-38
5.4.3 Filter Parameters .....	5-41
5.4.3.1 Modeling Values .....	5-41
5.4.3.2 Initial Conditions .....	5-41
5.4.3.3 Tuning Values .....	5-42
5.5 Summary .....	5-42
VI. Procedures and Results .....	6-1
6.1 Introduction .....	6-1



	Page
6.2 Software Validation .....	6-3
6.3 Coordinate Transformations of the Center-of-Mass Error .....	6-4
6.4 Six-State Filter Performance Analysis .....	6-8
6.5 One-State Filter Performance Analysis .....	6-10
6.6 Eight-State Filter Performance Analysis .....	6-14
6.7 One-State vs. Two-State Center-of-Mass Filter Comparison .....	6-15
6.8 Studies and Investigations .....	6-18
6.8.1 Low-Energy Laser Sensor Sensitivity .....	6-18
6.8.2 Intensity Centroid Movement .....	6-19
6.8.3 Filter Dynamics Tuning .....	6-22
6.9 Summary .....	6-24
VII. Conclusions and Recommendations .....	7-1
7.1 Introduction .....	7-1
7.2 Conclusions .....	7-1
7.2.1 One-State vs. Two-State Center-of-Mass Estimation .....	7-1
7.2.2 Hardbody Binary vs. Reflectivity Model .....	7-2
7.2.3 Low-Energy Laser Sweep .....	7-3
7.2.4 Doppler Shift Investigation .....	7-4
7.2.5 Atmospheric Modeling .....	7-4
7.2.6 Variable Target Dynamics Tuning .....	7-5
7.3 Recommendations .....	7-5
7.3.1 One-State Center-of-Mass Filter .....	7-5
7.3.2 "Apparent" Intensity Centroid Movement .....	7-6
7.3.3 Improve Atmospheric and Bending/Vibration Modeling ...	7-7
7.3.4 Variable Target Dynamics Tuning .....	7-7
7.3.5 Alternate Low-Energy Laser Sweeping Technique .....	7-8

	Page
Appendix A. Data Processing Statistics Method .....	A-1
Appendix B. Examples of Performance Plots .....	B-1
Appendix C. Six-State Filter Performance Plots Without Plume Pogo .....	C-1
Appendix D. Six-State Filter Performance Plots With Plume Pogo .....	D-1
Appendix E. One-State Center-of-Mass Filter Performance Plots Without Low-Energy Laser Sweep and Plume Pogo .....	E-1
Appendix F. One-State Center-of-Mass Filter Performance Plots Without Low-Energy Laser Sweep and With Plume Pogo .....	F-1
Appendix G. One-State Center-of-Mass Filter Performance Plots With Low-Energy Laser Sweep and Without Plume Pogo .....	G-1
Appendix H. One-State Center-of-Mass Filter Performance Plots With Low-Energy Laser Sweep and Plume Pogo .....	H-1
Appendix I. Eight-State Center-of-Mass Filter Performance Plots Without Low-Energy Laser Sweep and Plume Pogo .....	I-1
Appendix J. Eight-State Center-of-Mass Filter Performance Plots Without Low-Energy Laser Sweep and With Plume Pogo .....	J-1
Appendix K. Eight-State Center-of-Mass Filter Performance Plots With Low-Energy Laser Sweep and Without Plume Pogo .....	K-1
Appendix L. Eight-State Center-of-Mass Filter Performance Plots With Low-Energy Laser Sweep and Plume Pogo .....	L-1
Appendix M. Low-Energy Laser Sensitivity Analysis Plots .....	M-1
Appendix N. True Atmospheric and Bending/Vibration Plots .....	N-1
Bibliography .....	BIB-1
Vita .....	VITA-1

## *List of Figures*

Figure	Page
1.1. AFIT Tracking System .....	1-3
1.2. Multiple Model Filtering Algorithm .....	1-10
1.3. Data Processing Scheme Using FFT and IFFT .....	1-11
1.4. Linear Kalman Filter/Enhanced Correlator Algorithm .....	1-14
1.5. Greyscale Target Image .....	1-16
1.6. Thesis Objectives Flow Chart .....	1-22
3.1. Three Primary Coordinate Frames in Simulation Space .....	3-2
3.2. FLIR Image Plane .....	3-4
3.3. FLIR Plane, Trans-FLIR Plane, and ALT-ACT Plane .....	3-6
3.4. Pictorial of 8 x 8 FLIR Field-of-View .....	3-7
3.5. Target Image (Difference of Two Intensity Functions) in FLIR Field-of-View .....	3-8
3.6. Orientation of Target Gaussian Intensity Functions .....	3-10
3.7. Plume Intensity Centroid and Relationship with Target Velocity Vector on FLIR Image Plane .....	3-12
3.8. Target Intensity Centroid Inertial Velocity Geometry onto FLIR Image Plane .....	3-14
3.9. Target Intensity Centroid Image Projection Geometry onto FLIR Image Plane .....	3-16
3.10. Missile Trajectory in Inertial Space Relative to FLIR Image Plane .....	3-20
4.1. Computer Software Simulation Diagram of Truth Model and Kalman Filter .....	4-2
4.2. Outputs of three Monte Carlo runs .....	4-4
4.3. Filter Tuning Covariance Analysis .....	4-6
4.4. Target Image on $\alpha$ - $\beta$ Plane With "Pseudo" Angles .....	4-13
4.5. Atmospheric Turbulence Spectral Representation and Filter Approximation .....	4-16

Figure	Page
4.6. Dominant Vibration Response Spectrum . . . . .	4-20
4.7. Plume Pogo Oscillation Relative to Equilibrium Point . . . . .	4-26
4.8. Resulting Target Intensity Function on FLIR Image Plane for Difference Between Two Gaussian Intensity Functions . . . . .	4-28
4.9. FLIR Field-of-View Pixel Numbering Scheme . . . . .	4 31
4.10. True Intensity Centroid and Hardbody Binary Model in FLIR Image Plane .	4-36
4.11. Ideal Low-Energy Laser Scan at Target Location . . . . .	4-37
4.12. Six Cases of Low-Energy Laser Scan Crossing Hardbody . . . . .	4-40
4.13. Hardbody Reflectivity Model Relative to FLIR Image Plane . . . . .	4-42
4.14. Empirical Radar Reflection Data of Cylinder . . . . .	4-42
4.15. Hardbody Reflectivity Model Cross-Sectional Reflectivity Function . . . . .	4-44
4.16. Discrete Implementation of Cross-Sectional Reflectivity Function . . . . .	4-45
4.17. Hardbody Reflectivity Model Longitudinal Reflectivity Function . . . . .	4-46
4.18. Hardbody Binary Model Center-of-Mass with Low-Energy Laser Sweep . . . . .	4-49
4.19. Hardbody Reflectivity Model Center-of-Mass with Low-Energy Laser Sweep . . . . .	4-51
5.1. Data Processing for Two Filter Schemes Considered . . . . .	5-2
5.2. Enhanced Correlator/Linear Measurement Model Data Processing Algorithm . . . . .	5-10
5.3. DRFOV Rotation Scheme . . . . .	5-19
5.4. Data Processing Algorithm for Rotating Field-of-View . . . . .	5-20
5.5. DRFOV Rotation Geometry . . . . .	5-22
5.6. One-State Filter Estimate of Missile Hardbody Center-of-Mass . . . . .	5-27
5.7. Two-State Filter Estimate of Missile Hardbody Center-of-Mass . . . . .	5-38
6.1. Three Descriptions of Center-of-Mass Error . . . . .	6-6
6.2. "Apparent" Intensity Centroid Movement in FLIR Image Plane . . . . .	6-21
B.1. Example Time History Plot of Filter vs. Actual rms Errors . . . . .	B-2

Figure	Page
B.2. Example Time History Plot of Filter Error Statistics (Mean $\pm 1\sigma$ ) . . . . .	B-2
B.3. Example Time History Plot of Filter vs. Actual rms Errors With a Single Scan of Low-Energy Laser . . . . .	B-3
B.4. Example Time History Plot of Filter vs. Actual rms Errors With Low-Energy Laser Sweep . . . . .	B-3
C.1. Six-State Filter vs. Actual rms Target Azimuth Error Without Plume Pogo .	C-2
C.2. Six-State Filter vs. Actual rms Target Elevation Error Without Plume Pogo.	C-2
C.3. Six-State Filter Target Azimuth Error at $t_i^-$ Without Plume Pogo . . . . .	C-3
C.4. Six-State Filter Target Elevation Error at $t_i^-$ Without Plume Pogo . . . . .	C-3
C.5. Six-State Filter Target Azimuth Error at $t_i^+$ Without Plume Pogo . . . . .	C-4
C.6. Six-State Filter Target Elevation Error at $t_i^+$ Without Plume Pogo . . . . .	C-4
C.7. Six-State Filter Centroid Azimuth Error at $t_i^-$ Without Plume Pogo . . . . .	C-5
C.8. Six-State Filter Centroid Elevation Error at $t_i^-$ Without Plume Pogo . . . . .	C-5
C.9. Six-State Filter Centroid Azimuth Error at $t_i^+$ Without Plume Pogo . . . . .	C-6
C.10. Six-State Filter Centroid Elevation Error at $t_i^+$ Without Plume Pogo . . . . .	C-6
C.11. Six-State Filter vs. Actual rms Atmospheric Azimuth Error . . . . .	C-7
C.12. Six-State Filter vs. Actual rms Atmospheric Elevation Error . . . . .	C-7
C.13. Six-State Filter Atmospheric Azimuth Error at $t_i^-$ . . . . .	C-8
C.14. Six-State Filter Atmospheric Elevation Error at $t_i^-$ . . . . .	C-8
C.15. Six-State Filter Atmospheric Azimuth Error at $t_i^+$ . . . . .	C-9
C.16. Six-State Filter Atmospheric Elevation Error at $t_i^+$ . . . . .	C-9
D.1. Six-State Filter vs. Actual rms Target Azimuth Error With Plume Pogo . . .	D-2
D.2. Six-State Filter vs. Actual rms Target Elevation Error With Plume Pogo . .	D-2
D.3. Six-State Filter Target Azimuth Error at $t_i^-$ With Plume Pogo . . . . .	D-3
D.4. Six-State Filter Target Elevation Error at $t_i^-$ With Plume Pogo . . . . .	D-3
D.5. Six-State Filter Target Azimuth Error at $t_i^+$ With Plume Pogo . . . . .	D-4
D.6. Six-State Filter Target Elevation Error at $t_i^+$ With Plume Pogo . . . . .	D-4

Figure	Page
D.7. Six-State Filter Centroid Azimuth Error at $t_i^-$ With Plume Pogo . . . . .	D-5
D.8. Six-State Filter Centroid Elevation Error at $t_i^-$ With Plume Pogo . . . . .	D-5
D.9. Six-State Filter Centroid Azimuth Error at $t_i^+$ With Plume Pogo . . . . .	D-6
D.10. Six-State Filter Centroid Elevation Error at $t_i^+$ With Plume Pogo . . . . .	D-6
E.1. One-State Filter vs. Actual rms Center-of-Mass Magnitude Error for Binary Model Without Low-Energy Laser Sweep and Plume Pogo . . . . .	E-2
E.2. One-State Filter Center-of-Mass Magnitude Error at $t_i^-$ for Binary Model Without Low-Energy Laser Sweep and Plume Pogo . . . . .	E-3
E.3. One-State Filter Center-of-Mass Magnitude Error at $t_i^+$ for Binary Model Without Low-Energy Laser Sweep and Plume Pogo . . . . .	E-3
E.4. One-State Filter vs. Actual rms Center-of-Mass Azimuth Error for Binary Model Without Low-Energy Laser Sweep and Plume Pogo . . . . .	E-4
E.5. One-State Filter vs. Actual rms Center-of-Mass Elevation Error for Binary Model Without Low-Energy Laser Sweep and Plume Pogo . . . . .	E-4
E.6. One-State Filter Center-of-Mass Azimuth Error at $t_i^-$ for Binary Model Without Low-Energy Laser Sweep and Plume Pogo . . . . .	E-5
E.7. One-State Filter Center-of-Mass Elevation Error at $t_i^-$ for Binary Model Without Low-Energy Laser Sweep and Plume Pogo . . . . .	E-5
E.8. One-State Filter Center-of-Mass Azimuth Error at $t_i^+$ for Binary Model Without Low-Energy Laser Sweep and Plume Pogo . . . . .	E-6
E.9. One-State Filter Center-of-Mass Elevation Error at $t_i^+$ for Binary Model Without Low-Energy Laser Sweep and Plume Pogo . . . . .	E-6
E.10. One-State Filter vs. Actual rms Center-of-Mass Along-Track Error for Binary Model Without Low-Energy Laser Sweep and Plume Pogo . . . . .	E-7
E.11. One-State Filter vs. Actual rms Center-of-Mass Across-Track Error for Binary Model Without Low-Energy Laser Sweep and Plume Pogo . . . . .	E-7
E.12. One-State Filter Center-of-Mass Along-Track Error at $t_i^-$ for Binary Model Without Low-Energy Laser Sweep and Plume Pogo . . . . .	E-8
E.13. One-State Filter Center-of-Mass Across-Track Error at $t_i^-$ for Binary Model Without Low-Energy Laser Sweep and Plume Pogo . . . . .	E-8
E.14. One-State Filter Center-of-Mass Along-Track Error at $t_i^+$ for Binary Model Without Low-Energy Laser Sweep and Plume Pogo . . . . .	E-9

Figure	Page
E.15. One-State Filter Center-of-Mass Across-Track Error at $t_i^+$ for Binary Model Without Low-Energy Laser Sweep and Plume Pogo . . . . .	E-9
F.1. One-State Filter vs. Actual rms Center-of-Mass Magnitude Error for Binary Model Without Low-Energy Laser Sweep and With Plume Pogo . .	F-2
F.2. One-State Filter Center-of-Mass Magnitude Error at $t_i^-$ for Binary Model Without Low-Energy Laser Sweep and With Plume Pogo . . . . .	F-3
F.3. One-State Filter Center-of-Mass Magnitude Error at $t_i^+$ for Binary Model Without Low-Energy Laser Sweep and With Plume Pogo . . . . .	F-3
F.4. One-State Filter vs. Actual rms Center-of-Mass Azimuth Error for Binary Model Without Low-Energy Laser Sweep and With Plume Pogo . .	F-4
F.5. One-State Filter vs. Actual rms Center-of-Mass Elevation Error for Binary Model Without Low-Energy Laser Sweep and With Plume Pogo . .	F-4
F.6. One-State Filter Center-of-Mass Azimuth Error at $t_i^-$ for Binary Model Without Low-Energy Laser Sweep and With Plume Pogo . . . . .	F-5
F.7. One-State Filter Center-of-Mass Elevation Error at $t_i^-$ for Binary Model Without Low-Energy Laser Sweep and With Plume Pogo . . . . .	F-5
F.8. One-State Filter Center-of-Mass Azimuth Error at $t_i^+$ for Binary Model Without Low-Energy Laser Sweep and With Plume Pogo . . . . .	F-6
F.9. One-State Filter Center-of-Mass Elevation Error at $t_i^+$ for Binary Model Without Low-Energy Laser Sweep and With Plume Pogo . . . . .	F-6
F.10. One-State Filter vs. Actual rms Center-of-Mass Along-Track Error for Binary Model Without Low-Energy Laser Sweep and With Plume Pogo . .	F-7
F.11. One-State Filter vs. Actual rms Center-of-Mass Across-Track Error for Binary Model Without Low-Energy Laser Sweep and With Plume Pogo . .	F-7
F.12. One-State Filter Center-of-Mass Along-Track Error at $t_i^-$ for Binary Model Without Low-Energy Laser Sweep and With Plume Pogo . . . . .	F-8
F.13. One-State Filter Center-of-Mass Across-Track Error at $t_i^-$ for Binary Model Without Low-Energy Laser Sweep and With Plume Pogo . . . . .	F-8
F.14. One-State Filter Center-of-Mass Along-Track Error at $t_i^+$ for Binary Model Without Low-Energy Laser Sweep and With Plume Pogo . . . . .	F-9
F.15. One-State Filter Center-of-Mass Across-Track Error at $t_i^+$ for Binary Model Without Low-Energy Laser Sweep and With With Plume Pogo . . .	F-9
G.1. One-State Filter vs. Actual rms Center-of-Mass Magnitude Error for Reflectivity Model With Low-Energy Laser Sweep and Without Plume Pogo . . . . .	G-2

Figure	Page
G.2. One-State Filter Center-of-Mass Magnitude Error at $t_i^-$ for Reflectivity Model With Low-Energy Laser Sweep and Without Plume Pogo . . . . .	G-3
G.3. One-State Filter Center-of-Mass Magnitude Error at $t_i^+$ for Reflectivity Model With Low-Energy Laser Sweep and Without Plume Pogo . . . . .	G-3
G.4. One-State Filter vs. Actual rms Center-of-Mass Azimuth Error for Reflectivity Model With Low-Energy Laser Sweep and Without Plume Pogo . . . . .	G-4
G.5. One-State Filter vs. Actual rms Center-of-Mass Elevation Error for Reflectivity Model With Low-Energy Laser Sweep and Without Plume Pogo . . . . .	G-4
G.6. One-State Filter Center-of-Mass Azimuth Error at $t_i^-$ for Reflectivity Model With Low-Energy Laser Sweep and Without Plume Pogo . . . . .	G-5
G.7. One-State Filter Center-of-Mass Elevation Error at $t_i^-$ for Reflectivity Model With Low-Energy Laser Sweep and Without Plume Pogo . . . . .	G-5
G.8. One-State Filter Center-of-Mass Azimuth Error at $t_i^+$ for Reflectivity Model With Low-Energy Laser Sweep and Without Plume Pogo . . . . .	G-6
G.9. One-State Filter Center-of-Mass Elevation Error at $t_i^+$ for Reflectivity Model With Low-Energy Laser Sweep and Without Plume Pogo . . . . .	G-6
G.10. One-State Filter vs. Actual rms Center-of-Mass Along-Track Error for Reflectivity Model With Low-Energy Laser Sweep and Without Plume Pogo . . . . .	G-7
G.11. One-State Filter vs. Actual rms Center-of-Mass Across-Track Error for Reflectivity Model With Low-Energy Laser Sweep and Without Plume Pogo . . . . .	G-7
G.12. One-State Filter Center-of-Mass Along-Track Error at $t_i^-$ for Reflectivity Model With Low-Energy Laser Sweep and Without Plume Pogo . . . . .	G-8
G.13. One-State Filter Center-of-Mass Across-Track Error at $t_i^-$ for Reflectivity Model With Low-Energy Laser Sweep and Without Plume Pogo . . . . .	G-8
G.14. One-State Filter Center-of-Mass Along-Track Error at $t_i^+$ for Reflectivity Model With Low-Energy Laser Sweep and Without Plume Pogo . . . . .	G-9
G.15. One-State Filter Center-of-Mass Across-Track Error at $t_i^+$ for Reflectivity Model With Low-Energy Laser Sweep and With Without Plume Pogo . . . . .	G-9
H.1. One-State Filter vs. Actual rms Center-of-Mass Magnitude Error for Reflectivity Model With Low-Energy Laser Sweep and Plume Pogo . . . . .	H-2
H.2. One-State Filter Center-of-Mass Magnitude Error at $t_i^-$ for Reflectivity Model With Low-Energy Laser Sweep and Plume Pogo . . . . .	H-3



Figure	Page
H.3. One-State Filter Center-of-Mass Magnitude Error at $t_i^+$ for Reflectivity Model With Low-Energy Laser Sweep and Plume Pogo . . . . .	H-3
H.4. One-State Filter vs. Actual rms Center-of-Mass Azimuth Error for Reflectivity Model With Low-Energy Laser Sweep and Plume Pogo . . . . .	H-4
H.5. One-State Filter vs. Actual rms Center-of-Mass Elevation Error for Reflectivity Model With Low-Energy Laser Sweep and Plume Pogo . . . . .	H-4
H.6. One-State Filter Center-of-Mass Azimuth Error at $t_i^-$ for Reflectivity Model With Low-Energy Laser Sweep and Plume Pogo . . . . .	H-5
H.7. One-State Filter Center-of-Mass Elevation Error at $t_i^-$ for Reflectivity Model With Low-Energy Laser Sweep and Plume Pogo . . . . .	H-5
H.8. One-State Filter Center-of-Mass Azimuth Error at $t_i^+$ for Reflectivity Model With Low-Energy Laser Sweep and Plume Pogo . . . . .	H-6
H.9. One-State Filter Center-of-Mass Elevation Error at $t_i^+$ for Reflectivity Model With Low-Energy Laser Sweep and Plume Pogo . . . . .	H-6
H.10. One-State Filter vs. Actual rms Center-of-Mass Along-Track Error for Reflectivity Model With Low-Energy Laser Sweep and Plume Pogo . . . . .	H-7
H.11. One-State Filter vs. Actual rms Center-of-Mass Across-Track Error for Reflectivity Model With Low-Energy Laser Sweep and Plume Pogo . . . . .	H-7
H.12. One-State Filter Center-of-Mass Along-Track Error at $t_i^-$ for Reflectivity Model With Low-Energy Laser Sweep and Plume Pogo . . . . .	H-8
H.13. One-State Filter Center-of-Mass Across-Track Error at $t_i^-$ for Reflectivity Model With Low-Energy Laser Sweep and Plume Pogo . . . . .	H-8
H.14. One-State Filter Center-of-Mass Along-Track Error at $t_i^+$ for Reflectivity Model With Low-Energy Laser Sweep and Plume Pogo . . . . .	H-9
H.15. One-State Filter Center-of-Mass Across-Track Error at $t_i^+$ for Reflectivity Model With Low-Energy Laser Sweep and With Plume Pogo . . . . .	H-9
I.1. Eight-State Filter vs. Actual rms Center-of-Mass Azimuth Error for Binary Model Without Low-Energy Laser Sweep and Plume Pogo . . . . .	I-2
I.2. Eight-State Filter vs. Actual rms Center-of-Mass Elevation Error for Binary Model Without Low-Energy Laser Sweep and Plume Pogo . . . . .	I-2
I.3. Eight-State Filter Center-of-Mass Azimuth Error at $t_i^-$ for Binary Model Without Low-Energy Laser Sweep and Plume Pogo . . . . .	I-3
I.4. Eight-State Filter Center-of-Mass Elevation Error at $t_i^-$ for Binary Model Without Low-Energy Laser Sweep and Plume Pogo . . . . .	I-3

Figure	Page
I.5. Eight-State Filter Center-of-Mass Azimuth Error at $t_i^+$ for Binary Model Without Low-Energy Laser Sweep and Plume Pogo . . . . .	I-4
I.6. Eight-State Filter Center-of-Mass Elevation Error at $t_i^+$ for Binary Model Without Low-Energy Laser Sweep and Plume Pogo . . . . .	I-4
I.7. Eight-State Filter vs. Actual rms Center-of-Mass Along-Track Error for Binary Model Without Low-Energy Laser Sweep and Plume Pogo . . . . .	I-5
I.8. Eight-State Filter vs. Actual rms Center-of-Mass Across-Track Error for Binary Model Without Low-Energy Laser Sweep and Plume Pogo . . . . .	I-5
I.9. Eight-State Filter Center-of-Mass Along-Track Error at $t_i^-$ for Binary Model Without Low-Energy Laser Sweep and Plume Pogo . . . . .	I-6
I.10. Eight-State Filter Center-of-Mass Across-Track Error at $t_i^-$ for Binary Model Without Low-Energy Laser Sweep and Plume Pogo . . . . .	I-6
I.11. Eight-State Filter Center-of-Mass Along-Track Error at $t_i^+$ for Binary Model Without Low-Energy Laser Sweep and Plume Pogo . . . . .	I-7
I.12. Eight-State Filter Center-of-Mass Across-Track Error at $t_i^+$ for Binary Model Without Low-Energy Laser Sweep and Plume Pogo . . . . .	I-7
J.1. Eight-State Filter vs. Actual rms Center-of-Mass Azimuth Error for Binary Model Without Low-Energy Laser Sweep and With Plume Pogo . .	J-2
J.2. Eight-State Filter vs. Actual rms Center-of-Mass Elevation Error for Binary Model Without Low-Energy Laser Sweep and With Plume Pogo . .	J-2
J.3. Eight-State Filter Center-of-Mass Azimuth Error at $t_i^-$ for Binary Model Without Low-Energy Laser Sweep and With Plume Pogo . . . . .	J-3
J.4. Eight-State Filter Center-of-Mass Elevation Error at $t_i^-$ for Binary Model Without Low-Energy Laser Sweep and With Plume Pogo . . . . .	J-3
J.5. Eight-State Filter Center-of-Mass Azimuth Error at $t_i^+$ for Binary Model Without Low-Energy Laser Sweep and With Plume Pogo . . . . .	J-4
J.6. Eight-State Filter Center-of-Mass Elevation Error at $t_i^+$ for Binary Model Without Low-Energy Laser Sweep and With Plume Pogo . . . . .	J-4
J.7. Eight-State Filter vs. Actual rms Center-of-Mass Along-Track Error for Binary Model Without Low-Energy Laser Sweep and With Plume Pogo . .	J-5
J.8. Eight-State Filter vs. Actual rms Center-of-Mass Across-Track Error for Binary Model Without Low-Energy Laser Sweep and With Plume Pogo . .	J-5
J.9. Eight-State Filter Center-of-Mass Along-Track Error at $t_i^-$ for Binary Model Without Low-Energy Laser Sweep and With Plume Pogo . . . . .	J-6

Figure	Page
J.10. Eight-State Filter Center-of-Mass Across-Track Error at $t_i^-$ for Binary Model Without Low-Energy Laser Sweep and With Plume Pogo . . . . .	J-6
J.11. Eight-State Filter Center-of-Mass Along-Track Error at $t_i^+$ for Binary Model Without Low-Energy Laser Sweep and With Plume Pogo . . . . .	J-7
J.12. Eight-State Filter Center-of-Mass Across-Track Error at $t_i^+$ for Binary Model Without Low-Energy Laser Sweep and With With Plume Pogo . . . . .	J-7
K.1. Eight-State Filter vs. Actual rms Center-of-Mass Azimuth Error for Reflectivity Model With Low-Energy Laser Sweep and Without Plume Pogo . . . . .	K-2
K.2. Eight-State Filter vs. Actual rms Center-of-Mass Elevation Error for Reflectivity Model With Low-Energy Laser Sweep and Without Plume Pogo . . . . .	K-2
K.3. Eight-State Filter Center-of-Mass Azimuth Error at $t_i^-$ for Reflectivity Model With Low-Energy Laser Sweep and Without Plume Pogo . . . . .	K-3
K.4. Eight-State Filter Center-of-Mass Elevation Error at $t_i^-$ for Reflectivity Model With Low-Energy Laser Sweep and Without Plume Pogo . . . . .	K-3
K.5. Eight-State Filter Center-of-Mass Azimuth Error at $t_i^+$ for Reflectivity Model With Low-Energy Laser Sweep and Without Plume Pogo . . . . .	K-4
K.6. Eight-State Filter Center-of-Mass Elevation Error at $t_i^+$ for Reflectivity Model With Low-Energy Laser Sweep and Without Plume Pogo . . . . .	K-4
K.7. Eight-State Filter vs. Actual rms Center-of-Mass Along-Track Error for Reflectivity Model With Low-Energy Laser Sweep and Without Plume Pogo . . . . .	K-5
K.8. Eight-State Filter vs. Actual rms Center-of-Mass Across-Track Error for Reflectivity Model With Low-Energy Laser Sweep and Without Plume Pogo . . . . .	K-5
K.9. Eight-State Filter Center-of-Mass Along-Track Error at $t_i^-$ for Reflectivity Model With Low-Energy Laser Sweep and Without Plume Pogo . . . . .	K-6
K.10. Eight-State Filter Center-of-Mass Across-Track Error at $t_i^-$ for Reflectivity Model With Low-Energy Laser Sweep and Without Plume Pogo . . . . .	K-6
K.11. Eight-State Filter Center-of-Mass Along-Track Error at $t_i^+$ for Reflectivity Model With Low-Energy Laser Sweep and Without Plume Pogo . . . . .	K-7
K.12. Eight-State Filter Center-of-Mass Across-Track Error at $t_i^+$ for Reflectivity Model With Low-Energy Laser Sweep and With Without Plume Pogo . . . . .	K-7
L.1. Eight-State Filter vs. Actual rms Center-of-Mass Azimuth Error for Reflectivity Model With Low-Energy Laser Sweep and Plume Pogo . . . . .	L-2

Figure	Page
L.2. Eight-State Filter vs. Actual rms Center-of-Mass Elevation Error for Reflectivity Model With Low-Energy Laser Sweep and Plume Pogo . . . . .	L-2
L.3. Eight-State Filter Center-of-Mass Azimuth Error at $t_i^-$ for Reflectivity Model With Low-Energy Laser Sweep and Plume Pogo . . . . .	L-3
L.4. Eight-State Filter Center-of-Mass Elevation Error at $t_i^-$ for Reflectivity Model With Low-Energy Laser Sweep and Plume Pogo . . . . .	L-3
L.5. Eight-State Filter Center-of-Mass Azimuth Error at $t_i^+$ for Reflectivity Model With Low-Energy Laser Sweep and Plume Pogo . . . . .	L-4
L.6. Eight-State Filter Center-of-Mass Elevation Error at $t_i^+$ for Reflectivity Model With Low-Energy Laser Sweep and Plume Pogo . . . . .	L-4
L.7. Eight-State Filter vs. Actual rms Center-of-Mass Along-Track Error for Reflectivity Model With Low-Energy Laser Sweep and Plume Pogo . . . . .	L-5
L.8. Eight-State Filter vs. Actual rms Center-of-Mass Across-Track Error for Reflectivity Model With Low-Energy Laser Sweep and Plume Pogo . . . . .	L-5
L.9. Eight-State Filter Center-of-Mass Along-Track Error at $t_i^-$ for Reflectivity Model With Low-Energy Laser Sweep and Plume Pogo . . . . .	L-6
L.10. Eight-State Filter Center-of-Mass Across-Track Error at $t_i^-$ for Reflectivity Model With Low-Energy Laser Sweep and Plume Pogo . . . . .	L-6
L.11. Eight-State Filter Center-of-Mass Along-Track Error at $t_i^+$ for Reflectivity Model With Low-Energy Laser Sweep and Plume Pogo . . . . .	L-7
L.12. Eight-State Filter Center-of-Mass Across-Track Error at $t_i^+$ for Reflectivity Model With Low-Energy Laser Sweep and Plume Pogo . . . . .	L-7
M.1. Study: Eight-State Filter vs. Actual rms Center-of-Mass Azimuth Error for Reflectivity Model With Low-Energy Laser Sweep and Plume Pogo . . . . .	M-2
M.2. Study: Eight-State Filter vs. Actual rms Center-of-Mass Elevation Error for Reflectivity Model With Low-Energy Laser Sweep and Plume Pogo . . . . .	M-2
M.3. Study: Eight-State Filter Center-of-Mass Azimuth Error at $t_i^-$ for Reflectivity Model With Low-Energy Laser Sweep and Plume Pogo . . . . .	M-3
M.4. Study: Eight-State Filter Center-of-Mass Elevation Error at $t_i^-$ for Reflectivity Model With Low-Energy Laser Sweep and Plume Pogo . . . . .	M-3
M.5. Study: Eight-State Filter Center-of-Mass Azimuth Error at $t_i^+$ for Reflectivity Model With Low-Energy Laser Sweep and Plume Pogo . . . . .	M-4
M.6. Study: Eight-State Filter Center-of-Mass Elevation Error at $t_i^+$ for Reflectivity Model With Low-Energy Laser Sweep and Plume Pogo . . . . .	M-4

Figure	Page
M.7. Study: Eight-State Filter vs. Actual rms Center-of-Mass Along-Track Error for Reflectivity Model With Low-Energy Laser Sweep and Plume Pogo . . .	M-5
M.8. Study: Eight-State Filter vs. Actual rms Center-of-Mass Across-Track Error for Reflectivity Model With Low-Energy Laser Sweep and Plume Pogo . . .	M-5
M.9. Study: Eight-State Filter Center-of-Mass Along-Track Error at $t_i^-$ for Reflectivity Model With Low-Energy Laser Sweep and Plume Pogo . . . . .	M-6
M.10. Study: Eight-State Filter Center-of-Mass Across-Track Error at $t_i^-$ for Reflectivity Model With Low-Energy Laser Sweep and Plume Pogo . . . . .	M-6
M.11. Study: Eight-State Filter Center-of-Mass Along-Track Error at $t_i^+$ for Reflectivity Model With Low-Energy Laser Sweep and Plume Pogo . . . . .	M-7
M.12. Study: Eight-State Filter Center-of-Mass Across-Track Error at $t_i^+$ for Reflectivity Model With Low-Energy Laser Sweep and Plume Pogo . . . . .	M-7
N.1. Truth Model Atmospheric States: $x_3 + x_4$ . . . . .	N-2
N.2. Truth Model Atmospheric States: $x_6 + x_7$ . . . . .	N-2
N.3. Truth Model Bending/Vibration State: $x_9$ . . . . .	N-3
N.4. Truth Model Bending/Vibration State: $x_{11}$ . . . . .	N-3

## *List of Tables*

Table	Page
1.1. Kalman Filter and Correlation Tracker Statistics Comparison . . . . .	1-8
6.1. Target and Intensity Centroid Statistics Without Plume Pogo . . . . .	6-9
6.2. Target and Intensity Centroid Statistics With Plume Pogo . . . . .	6-9
6.3. One-State Filter Statistics Without Sweep and Pogo for Binary Model . . .	6-11
6.4. One-State Filter Statistics Without Sweep and With Pogo for Binary Model . . . . .	6-11
6.5. One-State Filter Statistics With Sweep and Without Pogo for Binary Model . . . . .	6-12
6.6. One-State Filter Statistics With Sweep and Pogo for Binary Model . . . . .	6-12
6.7. One-State Filter Statistics With Sweep and Without Pogo for Reflectivity Model . . . . .	6-12
6.8. One-State Filter Statistics With Sweep and Pogo for Reflectivity Model . . .	6-12
6.9. Eight-State Filter Statistics Without Sweep and Pogo for Binary Model . . .	6-15
6.10. Eight-State Filter Statistics Without Sweep and With Pogo for Binary Model . . . . .	6-15
6.11. Eight-State Filter Statistics With Sweep and Without Pogo for Binary Model . . . . .	6-16
6.12. Eight-State Filter Statistics With Sweep and Pogo for Binary Model . . . . .	6-16
6.13. Eight-State Filter Statistics With Sweep and Without Pogo for Reflectivity Model . . . . .	6-16
6.14. Eight-State Filter Statistics With Sweep and Pogo for Reflectivity Model . .	6-16
6.15. Six-State Filter Target and Intensity Centroid Statistics for Trajectory at 75° . . . . .	6-23
6.16. One-State Filter Center-of-Mass Statistics for Trajectory at 75° . . . . .	6-23

## *List of Symbols*

Symbol	Page
SDI .....	1-1
FLIR .....	1-1
IR .....	1-2
AFIT .....	1-2
AFWL .....	1-4
FOV .....	1-4
SNR .....	1-8
BM .....	1-9
CTR .....	1-9
MMAF .....	1-9
<b>P</b> .....	1-9
<b>K</b> .....	1-9
$z(t_i)$ .....	1-12
FFT .....	1-12
IFFT .....	1-12
<b>H</b> .....	1-12
<b>h</b> .....	1-12
MAP .....	1-15
AR .....	1-16
RRFOV .....	1-18
<b>Q</b> .....	1-18
RSFOV .....	1-19
DRFOV .....	1-19
$\hat{x}_0$ .....	2-1

Symbol	Page
$E$ .....	2-1
$\mathbf{x}(t_0)$ .....	2-1
$\mathbf{P}_0$ .....	2-1
$\mathbf{Z}(t_i)$ .....	2-2
$\mathbf{x}(t_i)$ .....	2-2
$\hat{\mathbf{x}}(t_i^+)$ .....	2-2
$\mathbf{P}(t_i^+)$ .....	2-2
$\mathbf{F}(t)$ .....	2-2
$\mathbf{x}(t)$ .....	2-2
$\mathbf{B}(t)$ .....	2-2
$\mathbf{u}(t)$ .....	2-2
$\mathbf{G}(t)$ .....	2-2
$\mathbf{w}(t)$ .....	2-2
$\mathbf{Q}(t)$ .....	2-2
$\mathbf{x}(t_{i+1})$ .....	2-3
$\Phi(t_{i+1}, t_i)$ .....	2-3
$\mathbf{B}_d(t_i)$ .....	2-3
$\mathbf{u}(t_i)$ .....	2-3
$\mathbf{G}_d(t_i)$ .....	2-3
$\mathbf{w}_d(t_i)$ .....	2-3
$\mathbf{Q}_d(t_i)$ .....	2-3
$\mathbf{H}(t_i)$ .....	2-4
$\mathbf{v}(t_i)$ .....	2-4
$\mathbf{R}$ .....	2-4
$\hat{\mathbf{x}}(t/t_i)$ .....	2-4
$\mathbf{P}(t/t_i)$ .....	2-4



Symbol	Page
$\mathbf{R}(t_i)$ .....	2-5
$\mathbf{x}_n(t_0)$ .....	2-6
$t$ .....	2-6
$t_i$ .....	2-6
$\mathbf{z}_n(t_i)$ .....	2-6
$\mathbf{x}_n(t_i)$ .....	2-6
$\mathbf{x}_n(t)$ .....	2-7
$\delta\mathbf{x}(t)$ .....	2-7
$\hat{\mathbf{x}}(t/t_i)$ .....	2-8
$\mathbf{P}(t/t_i)$ .....	2-8
$\alpha - \beta - r$ .....	3-1
AI T-ACT .....	3-1
trans-FLIR .....	3-1
$\theta$ .....	3-1
$\mathbf{e}_x$ .....	3-2
$\mathbf{e}_y$ .....	3-2
$\mathbf{e}_z$ .....	3-2
$\mathbf{e}_v$ .....	3-3
$\mathbf{e}_{pv}$ .....	3-3
$\mathbf{e}_{ppv}$ .....	3-3
$\mathbf{e}_r$ .....	3-3
$\mathbf{e}_\alpha$ .....	3-3
$\mathbf{e}_\beta$ .....	3-3
LOS .....	3-3
$\alpha'$ .....	3-5
$\beta'$ .....	3-5

Symbol	Page
$\theta_l$ .....	3-5
$x_{\text{FLIR}}$ .....	3-5
$y_{\text{FLIR}}$ .....	3-5
$x_{\text{peak}}$ .....	3-9
$y_{\text{peak}}$ .....	3-9
$x$ .....	3-9
$y$ .....	3-9
$\Delta x$ .....	3-9
$\Delta y$ .....	3-9
$\sigma_v$ .....	3-9
$\sigma_{pv}$ .....	3-9
$r_h$ .....	3-13
$v_x$ .....	3-14
$v_z$ .....	3-14
$v_y$ .....	3-15
$v_{\perp\text{LOS}}$ .....	3-16
$\mathbf{v}$ .....	3-16
$\gamma$ .....	3-16
$F_G$ .....	3-18
$G$ .....	3-18
$m_1, m_2$ .....	3-18
<b>F</b> .....	3-18
$m$ .....	3-18
<b>a</b> .....	3-18
$k_p$ .....	3-20
$(\cdot, \cdot)$ .....	4-i

Symbol	Page
$\mathbf{z}_t(\cdot, \cdot)$ .....	4-1
$\mathbf{w}_t(\cdot, \cdot)$ .....	4-1
$\mathbf{v}_t(\cdot, \cdot)$ .....	4-1
$\omega$ .....	4-1
$\mathbf{y}_t(t, \cdot)$ .....	4-2
$\mathbf{C}_t(t)$ .....	4-2
$\mathbf{x}_t(t, \cdot)$ .....	4-2
$\hat{\mathbf{y}}(t_i^-)$ .....	4-2
$\mathbf{C}(t_i)$ .....	4-2
$\hat{\mathbf{y}}(t_i^+)$ .....	4-2
$\hat{\mathbf{x}}(t_i^+)$ .....	4-2
$\mathbf{e}_t(t_i^-, \cdot)$ .....	4-3
$\mathbf{e}_t(t_i^+, \cdot)$ .....	4-3
$\mathbf{P}_e(\cdot)$ .....	4-5
$x_c, y_c$ .....	4-7
$x_d, y_d$ .....	4-7
$x_a, y_a$ .....	4-7
$x_b, y_b$ .....	4-7
$x_p$ .....	4-7
$\mathbf{Q}_{td}$ .....	4-10
$\mathbf{B}_{td}$ .....	4-10
$\mathbf{x}_t$ .....	4-10
$\mathbf{x}_d$ .....	4-11
$\mathbf{x}_a$ .....	4-11
$\mathbf{x}_b$ .....	4-11
$\mathbf{x}_p$ .....	4-11

Symbol	Page
$\Phi_t$ .....	4-11
$w_{da}(t_i)$ .....	4-12
$w_{db}(t_i)$ .....	4-12
$w_{dp}(t_i)$ .....	4-12
$\Delta t$ .....	4-14
$K_a$ .....	4-16
$\Phi\Delta t$ .....	4-18
$K_b$ .....	4-20
$\zeta_b$ .....	4-20
$\zeta_p$ .....	4-24
$K_p$ .....	4-24
$v_t$ .....	4-28
$A_p$ .....	4-29
$n_{jk}(t_i)$ .....	4-30
$b_{jk}(t_i)$ .....	4-30
$\sqrt{\epsilon}$ .....	4-32
$\mathbf{I} \delta_{ij}$ .....	4-32
$v_f$ .....	4-35
$ML_{FLIR}$ .....	4-36
$ML_{Actual}$ .....	4-36
$\theta_f$ .....	4-37
$L_o(t_i)$ .....	4-41
$\mu$ .....	4-46
$R_T$ .....	4-47
$A_i$ .....	4-47
$F(\gamma)$ .....	4-47

Symbol	Page
$\mathbf{v}_{jk}$ .....	4-53
$\tau_x$ .....	5-5
$\tau_y$ .....	5-5
$\Phi_f \Delta t$ .....	5-5
$t_i^-$ .....	5-5
$t_i^+$ .....	5-5
$\mathbf{Q}_{df}$ .....	5-7
$\hat{x}_1(t_{i+1}^-)$ .....	5-9
$\hat{x}_2(t_{i+1}^-)$ .....	5-9
$\hat{\mathbf{I}}(t_i)$ .....	5-15
$\mathbf{I}(t_i)$ .....	5-15
$F\{\cdot\}$ .....	5-16
$\mathbf{g}(x, y)$ .....	5-16
$l(x, y)$ .....	5-16
$\mathbf{G}(f_x, f_y)$ .....	5-16
$\mathbf{L}^*(f_x, f_y)$ .....	5-16
$\mathbf{H}_f$ .....	5-17
$\mathbf{v}_f(t_i)$ .....	5-17
$\mathbf{K}(t_i)$ .....	5-18
$\mathbf{x}_f(t_i^+)$ .....	5-18
$\mathbf{P}_f(t_i^+)$ .....	5-18
$\mathbf{R}_f$ .....	5-18
$\hat{\psi}$ .....	5-22
$x_{offset}$ .....	5-38
$y_{offset}$ .....	5-38
$\lambda$ .....	6-5

Symbol	Page
$\eta$ .....	6-5
$\mathbf{P}'$ .....	6-5
$\mathbf{T}$ .....	6-5
$\mathbf{T}^T$ .....	6-5
$\bar{E}(t_i)$ .....	A-2
$\sigma^2(t_i)$ .....	A-2
$x_{truth_n}(t_i)$ .....	A-2
$\hat{x}_{filter_n}(t_i)$ .....	A-2
$N$ .....	A-2

## *Abstract*

The Electrical Engineering Department at the Air Force Institute of Technology has been investigating the capabilities of Kalman filter algorithms to improve tracking performance of short- and long-ranged airborne targets. Previous research has included linear and extended (nonlinear) Kalman filters. Filter configurations have used multiple model adaptive filter structures and a Kalman filter/correlator tracker arrangement. The performance of the Kalman filter tracker has shown substantial improvements over conventional correlation trackers in tracking airborne targets on benign trajectories to highly dynamic maneuvers up to 20-g's, without loss of lock.

In the tracking scenario, a forward looking infrared radar (FLIR) sensor provides measurements to update filter estimates of the (state) variables of interest. The filter algorithm then propagates the state estimates to the next sample time. The states have included position, velocity, and acceleration of the target's intensity centroid as well as atmospheric states. Recently, a low-energy laser, scanned along the filter's estimate of the target velocity vector, has provided additional measurements to a separate Kalman filter for estimating the hardbody center-of-mass of a missile at a range of two-thousand kilometers.

This thesis furthers the investigation of tracking the center-of-mass of a missile using FLIR measurements and low-energy laser illumination of the missile hardbody. The aiming of the laser is affected by the accuracy of a filter's estimate of the intensity centroid, which in turn is affected by atmospheric jitter and vibration/bending of the space-based platform. In this research, a linear correlator/Kalman filter provides estimates to compensate for the atmospheric jitter and vibration/bending modeled in the computer-simulated truth model, and it estimates the location of the apparent intensity centroid of the target's plume. This filter provides the best attributes of the standard correlator tracker and

the Kalman filter: the correlator uses the FLIR measurement data to provide a template of the size and shape of the intensity centroid to develop offset tracking errors, provided to the filter as "pseudo-measurements"; and the Kalman filter, with its internal dynamics model, provides estimates of the state variables, and propagates the estimates to the next sample time.

Two filter estimation processes are considered in this research. In the first arrangement, a six-state linear correlator/Kalman filter with two position states, two velocity states, and two atmospheric jitter states provides estimates of the location of the target intensity centroid and velocity vector. A low-energy laser is scanned along the estimated velocity vector from the intensity centroid estimate to illuminate the missile hardbody, in order to obtain measurements of the center-of-mass for a separate one-state filter, which is tracking the hardbody center-of-mass without assuming that it is necessarily displaced along the estimated velocity vector from the intensity centroid. The second arrangement, consists of an eight-state filter, which augments the six-state filter described with two additional bias states to estimate the hardbody center-of-mass. The bias states are also used to provide the low-energy laser scanning direction following an initial reflection using the six-state filter velocity vector estimate.

An ideal hardbody of a missile is modeled as an ideal reflector ("on" or "off"), and the test results are compared to a more realistic hardbody reflectivity model. The reflectivity model considers the curvature of the missile and the angle to the low-energy laser source (FLIR image plane). The testing is accomplished both with and without a plume pogo (oscillatory) motion that is modeled in the truth model, which has a frequency of 10 Hertz and an amplitude of approximately 34 meters. The research also includes a study of using a single low-energy laser scan vs. a sweep (multiple scans) to obtain the center-of-mass measurements.



The results of the one-state filter in estimating the center-of-mass provides the same performance as the two center-of-mass states in the eight-state filter. The single scan of the low-energy laser provides laser reflection measurements only 10-20% of the time, while the method of sweeping the low-energy laser provides a measurement at each sample time. For the single scan of the low-energy laser, both filters have mean error estimates of the center-of-mass on the order of 2 meters with a standard deviation of approximately 8 meters, with the plume pogo applied to the intensity centroid. When the low-energy laser sweep is used, the errors for both filters are on the order of .0005 meters (less than 1.0 inch) with a standard deviation of 0.25 meters (less than 10.0 inches), with the plume pogo applied to the intensity centroid. The enhanced reflectivity model provides the same performance trends as the hardbody binary model; however, it is shown that the performance of the realistic reflectivity model is dependent on the sensitivity of the low-energy laser sensor.

It is determined that the cause of the apparent movement of the intensity centroid is caused by the inaccuracy of the filter's estimate provided to point the FLIR line-of-sight vector at the next predicted position of the target. This condition results in the small number of successful single low-energy laser scan reflections; the condition is overcome by the low-energy laser sweep.

# Kalman Filter Tracking of a Reflective Target Using Forward Looking Infrared Measurements and Laser Illumination

## *I. Introduction*

Research is the first step in determining how an idea may be implemented. Most advances in technology are directly attributable to previously accomplished research. If the results of the research are developed into a physical use, there may be additional technological advances made in design and fabrication of materials, and in building processes. Additionally, the combination of independently developed technologies can create new systems which may not have been otherwise realized.

The research outlined in this thesis is such an effort. It uses the attributes of three independently developed technologies to conduct research into a missile tracking system for the Strategic Defense Initiative (SDI). The three technologies involved in the research are: the Kalman filter, the forward looking infrared (FLIR) sensor, and the laser. The research is accomplished using computer simulations.

The concept of the Kalman filter was first published by 1960 [7, 8]. Based on a dynamics model of the system, the filter algorithm uses external measurements to estimate the optimum value of a desired state vector. The recursive nature of the filter makes it very desirable since it reduces computational loading. Kalman filtering is recognized as being an ideal solution to navigation data processing problems for both space and terrestrial vehicles [1]. A Kalman filter was a part of the Apollo space vehicle navigation system, and filters are currently being used in military navigation systems [1]. In addition to improving navigation solutions, the algorithm has shown improved performance over the conventional

correlation tracker in tracking benign to highly dynamic targets [2, 3, 6, 9, 10, 11, 21, 22, 24, 25, 26, 27, 28, 29, 30].

Since the early 1920's, IR has been exploited in sciences, engineering, medicine, space sciences, industry and commercial enterprises. The military expanded research of the infrared (IR) spectrum during the 1940's. In military applications, IR is used with search and tracking devices for aircraft particularly when passive sensors are desired so as not to broadcast to a target that is being tracked, and in seeking and homing devices for guided missiles. The FLIR sensor is just one of the many applications of IR technology. [5]

Since the development of the first laser in the Hughes Research Laboratories in 1960, the laser has found uses in medical, industrial, scientific, and military applications [9]. The military interest in the laser is due to its ability to transmit a narrow beam of high energy to a target almost instantaneously. If a high-energy laser is focused on a target long enough, the laser can literally burn through the skin of the vehicle and destroy it.

The Air Force Institute of Technology (AFIT) has been engaged in the development of improved short- and long-ranged tracking systems for the past twelve years. The Kalman filter, the FLIR, and the laser technologies complement each other as applied to the AFIT-research scenario (Figure 1.1) for ground- and space-based tracking systems: (1) the FLIR senses the intensity centroid of a target vehicle's exhaust plume; (2) the Kalman filter uses the FLIR information to update its system state estimates and predicts the future position of the vehicle's intensity centroid and velocity vector; (3) a low energy laser is scanned along the estimated velocity vector from the intensity centroid so as to intercept the vehicle; (4) as the vehicle is scanned by the low-energy laser, the reflection is received by a laser sensor co-located with the FLIR; (5) upon completion of a scan across the target, the center of mass of the vehicle is estimated by the filter and vehicle lock is established; and,

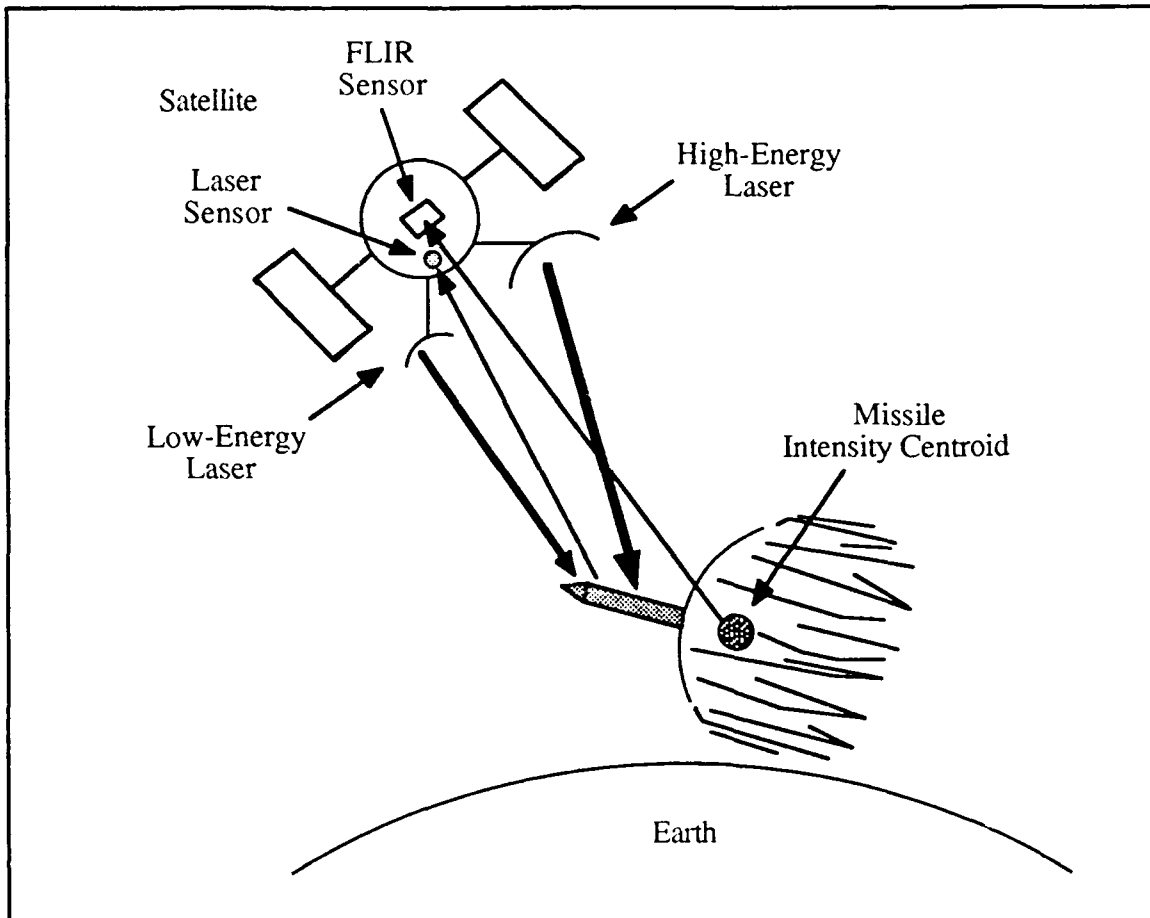


Figure 1.1. AFIT Tracking System

(6) following lock-on, the high energy laser is fired on the vehicle using the pointing information provided by the Kalman filter. As described, this system requires a high-energy laser, an accurate pointing system, and an accurate estimate of the target position. Many technological advances are necessary before the tracking system can be implemented over a distance of many hundreds of kilometers. The FLIR sensor must be able to detect and differentiate between minute changes in the target and background clutter over the long distance. Following a successful acquisition, the tracking system must then maintain lock on the target for a continuous amount of time for the high-energy laser to affect the target with its energy. If this is not accomplished, the laser will benignly "paint" the target. To understand the critical aspect of the tracking system, consider the aiming angle accuracy

required. The angle must be correct to within four one-hundred-thousandths of one degree (0.7 microradians) to track a typical missile at a distance of 2000 kilometers [27].

### *1.1 Background*

The Air Force Weapons Laboratory (AFWL) at Kirtland Air Force Base, New Mexico, has sponsored research for the purpose of developing tracking algorithms in support of SDI development beginning with the initial thesis [21] in 1978. This section provides a general overview of the AFIT-developed tracking system.

The AFIT tracking system, in its present state, consists of two sources of measurement inputs to two separate Kalman filters: the FLIR measurement and the reflected low-energy laser measurement. The measurements are readily identified in Figure 1.1. The FLIR obtains its information from the surrounding medium without providing a stimulus, while the laser measurement consists of firing a low-energy laser at the target to obtain a reflection. The former is considered a passive measurement, while the latter is an active measurement.

The FLIR consists of a 300 x 500 dimensional array of pixels, or picture elements. Each pixel is able to detect infrared radiation (IR) through an angle of 15 microradians in two orthogonal directions (azimuth and elevation). In the case of a missile target, the primary IR emission is produced by the hot gases of the target vehicle's exhaust. The array is reduced to an 8 x 8 tracking "window" in the FLIR plane to keep the mathematics manageable and reduce computational loading. This field-of-view (FOV) has proven to be satisfactory at close distances of twenty kilometers in maintaining track on targets flying benign trajectories to targets performing 20-g jinking maneuvers.

When the detectors of the 8 x 8 FOV are excited by a received signal, the measurement information is given to the Kalman filter algorithm which has been propagating the

optimum location of the target's intensity centroid since the last measurement. The filter computes the estimate of the target position and continuously commands a controller to center the target in the sensor FOV. Since the low-energy and high-energy laser share the FLIR optical aperture, the lasers are continually pointing at the estimated position of the target's intensity centroid.

The FLIR capabilities have been tested in a number of different ways as described in Section 1.2. However the use of a low-energy laser measurements to aid in the location of the target hardbody has not yet been fully examined. The simulation of the low-energy laser and its receiving sensor were initiated in the previous thesis [2]. This concept is very important to the advancement of this tracking problem, since the location of the hardbody cannot be identified from the FLIR data alone; the FLIR can only track the intensity centroid of the target. The low-energy laser is used to scan along the Kalman filter estimated velocity vector of the target. Once the reflection of the target is received by the laser sensor, which is co-located with the FLIR on the space-based platform, the Kalman filter algorithm will use the additional inputs to determine the center of mass of the target hardbody, and begin tracking.

The Kalman filter algorithm might be considered as the heart of the tracking acquisition process just described. This linear optimal estimator has replaced the previously employed correlation algorithm used by the AFWL. The potential increase in tracking performance of the Kalman filter over that of correlation tracking is readily understood from a comparison of the two processes. The correlation tracker operates under the simple principle that the current FLIR image data compared with the previous sampled data provides the necessary offset information to command the controller to the new estimate of the target's position. Since this cross-correlation of the data and the subsequent pointing of the tracker takes time, the tracking system has an inherent lag built into its response. Additionally, the correlation tracker cannot distinguish between actual target motion and

"apparent" target motion caused by atmospheric jitter phenomenon (to be discussed subsequently), and assumes that the detected translation in the image is directly proportional to the translation of the target in the spatial domain. The correlation scheme does not require explicit information about the target vehicle, the environment between the sensor and the target, or any sources of data corruption in the system. Thus it is a rather robust tracking technique. However, since the correlation algorithm does not consider these effects in the tracking solution, it is not considered to be an optimal tracker.

The inadequacies of the correlation tracker have been overcome by AFIT research [2, 3, 6, 9, 10, 11, 21, 22, 24, 25, 26, 27, 28, 29, 30] using linear and extended Kalman filtering techniques. The real world corruption (noise) found in the FLIR signal, atmospheric jitter, and the mechanical vibrations and bending of the optics hardware and platform are modeled into the filter algorithm to account for the errors in the tracking solution. Modeling of these error sources provides a significant increase in tracking performance over the correlation tracker in estimating the target position. Additionally, the (adaptively estimated) size, shape, and dynamics characteristics of the target are incorporated into the Kalman filter algorithm, which provides the ability to propagate the optimal estimate of the target position into the future.

The simulation "real world" truth model in this research provides modeling of the missile plume intensity centroid, and models a 3-dimensional reflective target onto the 2-dimensional FLIR plane. The truth model also incorporates a model of the atmospheric jitter [21], bending/vibration phenomenon [11], and the plume pogo effects [26]. The six-state filter in this research models the dynamics of the target and the atmospheric jitter phenomenon. Filter tuning, as discussed in Chapter IV and V, is used to compensate for mismodeling and/or the absence of explicit state variables, such as bending/vibration [10] and plume pogo effects [26] (in this case), in the filter model. The truth model is discussed in Chapter IV, and the three filter models used in this research are discussed in Chapter V.

## *1.2 Summary of AFIT Research*

This thesis advances the research of fifteen previous master's theses accomplished at AFIT in this area of study. Though other references are used to support this research project, by far the majority of the background information as well as the computer software development has been obtained from the AFIT graduate students [2, 3, 6, 9, 10, 11, 21, 22, 24, 25, 26, 27, 28, 29, 30]. Numerous papers [16, 17, 18, 19, 20, 31] have also been published describing the findings and accomplishments of the research. This section is devoted to the research advancement pertaining to each of the fifteen previous AFIT theses.

Research into tracking a target vehicle using a linear Kalman filter was started at AFIT in 1978 by Mercier [17, 21]. His primary emphasis was to compare the correlation tracker performance to that of an extended Kalman filter under identical conditions. The correlation algorithm used was obtained from the AFWL [21]. An eight-state real world truth model was developed consisting of two target position states and six atmospheric jitter states. The position states defined the target in each of two FLIR plane coordinate directions (azimuth and elevation), by accurately portraying target trajectories in three-dimensional space and projecting onto the FLIR image plane. The atmospheric effects were modeled by means of a third order shaping filter as given by the Analytic Sciences Corporation (TASC) [12]; three states defined the atmospheric distortion in each of the two FLIR plane coordinate directions. The Kalman filter dynamics model consisted of four states: two target position states and two atmospheric jitter states. As in the truth model, the two target position states defined the target position in each of two FLIR plane coordinate directions; the atmospheric jitter position states were defined in the same manner. In the filter the position and atmospheric states were each modeled as a first-order, zero-mean, Gauss-Markov processes. The FLIR provided sampled data measurements to the filter at a 30 Hertz (Hz) rate. The FLIR measurement noise due to



background clutter effects and internal FLIR noises were modeled in the filter as both temporally and spatially uncorrelated. The target was considered as a point source of light (i.e., a long range target) having benign dynamics. The corresponding Airy disc on the FLIR image plane was modeled as a bivariate Gaussian distribution with circular equal intensity contours. The correlation tracker and the extended Kalman filter were compared across three different signal-to-noise ratios (SNR) using a ten-run Monte Carlo analysis (Chapter III) to obtain the tracker error statistics. The results of the correlation tracker and the extended Kalman filter are shown in Table 1.1 for a Gaussian intensity function dispersion,  $\sigma_g$ , equal to one pixel. (For a Gaussian intensity function dispersion equal to one pixel, most of the useful information is contained in an area of about five pixels square.)

Table 1.1. Kalman Filter and Correlation Tracker Statistics Comparison [21]

Signal-to-Noise Ratio	Correlation Tracker		Extended Kalman Filter	
	Mean Error	$1\sigma$	Mean Error	$1\sigma$
20	7.0	8.0	0.0	0.2
10	8.0	10.0	0.0	0.2
1	15.0	30.0	0.0	0.8

Error in Pixels

While the correlation tracker showed dramatic degradation as the SNR was decreased, the Kalman filter showed only a minor change in its performance at the lowest SNR tested. The extended Kalman filter was shown to be superior to the correlation tracker by an order of magnitude in the root mean square (rms) tracking error, provided the models incorporated into the filter were a valid depiction of the tracking scenario. This success motivated a follow-on thesis to improve filter modeling and further increase the performance.

The research accomplished by Harnly and Jenson [6, 16] investigated modeling improvements in the filter and tested more dynamic target simulations. A comparison was made between a new six-state filter and a new eight-state filter. The six-state filter target dynamics model included the four previous states as well as two velocity states in the FLIR plane coordinates (azimuth and elevation); the dynamics model of the eight-state filter included two acceleration states in the FLIR plane coordinates as well. The acceleration was modeled as Brownian motion (BM) ( $\dot{\mathbf{a}} = \mathbf{w}$ , where  $\mathbf{w}$  is a zero-mean white Gaussian noise). The filter was also designed to perform residual monitoring of the rms errors. Residual monitoring allowed the filter to react adaptively, and maintain track, by quickly increasing the covariance values in the filter-computed  $\mathbf{P}$  matrix, which in turn increased the filter gain  $\mathbf{K}$ . (These terms are discussed in Chapter II and IV). A recommendation was also made to examine increasing the FOV during target jinking maneuvers to avoid losing lock. The intensity contours of the target were modeled as elliptical patterns as opposed to the earlier circular equal intensity contours in order to simulate closer range targets. The major axis of the target FLIR image was aligned with the estimated velocity vector. A number of different target trajectories were tested against the six-state and eight-state filters, and while the six-state filter performed well during jinking maneuvers, the eight-state filter performed better tracking high-g target maneuvers.

Other approaches to modeling the dynamics of the target in the filter were considered by Flynn [4]. He used the Brownian motion (BM) acceleration target dynamics model [6] and a constant turn rate (CTR) dynamics model. The CTR model portrayed the target behavior by modeling the acceleration as that associated with a constant rate of turn dynamics. Concatenating such constant turn rate segments together provides an accurate portrayal of manned target trajectories. Additionally, a Bayesian multiple model adaptive filter (MMAF) was developed using the BM dynamics model. A MMAF (Figure 1.2) consists of a bank of  $K$  independent Kalman filters, each of which is tuned to a specified

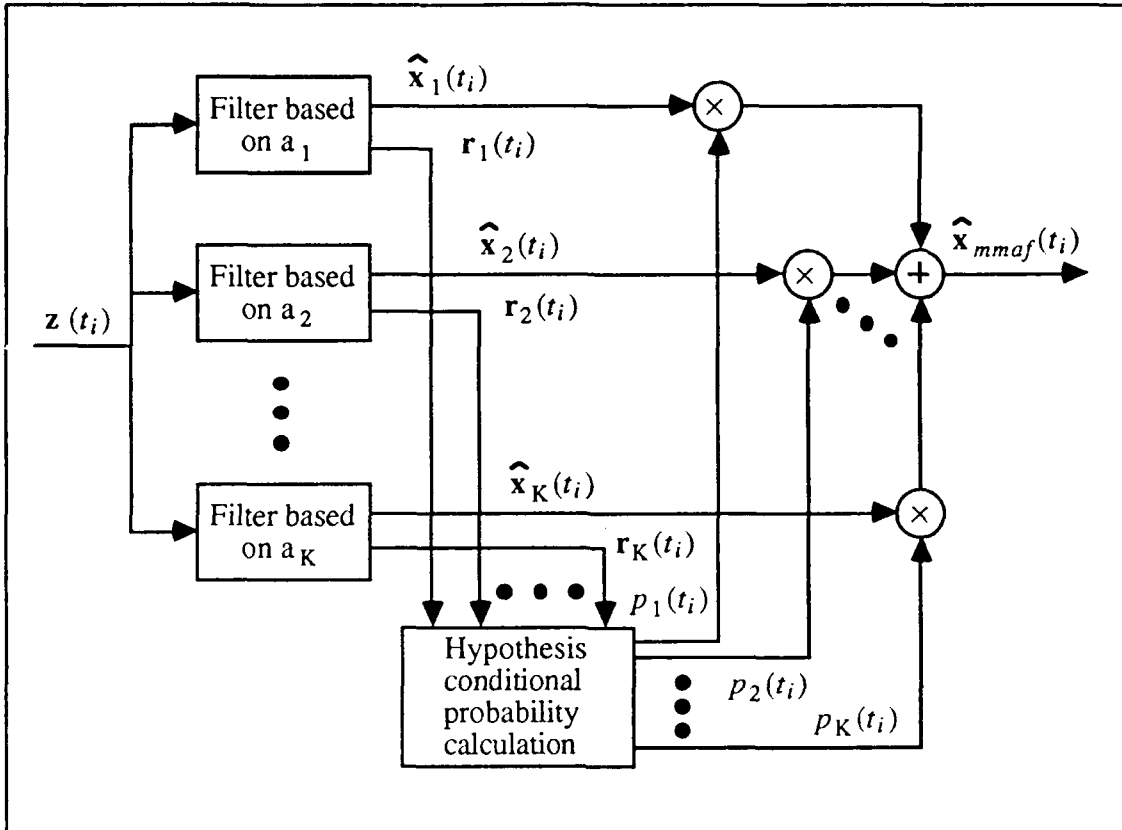


Figure 1.2. Multiple Model Filtering Algorithm

target dynamics characteristic. The time histories of the residuals of these  $K$  filters are processed to compute the conditional probability that each discrete parameter value is "correct". The residuals of the Kalman filter, based upon the "correct" model, are expected to be consistently smaller (relative to the filter's internally computed residual rms values) than the residuals of the other mismatched filters [4]. If that is true, then the multiple model adaptive filter algorithm appropriately weights that particular Kalman filter more heavily than the other Kalman filters. These values are used as weighting coefficients to produce a probability-weighted average of the elemental controller outputs [4]. Therefore, the state estimate is actually the probabilistically weighted average of the state estimate generated by each of the  $K$  separate Kalman filters. Testing of the three filter models was conducted for three different flight trajectories which included 2-g, 10-g, and 20-g pull-up maneuvers. Unfortunately, the residuals of the  $K$  Kalman filters did not

differ from each other enough to perform the weighting function properly, and MMAF did not track well. The BM and CTR filters both performed equally well at 2-g's. The CTR filter was found to be substantially better than the BM filter for 10-g and 20-g pull-up maneuvers.

Mercier had assumed that the filter had *a priori* knowledge of the target shape and intensity profile. Singletary [28] improved the realism in the target model by developing a model in the FLIR plane which included multiple hot spots. However, he returned to the case of very benign targets. The filter did not assume *a priori* knowledge of the target size, shape, or location. A new data processing scheme (Figure 1.3) was developed which

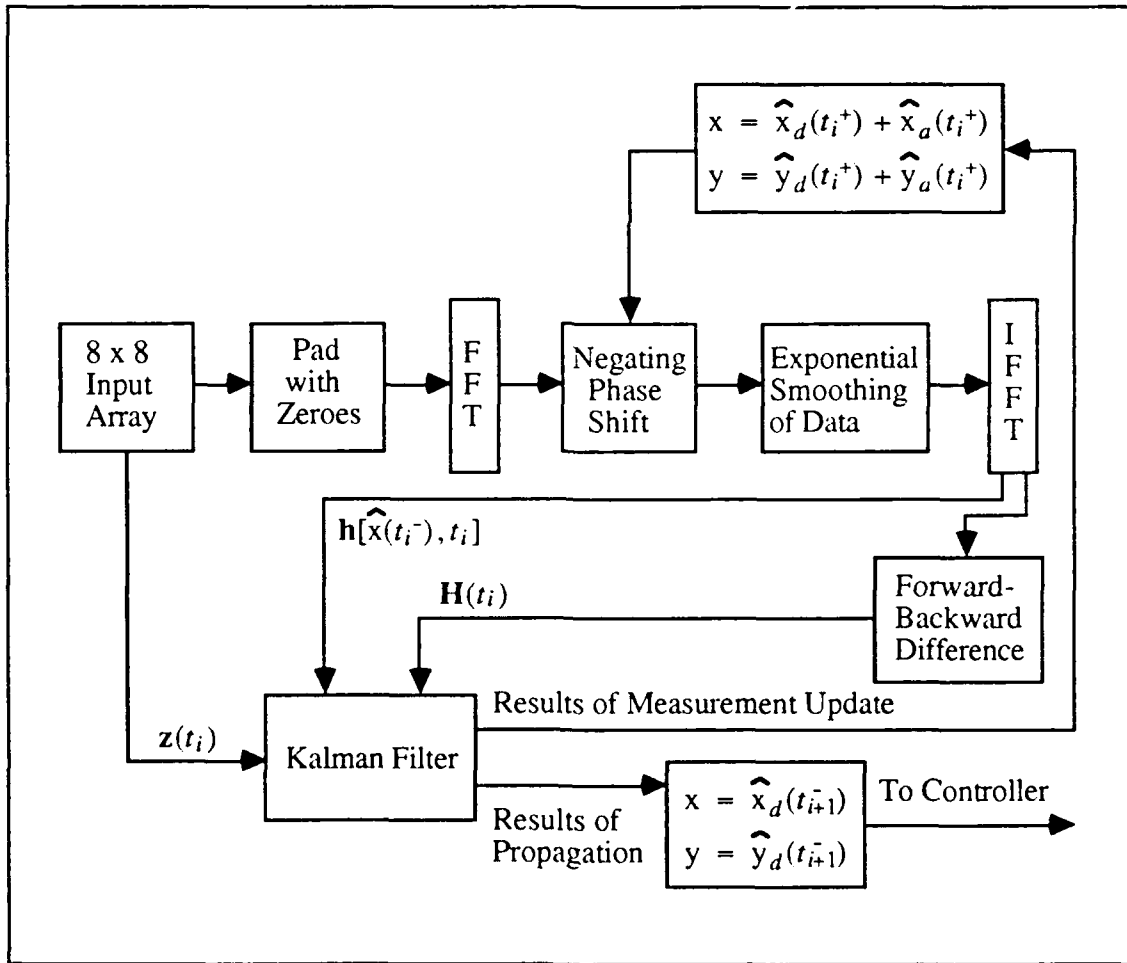


Figure 1.3. Data Processing Scheme using FFT and IFFT [28]

included the use of the Fast Fourier Transform (FFT) and the Inverse Fast Fourier Transform (IFFT). The plan included two data paths for processing the intensity measurements  $z(t_i)$ . On the first path, the  $8 \times 8$  array of intensity measurements from the FLIR are arranged into a 64-dimensional measurement vector. This measurement vector is applied to the extended Kalman filter (as in prior work). The purpose of the second path is to provide centered target shape functions to be time-averaged with previous centered shape functions in order to generate the estimated target image template ( $\mathbf{h}$  in Figure 1.3) and partial derivatives of it with respect to the states ( $\mathbf{H}$  in Figure 1.3). This requires the use of the shifting theorem of Fourier transforms. The shift theorem states that a translation of an image in the spatial domain results in a linear phase shift in the spatial frequency domain. To negate the translational effects in the spatial domain, the Fourier transform of the translated image is multiplied by the complex conjugate of the desired linear phase shift [28]. In essence, the translation of an intensity pattern in the spatial domain can be negated by multiplying its Fourier transform by the complex conjugate of the resulting linear phase shift [28]. The extended Kalman filter model, in path one, which was developed by Mercier [21] was used to provide the optimal estimate of the linear translation. The filter state estimates are used to develop the complex conjugate of the linear phase shift and provide the centered measurement functions. Before the IFFT is taken, the resulting centered pattern is exponentially smoothed to yield an approximation to averaging the result with previously centered frames of data, to minimize the effect of measurement noise. The result is a centered pattern with noise effects substantially reduced. Following the application of the IFFT, the spatial derivative is used to determine the linearized function of intensity measurements ( $\mathbf{H}$  of Figure 1.3) and the nonlinear function of intensity measurements ( $\mathbf{h}$  of Figure 1.3). These are both used by the Kalman filter in processing the next sampled measurement [28]. The results of this data processing scheme were inconclusive due to filter divergence problems. Despite the problems encountered with the filter, the concept was considered to have filter performance potential.

Rogers [27] continued the work of developing a Kalman filter tracker which could handle multiple-hot-spot targets with no *a priori* information as to the size, shape, intensity, or location of the target. However, he continued the application to benign target motion, as Singletery [28] had done before, in order to concentrate on the feasibility of adaptively identifying the target shape. Using digital signal processing on the FLIR data (as described above) to identify the target shape, the filter uses the information to estimate target offset from the center of the FOV, which in turn drives a controller to center the image in the FLIR plane. Algorithm improvements included replacing the Forward-backward difference block of Figure 1.3 with a partial differentiation operation accomplished as a simple multiplication before the IFFT block.

Rogers [27] also considered an alternative design that used the target image  $h$  (as generated in Figure 1.3) as a template for an enhanced correlator, as shown in Figure 1.4. The position offsets produced as outputs from the correlator were then used as "pseudo-measurement" inputs to a linear Kalman filter. Its performance was compared to the results of earlier extended Kalman filters that used the raw FLIR data as measurements [6]. The improved correlation algorithm of Figure 1.4 compares the FLIR image to an estimated template instead of the previous image, as is done in the standard correlator. This tracking concept is thus a hybrid of correlation tracking and Kalman filtering [27]. Although the extended Kalman filter performed well without *a priori* knowledge of the shape and location of the intensity centroid, the improved correlator used with the linear Kalman filter outperformed the extended Kalman filter while providing reduced computational loading.

Millner [22] and Kozemchak [9] tested an extended Kalman filter and the linear Kalman filter/enhanced correlation algorithm against close range, highly maneuverable targets. The linear four-state filter used in the previous research was replaced by an eight-state filter consisting of position, velocity, acceleration, and atmospheric jitter states in the two coordinates of the FLIR plane (azimuth and elevation). Two target dynamics models

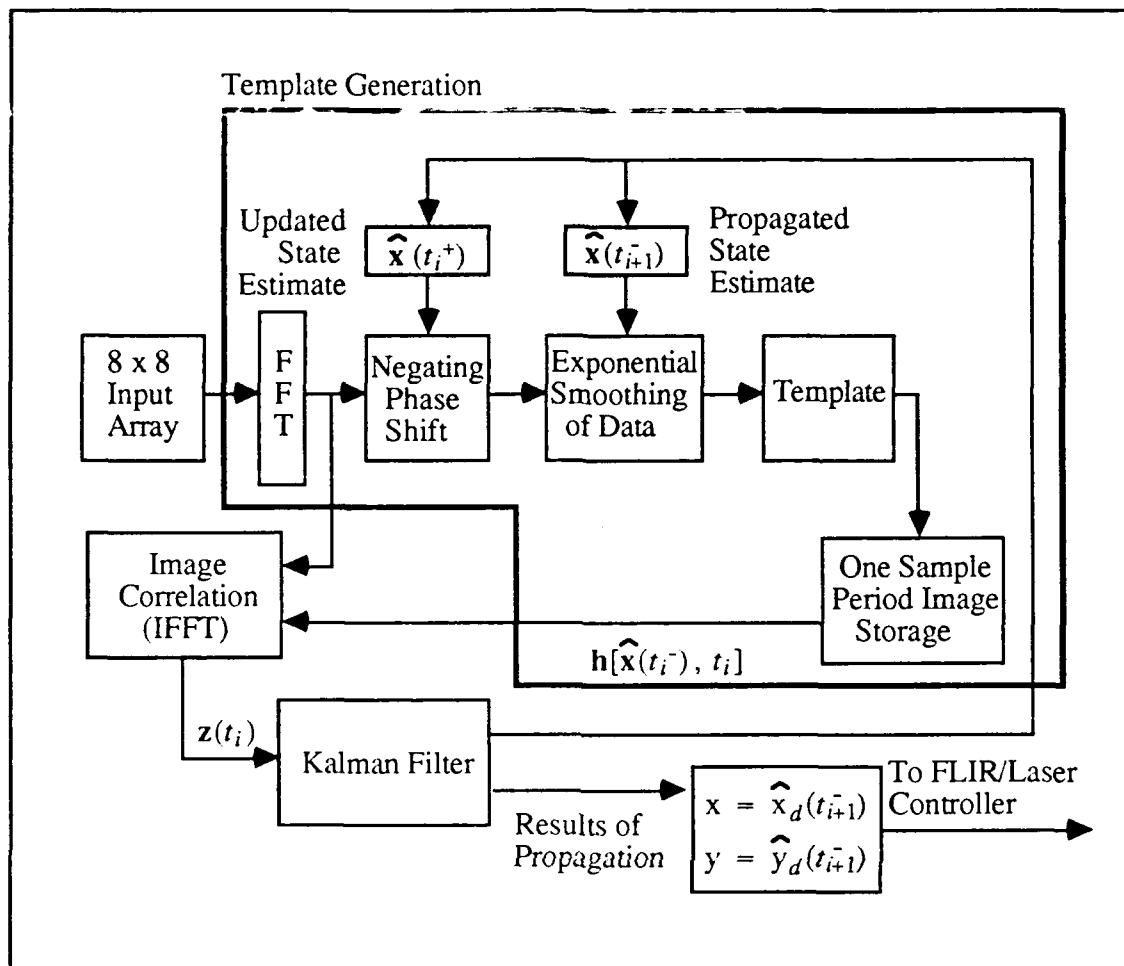


Figure 1.4. Linear Kalman Filter/Enhanced Correlator Algorithm [27]

were also developed. The target was first modeled as a first-order Gauss-Markov acceleration process, and secondly with a constant turn-rate model. Both filters performed well without *a priori* knowledge of the target size, shape, and location using the FFT data processing method for identifying the target shape function [27, 28]. However, at maneuvers approaching 5-g's, the filter performance degraded considerably. It was noted that the tracking was substantially better when the Kalman filter dynamics model closely matched the target trajectory.

The Bayesian MMAF technique [4] was reinvestigated by Suizu [29] based on the recommendations of the previous work. The MMAF (Figure 1.2) consisted of a Kalman

filter which was tuned for benign target maneuvers and obtained sampled measurement information from an 8 x 8 pixel FOV in the FLIR plane. A second filter was tuned for dynamic maneuvers and obtained sampled measurement information from a 24 x 24 pixel FOV in the FLIR plane. The technique allowed the MMAF to maintain track on benign target trajectories and highly maneuvering trajectories up to 20-g's at a distance of 20 kilometers. The MMAF was configured for both the linear Kalman filter/enhanced correlation algorithm [27] and the extended Kalman filter. The results of the MMAF tracking for both filters was very good. The state rms tracking error was on the order of 0.2 to 0.4 pixels (one pixel being equivalent to 20  $\mu$ rad on a side).

The potential of the MMAF technique with the FFT processing method was continued by Loving [11]. A third filter was added to the bank of filters which was tuned for intermediate target maneuvers and obtained sampled measurement information from the 8 x 8 FOV in the FLIR plane. This MMAF showed significant performance over all the previous filters. Additionally, a Maximum A Posteriori (MAP) algorithm was developed and compared with the Bayesian MMAF. The MAP algorithm differs from the Bayesian MMAF in that the MAP algorithm uses the residuals of the separate filters to select the one filter with the highest probabilistic validity, while the MMAF uses a probability-weighted average of all the filters in the bank. The MMAF and the MAP techniques produced similar results and delivered performance that surpassed previous filters.

Netzer [24] expanded the study of the MMAF algorithm. He investigated a steady-state bias error that resulted when tracking a target exhibiting a high-g constant turn-rate maneuver. A major cause of this bias is the MMAF mistuning the  $x$ -direction (azimuth) while maintaining lock on the highly dynamic  $y$ -direction (elevation) transient. This motivates the concept of individual  $x$ - and  $y$ -channel filters in the MMAF, which would allow adaptive filtering for the  $x$ - and  $y$ -channels independently [24]. The size of the FOV was also investigated. When a target came to within five kilometers of the FLIR platform,



the 8 x 8 FOV was saturated with the intensity centroid image, resulting in a loss of track. This analysis motivates a changing FOV to maintain lock for targets and also warrants the possibility of adding another Kalman filter which is tuned for extremely harsh maneuvers at close ranges. A study of the aspect ratio (AR) associated with target's intensity centroid was also accomplished to identify filter tracking characteristics for various target image functions [24]. This study used "greyscale plots" of the kind shown in Figure 1.5 to support the analysis. A greyscale plot is a pictorial display of an image in which shading of the image is used to indicate similar parameters. In this case, the plot indicates regions of varying levels of the intensity of the target image in a 24 x 24 pixel FOV. Four different AR of 0.2, 0.5, 5, and 10 were compared to the nominal AR of 1. The results showed that tracking was slightly impaired for images with AR as high as 5. The reduced performance

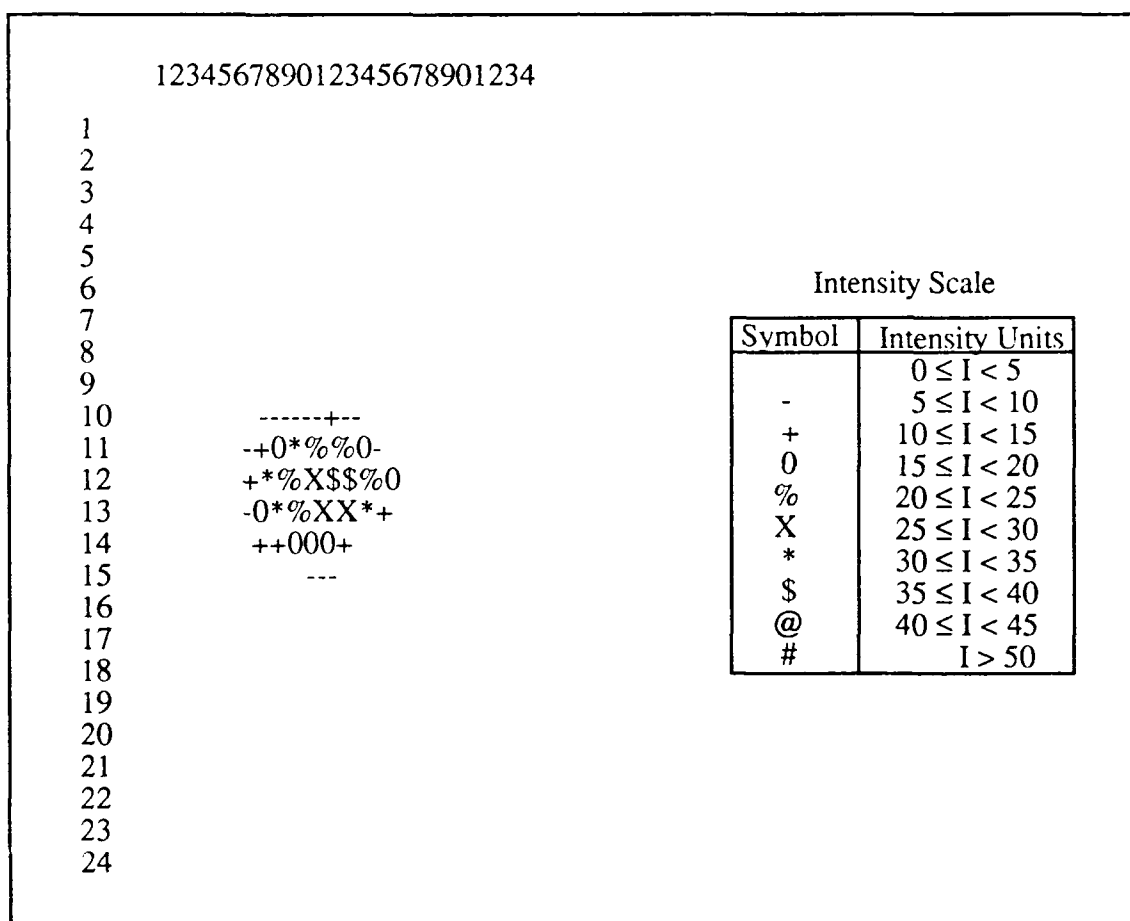


Figure 1.5. Greyscale Target Image [24]

is primarily along the semi-major axis of an elliptically modeled intensity centroid. Additionally a target-decoy experiment was conducted in which a high intensity decoy was also located in the FOV with the target. Since the decoy was modeled with different dynamics not given to the filter, it was hoped that the filter would reject the decoy. This was not the case; the filter locked onto the hotter decoy image. This indicates that the inability of the current filter algorithm to reject this type of bright hotspot requires isolating the target image in a small FOV or some other concept to ensure tracking of the desired target.

The previous research efforts [11, 24, 29] used Gauss-Markov acceleration models in the development of the MMAF. Tobin [30] implemented the CTR dynamics model in another MMAF. His results showed that the Gauss-Markov MMAF exhibited smaller bias errors while the CTR MMAF gave smaller steady state standard deviation errors; both filters had comparable rms errors. Motivated by earlier research [24], he also developed an 8 x 24 pixel FOV for both the  $x$ - and  $y$ -directions of the FLIR image plane. The results showed that the filter maintained lock on a target during a highly dynamic maneuver in the  $y$ -direction while maintaining substantially better steady state bias performance in the benign  $x$ -direction.

Leeney [10] expanded the previously used Gauss-Markov truth model by incorporating bending and vibrational states. The elemental filters in the MMAF were not modeled with this information through explicit state variables, but performed well up to a 10-g maneuver. A performance investigation was also conducted as to the effects of increasing the measurement update rate from the previously used 30 Hz to 50 Hz. The sampling rate of 50 Hz showed a minor performance improvement, but also increased the computational loading because of the higher rate. A preliminary study was also done on replacing the 8 x 24 pixel FOV in the  $x$ - and  $y$ -directions [30] on the FLIR plane with a single 8 x 24 pixel FOV, which is also known as the rotating rectangular field-of-view

(RRFOV). The idea was to align the long side of the rectangular FOV with the semi-major axis of the intensity centroid by aligning it with an estimate of the acceleration vector. (Actually, the higher precision velocity estimate was used instead of the noisier acceleration estimate, and it was assumed that the acceleration direction would be essentially orthogonal to the velocity vector direction.) Additionally, the five elemental Kalman filters in the MMAF bank would be reduced to four by using this FOV rotation scheme. The results were not conclusive, but the insight provided motivation to continue the study.

The RRFOV research was continued by Norton [25]. He discovered that the appropriate choice of the filter dynamics driving noise  $\mathbf{Q}$  dictated the filter's response to a high-g jinking maneuver, and that the size of the FOV could be reduced to an 8 x 8 pixel rotating FOV, which is also known as the rotating square field of view (RSFOV). His investigation showed that a non-rotating square FOV could provide good performance, but that the dynamics noise strength  $\mathbf{Q}$  matrix value must be large in the direction of the acceleration vector. A mathematical matrix transformation was developed which rotated the  $\mathbf{Q}$  matrix to keep the larger values aligned with the acceleration vector. A study of both the rotating FOV and rotating the  $\mathbf{Q}$  matrix provided advantages and disadvantages for each method. Both methods are affected by the tuning parameters used to represent the rms level of acceleration of the target, which also contributes to error biases. The rotating FOV improves the  $x$ -direction (azimuth) estimation for dominant  $y$ -direction (elevation) dynamics from previous MMAF algorithms, but does not improve  $y$ -direction estimation for dominant  $y$ -direction dynamics. Rotating the  $\mathbf{Q}$  matrix adaptively improves estimation of both  $x$ - and  $y$ -directions and improves the jink maneuver error transients, but is dependent on the orthogonality of the velocity and acceleration vectors and proper initial tuning parameters. The conclusion was that both methods employed together provide the ability to adjust filter characteristics to differentiate between harsh and benign dynamics in any orientation of target acceleration (rotating  $\mathbf{Q}$ ) while at the same time maintaining view

resolution in the directions of both benign and harsh dynamics (rotating FOV). Therefore, the combination allows for tracking highly maneuvering targets without sacrificing the resolution provided by the smaller RSFOV [25].

The research up to this point was primarily directed towards tracking aircraft and missiles from a ground-based FLIR plane. Rizzo [26] initiated research on a space-based platform which could track targets using the same filtering techniques. Since the linear Kalman filter/enhanced correlator algorithm had proven to be computationally more efficient than the extended Kalman Filter, it was chosen as the system filter. The plume "pogo" (oscillation) phenomenon of a missile in the boost phase of flight was modeled in the truth model and one of two filters used for the analysis. The pogo was modeled as a second order Gauss-Markov process, and applied in the direction of the missile velocity vector. The plan was to go adaptive on the pogo states using the MMAF algorithm, treating the pogo amplitude and oscillation frequency as uncertain parameters. Although the elemental filters were developed, no MMAF performance was accomplished.

Three rotation schemes were also developed and tested. The first scheme, referred to as the rotating field of view (RFOV), involved using the 8 x 8 FOV filter and aligning a single axis of the FLIR plane with the estimated velocity vector of the target; therefore one of the coordinate axes of the FOV would stay aligned with the oscillation of the plume. The second scheme, referred to as the diagonal rotating field of view (DRFOV), used the 8 x 8 FOV with the diagonal aligned with the oscillation of the plume. The motivation behind this scheme is that the 8 x 8 FOV is oriented in such a fashion will be able to "see" more of the target's intensity image, thus enabling the sensor to obtain more measurement information [26]. The third tracking scheme was the RRFOV developed from previous research [10, 30]. The RFOV, DRFOV, and the RRFOV algorithms [24] were tested along with the non-rotating field-of-view (NRFOV) filter. The NRFOV is the standard tracker used in previous studies [10, 24, 30]. The DRFOV scheme was shown to be

superior to the other three tested for providing enhanced tracking of a missile hardbody whose plume is undergoing a pogo phenomenon.

The eight-state filter (without pogo states) and the ten-state filter (with pogo states) surfaced a problem that may have gone unnoticed in previous work. Following tuning of the filters with the twelve-state truth model, it was discovered that the eight-state filter outperformed the ten-state filter. An investigation into the cause of the irregularity revealed that there was a serious observability problem in the ten-state filter, as well as a slight problem with the observability in the eight-state filter. The affected states were velocity and acceleration. A recommendation was made to remove the acceleration states in the ten-state filter, and to model the velocity states in this new eight-state filter as a first-order Gauss-Markov processes.

Eden [2] resumed the research of the space-based FLIR platform. The scope of the tracking problem was expanded by requiring the filter to track the hardbody of the missile rather than the intensity centroid of the FLIR. Since the FLIR could not supply the needed information about the hardbody relative to the image center of intensity to the Kalman filter, another measurement source was developed. Under the advisement of the AFWL, the new measurement source was identified as a low-energy laser. The laser provides actively acquired measurement data while the FLIR obtains its measurement information passively. The scheme called for a six-state Kalman filter (consisting of two position states, two velocity states, and two atmospheric jitter states) to provide a velocity vector estimate for the target. The low-energy laser is then scanned along this vector from the image center of intensity to intercept the hardbody. The hardbody was modeled as a rectangle with binary reflectivity. When the low-energy laser illuminates the hardbody, the reflection is received by a low-energy laser sensor on the platform. This information is provided to a single-state Kalman filter which estimates the distance between the center of mass and the center of intensity along the velocity vector direction. For this thesis, the laser beam width

at the target was modeled as 2.75 meters. The center-of-mass was defined as the midpoint of the scan across the hardbody if the centerline of the laser beam crossed the aft end of the missile and the top (nose) of the hardbody, or if the laser beam crossed the aft end and one of the sides of the hardbody. Another estimation of the center-of-mass was found as the center of the area of overlap between the hardbody and the laser beam if the laser beam centerline did not cross the hardbody. This case was found to occur along the aft corners of the hardbody when the laser did not completely cross the hardbody. The results of the laser scan showed that the interception of the laser with the hardbody occurred only 10-20% of the time. This low ratio of hitting the target was attributed to the six-state filter being tuned for estimating only the intensity centroid location on the FLIR plane and not for precise velocity estimation. Since the velocity vector must be accurately estimated for active illumination of the target to be a viable concept, it was recommended that the filter also be tuned for accurate velocity estimates.

### *1.3 Thesis Objectives*

This thesis follows the research of the previous thesis [2] with the support of all the work already accomplished by the AFIT students. The objectives of this thesis support the continued development of Kalman filter models and simulations which test the filter for tracking long-range targets. The two primary goals of this thesis, as described in the following paragraphs, are to design a new filter which determines the location of the target hardbody using the FLIR and low-energy laser measurement data, and to develop a three-dimensional reflective target in the FLIR plane. Secondary objectives include: the development of a laser sweeping technique to ensure a maximum number of reflectivity measurements from the low-energy laser; developing additional target trajectories which will test the three-dimensional reflectivity model at different orientations in the FLIR FOV; an investigation into using Doppler shift information to determine the hardbody location relative to the center of intensity; and improving the atmospheric model to account for

ionospheric and tropospheric distortions. A flow chart of the objectives for this thesis is shown in Figure 1.6.

As previously stated, this thesis emphasizes the development of a computer-simulated three-dimensional target onto the two-dimensional FLIR plane. Prior research [2] used a simulated two-dimensional missile model in the form of a rectangle in which the reflectivity was "on" or "off" (i.e., the reflectivity did not vary over the surface). This model is enhanced to account for the varying reflective surfaces of the target vehicle when a low energy laser is scanned along the hardbody. Before this is accomplished, the tracking

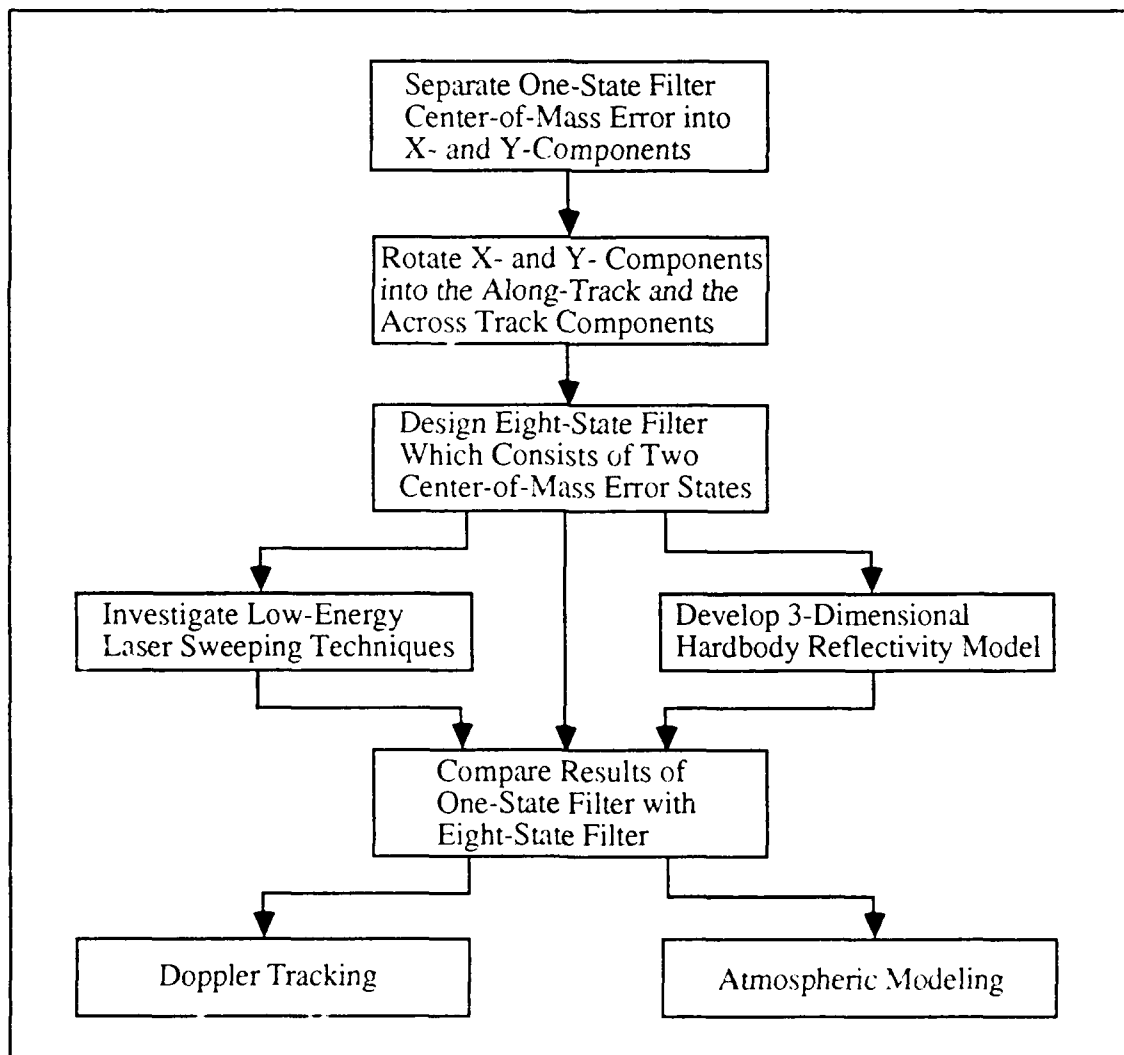


Figure 1.6. Thesis Objectives Flow Chart

error represented in the previous research [2] by a straight line between the estimated target center of mass and the true center of mass is separated into two components. This data is analyzed to determine in which direction (using azimuth and elevation or along-track and across-track as reference coordinate directions) the greatest error in the estimate exists. This information is used to design a new eight-state Kalman filter consisting of two position states, two velocity states, two atmospheric jitter states, and two tracking error states which depict the distances between the target center-of-mass and its image center of intensity. The new filter is measured against a previously developed truth model (composed of two target position states, six atmospheric jitter states, four vibration states, and two pogo states). In parallel with testing the new filter, a number of techniques are investigated to determine the best method of scanning the low-energy laser in order to locate the hardbody in the shortest amount of time. The single target trajectory used to test an earlier system [2] and two other trajectories are developed to take advantage of the new insights that the new target reflectivity model may provide. Another research area includes an investigation into using Doppler information to determine the measurement of the hardbody vs. center of intensity. Additionally, the atmospheric modeling is enhanced.

*1.3.1 Separation of Error Statistics on the FLIR Plane.* The determination of the location of the hardbody in the shortest amount of time is critical to the operation of SDI. From the FLIR data alone, there is no information on the location of the missile hardbody center of mass, but only the center of intensity of the infrared image of the hardbody/plume combination. An algorithm was added to the tracking system that would accept processed information about the offset of the missile hardbody center of mass from the apparent intensity centroid on the FLIR [2]. The sweeping of a low-energy laser up and down the estimated velocity vector from the estimated intensity centroid in the FLIR image plane was previously simulated [2] to determine the location of the vehicle. Then a midpoint line between the two points where the sweepline intersected the hardbody/background bound-



ary was calculated as an indication of the location of the hardbody center of mass. The error between this estimate of the simulated target's center of mass and its true center of mass was left as the straight-line-difference between the two points, and statistics were gathered [2] on the magnitude of this line. This gives no insight into the weighting of the error on the two-dimensional FLIR plane. The errors of the estimate and the true location of the simulated missile need to be separated to gain this additional information on Eden's model. Therefore, the scalar distance between the actual (simulated) missile center of mass and the estimated center of mass is separated into the two error components on the FLIR plane. These may be obtained in one of two ways: separated either into the  $x$ - and  $y$ - (azimuth and elevation) components, or into the along-track and across-track components. The second method is emphasized since it is thought that it gives better information relative to the principal axes directions of the error phenomenon. It is anticipated that along-track errors are small while across-track errors are large, since the latter is due to estimated velocity vector angular orientation errors (which are fundamentally larger than magnitude errors along the sweep direction) [15]. The information gained from this effort is analyzed and the filter is tuned to obtain the optimum estimates.

*1.3.2 Development of Eight-State Kalman Filter.* The knowledge gained from separating the tracking information of Eden's work is used to develop a new eight-state Kalman filter using Rizzo's [26] suggested four-state target dynamics model (two position states and two velocity states), which was developed by Eden [2], the two atmospheric jitter states from previous research, and two additional states to account for the two error components of the target's displacement of the center-of-mass from the intensity centroid. This filter is tested against Eden's two-Kalman filter design (which consists of the six-state filter and an additional one-state filter to estimate the distance from the center of intensity to the center-of-mass along the estimated velocity vector direction). When the eight-state filter design is accomplished, tuned, and tested with the previously developed twelve-state truth

model, the filter will be applied to a three-dimensional reflectivity target developed as a part of this research.

*1.3.3 Missile Reflectivity Model.* This research objective is one of the primary objectives of this thesis. It involves the development of a computer simulated three-dimensional missile model transformed onto the two-dimensional FLIR plane. This model is an enhancement of Eden's two-dimensional rectangle simulation on the FLIR plane. His model consisted of a binary-valued reflectivity function ("on" or "off"). The enhanced model may include a conical forward section (nose cone) and will account for the varying reflective surfaces of a missile by rounding the reflectivity function. With this model in simulation, the simulated low-energy laser will provide more representative measurement information to the Kalman filter since the varying reflectivity of the target will be modeled into the laser return sensor developed by Eden. The modeling approach may follow that used by Rizzo [26] to model the plume at high altitudes. The method to model the plume involved using a Gaussian intensity distribution from which a second Gaussian distribution, offset from the first, was subtracted. Under this method, half of a Gaussian density function would be used to model the reflectivity function of the forward end (nose) of the missile and a second half-density function would simulate the aft end of the missile. A straight line made between the two density functions completes the along-track shape. A Gaussian intensity distribution would model the across-track (rounded) surface of the missile. Another method considered involves enhancing the existing rectangular model [2] with discrete reflectivity line-segments along the longitudinal axis of the missile. Numerical weighting of the discrete line-segments would simulate the reflectivity of the surface when the low-energy laser strikes the surface. The chosen reflectivity model will provide additional information as the low-energy laser scans the vehicle. The calculated distance between the rise and fall-off of the low-energy laser return will provide information as to which part of the vehicle was swept by the laser with respect to the

dimensions of the model. This information will be used to obtain a better estimate of a probable location of the center of mass than the simple midpoint computation now incorporated.

*1.3.4 Laser Sweeping Technique Investigation.* When the FLIR information has been processed by the Kalman filter and the filter has determined the best estimate of the location of the center of intensity, the next step is to scan the low-energy laser to illuminate the vehicle and obtain further information for the filter to estimate the target's center of mass. However, since the estimate of the filter is based on noisy data, it is not highly probable that a fine-beam laser scan to this estimated point would consistently intercept the hardbody. A sweeping technique is needed to ensure illumination of the hardbody in the shortest time. The method may be a fixed procedure or it may be variable based on other information. Radar acquisition techniques such as cross-scanning or spiraling outward from an arbitrary "best guess" location of the target have been used to achieve lock-on. The best approach for the low-energy laser scan appears to be either a wide-beam straight-line sweep or a dithering sweep (which is similar to the cross-scanning technique). Additional information gained from the initial interception of the hardbody (as stated in Section 1.3.1) will be used to determine subsequent sweeping to determine the location of the center of mass. (Once the center of mass is realized, other parts of the vehicle may be easily identified from this reference point.)

*1.3.5 Filter Performance Evaluation.* With the enhanced model and the eight-state filter fully developed, an investigation into the new filter's performance will be further evaluated with the truth model (composed of two target position states: actually the result of accurate three-dimensional trajectory simulation and projection into the FLIR image plane; six atmospheric jitter states; four vibration states; and two pogo states). The initial testing (described in Section 1.3.2) will be done with the vibration and pogo states turned off (i.e., the dynamics driving noise set to zero). The two-state pogo model developed by Rizzo [26]

and the four-state vibration model developed by Leeney [10] will be turned on separately and together in the truth model. The filter's ability to determine the hardbody center of mass from an oscillating intensity centroid and with vibration inputs will be investigated. Some tuning of the filter may be required to be able to estimate the hardbody precisely enough in the face of the plume "pogo" phenomenon and the vibration effects.

*1.3.6 Trajectory Analysis.* The new target reflectivity model allows an opportunity to examine other trajectories. Eden's work considered a single trajectory which was perpendicular to the low-energy laser. This trajectory will also be used in this research to test the Kalman filter, the new reflectivity model, and the scanning techniques. The enhanced model of the missile and the modeled pogo effect with the different trajectories will provide a realistic simulation which will give insight into Kalman filter performance.

*1.3.7 Doppler Shift Analysis.* This area of study involves determining a measurement of the hardbody vs. the center of intensity using Doppler shift information. The missile provides a different Doppler return from that of the background as it moves along its trajectory, so Doppler information could be used to discern the hardbody from the background. The filter-estimated location of the intensity centroid and its velocity vector will be used in the same way as the low-energy laser scan concept. In the computer simulation, a Doppler scan is simulated in the same manner as a low-energy laser scan, through perhaps to different precision (i.e., measurement noise variance) of indicating the line of demarcation between the hardbody and the background.

*1.3.8 Improved Atmospheric Modeling.* Atmospheric modeling has been incorporated into the previous software to account for jitter affects. However, since the direction of the research direction has transitioned from aircraft to space-based systems, the atmospheric model must be enhanced. This objective is very important to the long term study. These atmospheric disturbances are especially important with the introduction of

active target illumination using the low-energy laser. The laser signal will be greatly attenuated and twice refracted before the information is received by the laser sensor. The information given to the Kalman filter will be distorted from the true information. This will require that atmospheric modeling in the filter compensate for the data and still arrive at the same estimate of the target center of mass location as if there were no atmosphere to affect the signal. There have been many attempts to model the constantly shifting atmosphere. The atmospheric properties considered as essential to the definition of the atmospheric particle interactions are the total density including fluctuations and cross-correlations, temperature, molecular, and atomic composition, electron density, ion composition, and solar flux. These properties are modeled in the 1959 ARDC Model [23]. When a new atmospheric model is developed for the truth model, the filter will be tested to determine how well it estimates the location of the hardbody in this refined tracking environment.

#### *1.4 Thesis Overview*

This chapter described the AFIT-developed tracking system consisting of a Kalman filter, a FLIR sensor, and a low-energy laser (with sensor). The background surrounding the development of this tracking system was provided, and included a review of the previous AFIT research accomplished over the past twelve years. Chapter II gives a mathematical summary of the linear Kalman filter and extended Kalman filter algorithms. Chapter III defines the simulation space used to provide orientations of the FLIR image plane and the target model in the computer program. The truth model dynamics and measurement models, which represent the real world environment in the simulation, are developed in Chapter IV. The dynamics and measurement models of the three Kalman filters used in this research are described in Chapter V. Chapter VI provides filter performance analyses and discusses other investigations conducted in this research. Chapter VII presents the final conclusions regarding this research and makes recommendations for further study.

## II. Kalman Filter Theory

### 2.1 Introduction

A Kalman filter is an optimal estimator that provides estimates of variables of interest (known as states) for a particular system. The filter estimates a state in terms of its conditional mean and covariance. The mean and covariance describe the conditional Gaussian distribution or density function for the states, conditioned on knowledge of the measurements received. The *a priori* statistics of the mean and covariance provided to the filter before the first measurement is received are defined respectively by:

$$\hat{\mathbf{x}}_o = E \{ \mathbf{x}(t_o) \} \quad (2-1)$$

$$\mathbf{P}_o = E \left\{ [\mathbf{x}(t_o) - \hat{\mathbf{x}}_o][\mathbf{x}(t_o) - \hat{\mathbf{x}}_o]^T \right\} \quad (2-2)$$

where the  $(\hat{\quad})$  notation indicates an estimated value, and  $E\{ \quad \}$  is the ensemble average of the possible outcomes.

For the application of tracking a target, the variable of interest is the position of the target. With its internal dynamics model of the target, the Kalman filter is able to predict the future position of the target. At a prescribed sample rate, the filter is updated with measurements provided by physical sensors. The filter propagates the state "conditioned" on this measurement time history  $\mathbf{Z}(t_i)$  given by:

$$\mathbf{Z}(t_i) = \begin{bmatrix} \mathbf{z}(t_1) \\ \vdots \\ \mathbf{z}(t_i) \end{bmatrix} \quad (2-3)$$

where  $\mathbf{z}(t_j)$  is the measurement data available at sample time  $(t_j)$ .

Then the conditional mean and covariance of the state variables are given respectively by:

$$\hat{\mathbf{x}}(t_i^+) = E \{ \mathbf{x}(t_i) | \mathbf{Z}(t_i) \} \quad (2-4)$$

$$\mathbf{P}(t_i^+) = E \left\{ [\mathbf{x}(t_i) - \hat{\mathbf{x}}(t_i^+)] [\mathbf{x}(t_i) - \hat{\mathbf{x}}(t_i^+)]^T | \mathbf{Z}(t_i) \right\} \quad (2-5)$$

The following sections provide a summary of the mathematical background for the linear Kalman filter and the extended Kalman filter. A complete development is available in references [12, 13].

## 2.2 Linear Kalman Filter

To implement the Kalman filter algorithm, a model of the system dynamics and discrete-time measurements must be available. A system may be modeled by a continuous linear system with sampled data linear measurements. The general continuous system model is of the form:

$$\dot{\mathbf{x}}(t) = \mathbf{F}(t)\mathbf{x}(t) + \mathbf{B}(t)\mathbf{u}(t) + \mathbf{G}(t)\mathbf{w}(t) \quad (2-6)$$

where

- $\mathbf{F}(t)$  = homogeneous state dynamics matrix
- $\mathbf{x}(t)$  = vector of states of interest
- $\mathbf{B}(t)$  = control input matrix
- $\mathbf{u}(t)$  = deterministic control input vector
- $\mathbf{G}(t)$  = driving noise input matrix
- $\mathbf{w}(t)$  = driving noise vector

and the mean and strength,  $\mathbf{Q}(t)$ , of the white Gaussian noise is given by:

$$E \{ \mathbf{w}(t) \} = \mathbf{0} \quad (2-7)$$

$$E \{ \mathbf{w}(t) \mathbf{w}^T(t + \tau) \} = \mathbf{Q}(t) \delta(\tau) \quad (2-8)$$

The equivalent discrete-time system model of Equation (2-6) is required to implement the algorithm on a digital computer. For a time-invariant system, the general form of the discrete-time state space form (denoted by the  $d$  subscript) of the linear Kalman filter is given by [12]:

$$\mathbf{x}(t_{i+1}) = \Phi(t_{i+1}, t_i) \mathbf{x}(t_i) + \mathbf{B}_d(t_i) \mathbf{u}(t_i) + \mathbf{G}_d(t_i) \mathbf{w}_d(t_i) \quad (2-9)$$

where

$\Phi(t_{i+1}, t_i)$  = the system state transition matrix defined as an n-by-n matrix that satisfies the differential equation and initial condition given by:

$$\frac{d[\Phi(t, t_0)]}{dt} = \mathbf{F}(t) \Phi(t, t_0) \quad (2-10)$$

$$\Phi(t_0, t_0) = \mathbf{I} \quad (2-11)$$

$\mathbf{x}(t_i)$  = discrete-time vector of states of interest  
 $\mathbf{B}_d(t_i)$  = discrete-time control input matrix  
 $\mathbf{u}(t_i)$  = discrete-time deterministic control input vector  
 $\mathbf{G}_d(t_i)$  = discrete-time driving noise input matrix  
 $\mathbf{w}_d(t_i)$  = discrete-time, independent, white Gaussian noise process  
with mean and covariance statistics defined by:

$$E \{ \mathbf{w}_d(t_i) \} = \mathbf{0} \quad (2-12)$$

$$E \{ \mathbf{w}_d(t_i) \mathbf{w}_d^T(t_j) \} = \begin{cases} \mathbf{Q}_d(t_i) & t_i = t_j \\ \mathbf{0} & t_i \neq t_j \end{cases} \quad (2-13)$$



where

$$\mathbf{Q}_d(t_i) = \int_{t_i}^{t_{i+1}} \Phi(t_{i+1}-\tau) \mathbf{G}(\tau) \mathbf{Q}(\tau) \mathbf{G}^T(\tau) \Phi^T(t_{i+1}-\tau) d\tau \quad (2-14)$$

The Kalman filter is given measurement information at a prescribed rate to improve its estimate of a desired state. The discrete measurement model is defined as follows:

$$\mathbf{z}(t_i) = \mathbf{H}(t_i)\mathbf{x}(t_i) + \mathbf{v}(t_i) \quad (2-15)$$

where

- $\mathbf{z}(t_i)$  = m-dimensional measurement vector
- $\mathbf{H}(t_i)$  = state observation matrix
- $\mathbf{x}(t_i)$  = vector of states of interest
- $\mathbf{v}(t_i)$  = white Gaussian measurement noise

The white Gaussian measurement noise  $\mathbf{v}$  is independent of both  $\mathbf{x}$  and  $\mathbf{w}$  for all time and has a mean and covariance,  $\mathbf{R}$ , given by:

$$E \{ \mathbf{v}(t_i) \} = \mathbf{0} \quad (2-16)$$

$$E \{ \mathbf{v}(t_i) \mathbf{v}^T(t_j) \} = \begin{cases} \mathbf{R} & t_i = t_j \\ \mathbf{0} & t_i \neq t_j \end{cases} \quad (2-17)$$

The state conditional mean and covariance estimates are propagated from time  $t_i^+$ , just after measurement incorporation at time  $t_i$ , to the next sample time just before measurement incorporation  $t_{i+1}^-$ , by numerical integration of the following propagation equations:

$$\dot{\hat{\mathbf{x}}}(t/t_i) = \mathbf{F}(t)\hat{\mathbf{x}}(t/t_i) \quad (2-18)$$

$$\dot{\mathbf{P}}(t/t_i) = \mathbf{F}(t)\mathbf{P}(t/t_i) + \mathbf{P}(t/t_i)\mathbf{F}^T(t) + \mathbf{G}(t)\mathbf{Q}(t)\mathbf{G}^T(t) \quad (2-19)$$

where the initial conditions are:

$$\hat{\mathbf{x}}(t_0) = \hat{\mathbf{x}}_0 \quad (2-20)$$

$$\mathbf{P}(t_0) = \mathbf{P}_0 \quad (2-21)$$

When a measurement becomes available,  $\hat{\mathbf{x}}$  and  $\mathbf{P}$  are updated using the following update equations:

$$\mathbf{K}(t_i) = \mathbf{P}(t_i^-) \mathbf{H}^T(t_i) [\mathbf{H}(t_i) \mathbf{P}(t_i^-) \mathbf{H}^T(t_i) + \mathbf{R}(t_i)]^{-1} \quad (2-22)$$

$$\hat{\mathbf{x}}(t_i^+) = \hat{\mathbf{x}}(t_i^-) + \mathbf{K}(t_i) [z(t_i^-) - \mathbf{H}(t_i) \hat{\mathbf{x}}(t_i^-)] \quad (2-23)$$

$$\mathbf{P}(t_i^+) = \mathbf{P}(t_i^-) - \mathbf{K}(t_i) \mathbf{H}(t_i) \mathbf{P}(t_i^-) \quad (2-24)$$

where  $\mathbf{K}$  is the time varying Kalman filter gain which continually changes due to the relative weighting of the covariances of the state estimates and the measurement uncertainties.

### 2.3 Extended Kalman Filter

An extended Kalman filter is used to estimate the states of a nonlinear stochastic system in cases where the system model and/or measurements of interest are not linear. Since it is desired to use a first-order filter, the nonlinear dynamics and measurement equations are linearized by performing a Taylor series expansion about the most recent value of the state estimate [12]. The series is then truncated after the first order terms which results in the linearized set of equations. Since the extended Kalman filter is a first order approximation of the solution, it does not produce an optimal estimate as does the linear Kalman filter for the linear class of problems.

A nonlinear system is described by the following stochastic differential equation:

$$\dot{\mathbf{x}}(t) = \mathbf{f}[\mathbf{x}(t), \mathbf{u}(t), t] + \mathbf{G}(t)\mathbf{w}(t) \quad (2-25)$$

where now the state dynamics vector,  $\mathbf{f}$ , is a nonlinear function of the state values  $\mathbf{x}(t)$ , system inputs  $\mathbf{u}(t)$ , and time  $t$ . The statistics of the white Gaussian noise are given by Equations (2-7) and (2-8).

The sampled-data measurements may also be a nonlinear function of the states and of time. The discrete measurement equation takes on the form:

$$\mathbf{z}(t_i) = \mathbf{h}[\mathbf{x}(t_i), t_i] + \mathbf{v}(t_i) \quad (2-26)$$

where  $\mathbf{h}$  is a nonlinear function of the state  $\mathbf{x}$  at time  $t_i$  and of time  $t_i$  itself. The statistics of  $\mathbf{v}$  at time  $t_i$  are given by Equations (2-16) and (2-17).

Given a nonlinear model, the method used to obtain a linear approximation is based on perturbation techniques. Assume a nominal solution,  $\mathbf{x}_n(\cdot)$ , with an initial condition  $\mathbf{x}_n(t_0) = \mathbf{x}_{n0}$ , is generated which satisfies the deterministic differential equation given by:

$$\dot{\mathbf{x}}_n(t) = \mathbf{f}[\mathbf{x}_n(t), \mathbf{u}(t), t] \quad (2-27)$$

where  $\mathbf{f}$  and  $\mathbf{u}(t)$  are the same as in Equation (2-24) and  $\mathbf{x}_n(t)$  are the nominal points along the nominal state trajectory. Additionally, define nominal measurements as noise-free measurements that would be taken along the nominal trajectory:

$$\mathbf{z}_n(t_i) = \mathbf{h}[\mathbf{x}_n(t_i), t_i] \quad (2-28)$$

where  $\mathbf{x}_n(t_i)$  is the nominal state value at sample time  $t_i$  and  $\mathbf{h}$  is the same as in Equation (2-26).

Now if a perturbation of the state from the assumed nominal trajectory is considered, the result can be found by subtracting Equation (2-27) from Equation (2-25). The stochastic equation then becomes:

$$[\dot{\mathbf{x}}(t) - \dot{\mathbf{x}}_n(t)] = \mathbf{f}[\mathbf{x}(t), \mathbf{u}(t), t] - \mathbf{f}[\mathbf{x}_n(t), \mathbf{u}(t), t] + \mathbf{G}(t)\mathbf{w}(t) \quad (2-29)$$

where the statistics of  $\mathbf{w}(t)$  are given by Equations (2-7) and (2-8). This equation can be expressed in a Taylor series expanded about a nominal solution,  $\mathbf{x}_n(t)$ , assuming that  $\mathbf{u}$  does not assume perturbation values:

$$[\dot{\mathbf{x}}(t) - \dot{\mathbf{x}}_n(t)] = \left. \frac{\partial \mathbf{f}[\mathbf{x}, \mathbf{u}(t), t]}{\partial \mathbf{x}} \right|_{\mathbf{x}=\mathbf{x}_n(t)} [\mathbf{x}(t) - \mathbf{x}_n(t)] + \text{h.o.t.} + \mathbf{G}(t)\mathbf{w}(t) \quad (2-30)$$

A linear approximation of Equation (2-30) is obtained by keeping only the first order term of the expansion:

$$\delta \dot{\mathbf{x}}(t) = \mathbf{F}[t; \mathbf{x}_n(t)] \delta \mathbf{x}(t) + \mathbf{G}(t)\mathbf{w}(t) \quad (2-31)$$

where

$$\mathbf{F}[t; \mathbf{x}_n(t)] \equiv \left. \frac{\partial \mathbf{f}[\mathbf{x}, \mathbf{u}(t), t]}{\partial \mathbf{x}} \right|_{\mathbf{x}=\mathbf{x}_n(t)} \quad (2-32)$$

Equation (2-32) is the first order approximation to the solution and is valid as long as the deviations are small enough for the higher order terms to be negligible. The strength of the white Gaussian noise  $\mathbf{w}(\cdot, \cdot)$  may be increased to account for the effect of the higher order terms which are neglected in the first order approximation.

Similarly, the effects of the state perturbation on the measurement are:

$$\delta \mathbf{z}(t_i) = \mathbf{H}[t_i; \mathbf{x}_n(t_i)] \delta \mathbf{x}(t_i) + \mathbf{v}(t_i) \quad (2-33)$$

where

$$\mathbf{H}[t_i; \mathbf{x}_n(t_i)] \equiv \left. \frac{\partial \mathbf{h}[\mathbf{x}, t_i]}{\partial \mathbf{x}} \right|_{\mathbf{x}=\mathbf{x}_n(t_i)} \quad (2-34)$$

The basic idea of the extended Kalman filter is to relinearize about each estimate  $\hat{\mathbf{x}}(t_i^+)$  once it has been computed [12]. The result is then propagated forward to time  $t_{i+1}$ , and updated if a measurement is available. The system is then relinearized about a new nominal trajectory. The filter accomplishes the propagation by integrating the following equations from  $t_i$  to  $t_{i+1}$ :

$$\dot{\hat{\mathbf{x}}}(t/t_i) = \mathbf{f}[\hat{\mathbf{x}}(t/t_i), \mathbf{u}(t), t] \quad (2-35)$$

$$\dot{\mathbf{P}}(t/t_i) = \mathbf{F}[t; \hat{\mathbf{x}}(t/t_i)]\mathbf{P}(t/t_i) + \mathbf{P}(t/t_i)\mathbf{F}^T[t; \hat{\mathbf{x}}(t/t_i)] + \mathbf{G}(t)\mathbf{Q}(t)\mathbf{G}^T(t) \quad (2-36)$$

where

$$\mathbf{F}[t; \hat{\mathbf{x}}(t/t_i)] \equiv \left. \frac{\partial \mathbf{f}[\mathbf{x}(t), \mathbf{u}(t), t]}{\partial \mathbf{x}} \right|_{\mathbf{x}=\hat{\mathbf{x}}(t/t_i)} \quad (2-37)$$

and the initial conditions are given by the results of the previous measurement update:

$$\hat{\mathbf{x}}(t_i/t_i) = \hat{\mathbf{x}}(t_i^+) \quad (2-38)$$

$$\mathbf{P}(t_i/t_i) = \mathbf{P}(t_i^+) \quad (2-39)$$

The filter update equations incorporate the measurement  $\mathbf{z}(t_i)$  given by:

$$\mathbf{K}(t_i) = \mathbf{P}(t_i^-)\mathbf{H}^T[t_i; \hat{\mathbf{x}}(t_i^-)] \left\{ \mathbf{H}[t_i; \hat{\mathbf{x}}(t_i^-)]\mathbf{P}(t_i^-)\mathbf{H}^T[t_i; \hat{\mathbf{x}}(t_i^-)] + \mathbf{R}(t_i) \right\}^{-1} \quad (2-40)$$

$$\hat{\mathbf{x}}(t_i^+) = \hat{\mathbf{x}}(t_i^-) + \mathbf{K}(t_i) \left\{ \mathbf{z}(t_i) - \mathbf{h}[\hat{\mathbf{x}}(t_i^-), t_i] \right\} \quad (2-41)$$

$$\mathbf{P}(t_i^+) = \mathbf{P}(t_i^-) - \mathbf{K}(t_i)\mathbf{H}[t_i; \hat{\mathbf{x}}(t_i^-)]\mathbf{P}(t_i^-) \quad (2-42)$$

where

$$\mathbf{H}[t_i; \hat{\mathbf{x}}(t_i^-)] \equiv \left. \frac{\partial \mathbf{h}[\mathbf{x}, t_i]}{\partial \mathbf{x}} \right|_{\mathbf{x}=\hat{\mathbf{x}}(t_i^-)} \quad (2-43)$$

A comparison of the extended Kalman filter propagation and update equations with the linear Kalman filter propagation and update equations reveals that, for linear vector functions  $\mathbf{f}[\mathbf{x}(t), \mathbf{u}(t), t]$  and  $\mathbf{h}[\mathbf{x}(t_i), t_i]$  from Equations (2-25) and (2-26), the extended Kalman filter relations reduce to the linear Kalman filter equations. Since the linear system model is completely representative of the first-order terms of the Taylor series expansion, the extended Kalman filter propagation and update equations reduce to the linear Kalman filter algorithm under the conditions [13].

#### 2.4 Summary

This chapter provided the mathematical background theory of the linear and extended Kalman filters. The linear Kalman filter is an optimal estimator, while the extended Kalman filter is a good approximation for nonlinear models. The limitations of the first order approximations inherent in extended Kalman filter algorithms are recognized, but the results have proven to be very good in previous AFIT theses associated with this application. For the computer simulation used in this research, the truth model (Chapter IV) is composed of linear and nonlinear functions, while the three Kalman filters studied have dynamics and measurement models (Chapter V) which are linear.

### *III. Simulation Space*

#### *3.1 Introduction*

The AFIT tracking scenario described in Chapter I is simulated on a digital computer. To accomplish the simulation, a "simulation space" is defined [6, 9, 24] to propagate the target along a realistic trajectory, and to provide a means of mathematically projecting the target's infrared image and velocity vector from a three-dimensional space into the FLIR plane's two-dimensional image plane. For the purpose of this thesis, the formulated simulation space is coded into a FORTRAN computer language for use on a digital computer. This chapter relates the simulation space to the target model, and covers the process of pointing the FLIR sensor at the target during tracking. The target trajectory is also presented.

#### *3.2 Coordinate Frames*

The simulation space is defined relative to three coordinate frames: a system inertial reference frame, a target reference frame, and an  $\alpha$ - $\beta$ - $r$  reference frame. There are also four special coordinate frames associated with the  $\alpha$ - $\beta$ - $r$  reference frame: the  $\alpha$ - $\beta$  (FLIR) plane, the absolute  $\alpha$ - $\beta$ - $r$  reference frame, the trans-FLIR plane, and the along-track/across-track (ALT-ACT) plane. The  $\alpha$ - $\beta$ - $r$  reference frame is used to translate the target's apparent intensity image onto the  $\alpha$ - $\beta$  (FLIR) image plane. The trans-FLIR plane is the FLIR plane translated to the target's true center of mass. The ALT-ACT frame is a rotation of the trans-FLIR plane by an angle  $\theta$ , shown in Figure 3.1, with one of the axes aligned along the longitudinal axis of the hardbody and the other being across the hardbody. Figure 3.1 shows the origin and the orientation of each of the three primary frames and their relationships to the other frames. A description of each reference frame is given in the following paragraphs.

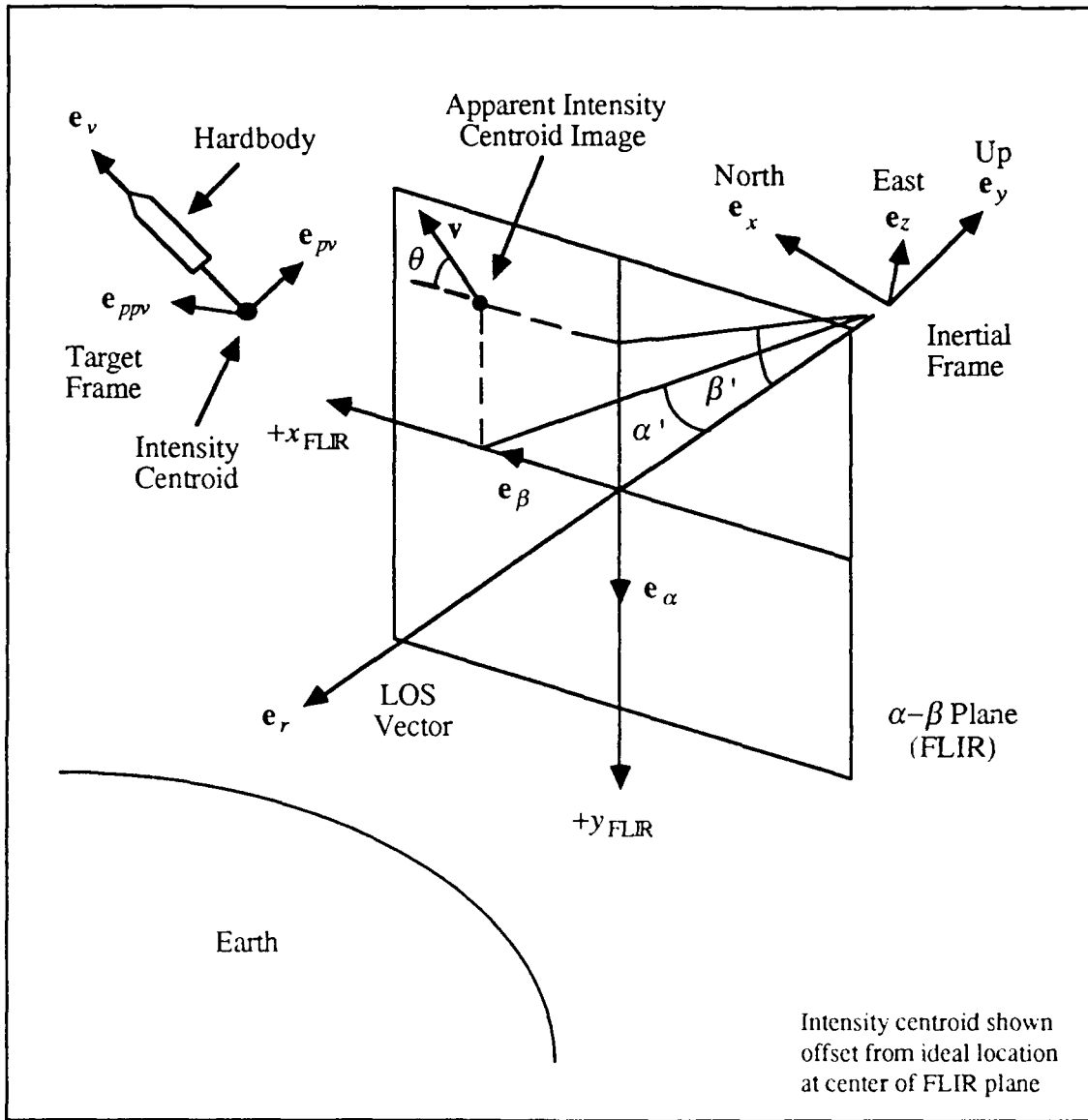


Figure 3.1. Three Primary Coordinate Frames in Simulation Space

3.2.1 *Inertial Reference Frame.* The inertial reference frame is an North-Up-East (NUE) frame located with its origin at the center of the FLIR sensor. The simulation of the target flight occurs in this frame. The unit vectors of this frame are represented by:

- $e_x$  - north, tangent to earth's surface, defines zero azimuth
- $e_y$  - up, perpendicular to the earth's surface
- $e_z$  - east, completes right-hand coordinate set



3.2.2 *Target Reference Frame.* The target reference frame has its origin at the center of mass of the target. The frame is orientated with one of the unit vectors pointing along the velocity vector of the target. The unit vectors of this frame are represented by:

- $\mathbf{e}_v$  - along the velocity vector
- $\mathbf{e}_{pv}, \mathbf{e}_{ppv}$  - define a plane perpendicular to the target velocity vector,  $\mathbf{e}_v$

where

the subscript 'v' indicates along the velocity vector

the subscript 'pv' indicates perpendicular to v

the subscript 'ppv' indicates perpendicular to both v and pv

3.2.3  *$\alpha$ - $\beta$ -r Reference Frame.* The  $\alpha$ - $\beta$ -r reference frame is defined by the azimuth angle  $\alpha'$  and the elevation angle  $\beta'$  measured with respect to the FLIR line-of-sight (LOS) vector  $\mathbf{e}_r$ . (The FLIR LOS vector  $\mathbf{e}_r$  defines the pointing direction of the FLIR FOV, which may not point directly at the target.) The true azimuth  $\alpha$  and the true elevation  $\beta$  are referenced from true north and the horizon. The purpose of this frame is to project the velocity and position of the target onto the FLIR plane. The unit vectors of this frame are represented by:

- $\mathbf{e}_r$  - coincident with the LOS vector; defines the pointing direction of the FLIR FOV
- $\mathbf{e}_\alpha, \mathbf{e}_\beta$  - define a plane perpendicular to  $\mathbf{e}_r$ , rotated from the inertial  $\mathbf{e}_x$  and  $\mathbf{e}_y$  by the azimuth angle  $\alpha$  and the elevation angle  $\beta$

3.2.4  *$\alpha$ - $\beta$  (FLIR Image) Plane.* As previously mentioned, this is a plane in the  $\alpha$ - $\beta$ -r reference frame. The FLIR plane is used to obtain the measurements of the position and the velocity vector components of the target's intensity centroid as the target propagates along its trajectory. (The target velocity vector in the FLIR plane is

geometrically derived, as described in Section 3.3.3; there are no measurements of this velocity vector.) Recall the FLIR sensor only provides information on the target's intensity centroid, and cannot supply information on the location of the target's hardbody. A view from the inertial frame through the FLIR plane is shown in Figure 3.2. As seen in Figures 3.1 and 3.2, the LOS vector  $e_r$  projects through the center of the the FLIR plane, and defines the pointing position for the FLIR sensor. When looking through the FLIR plane along the LOS vector, the FLIR  $x$ -axis ( $e_\alpha$ ) is positive to the right and the FLIR  $y$ -axis ( $e_\beta$ ) is positive down. This coordinate system allows for the distance to the target to be measured positive along the  $e_r$  vector, which completes the right-hand coordinate set. The LOS vector also serves as the aiming source for the low-energy and high-energy lasers.

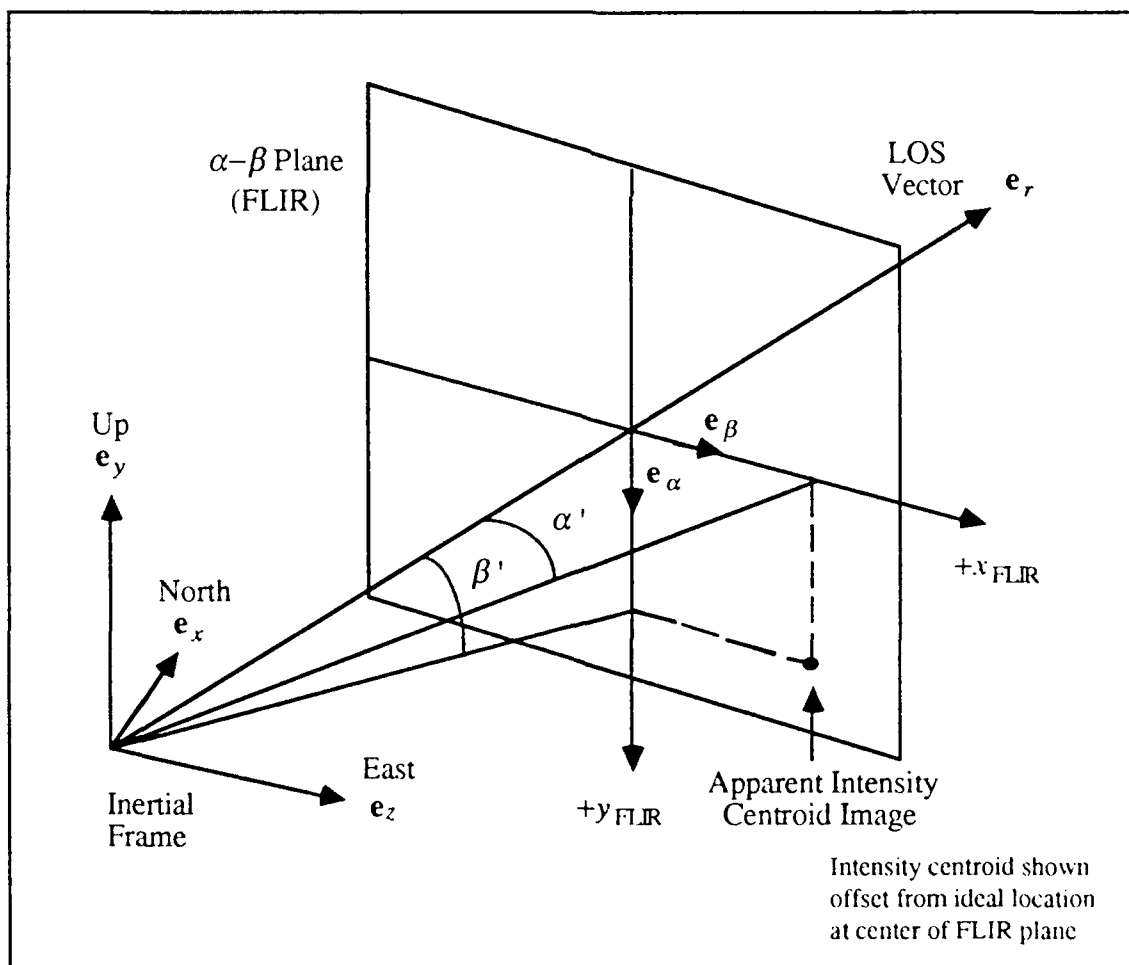


Figure 3.2. FLIR Image Plane

Since the distance to the target is so large (approximately 2,000 kilometers), the azimuth angle  $\alpha'$  and the elevation angle  $\beta'$ , shown in Figure 3.1 and 3.2, are considered very small, allowing the use of small angle approximations for the angles. Using the small angle approximations, then angles  $\alpha'$  and  $\beta'$  are linearly proportional to the cartesian coordinates  $x$  and  $y$  in the FLIR plane. The  $x$  and  $y$  distances from the center of the FLIR FOV are the errors associated with tracking the intensity centroid of the target. These errors are measured in pixels on the  $\alpha$ - $\beta$  plane.

*3.2.5 Absolute  $\alpha$ - $\beta$ - $r$  Reference Frame.* The absolute  $\alpha$ - $\beta$ - $r$  reference frame is similar to the  $\alpha$ - $\beta$ - $r$  reference frame except that the absolute frame is fixed in inertial space at the initial  $\alpha$ - $\beta$ - $r$  coordinates of the target. During the simulation, this coordinate system defines the pointing direction of the FLIR LOS vector  $\mathbf{e}_r$ , and is also used to define the true and filter estimated target positions and velocity components on the FLIR plane. The coordinates of the target position and velocity components are continuously updated from the start of the simulation.

*3.2.6 Trans-FLIR Plane.* Quadrant I of the FLIR plane (as seen through the FLIR plane towards the target) is shown with the trans-FLIR plane and ALT-ACT plane in Figure 3.3. The trans-FLIR plane is defined as the result of translating the center of the FLIR FOV to the true center-of-mass of the target hardbody. The frame is used to determine the  $x_{\text{FLIR}}$  and  $y_{\text{FLIR}}$  coordinate errors of the Kalman filter estimate of the hardbody center-of-mass for performance analysis.

*3.2.7 ALT/ACT Plane.* The ALT-ACT plane is shown in the FLIR plane in Figure 3.3. This plane is a rotation of the trans-FLIR plane by the true angle  $\theta_t$  of the target trajectory. The ALT-ACT plane is used to determine the tracking error mean and covariance, where the error is the difference between the estimate of the hardbody center-of-mass and the true center-of-mass in the target's along-track and across-track components.

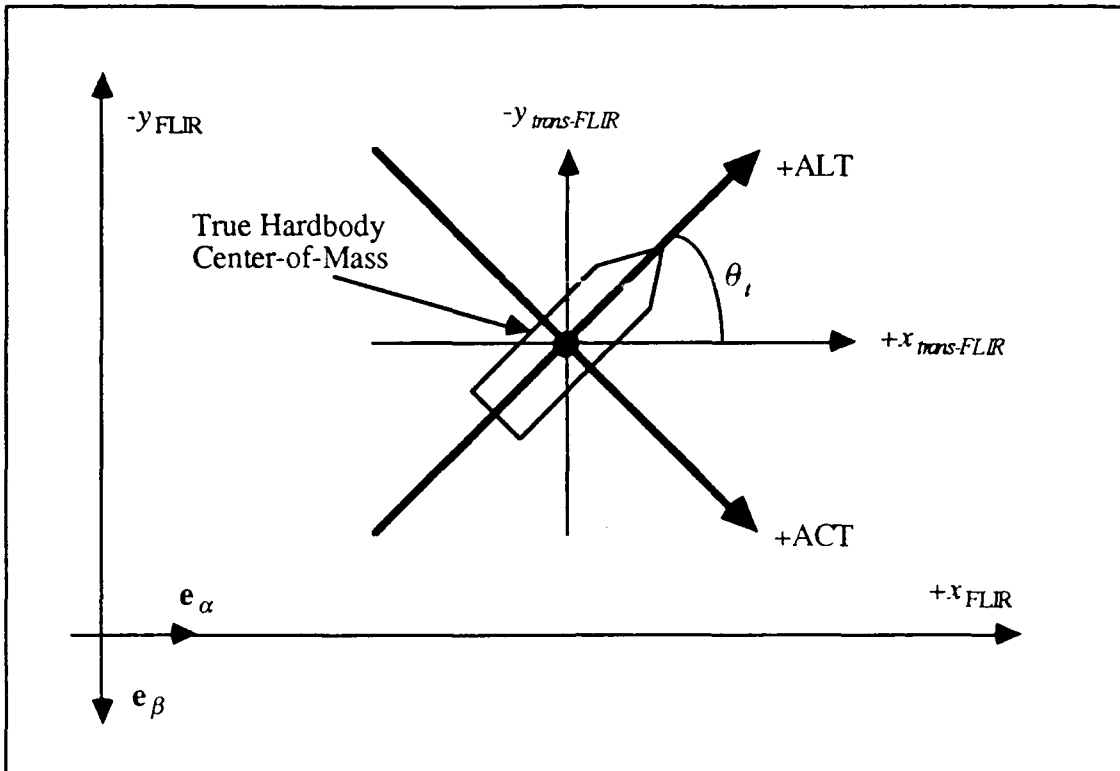


Figure 3.3. FLIR Plane, Trans-FLIR plane, and ALT-ACT plane

This frame provides an orientation of the center-of-mass errors which is easier to visualize. The previous thesis [2] estimated only the scalar magnitude of that error as measured in the FLIR plane. As mentioned in the objectives (Section 1.3), this thesis determines the FLIR  $x$ - and  $y$ -components of that error, then rotates the error to determine the along-track and across-track components of the error in the ALT-ACT plane.

### 3.3 FLIR Image Plane

The FLIR plane is of primary importance in determining the performance of the Kalman filter in tracking a target. The target flight trajectory occurs in the inertial coordinate system, while the projection of the target and its dynamics onto the FLIR plane provides a means of generating simulated measurements and estimating the target trajectories. The measure of success is found in the errors that are calculated in this plane. A description of the geometry comprising the FLIR plane is summarized in this section.

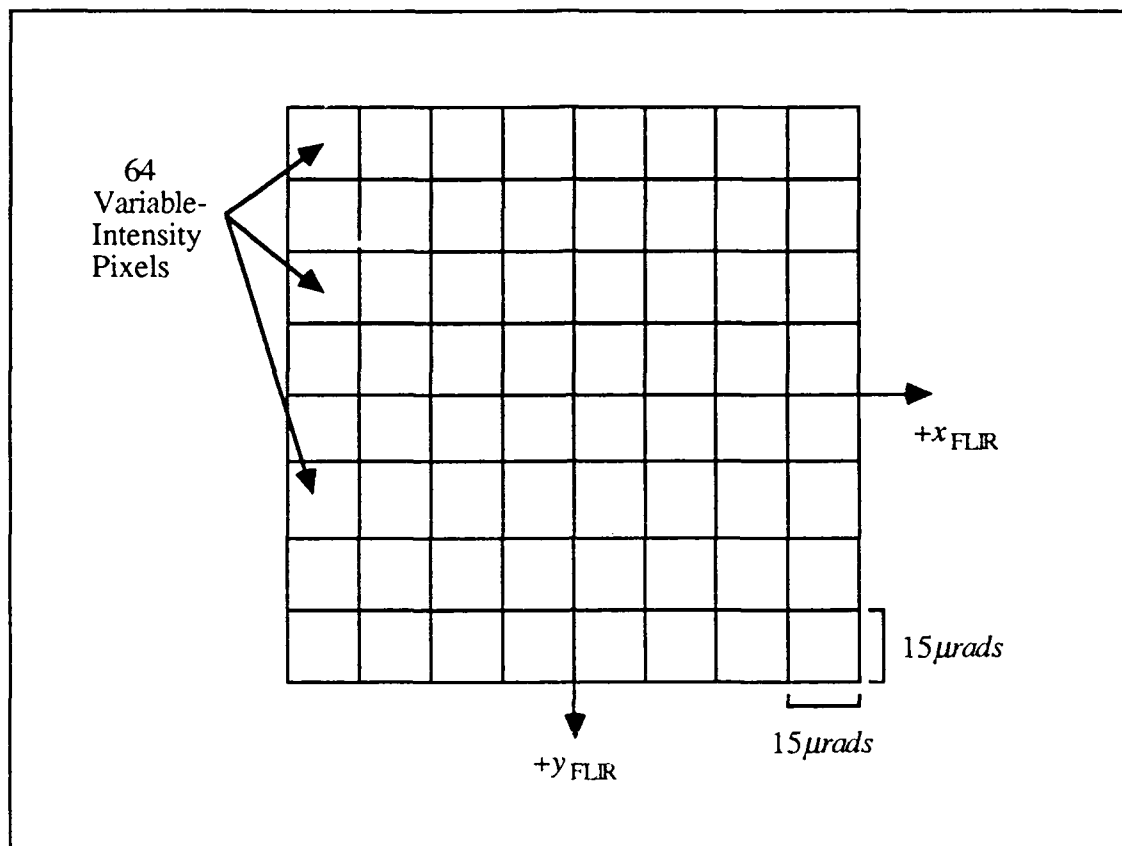


Figure 3.4. Pictorial of 8 x 8 FLIR Field-of-View

*3.3.1 FLIR Field-Of-View Geometry.* The FLIR FOV in this thesis consists of an 8 x 8 pixel array shown pictorially in Figure 3.4. The detected information provided by each pixel is a function of the varying intensity of the IR image and background noise. The resolution of each of the discrete pixel elements provides a measure with which the errors in the Kalman filter's estimate of the azimuth and elevation of the target's intensity centroid are determined. The units of the errors are in "pixels". The pixel length has typically been 20 microradians per side of each pixel. This value was reduced to 15 microradians [26] for studying the long range tracking of a missile target (i.e., 1 pixel = 15 microradians). The pixel distances and errors become meaningful in the simulation through a pixel proportionality constant denoted as  $k_p$  with units of radians/pixel. For this thesis the value of the pixel proportionality constant is  $k_p = 0.000015$  radians/pixel. At a distance of 2,000 kilometers, the relationship of pixels and meters is: 1 pixel  $\cong$  30 meters.

3.3.2 *Target Model on FLIR Image Plane.* The target intensity model, as viewed by the FLIR plane, is modeled using two Gaussian intensity functions as developed in a previous thesis [26]. The difference between these intensity functions represents the plume hotspot of the target, as shown in Figure 3.5. In addition, the target hardbody itself has recently been modeled as a rectangle in the FLIR plane [2]. As one of the primary objectives of this thesis, a better three-dimensional reflective target model is developed. The FLIR sensor can only "see" the IR intensity shape function of the target, therefore the intensity centroid model is emphasized. The modeling of the hardbody as it relates to the low-energy laser measurements, and the determination of the target center of mass, are discussed in Chapters IV and V.

The radiated energy from a single intensity function is modeled as a bivariate Gaussian distribution with elliptical constant intensity contours in the FLIR image plane. As mentioned above, the target's plume is modeled using two bivariate Gaussian densities.

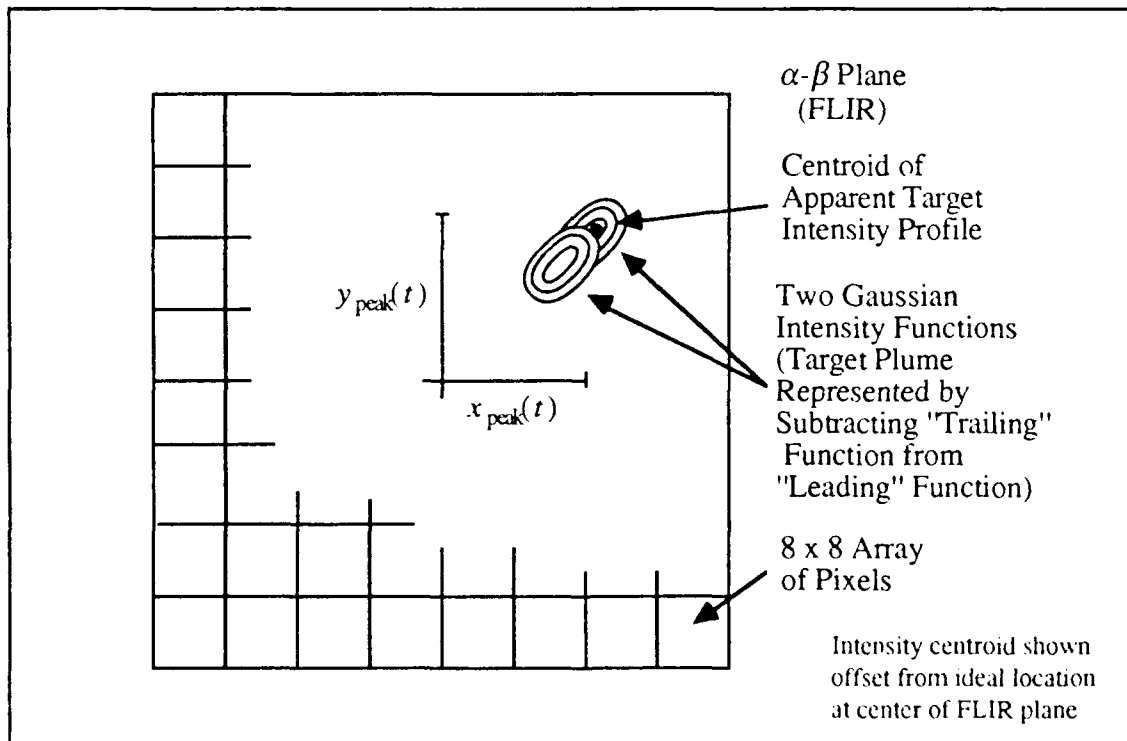


Figure 3.5. Target Image (Difference of Two Intensity Functions) in FLIR Field-of-View

One function is subtracted from the other (the "trailing" intensity function is subtracted from the "leading" intensity function), resulting in the contour map shapes shown in Figure 3.5. This simulation of the target plume represents a good approximation of empirically observed plume intensity profiles.

The bivariate Gaussian intensity function is given by the following equation:

$$I [x, y, x_{peak}(t), y_{peak}(t)] = I_{max} \exp[-0.5[\Delta x \ \Delta y] \mathbf{P}^{-1} [\Delta x \ \Delta y]^T] \quad (3-1)$$

where

- $\Delta x$  =  $(x - x_{peak}) \cos \theta_t + (y - y_{peak}) \sin \theta_t$
- $\Delta y$  =  $(y - y_{peak}) \cos \theta_t - (x - x_{peak}) \sin \theta_t$
- $\theta_t$  = true target orientation angle between the projection of the velocity vector perpendicular to the LOS vector and the  $x$ -axis in the FLIR plane
- $x, y$  = reference coordinate axes on the  $\alpha$ - $\beta$  plane
- $x_{peak}, y_{peak}$  = coordinates of the peak intensity of the single Gaussian intensity function
- $I_{max}$  = maximum intensity function
- $\mathbf{P}$  = 2 x 2 target dispersion matrix whose eigenvalues ( $\sigma_v^2$  and  $\sigma_{pv}^2$ ) define the dispersion of the elliptical constant intensity contours (along the velocity vector and perpendicular to that velocity vector, respectively in the  $\alpha$ - $\beta$  plane; see Sections 3.2 and 3.3.4)

The geometry of the two intensity functions that define the target to the FLIR sensor is shown in Figure 3.6. The spatial definition of the intensity functions along the  $\mathbf{e}_v$  axis is based on the assumption [26] that the dispersion of a missile's exhaust plume at high

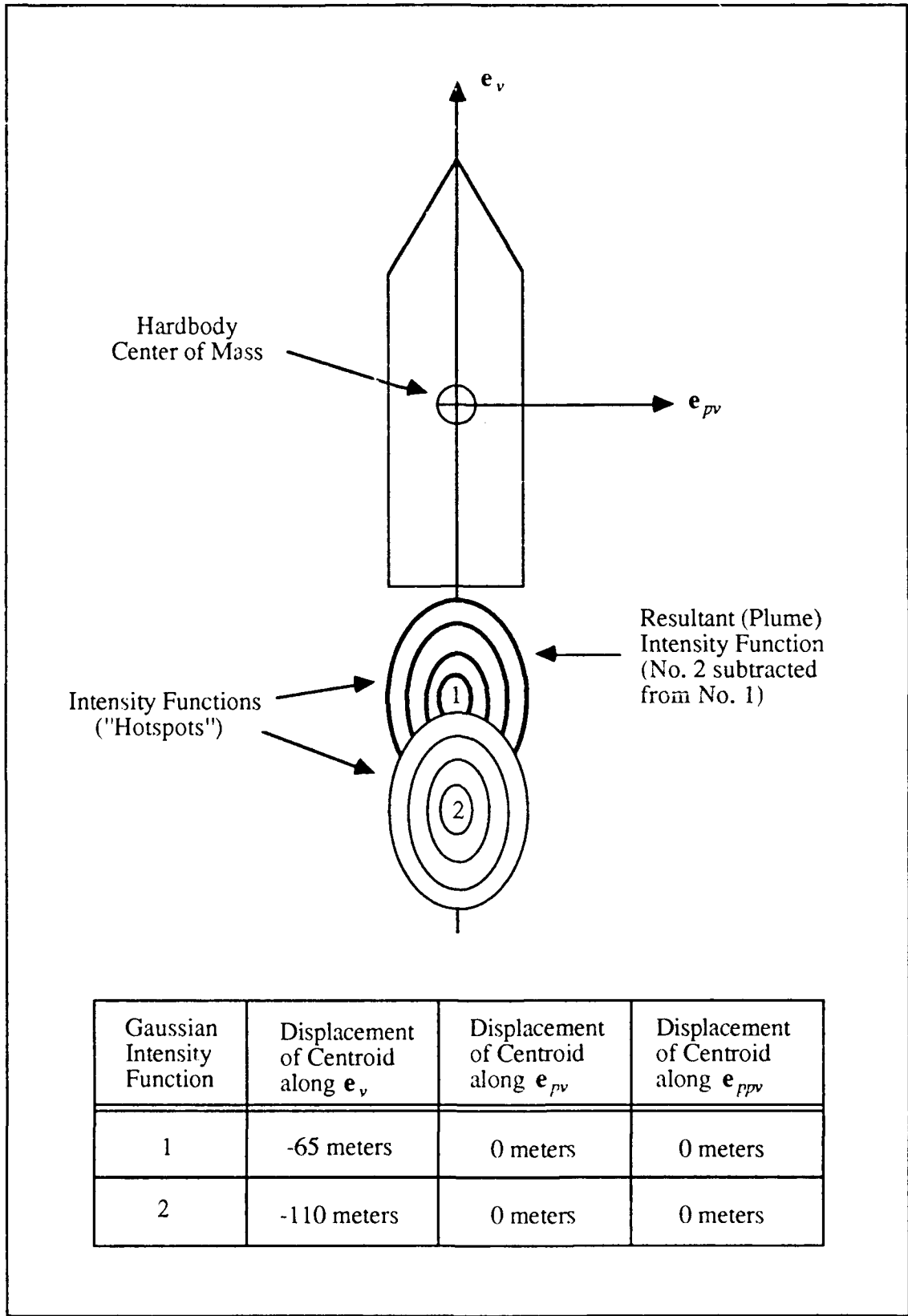


Figure 3.6. Orientation of Target Gaussian Intensity Functions



altitudes is approximately 20 *times* the diameter of the missile [26]. Additionally, at high altitudes the plume often appears to envelope the target, at least partially [26]. The model of the target hardbody was chosen to be 40 meters long by 3 meters in diameter. With this target geometry, the first centroid was placed 65 meters behind the target center of mass to simulate the composite centroid of the plume being close to the exhaust nozzle of the missile. The second intensity function was arbitrarily placed at 140 meters to simulate one of many different plume shapes. The shape of the plume, and the relative distance of the composite centroid of the plume with respect to the aft end of the target, can be varied by changing the location of the second intensity function.

In this simulation, the centroids of the two intensity functions remain fixed in the target frame (without the effect of plume pogo oscillations; see Chapters IV, and VI). The external forces acting on the target other than thrust and gravity are assumed negligible. Therefore, the sideslip angle and the angle of attack are considered to be zero. With these simplifications of the target, Figure 3.7 shows that the semi-major axis of the plume intensity centroid (difference between two elliptically-shaped Gaussian intensity functions) is aligned with the velocity vector's projection onto the FLIR image plane. These conservative assumptions provide for a simplified geometry while retaining the essential features of the trajectory simulation necessary for a valid performance analysis of the tracking system.

*3.3.3 Target Velocity Projection onto FLIR Image Plane.* As discussed in Section 3.2.1, the target is propagated through inertial space by the truth model (Chapter IV) in the simulation. The two intensity functions, which define the target's intensity profile, are projected onto the FLIR image plane (Section 3.3.2) as the simulation occurs. The general discrete-time state space form of the equation that models the target in the truth model is given by Equation (2-9):

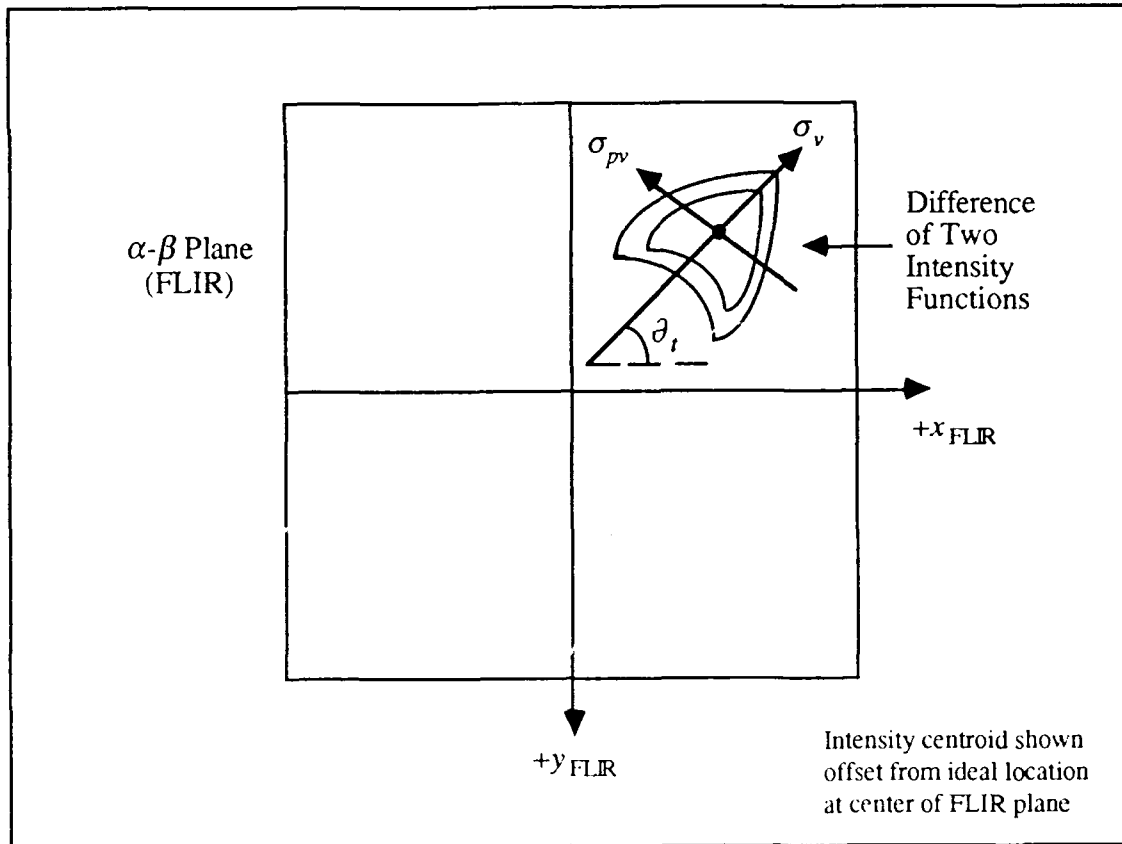


Figure 3.7. Plume Intensity Centroid and Relationship with Target Velocity Vector on FLIR Image Plane

$$\mathbf{x}(t_{i+1}) = \Phi(t_{i+1}, t_i) \mathbf{x}(t_i) + \mathbf{B}_d(t_i) \mathbf{u}(t_i) + \mathbf{G}_d(t_i) \mathbf{w}_d(t_i) \quad (2-9)$$

where

- $\Phi(t_{i+1}, t_i)$  = the system state transition matrix
- $\mathbf{x}(t_i)$  = discrete-time vector of states of interest
- $\mathbf{B}_d(t_i)$  = discrete-time control input matrix
- $\mathbf{u}(t_i)$  = discrete time deterministic control input vector
- $\mathbf{G}_d(t_i)$  = discrete-time driving noise input matrix
- $\mathbf{w}_d(t_i)$  = discrete-time, zero-mean, white Gaussian noise process with independent components

The target is propagated through 3-dimensional inertial space, and projected onto the FLIR plane. Equation (2-9) is used to express the desired time histories of the true azimuth  $\alpha(t_i)$  and true elevation  $\beta(t_i)$  angles (Section 3.2.3) as the solution to the state space model. Therefore, the azimuth angle  $\dot{\alpha}'$  and the elevation angle  $\dot{\beta}'$  are computed such that the result of the discrete-time forcing function  $\mathbf{B}_d(t_i)\mathbf{u}(t_i)$  passing through Equation (2-9) are the desired  $\alpha(t_i)$  and  $\beta(t_i)$  time histories. (In the simulation, the  $\mathbf{G}_d(t_i)\mathbf{w}_d(t_i)$  is not used in the generation of the  $\alpha(t_i)$  and  $\beta(t_i)$  time histories.) The truth model contains the deterministic control input matrix  $\mathbf{B}_d(t_i)$  and the deterministic input control vector  $\mathbf{u}(t_i)$ , while the three Kalman filters used in the simulation do not have control functions (i.e., they are not informed of the actual trajectory being performed by the target). The projection of the target's inertial velocity vector onto the FLIR image plane is given by the deterministic input vector :

$$\mathbf{u}_{1d}(t_i) = \left[ \dot{\alpha}'(t_i) \quad \dot{\beta}'(t_i) \right]^T \quad (3-2)$$

where

$$\begin{aligned} \mathbf{u}_{1d}(t_i) &= \text{2-dimensional true target deterministic input vector} \\ \dot{\alpha}'(t_i) &= \text{target azimuth rate in the FLIR plane} \\ \dot{\beta}'(t_i) &= \text{target elevation rate in the FLIR plane} \end{aligned}$$

This projection is based on the FLIR and target intensity centroid geometry shown in Figure 3.8 [6]. The horizontal projection of the range to the target's intensity centroid is given by  $r_h$ . The azimuth velocity is derived from Figure 3.8(b). From the diagram:

$$\alpha(t) = \arctan \left[ \frac{z(t)}{x(t)} \right] \quad (3-3)$$

Taking the time derivative of this equation and noting from Section 3.2.4 that  $\dot{\alpha}(t) = \dot{\alpha}'(t)$  gives the azimuth velocity in the FLIR plane as:

$$\dot{\alpha}'(t) = \dot{\alpha}(t) = \frac{x(t)v_z(t) - z(t)v_x(t)}{x^2(t) + z^2(t)} \quad (3-4)$$

where

$v_x, v_z$  = components of the target's inertial velocity in the  $e_x$  and  $e_z$  directions, respectively.

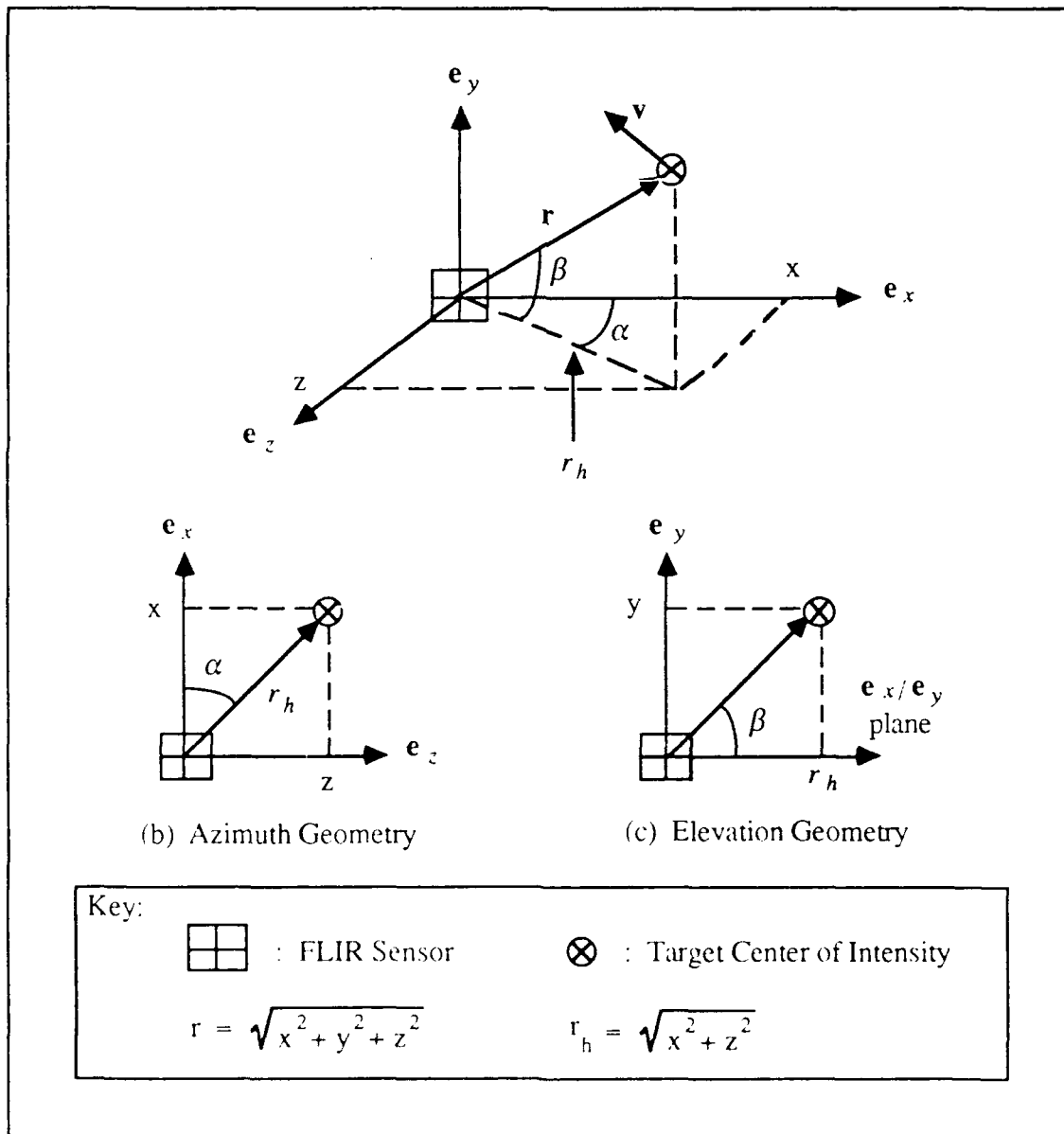


Figure 3.8. Target Intensity Centroid Inertial Velocity Geometry onto FLIR Image Plane

The elevation velocity is derived from Figure 3.8(c). From the diagram, it can be seen that:

$$\beta(t) = \arctan \left[ \frac{y(t)}{r_h(t)} \right] \quad (3-5)$$

Taking the time derivative of this equation and noting from Section 3.2.4 that  $\dot{\beta}(t) = \dot{\beta}'(t)$  gives the elevation velocity in the FLIR plane as:

$$\dot{\beta}'(t) = \dot{\beta}(t) = \frac{r_h(t)v_y(t) - y(t)\dot{r}_h(t)}{r_h^2(t)} \quad (3-6)$$

where

$$\dot{r}_h(t) = \frac{x(t)v_z(t) + z(t)v_x(t)}{r_h(t)}$$

$v_y$  = component of the target's inertial velocity in the  $e_y$  direction.

*3.3.4 Target Image Projection onto FLIR Image Plane.* As described in earlier research [2, 11, 26, 30], the target intensity centroid image projection geometry, shown in Figure 3.9, relates the current target intensity image to an initial "reference target" image on the FLIR plane. The reference image is oriented on the FLIR image plane to correspond to the largest apparent platform at a specified range. The angle  $\theta$  is defined from the positive  $x$  axis to the projection of the target's velocity vector on the FLIR image plane. The target intensity image in the FLIR plane, as shown in Figure 3.7, is defined by the dispersion along the principle axes of the intensity function's two bivariate Gaussian images as seen by the FLIR sensor:

$$\sigma_{pv} = \sigma_{pvo} \left( \frac{r_o}{r} \right) \quad (3-7)$$

$$\begin{aligned} \sigma_v &= \left( \frac{r_o}{r} \right) \left( \sigma_{pvo} + (\sigma_w - \sigma_{pwo}) \cos \delta \right) \\ &= \sigma_{pv} \left\{ 1 + \frac{v_{LOS}}{v} (AR - 1) \right\} \end{aligned} \quad (3-8)$$

where

$\sigma_{v_o}, \sigma_{p_{v_o}}$  = the initial dispersions of the target intensity functions along  $\mathbf{e}_v$  and  $\mathbf{e}_{p_v}$  in the target frame of the reference image

$\sigma_v, \sigma_{p_v}$  = the current dispersions of the target's image

$r_o$  = initial sensor-to-target range of the reference image

$r$  = current sensor-to-target range

$\mathbf{v}$  = initial velocity vector of the target

$v$  = magnitude of  $\mathbf{v}$

$\mathbf{v}_{\perp\text{LOS}}$  = projection of  $\mathbf{v}$  on the  $(\alpha-\beta)$  plane; i.e., the component of  $\mathbf{v}$  perpendicular to the LOS vector

$v_{\perp\text{LOS}}$  = magnitude of  $\mathbf{v}_{\perp\text{LOS}}$ :  $v_{\perp\text{LOS}} = \sqrt{\dot{\alpha}^2 + \dot{\beta}^2}$

$\gamma$  = angle between  $\mathbf{v}$  and the  $(\alpha-\beta)$  plane

AR =  $\frac{\sigma_{v_o}}{\sigma_{p_{v_o}}}$  : aspect ratio of the reference image

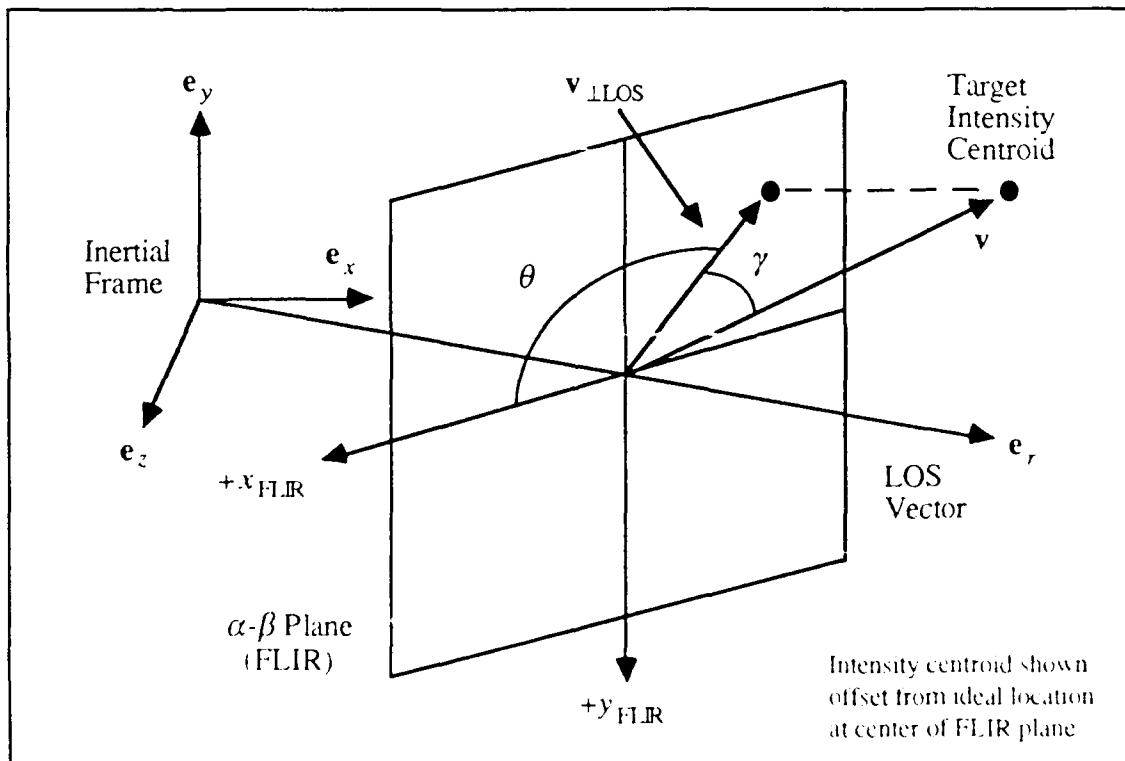


Figure 3.9. Target Intensity Centroid Image Projection Geometry onto FLIR Image Plane

The locations of the intensity functions are initialized in the target frame as a displacement from the target's center of mass. Then the hotspots are rotated by the target orientation angle,  $\theta_t$ , in the FLIR image plane (refer to Figure 3.7). As the target propagates through inertial space in the simulation, the output of the FLIR sensor is simulated by projecting the target's two intensity functions (which are used to create the simulated plume intensity centroid) onto the FLIR image plane. In previous AFIT research [2, 26, 25], these "hotspots" remained fixed with respect to the target frame, while the locations of the intensity functions in the FLIR plane changed as the target changed its orientation relative to the FLIR sensor. As a part of this research, the plume pogo phenomenon [26] is applied to the intensity centroids. With the pogo forcing input applied, the intensity functions do not remain fixed in the target frame relative to the target center-of-mass, and the composite image centroid oscillates along the velocity vector, producing an additional perturbation to the intensity functions in the FLIR plane.

### *3.4 FLIR Sensor Pointing Controller*

The FLIR sensor is directed to track the target based on the Kalman filter's propagated estimate of the target's position. The link between the filter command and proper positioning of the FLIR sensor is the pointing controller. Ideally, the command from the filter to the pointing controller, provides positioning of the FLIR sensor within one sample period (1/30 second). This would mean that the process of pointing the FLIR sensor would occur between the measurements provided to the filter by the FLIR sensor. However, due to mechanical servo lags, the positioning process is not actually accomplished completely before the next measurement is received. Furthermore, if the filter is not aware of the pointing lag at the time of a measurement update, the filter could interpret the motion of the FLIR as target motion and provide inaccurate estimates of future states [24].

A study was accomplished in a previous thesis [24] in which a controller model was studied to determine the necessity of including the controller dynamics lag in the simulation. The study revealed that the filter interprets the pointing controller time lags as due to atmospheric jitter. This implies some robustness on the part of the Kalman filter to perform nominal tracking in the presence of unmodeled actuator dynamics. Therefore, the controller in the simulation is an ideal lag-free model for this research.

### 3.5 Target Trajectory

The missile trajectory used in the simulation is a point mass influenced by a thrust force and a gravitational force, described by the following inverse square-law force field equation [26]:

$$F_G = \frac{Gm_1m_2}{r^2} \quad (3-9)$$

where

- $F_G$  = force of attraction between missile and the earth
- $G$  = universal gravitation constant
- $m_1, m_2$  = mass of earth and missile, respectively
- $r$  = distance between the earth's center and the missile center of gravity

For the purposes of this study, all other external forces on the missile (atmospheric drag, deterministic solar effects, etc.) are assumed negligible; and the missile is assumed to have constant mass over the simulation interval of ten seconds. To obtain an expression for the missile acceleration, Newton's second law gives:

$$\mathbf{F} = m\mathbf{a} \quad (3-10)$$

where

- $\mathbf{F}$  = external force(s) acting on the missile
- $m$  = constant mass of the missile
- $\mathbf{a}$  = inertial acceleration of the missile



From the derived inertial acceleration, the components of the missile's inertial velocity and position are obtained by integration techniques. The deterministic inertial position and velocity components are used to project the velocity onto the FLIR image plane (Sections 3.3.3 and 3.3.4), and the resulting FLIR plane position coordinates from the truth model propagation cycle represent the first two states in the truth model state vector of Equation (2-9). The thrust and mass parameters used to describe the simulated ballistic missile are based upon the Atlas missile specifications [26].

The initial conditions of the target's inertial position and velocity vectors for the simulation are:

$$\begin{aligned}e_x &= 27,000 \text{ meters} \\e_y &= 100,000 \text{ meters} \\e_z &= 2,000,000 \text{ meters} \\v_x &= -2500 \text{ meters/second} \\v_y &= 4330 \text{ meters/second} \\v_z &= 0 \text{ meters/second}\end{aligned}$$

With these initial conditions, the range of the target is on the order of 2,000 kilometers and traveling at a speed of 5,000 meters/second. Figure 3.10 shows the position of the target at the start of the simulation relative to the FLIR image plane. The relative magnitudes of the initial velocity components  $v_x$  and  $v_y$  form an initial velocity vector orientation angle of  $60^\circ$  for the target in the inertial frame. The components of acceleration are calculated based on the above mathematical discussion.

The initial condition in the  $e_z$  direction is made large to simulate the large effective range when considering an orbiting platform that is undergoing bending/vibrational effects. The reason that the  $e_z$  direction is chosen to generate a large effective range is because it is a "benign" axis when implementing the ballistic missile trajectory for this simulation. All

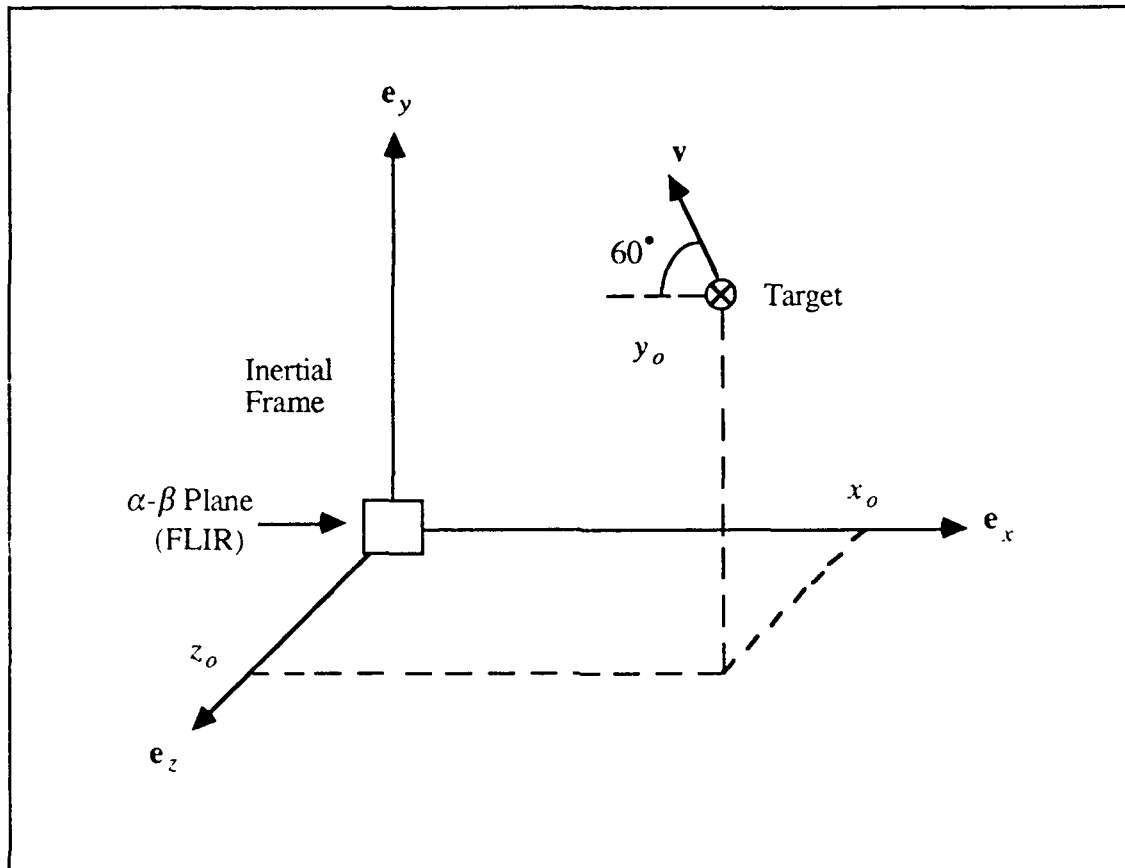


Figure 3.10. Missile Trajectory in Inertial Space Relative to FLIR Image Plane

of the missile dynamics are simulated to occur in a plane parallel to the inertial  $e_x$ - $e_y$  plane. Therefore, the  $e_z$  axis is basically used to scale the desired range when considering an orbiting optical platform in the simulation. The effective range is also used in determining the required pixel proportionality constant  $k_p$  (Section 4.3.1), as well as being involved in the various coordinate frame transformations that have been implemented in the simulation software over the past twelve years. The large initial component in  $e_z$  does not affect the true missile trajectory as generated by the mathematical development at the beginning of this section, since the only forces acting on the missile are assumed to be the thrust force and the force due to the earth's gravitational attraction. Both of these forces are simulated to occur in a plane parallel to the  $e_x$ - $e_y$  plane. [26]

### 3.6 Summary

This chapter described the coordinate reference frames used in the simulation to establish the target on the FLIR sensor. The three primary coordinate frames are: the inertial reference frame which is used to translate the target; the target reference frame which defines the axes of the missile; and the  $\alpha$ - $\beta$ - $r$  frame which is used to define the apparent image of the target's intensity centroid on the FLIR sensor. The target FLIR image is modeled as the difference of two Gaussian intensity functions with elliptical constant-intensity contours. The position and velocity of the target's intensity centroid is established on the FLIR image plane using geometric relationships between the inertial frame, the  $\alpha$ - $\beta$ - $r$  frame, and the target frame. The Trans-FLIR plane and the ALT-ACT frames are used to identify the target hardbody center-of-mass. The target is kept in the FLIR FOV by the commands received from the pointing controller which uses propagated Kalman filter data to point the FLIR sensor. The initial conditions of the target trajectory define a nominal Atlas missile at a distance of 2,000 kilometers from the space platform, and climbing at an angle of 60°. The trajectory is determined by the first two states of the truth model, which is covered in the next chapter.

## *IV. Truth Model*

### *4.1 Introduction*

The design process of a Kalman filter must include testing in the dynamic environment in which the filter will operate. Since it is difficult and expensive to test each filter modification in an actual real world, an alternative is to define a "real world" environment in a computer simulation. This simulated description of the real world is called a truth model. This model of the dynamic environment in which the filter will perform must contain as many states as needed to provide a realistic test for the filter. The Kalman filter is typically derived from this "truth model" by reducing the model to meet computer processing and memory requirements, while at the same time ensuring that it meets the performance specifications.

The truth model is developed by accomplishing data analysis on information obtained from instruments measuring physical phenomena of the real world environment. Then mathematical shaping filters [12] are developed and validated in the real world environment until the models meet, or exceed, the specifications required of the filter. It is essential to expend enough effort in its generation to be confident that it adequately represents the real world, since the ensuing performance evaluation and systematic design procedure of the Kalman filter is totally dependent upon this assumption [12].

A diagram of the computer simulation used to conduct a performance analysis of a Kalman filter design is shown in Figure 4.1. The truth model, which is a linear or non-linear  $n_t$ -dimensional state model, is driven by a zero-mean white Gaussian noise  $\mathbf{w}_t(\cdot, \cdot)$  that provides the real world measurements  $\mathbf{z}_t(\cdot, \cdot)$  to the Kalman filter under evaluation. The measurements are corrupted by a zero-mean white Gaussian noise  $\mathbf{v}_t(\cdot, \cdot)$ . (The notation  $(\cdot, \cdot)$  indicates a stochastic process as a function of the two arguments, time  $t$  and the elementary outcome  $\omega$ .) In actual operation, the filter obtains measurement data from

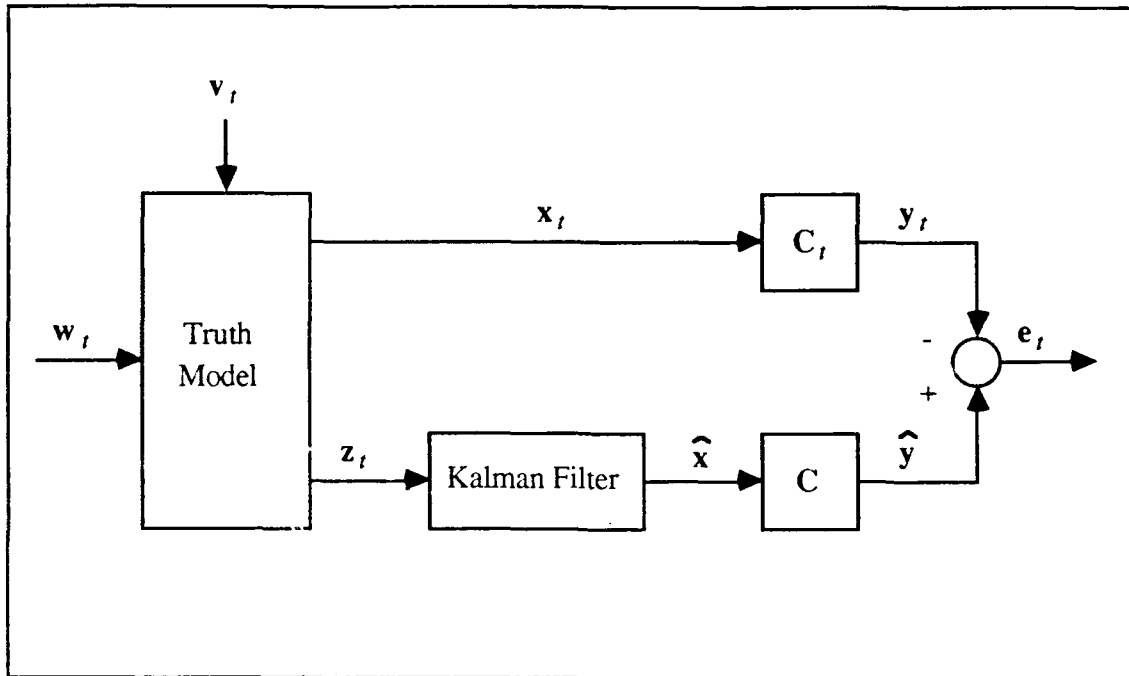


Figure 4.1. Computer Software Simulation Diagram of Truth Model and Kalman Filter [12]

physical sensors. The filter uses the measurement input to update the state estimates  $\hat{x}$ , and propagate its estimates to the next sample period.

The true state  $x_t$  from the truth model is related to the important variables of interest by a linear (or non-linear) transformation:

$$y_t(t, \cdot) = C_t(t) x_t(t, \cdot) \quad (4-1)$$

where  $y_t(t, \cdot)$  represents the real world variables of interest. The state estimate  $\hat{x}(\cdot, \cdot)$  from the Kalman filter is also processed by a linear transformation which is nominally the identity matrix since this will give all the states of interest estimated by the filter. Therefore, we obtain  $\hat{y}(t, \cdot)$  which is the estimate by the Kalman filter of the values of the variables of interest before and after the update:

$$\hat{y}(t_i^-) = C(t_i) \hat{x}(t_i^-) \quad (4-2)$$

$$\hat{y}(t_i^+) = C(t_i) \hat{x}(t_i^+) \quad (4-3)$$

The analysis of the Kalman filter performance with the truth model is determined by the difference, or "true error" of the filter estimates. The values of the errors may be obtained both before and after the measurement update:

$$\mathbf{e}_i(t_i^-, \cdot) = \hat{\mathbf{y}}(t_i^-, \cdot) - \mathbf{y}_i(t_i^-, \cdot) \quad (4-4)$$

$$\mathbf{e}_i(t_i^+, \cdot) = \hat{\mathbf{y}}(t_i^+, \cdot) - \mathbf{y}_i(t_i^+, \cdot) \quad (4-5)$$

For instance, the Kalman filter state vector for this thesis consists of two position states, two velocity states, two atmospheric jitter states, and two center of mass offset error states. The truth model consists two position states, six atmospheric jitter states, four vibration/bending states, and two plume pogo states. The truth model has a total of fourteen states while the Kalman filter has eight states, which means that the fourteen-state truth model gives (assuming the modeling is correct) a better representation of the real world than the model within the Kalman filter under test. Moreover, the filter is never "told" the actual trajectory simulated in the truth model, and the FLIR measurement generation and processing by the enhanced correlator is represented by a simple linear model within the filter. In this thesis, the primary interest is the error in the estimate of the hardbody location, which is a linear combination of the position states and the center of mass offset errors. Secondary interests include: the two target dynamics states, the two centroid intensity position states (for shape function identification), and the velocity error (to determine the sweepline orientation of the low-energy laser). Therefore, using Equations (4-4) and (4-5), the true error between position estimated by the filter and that estimated by the truth model is calculated. The statistics of this error indicate the quality of the tracking performance of the filter.

The purpose of the Kalman filter performance analysis is to characterize the errors in the filter's estimates. The analysis often also includes a sensitivity study to determine how the performance changes when the structure of the filter is adjusted (i.e., when states

are added to or subtracted from the filter, or when covariances are adjusted). The truth model may also be adjusted to simulate a changing sensor environment. Since the system is a stochastic process, the analysis is accomplished by examining the statistics of the error.

There are two different methods used to obtain the statistical information about the filter errors. One means is by using a Monte Carlo study, and the other is by using a covariance analysis. They both provide essentially the same information, however they each have differing limitations which makes them useful under different conditions.

The Monte Carlo analysis correctly provides statistical information on linear and nonlinear systems with Gaussian or non-Gaussian noises. The error analysis is accomplished by completing many computer runs of the filter, then obtaining the sample statistics from the average of the runs. Figure 4-2 shows the outputs of three such Monte Carlo computer simulation runs. The number of computer runs required to obtain good statistics on the filter errors is dependent on the application, but 10 to 20 runs are usually sufficient for most applications. (Ten runs are used to obtain the statistics for this thesis.) The computer time to accomplish many runs can be very costly and time-consuming.

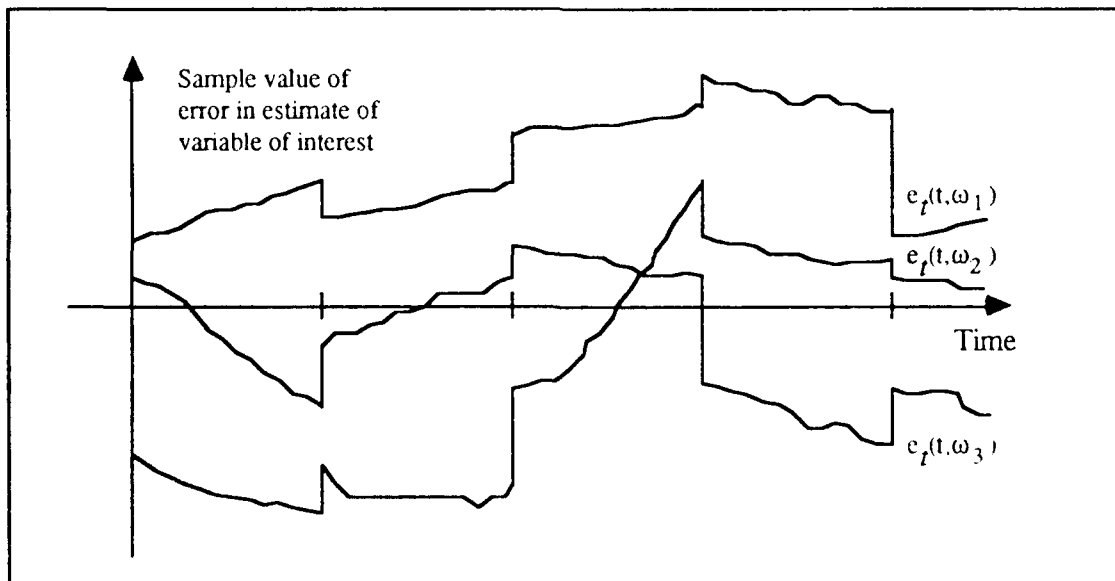


Figure 4.2. Outputs of Three Monte Carlo Runs [12]

An alternative to using the Monte Carlo method is to use a covariance analysis. A covariance analysis may be used if the truth model is in the form of a linear system driven by a white Gaussian noise which provides linear measurements to the filter that are corrupted by white Gaussian noises. A single computer run generates a time history of the covariance of the true estimation errors  $\mathbf{P}_e(\cdot)$  committed by the filter as given by Equations (4-4) and (4-5). The square roots of the diagonal terms of this matrix are the standard deviations ( $1\sigma$  values) of the estimates of the critical variables. These values are directly comparable to the results of the Monte Carlo method, but they are generated in a single computer run.

The Kalman filter design must provide the best possible performance estimation. Therefore, the filter must be "tuned" to obtain the optimal performance. This is accomplished by varying the initial uncertainty in the state estimates  $\mathbf{P}_0$ , strength of the white Gaussian dynamics noises  $\mathbf{Q}$ , and the uncertainty in the measurements as depicted by the measurement noise covariance  $\mathbf{R}$ . These parameters account for the actual noises and disturbances in the physical system, and provide a means of identifying how adequately the filter model represents the real world. A simple model (few states) has higher values of covariances or strengths of uncertainties/noises assigned while a complex model (many states) will have lower values assigned.

The covariance analysis can be a very effective tool in tuning the filter. Since a single computer simulation run provides a complete set of statistics, a run provides a basis to study performance changes when the covariance parameters of the filter are adjusted. The  $\mathbf{P}_0$  matrix determines the transient performance of the filter, while the  $\mathbf{Q}$  and  $\mathbf{R}$  matrices predominantly determine the steady-state performance. By properly selecting the noise terms  $\mathbf{Q}$  and  $\mathbf{R}$ , and the initial values for the covariance  $\mathbf{P}$  matrix, the actual estimation errors of the filter are reduced. Figure 4.3 shows three covariance runs during the process of tuning the  $\mathbf{P}$ ,  $\mathbf{Q}$ , and  $\mathbf{R}$  terms in a filter.



When a filter is properly tuned, an "error budget" may be established. An error budget is determined by individually turning on individual error sources (or groups of error sources) in the truth model to determine the separate effects of the sources. The analysis will indicate the rank order of importance of the error sources. This information can be used to reduce the filter states (replacing the removed states with white Gaussian noise of appropriate strength, as found by means of tuning).

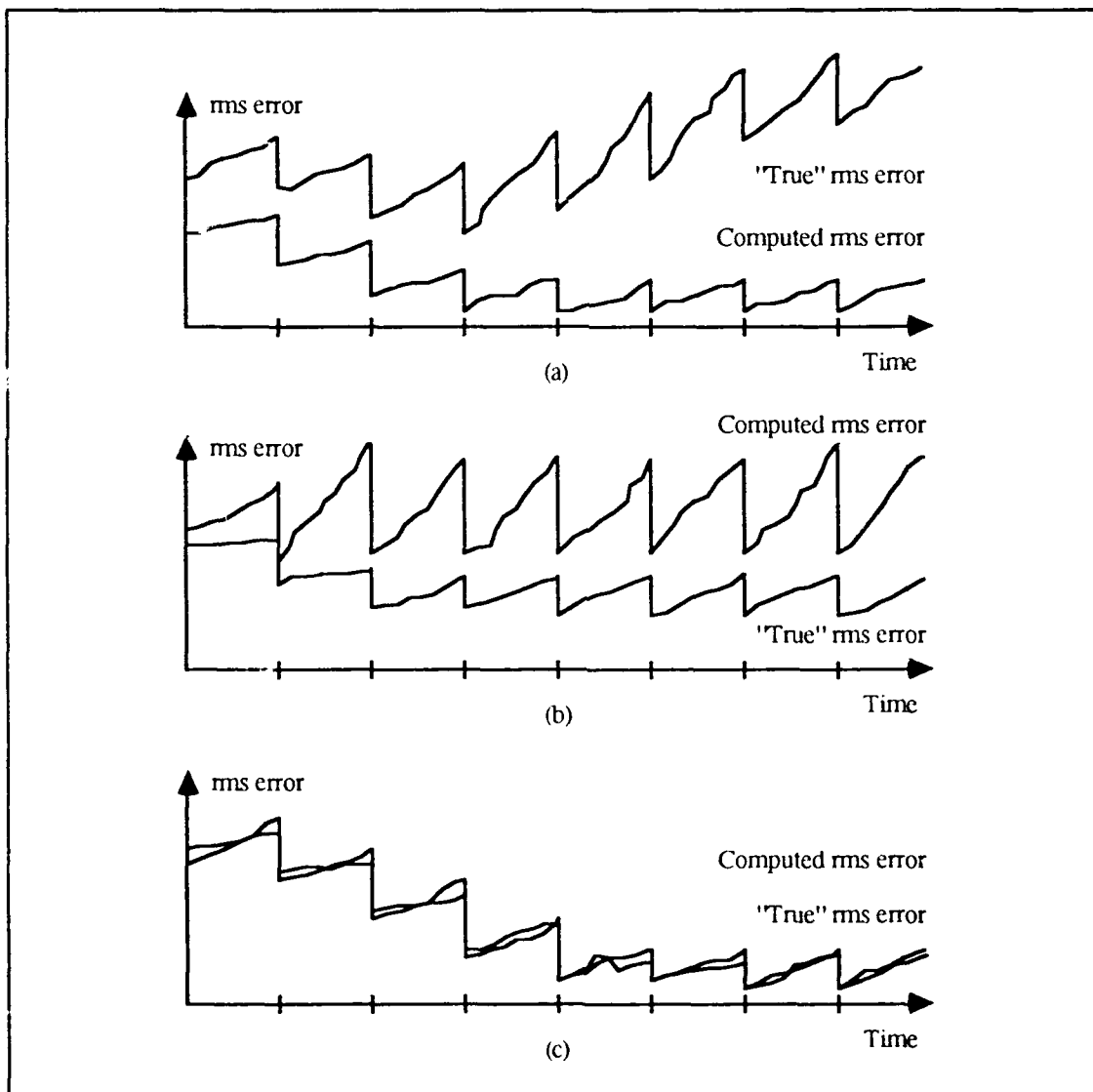


Figure 4.3. Filter Tuning Covariance Analysis: (a) the filter is weighting its internal model too heavily and underestimates its own errors; (b) the filter overestimates its own errors; (c) the filter is properly tuned [12]

## 4.2 State Description

The introduction of this chapter pointed out that the truth model should have as many states as necessary to give a good portrayal of the real world environment in which the filter will operate. The truth model used in this thesis is a result of past theses [10, 21, 26], and is composed of fourteen states. The states are as follows:

2 target dynamic states

6 atmospheric states

4 mechanical bending states

2 pogo oscillation states

The dynamics of the target's intensity centroid on the FLIR plane is the result of target dynamics, atmospheric jitter due to distorted infrared wavefronts, bending/vibration of the optical hardware, and pogo effects of the exhaust plume's oscillatory nature. The location of the true target image on the FLIR plane is measured in pixels from the center of the FOV in the  $x$  and  $y$  FLIR plane directions. The true target location is given by:

$$x_c = x_d + x_a + x_b + x_p \cos \theta_t \quad (4-6)$$

$$y_c = y_d + y_a + y_b - x_p \sin \theta_t \quad (4-7)$$

where

$x_c, y_c$  = target image intensity centroid coordinates

$x_d, y_d$  = coordinate deviation due to target dynamics

$x_a, y_a$  = coordinate deviation due to atmospheric jitter

$x_b, y_b$  = coordinate deviation due to bending/vibration of optical hardware

$x_p$  = coordinate deviation due to pogo oscillations along  
the velocity vector direction

$\theta_t$  = true target orientation angle (refer to Figure 3.7)

Equation (4-7) has a minus sign associated with the pogo component, due to the coordinate definition of the FLIR coordinate frame (refer to Section 3.2.4). The seven output states  $x_d, x_a, x_b, x_p, y_d, y_a, y_b$  comprise the output states, which are used to develop the fourteen stochastic differential equations necessary to describe the truth model mathematically. The states  $x_d$  and  $y_d$  are each modeled by first-order differential equations; the states  $x_b, y_b,$  and  $x_p$  are each modeled using second-order differential equations; and  $x_a$  and  $y_a$  are each modeled with third-order differential equations. The dynamics part of the truth model is made up of these fourteen differential equations when arranged in state-space form.

The rest of this chapter presents the dynamics model, the measurement models that give the Kalman filter periodic measurement updates, and the initial conditions of the truth model equations and target trajectory. Chapter III describes the simulation space in which the models are defined.

### 4.3 Dynamics Model

The mathematical representation for the fourteen-state truth model state vector is the augmentation of a two-state deterministic target dynamics model, a six-state stochastic atmospheric jitter model, a four-state bending/vibration model, and a two-state stochastic plume pogo model. The augmented system is described by a first-order, stochastic differential equation given by:

$$\dot{\mathbf{x}}_t(t) = \mathbf{F}_t \mathbf{x}_t(t) + \mathbf{B}_t \mathbf{u}_t(t) + \mathbf{G}_t \mathbf{w}_t(t) \quad (4-8)$$

where

- $\mathbf{F}_t$  = 14 x 14 time-invariant truth model plant matrix
- $\mathbf{x}_t(t)$  = 14-dimensional truth model state vector
- $\mathbf{B}_t$  = 14 x 2 time-invariant truth model distribution matrix
- $\mathbf{u}_t(t)$  = 2-dimensional deterministic input vector

- $\mathbf{G}_t$  = 14 x 14 noise distribution matrix, ( $\mathbf{G}_t = \mathbf{I}$ )  
 $\mathbf{w}_t(t)$  = 14-dimensional, white Gaussian noise process with unit strength components, and mean and covariance kernel statistics:

$$E\{\mathbf{w}_t(t)\} = \mathbf{0} \quad (4-9)$$

$$E\{\mathbf{w}_t(t)\mathbf{w}_t^T(t+\tau)\} = \mathbf{Q}_t\delta(\tau) \quad (4-10)$$

To simulate the target dynamics model on a digital computer, the following equivalent discrete-time solution to Equation (4-8) is found from linear algebra techniques [12]:

$$\mathbf{x}_t(t_{i+1}) = \Phi_t(t_{i+1}, t_i)\mathbf{x}_t(t_i) + \mathbf{B}_{td}\mathbf{u}_{td}(t_i) + \mathbf{G}_{td}\mathbf{w}_{td}(t_i) \quad (4-11)$$

where the state transition matrix  $\Phi_t(t_{i+1}, t_i)$  is given from solving the differential equation:

$$\frac{d\Phi_t(t, t_i)}{dt} = \mathbf{F}_t\Phi_t(t, t_i) \quad (4-12)$$

with the initial condition:  $\Phi_t(t_i, t_i) = \mathbf{I}$

and

- $\mathbf{x}_t(t_i)$  = 14-dimensional discrete-time truth model state vector  
 $\mathbf{B}_{td}$  = 14 x 2 discrete-time truth model distribution matrix  
 $\mathbf{u}_{td}(t_i)$  = 2-dimensional discrete-time input vector  
 $\mathbf{G}_{td}$  = 14 x 14 discrete-time noise distribution matrix, ( $\mathbf{G}_{td} = \mathbf{I}$ )  
 $\mathbf{w}_{td}(t_i)$  = 12-dimensional discrete-time, white Gaussian noise process with mean and covariance statistics:

$$E\{\mathbf{w}_{td}(t_i)\} = \mathbf{0} \quad (4-13)$$

$$E \left\{ \mathbf{w}_{td}(t_i) \mathbf{w}_{td}^T(t_i) \right\} = \mathbf{Q}_{td} = \int_{t_i}^{t_{i+1}} \Phi_t(t_{i+1}-\tau) \mathbf{G}_t \mathbf{Q}_t \mathbf{G}_t^T \Phi_t^T(t_{i+1}-\tau) d\tau \quad (4-14)$$

where  $\mathbf{Q}_t$  is defined in Equation (4-10). The discrete-time input distribution matrix  $\mathbf{B}_{td}$  is defined as:

$$\mathbf{B}_{td} = \int_{t_i}^{t_{i+1}} \Phi_t(t_{i+1}-\tau) \mathbf{B}_t d\tau \quad (4-15)$$

The discrete-time truth model, like the continuous-time case, consists of two target states, six atmospheric states, four mechanical bending/vibration states, and two plume pogo states. These states are realizable in the  $x$  and  $y$  coordinate axes of the FLIR plane. The fourteen states are oriented in the FLIR plane as:

$x_{FLIR}$	$y_{FLIR}$
1 target state	1 target state
3 atmospheric states	3 atmospheric states
2 bending/vibration states	2 bending/vibration states
2 plume pogo states	

where the plume pogo states are neither  $x_{FLIR}$  nor  $y_{FLIR}$ . These states are augmented into the truth model state vector:

$$\mathbf{x}_t = \begin{bmatrix} \mathbf{x}_d_{(2 \times 1)} \\ \text{---} \\ \mathbf{x}_a_{(6 \times 1)} \\ \text{---} \\ \mathbf{x}_b_{(4 \times 1)} \\ \text{---} \\ \mathbf{x}_p_{(2 \times 1)} \end{bmatrix} \quad (4-16)$$

where

- $\mathbf{x}_d$  = 2-dimensional target dynamics state vector
- $\mathbf{x}_a$  = 6-dimensional atmospheric state vector
- $\mathbf{x}_b$  = 4-dimensional bending/vibration state vector
- $\mathbf{x}_p$  = 2-dimensional plume pogo state vector

The discrete-time truth model state transition matrix  $\Phi_t$  is given as:

$$\Phi_t = \begin{bmatrix} \Phi_{d(2 \times 2)} & \mathbf{0}_{(2 \times 2)} & \mathbf{0}_{(2 \times 4)} & \mathbf{0}_{(2 \times 2)} \\ \mathbf{0}_{(6 \times 2)} & \Phi_{a(6 \times 6)} & \mathbf{0}_{(6 \times 4)} & \mathbf{0}_{(6 \times 2)} \\ \mathbf{0}_{(4 \times 2)} & \mathbf{0}_{(4 \times 6)} & \Phi_{b(4 \times 4)} & \mathbf{0}_{(4 \times 2)} \\ \mathbf{0}_{(2 \times 2)} & \mathbf{0}_{(2 \times 6)} & \mathbf{0}_{(2 \times 4)} & \Phi_{p(2 \times 2)} \end{bmatrix} \quad (4-17)$$

The discrete-time truth model distribution matrix  $\mathbf{B}_{td}$  is given by:

$$\mathbf{B}_{td} = \begin{bmatrix} \mathbf{B}_{dd(2 \times 2)} \\ \mathbf{0}_{(6 \times 2)} \\ \mathbf{0}_{(4 \times 2)} \\ \mathbf{0}_{(2 \times 2)} \end{bmatrix} \quad (4-18)$$

The discrete-time truth model white Gaussian noise process  $\mathbf{w}_{td}$  is given by:

$$\mathbf{w}_{td} = \begin{bmatrix} \mathbf{0}_{(2 \times 1)} \\ \mathbf{w}_{da(6 \times 1)} \\ \mathbf{w}_{db(4 \times 1)} \\ \mathbf{w}_{dp(2 \times 1)} \end{bmatrix} \quad (4-19)$$

where

- $w_{da}(t_i)$  = 6-dimensional discrete-time, white Gaussian noise  
related to atmospheric jitter states
- $w_{db}(t_i)$  = 4-dimensional discrete-time, white Gaussian noise  
related to bending states
- $w_{dp}(t_i)$  = 2-dimensional discrete-time, white Gaussian noise  
related to plume pogo states

From Equations (4-11) and (4-16) through (4-19), it can be seen that the truth model is in a block diagonal form, which permits the models for target dynamics, atmospheric jitter, bending/vibration, and plume pogo to be presented separately. The following sections provide a detailed evaluation of each of the discrete state models which form the stochastic discrete-time truth model.

*4.3.1 Target Model State Description.* The  $\alpha$ - $\beta$  plane (FLIR image plane, Section 3.2.4) is coincident with the FLIR sensor FOV (Figure 3.3), and perpendicular to the LOS vector  $\mathbf{e}_r$ . In the simulation, the 3-dimensional target dynamics are projected onto the FLIR image plane. As discussed in Section 3.2.4, the position and velocity components of the target's intensity centroid are obtained from the azimuth and elevation displacement angles ( $\alpha'$  and  $\beta'$ , respectively). Since the distance to the target is simulated as 2,000 kilometers, small angle approximations are used in approximating the angle displacements to the cartesian coordinate system of the FLIR image plane. These "pseudo" angles  $\alpha'$  and  $\beta'$  are referenced from the current LOS vector, as shown in Figure 4.4.

The pseudo angles  $\alpha'$  and  $\beta'$  are measured in microradians, and the linear translational coordinates  $x_d$  and  $y_d$ , which locate the target intensity function on the FLIR plane, are measured in pixels of displacement from the center of the FLIR FOV. These two measurements are related by the pixel proportionality constant  $k_p$ , which is the angular

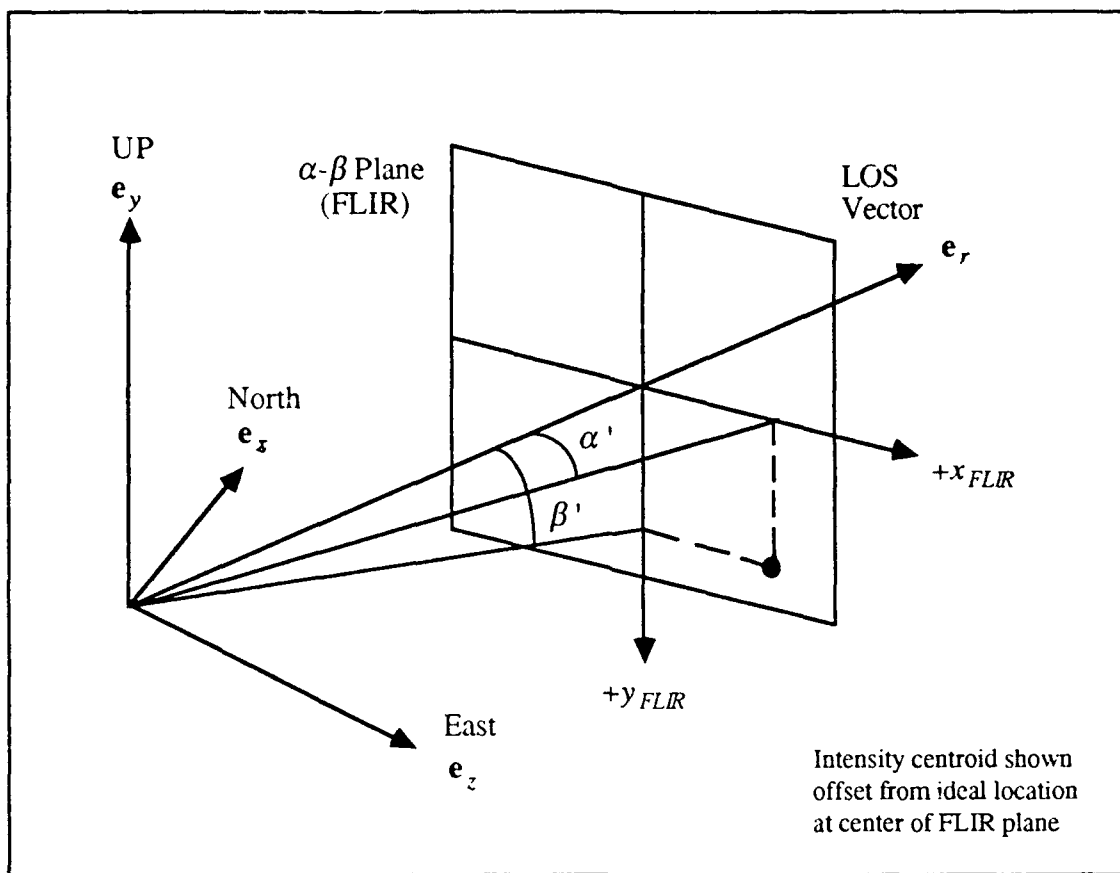


Figure 4.4. Target Image on  $\alpha$ - $\beta$  Plane with "Pseudo" Angles

FOV of a single pixel. The pixel proportionality constant used in this research is approximately 15 microradians/pixel. This value is carried over from previous research [2, 26]. Prior to this current value for the pixel proportionality constant, the value of 20 microradians/pixel was used [4, 6, 9, 10, 11, 21, 22, 24, 25, 27, 28, 29, 30]. The value was reduced for the study of long-range targets to improve the resolution of the target's intensity centroid on the FLIR image plane. This finer resolution of the FLIR allows the  $8 \times 8$  FOV to "see" the shape of the target's intensity function.

The derivation of the state space model of the target dynamics begins by assuming that the azimuth and elevation rates ( $\dot{\alpha}'$  and  $\dot{\beta}'$ , respectively) remain essentially constant over each sample period  $\Delta t$  (i.e.,  $t_{i+1} - t_i$ ). Then the discrete targets dynamics model is:



$$x_d(t_{i+1}) = x_d(t_i) + \frac{(\dot{\alpha}')(\Delta t)}{k_p} \quad (4-20)$$

$$y_d(t_{i+1}) = y_d(t_i) - \frac{(\dot{\beta}')(\Delta t)}{k_p} \quad (4-21)$$

Arranging these equations in state space form yields:

$$\mathbf{x}_d(t_{i+1}) = \Phi_d(t_{i+1}, t_i)\mathbf{x}_d(t_i) + \mathbf{B}_d \mathbf{u}_d(t_i) \quad (4-22a)$$

$$\begin{bmatrix} x_d(t_{i+1}) \\ y_d(t_{i+1}) \end{bmatrix} = \begin{bmatrix} 1 & 0 \\ 0 & 1 \end{bmatrix} \begin{bmatrix} x_d(t_i) \\ y_d(t_i) \end{bmatrix} + \begin{bmatrix} \frac{\Delta t}{k_p} & 0 \\ 0 & -\frac{\Delta t}{k_p} \end{bmatrix} \begin{bmatrix} \dot{\alpha}'(t_i) \\ \dot{\beta}'(t_i) \end{bmatrix} \quad (4-22b)$$

where

$$\dot{\alpha}'(t_i) = \frac{d\alpha'}{dt}, \text{ measured in microradians/second and constant over the time interval } \Delta t$$

$$\dot{\beta}'(t_i) = \frac{d\beta'}{dt}, \text{ measured in microradians/second and constant over the time interval } \Delta t$$

$$\Delta t = \text{sample time interval, } t_{i+1} - t_i$$

$$k_p = \text{pixel proportionality constant (15 microradians/pixel)}$$

Using these relationships in block form of the overall truth model, by inspection of Equation (4-17), the upper left block is:

$$\Phi_d_{(2 \times 2)} = \begin{bmatrix} 1 & 0 \\ 0 & 1 \end{bmatrix} \quad (4-23)$$

and the upper block of Equation (4-18) is:

$$\mathbf{B}_d d_{(2 \times 2)} = \begin{bmatrix} \frac{\Delta t}{k_p} & 0 \\ 0 & -\frac{\Delta t}{k_p} \end{bmatrix} \quad (4-24)$$

and the input vector in Equation (4-11) is given by:

$$\mathbf{u}_{t_d(2 \times 2)} = \begin{bmatrix} \dot{\alpha}'(t_i) \\ \dot{\beta}'(t_i) \end{bmatrix} \quad (4-25)$$

The minus sign of the lower right term in Equation (4-24) is due to the difference in the  $y$  axis orientations between the inertial coordinate frame and the FLIR coordinate plane (refer to Figures 3.1 and 3.2).

The two target dynamic states of Equation (4-16) are used to propagate the missile along its trajectory. The trajectory is represented on the FLIR image plane by the  $x_d$  and  $y_d$  position coordinates. This truth model deterministic trajectory could have been contained in "look-up" tables, where the exact coordinates of the missile's position are stored for every time increment of the simulation. There are two advantages to representing the deterministic truth model in the form of Equation (4-22). First, Equation (4-22) can be substituted back into Equation (4-10) to form a single augmented vector differential equation that defines the truth model. Second, since Equation (4-22) is in state space form, white (or time-correlated) noise can be added, if desired, to account for non-deterministic type terms such as wind-buffeting or solar effects acting on the missile's hardbody. The latter advantage can provide further testing of the Kalman filter algorithm.

*4.3.2 Atmospheric Jitter Model.* The atmospheric jitter model used in the simulation was developed in coordination with the AFWL [21]. The process used to model the translational displacement of the intensity function due to disturbances in the atmosphere is based on a study by The Analytic Sciences Corporation [21]. Using power spectral density characteristics, the atmospheric jitter phenomenon is modeled as the output of a third-order shaping filter driven by white Gaussian noise [21]. The empirical power spectral density and the shaping filter approximation are shown graphically in Figure 4.5.

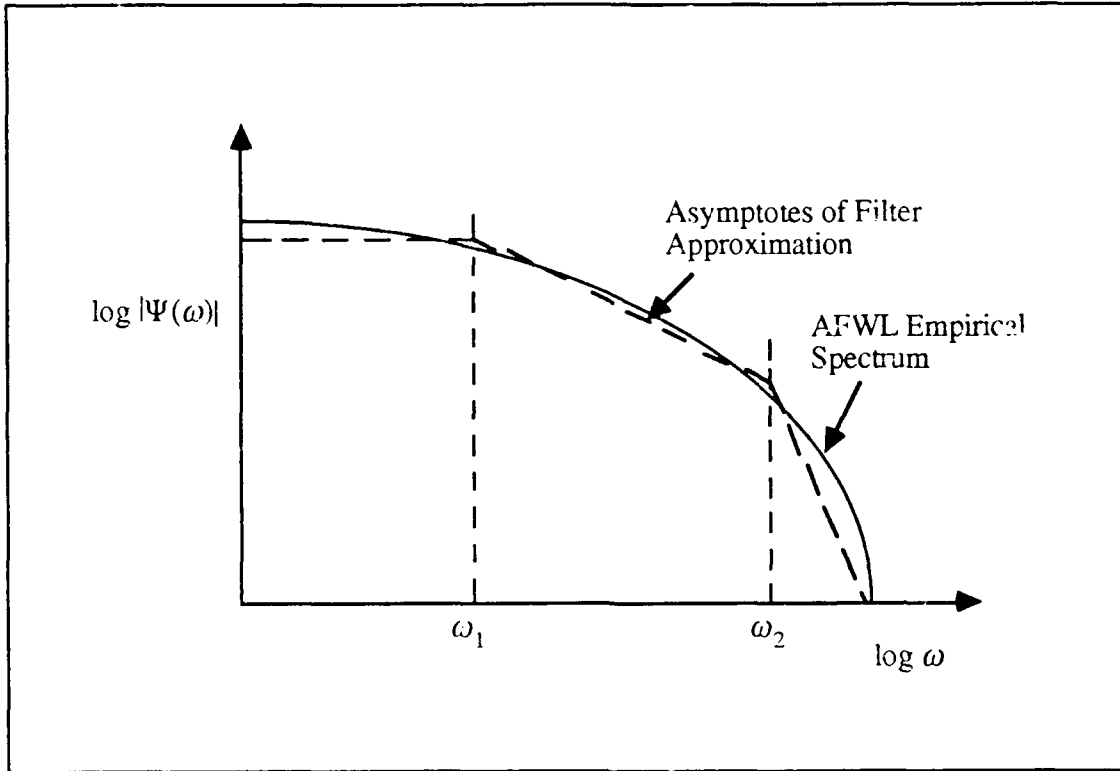


Figure 4.5. Atmospheric Turbulence Spectral Representation and Filter Approximation [21]

With this model, one can identify the effects of the atmospheric disturbance on the FLIR plane target image. The Laplace domain representation of this shaping filter transfer function is given by:

$$\frac{x_a(s)}{w_a(s)} = \frac{K_a \omega_1 \omega_2^2}{(s + \omega_1)(s + \omega_2)^2} \quad (4-26)$$

where

- $x_a$  = output of shaping filter
- $w_a$  = zero-mean, scalar, unit-strength white Gaussian noise
- $K_a$  = gain, adjusted for desired atmospheric jitter rms value
- $\omega_1$  = break frequency, 14.14 radians/second
- $\omega_2$  = double-pole break frequency, 659.5 radians/second

The atmospheric jitter model in the  $y_{\text{FLIR}}$  direction is identically modeled as the shaping filter in the  $x_{\text{FLIR}}$  direction, where  $y_a$  is the same output of the shaping filter defined in Equation (4-26). The two shaping filters are assumed to be independent of each other. Each shaping filter is composed of three states to comprise the six atmospheric states of the second block on the right side of Equation (4-16). The atmospheric jitter can be expressed in Jordan canonical form as [21]:

$$\dot{\mathbf{x}}_a(t) = \mathbf{F}_a \mathbf{x}_a(t) + \mathbf{G}_a \mathbf{w}_a(t) \quad (4-27)$$

where

- $\mathbf{F}_a$  = 6 x 6 time-invariant atmospheric plant matrix
- $\mathbf{x}_a(t)$  = 6-dimensional atmospheric state vector
- $\mathbf{G}_a$  = 2 x 6 noise distribution matrix
- $\mathbf{w}_a(t)$  = 2-dimensional, independent, white Gaussian noise process with unit strength components, and mean and covariance statistics:

$$E\{\mathbf{w}_a(t)\} = \mathbf{0} \quad (4-28)$$

$$E\{\mathbf{w}_a(t)\mathbf{w}_a^T(t+\tau)\} = \mathbf{Q}_a \delta(\tau) = \begin{bmatrix} 1 & 0 \\ 0 & 1 \end{bmatrix} \delta(\tau) \quad (4-29)$$

The atmospheric plant matrix  $\mathbf{F}_a$  is defined as:

$$\mathbf{F}_a = \begin{bmatrix} -\omega_1 & 0 & 0 & 0 & 0 & 0 \\ 0 & -\omega_2 & 0 & 0 & 0 & 0 \\ 0 & 0 & -\omega_2 & 0 & 0 & 0 \\ 0 & 0 & 0 & -\omega_1 & 0 & 0 \\ 0 & 0 & 0 & 0 & -\omega_2 & 0 \\ 0 & 0 & 0 & 0 & 0 & -\omega_2 \end{bmatrix} \quad (4-30)$$

The noise distribution matrix  $\mathbf{G}_a$  is:

$$\mathbf{G}_a = \begin{bmatrix} \frac{K_a^2 \omega_1 \omega_2^2}{(\omega_1 - \omega_2)^2} & 0 \\ -\frac{K_a^2 \omega_1 \omega_2^2}{(\omega_1 - \omega_2)} & 0 \\ \frac{K_a^2 \omega_1 \omega_2^2}{(\omega_1 - \omega_2)} & 0 \\ 0 & \frac{K_a^2 \omega_1 \omega_2^2}{(\omega_1 - \omega_2)^2} \\ 0 & -\frac{K_a^2 \omega_1 \omega_2^2}{(\omega_1 - \omega_2)} \\ 0 & \frac{K_a^2 \omega_1 \omega_2^2}{(\omega_1 - \omega_2)} \end{bmatrix} \quad (4-31)$$

To simulate the atmospheric jitter model on a digital computer, the discrete-time equivalent to Equation (4-27) is the atmospheric jitter partition of the augmented truth model in Equation (4-10), and is given by:

$$\mathbf{x}_a(t_{i+1}) = \Phi_a(t_{i+1}, t_i) \mathbf{x}_a(t_i) + \mathbf{w}_{da}(t_i) \quad (4-32)$$

The state transition matrix in Jordan canonical form for the time-invariant plant matrix  $\Phi_a$  of Equation (4-27) is given by [21]:

$$\Phi_a(\Delta t) = \begin{bmatrix} \Phi_{a11} & 0 & 0 & 0 & 0 & 0 \\ 0 & \Phi_{a22} & \Phi_{a23} & 0 & 0 & 0 \\ 0 & 0 & \Phi_{a33} & 0 & 0 & 0 \\ 0 & 0 & 0 & \Phi_{a44} & 0 & 0 \\ 0 & 0 & 0 & 0 & \Phi_{a55} & \Phi_{a56} \\ 0 & 0 & 0 & 0 & 0 & \Phi_{a66} \end{bmatrix} \quad (4-33)$$

where

$$\begin{aligned}
 \Phi_{a11} &= \Phi_{a44} = \exp(-\omega_1 \Delta t) \\
 \Phi_{a22} &= \Phi_{a55} = \exp(-\omega_2 \Delta t) \\
 \Phi_{a23} &= \Phi_{a56} = \Delta t \exp(-\omega_2 \Delta t) \\
 \Phi_{a33} &= \Phi_{a66} = \exp(-\omega_2 \Delta t) \\
 \Delta t &= \text{sample time interval, } t_{i+1} - t_i
 \end{aligned}$$

The 6-dimensional, discrete-time, white Gaussian noise  $\mathbf{w}_{da}(t_i)$  process has mean and covariance statistics defined by:

$$E\{\mathbf{w}_{da}(t_i)\} = \mathbf{0} \quad (4-34)$$

$$E\{\mathbf{w}_{da}(t_i)\mathbf{w}_{da}^T(t_i)\} = \mathbf{Q}_{da} = \int_{t_i}^{t_{i+1}} \Phi_a(t_{i+1}-\tau) \mathbf{G}_a \mathbf{Q}_a \mathbf{G}_a^T \Phi_a^T(t_{i+1}-\tau) d\tau \quad (4-35)$$

*4.3.3 Bending/Vibration Model.* The mechanical bending states, which occupy the third block in Equation (4-16), were added to the truth model [10] to account for the vibrational phenomenon that exists for a non-rigid optical platform involved in collecting the IR image data of the plume. Based on tests at the AFWL, it was concluded that the bending phenomenon in both the  $x_{\text{FLIR}}$  and  $y_{\text{FLIR}}$  directions can be represented by the output of a second-order shaping filter driven by white Gaussian noise. The second order model is a good representation of the bending/vibration phenomenon. The dominant vibration response and the filter approximation are shown graphically in Figure 4.6. The Laplace domain transfer function for the bending model is [10]:

$$\frac{x_b(s)}{w_b(s)} = \frac{K_b \omega_{nb}^2}{s^2 + 2\zeta_b \omega_{nb} s + \omega_{nb}^2} \quad (4-36)$$

where

- $x_b$  = mechanical bending disturbance
- $w_b$  = zero-mean, unit strength, white Gaussian noise
- $K_b$  = gain adjustment to obtain desired rms bending output,  
( $K_b^2 = 5 \times 10^{-13} \text{ rad}^4/\text{sec}^4$ )
- $\zeta_b$  = damping coefficient, equal to 0.15
- $\omega_{nb}$  = undamped natural frequency for bending, ( $\omega_{nb} = \pi \text{ rad/sec}$ )

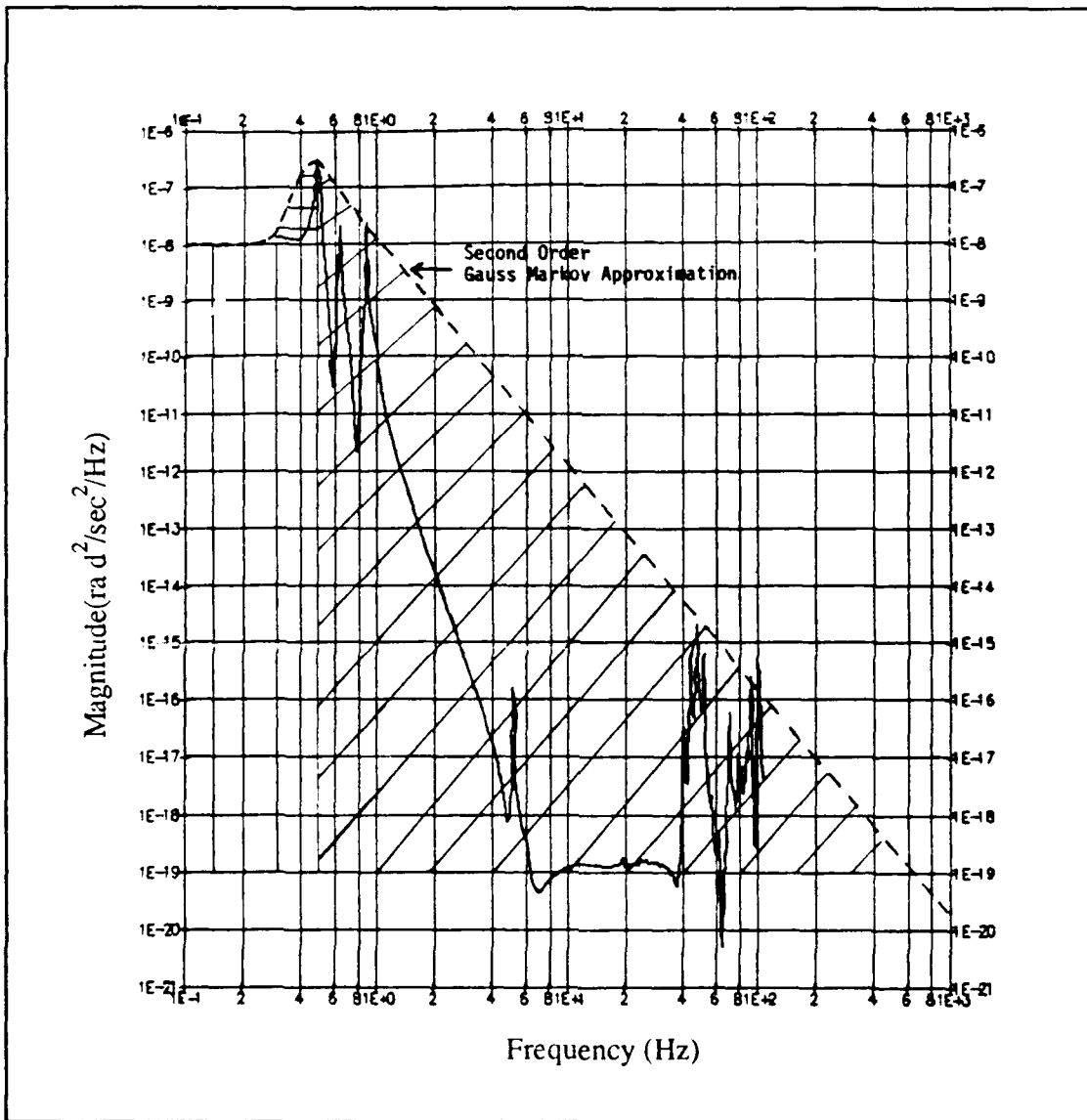


Figure 4.6. Dominant Vibration Response Spectrum [10]

The bending/vibration model in the  $y_{FLIR}$  direction is identically modeled as the shaping filter in the  $x_{FLIR}$  direction, where  $y_b$  is the same output of the shaping filter defined in Equation (4-36). The two shaping filters are assumed to be independent of each other. Each shaping filter is composed of two states to comprise the four bending/vibration states of the third block on the right side of Equation (4-16).

The linear stochastic differential equation that describes the bending/vibration is given by:

$$\dot{\mathbf{x}}_b(t) = \mathbf{F}_b \mathbf{x}_b(t) + \mathbf{G}_b \mathbf{w}_b(t) \quad (4-37)$$

where

- $\mathbf{F}_b$  = 4 x 4 time-invariant bending plant matrix
- $\mathbf{x}_b(t)$  = 4-dimensional mechanical bending state vector
- $\mathbf{G}_b$  = 4 x 2 noise distribution matrix
- $\mathbf{w}_b(t)$  = 2-dimensional, independent, white Gaussian noise process with unit strength components:

$$E\{\mathbf{w}_b(t)\} = \mathbf{0} \quad (4-38)$$

$$E\{\mathbf{w}_b(t)\mathbf{w}_b^T(t+\tau)\} = \mathbf{Q}_b \delta(\tau) = \begin{bmatrix} 1 & 0 \\ 0 & 1 \end{bmatrix} \delta(\tau) \quad (4-39)$$

The bending vibration plant  $\mathbf{F}_b$  is defined as:

$$\mathbf{F}_b = \begin{bmatrix} 0 & 1 & 0 & 0 \\ -\omega_{nb}^2 & -2\zeta_b \omega_{nb} & 0 & 0 \\ 0 & 0 & 0 & 1 \\ 0 & 0 & -\omega_{nb}^2 & -2\zeta_b \omega_{nb} \end{bmatrix} \quad (4-40)$$



The noise distribution matrix  $\mathbf{G}_b$  is:

$$\mathbf{G}_b = \begin{bmatrix} 0 & 0 \\ K_b \omega_n^2 & 0 \\ 0 & 0 \\ 0 & K_b \omega_n^2 \end{bmatrix} \quad (4-41)$$

To simulate the bending/vibration model on a digital computer, the discrete-time equivalent to Equation (4-37) is the bending/vibration partition of the augmented truth model in Equation (4-10), and is given by:

$$\mathbf{x}_b(t_{i+1}) = \Phi_b(t_{i+1}, t_i) \mathbf{x}_b(t_i) + \mathbf{w}_{db}(t_i) \quad (4-42)$$

The state transition matrix in Jordan canonical form for the time-invariant plant matrix  $\Phi_b$  of Equation (4-37) is given by [10]:

$$\Phi_b(\Delta t) = \begin{bmatrix} \Phi_{b11} & \Phi_{b12} & 0 & 0 \\ \Phi_{b21} & \Phi_{b22} & 0 & 0 \\ 0 & 0 & \Phi_{b33} & \Phi_{b34} \\ 0 & 0 & \Phi_{b43} & \Phi_{b44} \end{bmatrix} \quad (4-43)$$

where

$$\Phi_{b11} = \Phi_{b33} = \exp(-\sigma_b \Delta t) [\cos(\omega_b \Delta t) + \frac{\sigma_b}{\omega_b} \sin(\omega_b \Delta t)]$$

$$\Phi_{b12} = \Phi_{b34} = \exp(-\sigma_b \Delta t) [\frac{1}{\sigma_b} \sin(\omega_b \Delta t)]$$

$$\Phi_{b21} = \Phi_{b43} = \exp(-\sigma_b \Delta t) [-1 - (\frac{\sigma_b}{\omega_b})^2 \sin(\omega_b \Delta t)]$$

$$\Phi_{b22} = \Phi_{b44} = \exp(-\sigma_b \Delta t) [\cos(\omega_b \Delta t) - \frac{\sigma_b}{\omega_b} \sin(\omega_b \Delta t)]$$

$$\Delta t = \text{sample time interval, } t_{i+1} - t_i$$

$$\sigma_b = \text{real part of the root of the characteristic equation in Equation (4-36), } (\sigma_b = -0.47124 \text{ second}^{-1})$$

$$\omega_b = \text{imaginary part of the root of the characteristic equation in Equation (4-36), } (\omega_b = 3.10605 \text{ radians/second})$$

The 4-dimensional, discrete-time, white Gaussian noise process vector  $\mathbf{w}_{db}(t_i)$  has mean and covariance statistics:

$$E \{ \mathbf{w}_{db}(t_i) \} = \mathbf{0} \quad (4-44)$$

$$E \{ \mathbf{w}_{db}(t_i) \mathbf{w}_{db}^T(t_i) \} = \mathbf{Q}_{db} = \int_{t_i}^{t_{i+1}} \Phi_b(t_{i+1}-\tau) \mathbf{G}_b \mathbf{Q}_b \mathbf{G}_b^T \Phi_b^T(t_{i+1}-\tau) d\tau \quad (4-45)$$

*4.3.4 Plume Pogo Model.* The plume pogo model was developed [26] to account for the oscillatory plume phenomenon of a typical missile in the boost phase of flight. Though experimental data was unavailable, a second-order Gauss-Markov model was developed using physical insight, and visual observation of the pogo effect on various missiles in flight. The model allows for the study of the amplitude and frequency characteristics of the oscillatory nature of the plume, and the effect this phenomenon has on tracking a missile using a Kalman filter.

To implement the pogo phenomenon in the 8 x 8 FOV, the non-oscillating plume is designed to "fit" into a 5 x 5 FOV window (within the 8 x 8 FLIR FOV). Based on this assumption, and the 2,000 kilometer range of the target from the FLIR plane, the referenced hotspot dispersion in the  $\mathbf{e}_{pv}$  direction of the target frame (Equation 3-8) is chosen to be 1 pixel when projected onto the FLIR image plane. With an intensity centroid aspect ratio of 1.5, the hotspot dispersion along the  $\mathbf{e}_v$  direction is 1.5 pixels when projected onto the FLIR image plane. The pixel proportionality constant  $k_p$  required to meet these specifications is on the order of 15 microradians/pixel, as presented in Section 4.3.1.

The second-order shaping filter driven by white Gaussian noise is described in the Laplace domain by the following transfer function:

$$\frac{x_p(s)}{w_p(s)} = \frac{K_p \omega_{np}^2}{s^2 + 2\zeta_p \omega_{np} s + \omega_{np}^2} \quad (4-46)$$

where

- $x_p$  = plume pogo shaping filter output along the direction of the velocity vector
- $w_p$  = zero-mean, unit strength, white Gaussian noise
- $\zeta_p$  = assumed damping coefficient, ( $\zeta = 0.05$ )
- $\omega_{np}$  = nominal undamped natural frequency for pogo; assumed range is 0.1 - 10 Hertz, with a nominal value of 1.0 Hertz
- $K_p$  = gain adjustment to obtain desired rms pogo amplitude determined by [26]:

$$K_p = 2\sigma_p \sqrt{\frac{\zeta_p}{\omega_{np}}} \quad (4-47)$$

where

- $\sigma_p$  = desired rms pogo along the velocity vector of the missile

Oscillations due to this effect are modeled along the direction of the missile velocity vector. The mathematical expression that describes the pogo effect takes the form of a two-state linear stochastic differential equation given by:

$$\dot{\mathbf{x}}_p(t_i) = \begin{bmatrix} 0 & 1 \\ -\omega_{np}^2 & -2\zeta_p \omega_{np} \end{bmatrix} \mathbf{x}_p(t) + \begin{bmatrix} 0 \\ K_p \omega_{np} \end{bmatrix} w_p(t) \quad (4-48)$$

where

- $\mathbf{x}_p(t)$  = 2-dimensional pogo state vector derived from Equation (4-46)
- $w_p(t)$  = 1-dimensional zero-mean, white Gaussian noise of unit strength:

$$E \{w_p(t)\} = 0 \quad (4-49)$$

$$E \{w_p(t)w_p(t+\tau)\} = Q_p \delta(t-\tau); \quad Q_p = 1 \quad (4-50)$$

To simulate the pogo model on a digital computer, the following equivalent discrete-time model for Equation (4-48) is the pogo partition of the augmented truth model in Equation (4-10):

$$\mathbf{x}_p(t_{i+1}) = \Phi_p(t_{i+1}, t_i)\mathbf{x}_p(t_i) + \mathbf{w}_{dp}(t_i) \quad (4-51a)$$

$$\mathbf{x}_p(t_{i+1}) = \begin{bmatrix} \Phi_{p11}(\Delta t) & \Phi_{p12}(\Delta t) \\ \Phi_{p21}(\Delta t) & \Phi_{p22}(\Delta t) \end{bmatrix} \mathbf{x}_p(t_i) + \mathbf{w}_{dp}(t_i) \quad (4-51b)$$

where

$$\Phi_{p11}(\Delta t) = \frac{1}{\sqrt{1-\zeta_p^2}} \exp(-\zeta_p \omega_{np} \Delta t) \sin[\omega_{np} \sqrt{1-\zeta_p^2} \Delta t + \arctan(\frac{\sqrt{1-\zeta_p^2}}{\zeta_p})]$$

$$\Phi_{p12}(\Delta t) = \frac{-\omega_{np}}{\sqrt{1-\zeta_p^2}} \exp(-\zeta_p \omega_{np} \Delta t) \sin(\omega_{np} \sqrt{1-\zeta_p^2} \Delta t)$$

$$\Phi_{p21}(\Delta t) = \frac{-\omega_{np}}{\sqrt{1-\zeta_p^2}} \exp(-\zeta_p \omega_{np} \Delta t) \sin(\omega_{np} \sqrt{1-\zeta_p^2} \Delta t)$$

$$\Phi_{p22}(\Delta t) = \frac{1}{\sqrt{1-\zeta_p^2}} \exp(-\zeta_p \omega_{np} \Delta t) \sin[\omega_{np} \sqrt{1-\zeta_p^2} \Delta t + \arctan(\frac{\sqrt{1-\zeta_p^2}}{-\zeta_p}) + \pi]$$

$$\Delta t = \text{sample time interval, } t_{i+1} - t_i$$

The 2-dimensional, discrete-time, white Gaussian noise process  $\mathbf{w}_{dp}(t_i)$  has mean and covariance statistics:

$$E \{\mathbf{w}_{dp}(t_i)\} = \mathbf{0} \quad (4-52)$$

$$E \{\mathbf{w}_{dp}(t_i)\mathbf{w}_{dp}^T(t_i)\} = \mathbf{Q}_{dp} = \int_{t_i}^{t_{i+1}} \Phi_p(t_{i+1}-\tau) \mathbf{G}_p \mathbf{Q}_p \mathbf{G}_p^T \Phi_p^T(t_{i+1}-\tau) d\tau \quad (4-53)$$

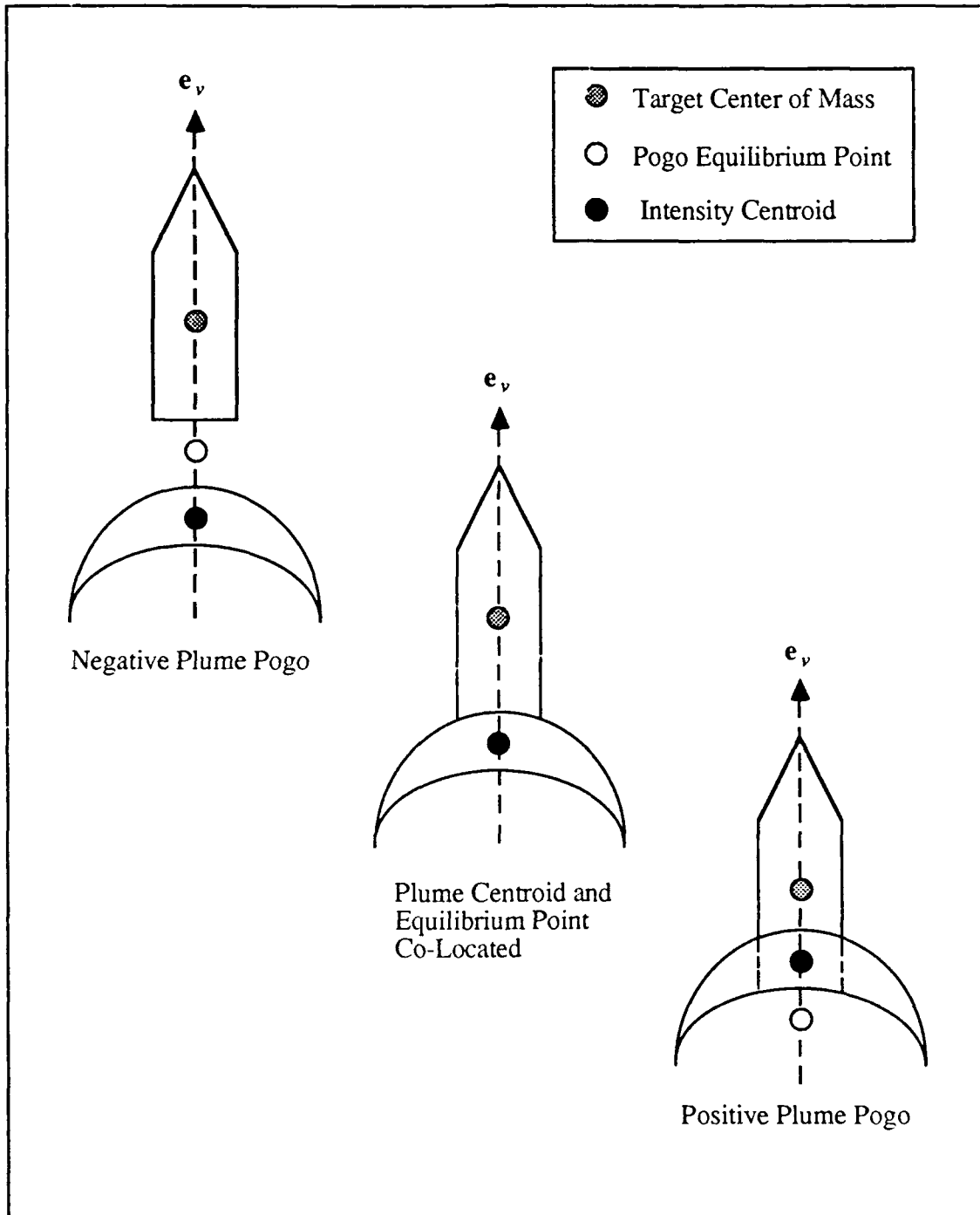


Figure 4.7. Plume Pogo Oscillation Relative to the Equilibrium Point

The 2-dimensional pogo state vector represents the position of the plume image intensity centroid and its velocity along the longitudinal axis of the missile. As shown in Figure 4.7, the plume oscillates about an equilibrium point also located on the longitudinal

axis. The location of this equilibrium point is defined by the initial positions of the two intensity functions in the target coordinate frame (refer to Section 3.3.2 and Figure 3.6). The equilibrium point remains equidistant from the hard body center-of-mass throughout the simulation. Figure 4.7 shows the location of the equilibrium point relative to the plume's centroid for both positive and negative pogo. (The crescent-shaped plume shown in Figure 4.7 is one of many equal-intensity contour lines of the actual plume.) For the simulation, it is assumed that the velocity vector lies coincident with the longitudinal axis of the missile. As stated in Section 3.5, the angle of attack and sideslip angle of the missile are also assumed negligible, and have zero values for the simulation. [26]

#### *4.4 Measurement Models*

In the simulation, the truth model provides discrete measurements to the filter in place of the real world measurements from physical sensors. The Kalman filter depends on the accuracy of these measurements to update its state estimate, then propagates the result to the next measurement update. Two different types of measurements are provided to the filter during the course of the simulation. The 8 x 8 pixel FLIR sensor array provides measurements on the position of the intensity centroid of the target, while the low-energy laser and associated sensor provide information on the location of the target hardbody center-of-mass relative to the target center of intensity. The FLIR measurement is given to the filter every 1/30 second. The filter estimation of the intensity centroid is used as a starting point for the low-energy laser scan. For the one-state center-of-mass filter, the low-energy laser is scanned along the filter estimated velocity vector. For the eight-state filter, which is an augmentation of the six-state FLIR filter and a two-state center-of-mass filter, the low-energy laser is scanned along the six-state filter estimated velocity vector until the first reflection; then on subsequent low-energy laser scanning, the laser scan direction is based on the two-state filter estimate of the scan direction (using the two filter estimated bias states). For both filters, a center-of-mass measurement is provided to the

filter only if the laser "hits" the hardbody (i.e., laser reflection occurs). Sweeping of the low-energy laser about the velocity vector provides increased reflection returns, and improves the estimate of the hardbody center-of-mass; this is discussed in more detail in Sections 5.3 and 5.4. The measurement models, which are used to simulate the 8 x 8 FLIR sensor array and the low-energy laser reflection returns, are discussed in the following two sections.

*4.4.1 FLIR Model.* The FLIR sensor is composed of an 8 x 8 array of pixels which are sensitive to IR signals (actually extracted out of a larger total array of 300 x 500 pixels), and tracks the plume intensity centroid, or "hotspot", of the target. As discussed in Section 3.3.2, the intensity function of the missile's plume projection on the FLIR focal plane is modeled as the difference of two bivariate Gaussian intensity functions, as shown in Figure 3.5, and also in Figure 4.8. The form of the (non-Gaussian) plume is obtained

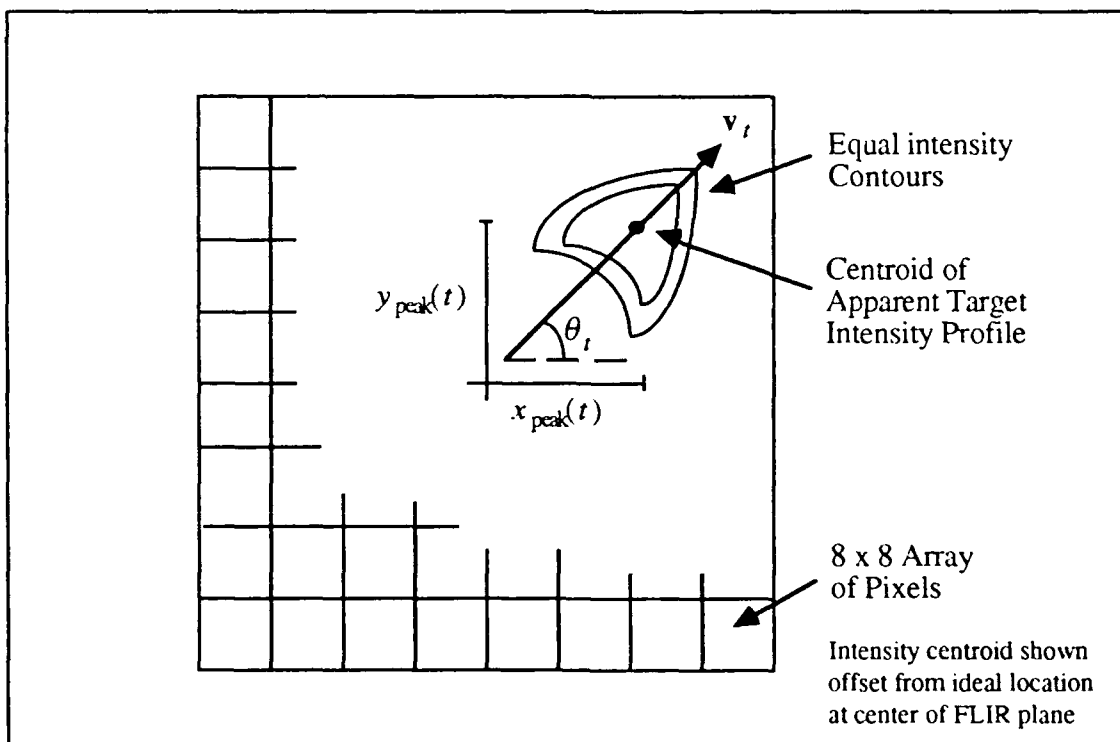


Figure 4.8. Resulting Target Intensity Function on FLIR Image Plane for Difference Between Two Gaussian Intensity Functions

by subtracting the "trailing" intensity function from the "leading" intensity function (as shown in Figures 3.5 and 3.6), the characteristic size and shape of a ballistic missile's plume at a particular altitude is well modeled. This data is corrupted by spatially correlated and temporally uncorrelated background noise according to models of actual data taken from a FLIR sensor looking at various backgrounds [25].

For this model to be useful, several parameters must be known: the size of the major and minor axes of the elliptical contours of each bivariate Gaussian function, and the orientation of the principal axes in the FLIR image plane. The intensity measurement produced by each pixel of the FLIR FOV is the average intensity on that pixel that results from the sum of the target's intensity function, and the correlated background and FLIR noises. For the 8 rows and the 8 columns of the FOV, the intensity measurement corresponding to the pixel in the  $j^{th}$  row and  $k^{th}$  column at sampling time  $t_i$  is given by:

$$z_{jk}(t_i) = \frac{1}{A_p} \int_{\text{pixel},k} \left\{ I_1[x,y,x_{\text{peak}_1}(t_i),y_{\text{peak}_1}(t_i)] - I_2[x,y,x_{\text{peak}_2}(t_i),y_{\text{peak}_2}(t_i)] \right\} dx dy + n_{jk}(t_i) + b_{jk}(t_i) \quad (4-54)$$

where

- $z_{jk}(t_i)$  = output of pixel in the  $j^{th}$  row and  $k^{th}$  column
- $A_p$  = area of one pixel
- $I_1, I_2$  = intensity function of first and second Gaussian intensity function, respectively
- $x, y$  = coordinates of any point within pixel  $jk$
- $x_{\text{peak}_1}, y_{\text{peak}_1}$  = coordinates of maximum point of the first Gaussian intensity function
- $x_{\text{peak}_2}, y_{\text{peak}_2}$  = coordinates of maximum point of the second Gaussian intensity function



- $n_{jk}(t_i)$  = effect of internal FLIR sensor noise on pixel  
in the  $j^{th}$  row and  $k^{th}$  column
- $b_{jk}(t_i)$  = effect of spatially correlated background noise on pixel  
in the  $j^{th}$  row and  $k^{th}$  column

The FLIR sensor noise,  $n_{jk}(t_i)$ , is the result of thermal noise and dark current in the IR sensitive detectors (pixels). This noise is assumed to be a corrupted noise which is both temporally and spatially uncorrelated [26]. The spatially correlated background noise  $b_{jk}(t_i)$  development is covered in the next section.

*4.4.1.1 Spatially Correlated Background Noise.* The existence of spatially correlated background noise,  $b_{jk}(t_i)$ , in FLIR data was observed during a tracking operation by personnel at the AFWL. The data analyzed was obtained as the sensor tracked an approaching air-to-air missile. The FLIR started tracking the missile with a background of clear blue skies, and changed to ground clutter when the missile descended below the horizon. The data analysis concluded that spatial correlation existed in the background with a correlation distance of approximately two pixels [6].

In the simulation, the spatially correlated background noise,  $b_{jk}(t_i)$ , is represented in the FLIR plane as a radially symmetric, exponentially decaying pattern characterized by the distance of approximately two pixels in the FLIR image plane for the correlation to drop an order of magnitude (i.e., essentially to zero). This effect is accomplished by maintaining non-zero correlation coefficients between each pixel and its two closest neighbors symmetrically in all directions (i.e., including first and second neighboring pixels). The 8 x 8 pixel FOV provides 64 measurements, numbered from 1 to 64 starting from the left hand corner of the array and proceeding across the rows, as shown in Figure 4.9 [6]. The generation of spatially correlated white Gaussian noises is accomplished by allowing non-zero cross correlations between the measurement noises  $b_{jk}(t_i)$  associated with each of the

1	2	3	4	5	6	7	8
9	10	11	12	13	14	15	16
17	18	19	20	21	22	23	24
25	26	27	28	29	30	31	32
33	34	35	36	37	38	39	40
41	42	43	44	45	46	47	48
49	50	51	52	53	54	55	56
57	58	59	60	61	62	63	64

Figure 4.9. FLIR Field-of-View Pixel Numbering Scheme

64 pixels of Figure 4.9. Then the matrix of the correlated measurement noise in Equation (4-54) is:

$\mathbf{b}(t_i)$  = 64-dimensional vector of spatially  
correlated noise with statistics:

$$E\{\mathbf{b}(t_i)\} = \mathbf{0} \quad (4-55)$$

$$E\{\mathbf{b}(t_i)\mathbf{b}^T(t_j)\} = \mathbf{R} \delta_{ij} \quad (4-56)$$

where  $\mathbf{R}$  is a 64 x 64 measurement noise covariance matrix. This matrix describes the spatial correlation between pixels, and is given by [6]:

$$\mathbf{R} = \sigma_R^2 \begin{bmatrix} 1 & r_{1,2} & r_{1,3} & \cdots & r_{1,64} \\ r_{1,2} & 1 & r_{2,3} & \cdots & r_{2,64} \\ r_{1,3} & r_{2,3} & 1 & \cdots & r_{3,64} \\ \cdots & \cdots & \cdots & \cdots & \cdots \\ r_{1,64} & r_{2,64} & r_{3,64} & \cdots & 1 \end{bmatrix} \quad (4-57)$$

where  $\sigma_R^2$  is the variance of each scalar noise and the correlation coefficients  $r_{j,k}$  are evaluated to reflect the radially symmetric, exponentially decaying pattern described previously. The specific realizations of the spatially correlated noise matrix  $\mathbf{b}$  are simulated using a Cholesky square root decomposition of  $\mathbf{R}$  and a Gaussian noise generator with unit variance. The 64-dimensional spatially correlated background noise  $\mathbf{b}(t_i)$  is modeled as:

$$\mathbf{b}(t_i) = \sqrt[3]{\mathbf{R}} \mathbf{b}'(t_i) \quad (4-58)$$

where

$$\sqrt[3]{\quad} = \text{Cholesky square root}$$

$$\mathbf{b}'(t_i) = \text{64-dimensional vector of discrete, independent white Gaussian noise with statistics:}$$

$$E\{\mathbf{b}'(t_i)\} = \mathbf{0} \quad (4-59)$$

$$E\{\mathbf{b}'(t_i)\mathbf{b}'^T(t_j)\} = \mathbf{I} \delta_{ij} \quad (4-60)$$

where  $\mathbf{I}$  is a 64 x 64 matrix.

As previously stated, the spatial correlation model is represented in the FLIR plane as a radially symmetric, exponentially decaying pattern. A correlation distance of one pixel is used in the simulation since it fits the data for the first neighboring pixel and is essentially zero for the second neighboring pixel and beyond. Additionally, the exponential model prevents the  $\mathbf{R}$  matrix from becoming ill-conditioned (i.e.,  $\mathbf{R}$  remains positive definite, which allows the Cholesky square root to be taken).

*4.4.2 Low-Energy Laser Reflection Models.* The laser reflection measurement model simulates the low-energy laser reflecting off the target hardbody (refer Figure 1.1). In the previous thesis [2], the reflection model consisted of a binary-valued reflectivity function. Therefore, reflection information was equally obtained over the entire vehicle.

The hardbody reflectivity model, developed in this thesis, is enhanced to include a varying reflection surface over the vehicle. The reflection return from this latter scenario provides an increase in the realism of the simulation. In the simulation and this thesis document, the hardbody models are depicted in the  $\alpha$ - $\beta$  (FLIR) plane relative to the plume intensity centroid. However, it is important to remember that the FLIR can only "see", and determine dynamic parameters relating to, the intensity centroid of the plume, and can not provide any information concerning the hardbody.

The purpose of the low-energy laser reflection measurement is to provide an input to the Kalman filter for estimating the center-of-mass of the target hardbody relative to the target plume center of intensity. The identification of the hardbody center-of-mass [2, 26] is a recent request by the AFWL to study the possibility of tracking the actual hardbody of the missile as opposed to the intensity centroid. The scenario, as previously discussed in Chapter I, calls for the FLIR sensor to provide measurement information on the position of the intensity centroid to a Kalman filter. The filter processes the FLIR measurement, and provides an updated estimate of the target's velocity vector along which a low-energy laser is scanned to obtain a reflection (although the eight-state filter uses its two offset estimates to determine the sweep direction, rather than the estimated velocity direction; see next paragraph for further detail). A second Kalman filter uses the center-of-mass measurement to update its estimate of the offset between the FLIR target intensity centroid and the hardbody center-of-mass, and propagates the estimate to the next sample period.

Although the reflection models discussed in this chapter are part of the truth model, the description of the measurement models should be understood in the context of the Kalman filter(s) using the measurements. Therefore, a short description of the filter configurations used in this thesis is now provided. In this thesis the center-of-mass estimate is accomplished using two filter-processing schemes, and two low-energy laser reflection models (of the hardbody). In the first configuration, a six-state (FLIR) filter is

used to obtain estimates of the position and orientation angle of the intensity centroid in the FLIR plane. A one-state center-of-mass filter (which is independent of the six-state filter) uses the measurements obtained from scanning a low-energy laser along the estimated velocity vector (computed from the information provided by the six-state filter) to update its estimate of the hardbody center-of-mass. In the second configuration, an eight-state filter, composed of the same six-state filter and two center-of-mass states, performs the same basic estimations as the six-state/one-state configuration. The two states used for estimating the center-of-mass obtains center-of-mass measurements as a result of the low-energy laser scan along the velocity vector until the first laser reflection occurs, at which time the filter's two center-of-mass states in the  $x_{FLIR}$  and  $y_{FLIR}$  directions are used to estimate the laser scanning angle. The two center-of-mass states in the eight-state filter are independent of the other six states in the filter.

The low-energy laser scan from the intensity centroid along either the six-state filter's estimate of the velocity vector or the direction provided by the two bias states of the eight filter, provides a computed center-of-mass measurement to the filter only if the laser crosses the missile hardbody. The calculation of the center-of-mass measurement is accomplished as the midpoint between the initial and final intersections of the low-energy laser and the hardbody.

The low-energy laser binary model developed in the previous thesis [2] and the enhanced reflectivity model developed in this thesis are presented in the next two sections, with only a single scan of the low-energy laser considered in the presentation. A low-energy laser sweep technique, developed as a part of this thesis effort, is presented later in this section. (As defined in this document, a low-energy scan is a single attempt to obtain a reflection from the hardbody, and a low-energy laser sweep is a series of laser scans.) The low-energy laser sweep ensures a reflection from the target hardbody, providing a new center-of-mass measurement for the filter (one-state or eight-state) at each sample time.

The low-energy laser sweep is applicable to both the binary model and the reflectivity model, although the computation of the center-of-mass differs due to the properties of each model (Section 4.4.3).

*4.4.2.1 Hardbody Binary Model.* In the previously used hardbody binary measurement model [2], the target is represented as a rectangle with its longitudinal axis aligned with the true velocity vector in the FLIR image plane. The target hardbody, like the intensity centroid, is propagated along the inertial trajectory by the first two states of the truth model. The low-energy laser scan at the target is also simulated as a rectangle. The smaller side (width) of the low-energy laser rectangle represents a realistic finite width of a laser after it has traveled 2,000 kilometers, and the longer side represents the result of the purposeful scan of the laser. In the simulation of the six-state/one-state filter combination, after the FLIR measurement is incorporated into the filter algorithm, the updated target orientation angle  $\theta_f$  is used to determine the orientation of the laser beam scan at the target. Once the low-energy laser is "scanned" along the filter estimated velocity vector  $\mathbf{v}_f$  (using the six-state filter estimate), the intersection of the rectangles determines if the laser "hit" the target. (In the eight-state filter, the scan direction is determined by the two components of the estimated offset rather than by the estimated velocity direction.) Figure 4.10 shows the binary model as it appears in the FLIR image plane. The four corners of the hardbody define the rectangular model, the center of which is the true center-of-mass, offset from the intensity centroid. In the simulation this offset distance is arbitrarily defined as the distance from the center of the two Gaussian intensity functions, which define the target plume model (Figure 3.6), to the hardbody center-of-mass (87.5 meters or 2.9167 pixels). This distance relates well with the location of the plume intensity functions developed in a previous thesis [26].

Since the target propagates along its trajectory in 3-dimensional inertial space, as described in Section 3.5, the hardbody model is projected into the 2-dimensional FLIR

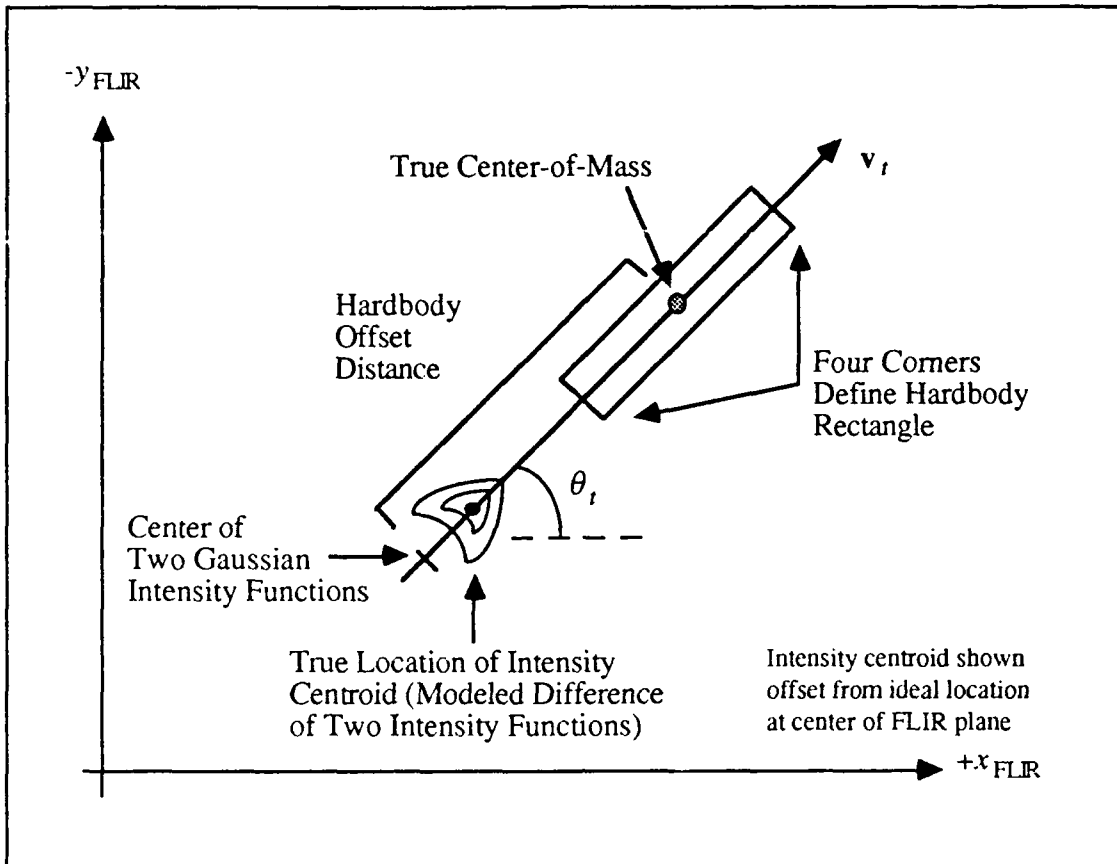


Figure 4.10. True Intensity Centroid and Hardbody Binary Model in FLIR Image Plane

plane. The projection of the 3-dimensional missile onto the 2-dimensional FLIR plane involves the target projection geometry of Section 3.3.4. From Figure 3.8, the projection of the length of the target hardbody onto the FLIR image plane is:

$$ML_{FLIR} = ML_{Actual} \cos \gamma \quad (4-61)$$

where

$$\begin{aligned} ML_{FLIR} &= \text{FLIR plane projection of missile length} \\ ML_{Actual} &= \text{true missile length in pixels} \\ \gamma &= \text{angle between } \mathbf{v}_t \text{ and the FLIR plane} \end{aligned}$$

Since the missile is cylindrical, the 3-dimensional projection of the missile diameter onto the FLIR plane is equal to its diameter. In the simulation, the length of the missile is 40 meters (1.333 pixels), and the width is 3 meters (0.1 pixels).

The low-energy laser rectangle (which represents a scan at the target location) is oriented with one end of the centerline located at the filter's estimate of the center-of-intensity location (the center of the FLIR FOV), as shown in Figure 4.11. The diagram in Figure 4.11 suggests that the filter estimates of the intensity centroid, the orientation angle  $\theta_f$ , and the computed velocity vector  $\mathbf{v}_f$  are equal to the truth model values, which is not generally true. The real world description is presented in Chapter V.

The second endpoint of the low-energy laser scan rectangle is determined by projecting the low-energy laser three times the truth model offset distance between the hardbody center-of-mass and the intensity centroid ( $3 \times 87.5$  meters = 262.5 meters or 8.75 pixels). This length ensures the low-energy laser model is long enough to scan the entire hardbody with an oscillating plume. (The affect of the plume pogo phenomenon is

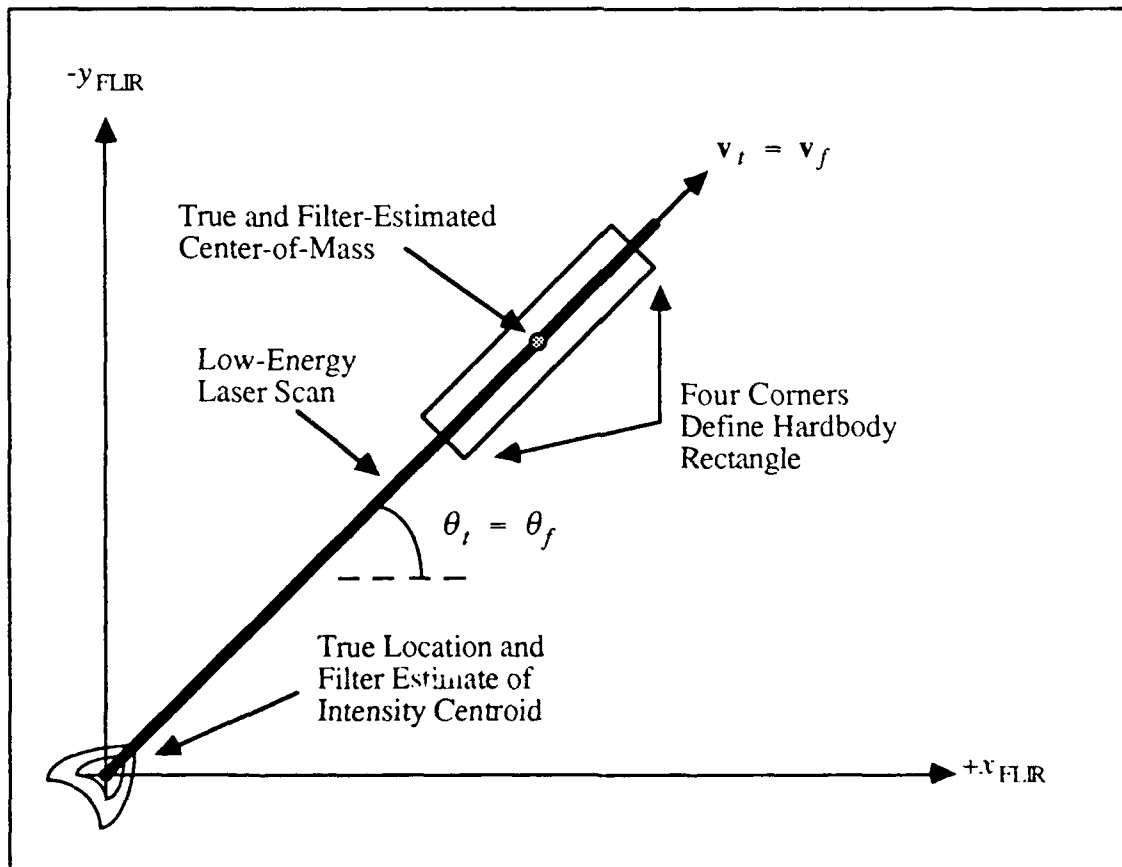


Figure 4.11. Ideal Low-Energy Laser Scan at Target Location



discussed in Chapter VI.) The location of the low-energy laser's second centerline endpoint is determined as:

$$x_p = x_c + L \cos \theta_f \quad (4-62)$$

$$y_p = y_c - L \sin \theta_f \quad (4-63)$$

where

- $x_p, y_p$  = the FLIR plane coordinates of the second centerline endpoint of the laser rectangle
- $x_c, y_c$  = the FLIR plane intensity centroid coordinates
- $L$  = the length of the laser rectangle
- $\theta_f$  = six-state (FLIR) filter (or eight-state center-of-mass bias states') estimate of velocity vector orientation angle

In the simulation, if the low-energy laser scan does not cross the hardbody (i.e., the missile rectangle and the laser rectangle do not overlap), the filter does not do an update, and it then propagates the updated state estimate(s) and covariance value(s) to the next sample period. When the low-energy laser scan results in a laser "hit", an estimate of the center-of-mass is computed based upon the intersection of the hardbody and the low-energy laser rectangles.

The scenario for determining the center-of-mass measurement for the one-state filter, or the two center-of-mass states in the eight-state filter, follows previous theses [2, 26]. The FLIR provides measurement information (which is processed by an enhanced correlation algorithm, Chapter V) to the filter on the position of the target's intensity centroid and orientation angle  $\theta_f$ . The updated filter estimate of the location of the intensity centroid is used to aim the low-energy laser at the intensity centroid, and scan the low-energy laser along the six-state filter's estimated target velocity vector in the case of the one-state center-of-mass filter, or along the eight-state center-of-mass bias states' estimate

of the velocity vector (once the first laser reflection is received by the low-energy laser sensor).

The truth model low-energy laser sensor receives the reflection of the low-energy laser off the hardbody (refer to Figure 1.1), and provides noise-corrupted center-of-mass measurements to the filter. There are six possible low-energy laser/hardbody intercepts that are considered in the simulation when the low-energy laser is scanned along the (one-state or eight-state) filter-estimated velocity vector. The cases are shown in Figure 4.12. The previous thesis [2] considered the first three cases (a), (b), and (c) of the low-energy laser initially crossing the aft end (bottom) of the hardbody and continuing across to a side or the forward end (top) of the hardbody. For this thesis, three additional cases are provided in the simulation, (d), (e), and (f), which consider the low-energy laser initially crossing either side of the hardbody and continuing through the forward end of the hardbody, and the case of the laser crossing both sides of the hardbody. These additional cases were essential due to the apparent "jitter" of the target on the FLIR plane, as discussed in Chapter V and VI.

For a single low-energy laser scan, non-sweep condition, the center-of-mass is calculated as the midpoint of the laser centerline segment that covers the hardbody. For this type of measurement acquisition, the accuracy of the center-of-mass computation depends on the orientation of the laser scan and the hardbody. The optimum orientation for a single-scan scenario is affected by the accuracy of the six-state filter's estimate of the intensity centroid location and the target orientation angle estimate. With only a single scan and the calculation of the center-of-mass dependent on an optimum scan of the low-energy laser across the hardbody, it is apparent from Figure 4.12 that the measurement provided to the filter is inaccurate. Repeated scans of the low-energy laser (i.e., a sweep) to intercept the hardbody gives better results, as described later in Section 4.4.3. The center-of-mass measurement is computed as an offset from the filter-estimated intensity centroid. Before

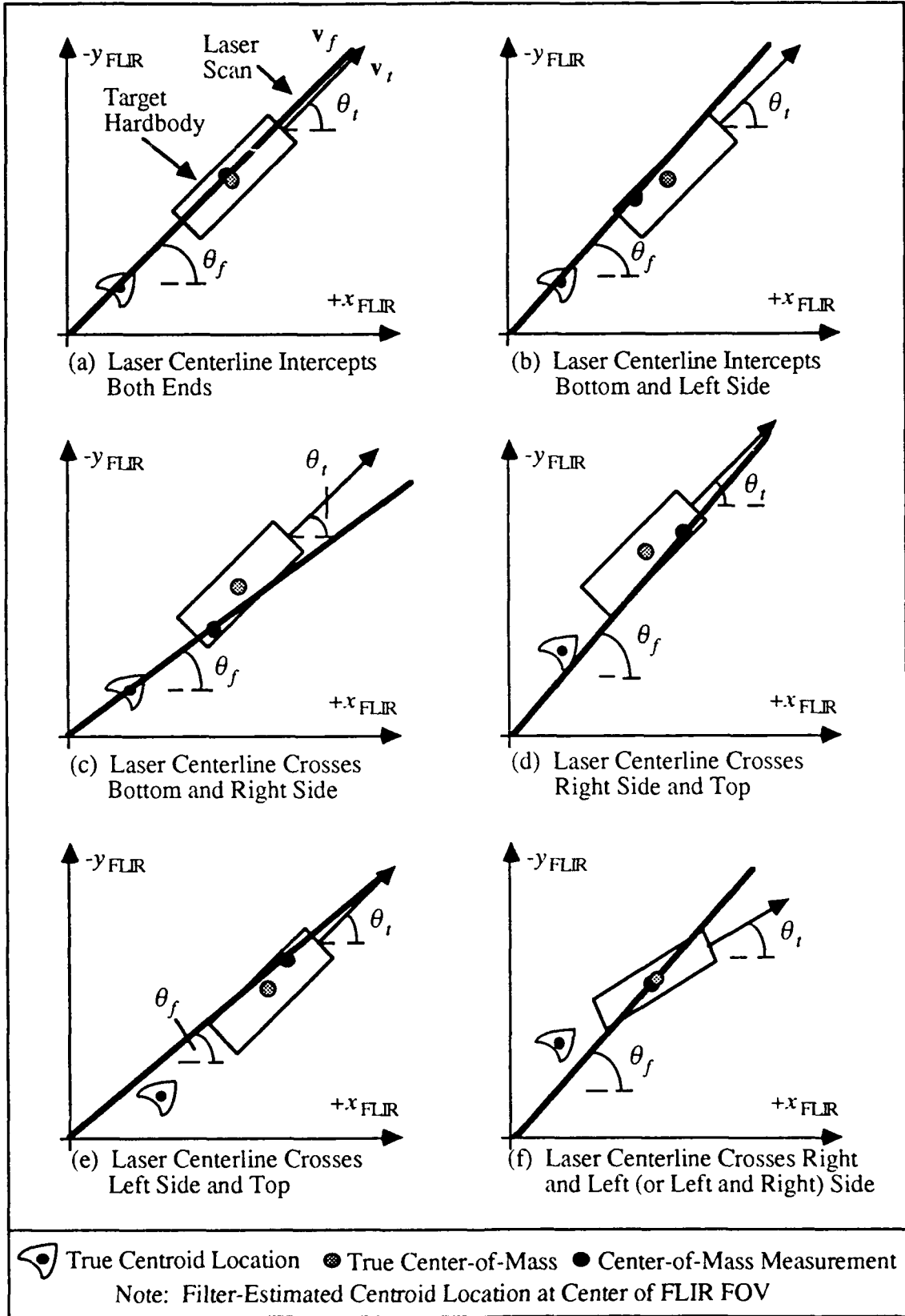


Figure 4.12. Six Cases of Low-Energy Laser Scan Crossing Hardbody

being provided to the filter, the offset measurement is corrupted with white Gaussian noise.

The low-energy laser sensor measurement model becomes:

$$z(t_i) = L_o(t_i) + v(t_i) \quad (4-64)$$

where

$z(t_i)$  = low-energy laser sensor output at time  $t_i$

$L_o(t_i)$  = offset between center-of-mass and the intensity centroid

$v(t_i)$  = discrete, white Gaussian measurement noise with statistics:

$$E\{v(t_i)\} = 0 \quad (4-65)$$

$$E\{v(t_i)v(t_j)\} = \begin{cases} R & t_i = t_j \\ 0 & t_i \neq t_j \end{cases} \quad (4-66)$$

where R is the variance of the white Gaussian measurement noise v.

*4.4.2.2 Hardbody Reflectivity Model.* In addition to the enhancements made to the hardbody binary model of the previous section, a hardbody reflectivity model is also developed for this thesis. While the hardbody binary model gives an "on or off" indication of a laser reflection, the hardbody reflectivity model provides a more realistic portrayal of a missile by considering the curvature of the missile and the target image projection angle  $\gamma$ , shown in Figure 3.9. The reflectivity design chosen for this research consists of the rectangular hardbody model of the previous thesis [2] modified to include 29 discrete-weighted line-segments along the length of the model. The target image projection angle  $\gamma$  provides a scaling factor of the reflection function if the missile centerline is oriented other than  $90^\circ$  to the FLIR image plane. The concept of the hardbody reflectivity model is shown in Figure 4.13 relative to the FLIR image plane.

The hardbody reflectivity model is based on the empirical data, shown in Figure 4.14, obtained from the 6585<sup>th</sup> Test Group, Holloman AFB, NM [3]. The data was

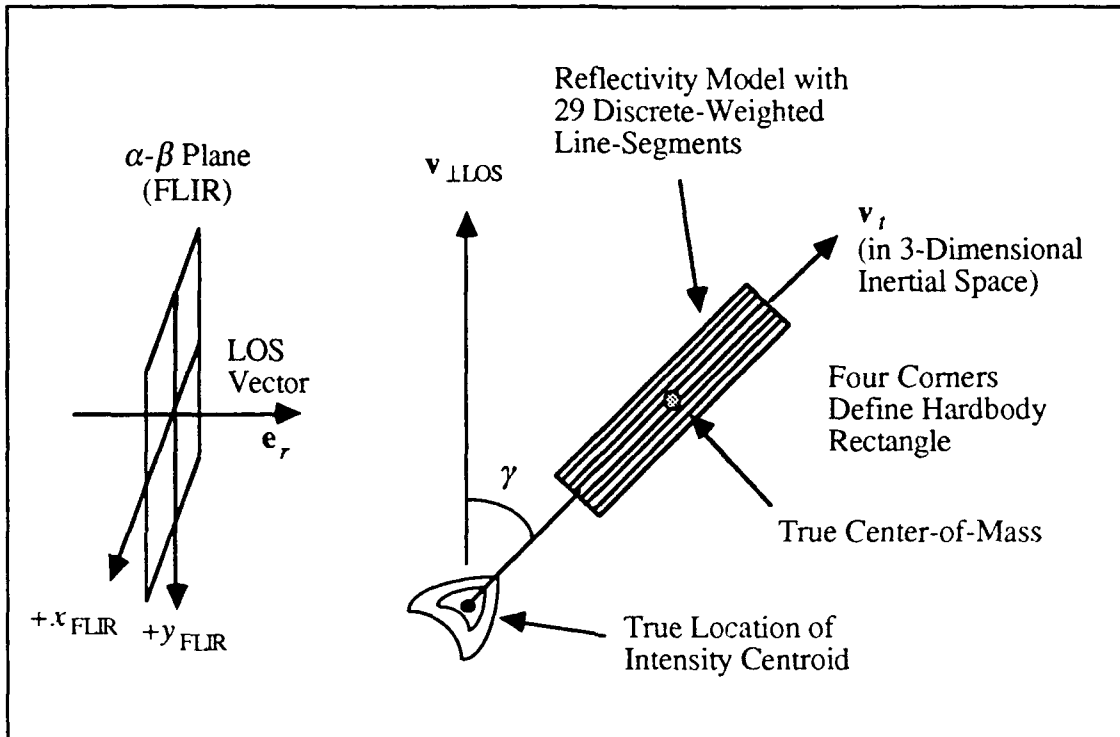


Figure 4.13. Hardbody Reflectivity Model Relative to FLIR Image Plane

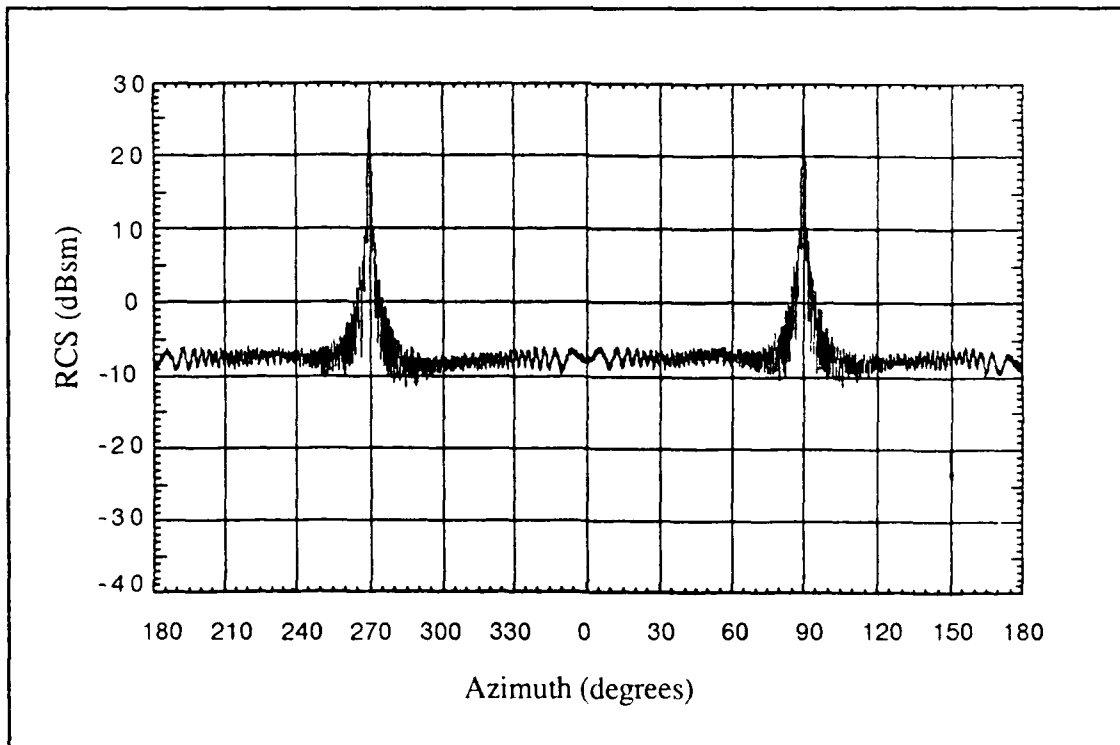


Figure 4.14. Empirical Radar Reflection Data of Cylinder [3]

obtained from a radar return off a 20 x 249 inch cylinder with hemispherical endcaps as it was rotated longitudinally in the plane of the radar source. This information is considered similar to the reflection return of the low-energy laser off the missile hardbody. Though the data was obtained from rotating the cylinder about its diameter, the data also represents a good approximation for the case of a radar scan across the diameter of the cylinder.

The information provided in the empirical graph of Figure 4.14 is incorporated into the cross-sectional and longitudinal reflectivity functions which define the hardbody reflectivity model. The cross-sectional reflectivity function models the curvature of the cylindrical hardbody, while the longitudinal reflectivity serves as a scaling factor determined by the projection angle  $\gamma$  (see Figures 3.9 and 4.13). The development of the two reflectivity functions for the hardbody reflectivity function is presented in the following paragraphs.

The model of the cross-sectional reflectivity function, which closely duplicates the important aspects of Figure 4.14, is shown in Figure 4.15. The graph of Figure 4.14 shows that if the cylinder is other than perpendicular to the source, there is a substantial reduction in signal return (reflection), and a non-zero threshold of the graphical data occurs at approximately 15 degrees off both sides of the peak reflections at 90° and 270°. This angle is applied to the 3.0 meter cross-section of the two-dimensional binary model. Using geometric techniques, the threshold at the 15 degree point is transformed to approximately 0.7 meters off the centerline of the missile. Therefore, the strength of the received signal is a constant value from 0.7 meters to the radius at 1.5 meters. The amplitude of the data is incorporated into the model by adding 14 offset line segments on either side of the centerline of the binary model (for a total of 29 discrete line segments). This offset scheme represents a discrete sensitivity of 0.1 meters (approximately 4 inches) across the 2-dimensional hardbody longitudinal axis. The amplitude of the cross-sectional reflectivity

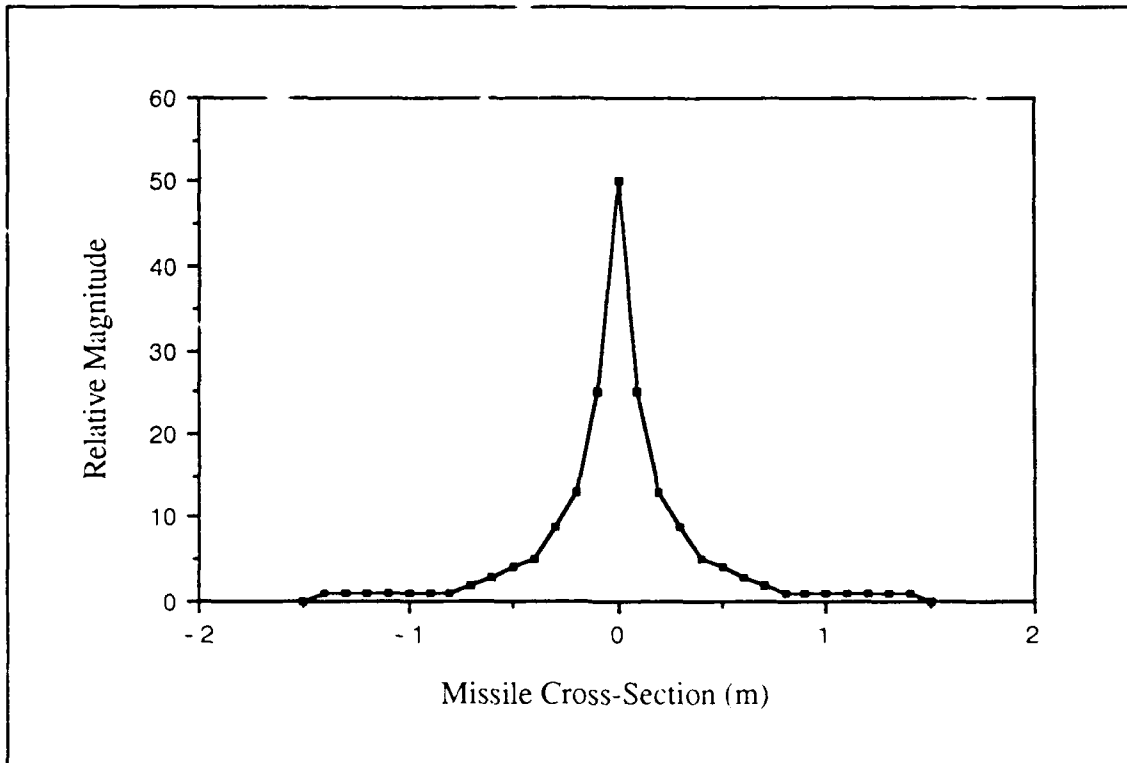


Figure 4.15. Hardbody Reflectivity Model Cross-Sectional Reflectivity Function

function consists of reflection magnitudes corresponding to the empirical data of Figure 4.14. For this thesis, an arbitrary value of 50 (units of magnitude of reflection) is used to represent the peak reflection of the cross-sectional reflectivity function's center line segment; the remaining line segments are scaled according to the empirical data of Figure 4.14. The results of the scaling produced the cross-sectional reflectivity function shown in Figure 4.15.

In the computer software, the scaled reflection magnitudes are assigned to the 29 discrete line-segments along the longitudinal axis of the 2-dimensional hardbody. The reflection magnitude assigned to each line segment is determined by the cross-sectional reflectivity function of Figure 4.15. The discrete implementation of the cross-sectional reflectivity function is shown in Figure 4.16. Notice that the reflectivity function also yields that the portions of the original rectangle far from the missile centerline have zero

reflection, therefore the effective reflective surface area of the hardbody is less than that of the binary model. As is discussed later, the effective surface area "visible" to the low-energy laser sensor is a function of the sensitivity of the sensor.

As previously stated, the longitudinal reflectivity function is related to the target image projection angle  $\gamma$ , which projects the target in the 3-dimensional inertial frame into the 2-dimensional FLIR plane, as shown in Figure 4.13. The longitudinal reflectivity function is represented by a function similar to the cross-sectional reflectivity function. The ordinate axis consists of the longitudinal angular offset from  $90^\circ$  to the low-energy laser source (i.e., from the FLIR plane), and the abscissa axis is the scaling factor associated with angular offset. The longitudinal reflectivity function is shown in Figure 4.17.

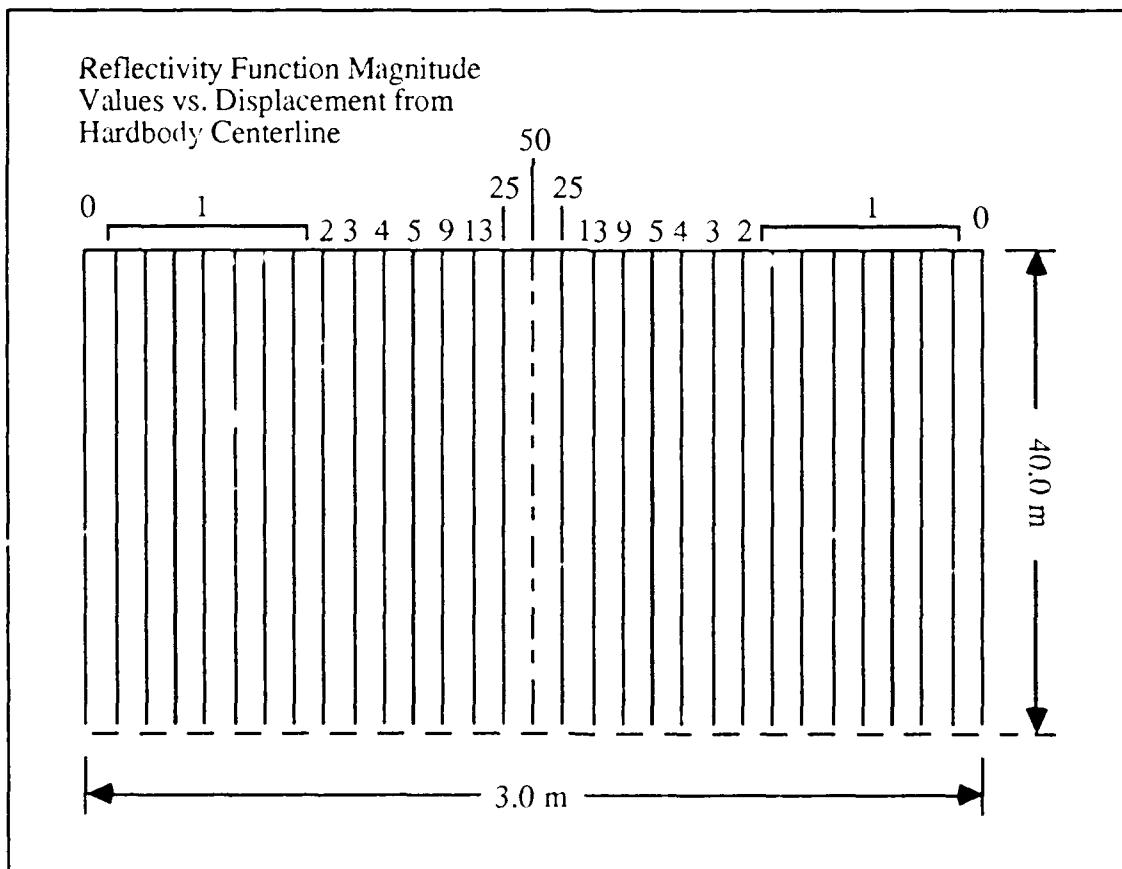


Figure 4.16. Discrete Implementation of Cross-Sectional Reflectivity Function



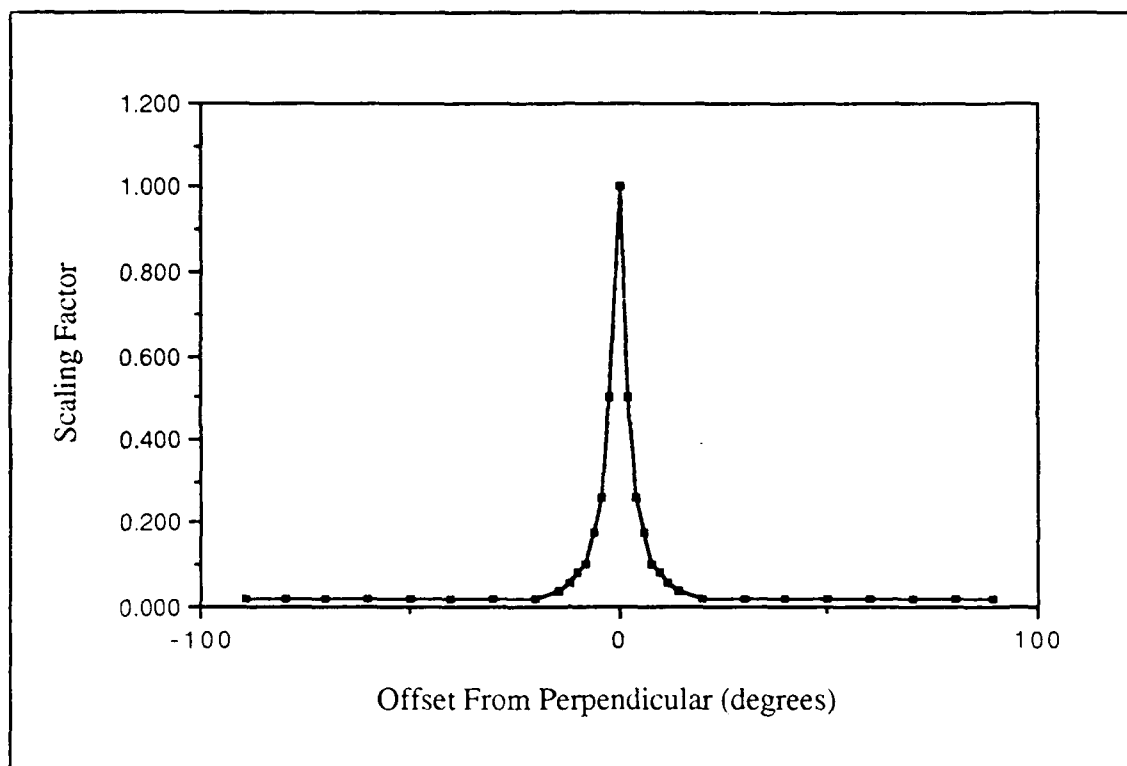


Figure 4.17. Hardbody Reflectivity Model Longitudinal Reflectivity Function

The sensitivity level of the low-energy laser sensor is also a factor in determining the reflectivity received at the sensor. This sensitivity is represented in the simulation as a threshold limit below which the low-energy laser sensor can not detect the reflection return. This factor, represented as  $\mu$ , also contains any noise associated with the sensor. As an example of the reflectivity model in the simulation, consider the hardbody at an angle of  $20^\circ$  to the FLIR image plane. In this orientation, the maximum amount of reflection energy received at the sensor is 50 (units of magnitude) times a scaling factor of 0.02, which gives 1.0 (units of magnitude). However, if the low-energy laser sensor sensitivity is also 1.0 (units of magnitude), then the sensor will not detect the reflection; the low-energy laser sensor sensitivity, in this case, must be less than 1.0 to detect the reflection off the missile hardbody. As this example shows, the sensitivity factor  $\mu$  of the low-energy laser sensor can represent the physical limitations of the sensor.

From the discussion the total reflectivity function is represented by:

$$R_T = \sum_{n=1}^m \mu [A_i F(\gamma)] \quad (4-67)$$

where

- $R_T$  = total reflectivity received by the low-energy laser sensor  
 $m$  = number of line segments crossed by laser scan; Figure 4.16  
 $\mu(\cdot)$  = sensitivity threshold function of low-energy laser sensor,

$$\mu(a) = \begin{cases} a & \text{if } a \geq \text{threshold} \\ 0 & \text{if } a < \text{threshold} \end{cases}$$

- $A_i$  = cross-sectional reflectivity function reflection amplitude  
 of the  $i$ th discrete line segment  
 $F(\gamma)$  = longitudinal reflectivity scaling function, where  $\gamma$  is the angle  
 between target  $\mathbf{v}$  and the  $\alpha$ - $\beta$  plane; Section 3.3.4, Figure 3.9  
 and Figure 4.13

The center-of-mass measurements provided to the filter by the enhanced reflectivity model are the same as the binary model for a single scan concept. The projection of the hardbody reflectivity model onto the FLIR image plane is given in Equation (4-61), and the positioning of the low-energy laser in the simulation is given by Equations (4-62) and (4-63). The low-energy laser hardbody crossings are the same as for the binary model, shown in Figure 4.12. The Kalman filter measurement Equations (4-64), (4-65), and (4-66) are also applicable to the hardbody reflectivity model.

**4.4.3 Low-Energy Laser Sweeping of Hardbody.** The previous two sections describe the hardbody binary and reflectivity models used for this research. The center-of-mass computation in the discussion consists of the midpoint of the low-energy laser

crossing of the hardbody. Additionally, a single low-energy laser scan is considered in the discussion, so the accuracy of the center-of-mass measurement is dependent upon the orientation of the low-energy laser crossing the hardbody (Figure 4-12). The single laser scan provides only 15-20% low-energy laser "hits" (reflection returns), as determined in previous research [2], and verified in this research. This results in fewer measurements for the Kalman filter than desired, which degrades filter performance.

The reason for the small number of low-energy laser reflection returns is found in this research to relate to the Kalman filter's positioning information provided to the FLIR pointing controller (Section 3.4). The filter provides its propagated estimate of the next position of the target's intensity centroid to point the FLIR LOS vector  $\mathbf{e}_r$ . This problem is not evident if the Kalman filter tracker is tracking the intensity centroid, but for tracking the hardbody, the accuracy of the propagated estimate for pointing the FLIR sensor is critical to the low-energy laser concept considered in this research, since the low-energy laser is fired through the FLIR plane aperture (i.e., one end of the laser scan rectangle in Figure 4.12 should actually be at the origin, since that origin is placed at the predicted intensity centroid location). As pointed out in the Chapter I, the tracking system must perform acquisition and lock-on of the target in the shortest time possible, with "pinpoint" accuracy. The problem with pointing of the FLIR sensor is covered as a thesis investigation in Chapter VI. The following two sections consider the problem of accurately determining the center-of-mass of the hardbody binary and reflectivity models despite the pointing problem to verify the feasibility of the concept.

*4.4.3.1 Center-of-Mass Computation with Binary Model.* The design of the low-energy laser sweep uses the previously developed low-energy laser scan [2]. However, rather than performing a single scan of the low-energy laser, the initial laser scan is offset clockwise from the filter estimated velocity vector, as shown in Figure 4.18, and a sweep (a series of low-energy laser scans) is implemented in the counter-clockwise

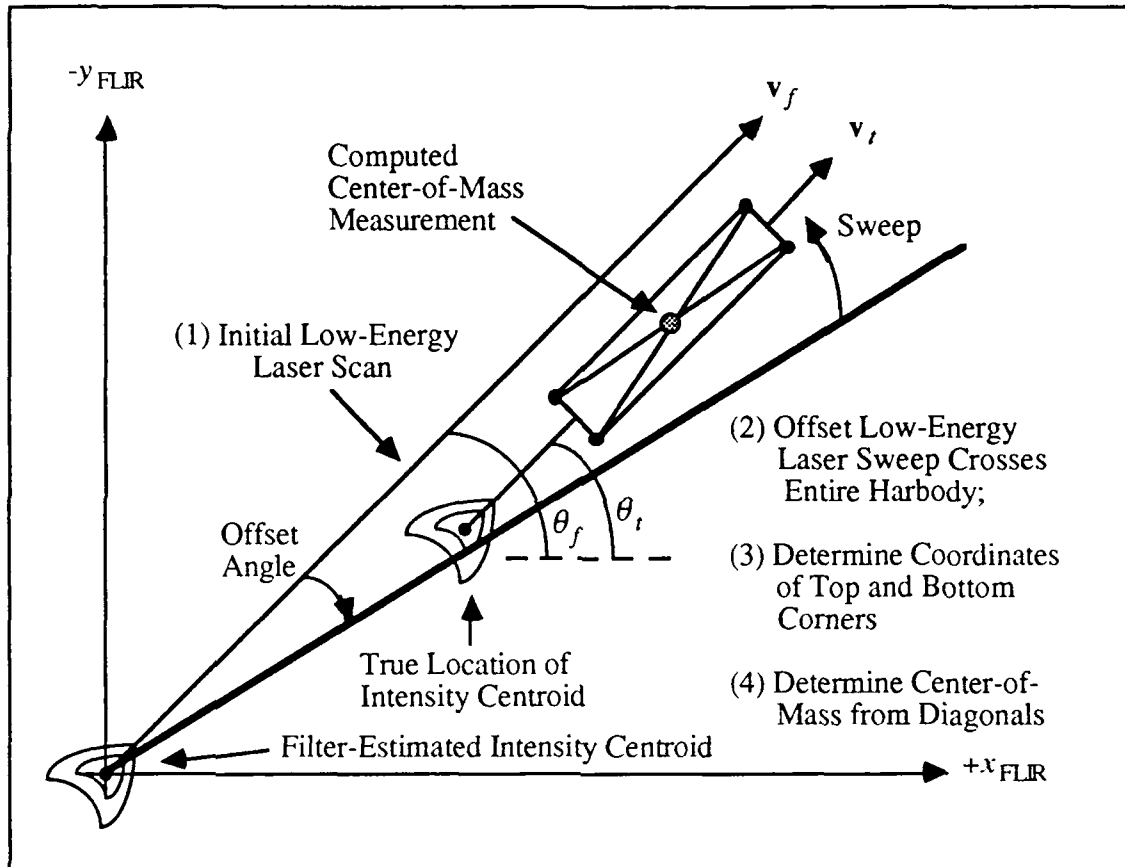


Figure 4.18. Hardbody Binary Model Center-of-Mass with Low-Energy Laser Sweep

direction so as to illuminate the entire hardbody. For this thesis the offset required is  $30^\circ$  without the plume pogo applied, and  $35^\circ$  with the plume pogo applied. This offset size is determined by a study of the "apparent" movement of the intensity centroid in the FLIR plane (which is actually due to the inaccurate positioning of the FLIR FOV on the target). (The movement of the centroid in the FLIR plane is also seen in the  $\hat{x}_d(t_i^-)$  plot, discussed in Chapter VI). The coarse sweep increment is chosen as 0.1 degrees to ensure that the closest coordinates to the corners of the binary model are obtained for the initial crossing of the hardbody, then 0.05 degree increments are used for the remainder of the laser sweep across the hardbody itself.

The determination of the hardbody binary model center-of-mass is computed from locating the initial forward (top) and aft (bottom) crossing coordinates of the hardbody in

the FLIR plane of the low-energy laser, and the final forward and aft crossing coordinates of the hardbody as the low-energy laser completes the sweep. The coordinates provide two measure of the center-of-mass, computed as the crossing point of the diagonals of the forward and aft coordinates obtained from the low-energy laser sweep, as seen in Figure 4.18. The low-energy laser crossing conditions given in Figure 4-12 apply as the low-energy laser crosses the hardbody.

*4.4.3.2 Center-of-Mass Computation with Reflectivity Model.* The computation of the hardbody reflectivity model center-of-mass using the low-energy laser sweep technique follows the same procedures as described for the hardbody binary model, except the computation of the center-of-mass is computed in a different manner. Since the "corners" of the reflectivity model are not visible to the low-energy laser sensor, these points cannot be used as they are with the hardbody binary model. Instead, the maximum reflection intensities of the forward and aft ends of the hardbody are obtained as the low-energy laser crosses the hardbody. The center-of-mass is computed as the midpoint between the forward and aft coordinates of the maximum reflection return. The low-energy laser sweep for determining the hardbody reflectivity model center-of-mass is shown in Figure 4-19. As previously stated, unlike the hardbody binary model, the reflection from the hardbody reflectivity model that is available to the low-energy laser sensor is dependent on the orientation of the hardbody with respect to the FLIR image plane, and the sensitivity of the low-energy laser sensor.

## *4.5 Truth Model Parameters*

The truth model parameters assigned to variables, and initial conditions are presented in this section. The parameters may appear in other parts of this thesis; however, the values are repeated here to provide a consolidated listing for the reader.

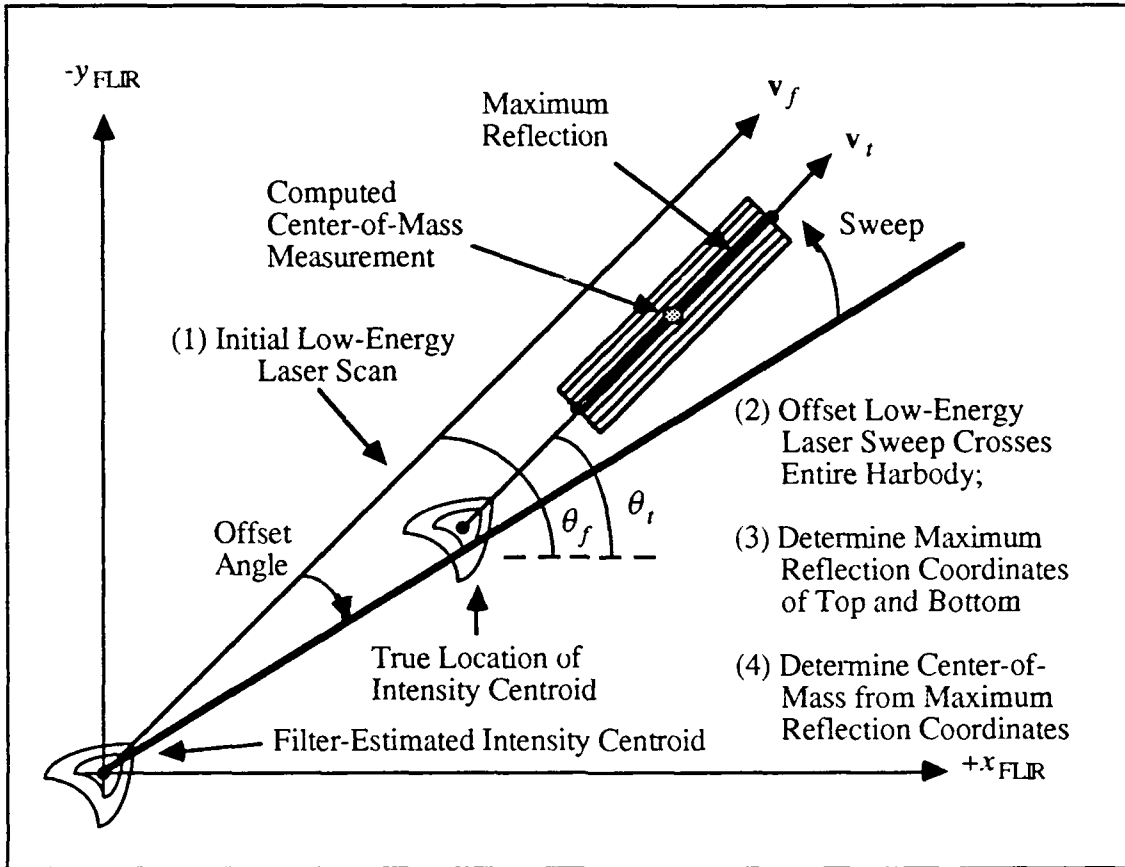


Figure 4.19. Harbbody Reflectivity Model Center-of-Mass with Low-Energy Laser Sweep

4.5.1 *Target Trajectory Initial Conditions.* The target trajectory is covered in Section 3.5. The initial conditions of the target's inertial position and velocity vectors for the simulation are:

$$\begin{aligned}
 e_x &= 27,000 \text{ meters} \\
 e_y &= 100,000 \text{ meters} \\
 e_z &= 2,000,000 \text{ meters} \\
 v_x &= -2500 \text{ meters/second} \\
 v_y &= 4330 \text{ meters/second} \\
 v_z &= 0 \text{ meters/second}
 \end{aligned}$$

The relative magnitudes of the initial velocity components,  $v_x$  and  $v_y$ , form an initial velocity vector orientation angle of  $60^\circ$  for the target in the inertial frame.

*4.5.2 Target Model, Dimensions, and Orientation.* For this thesis, the target model consists of an intensity centroid model and a hardbody binary or enhanced reflectivity model. Each of the two bivariate Gaussian intensity functions (differenced to produce the plume image) is modeled with elliptical constant-intensity loci with an aspect ratio of 1.5 and a semi-minor axis of one. The hardbody binary and reflectivity models are represented by a rectangle in the FLIR image plane. The hardbody is 40 meters (1.33 pixels) long and 3 meters (0.1 pixels) in diameter. For this study the offset distance of the hardbody center-of-mass from the intensity centroid is 87.5 meters (2.92 pixels). In the simulation, the intensity centroid and the longitudinal axis of the hardbody are aligned with the velocity vector, and the hardbody has zero sideslip and zero angle-of-attack.

*4.5.3 Intensity Functions.* The maximum intensity value of each intensity functions in Equation (3-1) is 20 intensity units. The two Gaussian bivariate intensity functions, which represent the plume hotspots, are centered at 65 meters and 110 meters behind the missile.

*4.5.4 Atmospheric Jitter.* The variance and mean squared value for the atmospheric jitter process in the truth model, given by  $x_a$  and  $y_a$  in Equations (4-6) and (4-7), is 0.2 pixels<sup>2</sup> [30].

*4.5.5 Bending/Vibration.* The values used for the second-order transfer function that models the bending/vibration phenomenon (Equation 4-36) are:  $K_b^2 = 5 \times 10^{-13}$  rad<sup>4</sup>/sec<sup>4</sup>;  $\zeta_b = 0.15$ ;  $\omega_{nb} = \pi$  rad/sec.

*4.5.6 Plume Pogo Characteristics.* For this research, the frequency of the pogo oscillation is 10 Hertz and the pogo rms value is 33.6 meters (1.12 pixels). These values

represent the maximum pogo oscillation as determined in previous research [26]. The size of the plume relative to the hardbody is on the order of 30 times the diameter of the missile at the altitudes of interest [26].

*4.5.7 Spatially Correlated Background Noise.* The rms value of  $v_{jk}$ , which is the summed effect of the spatially correlated background noise  $b_{jk}$  and the FLIR sensor noise  $n_{jk}$  in Equation (4-54), is one. This produces a signal-to-noise ratio of 20, which is typical of many tracking scenarios of current interest [26].

*4.5.8 Low-Energy Laser Measurement Dimensions.* The calculation of the center-of-mass is found using a low-energy laser beam scan represented as a rectangle at the target. The length of the laser beam scan is 262.5 meters (8.75 pixels), which is three times the truth model hardbody offset distance. The laser beam width is 0.1 meters (approximately 4.0 inches). The measurement noise associated with the low-energy laser sensor is obtained by taking 1.0 % of the length of the hardbody, and dividing by the pixel proportionality constant  $k_p$  times the range to the target, giving a variance (rms value) of 0.000178 pixels<sup>2</sup>. (This value is a refinement of the value used in the previous thesis [2] of 0.004444 pixels<sup>2</sup>, obtained using 5.0% of the length of the hardbody.)

*4.5.9 Reflectivity Measurement Model.* The variable  $\mu$  represents the threshold of the low-energy laser sensor. The value of the low-energy laser sensor threshold must be less than 1.0 (units of magnitude reflection) to detect the peak intensity reflection from the hardbody for a projection angle  $\gamma$  greater than, or equal to, 16°.

## 4.6 Summary

This chapter presented the mathematical description of the truth model used in the simulation. The model dynamics consist of two deterministic target trajectory states, six stochastic atmospheric jitter states, four stochastic bending/vibration states, and two



stochastic plume pogo states. The infrared measurement model consists of a combination of the Gaussian intensity functions with the result being non-Gaussian. The measurements from the FLIR sensor are subject to spatially and temporally uncorrelated FLIR sensor noise, and spatially correlated and temporally uncorrelated background noise. The low-energy laser measurement model provides information to the filter on the location of the hardbody center-of-mass relative to the estimated center of intensity. The availability of the measurement is dependent on the accuracy of the filter estimates of the intensity centroid position and low-energy laser scan orientation angle in the FLIR image plane. The hardbody binary and refined reflectivity measurement models were described and related to the measurements obtained for the Kalman filter. The reflectivity model provides a realistic portrayal of the real world environment, and has a smaller effective cross-sectional area, which is a function of the sensitivity of the low-energy laser sensor. A sweep technique was described which ensures that a measurement is available at each Kalman filter sample period. The parameters and initial conditions of the truth model were also presented in this chapter.

## *V. Filter Models*

### *5.1 Introduction*

The Kalman filter, in the AFIT tracking scenario of Figure 1.1, uses its internal dynamics model and the periodic measurements provided by the FLIR sensor and low-energy laser sensor, to update the filter states. The filter then propagates the states to the next measurement sample time. The filter maintains lock on the target depending on the accuracy of its internal dynamics model and the measurements it receives from the FLIR and low-energy laser sensors (Chapter IV).

The Kalman filter dynamics model is a reduced and simplified version of the simulation truth model. The filter algorithm is limited to the least number of necessary states in order to process the state estimates in the shortest possible time. Increasing the number of states can inhibit the number of measurements that can be processed by the filter or the implementable sample rate, and subsequently reduce filter performance.

This thesis study uses three linear Kalman filter models: a six-state (FLIR) filter, a one-state (center-of-mass) filter, and an eight-state filter composed of the six-state filter and two additional states to estimate the center-of-mass. In this research, the combination of the six-state filter and the one-state state filter performance in estimating the center-of-mass of the missile hardbody is compared to that of the eight-state filter. The six-state filter, common to both filter schemes, is a development from a previous thesis [2, 26], which uses an enhanced correlator [27] to process FLIR measurements before being provided to the filter. Figure 5.1 shows the data processing for both filter schemes. In the case of the six-state/one-state filter scheme, following the filter update of the states, a low-energy laser is scanned along the estimated velocity vector. If a laser reflection is received by the low-energy laser sensor, this measurement information is provided to a separate one-state filter [2] to estimate the hardbody center-of-mass distance from the estimated center of intensity.

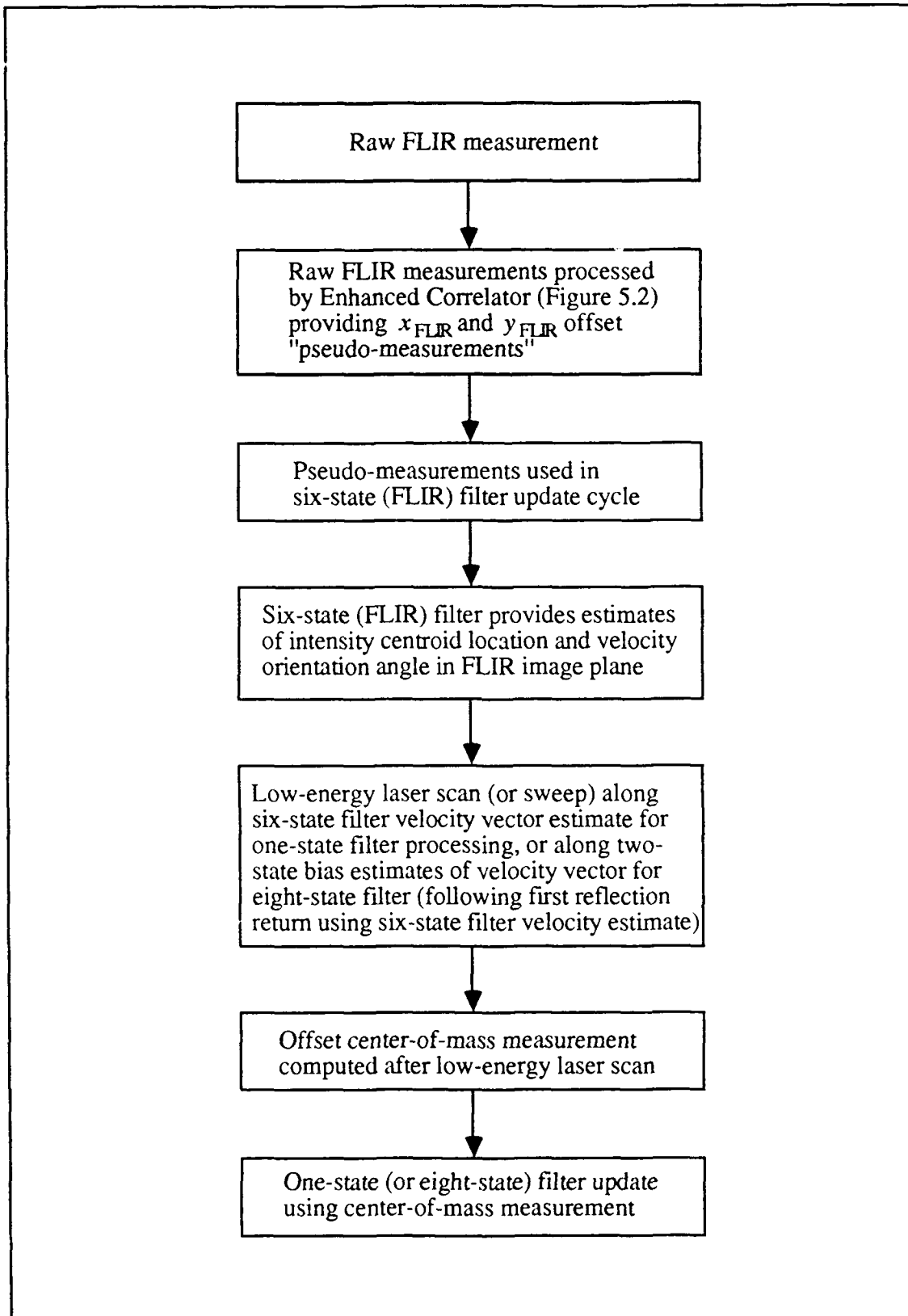


Figure 5.1. Data Processing for Two Filter Schemes Considered

In the second filter scheme, an eight-state filter (developed in this thesis) augments the original six-state filter with two additional states to estimate the FLIR  $x$  and  $y$  coordinates of the hardbody center-of-mass displacement from the intensity centroid. It uses its two center-of-mass bias states to determine the scan of the low-energy laser, following an initial low-energy laser scan using the six-state filter estimate of the target velocity vector. The dynamics and measurement models for each of the filters is covered in the following sections, as well as the enhanced correlation algorithm, and a FLIR FOV rotation scheme which maximizes the use of the FLIR viewing surface by rotating the diagonal of the FLIR FOV along the estimated velocity vector of the target.

## 5.2 Six-State Filter

The six-state filter model is a development over twelve years of research [2, 6, 21, 22, 26, 27]. The filter consists of two target position states, two target velocity states, and two atmospheric jitter position states. The filter is the same as that used in the previous thesis, except for choice of tuning parameters (Section 5.2.3). The proper tuning of the six-state filter is essential to the tracking of the intensity centroid, as well as to providing accurate estimation of the target velocity vector along which to scan the low-energy laser, and estimate the hardbody center-of-mass location.

*5.2.1 Dynamics Model.* The six-state filter dynamics model is a reduced version of an eight-state filter which included two acceleration states [26]. The acceleration states were eliminated from the model due to observability problems [2, 26]. The six-state Kalman filter used in this research is based upon the state vector:

$$\mathbf{x}_f = \begin{bmatrix} x_1 \\ x_2 \\ x_3 \\ x_4 \\ x_5 \\ x_6 \end{bmatrix} = \begin{bmatrix} x_d \\ y_d \\ v_x \\ v_y \\ x_a \\ y_a \end{bmatrix} \quad (5-1)$$

where

- $x_d$  = x component of centroid position (azimuth), relative to center of FOV
- $y_d$  = y component of centroid position (elevation), relative to center of FOV
- $v_x$  = x component of centroid velocity
- $v_y$  = y component of centroid velocity
- $x_a$  = x component of atmospheric jitter
- $y_a$  = y component of atmospheric jitter

The six states are coordinatized in the  $\alpha$ - $\beta$  (FLIR) plane. The target velocity and atmospheric jitter position states are each modeled as an exponentially time-correlated first-order Gauss-Markov process. A comparison of the filter states with the truth model states in Equation (4-16) shows that the atmospheric jitter model is reduced from the six states defined in the truth model to two states in the filter model. The filter model does not consider the the high frequency effect of the double pole in Equation (4-26). Therefore, the order of the filter's atmospheric model is reduced. The atmospheric state reduction does not greatly affect the filter's performance since the dominant characteristic of the atmospheric jitter is contained in the first-order term. The bending/vibration states are not modeled in the filter since past research [10] found no significant degradation in filter performance without these states. The pogo states are not modeled in the filter for this research. (The pogo effect is to be investigated to determine if it is necessary to model the plume oscillation in the filter.) The six-state filter model is described by the following time-invariant, linear stochastic differential equation:

$$\dot{\mathbf{x}}_f(t) = \mathbf{F}_f \mathbf{x}_f(t) + \mathbf{G}_f \mathbf{w}_f(t) \quad (5-2)$$

where

- $\mathbf{F}_f$  = 6 x 6 time-invariant system matrix
- $\mathbf{x}_f(t)$  = 6-dimensional filter state vector
- $\mathbf{G}_f$  = 6 x 4 time-invariant noise distribution matrix
- $\mathbf{w}_f(t)$  = 4-dimensional, white Gaussian noise process with independent components, and mean and covariance statistics:

$$E\{\mathbf{w}_f(t)\} = \mathbf{0} \quad (5-3)$$

$$E\{\mathbf{w}_f(t)\mathbf{w}_f^T(t+\tau)\} = \mathbf{Q}_f\delta(\tau) \quad (5-4)$$

The time-invariant system matrix  $\mathbf{F}_f$  is:

$$\mathbf{F}_f = \begin{bmatrix} 0 & 0 & 1 & 0 & 0 & 0 \\ 0 & 0 & 0 & 1 & 0 & 0 \\ 0 & 0 & -\frac{1}{\tau_x} & 0 & 0 & 0 \\ 0 & 0 & 0 & -\frac{1}{\tau_y} & 0 & 0 \\ 0 & 0 & 0 & 0 & -\frac{1}{\tau_{a_x}} & 0 \\ 0 & 0 & 0 & 0 & 0 & -\frac{1}{\tau_{a_y}} \end{bmatrix} \quad (5-5)$$

The noise distribution matrix  $\mathbf{G}_f$  is:

$$\mathbf{G}_f = \begin{bmatrix} 0 & 0 & 0 & 0 \\ 0 & 0 & 0 & 0 \\ 1 & 0 & 0 & 0 \\ 0 & 1 & 0 & 0 \\ 0 & 0 & 1 & 0 \\ 0 & 0 & 0 & 1 \end{bmatrix} \quad (5-6)$$

The strength of the white Gaussian noise  $\mathbf{w}_f$ , given by  $\mathbf{Q}_f$ , is:

$$\mathbf{Q}_f = \begin{bmatrix} \frac{2\sigma_x^2}{\tau_x} & 0 & 0 & 0 \\ 0 & \frac{2\sigma_y^2}{\tau_y} & 0 & 0 \\ 0 & 0 & \frac{2\sigma_{a_x}^2}{\tau_{a_x}} & 0 \\ 0 & 0 & 0 & \frac{2\sigma_{a_y}^2}{\tau_{a_y}} \end{bmatrix} \quad (5-7)$$

where

- $\tau_x, \tau_y$  = correlation times for the intensity centroid  $x$  and  $y$  velocities
- $\tau_{a_x}, \tau_{a_y}$  = correlation time for the atmospheric jitter position process in the  $x$  and  $y$  directions
- $\sigma_x^2, \sigma_y^2$  = variance and mean-squared value for the intensity centroid  $x$  and  $y$  velocities
- $\sigma_{a_x}^2, \sigma_{a_y}^2$  = variance and mean-squared value for the atmospheric jitter position process

To simulate the filter dynamics model on a digital computer, the discrete-time filter propagation equations [12] are used to propagate the state estimates and error covariance forward to the next measurement update:

$$\hat{\mathbf{x}}_f(t_{i+1}^-) = \Phi_f(\Delta t) \hat{\mathbf{x}}_f(t_i^+) \quad (5-8)$$

$$\mathbf{P}_f(t_{i+1}^-) = \Phi_f(\Delta t) \mathbf{P}_f(t_i^+) \Phi_f^T(\Delta t) + \mathbf{Q}_{df} \quad (5-9)$$

where

- $\hat{\mathbf{x}}_f(t_i)$  = filter estimate of the 6-dimensional state vector
- $\Phi_f(\Delta t)$  = 6 x 6 time-invariant state transition matrix for propagation  
over the sample period:  $\Delta t = t_{i+1} - t_i$
- $\mathbf{P}_f(t_i)$  = 6 x 6 filter covariance matrix
- $(t_i^-)$  = time instant before FLIR measurement is incorporated into  
the estimate at time  $t_i$
- $(t_i^+)$  = time instant after FLIR measurement is incorporated into  
the estimate at time  $t_i$
- $\mathbf{Q}_{df}$  = 6 x 6 filter dynamics noise covariance given by:

$$\mathbf{Q}_{df} = \int_{t_i}^{t_{i+1}} \Phi_f(t_{i+1}-\tau) \mathbf{G}_f \mathbf{Q}_f \mathbf{G}_f^T \Phi_f^T(t_{i+1}-\tau) d\tau \quad (5-10)$$

The time-invariant state transition matrix  $\Phi_f(\Delta t)$  is:

$$\Phi_f(\Delta t) = \begin{bmatrix} 1 & 0 & \Phi_{13} & 0 & 0 & 0 \\ 0 & 1 & 0 & \Phi_{24} & 0 & 0 \\ 0 & 0 & \Phi_{33} & 0 & 0 & 0 \\ 0 & 0 & 0 & \Phi_{44} & 0 & 0 \\ 0 & 0 & 0 & 0 & \Phi_{55} & 0 \\ 0 & 0 & 0 & 0 & 0 & \Phi_{66} \end{bmatrix} \quad (5-11)$$



where

$$\Phi_{13} = \tau_x [1 - \exp(-\frac{\Delta t}{\tau_x})]$$

$$\Phi_{24} = \tau_y [1 - \exp(-\frac{\Delta t}{\tau_y})]$$

$$\Phi_{33} = \exp(-\frac{\Delta t}{\tau_x})$$

$$\Phi_{44} = \exp(-\frac{\Delta t}{\tau_y})$$

$$\Phi_{55} = \exp(-\frac{\Delta t}{\tau_a})$$

$$\Phi_{66} = \exp(-\frac{\Delta t}{\tau_a})$$

$\Delta t$  = sample time interval,  $t_{i+1} - t_i$

The filter dynamics noise covariance  $\mathbf{Q}_{df}$  is:

$$\mathbf{Q}_{df} = \begin{bmatrix} q_{df11} & 0 & q_{df13} & 0 & 0 & 0 \\ 0 & q_{df22} & 0 & q_{df24} & 0 & 0 \\ q_{df31} & 0 & q_{df33} & 0 & 0 & 0 \\ 0 & q_{df42} & 0 & q_{df44} & 0 & 0 \\ 0 & 0 & 0 & 0 & q_{df55} & 0 \\ 0 & 0 & 0 & 0 & 0 & q_{df66} \end{bmatrix} \quad (5-12)$$

where

$$q_{df11} = 2\sigma_x^2 \tau_x \{ (\Delta t) - 2\tau_x [1 - \exp(-\frac{\Delta t}{\tau_x})] + \frac{\tau_x}{2} [1 - \exp(-\frac{2(\Delta t)}{\tau_x})] \}$$

$$q_{df22} = 2\sigma_y^2 \tau_y \{ (\Delta t) - 2\tau_y [1 - \exp(-\frac{\Delta t}{\tau_y})] + \frac{\tau_y}{2} [1 - \exp(-\frac{2(\Delta t)}{\tau_y})] \}$$

$$q_{df13} = 2\sigma_x^2 \{ 2\tau_x [1 - \exp(-\frac{\Delta t}{\tau_x})] - \frac{\tau_x}{2} [1 - \exp(-\frac{2(\Delta t)}{\tau_x})] \}$$

$$q_{df24} = 2\sigma_y^2 \{ 2\tau_y [1 - \exp(-\frac{\Delta t}{\tau_y})] - \frac{\tau_y}{2} [1 - \exp(-\frac{2(\Delta t)}{\tau_y})] \}$$

$$q_{df31} = q_{df13}$$

$$q_{df33} = \sigma_x^2 [1 - \exp(-\frac{2(\Delta t)}{\tau_x})]$$

$$q_{df42} = q_{df24}$$

$$q_{df44} = \sigma_y^2 [1 - \exp(-\frac{2(\Delta t)}{\tau_y})]$$

$$q_{df55} = \sigma_{a_x}^2 [1 - \exp(-\frac{2(\Delta t)}{\tau_{a_x}})]$$

$$q_{df66} = \sigma_{a_y}^2 [1 - \exp(-\frac{2(\Delta t)}{\tau_{a_y}})]$$

$$\Delta t = \text{sample time interval, } t_{i+1} - t_i$$

For a non-rotating FOV (NRFOV) FLIR sensor, the propagated intensity centroid position states  $\hat{x}_1(t_{i+1})$  and  $\hat{x}_2(t_{i+1})$  are applied as control signals to the pointing controller (Section 3.4). The pointing controller points the FLIR sensor centerline (LOS vector,  $\mathbf{e}_r$ ) at the filter-estimated position of the target's center of intensity following the filter's propagation of the state estimates. In addition to the position signals, for a diagonal rotating FOV (DRFOV) FLIR sensor, the filter's estimates of the velocity states  $\hat{x}_3(t_{i+1})$  and  $\hat{x}_4(t_{i+1})$  are used to rotate the FOV to align the filter's estimate of the velocity vector with the diagonal of the FOV (Section 5.2.2.4).

*5.2.2 FLIR Measurement Model.* This section discusses the data processing algorithm used to process the FLIR measurement information to update the Kalman filter. The computer simulation for this thesis uses an enhanced correlation algorithm, shown in Figure 5.2, which was developed in a previous thesis [27]. This algorithm combines the best features of a standard correlation tracker and a Kalman filter. The correlation tracker provides template generation of the intensity function, while the Kalman filter uses its internal dynamics model to provide future estimates of the intensity function position based on the template information. The correlator provides "measurements" of position offsets of the target centroid that are well represented by linear models; therefore, a linear Kalman filter is used as opposed to the nonlinear extended Kalman filter.

The enhanced correlation algorithm uses the properties of the Fourier transform to process the raw FLIR measurements to identify the target intensity shape function

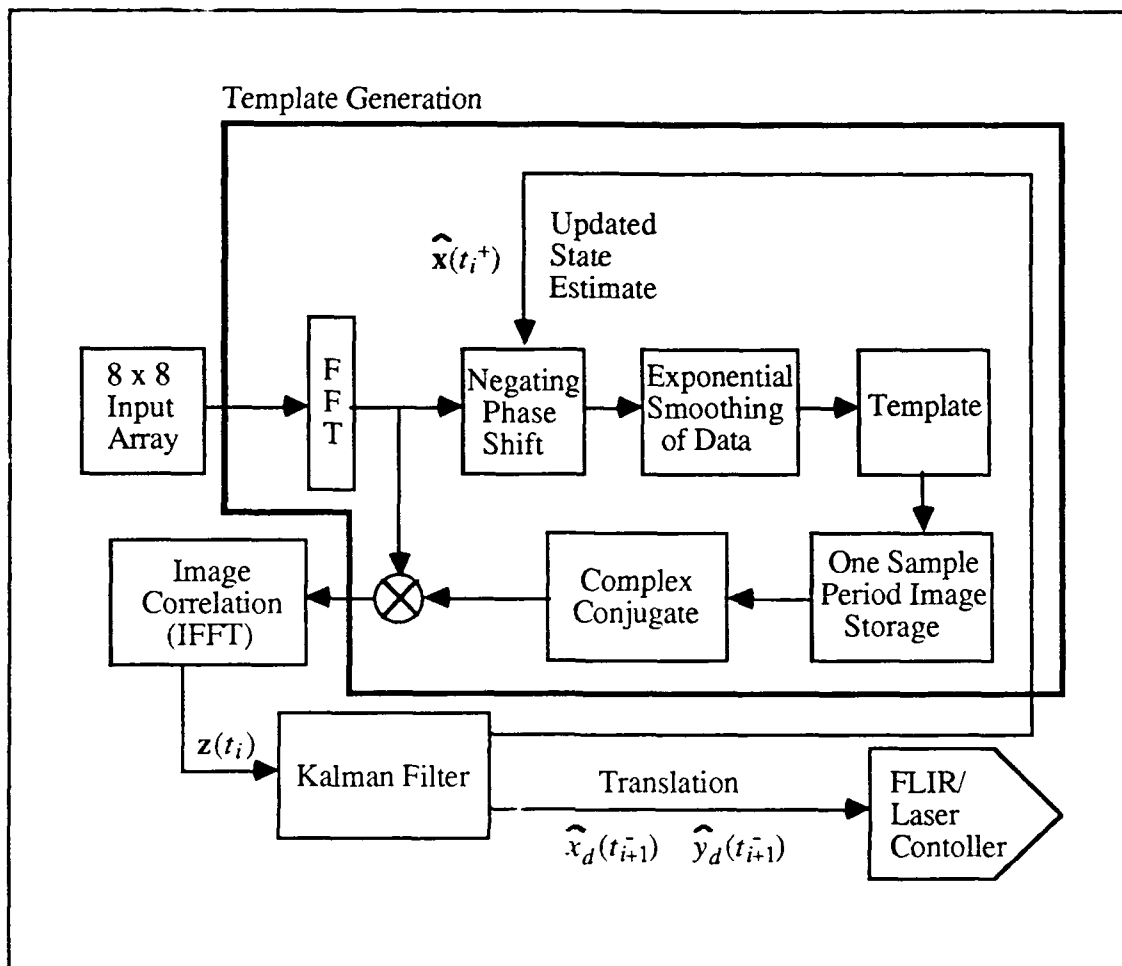


Figure 5.2. Enhanced Correlator/Linear Measurement Model Data Processing Algorithm

(template) through the noise-corrupted data, and provides computational efficiency. Specifically, the "shifting property" of the Fourier domain is used with updated filter estimates to center the template in the FLIR plane. The enhanced correlation algorithm is explained in more detail in the next section.

The enhanced correlation algorithm is affected by a FLIR plane rotation scheme, which maximizes the use of the available surface area of the FLIR 8 x 8 FOV. The rotation of the 8 x 8 FLIR plane was investigated in earlier research for high-g dynamic target maneuvering [25, 26]. The diagonal rotating FOV (Section 5.2.2.5) aligns the filter estimated target velocity vector with the diagonal of the FLIR plane to keep the target in the

FOV during any type of maneuvering. This feature is not necessary for the relatively benign trajectory of a missile, but it is considered in this research as a tracking option. The rotation of the FLIR plane requires that rotations are also performed on data going into and out of the the enhanced correlation algorithm. The DRFOV rotation of the FLIR image plane is covered in Section 5.2.2.5.

*5.2.2.1 Enhanced Correlation Algorithm* The FLIR sensor provides "raw" measurement information concerning the location of the apparent intensity function of the target on the FLIR plane. Before this information is given to the filter, it is processed through an enhanced correlation algorithm, shown in Figure 5.2. The original thesis work [21] showed that a Kalman filter outperformed a standard correlation tracker (Table 1.2). However, a later thesis [27] suggested that an enhanced correlation algorithm could replace the 64-dimensional measurement model used as the basis for an extended Kalman filter that processed raw FLIR measurement data directly. A linear Kalman filter is used with the enhanced correlation algorithm since the output measurements to the filter are linear measurements. The enhanced correlation algorithm is "enhanced" over the standard correlation algorithm in the following ways [26]:

1. The most current FLIR data frame is correlated with a template (which is an estimate of the target's intensity function), as opposed to correlation with the previous FLIR data frame.
2. Instead of outputting the peak of the correlation function, the enhanced correlator outputs the center of mass of the portion of the correlation function (intensity centroid) which is greater than some predetermined lower bound. This technique is known as "thresholding". As a result, the enhanced correlator does not suffer the problem of distinguishing global peaks from local peaks, as do many conventional "peak-finding" correlation algorithms.

3. Using the enhanced correlation algorithm, the FLIR/laser pointing commands are determined via the Kalman filter propagation cycle estimates, as opposed to the output of a standard correlation algorithm.
4. The Kalman filter state estimate  $\hat{\mathbf{x}}(t_i^+)$  is used to center the template, so the offsets seen in the enhanced correlation algorithm should be smaller than in the conventional correlator described in [21]. This increases the amount of "overlap" between the actual FLIR data and the stored template, thus improving overall performance.

The enhanced correlation algorithm uses the 8 x 8 array of target intensities obtained by the FLIR measurement, to establish a 64-element shape function from the target intensity profile (Section 4.4.1). The intensity functions are centered on the FLIR plane by the "shifting property" of the Fourier Transform, i.e., negating phase shifts are applied in the spatial frequency domain, which is the domain that the correlation takes place (Section 5.2.2.2). Exponential smoothing, as indicated in Figure 5.2, is then used to average the result with previously centered images, to yield an updated template. The current FLIR data is correlated against the template of the previously stored shape function (Section 5.2.2.3) that has been centered on the FLIR image plane. The outputs of the enhanced correlation algorithm are two linear offsets  $x_c$  and  $y_c$  that yield highest correlation of the current data with the template. These "pseudo-measurements" (Section 5.2.2.4) are then fed into a linear Kalman filter update cycle. The Kalman filter updates the states based on the pseudo-measurements and its internal models, then propagates the updated state estimates,  $\hat{\mathbf{x}}_d(t_{i+1})$ , to the next measurement (sample). The target position estimates,  $\hat{x}_d(t_{i+1})$  and  $\hat{y}_d(t_{i+1})$ , are applied to the FLIR/laser controller which centers the FLIR FOV and laser sensors to point in the direction of the predicted location of the target at the next sample time (Section 3.4). The filter also provides the updated estimate,  $\hat{\mathbf{x}}_d(t_i^+)$ , which is

used to center the FLIR intensity profile to be included in the template generation for the next measurement.

*5.2.2.2 Data Processing in the Fourier Domain.* All of the information of a two-dimensional intensity pattern can be preserved by a set of eigenvalues and eigenfunctions. However, to retain all of the information of a profile could require an infinite set of eigenvalues and eigenfunctions. Therefore, it is desirable to process the FLIR measurement data in a coordinate system which has properties more conducive to recognizing patterns in the spatial coordinate system. As described in the previous sections, the Kalman filter uses the pseudo-measurements (correlator outputs) derived from raw intensity functions to update the state estimates. Noise-corrupted FLIR data is processed through the enhanced correlation algorithm to determine the target's intensity profile (template). The process of determining the target intensity template from the noisy data is readily accomplished in the Fourier domain. Additionally, the "translational shift" for centering the template is easily accomplished in the Fourier domain; the difficult correlation in the time domain is a simple multiplication in the Fourier domain. Fourier transforms also lend themselves well to optical implementation, which reduces the computer resources required.

*5.2.2.3 Template Generation.* The template, shown by the boxed in area of Figure 5.2, reconstructs the shape, size, and location of the intensity centroid using the raw noise-corrupted FLIR measurements as its input. The outputs of the correlator are the two linear  $x$  and  $y$  coordinate FLIR measurements, which are provided to the Kalman filter. These measurements are referred to as "pseudo-measurements" due to the preprocessing that is done on the raw FLIR data before being given to the filter. This section and the following section explain the generation of the template and the resulting pseudo-measurements by discussing the significance of each of the template generation blocks of Figure 5.2.

The template generation begins with an input of a FLIR frame of data to the enhanced correlator of Figure 5.2. Using the property of the fast Fourier transform (FFT), which states that a translational shift in the spatial domain is equivalent to a linear phase shift in the frequency domain, the phase shift is computed by:

$$F\{g(x - x_{shift}, y - y_{shift})\} = G(f_x, f_y)\exp\{-j 2\pi((f_x \cdot x_{shift} + f_y \cdot y_{shift}))\} \quad (5-13)$$

where

$$\begin{aligned} F\{\cdot\} &= \text{Fourier Transform operator} \\ g(x, y) &= \text{2-dimensional spatial data array} \\ G(f_x, f_y) &= F\{g(x, y)\} \\ f_x, f_y &= \text{spatial frequencies} \end{aligned}$$

The Fourier transform is implemented in the software using the Cooley-Tukey algorithm [27]. After the raw data is transformed into the Fourier domain by the FFT, the target shape function is "centered on the FLIR plane" by phase shifting the transformed function an amount equal to:

$$x_{shift}(t_i) = \hat{x}_d(t_i^+) + \hat{x}_a(t_i^+) \quad (5-14)$$

$$y_{shift}(t_i) = \hat{y}_d(t_i^+) + \hat{y}_a(t_i^+) \quad (5-15)$$

where  $\hat{x}_d$ ,  $\hat{y}_d$ ,  $\hat{x}_a$ , and  $\hat{y}_a$  are the state estimates described by Equation (5-1).

Once the data is centered on the FLIR plane, it is incorporated into an updated template for the next sample period. In the simulation, the Kalman filter's first update cycle is bypassed to form the initial correlation template.

Temporal averaging of centered images using a true finite memory averager could require a large computer memory. A template, used in a finite memory averager [13], is normally accomplished by averaging over the  $N$  most recent centered intensity functions.

The memory size  $N$  is chosen according to how rapidly the shape functions change. Highly dynamic intensity functions require small values of  $N$ , while slowly varying functions use large  $N$  values. The averaging is intended to accentuate the target intensity function and to attenuate the corrupting background and FLIR noises. To overcome the computer storage problem, the enhanced correlation algorithm employs an "exponential smoothing" technique which reduces the storage requirement to a single FLIR frame of data. Exponential smoothing yields a very good approximation of  $N$  averaged samples of data. The template is maintained by the exponential smoothing algorithm given by:

$$\hat{\mathbf{I}}(t_i) = \gamma \mathbf{I}(t_i) + (1 - \gamma) \hat{\mathbf{I}}(t_{i-1}) \quad (5-16)$$

where

$$\begin{aligned} \hat{\mathbf{I}}(t_i) &= \text{"smoothed estimate" of the target's intensity function} \\ &\quad \text{(i.e., the template)} \\ \mathbf{I}(t_i) &= \text{"raw" intensity function from the current FLIR data frame} \\ \gamma &= \text{smoothing constant: } 0 < \gamma \leq 1 \end{aligned}$$

The smoothing constant  $\gamma$  is comparable to the  $N$  value of the true finite memory averager. From Equation (5-16), it can be seen that large values of  $\gamma$  emphasize the current data frame, which corresponds to small  $N$  values in the finite memory filter. Based on previous studies [11, 29], a smoothing constant of  $\gamma = 0.1$  is used for this thesis.

With the formation and storage of the correlation template for the next sample period, the current FLIR measurement is compared to the previously stored template obtained from the last sample time. This cross-correlation between the current measurement and the template is accomplished in the Fourier domain. The results from the cross-correlation are the  $x$  and  $y$  FLIR plane pseudo-measurements provided to the linear Kalman filter.



5.2.2.4 "Pseudo-Measurements". The current FLIR measurement frame is used to form the template for the next sample update, and is cross-correlated with the previous template in the Fourier domain (Figure 5.2) to determine the position offsets from the center of the FOV to the centroid of the target intensity image. The cross-correlation is computed by taking the inverse fast Fourier transform (IFFT) of the equation [27]:

$$F\{g(x, y) * l(x, y)\} = G(f_x, f_y)L^*(f_x, f_y) \quad (5-17)$$

where

- $F\{\cdot\}$  = Fourier Transform operator
- $g(x, y)$  = measured target intensity function of the current FLIR data frame
- $l(x, y)$  = expected target intensity function (i.e., the template)
- $g(x, y) * l(x, y)$  = cross-correlation of  $g(x, y)$  and  $l(x, y)$
- $G(f_x, f_y)$  =  $F\{g(x, y)\}$
- $L^*(f_x, f_y)$  = complex conjugate of  $F\{l(x, y)\}$

Once the IFFT is accomplished on the data, the correlation function,  $g(x, y) * l(x, y)$ , is "thresholded" at 30% of the function's maximum value; values below this threshold level are set to zero [11, 24]. The location of the center-of-mass of the thresholded function represents the relative displacement between the current FLIR data frame and the template. The result of the IFFT is the offset of the thresholded FLIR intensity centroid from the center of the FLIR FOV. This offset is assumed to be the result of the summed effects of target dynamics, atmospheric jitter, and measurement noise. The x- and y-component offsets out of the correlator are the pseudo-measurements provided to the Kalman filter. The offset measurements are modeled by:

$$x_{offset} = x_d + x_a + v_{f1} \quad (5-18)$$

$$y_{offset} = y_d + y_a + v_{f2} \quad (5-19)$$

where  $x_d$ ,  $y_d$ ,  $x_a$ , and  $y_a$  are as defined in Equation (5-1), and  $v_{f1}$  and  $v_{f2}$  are the measurement noises associated with each offset coordinate. The state space representation of Equations (5-18) and (5-19) is:

$$\mathbf{z}(t_i) = \mathbf{H}_f \mathbf{x}_f(t_i) + \mathbf{v}_f(t_i) \quad (5-20)$$

where

$$\begin{aligned} \mathbf{z}(t_i) &= [x_{offset}(t_i), y_{offset}(t_i)]^T \\ \mathbf{H}_f &= 2 \times 6 \text{ measurement matrix} \\ \mathbf{x}_f(t_i) &= \text{state vector of Equation (5-1)} \\ \mathbf{v}_f(t_i) &= 2\text{-dimensional, discrete, white Gaussian} \\ &\quad \text{measurement noise with statistics:} \end{aligned}$$

$$E \{ \mathbf{v}(t_i) \} = \mathbf{0} \quad (5-21)$$

$$E \{ \mathbf{v}(t_i) \mathbf{v}(t_j) \} = \begin{cases} \mathbf{R} & t_i = t_j \\ \mathbf{0} & t_i \neq t_j \end{cases} \quad (5-22)$$

The FLIR measurement matrix  $\mathbf{H}_f$  is:

$$\mathbf{H}_f = \begin{bmatrix} 1 & 0 & 0 & 0 & 1 & 0 \\ 0 & 1 & 0 & 0 & 0 & 1 \end{bmatrix} \quad (5-23)$$

The measurement noise  $\mathbf{v}_f(t_i)$  reflects the corrupting effects of the spatially correlated background noise (Section 4.5.7), the FLIR sensor noise, and the errors due to the FFT/IFFT processes. The covariance matrix  $\mathbf{R}_f$  (with units of pixels<sup>2</sup>) associated with this cumulative error is [6, 22, 27]:

$$\mathbf{R}_f = \begin{bmatrix} 0.00363 & 0 \\ 0 & 0.00598 \end{bmatrix} \quad (5-24)$$

Due to the linearity of this measurement model, the Kalman filter processes the correlator pseudo-measurements of Equation (5-20) using a linear update cycle. This update cycle is defined by the equations [12]:

$$\mathbf{K}(t_i) = \mathbf{P}_f(t_i^-) \mathbf{H}_f^T [\mathbf{H}_f \mathbf{P}_f(t_i^-) \mathbf{H}_f^T + \mathbf{R}]^{-1} \quad (5-25)$$

$$\hat{\mathbf{x}}_f(t_i^+) = \hat{\mathbf{x}}_f(t_i^-) + \mathbf{K}(t_i) [\mathbf{z}(t_i) - \mathbf{H}_f \hat{\mathbf{x}}_f(t_i^-)] \quad (5-26)$$

$$\mathbf{P}_f(t_i^+) = \mathbf{P}_f(t_i^-) - \mathbf{K}(t_i) \mathbf{H}_f \mathbf{P}_f(t_i^-) \quad (5-27)$$

where

- $\mathbf{K}(t_i)$  = 6 x 2 filter gain matrix
- $\mathbf{P}_f(t_i)$  = 6 x 6 filter covariance matrix
- $\mathbf{H}_f$  = 2 x 6 measurement matrix; Equation (5-23)
- $\mathbf{R}_f$  = 2 x 2 measurement noise covariance matrix; Equation (5-24)
- $\hat{\mathbf{x}}_f(t_i)$  = 6-dimensional estimated state vector; Equation (5-1)
- $\mathbf{z}(t_i)$  = 2-dimensional measurement vector; Equation (5-20)
- $(t_i^-)$  = time instant immediately before measurements are incorporated at time  $t_i$
- $(t_i^+)$  = time instant immediately after measurements are incorporated at time  $t_i$

**5.2.2.5 Field-of-View Rotation** The FOV used in this research is an 8 x 8 diagonal rotating FOV (DRFOV). Previous research [10] investigated a larger 24 x 24 FOV to ensure tracking of the target during high-g maneuvers. Additionally, further research [25, 26] investigated different orientations and rotation schemes of an 8 x 8 FOV.

The DRFOV essentially accomplished the same objective as the larger 24 x 24 FOV. The DRFOV scheme is shown in Figure 5.3. It incorporates the maximum benefit from the 8 x 8 FLIR FOV by continually aligning the diagonal of the FLIR plane along the filter-estimated velocity vector of the target. Since a missile target exhibits a rather benign dynamic trajectory, and based on the previous research accomplished (Section 1.2), the 8 x 8 DRFOV is capable of ensuring that the target remains in the FOV at all times under the constraints of the testing, which initially includes no staging and no plume pogo phenomenon. It is possible that staging events may create acceleration characteristics which could warrant a closer investigation of the size and/or orientation of the FLIR FOV. In addition to staging, the maximum amplitude of the plume's pogo along the longitudinal axis could possibly cause the 8 x 8 FOV tracker to lose lock on the target. The effect of the plume pogo on the filter performance on the FLIR FOV is evaluated in this research (Chapter VI).

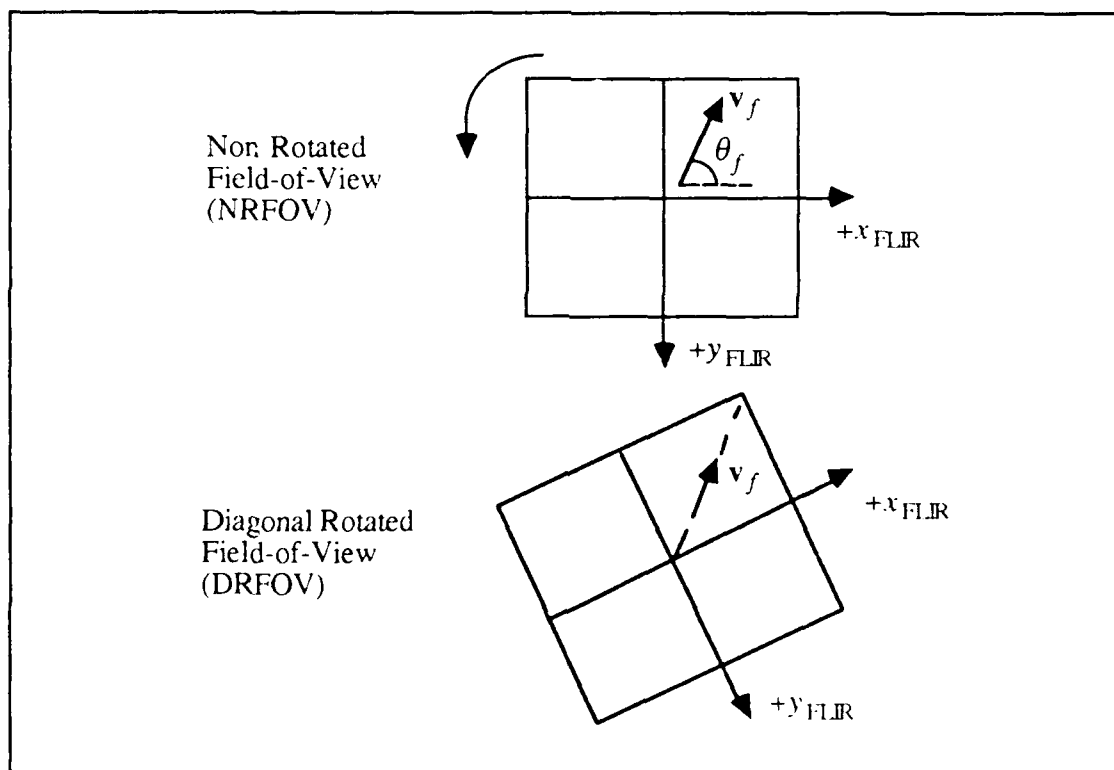


Figure 5.3. DRFOV Rotation Scheme [26]

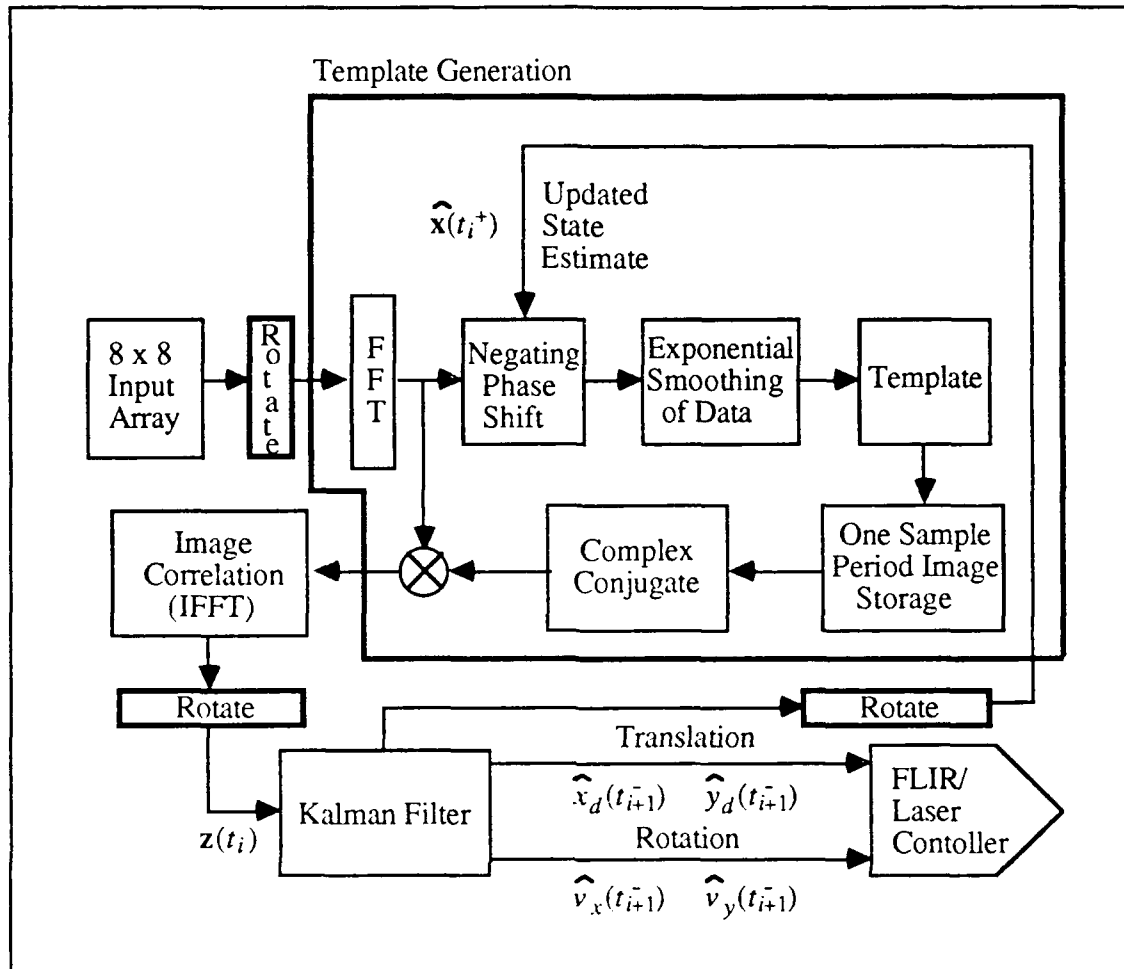


Figure 5.4. Data Processing Algorithm for Rotating Field-of View [26]

The incorporation of the DRFOV requires that the structure of the data processing algorithm is modified to provide commanding of the controller to rotate the FOV plane, and to ensure that the states, residuals, and measurements are processed in the non-rotated FOV. The changes to the enhanced correlation algorithm (Figure 5.2) are shown in Figure 5.4 when the FLIR FOV is rotated.

It is interesting to compare the data processing algorithms of previous theses with the current algorithm. The original data processing algorithm [28] is shown in Figure 1.3, and the first enhanced correlation algorithm [27] is shown in Figure 1.4. Additionally, a comparison should be made with the enhanced correlation algorithm with a non-rotated

FLIR FOV (Figure 5.2). The operation of the DRFOV and the data processing algorithm modifications are discussed in the following paragraphs. (Refer to Figure 5.4 throughout the discussion.) The description of the enhanced correlation algorithm without a rotated FOV is found in the previous four sections of this chapter.

As discussed in a previous thesis [26], the design of the DRFOV rotation scheme is dependent upon the filter's estimate of the target's positive velocity orientation angle  $\hat{\theta}_f$ . This angle is the filter's estimate of  $\theta_f$ , shown in Figures 3.7 and 4.8. The filter's estimate of  $\hat{\theta}_f$  is given by:

$$\hat{\theta}_f = \arctan \left[ \frac{-\hat{v}_y}{\hat{v}_x} \right] \quad (5-28)$$

The terms  $\hat{v}_x$  and  $\hat{v}_y$  are the third and fourth states of the six-state filter's state vector. Therefore, in addition to providing the translational velocity states, the filter is also estimating the velocity orientation angle. The filter can provide control inputs to the FLIR sensor and perform both a translation of the center of the FOV and a rotation of the FOV during on-line processing of the algorithm. The negative sign in the numerator of Equation (5-28) is due to the FLIR coordinate frame discussed in Section 3.2.4 and shown in Figure 3.2. The filter velocity vector orientation angle  $\theta$  in the FLIR plane (Figure 3.9) is positive in the counter-clockwise direction from the positive  $x$ -axis looking from the inertial reference frame through the FLIR plane at the target along the LOS ( $\mathbf{e}_r$ ) vector.

In the computer simulation, the rotation of the FLIR sensor for the DRFOV scheme is accomplished by applying the incoming FLIR measurements to a rotation matrix before the data is applied to the data processing algorithm. This rotation is shown in Figure 5.3 as the "Rotate" block following the incoming  $8 \times 8$  input array (FLIR measurements). The amount of rotation is dependent on the angle  $\hat{\theta}_f$  given by Equation (5-28). The actual rotation of the FLIR plane is further simulated by performing a rotation on the Gaussian

intensity functions rather than the FLIR plane itself. For example, for a positive velocity orientation, a negative rotation is accomplished on the location and orientation of the individual Gaussian intensity functions. Conversely, a negative rotation of the FLIR plane is accomplished for a negative velocity orientation, by performing a positive rotation on the location and orientation of the individual Gaussian intensity functions. For the DRFOV the rotation angle needed to align the target velocity vector with a diagonal of the FOV is determined by:

$$\hat{\psi} = \hat{\theta}_f - \frac{\pi}{4} \quad (5-29)$$

where  $\hat{\psi}$  is the estimate of the necessary rotation angle based on  $\hat{\theta}_f$  to rotate the filter's estimate of the velocity vector along the diagonal of the FLIR plane, as shown in Figure 5-5.

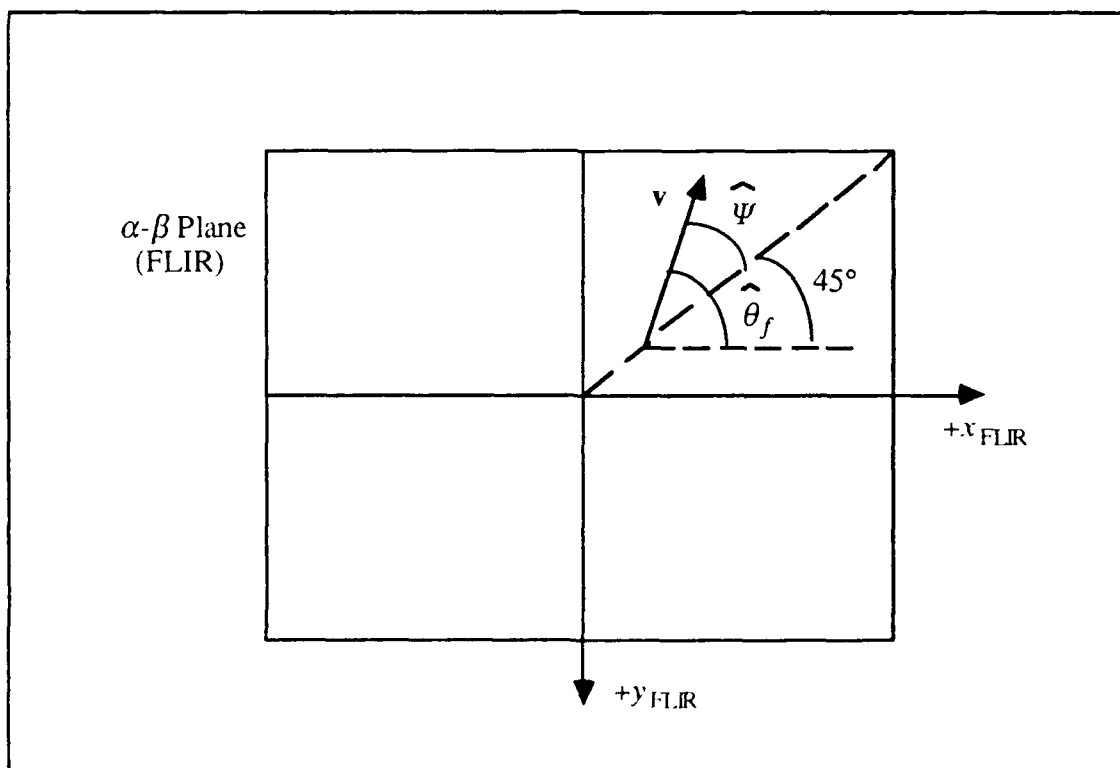


Figure 5.5. DRFOV Rotation Geometry

The angle obtained from Equation (5-29) is used to rotate the two intensity functions used to model the target plume. Each of the intensity functions, defined by Equation (3-1), is rotated using the rotation algorithm given by [25]:

$$\begin{bmatrix} x'_{peak} \\ y'_{peak} \end{bmatrix} = \begin{bmatrix} \widehat{\cos\psi} & -\widehat{\sin\psi} \\ \widehat{\sin\psi} & \widehat{\cos\psi} \end{bmatrix} \begin{bmatrix} x_{peak} \\ y_{peak} \end{bmatrix} \quad (5-30)$$

where the primed variables correspond to the rotated coordinate system.

The bivariate Gaussian intensity function of Equation (3-1) is then given by [25]:

$$I [x', y', x'_{peak}(t), y'_{peak}(t)] = I_{max} \exp[-0.5[\Delta x' \Delta y'] \mathbf{P}^{-1} [\Delta x' \Delta y']^T] \quad (5-31)$$

where

$$\Delta x' = (x' - x'_{peak}) \cos \Delta\theta + (y' - y'_{peak}) \sin \Delta\theta$$

$$\Delta y' = (y' - y'_{peak}) \cos \Delta\theta - (x' - x'_{peak}) \sin \Delta\theta$$

$$\Delta\theta = \text{difference between the truth model velocity orientation angle and the filter computed velocity orientation angle (i.e., } \Delta\theta = \theta_t - \widehat{\theta}_f \text{)}$$

$$x', y' = \text{rotated coordinates from the original FLIR coordinate frame via the same rotation matrix used in Equation (5-31)}$$

$$x'_{peak}, y'_{peak} = \text{rotated coordinates of the peak intensity of the single Gaussian intensity function}$$

$$I_{max} = \text{maximum intensity function}$$

$$\mathbf{P} = 2 \times 2 \text{ target dispersion matrix whose eigenvalues define the dispersion of the elliptical constant intensity contours (along the velocity vector and perpendicular to that velocity vector, respectively) in the } \alpha\text{-}\beta \text{ (FLIR) plane (Sections 3.2 and 3.3.4)}$$



Once the incoming FLIR measurements are rotated to align the diagonal of the FLIR plane with the estimated target velocity vector, the data processing algorithm shown in Figure 5.4 operates in the same manner as previously described, but now the data is transformed into a rotated coordinate system. Figure 5.4 also shows two other rotations on data before it enters or leaves the data processing algorithm. The translational shifts to center the incoming FLIR data, given by Equations (5-14) and (5-15), are accomplished in the correlation algorithm. The shift information is computed by the Kalman filter in the filter coordinate system, while the image data is represented in a rotated coordinate system simulating the DRFOV. Therefore, to implement the DRFOV data processing algorithm, the translational shift data from the filter is rotated by the same transformation that was used on the FLIR measurement data:

$$\begin{bmatrix} x'_{shift} \\ y'_{shift} \end{bmatrix} = \begin{bmatrix} \hat{\cos}\psi & -\hat{\sin}\psi \\ \hat{\sin}\psi & \hat{\cos}\psi \end{bmatrix} \begin{bmatrix} x_{shift} \\ y_{shift} \end{bmatrix} \quad (5-32)$$

where  $x_{shift}$  and  $y_{shift}$  are given by Equations (5-14) and (5-15).

The transformation given by Equation (5-32) is accomplished in the "Rotate" block following the Kalman filter shown in Figure 5.4. Now the current image data and the filter's estimate of the target centroid, given by the shift Equations (5-14) and (5-15), are both in the rotated coordinate frame, and the template generation proceeds as described in Section 5.2.2.3.

The third rotation required is shown in Figure 5.4 by the "Rotate" block following the IFFT. The outputs of the IFFT are the linear  $x_{FLIR}$  and  $y_{FLIR}$  offsets between the current data image and the centered template from the previous sample period. These offsets, given by Equations (5-18) and (5-19), are the pseudo-measurements described in Section 5.2.2.4. The correlator provides these linear measurements to the Kalman filter for

its update cycle. Since the Kalman filter processes the measurements in the unrotated filter coordinate frame and the linear offsets from the enhanced correlator are in the rotated frame, the measurements must be rotated opposite to the rotations performed on the filter shift data and the intensity function peaks. The rotation, shown by the "Rotate" block of Figure 5.4, is given by:

$$\begin{bmatrix} z_1 \\ z_2 \end{bmatrix} = \begin{bmatrix} \widehat{\cos\psi} & \widehat{\sin\psi} \\ -\widehat{\sin\psi} & \widehat{\cos\psi} \end{bmatrix} \begin{bmatrix} z'_1 \\ z'_2 \end{bmatrix} \quad (5-33)$$

where  $z_1$  and  $z_2$  are the components of the two-dimensional measurement vector of Equation (5-20) in the filter coordinate frame. The measurements  $z'_1$  and  $z'_2$  are the linear offsets provided by the enhanced correlator in the rotated FOV.

*5.2.3 Filter Parameters.* This section describes the modeling parameters, initial conditions, and tuning parameters for the six-state filter used in this research. There may be some duplication of information. This is purposefully done to ensure the reader has knowledge of pertinent parameter values during the course of reading the document, as well as a single reference place for the information.

*5.2.3.1 Modeling Values.* The filter target dynamics correlation time constants  $\tau_x$  and  $\tau_y$  for this research are both equal to 8.5 seconds. These values represent a target with rather benign dynamics. The atmospheric correlation time constants  $\tau_{a_x}$  and  $\tau_{a_y}$  are both set equal to 0.0707 seconds in the simulation.

*5.2.3.2 Initial Conditions.* In the tracking simulation, the filter is initialized to zero error for the position and velocity states. These are not realistic initial conditions for the filter in the real world, however since the values are established from previous research [30], these initial conditions remain the same. The position states  $x_1$  and  $x_2$  are initialized with the intensity centroid of the target centered in the FLIR FOV. The velocity states  $x_3$

and  $x_4$  are initialized in accordance with the target's initial trajectory conditions (Section 3.5 and 4.5.2), and the transformation Equations (3-4) and (3-6). The atmospheric states  $x_5$  and  $x_6$  are initialized to zero.

The initial state covariance matrix  $\mathbf{P}(t_0)$  is:

$$\mathbf{P}(t_0) = \begin{bmatrix} 10 & 0 & 0 & 0 & 0 & 0 \\ 0 & 10 & 0 & 0 & 0 & 0 \\ 0 & 0 & 2000 & 0 & 0 & 0 \\ 0 & 0 & 0 & 2000 & 0 & 0 \\ 0 & 0 & 0 & 0 & .2 & 0 \\ 0 & 0 & 0 & 0 & 0 & .2 \end{bmatrix} \quad (5-34)$$

where the position states  $x_1$  and  $x_2$  and the atmospheric states  $x_5$  and  $x_6$  have units of pixels<sup>2</sup>; the velocity states  $x_3$  and  $x_4$  have units of pixels<sup>2</sup>/seconds<sup>2</sup>.

The measurement covariance matrix  $\mathbf{R}_f$  (with units of pixels<sup>2</sup>) is [18, 27]:

$$\mathbf{R}_f = \begin{bmatrix} 0.00363 & 0 \\ 0 & 0.00598 \end{bmatrix} \quad (5-35)$$

*5.2.3.3 Tuning Values.* The filter dynamics variances  $\sigma_x^2$  and  $\sigma_y^2$  are both set equal to 800 pixels<sup>2</sup>/seconds<sup>2</sup> without plume pogo applied to the intensity centroid, and also with plume pogo applied. The atmospheric variances  $\sigma_{a_x}^2$  and  $\sigma_{a_y}^2$  are both set equal to 0.2 pixels<sup>2</sup>. This corresponds to the truth model value of 0.2 pixels<sup>2</sup>.

### 5.3 One-State Filter

The one-state (center-of-mass) filter generated in the previous research [2] estimates the distance from the center of intensity to the hardbody center-of-mass using the updated six-state (FLIR) filter states. This one-state (center-of-mass) filter uses the six-state (FLIR) filter's estimate of the target's velocity vector to obtain measurements from the low-energy

laser scan, which the filter uses to estimate the hardbody center-of-mass location. The center-of-mass position offset estimate is calculated as a bias distance along the estimated velocity direction from the filter's estimate of the intensity centroid. The measurement provided to the center-of-mass filter is from a low-energy laser sensor, which receives the reflections of a low-energy laser scanned along the FLIR filter's estimated velocity vector direction, emanating from the estimated center of intensity location. Figure 5.6 shows the physical representation of estimating the hardbody center-of-mass for the one-state (center-of-mass) filter, and the dependence of the one-state filter on the FLIR filter's estimate of the intensity centroid location and the estimated velocity vector of the target. Except for the dependence on the FLIR filter to provide the centroid velocity estimates, the center-of-mass filter computations are independent of the FLIR filter. Additionally, the FLIR filter has no knowledge of the existence of the center-of-mass filter.

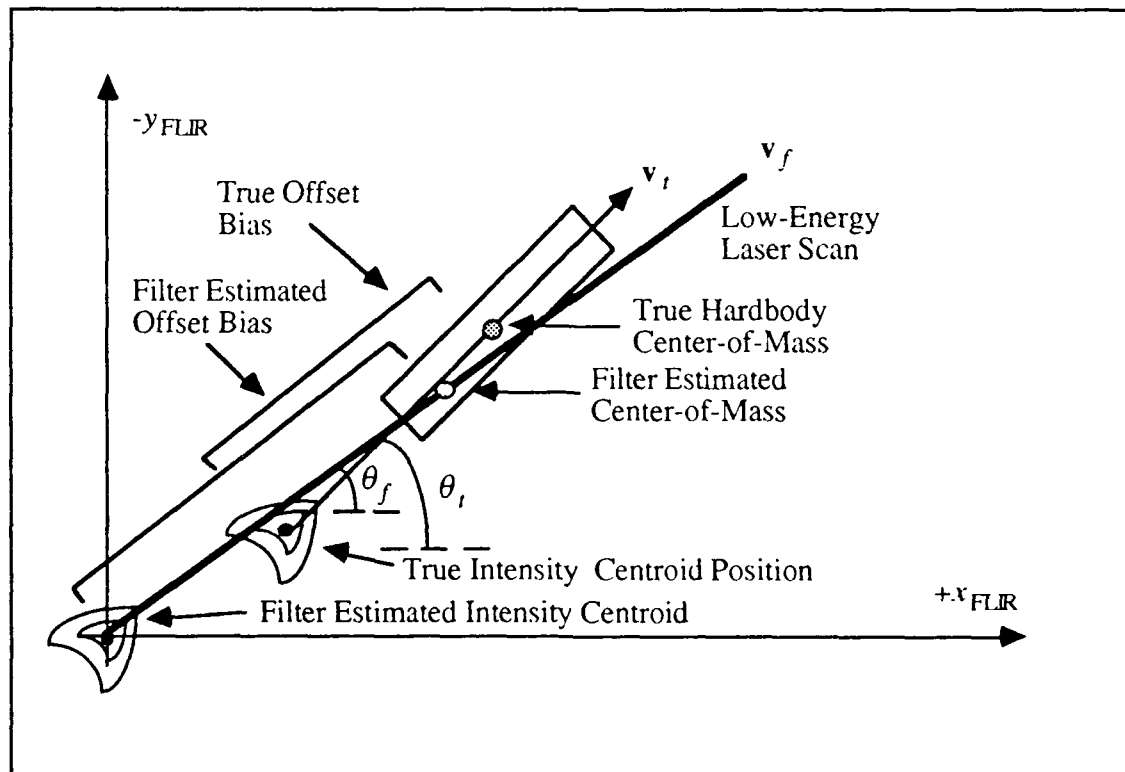


Figure 5.6. One-State Filter Estimate of Missile Hardbody Center-of-Mass

5.3.1 *Dynamics Model.* As previously stated, the offset between the intensity centroid and the hardbody center-of-mass is represented as a bias. Therefore, the dynamics model for the one-state filter is a simple integrator, with driving pseudo-noise for filter tuning purposes. The single-state representation of the linear, time-invariant, stochastic differential equation is given by:

$$\dot{x}_f(t) = F_f x_f(t) + G_f w_f(t) \quad (5-36)$$

where

- $F_f$  = 0 (since the model is represented as a bias)
- $x_f(t)$  = state representing offset distance between missile center-of-mass and intensity centroid
- $G_f$  = time-invariant noise distribution matrix;  $G_f = 1$
- $w_f(t)$  = independent, white Gaussian noise process with mean and covariance statistics:

$$E\{w_f(t)\} = 0 \quad (5-37)$$

$$E\{w_f(t)w_f(t+\tau)\} = Q_f \delta(\tau) \quad (5-38)$$

To simulate the filter dynamics model on a digital computer, the scalar discrete-time propagation Equations (5-8) and (5-9) are used to propagate the state estimates and error covariance forward to the next measurement update:

$$\hat{x}_f(t_{i+1}^-) = \Phi_f(\Delta t) \hat{x}_f(t_i^+) \quad (5-39)$$

$$P_f(t_{i+1}^-) = \Phi_f(\Delta t) P_f(t_i^+) \Phi_f(\Delta t) + Q_{df} \quad (5-40)$$

where

- $\hat{x}_f(t_i)$  = filter estimate of the 1-dimensional state vector
- $\Phi_f(\Delta t)$  = time-invariant state transition scalar for propagation over the sample period:  $\Delta t = t_{i+1} - t_i$ ;  $\Phi_f(\Delta t) = 1$
- $P_f(t_i)$  = filter variance

- $(t_i^-)$  = time instant before FLIR measurement is incorporated into the estimate at time  $t_i$   
 $(t_i^+)$  = time instant after FLIR measurement is incorporated into the estimate at time  $t_i$   
 $Q_{df}$  = filter dynamic noise covariance given by:

$$Q_{df} = \int_{t_i}^{t_{i+1}} \Phi_f(t_{i+1}-\tau) G_f Q_f G_f^T \Phi_f^T(t_{i+1}-\tau) d\tau \quad (5-41)$$

where  $Q_{df} = \Phi_f(\Delta t)$  since  $G_f = \Phi_f = 1$ .

5.3.2 *Measurement Model.* The low-energy laser measurement is provided to the filter if the laser intercepts the hardbody, and a reflection is received by the low-energy laser sensor. The measurement is a noise-corrupted bias given by the offset distance between the FLIR filter's estimate of the intensity centroid and the computed center-of-mass determined using the low-energy laser scan. The discrete-time measurement model is the scalar version of Equation (5-20), given by:

$$z(t_i) = H_f x_f(t_i) + v_f(t_i) \quad (5-42)$$

where

- $z(t_i)$  = offset measurement given as the distance from the FLIR filter estimated intensity centroid and the computed center-of-mass  
 $H_f$  = measurement distribution,  $H_f = 1$   
 $x_f(t_i)$  = center-of-mass offset state  
 $v_f(t_i)$  = discrete, white Gaussian measurement noise with statistics:

$$E \{v(t_i)\} = 0 \quad (5-43)$$

$$E \{v(t_i)v(t_j)\} = \begin{cases} R_f & t_i = t_j \\ 0 & t_i \neq t_j \end{cases} \quad (5-44)$$

where  $R_f = R_r$  (true measurement variance) = 0.000178 pixels<sup>2</sup>.

Due to the linearity of this measurement model, the Kalman filter processes the computed center-of-mass measurements of Equation (5-42) using a linear update cycle. This update cycle is defined by the scalar version of Equations (5-25), (5-26), and (5-27), given by:

$$K(t_i) = P_f(t_i^-) H_f^T [H_f P_f(t_i^-) H_f^T + R]^{-1} \quad (5-45)$$

$$\hat{x}_f(t_i^+) = \hat{x}_f(t_i^-) + K(t_i)[z(t_i) - H_f \hat{x}_f(t_i^-)] \quad (5-46)$$

$$P_f(t_i^+) = P_f(t_i^-) - K(t_i) H_f P_f(t_i^-) \quad (5-47)$$

where

- $K(t_i)$  = filter gain
- $P_f(t_i)$  = filter covariance
- $H_f$  = measurement distribution matrix,  $H_f = 1$
- $R_f$  = measurement noise variance
- $x_f(t_i)$  = center-of-mass offset state
- $z(t_i)$  = scalar measurement, Equation (5-40)
- $(t_i^-)$  = time instant immediately before measurements are incorporated at time  $t_i$
- $(t_i^+)$  = time instant immediately after measurements are incorporated at time  $t_i$

**5.3.3 Filter Parameters.** This section describes the modeling parameters, initial conditions, and tuning parameters for the one-state filter used in this research.

**5.3.3.1 Modeling Values.** The one-state dynamics model is a simple integrator with driving pseudo-noise, for filter tuning purposes. The strength of the white Gaussian noise driving the integrator given in Equations (5-38) is given in Section 5.2.3.3 for the low-energy laser scan and sweep configurations tested.

*5.2.3.2 Initial Conditions.* In the tracking simulation, the filter center-of-mass offset state is initialized to a 1.0 pixel error. This value represents an arbitrary value with which to test the filter performance. The initial variance is 0.2 pixels<sup>2</sup>. This value is selected to reflect the confidence of the initial state value.

*5.2.3.3 Tuning Values.* The filter was tested with and without a sweeping of the low-energy laser following the initial scan. (The results of the testing is covered in Chapter VI.) For the case without a low-energy laser sweep, a filter dynamics strength value of 0.3 pixels<sup>2</sup>/seconds<sup>2</sup> is used without plume pogo applied to the intensity centroid, and 0.35 pixels<sup>2</sup>/seconds<sup>2</sup> is used when plume pogo was applied. For the case with a low-energy laser sweep, a filter dynamics strength value of 0.7 pixels<sup>2</sup>/seconds<sup>2</sup> is used for the cases with and without plume pogo applied to the intensity centroid.

The value for the true and filter measurement noise variance of the center-of-mass estimate is equal to 0.000178 pixels<sup>2</sup>. This value is arbitrarily determined as 1.0% of the length of the hardbody (in meters); the conversion to pixels<sup>2</sup> is accomplished by dividing the 0.4 meters by the pixel proportionality constant  $k_p$  times the range to the target, and squaring the result. (The value of the measurement noise variance is a change from the previous thesis [2] value of 0.004444 pixels<sup>2</sup> to reflect the accuracy of the measurements obtained in this research.) The truth model offset distance (to be estimated by the filter) of the true hardbody center-of-mass from the midpoint between the two Gaussian intensity functions (Figure 3.5 and 3.6), is determined as 87.5 meters (2.917 pixels).

## *5.4 Eight-State Filter*

*5.4.1 Dynamics Model.* The eight-state filter is composed of the six-state filter (Section 5.1) augmented with a modification of the one-state filter (Section 5.2). The six-state (FLIR) part of the filter is designed to operate independently as it does when used in conjunction with the previous one-state (center-of-mass) filter. The two additional states



comprise the  $x$  and  $y$  center-of-mass offset components, whereas the one-state filter only estimated a scalar distance that was presumed to be along the estimated velocity direction from the center of intensity. This part of the filter is independent of the FLIR part of the filter, except for the dependence on centroid intensity information. The eight-state Kalman filter used in this research is based upon the state vector:

$$\mathbf{x}_f = \begin{bmatrix} x_1 \\ x_2 \\ x_3 \\ x_4 \\ x_5 \\ x_6 \\ x_7 \\ x_8 \end{bmatrix} = \begin{bmatrix} x_d \\ y_d \\ v_x \\ v_y \\ x_a \\ y_a \\ x_o \\ y_o \end{bmatrix} \quad (5-48)$$

where

- $x_d$  =  $x$  component of centroid position (azimuth), relative to center of FOV
- $y_d$  =  $y$  component of centroid position (elevation), relative to center of FOV
- $v_x$  =  $x$  component of centroid velocity
- $v_y$  =  $y$  component of centroid velocity
- $x_a$  =  $x$  component of atmospheric jitter
- $y_a$  =  $y$  component of atmospheric jitter
- $x_o$  =  $x$  component of center-of-mass offset
- $y_o$  =  $y$  component of center-of-mass offset

The first six states are as described in Section 5.1. The offset states  $x_o$  and  $y_o$  estimate the  $x$  and  $y$  bias components of the center-of-mass offset between the filter's estimate of the intensity centroid and the target center-of-mass. The eight-state filter is the same as the working combination of the six-state filter and the one-state filter, except that the one-state center-of-mass offset estimate is replaced by the  $x$  and  $y$  bias components in

the eight-state filter. The eight-state filter model is described by the following time-invariant, linear stochastic differential equation:

$$\dot{\mathbf{x}}_f(t) = \mathbf{F}_f \mathbf{x}_f(t) + \mathbf{G}_f \mathbf{w}_f(t) \quad (5-49)$$

where

- $\mathbf{F}_f$  = 8 x 8 time-invariant system matrix
- $\mathbf{x}_f(t)$  = 8-dimensional filter state vector
- $\mathbf{G}_f$  = 8 x 6 time-invariant noise distribution matrix
- $\mathbf{w}_f(t)$  = 6-dimensional independent, white Gaussian noise process with mean and covariance statistics:

$$E\{\mathbf{w}_f(t)\} = \mathbf{0} \quad (5-50)$$

$$E\{\mathbf{w}_f(t)\mathbf{w}_f^T(t+\tau)\} = \mathbf{Q}_f \delta(\tau) \quad (5-51)$$

The time-invariant system matrix  $\mathbf{F}_f$  is:

$$\mathbf{F}_f = \begin{bmatrix} 0 & 0 & 1 & 0 & 0 & 0 & 0 & 0 \\ 0 & 0 & 0 & 1 & 0 & 0 & 0 & 0 \\ 0 & 0 & -\frac{1}{\tau_x} & 0 & 0 & 0 & 0 & 0 \\ 0 & 0 & 0 & -\frac{1}{\tau_y} & 0 & 0 & 0 & 0 \\ 0 & 0 & 0 & 0 & -\frac{1}{\tau_{a_x}} & 0 & 0 & 0 \\ 0 & 0 & 0 & 0 & 0 & -\frac{1}{\tau_{a_y}} & 0 & 0 \\ 0 & 0 & 0 & 0 & 0 & 0 & 0 & 0 \\ 0 & 0 & 0 & 0 & 0 & 0 & 0 & 0 \end{bmatrix} \quad (5-52)$$

The noise distribution matrix  $\mathbf{G}_f$  is:

$$\mathbf{G}_f = \begin{bmatrix} 0 & 0 & 0 & 0 & 0 & 0 \\ 0 & 0 & 0 & 0 & 0 & 0 \\ 1 & 0 & 0 & 0 & 0 & 0 \\ 0 & 1 & 0 & 0 & 0 & 0 \\ 0 & 0 & 1 & 0 & 0 & 0 \\ 0 & 0 & 0 & 1 & 0 & 0 \\ 0 & 0 & 0 & 0 & 1 & 0 \\ 0 & 0 & 0 & 0 & 0 & 1 \end{bmatrix} \quad (5-53)$$

The strength of the white Gaussian noise  $\mathbf{w}_f$ , given by  $\mathbf{Q}_f$ , is:

$$\mathbf{Q}_f = \begin{bmatrix} \frac{2\sigma_x^2}{\tau_x} & 0 & 0 & 0 & 0 & 0 \\ 0 & \frac{2\sigma_y^2}{\tau_y} & 0 & 0 & 0 & 0 \\ 0 & 0 & \frac{2\sigma_{a_x}^2}{\tau_{a_x}} & 0 & 0 & 0 \\ 0 & 0 & 0 & \frac{2\sigma_{a_y}^2}{\tau_{a_y}} & 0 & 0 \\ 0 & 0 & 0 & 0 & Q_{o_x} & 0 \\ 0 & 0 & 0 & 0 & 0 & Q_{o_y} \end{bmatrix} \quad (5-54)$$

where

- $\tau_x, \tau_y$  = correlation times for the intensity centroid x and y velocities
- $\tau_{a_x}, \tau_{a_y}$  = correlation time for the atmospheric jitter position process  
in the x and y directions

$\sigma_x^2, \sigma_y^2$  = variance and mean-squared value for the intensity centroid  
x and y velocities

$\sigma_{a_x}^2, \sigma_{a_y}^2$  = variance and mean-squared value for the atmospheric jitter  
position process

$Q_{o_x}$  = noise strength associated with the x bias offset component  
for determining the center-of-mass estimate

$Q_{o_y}$  = noise strength associated with the y bias offset component  
for determining the center-of-mass estimate

To simulate the filter dynamics model on a digital computer, the discrete-time propagation equations [12] are used to propagate the state estimates and error covariance forward to the next measurement update:

$$\hat{\mathbf{x}}_f(t_{i+1}^-) = \Phi_f(\Delta t) \hat{\mathbf{x}}_f(t_i^+) \quad (5-55)$$

$$\mathbf{P}_f(t_{i+1}^-) = \Phi_f(\Delta t) \mathbf{P}_f(t_i^+) \Phi_f^T(\Delta t) + \mathbf{Q}_{df} \quad (5-56)$$

where

$\hat{\mathbf{x}}_f(t_i)$  = filter estimate of the 8-dimensional state vector

$\Phi_f(\Delta t)$  = 8 x 8 time-invariant state transition matrix for propagation  
over the sample period:  $\Delta t = t_{i+1} - t_i$

$\mathbf{P}_f(t_i)$  = 8 x 8 filter covariance matrix

$(t_i^-)$  = time instant before FLIR measurement is incorporated into  
the estimate at time  $t_i$

$(t_i^+)$  = time instant after FLIR measurement is incorporated into  
the estimate at time  $t_i$

$\mathbf{Q}_{df}$  = 8 x 8 filter dynamics noise covariance given by:

$$Q_{df} = \int_{t_i}^{t_{i+1}} \Phi_f(t_{i+1}-\tau) G_f Q_f G_f^T \Phi_f^T(t_{i+1}-\tau) d\tau \quad (5-57)$$

The time-invariant state transition matrix  $\Phi_f(\Delta t)$  is:

$$\Phi_f(\Delta t) = \begin{bmatrix} 1 & 0 & \Phi_{13} & 0 & 0 & 0 & 0 & 0 \\ 0 & 1 & 0 & \Phi_{24} & 0 & 0 & 0 & 0 \\ 0 & 0 & \Phi_{33} & 0 & 0 & 0 & 0 & 0 \\ 0 & 0 & 0 & \Phi_{44} & 0 & 0 & 0 & 0 \\ 0 & 0 & 0 & 0 & \Phi_{55} & 0 & 0 & 0 \\ 0 & 0 & 0 & 0 & 0 & \Phi_{66} & 0 & 0 \\ 0 & 0 & 0 & 0 & 0 & 0 & \Phi_{77} & 0 \\ 0 & 0 & 0 & 0 & 0 & 0 & 0 & \Phi_{88} \end{bmatrix} \quad (5-58)$$

where

$$\Phi_{13} = \tau_x [1 - \exp(-\frac{\Delta t}{\tau_x})]$$

$$\Phi_{24} = \tau_y [1 - \exp(-\frac{\Delta t}{\tau_y})]$$

$$\Phi_{33} = \exp(-\frac{\Delta t}{\tau_x})$$

$$\Phi_{44} = \exp(-\frac{\Delta t}{\tau_y})$$

$$\Phi_{55} = \exp(-\frac{\Delta t}{\tau_a})$$

$$\Phi_{66} = \exp(-\frac{\Delta t}{\tau_a})$$

$$\Phi_{77} = \Phi_{88} = 1$$

$$\Delta t = \text{sample time interval, } t_{i+1} - t_i$$

The filter dynamics noise covariance  $\mathbf{Q}_{df}$  is:

$$\mathbf{Q}_{df} = \begin{bmatrix} q_{df11} & 0 & q_{df13} & 0 & 0 & 0 & 0 & 0 \\ 0 & q_{df22} & 0 & q_{df24} & 0 & 0 & 0 & 0 \\ q_{df31} & 0 & q_{df33} & 0 & 0 & 0 & 0 & 0 \\ 0 & q_{df42} & 0 & q_{df44} & 0 & 0 & 0 & 0 \\ 0 & 0 & 0 & 0 & q_{df55} & 0 & 0 & 0 \\ 0 & 0 & 0 & 0 & 0 & q_{df66} & 0 & 0 \\ 0 & 0 & 0 & 0 & 0 & 0 & q_{df77} & 0 \\ 0 & 0 & 0 & 0 & 0 & 0 & 0 & q_{df88} \end{bmatrix} \quad (5-59)$$

where

$$q_{df11} = 2\sigma_x^2 \tau_x \{(\Delta t) - 2\tau_x [1 - \exp(-\frac{\Delta t}{\tau_x})] + \frac{\tau_x}{2} [1 - \exp(-\frac{2(\Delta t)}{\tau_x})]\}$$

$$q_{df22} = 2\sigma_y^2 \tau_y \{(\Delta t) - 2\tau_y [1 - \exp(-\frac{\Delta t}{\tau_y})] + \frac{\tau_y}{2} [1 - \exp(-\frac{2(\Delta t)}{\tau_y})]\}$$

$$q_{df13} = 2\sigma_x^2 \{2\tau_x [1 - \exp(-\frac{\Delta t}{\tau_x})] - \frac{\tau_x}{2} [1 - \exp(-\frac{2(\Delta t)}{\tau_x})]\}$$

$$q_{df24} = 2\sigma_y^2 \{2\tau_y [1 - \exp(-\frac{\Delta t}{\tau_y})] - \frac{\tau_y}{2} [1 - \exp(-\frac{2(\Delta t)}{\tau_y})]\}$$

$$q_{df31} = q_{df13}$$

$$q_{df33} = \sigma_x^2 [1 - \exp(-\frac{2(\Delta t)}{\tau_x})]$$

$$q_{df42} = q_{df24}$$

$$q_{df44} = \sigma_y^2 [1 - \exp(-\frac{2(\Delta t)}{\tau_y})]$$

$$q_{df55} = \sigma_{a_x}^2 [1 - \exp(-\frac{2(\Delta t)}{\tau_{a_x}})]$$

$$q_{df66} = \sigma_{a_y}^2 [1 - \exp(-\frac{2(\Delta t)}{\tau_{a_y}})]$$

$$q_{df77} = \mathbf{Q}_{o_x} \Delta t$$

$$q_{df88} = \mathbf{Q}_{o_y} \Delta t$$

$$\Delta t = \text{sample time interval, } t_{i+1} - t_i$$

where  $\mathbf{Q}_{o_x}$  and  $\mathbf{Q}_{o_y}$  are as described in Equation (5-54).

5.4.2 *Measurement Models.* The FLIR measurement model is the same as for the six-state filter discussed in Section 5.2.2. There are two separate update cycles in the eight-state filter to provide FLIR measurements to the six-state (FLIR) part of the filter, and to provide center-of-mass measurements to the two-state (center-of-mass) part of the filter; first the FLIR measurement update cycle is performed, then the center-of-mass update cycle is performed if the low-energy laser scan (or sweep) results in a reflection return from the hardbody. For the FLIR measurement, the  $\mathbf{H}_f$  matrix given in Equation (5-23) becomes a  $2 \times 8$  matrix, with zeros in columns seven and eight, to satisfy the measurement independence of the first six-states from the last two center-of-mass bias states. (The low-energy laser measurement  $\mathbf{H}_f$  matrix is covered in this section.) The FLIR measurement covariance matrix  $\mathbf{R}_f$  given by Equation (5-24) and the low-energy laser measurement covariance matrix (covered in this section) are augmented into a  $4 \times 4$  diagonal matrix. The eight-state filter's low-energy laser measurement model, shown in Figure 5.7, is the same

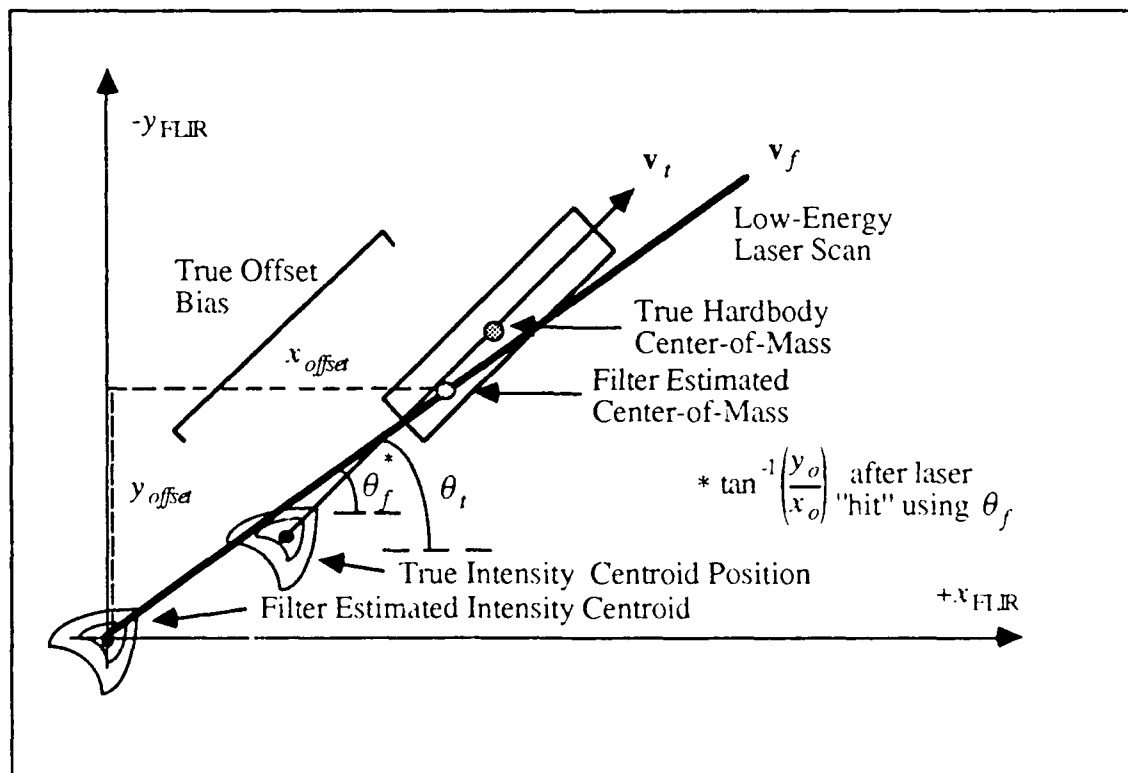


Figure 5.7. Two-State Filter Estimate of Missile Hardbody Center-of-Mass

as the one-state filter noise-corrupted measurement model of Equation (5-42), except that the eight-state filter model consists of the  $x$  and  $y$  offsets of the measurement. The discrete-time low-energy laser measurement model is given by:

$$\mathbf{z}(t_i) = \mathbf{H}_f \mathbf{x}_f(t_i) + \mathbf{v}_f(t_i) \quad (5-60)$$

where

$\mathbf{z}(t_i)$  =  $x$  and  $y$  offset measurements of the distance between the FLIR filter estimated intensity centroid and the computed center-of-mass, where the straightline measurement, given by Equation (5-42), is resolved into two components as:

$$\begin{aligned} & z(t_i) (\cos \theta_f) \\ & z(t_i) (-\sin \theta_f) \end{aligned}$$

(The minus sign in the second measurement is necessary due to the sign convention of the  $\alpha$ - $\beta$  (FLIR) plane, (Figure 3.1))

$\mathbf{H}_f$  = 2 x 8 measurement distribution matrix  
 $\mathbf{x}_f(t_i)$  = 8-dimensional filter state  
 $\mathbf{v}_f(t_i)$  = discrete, white Gaussian measurement noise with mean and covariance statistics:

$$E \{ \mathbf{v}(t_i) \} = \mathbf{0} \quad (5-61)$$

$$E \{ \mathbf{v}(t_i) \mathbf{v}(t_j) \} = \begin{cases} \mathbf{R}_f & t_i = t_j \\ \mathbf{0} & t_i \neq t_j \end{cases} \quad (5-62)$$

The low-energy laser measurement matrix  $\mathbf{H}_f$  is:

$$\mathbf{H}_f = \begin{bmatrix} 0 & 0 & 0 & 0 & 0 & 0 & 1 & 0 \\ 0 & 0 & 0 & 0 & 0 & 0 & 0 & 1 \end{bmatrix} \quad (5-63)$$

The measurement covariance matrix  $\mathbf{R}_f$  (with units of pixels<sup>2</sup>) is:

$$\mathbf{R}_f = \begin{bmatrix} 0.000178 & 0 \\ 0 & 0.000178 \end{bmatrix} \quad (5-64)$$



where the values of  $\mathbf{R}_f$  are the same as the value used in the one-state filter, since the uncertainty of the estimate in the  $x$  and  $y$  directions is not known. (Sensitivity studies, which are not covered in this thesis, may reveal that the  $x$  and  $y$  covariances are not equal.)

Due to the linearity of this measurement model, the Kalman filter processes the FLIR measurements of Equation (5-20) and the computed center-of-mass measurements of Equation (5-60) using a linear update cycle. Since the first six-states are decoupled from the two center-of-mass states, the FLIR measurements are unaffected by the center-of-mass measurements, and center-of-mass measurements are not affected by the FLIR measurements. The two, uncoupled update cycles are defined by Equations (5-25), (5-26), and (5-27), given by:

$$\mathbf{K}(t_i) = \mathbf{P}_f(t_i^-) \mathbf{H}_f^T [\mathbf{H}_f \mathbf{P}_f(t_i^-) \mathbf{H}_f^T + \mathbf{R}]^{-1} \quad (5-65)$$

$$\hat{\mathbf{x}}_f(t_i^+) = \hat{\mathbf{x}}_f(t_i^-) + \mathbf{K}(t_i) [\mathbf{z}(t_i) - \mathbf{H}_f \hat{\mathbf{x}}_f(t_i^-)] \quad (5-66)$$

$$\mathbf{P}_f(t_i^+) = \mathbf{P}_f(t_i^-) - \mathbf{K}(t_i) \mathbf{H}_f \mathbf{P}_f(t_i^-) \quad (5-67)$$

where

- $\mathbf{K}(t_i)$  = 2 x 8 filter gain matrix
- $\mathbf{P}_f(t_i)$  = 8 x 8 filter covariance matrix
- $\mathbf{H}_f$  = 2 x 8 measurement matrix; Equation (5-63)
- $\mathbf{R}_f$  = 2 x 2 measurement noise matrix; Equation (5-64)
- $\mathbf{x}_f(t_i)$  = 8-dimensional state vector; Equation (5-48)
- $\mathbf{z}(t_i)$  = 2-dimensional laser measurement matrix; Equation (5-60)
- $(t_i^-)$  = time instant immediately before measurements are incorporated at time  $t_i$
- $(t_i^+)$  = time instant immediately after measurements are incorporated at time  $t_i$

5.4.3 *Filter Parameters.* This section describes the modeling parameters, initial conditions, and tuning parameters for the eight-state filter used in this research.

5.4.3.1 *Modeling Values.* The filter target dynamics and atmospheric jitter characteristics of the eight-state filter are the same as the six-state filter (Section 5.2.3.1).

5.4.3.2 *Initial Conditions.* The initial conditions for the first six states of the eight-state filter are the same as for the six-state filter (Section 5.2.3.2). The initial conditions for states  $x_7$  and  $x_8$  are 0.5 and -0.5 pixels. These magnitudes provide the equivalent initial condition as the one-state filter (for filter performance comparison purposes). The minus sign in front of the  $x_8$  initial condition is due to the coordinate system of the  $\alpha$ - $\beta$  (FLIR) plane (Figure 3.1). This gives the state the proper sign convention.

The initial state covariance matrix  $\mathbf{P}(t_0)$  is:

$$\mathbf{P}(t_0) = \begin{bmatrix} 10 & 0 & 0 & 0 & 0 & 0 & 0 & 0 \\ 0 & 10 & 0 & 0 & 0 & 0 & 0 & 0 \\ 0 & 0 & 2000 & 0 & 0 & 0 & 0 & 0 \\ 0 & 0 & 0 & 2000 & 0 & 0 & 0 & 0 \\ 0 & 0 & 0 & 0 & .2 & 0 & 0 & 0 \\ 0 & 0 & 0 & 0 & 0 & .2 & 0 & 0 \\ 0 & 0 & 0 & 0 & 0 & 0 & .2 & 0 \\ 0 & 0 & 0 & 0 & 0 & 0 & 0 & .2 \end{bmatrix} \quad (5-68)$$

where the position states  $x_1$  and  $x_2$ , the atmospheric states  $x_5$  and  $x_6$ , and the center-of-mass states  $x_7$  and  $x_8$  have units of pixels<sup>2</sup>; the velocity states  $x_3$  and  $x_4$  have units of pixels<sup>2</sup>/seconds<sup>2</sup>.

The measurement covariance matrix  $\mathbf{R}_f$  (with units of pixels<sup>2</sup>) is:

$$\mathbf{R}_f = \begin{bmatrix} 0.00363 & 0 & 0 & 0 \\ 0 & 0.00598 & 0 & 0 \\ 0 & 0 & 0.000178 & 0 \\ 0 & 0 & 0 & 0.000178 \end{bmatrix} \quad (5-69)$$

5.4.3.3 *Tuning Values.* The filter dynamics variances  $\sigma_x^2$  and  $\sigma_y^2$  are both set equal to 800 pixels<sup>2</sup>/seconds<sup>2</sup>. For the single low-energy laser scan (i.e., no sweep), the filter dynamic variances of the center-of-mass states,  $x_7$  and  $x_8$ , are 0.25 pixels<sup>2</sup> and 0.35 pixels<sup>2</sup>, respectively, without plume pogo applied to the intensity centroid; the variances with plume pogo applied are 0.25 pixels<sup>2</sup> and 0.40 pixels<sup>2</sup>, respectively. For a low-energy laser sweep, the filter dynamic variances of  $x_7$  and  $x_8$  are 1.0 pixels<sup>2</sup> and 1.4 pixels<sup>2</sup> for both the cases with and without plume pogo applied to the intensity centroid. The atmospheric jitter variances  $\sigma_{a_x}^2$  and  $\sigma_{a_y}^2$  are both set equal to 0.2 pixels<sup>2</sup>. This corresponds to the truth model value of 0.2 pixels<sup>2</sup>.

#### 5.4 Summary

This chapter presented the three filter models used in the course of performing research into determining if low-energy laser measurements can be used with FLIR sensor measurements to determine the location of the center-of-mass of the missile hardbody. The six-state filter and the one-state filter are previously developed filters [2, 4, 6, 9, 10, 11, 21, 22, 24, 25, 26, 27, 28, 29, 30]. The eight-state filter, developed in this thesis, is an augmentation of the six-state filter and two-states to estimate the  $x$  and  $y$  components of the location of the center-of-mass of the missile hardbody. The six-state filter and the one-state filter operate independently in determining the center-of-mass of the hardbody, except for the need by the one-state filter to use the six-state filter's updated estimates of the intensity centroid position and velocity. The eight-state filter operates in a similar manner. A performance analysis of these filters is presented with respect to a single scan of the low-energy laser, and with a sweep of the low-energy laser, in Chapter VI.

## *VI. Procedures and Results*

### *6.1 Introduction*

This chapter presents the results of the research objectives given in Chapter I and the findings of three studies conducted during the course of the research. The Doppler investigation and the atmospheric modeling improvements were not accomplished, however the research of this thesis provided insight into both topics, which are covered in Chapter VII. The three studies/investigations include: low-energy laser sensitivity study; intensity centroid movement in the FLIR image plane investigation; and a six-state filter dynamics noise trajectory study. The diagonal rotating field-of-view (DRFOV) was not used in this research due to possible problems with the rotation algorithm. Since the benign dynamics of a missile do not require the maximum efficiency of the FLIR image plane, the testing was not affected. The DRFOV is discussed in Chapter VII as a possible solution to obtaining a reflection from the hardbody with a single scan of the low-energy laser.

The configuration of the truth model is such that the atmospheric jitter and bending/vibration models are activated during all simulation runs. The truth model plume pogo model is turned on and off to test the six-state/one-state filter performance and the eight-state filter performance in estimating the center-of-mass without, and with plume pogo applied to the intensity centroid. (This research is primarily interested in the one-state center-of-mass filter performance and the two-state center-of-mass part of the eight-state filter. The one-state filter is referred to by this name since it is a separate filter, while the two-state center-of-mass augmented filter is part of the eight-state filter, therefore it is referred to as the eight-state filter with reference to the center-of-mass estimates.) The low-energy laser is used as a single scan along the filter-estimated sweep direction (i.e., no sweep) and as a sweep (multiple scanning) to test both center-of-mass filters for the cases

when few successful measurements are provided, and when measurements are provided at every sample period (1/30 second). The hardbody binary model is tested in various configurations: without low-energy laser sweep and without plume pogo; without low-energy laser sweep and with plume pogo; with low-energy laser sweep and without plume pogo; and with low-energy laser sweep and with plume pogo. The enhanced hardbody reflectivity model is only tested with the filters using a low-energy sweep, and without and with plume pogo applied to the intensity centroid. (For this thesis, since emphasis is placed on obtaining an accurate measurement of the center-of-mass for the filter, the reflectivity model is designed exclusively for use with a low-energy laser sweep; the software can be altered to also include the non-sweep condition.)

Each simulation run consists of 10 Monte Carlo runs over a 10 second period of the target's trajectory. The collection of the statistics of the filter's actual rms mean error, the filter's computed mean error, and the actual standard deviation ( $\sigma$ ) of the error is given in Appendix A. The statistical data is collected from 2 to 10 seconds to avoid having the transient performance from influencing the steady-state results. The statistics data is presented both graphically in the appendices (which are referred to throughout the discussion of this chapter), and in tabular form within the text of this chapter. Appendix B gives a description of the two types of performance plots used in the analysis of the filters, and also provides example plots with annotations.

Before beginning the filter analysis, two sections are devoted to providing the reader with the background necessary for a more thorough understanding of the data reported in this chapter. In Section 6.2, the software validation accomplished during the course of the research is given to provide reader confidence that every effort is made to ensure the data results are accurate. In Section 6.3, the simulation coordinate frames, given in Section 3.2, are discussed relative to the three descriptions of the filter estimated center-of-mass error: the straight-line magnitude error  $m$ ; the  $x$  and  $y$  components of the error;

and the along-track (ALT) and across-track (ACT) components of the error, defined as along and across the centerline of the missile, respectively.

## *6.2 Software Validation*

During the course of this thesis research, the software and the modeling techniques were continuously scrutinized to avoid misrepresenting the data obtained from the simulation runs. In many cases, the software was revalidated with results from previous theses, and in some cases, the software was changed to correct coding errors. Additionally, emphasis was placed on ensuring that correct modeling values were used in the truth model and the filter models. This self-imposed part of the thesis research was considered as important as the thesis objectives, since without having confidence that the software and modeling are correct, the results, at best, are questionable. The following paragraphs discuss some of the more important software findings.

The most significant finding of incorrect software implementation was the noise (random number) generator. In the process of accomplishing runs over different time intervals (of 7 and 8 seconds) due to a software missile trajectory problem, it was noted that the statistics changed dramatically. The problem was isolated to the random number generator (which provides the white Gaussian noise in the simulation). A proven reliable random number generator with a longer correlation time (i.e., longer time between any possible repetition of numbers) was installed into the software, which corrected a data bias problem that was also under investigation. The missile trajectory problem is due to the simulated hardbody crossing the  $y$ - $z$  plane inertial coordinate system. The problem occurs due to the representation of the hardbody in the software; upon crossing the  $y$ - $z$  plane, the missile model requires both positive and negative  $x$  coordinates to define the hardbody, for which the simulation model is not equipped. The trajectory of the missile initial conditions were changed, without compromising the study, to avoid this software limitation.

In the process of determining the cause of the bias problem, which was corrected by the replacement of the random noise generator, the correlation algorithm was investigated (as a potential source of the problem). The correlation algorithm provides the position offset "pseudo-measurements" of the target's location to the six-state Kalman filter; therefore, it was suspected that the correlator may be providing biased measurements. The statistics of the correlator were gathered, which provided a validation of the accuracy of the correlator measurements: the  $x$  offset mean measurement was found to be 0.002 pixels with a standard deviation of 0.025 pixels, and the  $y$  offset measurement was found to be - 0.003 pixels with a standard deviation of 0.030 pixels (where a pixel  $\cong$  30 meters for the 2,000 kilometer distance of the target from the FLIR image plane). These standard deviation values indicate an increase in performance over that determined by [10], where the  $x$  offset measurement standard deviation was determined as 0.060 pixels and the  $y$  offset measurement standard deviation was given as 0.077 pixels. This difference may be due to changing the random number generator.

The modeling parameter values of the truth model, and the modeling and tuning parameter values of the filter models, were also investigated. The truth model value of the atmospheric jitter standard deviation was corrected to the 0.2 pixels defined in [26]. The other values were all found to be correct, and the filter parameters were changed, due to tuning requirements, as described in Sections 5.2.3, 5.3.3, and 5.4.3.

### *6.3 Coordinate Transformations of the Center-of-Mass Error*

One of the thesis objectives described in Section 1.3 is to compare the one-state filter [2] center-of-mass estimate with that of the two-state partition of an eight-state filter developed in this thesis for refined estimation of that center-of-mass location. Another objective is to portray the one-state filter results in the  $x$  and  $y$  coordinates, and in the ALT and ACT coordinates of the missile hardbody. The trans-FLIR coordinate system and the

ALT-ACT coordinate system, described in Section 3.2, are used to transform the magnitude error  $m$  [2] into  $x$  and  $y$  errors, and into the ALT and ACT offset errors. Additionally, the  $x$  and  $y$  center-of-mass states of the eight-state filter are also transformed into the ALT-ACT frame for comparison with the one-state filter in this coordinate system. The standard deviation of the filter-computed error is also transformed to obtain tuning insight into each of the coordinate systems. This error description analysis may provide improvements in representing the filter errors, and could also give insight concerning which coordinate frame the filter should be tuned to obtain optimum performance. The three different descriptions of the center-of-mass error are shown in Figure 6.1.

The transformation of the magnitude  $m$  error for the one-state filter into the ALT-ACT coordinate system is accomplished by determining the angle  $\lambda$  in Figure 6.1(a) using the  $x$  and  $y$  error values of (b) to determine  $\eta$ . The angle  $\lambda$  is found by:

$$\lambda = \theta_t - \eta \quad (6-1)$$

where  $\theta_t$  is the true orientation angle of the target trajectory. (The true orientation angle  $\theta_t$  is used, as opposed to  $\theta_f$ , since the errors must be represented in a fixed, known coordinate system.) Then the ALT and ACT components of the error are:

$$\text{ALT} = m \cos \lambda \quad (6-2)$$

$$\text{ACT} = m \sin \lambda \quad (6-3)$$

Equations (6-1) through (6-3) are also used for the eight state filter, where the  $x$  and  $y$  for determining  $\eta$  are the errors from the two center-of-mass states.

For the one-state filter, the filter-computed error variance is transformed into the  $x$  and  $y$  coordinate system using:

$$\mathbf{P}' = \mathbf{T} \mathbf{P} \mathbf{T}^T \quad (6-4)$$



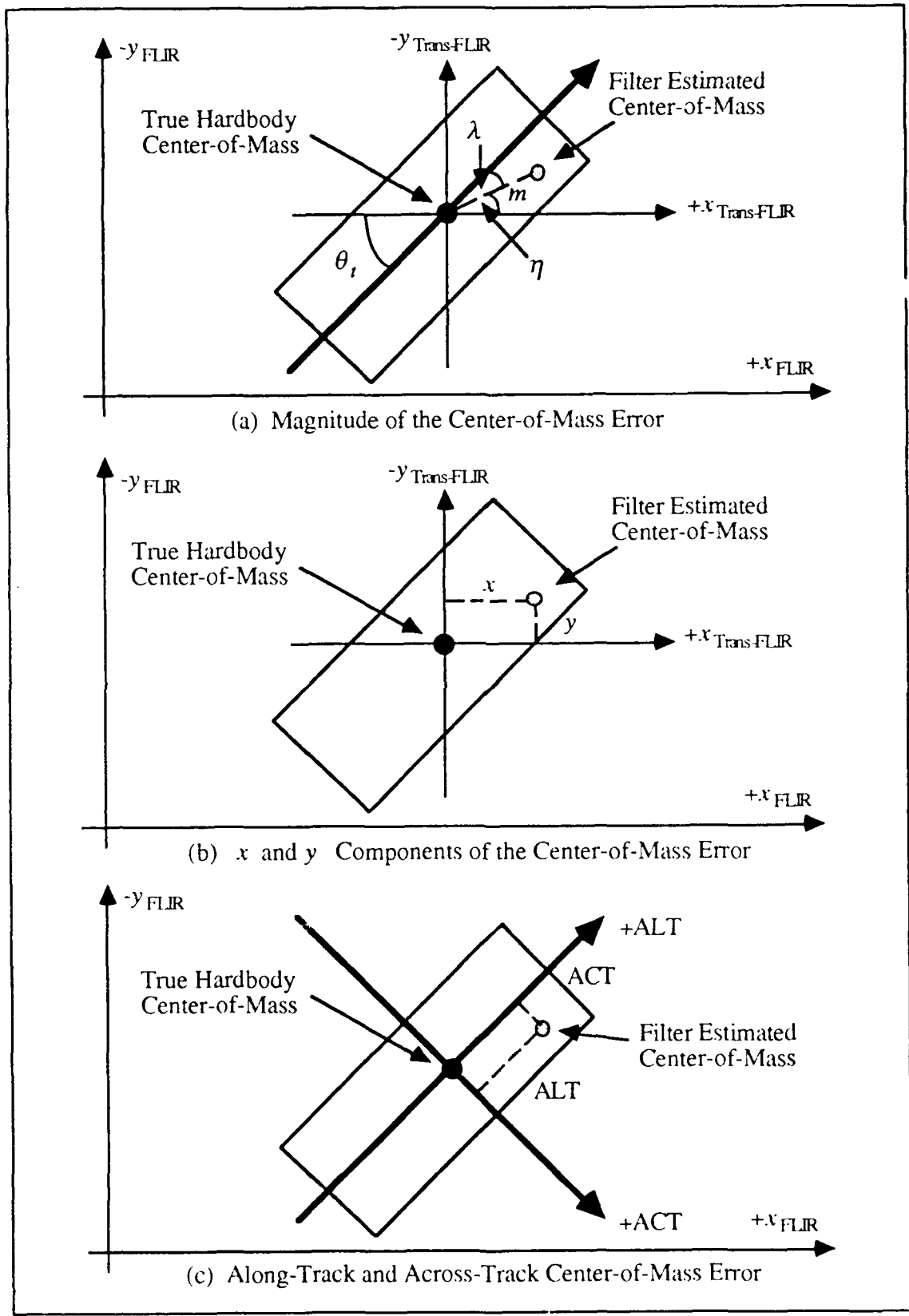


Figure 6.1. Three Descriptions of Center-of-Mass Error

where

- $\mathbf{P}'$  = 2 x 2 covariance matrix in the trans-FLIR plane
- $P$  = scalar error variance obtained from one-state filter statistics
- $\mathbf{T}$  = 1 x 2 transformation matrix given by:

$$\mathbf{T} = \begin{bmatrix} \cos\theta_t & \sin\theta_t \end{bmatrix} \quad (6-5)$$

Then to transform  $\mathbf{P}'$  into the ALT-ACT coordinates, a second transformation is performed:

$$\mathbf{P}'' = \mathbf{T} \mathbf{P}' \mathbf{T}^T \quad (6-6)$$

where

- $\mathbf{P}''$  = 2 x 2 covariance matrix in the ALT-ACT plane
- $\mathbf{P}'$  = 2 x 2 error covariance matrix
- $\mathbf{T}$  = 2 x 2 transformation matrix given by:

$$\mathbf{T} = \begin{bmatrix} \cos\theta_t & \sin\theta_t \\ -\sin\theta_t & \cos\theta_t \end{bmatrix} \quad (6-7)$$

The eight-state filter error consists of the  $x$  and  $y$  components of the two center-of-mass states  $x_7$  and  $x_8$ , respectively. The transformation of the error covariances into the ALT-ACT coordinate frame is accomplished using Equation (6-6) with the transformation matrix of Equation (6-7).

The diagonal terms of the resulting error covariance matrices are plotted with the filter's actual rms error, as described in Appendix B. The cross terms of the transformed error covariance matrix for the one-state and the eight-state transformations are small in all cases.

#### 6.4 Six-State Filter Performance Analysis

With the understanding of the previous two sections, this section and the following three sections discuss the performance of the three filters used during this research. The six-state filter, as pointed out in Chapter I, is a development from previous theses [2, 26]. The filter is not changed from the previous research. The evaluation of filter performance is improved with the replacement of the random noise generator, discussed in Section 6.2. The primary purpose of the six-state filter is to track the intensity centroid of the missile using FLIR measurements to update its algorithm, then the filter propagates the estimate to the next sample time. This propagation estimate at  $t_i^-$  is used to command the pointing controller (Section 3.4) to position the FLIR plane before the next sample time.

The filter error statistics are shown in Table 6.1 for the case without plume pogo applied to the intensity centroid, and Table 6.2 gives the filter error statistics for the case of plume pogo being applied to the intensity centroid at 10 Hertz with an amplitude of approximately 34.0 meters (1.12 pixels). This plume pogo represents the maximum frequency and amplitude researched by [26]. The filter performance is slightly degraded when plume pogo is applied, as is expected since the filter is not currently modeling the plume pogo phenomenon. The degradation is more significant for the standard deviation at  $t_i^-$  for the target position and apparent intensity centroid position than at  $t_i^+$ , which means that the filter has a much harder time of tracking the missile with the realistic plume pogo phenomenon applied. A solution to this problem could be the addition of two plume pogo states to the filter.

The performance plots of the six-state filter are shown in Appendix C and Appendix D. The plots in Appendix C pertain to the non-oscillating intensity centroid, and Appendix D contains the plots when plume pogo is applied to the centroid. Filter tuning is the same for both cases. (The reason for not retuning the filter for the application of plume pogo is discussed in the next paragraph.) A comparison of Tables 6.1 and 6.2, and Figures C.4,

### 6.1. Target and Intensity Centroid Statistics Without Plume Pogo

Averaged Error	mean ( $t_i^-$ )	mean ( $t_i^+$ )	$1\sigma$ ( $t_i^-$ )	$1\sigma$ ( $t_i^+$ )
Target ( $\hat{x}_d$ )	- 0.059	- 0.017	0.769	0.709
Target ( $\hat{y}_d$ )	0.125	0.054	0.926	0.877
Centroid ( $\hat{x}_c$ )	- 0.056	0.006	0.512	0.172
Centroid ( $\hat{y}_c$ )	0.083	- 0.022	0.545	0.253

Error in Pixels

Table 6.2. Target and Intensity Centroid Statistics With Plume Pogo

Averaged Error	mean ( $t_i^-$ )	mean ( $t_i^+$ )	$1\sigma$ ( $t_i^-$ )	$1\sigma$ ( $t_i^+$ )
Target ( $\hat{x}_d$ )	- 0.047	- 0.006	0.907	0.809
Target ( $\hat{y}_d$ )	0.179	0.109	1.163	1.102
Centroid ( $\hat{x}_c$ )	- 0.040	0.022	1.094	0.216
Centroid ( $\hat{y}_c$ )	0.129	- 0.025	1.693	0.223

Error in Pixels

C.8 , D.4, and D.8, show a significant increase in the standard deviation of the target and intensity centroid estimates at  $t_i^-$  with plume pogo. The target values at  $t_i^-$  are the pointing errors of the FLIR FOV. The consequence of these errors is discussed in Section 6.8.2.

Appendix C also contains the filter statistics for the estimation of the atmospheric jitter phenomenon. The atmospheric performance plots are shown in Figures C.11 through C.16. During the six-state filter tuning it was determined that the filter's atmospheric jitter variance is strongly coupled with the dynamics noise of the filter. Though the filter atmospheric jitter variance is the same as the truth model value, the plotted atmospheric jitter computed error was below the actual rms error plot. Attempts to tune the atmospheric model created significant loss in tuning ability of the dynamics noise values for the filter estimated position states. It was decided to leave the atmospheric jitter variance at the truth model value of 0.2, and tune the dynamics noise for the best possible

performance. Under these conditions, following many different dynamics noise values, the tuning of the six-state filter used the same values as previous thesis [2, 26] (see Section 5.2.3.3). The tuning of the dynamics noise, as shown in Figures C.1, C.2, D.1, and D.2, is the maximum which could be obtained.

### *6.5 One-State Filter Performance Analysis*

The testing of the one-state center-of-mass filter is accomplished for a variety of configurations. The filter is tested with a single scan of the low-energy laser, and with a sweep (i.e., multiple scanning) of the low-energy laser. The single low-energy laser scan, due to the 10-20% reflections obtained for a simulation run, represents the case of minimum measurements to the filter; on the other hand, the low-energy laser sweep method provides a measurement to the filter at each sample time (i.e., 100% reflections). The filter is also tested with and without the plume pogo applied to the intensity centroid. This tests the filter's robustness, which is the ability of the filter to adapt to an environment different from the one which it was designed. The filter is also tested with the hardbody binary model and the hardbody reflectivity model, described in Chapter IV. The tuning values of the filter are given in Section 5.3.3. The filter performance of the one-state filter is much better than expected.

The tabular time-averaged performance results of the one-state filter testing are given in Tables 6.3 through 6.8. Tables 6.3 through 6.6 are the results using the hardbody binary model without and with plume pogo, and without and with a low-energy laser sweep. Tables 6.7 and 6.8 are with the hardbody reflectivity model results for the case of a low-energy laser sweep, and without and with plume pogo applied to the intensity centroid. (As mentioned in the introduction to this chapter, for this thesis, the reflectivity model is designed exclusively for use with a low-energy laser sweep.) As described in Section 4.4.3, the hardbody reflectivity model computes the center-of-mass differently than the

Table 6.3. One-State Filter Statistics Without Sweep and Pogo for Binary Model

Averaged Error	mean ( $t_i^-$ )	mean ( $t_i^+$ )	$1\sigma$ ( $t_i^-$ )	$1\sigma$ ( $t_i^+$ )
Magnitude ( $\widehat{m}_o$ )	0.060	0.060	0.205	0.204
$\widehat{x}_o$	0.037	0.037	0.212	0.212
$\widehat{y}_o$	0.043	0.048	0.240	0.239
$\widehat{ALT}$	-0.060	-0.060	0.205	0.204
$\widehat{ACT}$	-0.007	-0.007	0.244	0.244

Error in Pixels

Table 6.4. One-State Filter Statistics Without Sweep and With Pogo for Binary Model

Averaged Error	mean ( $t_i^-$ )	mean ( $t_i^+$ )	$1\sigma$ ( $t_i^-$ )	$1\sigma$ ( $t_i^+$ )
Magnitude ( $\widehat{m}_o$ )	-0.072	-0.072	0.231	0.229
$\widehat{x}_o$	0.010	0.010	0.231	0.230
$\widehat{y}_o$	0.078	0.078	0.270	0.269
$\widehat{ALT}$	-0.072	-0.072	0.231	0.230
$\widehat{ACT}$	0.030	0.030	0.262	0.262

Error in Pixels

hardbody binary model due to the reflective nature of the model design, therefore filter performance also gives an indication of the effectiveness of the enhanced hardbody reflectivity model.

The performance plots of the one-state filter are provided in Appendices E, F, G, and H. Each set of plots for a particular configuration of testing show the center-of-mass error as a magnitude, in the x and y components of the magnitude error, and in the ALT-ACT components of the magnitude error, as described in Section 6.3. Keep in mind that the one-state filter has only one state to tune, therefore following the transformation of the errors into the x and y components of the magnitude error, or the ALT-ACT components of the error, the filter may not appear to be tuned in the transformed coordinate frame. This condition provides insight into which coordinate system should be used to tune the filter. (This subject is accomplished as an independent study in Section 6.8.3.)

Table 6.5. One-State Filter Statistics With Sweep and Without Pogo for Binary Model

Averaged Error	mean ( $t_i^-$ )	mean ( $t_i^+$ )	$1\sigma (t_i^-)$	$1\sigma (t_i^+)$
Magnitude ( $\widehat{m}_o$ )	0.000	0.000	0.149	0.013
$\widehat{x}_o$	-0.003	0.000	0.076	0.007
$\widehat{y}_o$	0.000	0.000	0.129	0.011
$\widehat{ALT}$	0.000	0.000	0.149	0.013
$\widehat{ACT}$	0.003	0.000	0.012	0.001

Error in Pixels

Table 6.6. One-State Filter Statistics With Sweep and Pogo for Binary Model

Averaged Error	mean ( $t_i^-$ )	mean ( $t_i^+$ )	$1\sigma (t_i^-)$	$1\sigma (t_i^+)$
Magnitude ( $\widehat{m}_o$ )	0.000	0.001	0.171	0.013
$\widehat{x}_o$	-0.003	0.000	0.085	0.006
$\widehat{y}_o$	0.001	-0.001	0.149	0.011
$\widehat{ALT}$	0.000	0.000	0.171	0.013
$\widehat{ACT}$	0.003	0.000	0.015	0.001

Error in Pixels

Table 6.7. One-State Filter Statistics With Sweep and Without Pogo for Reflectivity Model

Averaged Error	mean ( $t_i^-$ )	mean ( $t_i^+$ )	$1\sigma (t_i^-)$	$1\sigma (t_i^+)$
Magnitude ( $\widehat{m}_o$ )	0.000	0.000	0.149	0.013
$\widehat{x}_o$	-0.003	0.000	0.076	0.006
$\widehat{y}_o$	0.000	0.000	0.129	0.011
$\widehat{ALT}$	0.000	0.000	0.149	0.013
$\widehat{ACT}$	0.003	0.000	0.012	0.001

Error in Pixels

Table 6.8. One-State Filter Statistics With Sweep and Pogo for Reflectivity Model

Averaged Error	mean ( $t_i^-$ )	mean ( $t_i^+$ )	$1\sigma (t_i^-)$	$1\sigma (t_i^+)$
Magnitude ( $\widehat{m}_o$ )	0.000	0.000	0.171	0.013
$\widehat{x}_o$	-0.003	0.000	0.085	0.006
$\widehat{y}_o$	0.001	0.000	0.149	0.011
$\widehat{ALT}$	0.000	0.000	0.171	0.013
$\widehat{ACT}$	0.003	0.000	0.015	0.001

Error in Pixels

For the case of a single low-energy laser scan without plume pogo applied, refer to Table 6.3 and Appendix E. The percentage of measurements the filter successfully received is approximately 20% of the total sample periods during the simulation. The filter performance shows that it is tracking well but with an average mean error of approximately 0.060 pixels (1.8 meters) and an average standard deviation of approximately 0.2 pixels (6.0 meters). Although the filter performs consistently, it does not meet the accuracy requirements as described in Chapter I. For the case of the low-energy laser scan and the plume pogo applied to the intensity centroid, refer to Table 6.4 and Appendix F. The filter performance degrades very little from the case without plume pogo, which provides insight into the robustness of the filter. The number of low-energy laser reflection returns (resulting in measurements for the filter) remained on the order of 20%. Notice the complete loss of measurements in the plots of Appendix F at 7 seconds into the simulation; the filter recovers quite well following the receipt of another measurement. Also notice from Figures E.1 and F.1, that the filter is tuned rather well for both the cases just discussed, however this is not reflected in the  $x$  coordinate of the error (Figures E.4 and F.4) or the ACT coordinate of the error (Figures E.11 and F.11), while the  $y$  coordinate of the error (Figures E.5 and F.5) and the ALT coordinate of the error (Figures E.10 and F.10) are tuned. This is explained by noting that the trajectory of the missile in the simulation is primarily in the  $y$  direction, which results in the filter tuning affecting this direction more than the  $x$  direction, and since the filter is tuned in the near-ALT direction of the missile, this coordinate error is also tuned much better than the ACT direction.

The hardbody binary model and the enhanced reflectivity model are both tested for the filter with a low-energy laser sweep, and without and with plume pogo applied to the intensity centroid. The sweep of the low-energy laser, as described in Section 4.4.3 for the hardbody binary model and the reflectivity model, provides laser reflection returns at each sample time for the filter. Tables 6.5 through 6.8 give the results of the testing for both



models. However, since the hardbody binary model and the reflectivity model results are almost identical, only the reflectivity model plots presented, as found in Appendices G and H. A close look at the results in Tables 6.5 through 6.8 indicates that without or with pogo applied, there is a mean error of less than one-inch. (0.001 pixels  $\cong$  1.2 inches). The standard deviation of the error, even with pogo applied, is approximately 0.008 pixels (10.0 inches). The plots shown in the appendices provide the visual analysis of the tabular data. The effect of the pogo on the filter is seen in the plots of Appendix H; however, as with the single laser scan, the filter adjusts to the pogo oscillations very well. Notice in the plots of the ACT coordinate of the error that, as with the single low-energy laser scan, the filter is not tuned for this direction. This is not the case when there are two states to estimate (and tune), as is the case for the eight-state filter.

### *6.6 Eight-State Filter Performance Analysis*

The eight-state filter performance is a mirror image of that of the one-state filter. Tables 6.9 and 6.10 give the hardbody binary model results for a single low-energy laser scan without and with plume pogo applied, and Appendices I and J give the corresponding performance plots. Tables 6.11 through 6.14 give the results of the hardbody binary model and the hardbody reflectivity model for the case with a low-energy laser sweep, and without and with plume pogo applied to the intensity centroid; Appendices K and L contain the associated performance plots of the filter (using the enhanced hardbody reflectivity model). The eight-state filter performance plots consist of the  $x$  and  $y$  coordinates (of the two center-of-mass states  $x_7$  and  $x_8$ ), and the ALT and ACT coordinate errors. Notice that, with two states to tune the filter, the filter is tuned well in both coordinate frames. Refer to Section 5.4.3 for the eight-state filter tuning values. This filter also has a mean error less than one-inch and a standard deviation of 10.0 inches for a low-energy laser sweep with plume pogo applied.

Table 6.9. Eight-State Filter Statistics Without Sweep and Pogo for Binary Model

Averaged Error	mean ( $t_i^-$ )	mean ( $t_i^+$ )	$1\sigma$ ( $t_i^-$ )	$1\sigma$ ( $t_i^+$ )
$\hat{x}_o$	0.047	0.047	0.211	0.210
$\hat{y}_o$	0.046	0.046	0.245	0.245
$\widehat{ALT}$	-0.064	-0.064	0.205	0.205
$\widehat{ACT}$	-0.017	-0.017	0.248	0.248

Error in Pixels

Table 6.10. Eight-State Filter Statistics Without Sweep and With Pogo for Binary Model

Averaged Error	mean ( $t_i^-$ )	mean ( $t_i^+$ )	$1\sigma$ ( $t_i^-$ )	$1\sigma$ ( $t_i^+$ )
$\hat{x}_o$	0.050	0.049	0.228	0.228
$\hat{y}_o$	0.061	0.061	0.256	0.255
$\widehat{ALT}$	-0.078	-0.078	0.215	0.215
$\widehat{ACT}$	-0.012	-0.012	0.265	0.265

Error in Pixels

### 6.7 One-State vs. Two-State Center-of-Mass Filter Comparison

One of the primary objectives of this thesis is to compare the performance of the one-state center-of-mass filter with that of the two-state center-of-mass estimator within the eight-state filter. Another objective of the thesis is to evaluate a realistic reflectivity model of the missile hardbody. Since the testing of the filters used both of the hardbody models, this section compares the performance of the one-state and two-state center-of-mass filters, and provides an additional comparison of the two hardbody models.

By performing a comparison of the tabular one-state filter performance data in Tables 6.3 through 6.8 with the performance data of the eight-state center-of-mass filter (states  $x_7$  and  $x_8$ ) in Tables 6.9 through 6.14, it is clear there is no advantage of having two states to estimate the hardbody center-of-mass. As can be seen in the tabular data and

Table 6.11. Eight-State Filter Statistics With Sweep and Without Pogo for Binary Model

Averaged Error	mean ( $t_i^-$ )	mean ( $t_i^+$ )	$1\sigma (t_i^-)$	$1\sigma (t_i^+)$
$\hat{x}_o$	0.000	0.000	0.196	0.007
$\hat{y}_o$	0.000	0.000	0.210	0.011
$\widehat{ALT}$	0.000	0.000	0.170	0.013
$\widehat{ACT}$	0.000	0.000	0.246	0.002

Error in Pixels

Table 6.12. Eight-State Filter Statistics With Sweep and Pogo for Binary Model

Averaged Error	mean ( $t_i^-$ )	mean ( $t_i^+$ )	$1\sigma (t_i^-)$	$1\sigma (t_i^+)$
$\hat{x}_o$	0.000	0.000	0.191	0.006
$\hat{y}_o$	0.000	0.000	0.221	0.011
$\widehat{ALT}$	0.000	0.000	0.170	0.013
$\widehat{ACT}$	0.000	0.000	0.239	0.002

Error in Pixels

Table 6.13. Eight-State Filter Stat. With Sweep and Without Pogo for Reflectivity Model

Averaged Error	mean ( $t_i^-$ )	mean ( $t_i^+$ )	$1\sigma (t_i^-)$	$1\sigma (t_i^+)$
$\hat{x}_o$	0.000	0.000	0.200	0.007
$\hat{y}_o$	0.000	0.000	0.210	0.011
$\widehat{ALT}$	0.000	0.000	0.149	0.013
$\widehat{ACT}$	0.000	0.000	0.246	0.002

Error in Pixels

Table 6.14. Eight-State Filter Statistics With Sweep and Pogo for Reflectivity Model

Averaged Error	mean ( $t_i^-$ )	mean ( $t_i^+$ )	$1\sigma (t_i^-)$	$1\sigma (t_i^+)$
$\hat{x}_o$	0.000	0.000	0.191	0.006
$\hat{y}_o$	0.000	0.000	0.221	0.011
$\widehat{ALT}$	0.000	0.000	0.170	0.013
$\widehat{ACT}$	0.000	0.000	0.239	0.002

Error in Pixels

the plots in the appendix, the principle error is in the ALT direction, therefore the one-state filter, which is basically tuned for the ALT direction (as shown in the ALI tuning plots of the Appendix E through H), performs as well as the two-state filter. The data also shows that the ACT direction (for which the one-state filter is not tuned) has relatively small errors, so the one-state filter does not lose performance estimation of the center-of-mass with its single (ALT) state. This condition exists since the missile has such a benign trajectory in the cross axis of flight (i.e., the ACT direction).

For the one-state filter, the six-state filter's estimate of the target velocity vector is used to determine the low-energy laser single scan of the target, while the eight-state filter center-of-mass states (states  $x_7$  and  $x_8$ ) are used to estimate the sweep angle following an initial reflection return using the velocity vector estimate. (The purpose of this scanning scenario is to provide the two center-of-mass states with good initial conditions.) The true velocity vector for the 10 second flight is:  $\theta_f = 59.95^\circ$ . The statistics gathered for the six-state filter estimate of the velocity vector are:  $\theta_f = 59.59^\circ$  with  $\sigma = \pm 0.03^\circ$ . The two bias states of the eight-state filter statistics for estimating the velocity vector are determined as:  $\tan^{-1} y_o/x_o = 59.30^\circ$  with  $\sigma = \pm 0.41^\circ$ . While the six-state filter estimate is more precise, the number of low-energy laser measurements for the one-state filter and the eight-state filter is approximately 10-20% for a single laser scan. The sample period of 30 Hz was increased to 50 Hz to determine if an increased sampling period would create more measurements; however, this did not improve the number of low-energy laser reflections. (In fact, the percentage of possible laser measurements decreased to 10%.) The measurement problem for both filters is solved by implementing the low-energy laser sweep, which provides a measurement to the filter at each sample time. (The low-energy laser sweep method is discussed further in Chapter VII.) The problem of obtaining a measurement at each sample time using a single low-energy laser scan is discussed in Section 6.8.1.

## 6.8 Studies and Investigations

Three studies evolved during the research of this thesis. The first study involves the hardbody reflectivity model developed for this thesis. The hardbody reflectivity model provides a more realistic portrayal of the real world, and therefore creates a lower probability of obtaining measurements for the filter with its realistic modeling, compared to the hardbody binary model. This study is conducted to show the effects of losing reflection measurements due to the lower threshold limitations of the low-energy laser sensor in the spaced-based platform (Figure 1.1). In another study, an investigation into the problem of not obtaining a higher percentage of laser reflection measurements, given the accuracy of the filter-estimated velocity vector (given in Section 6.7), for a single low-energy laser scan is discussed. The last study considers the performance advantages of tuning the Kalman filters (used in this research) in the ALT-ACT coordinates, as opposed to the  $x$  and  $y$  FLIR coordinates.

*6.8.1 Low-Energy Laser Sensor Sensitivity.* The introduction of the hardbody reflectivity model creates more realistic uncertainties in obtaining measurements for the Kalman filter. The design of the reflectivity model includes a low-energy laser sensor, which may be thresholded to reflect a physical design limitation of the space-based hardware. This testing also gives insight into the filter's need to have good measurement updates to perform its tracking function.

The trajectory of the missile in the simulation, as given in Section 3.5, creates a projection angle  $\gamma$  (Figures 3.9 and 4.13), between the missile and the FLIR image plane, from  $1.52^\circ$  to  $2.84^\circ$  during the course of the 10 second computer run. Therefore, this range of  $\gamma$  gives a discrete value of the longitudinal reflectivity function as 0.5, as described in Section 4.4.2.2. If the low-energy laser sensitivity is set to 25, then the missile reflection would be invisible to the sensor (i.e., 50 units of cross-sectional

reflection magnitude times 0.5 for the value of the longitudinal reflectivity function scaling factor gives 25 units of reflection magnitude, and  $25 - 25 = 0$ . (In this case, the low-energy laser sensitivity must have a value less than 25 units of reflection magnitude to detect a reflection return from the hardbody). To test the reflectivity model software, the initial condition of the  $z$  velocity component in the inertial reference frame is changed from zero to 180.0 meters/second. This creates a new missile trajectory, which gives a range of the  $\gamma$  angle from  $3.91^\circ$  to  $5.09^\circ$ . Therefore, if the low-energy laser sensitivity is 9.0 units of reflection magnitude (for a  $\gamma$  angle range up to  $7.0^\circ$ ), the sensor will lose the target as the  $\gamma$  angle exceeds  $5.0^\circ$ , which requires a low-energy laser sensitivity value less than 9.0 units of reflection magnitude. The test is accomplished using the eight-state filter with the hardbody reflectivity model, and a low-energy laser sweep with plume pogo applied to the intensity centroid. The results would probably be the same for the one-state filter with the same low-energy laser sensor sensitivity, but was not tested. The test results of the eight-state filter are shown in Appendix M (compare with Appendix L). As expected, the filter lost lock on the target as the projection angle  $\gamma$  exceeded  $5.0^\circ$ . This shows the requirement for adequate sensor technology to meet the needs of the tracking system.

*6.8.2 Intensity Centroid Movement.* The most curious problem encountered during this thesis is the "apparent" movement of the intensity centroid on the FLIR image plane. The target velocity estimates of the six-state filter are accurate enough (as given in Section 6.7) that a single low-energy laser scan along the velocity vector should provide a reflection each sample time, but this is not the case. To overcome this problem, the low-energy laser sweep technique was developed in this thesis, which provides measurements to the filter at each sample time. The low-energy laser offset angle, described in Section 4.4.3, needed to be  $30^\circ$  when plume pogo was not applied to the intensity centroid, and  $35^\circ$  when plume pogo is applied. (This required offset to sweep the low-energy laser equates to approximately a 1.0 pixel (30 meter) standard deviation of the intensity

centroid.) Initially, the atmospheric jitter or the bending/vibration phenomenon was suspected of being the problem. The filter models the atmospheric jitter, and as shown in Appendix C, Figures C.11 through C.16, the filter is well tuned and the errors are zero mean with a consistent standard deviation of 0.5 pixels (15 meters) at  $t_i^-$  and at  $t_i^+$ . The bending/vibration phenomenon is not modeled by the filter, and as determined by [10], does not affect filter performance substantially. However, to be certain these physically modeled phenomenon did not cause the movement of the intensity centroid, the truth model plots of the atmospheric jitter and the bending/vibration phenomenon over the simulation were obtained, as shown in Appendix N. The results show that the atmospheric jitter and the bending/vibration phenomenon could not cause the large magnitude centroid movement that is being exhibited. Additionally, as mentioned in Section 6.7, the sample period of 30 Hz was increased to 50 Hz to determine if a shortened sampling period would create more measurements. This did not improve the number of low-energy laser reflections, and by the increased number of potential laser measurements due to the increased sampling rate, the percentage of successful laser reflections actually decreased from 20% to 10%.

The solution to the problem of the centroid movement is related to the propagated estimate of the six-state filter at  $t_i^-$  (just before the next sample time). This propagated estimate is used to command the FLIR sensor pointing controller (Section 3.4) to point the FLIR plane LOS vector  $\mathbf{e}_r$ . If the propagated estimate is in error, then the center of the FLIR plane will not be positioned correctly to obtain a low-energy laser reflection return from the missile hardbody when the laser is scanned along the velocity vector (or the two-state filter bias estimated scan direction). Therefore the "apparent" movement of the intensity centroid is due to the positioning of the FLIR plane, and not to the centroid itself, as was initially suspected. This apparent movement of the intensity centroid in the FLIR plane can be seen in the six-state filter performance plots of the  $x$  and  $y$  target location estimates at  $t_i^-$ , shown in Figures C.3, C.4, D.3, and D.4. (The approximate 1.0 to 1.5

pixel standard deviation shown in the plots compares well with the experimental results obtained of the centroid movement in the process of determining the required angle offset of the low-energy laser from the filter-estimated velocity vector  $\theta_f$  for the sweep technique.) Figure 6.2 shows pictorially the reason for the apparent movement of the intensity centroid. Since the low-energy laser is fired through the LOS vector  $e_r$  of the FLIR plane, the FLIR must be locked onto the intensity centroid to obtain a high percentage of low-energy laser reflection returns for a single scan. Figure 6.2 shows the intensity centroid in the FLIR FOV for three different times in the trajectory in an apparent oscillatory motion about the center of the FLIR plane. Since the low-energy laser is fired from the center of the FLIR plane along the velocity vector, the first and third low-energy laser firings in Figure 6.2 result in no reflection returns; the middle case results in a reflection return, which also provides the filter with a measurement update. Some possible solutions to this problem are discussed in Chapter VII.

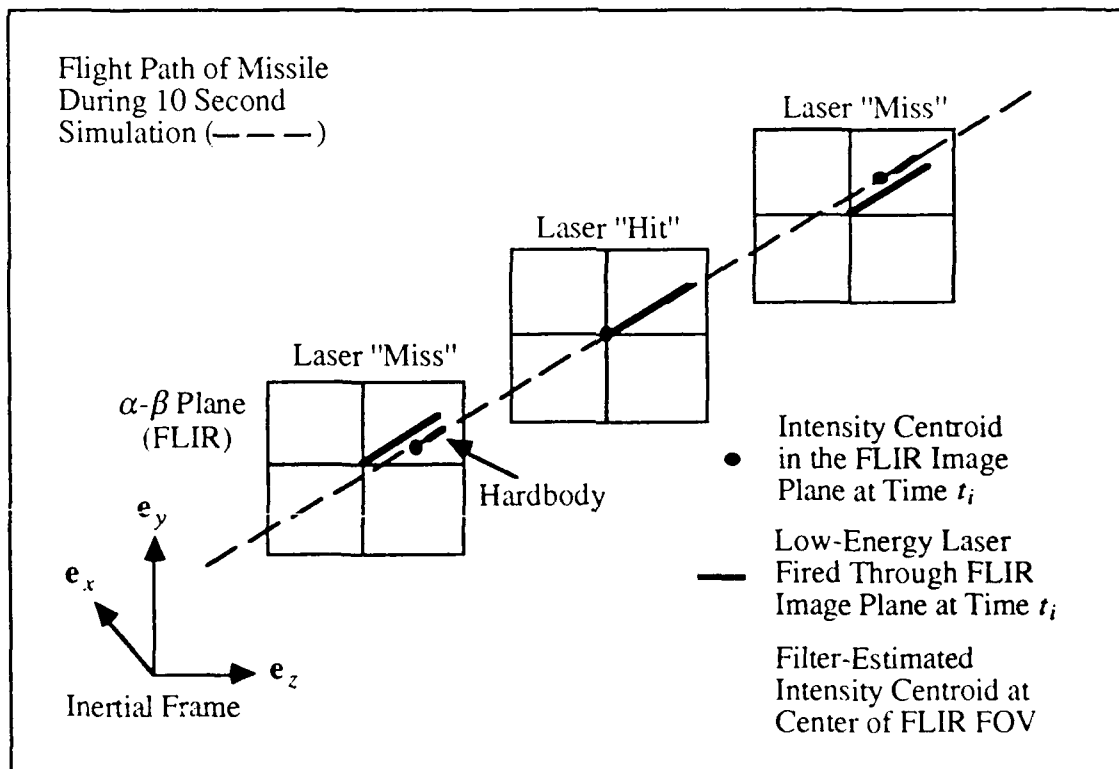


Figure 6.2. "Apparent" Intensity Centroid Movement in FLIR Image Plane



*6.8.3 Filter Dynamics Tuning.* In previous research, as in this thesis, filter tuning has been accomplished in the  $x$  and  $y$  FLIR coordinate system. However, it is proposed that the optimal tuning of the filter is most likely accomplished in the missile coordinate frame, the ALT-ACT frame. This applies to the FLIR filter as well as to the center-of-mass filter. Furthermore, in the trajectory of the missile tracking study [2, 26], the filter has been tuned for a single trajectory with an orientation angle of  $60^\circ$ , therefore it is suspected that there could be a performance degradation if the target trajectory is altered without retuning the filter.

The testing of this hypothesis was accomplished by adjusting the trajectory to approximately  $75^\circ$ ; the target's initial  $x_o$  and  $y_o$  velocities were changed to -1294 meters/second and 4829 meters/second, respectively, while keeping the  $z_o$  velocity zero (Section 3.5), and maintaining the speed of the missile at 5,000 meters/second. The filter remained tuned for the  $60^\circ$  trajectory. The six-state/one-state filter configuration was used for the test with the enhanced hardbody reflectivity model, and a low-energy laser sweep with plume pogo applied to the intensity centroid. The results of the simulation run are shown in Tables 6.15 and 6.16 for the target and intensity centroid estimates by the six-state filter, and for the one-state filter estimates of the center-of-mass coordinates, respectively. A comparison of these results with those obtained from the  $60^\circ$  trajectory, Tables 6.2 and 6.8, shows areas of performance improvement and performance loss for the filters. The six-state-filter results show an overall improvement in the  $x$  and  $y$  directions of the target and intensity centroid estimates at  $t_i^+$ . The  $x$  component error standard deviation also shows improvement at  $t_i^-$ , while the  $y$  direction standard deviation performance is degraded by almost 0.2 pixels (6.0 meters). This means that the filter is providing the pointing controller with worse estimates than for its tuned condition at the  $60^\circ$  trajectory. The one-state filter estimates of the center-of-mass shows an overall mean and standard deviation performance improvement in the  $x$  direction at both  $t_i^-$  and  $t_i^+$ ,

Table 6.15. Six-State Filter Target and Intensity Centroid Statistics for Trajectory at 75°

Averaged Error	mean ( $t_i^-$ )	mean ( $t_i^+$ )	$1\sigma$ ( $t_i^-$ )	$1\sigma$ ( $t_i^+$ )
Target ( $\hat{x}_d$ )	- 0.031	- 0.010	0.821	0.749
Target ( $\hat{y}_d$ )	0.144	0.066	1.227	1.070
Centroid ( $\hat{x}_c$ )	- 0.042	- 0.010	0.728	0.209
Centroid ( $\hat{y}_c$ )	0.087	- 0.029	1.877	0.250

Error in Pixels

Table 6.16. One-State Filter Center-of-Mass Statistics for Trajectory at 75°

Averaged Error	mean ( $t_i^-$ )	mean ( $t_i^+$ )	$1\sigma$ ( $t_i^-$ )	$1\sigma$ ( $t_i^+$ )
Magnitude ( $\hat{m}_o$ )	-0.008	-0.005	0.245	0.229
$\hat{x}_o$	0.001	0.001	0.076	0.008
$\hat{y}_o$	0.008	0.005	0.234	0.028
ALT	-0.008	-0.005	0.245	0.029
ACT	0.000	0.000	0.030	0.002

Error in Pixels

while the y direction performance is degraded. This error may not appear significant at first, but the mean error has increased from 0.0005 pixels (less than 1.0 inch) to 0.008 pixels (nearly 10.0 inches), and the standard deviation at  $t_i^+$  has increased from 0.011 pixels (13.0 inches) to 0.028 pixels (33.0 inches). (Notice that the ALT error is associated with the magnitude error and the error in the y direction, in this case.)

The results at the 75° trajectory are considered to be a large deviation from the results obtained with the tuned filters at the 60° trajectory. Even at this small angle of change, the tuned filter performance is degraded substantially. (Further testing at angles below 60° were hampered by software limitations.) Though there was insufficient time in this thesis to test the idea, it appears that the optimum tuning of the filters occurs in the ALT-ACT coordinate frame. Additionally, since initial acquisition of a target could be in any orientation, a variably-tuned filter may be necessary to track the target in different

trajectory orientations. The strength of the dynamics variance for tuning the filter would possibly be a function of the FLIR projection angles  $\theta$  and  $\gamma$  (Figures 3.9 and 4.13).

## 6.9 Summary

This chapter presented the results and findings of this thesis. The one-state center-of-mass filter performs as well as the two states devoted to estimating the center-of-mass in the eight-state filter. The reason for this outcome is related to the benign trajectory of the simulated missile target. Since the ACT component in flight does not change, a one-state filter estimating the ALT component of the missile dynamics provides excellent tracking performance. Moreover, the missile velocity direction is a good search direction for finding the hardbody center-of-mass from the infrared image center of intensity, provided that the latter is located precisely in the FLIR image plane. The "apparent" movement of the intensity centroid, which motivated the low-energy laser sweep, is the result of the large standard deviation associated with the propagated filter estimates used to point the FLIR plane. Although the problem was overcome by the use of a low-energy laser sweep, the time required to perform the sweep is not considered a final solution to the problem. The use of the ALT-ACT coordinate system to provide another description of the center-of-mass errors also gave insight into using this coordinate system to tune the filter as well. A trajectory test showed that there were changes in the performance of both the six state filter and the one-state filter when the trajectory was changed without retuning the filter. The initial acquisition of a target could be in any orientation, therefore a variably-tuned filter may be necessary to track the target in different trajectory orientations in the FLIR image plane. The hardbody reflectivity model provided the same basic performance trends as the hardbody binary model. However, it was also shown that there are physical hardware constraints associated with the low-energy laser sensor sensitivity.

## *VII. Conclusions and Recommendations*

### *7.1 Introduction*

This chapter gives the the conclusions of this thesis and makes recommendations for further research. It should be pointed out that not all the objectives described in Chapter I were completed, but other objectives developed during the research were accomplished instead. As is the case with any endeavor subjected to limited time, considerations and decisions were made to optimize the time devoted to current versus further research, even if the objectives needed to be altered.

### *7.2 Conclusions*

This thesis has developed a number of conclusions through the accomplishment of the research objectives, and the additional studies conducted during the course of this thesis. Chapter VI presented the *findings of the research, and also provided some conclusions and recommendations for further study.* The following sections consolidate previous conclusions with other insights obtained in this research, and makes further recommendations for continued research into tracking a missile hardbody using a Kalman filter with FLIR and low-energy laser measurements.

*7.2.1 One-State vs. Two-State Center-of-Mass Estimation.* One of the primary objectives of this thesis was to test a one-state filter, designed to estimate the center-of-mass of a missile hardbody using FLIR and low-energy laser measurements, against an eight-state filter with two states to estimate the center-of-mass. The one-state filter presumes that the direction of the offset between the hardbody center-of-mass and the infrared image center of intensity is well approximated by the filter-estimated velocity direction in the FLIR image plane. In contrast, the eight-state filter estimates the two components of the this offset in the FLIR image plane, without presuming such

directionality. The one-state filter and the eight-state filter are tested: without plume pogo of the intensity centroid and with plume pogo applied; with a single scan of the low-energy laser and with a sweep; and with the hardbody binary model and with the hardbody reflectivity model. The one-state filter performs as well in each case as the eight-state filter. The absence of measurements for the single-scan of the low-energy laser provides poor performance with an average mean error of 2.0 meters and a standard deviation of  $\pm 8.0$  meters. This aspect of the testing shows the reliance of the filter on good measurements at each sample update: for these tests there are many sample periods in which the low-energy laser did not intercept the missile hardbody so that there are no successful measurements for updating the center of mass state variable estimates. Additionally, an increase in the sample period from 30 Hz to 50 Hz shows no performance increase. The respective average mean error and standard deviation for the filters, for the case of plume pogo and a low-energy laser sweep for both the hardbody binary model and the reflectivity model, is found to be on the order of 1.0 inch and a standard deviation of  $\pm 10.0$  inches. These are much better statistics than expected, and the one-state filter performance is even more surprising. However, following the evaluation of the data, the one-state filter performance is logical. The data shows that the error is much greater in the along-track (ALT) direction than in the across-track (ACT) direction, therefore, the one-state filter performs well since it is tuned for the ALT direction. From this research it appears that a one-state filter is sufficient to estimate the center-of-mass of the hardbody, given the rather benign trajectory of a missile in flight. Since the objective of the tracking problem described in Chapter I emphasizes time as a critical issue, the need for only one state to perform the hardbody estimates provides a decrease in computer processing time to process the Kalman filter algorithm.

*7.2.2 Hardbody Binary vs. Reflectivity Model.* The design of the enhanced hardbody reflectivity model is accomplished to provide increased realism in the simulation.

The model includes the curvature of the missile and its angular orientation with respect to the FLIR plane, as factors in reducing the reflection strength of the low-energy laser return signal. Since the emphasis is placed on achieving a good measurement for the filter, the reflectivity model is designed for a low-energy laser sweep (but could be adapted to a single low-energy laser scan as well). The low-energy laser sensor is designed to allow thresholding to simulate a design hardware limitation. For all cases in which the low-energy laser could detect the low-energy laser reflection return, the performance of the hardbody reflectivity model in providing measurements is equal to the binary model. The discrete-valued design of the model created instances of the low-energy laser "jumping over" the peak intensity reflection (needed for the center-of-mass calculation), and this is overcome by decreasing the sweep increments of the low-energy laser sweep across the hardbody. The model is tested for the case of a design limitation associated with the low-energy laser, and as expected, when the low-energy laser could no longer sense the low-energy laser reflections, the filter diverged for lack of measurement updates, and lost track of the missile (however, the FLIR filter continued to track the intensity centroid).

*7.2.3 Low-Energy Laser Sweep.* The design of the low-energy laser sweep is implemented in the software due to the uncertainty as to why the low-energy laser was only crossing the hardbody approximately 20% of the time. Since a Kalman filter relies on frequent measurement updates, the early solution was to provide the updates to test the filter performance, then determine the problem associated with the need for the sweep routine. The low-energy laser sweep routine is not an optimal tool for obtaining filter measurements. The routine increased computer run time, and therefore the overall tracking scheme described in Chapter I would be degraded. However, the low-energy laser sweep provides the analysis that concludes a one-state filter can provide accurate estimates of the hardbody center-of-mass if measurements are provided to the filter at each sample time. The low-energy laser sweep routine should be used in the simulation, until the problem of

obtaining a reflection from a single scan of the low-energy laser is solved; this will provide continued testing of the center-of-mass filter with the necessary measurement updates. The scan could also be altered to supply fewer than the optimal number of measurements (i.e., missing some measurements for updating) to determine where the filter performance breaks down.

*7.2.4 Doppler Shift Investigation.* As mentioned in the opening of this chapter, the Doppler investigation was not directly accomplished. However, the Doppler phenomenon is similar to the low-energy laser sweep developed for this thesis. The low-energy laser sweep illuminates the vehicle in much the same way as a Doppler frequency return would "illuminate" the hardbody against the background. Therefore, the low-energy laser in the simulation can represent the Doppler frequency shift, by changing the simulation cross-sectional intensity function to be constant over its entire surface. The accuracy with which the line of demarcation between the hardbody and the background is discerned might also be varied. The results of this testing would possibly give the same results as found in the low-energy laser testing: the low-energy laser sensor technology is a limiting factor in detecting a reflection return, and it is suspected that the same would be true for a Doppler shift sensor in detecting the noise corrupted frequency shift between the missile hardbody and the background.

*7.2.5 Atmospheric Modeling.* The need for improved atmospheric modeling was explained in the thesis objectives in Chapter I. Unfortunately, this objective was not accomplished, and is left for a future thesis to put the "near perfect" filter tracking to the test by increasing the realism of the atmospheric distortion on the laser signal. For this thesis, the laser traveled unhindered both to and from the target. In the real world, of course, this is not the case. The atmosphere creates bending and refraction of the laser beam, as well as reducing the sending strength of the signal at the target and the reflected signal strength at the low-energy laser sensor.

*7.2.6 Variable Target Dynamics Tuning.* This topic arises from the representation of the filter center-of-mass errors being described in the ALT-ACT reference frame. The results of the testing revealed that the one-state filter is rather well-tuned in the ALT direction, while it is slightly overtuned in the ACT direction. However, since the one-state filter is tuned for the ALT direction (by default), its performance in the ALT direction is not surprising. Using the six-state filter and the one-state filter, the trajectory of the missile in the simulation was changed from  $60^\circ$  to  $75^\circ$ . There were both good and bad performance advantages changes for both filters. The performance changes (both good and bad) indicate that the filter may need adaptive, or variable, tuning to cope with the different possibilities of a target orientation in the FLIR plane. The variable tuning may need to be a function of the FLIR and target projection angles, which define the 3-dimensional model in the 2-dimensional FLIR plane.

### *7.3 Recommendations*

The following recommendations are suggested for further study in using a Kalman filter to track a missile hardbody using FLIR and laser measurements. Many of the recommendations have previously been mentioned, however they are provided here as a reference source for the reader.

*7.3.1 One-State Center-of-Mass Filter.* The one-state filter performed much better than anticipated. Its continued testing will provide increased confidence in the findings of this thesis, that a one-state estimator provides accurate estimation of the hardbody center-of-mass. The low-energy laser sweep routine and the hardbody reflectivity model provide testing aspects of the filter under different, more realistic conditions. The low-energy laser scan can be made to provide less than optimal amounts of measurements to the filter to test the point at which the filter performance significantly degrades. This type of testing should be repeated for the addition of other models that improve the realism of the simulation.



Improving the atmospheric model would be one such case. Additionally the filter should be tuned in the ALT-ACT frame and subjected to testing in a number of flight orientations to measure the adaptation of the filter under a variable tuning arrangement.

*7.3.2 "Apparent" Intensity Centroid Movement.* The accurate one-sample period prediction estimation of the six-state filter, to command the pointing controller, is currently the only problem in the way of being able to obtain reflection measurements at each sample time using a single scan of the low-energy laser. As previously mentioned, the low-energy laser sweep routine is not an optimum method of obtaining the measurements. The tuning of the FLIR filter in the ALT-ACT coordinate frame may assist in the filter estimating the location to next point the FLIR line-of-sight vector. Additionally, the state that is saved by the success of the one-state filter for estimating the hardbody center-of-mass, could be replaced with two plume pogo states to estimate the movement of the intensity centroid when the realistic plume pogo is applied. The one-state filter is not affected by the application of the plume pogo, however the six-state filter estimate of the target location and apparent intensity centroid location was significantly degraded. (An obvious question is why didn't the six-state filter degradation affect the performance of the one-state filter estimate? The answer is that the measurement provided to the filter is associated with the location of the intensity centroid at a particular sample time in the FLIR image plane, therefore an accurate measurement of the center-of-mass offset in the FLIR image plane is obtained from the estimated intensity centroid location despite large errors in the centroid estimate.) If the pogo is estimated well, the standard deviation of the centroid estimate may be reduced. Furthermore, if the tuning of the filter in the ALT-ACT frame is valid, the filter estimate may improve significantly. From this discussion, a nine-state filter is proposed that consists of the six-state filter (with its two position states, two velocity states, and two atmospheric jitter states), one state for estimating the hardbody center-of-

mass, and two states for estimating the plume pogo. (Additional states may also be necessary to estimate further changes to the atmospheric model.)

Another possible solution to the problem of obtaining a reflection return with each single scan of the low-energy laser may be with the diagonal rotating field-of-view (DRFOV) [26]. The DRFOV was not used in this thesis. By aligning the filter-estimated velocity vector (which is accurately estimated by the filter) along the diagonal of the FLIR plane, then firing the low-energy laser along the velocity vector has the potential to dramatically increase the number of low-energy laser reflections obtained using a single scan. The DRFOV was used by [2] to obtain the FLIR sensor measurements of the target's intensity centroid in the rotated field-of-view, however the low-energy laser was not fired in the direction of the missile hardbody in this rotated frame.

*7.3.3 Improve Atmospheric and Bending/Vibration Modeling.* The improved modeling of the atmospheric disturbances in the simulation requires changes to the truth model, and possible changes to the filter as well. With the improved hardbody reflectivity model and low-energy laser sensor, an improved atmospheric model will provide a more accurate analysis of the one-state filter to track the missile hardbody. The bending vibration modeling should also be examined, since the current modeling relates to a close-range target. With the long-range missile target considered, the bending/vibration phenomenon is significantly amplified over the greater distance.

*7.3.4 Variable Target Dynamics Tuning.* The investigation of the ALT-ACT coordinate frame has created insight into tuning filters in this frame as opposed to the  $x$  and  $y$  FLIR plane coordinate system. This method warrants investigation since it may help in more accurately estimating the location to point the FLIR sensor, which could improve the number of successful measurements obtained from the low-energy laser scan. The filter

tuning may also need to be adaptive, or variable, to provide good tracking for different target trajectory orientations.

*7.3.5 Alternate Low-Energy Laser Sweeping Technique.* The low-energy laser sweep developed for this thesis is one possible sweeping method to ensure that a measurement is available to the filter at each update time. As previously mentioned, a sweep is not necessarily desired, but if the filter estimation to point the FLIR plane does not improve, or improves but not well enough to obtain the necessary measurements required for good filter performance, a low-energy laser sweep may be required. An alternate sweeping technique consists of a sinusoidal scan from the intensity centroid along the filter estimated velocity vector. The variables of the sweep are frequency and amplitude. This sweeping method could prove to be more efficient than the current method, if a low-energy laser sweep continues to be necessary.

## Appendix A. Data Processing Statistics Method

The performance of the Kalman filters used in this thesis is evaluated using ten Monte Carlo computer runs. A Monte Carlo analysis involves collecting statistical information generated from simulating samples of stochastic processes [12]. Previous research has demonstrated that ten Monte Carlo runs provide sufficient convergence to the actual statistics resulting from an infinite number of runs [4, 5, 21].

In the simulation, the truth model generates simulated physical effects such as atmospheric jitter, mechanical bending, and plume pogo, to provide a realistic representation of the target in the real world as it is propagated through inertial space. As the target moves along its trajectory, the Kalman filter attempts to track the target using its internal dynamics model and periodic measurements provided by modeled hardware (ex: FLIR sensor, low-energy laser and sensor). After collecting  $N$  samples of truth model and filter model data for ten separate Monte Carlo runs, the true error statistics can be approximated by computing the sample mean error and variance of the error for the ten runs. These sample statistics provide a measure of the filter's performance.

The sample mean error and variance of the error for a filter's estimates are computed by:

$$\bar{E}(t_i) = \frac{1}{N} \sum_{n=1}^N \left[ x_{truth_n}(t_i) - \hat{x}_{filter_n}(t_i) \right] \quad (A-1)$$

$$\sigma^2(t_i) = \frac{1}{N-1} \sum_{n=1}^N \left[ x_{truth_n}(t_i) - \hat{x}_{filter_n}(t_i) \right]^2 - \frac{N}{N-1} \bar{E}^2(t_i) \quad (A-2)$$

where

- $\bar{E}(t_i)$  = sample mean of the error of interest at time  $t_i$
- $\sigma^2(t_i)$  = sample variance of the error of interest at time  $t_i$
- $x_{truth_n}(t_i)$  = truth model value of the variable of interest at time  $t_i$  during simulation  $n$
- $\hat{x}_{filter_n}(t_i)$  = filter estimate of the variable of interest at time  $t_i$  during simulation  $n$
- $N$  = number of Monte Carlo runs

The variables of interest for this simulation are the position of the target's intensity centroid in azimuth and elevation ( $x_d$  and  $y_d$  respectively), the velocity states ( $v_x$  and  $v_y$ ), the offsets in azimuth and elevation due to atmospheric jitter ( $x_a$  and  $y_a$ , respectively), and the offsets of the target hardbody center-of-mass from the intensity centroid in azimuth and elevation ( $x_o$  and  $y_o$ , respectively). Statistics on the variables for target's position and target center-of-mass in azimuth and elevation provides for evaluation of the filter's performance. The error committed in estimating the apparent location of the intensity centroid of the target's image on the FLIR plane is also important, since it provides an indication of how well the filter algorithm is adaptively determining the target's shape function and centroid location. The location of the intensity centroid is needed to center the the data on the FLIR plane for use in the correlation algorithm's template generation.

The statistics are calculated before the measurement update at  $(t_i^-)$  and after the update at  $(t_i^+)$  for all sample times  $t_i$ . They are reduced further to obtain average scalar values over the time of the run, by temporally averaging the mean error and standard deviation ( $\sigma$ ) time histories over the last eight seconds of the ten second simulation used in this thesis. The first two seconds are not used to ensure that the data reflects only steady-state performance. The errors are measured in units of pixels, where a pixel is 15 microradians on a side (or approximately 30 meters at a distance of 2,000 kilometers).

## *Appendix B. Examples of Performance Plots*

In this thesis, there are two different types of data plots used to assess the performance of the three filters evaluated. The first type of performance plot, shown in Figure B.1, provides filter tuning information, by comparing the actual rms error of the filter vs. the filter-computed rms error, i.e., how well the filter "thinks" it is performing. The second type of performance plot, shown in Figure B.2, provides a primary tracking performance evaluation. The plot shows the sample mean filter error (for a particular state or parameter) averaged over the ten Monte Carlo computer runs, and also shows the average  $\pm 1\sigma$  (sample standard deviation) for the ten runs. The mean  $\pm 1\sigma$  data plots are generated just before the filter receives its measurement (from FLIR or low-energy laser scan) at  $t_i^-$ , and after the measurement update is incorporated into the filter at  $t_i^+$ . The filter's state estimates after the measurement is incorporated at  $t_i^+$ , provides the lowest average mean error and the smallest  $\pm 1\sigma$ . A filter tracker with a larger standard deviation is ineffective in tracking, and in the case of this thesis, in scanning a low-energy laser to obtain a reflection return from a missile hardbody.

The state estimates of the target azimuth ( $x$ ) and elevation ( $y$ ) position at  $t_i^-$ , estimated at the previous time  $t_{i-1}$ , are used to generate the control signals for the FLIR sensor pointing controller (Section 3.4) to point the FLIR sensor. The position errors at time  $t_i^-$ , which are less accurate than just after the measurement at time  $t_i^+$ , result in an "apparent" movement of the intensity centroid in the FLIR plane (Section 6.8.2).

The filter vs. actual true rms error plots shown in Figures B.3 and B.4 are examples from estimating the center-of-mass of the hardbody, with and without a low-energy laser sweep. In the case of a single low-energy laser scan (i.e., no sweep), for this thesis, the filter-computed error can be discerned from the true rms error by knowing that the filter error is more stable in visual appearance on the plots than the rms error.

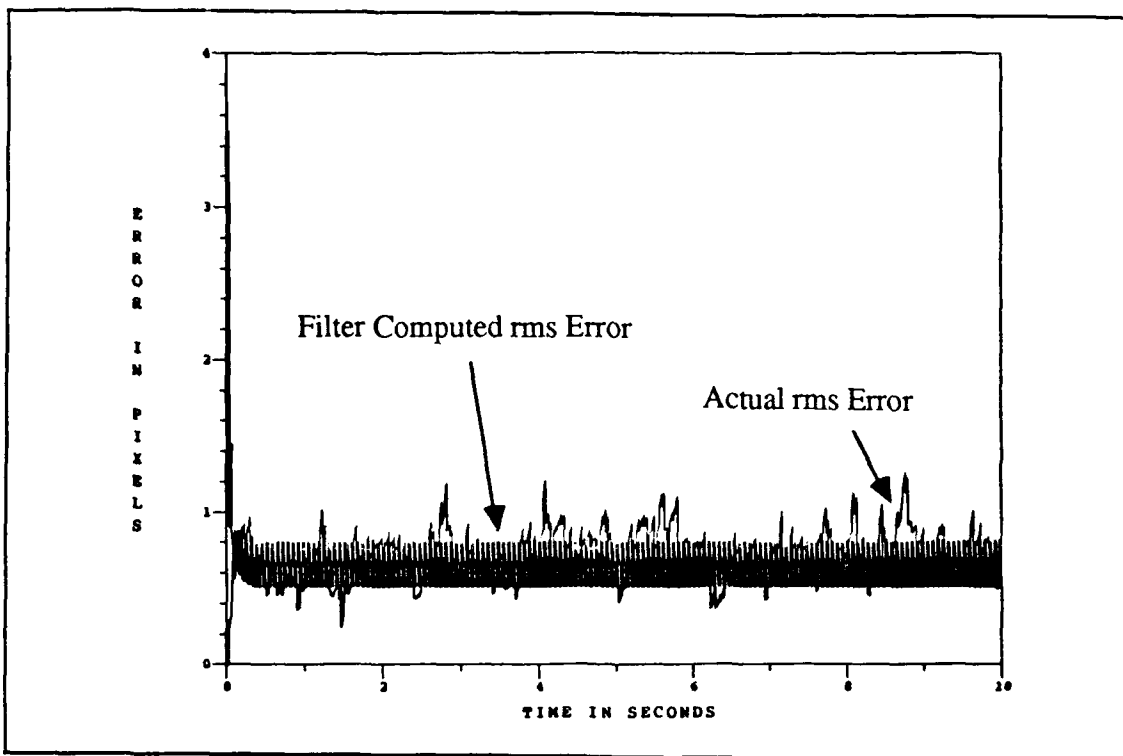


Figure B.1. Example Time History Plot of Filter vs. Actual rms Errors

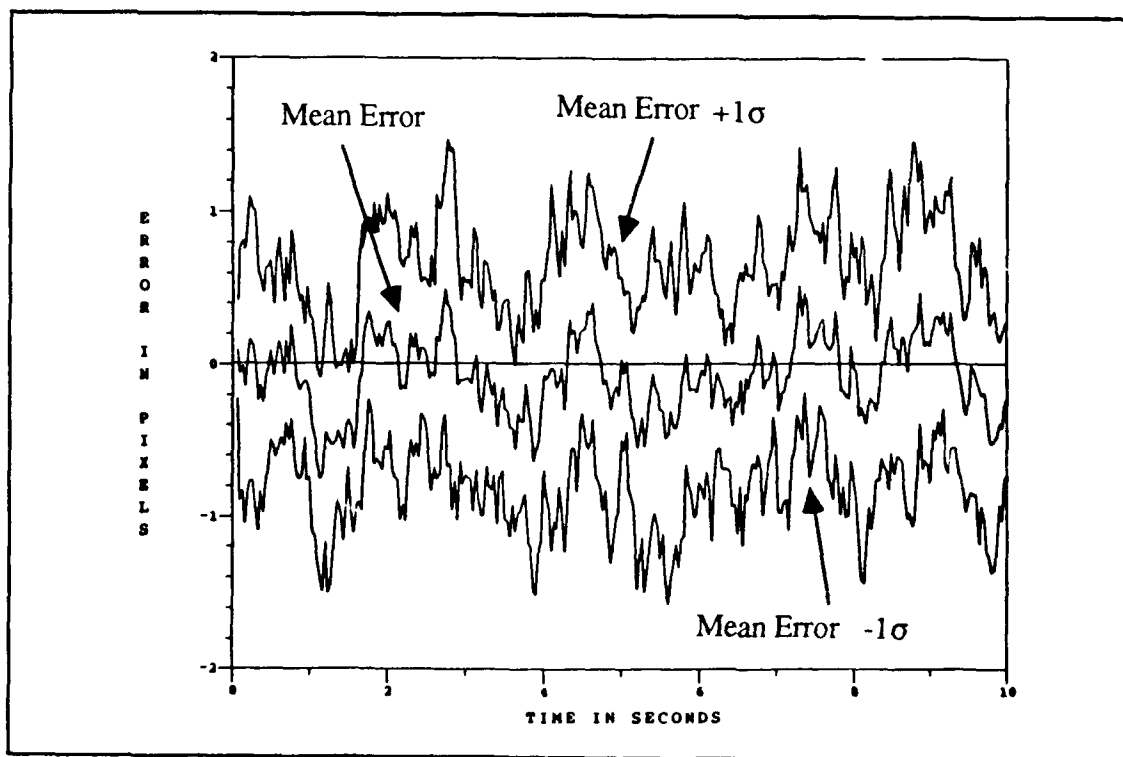


Figure B.2. Example Time History Plot of Filter Error Statistics (Mean  $\pm 1\sigma$ )

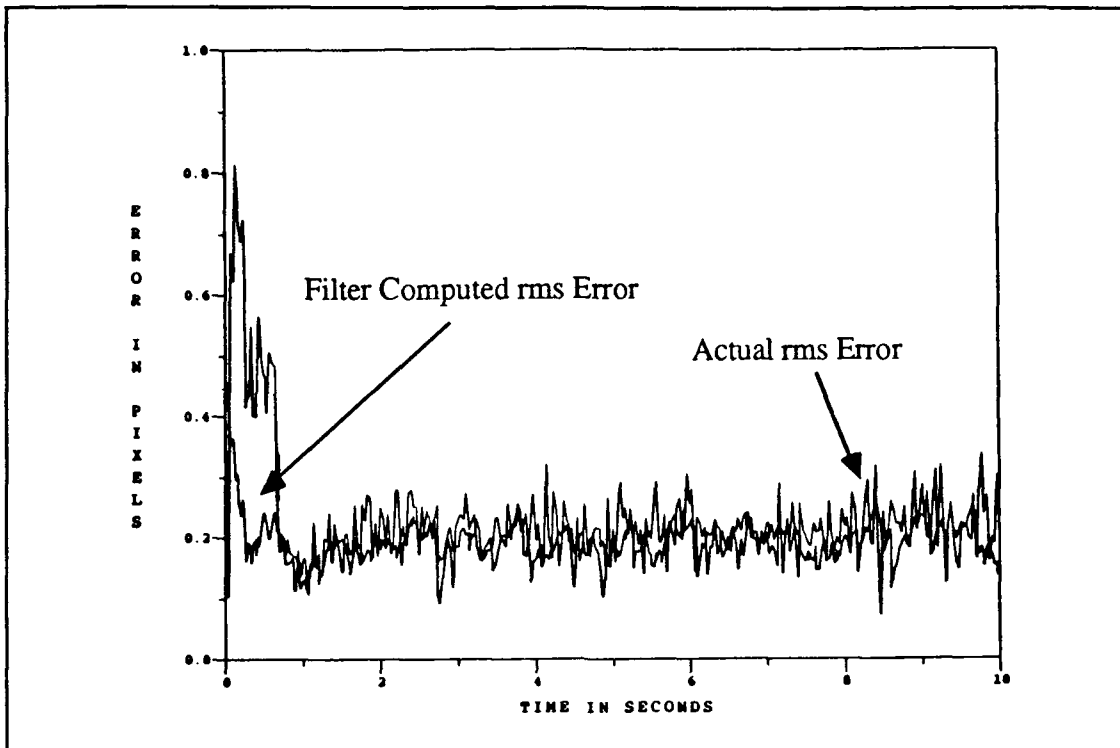


Figure B.3. Example Time History Plot of Filter vs. Actual rms Errors With a Single Scan of Low-Energy Laser (i.e., No Sweep)

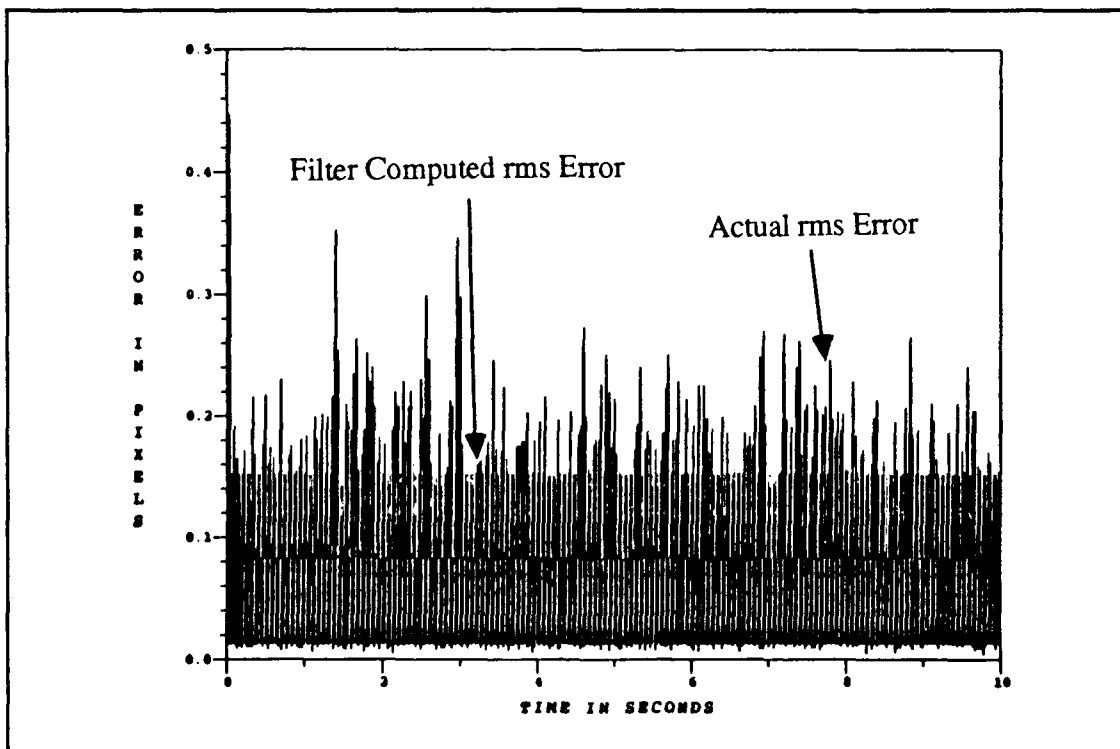


Figure B.4. Example Time History Plot of Filter vs. Actual rms Errors With Low-Energy Laser Sweep



## *Appendix C. Six-State Filter Performance Plots Without Plume Pogo*

This appendix contains the six-state (FLIR) filter error plots for the case of no plume pogo of the intensity centroid. The errors are labeled in the azimuth ( $x$ ) and elevation ( $y$ ) directions in the FLIR image plane. The filter error plots for the modeled atmospheric error are also contained in this appendix. The atmospheric data shown in the plots is the same for all configurations of filter testing considered in this thesis, since the six-state filter tuning and atmospheric parameters remain the same for all testing. For the discussion pertaining to these plots, refer to Chapter VI, Section 6.4.

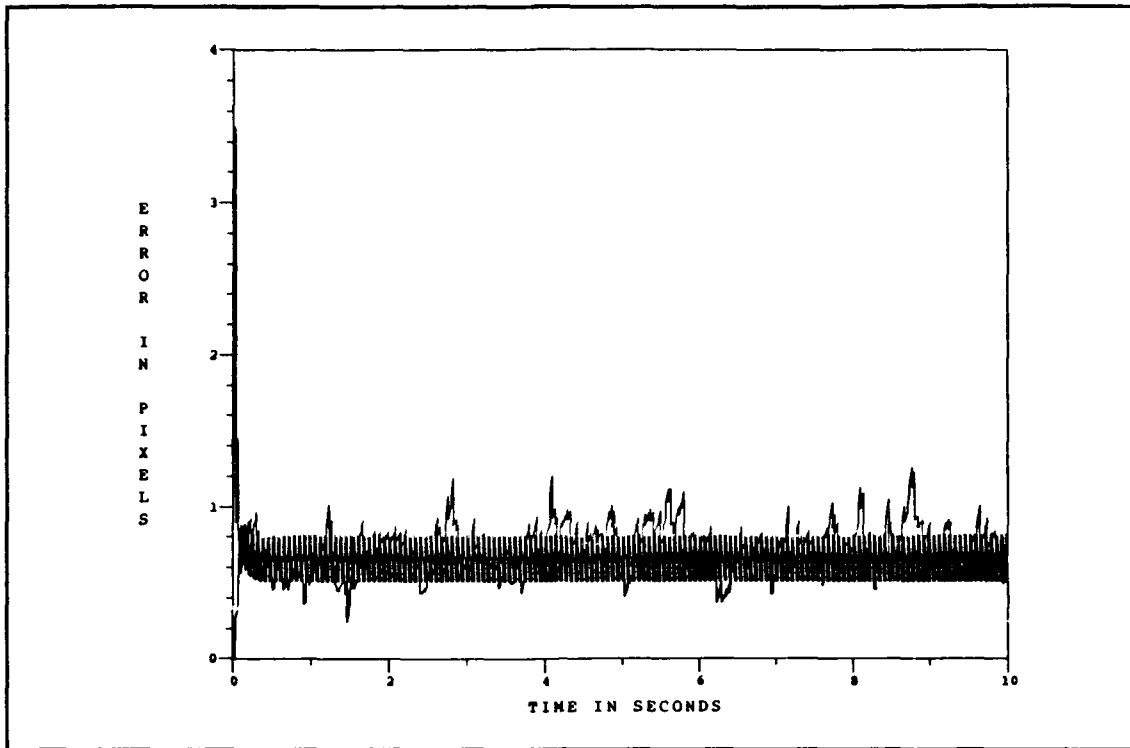


Figure C.1. Six-State Filter vs. Actual rms Target Azimuth Error Without Plume Pogo

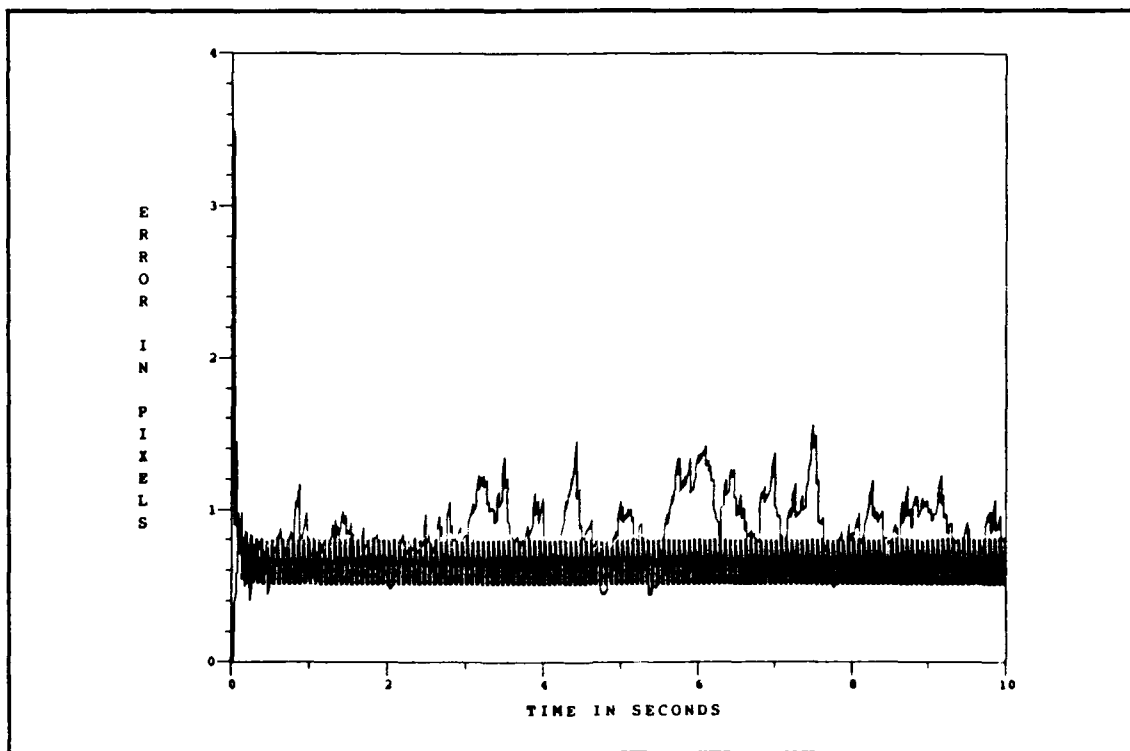


Figure C.2. Six-State Filter vs. Actual rms Target Elevation Error Without Plume Pogo

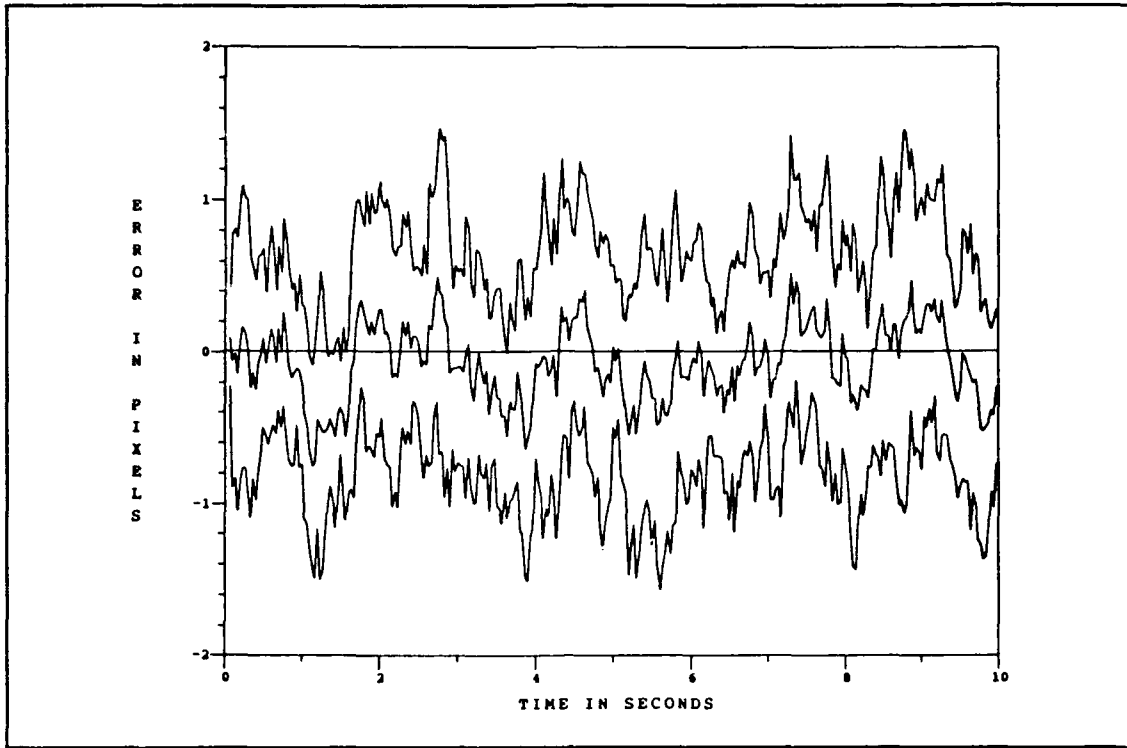


Figure C.3. Six-State Filter Target Azimuth Error at  $t_i$  - Without Plume Pogo

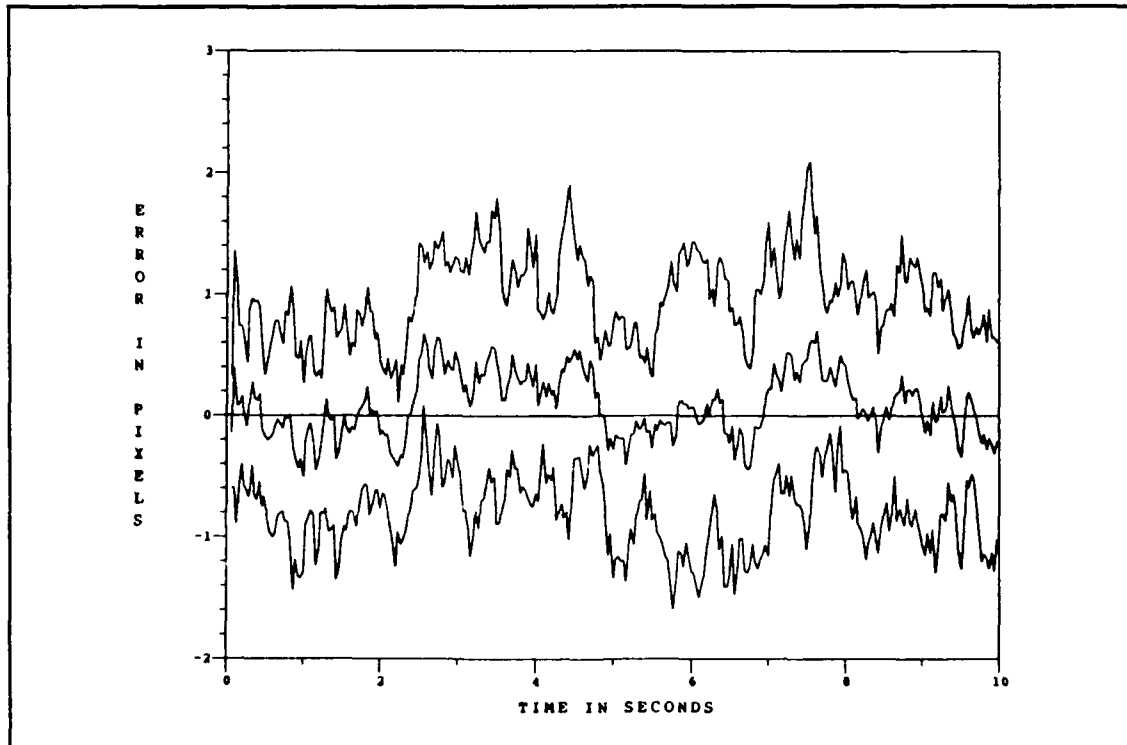


Figure C.4. Six-State Filter Target Elevation Error at  $t_i$  - Without Plume Pogo

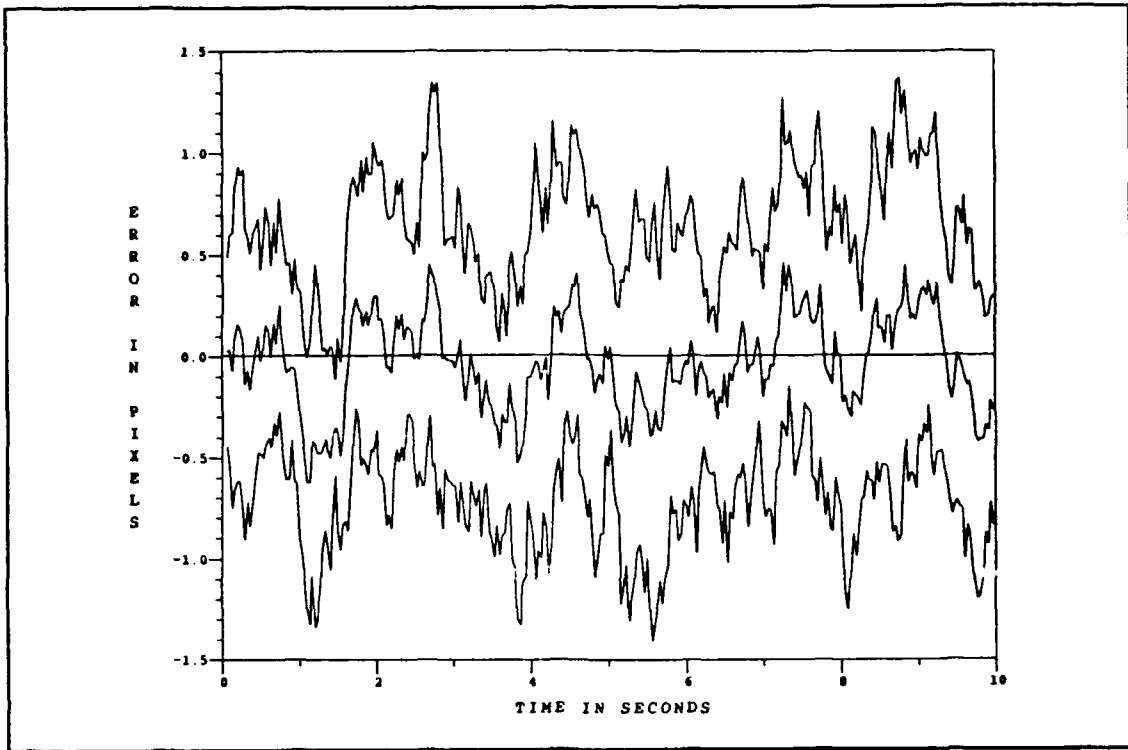


Figure C.5. Six-State Filter Target Azimuth Error at  $t_i +$  Without Plume Pogo

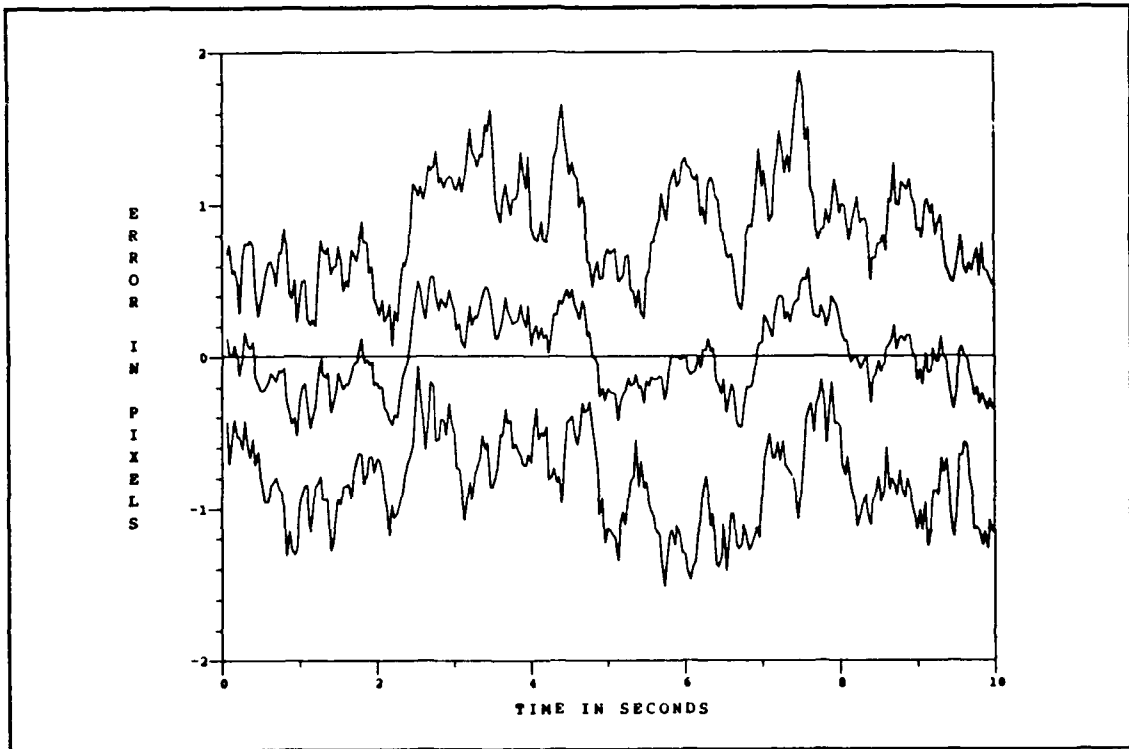


Figure C.6. Six-State Filter Target Elevation Error at  $t_i +$  Without Plume Pogo

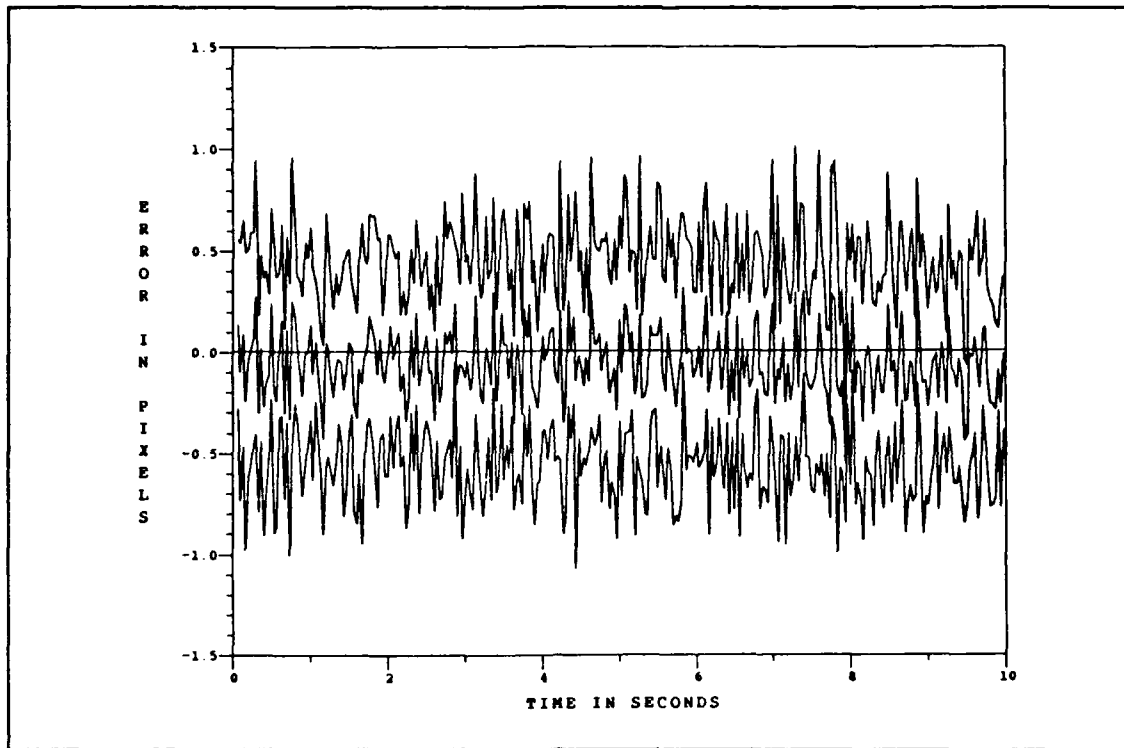


Figure C.7. Six-State Filter Centroid Azimuth Error at  $t_i$  - Without Plume Pogo

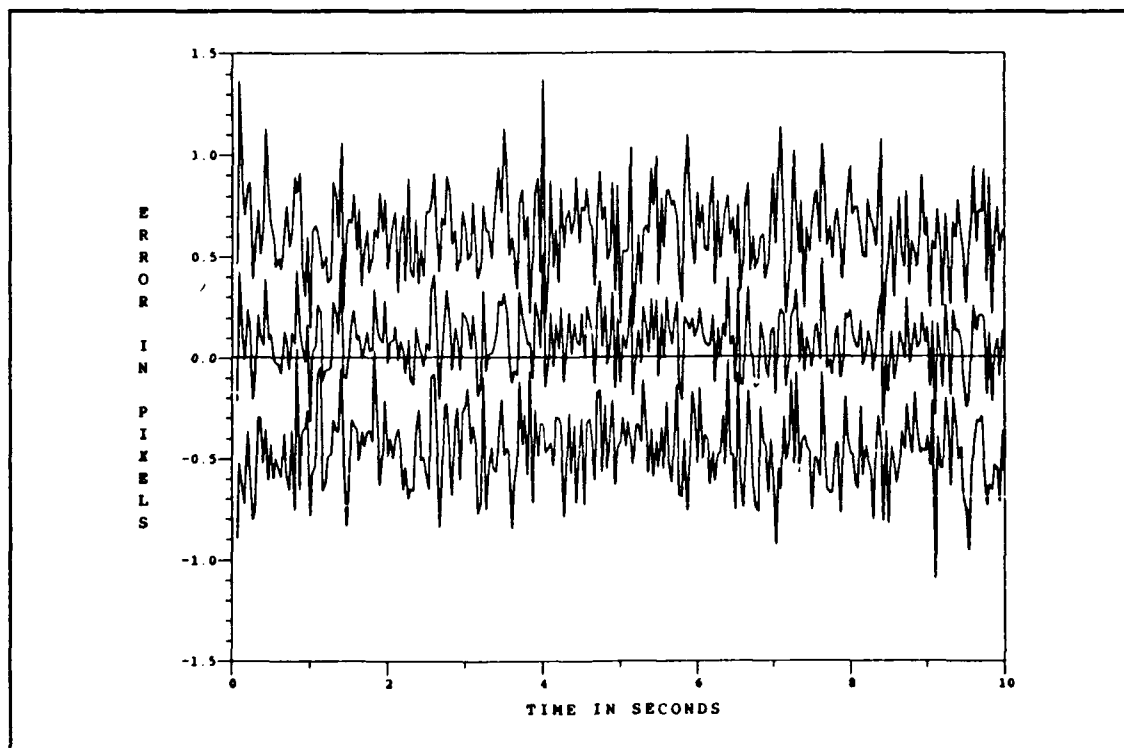


Figure C.8. Six-State Filter Centroid Elevation Error at  $t_i$  - Without Plume Pogo

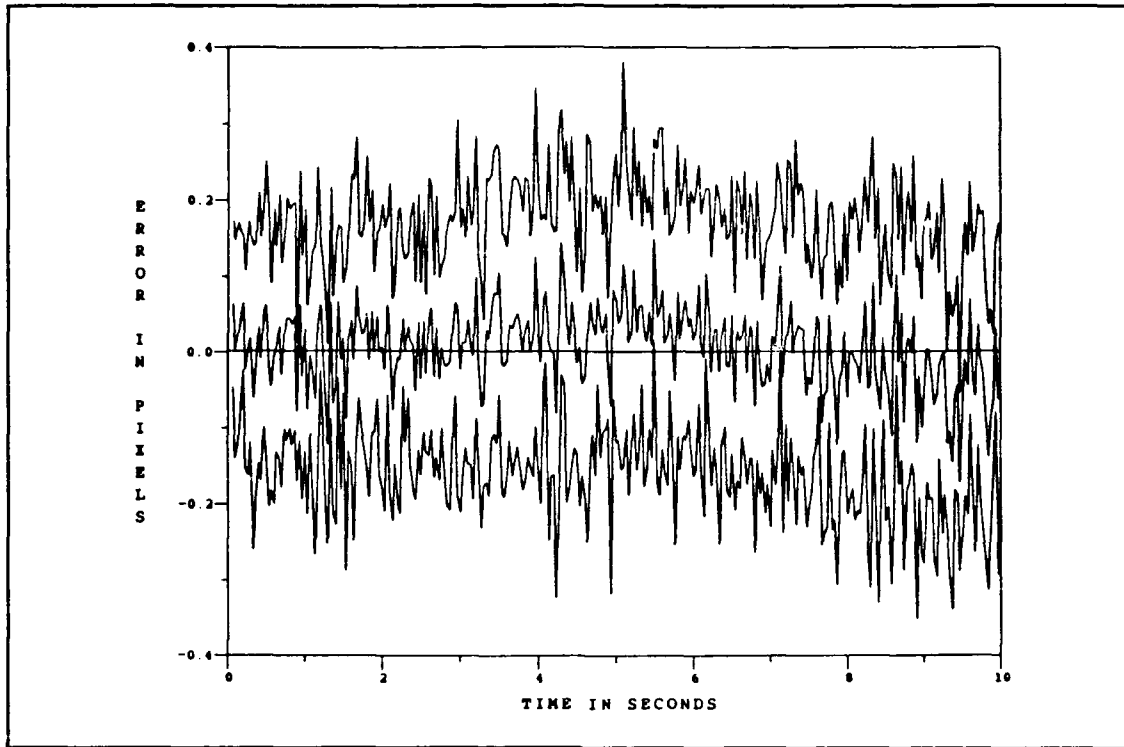


Figure C.9. Six-State Filter Centroid Azimuth Error at  $t_i +$  Without Plume Pogo

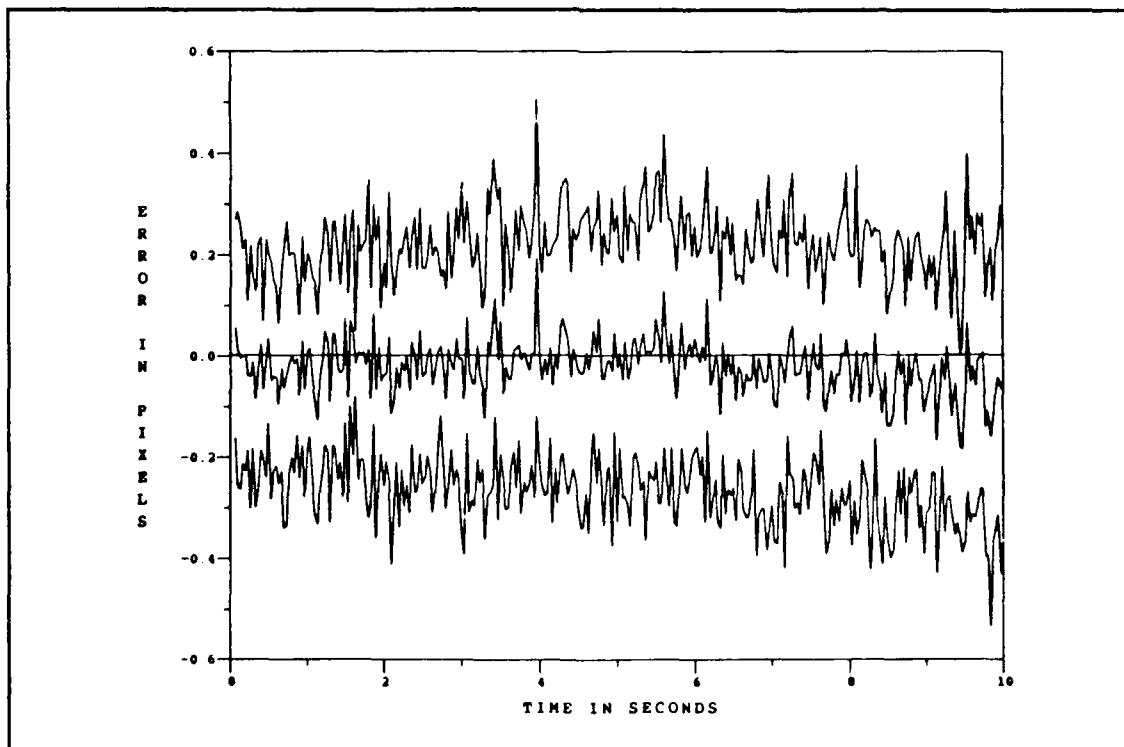


Figure C.10. Six-State Filter Centroid Elevation Error at  $t_i +$  Without Plume Pogo

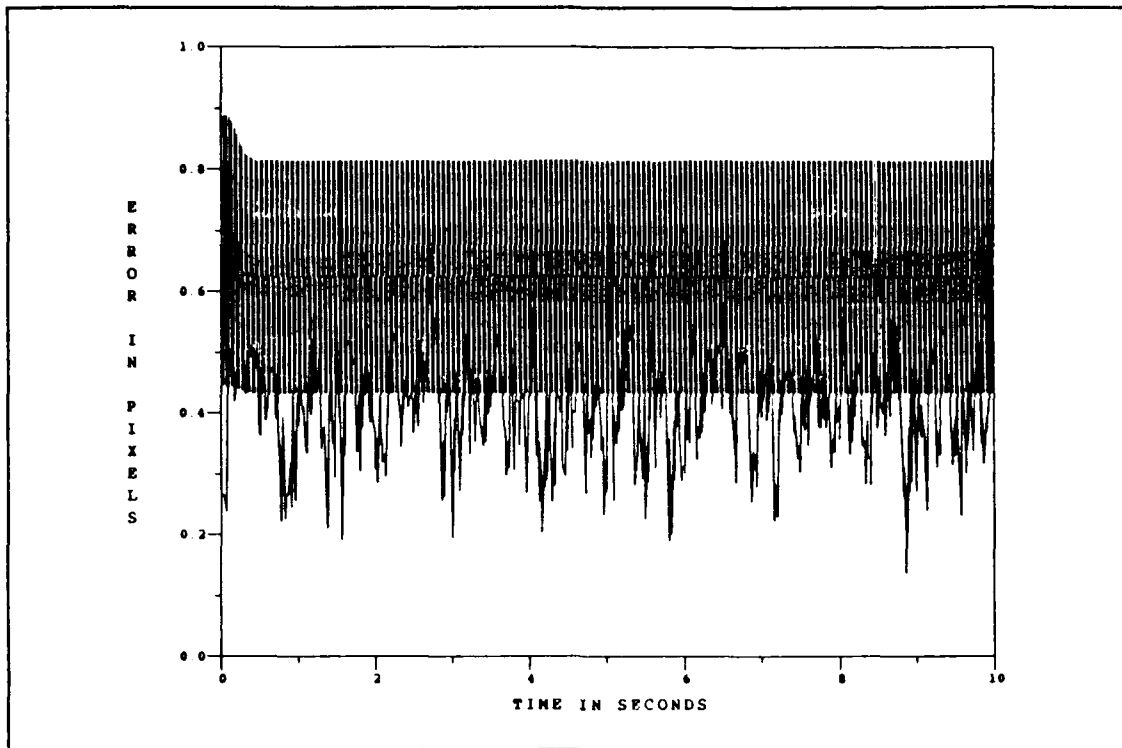


Figure C.11. Six-State Filter vs. Actual rms Atmospheric Azimuth Error

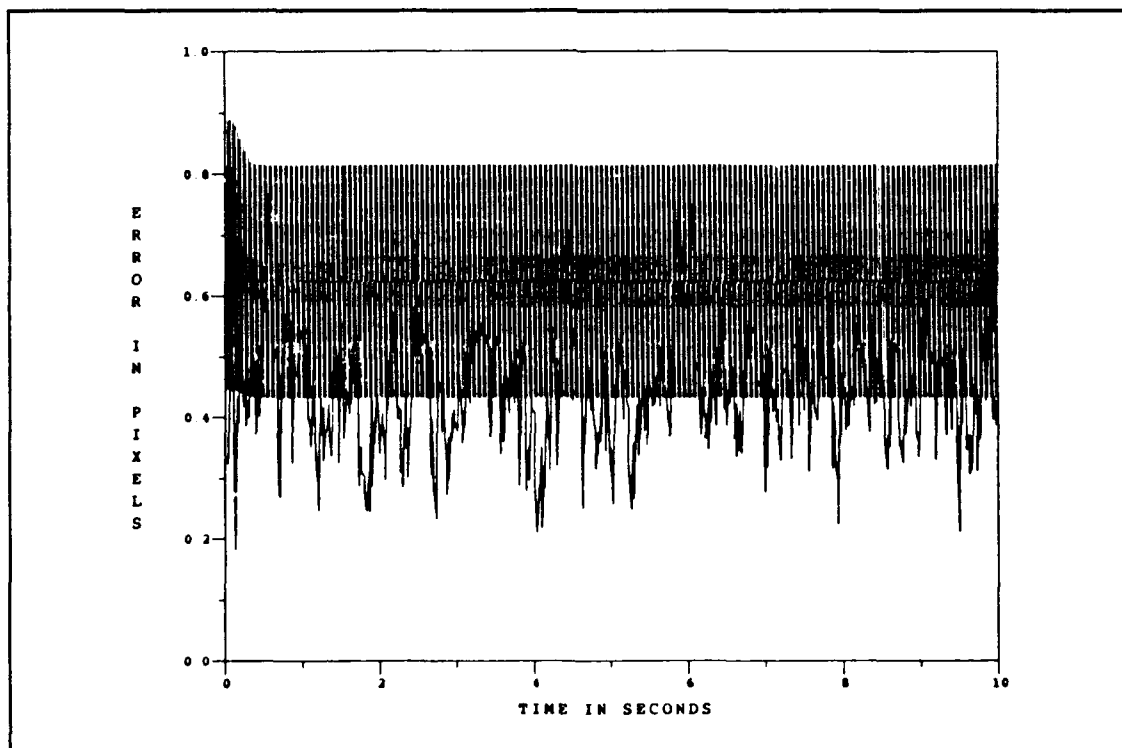


Figure C.12. Six-State Filter vs. Actual rms Atmospheric Elevation Error

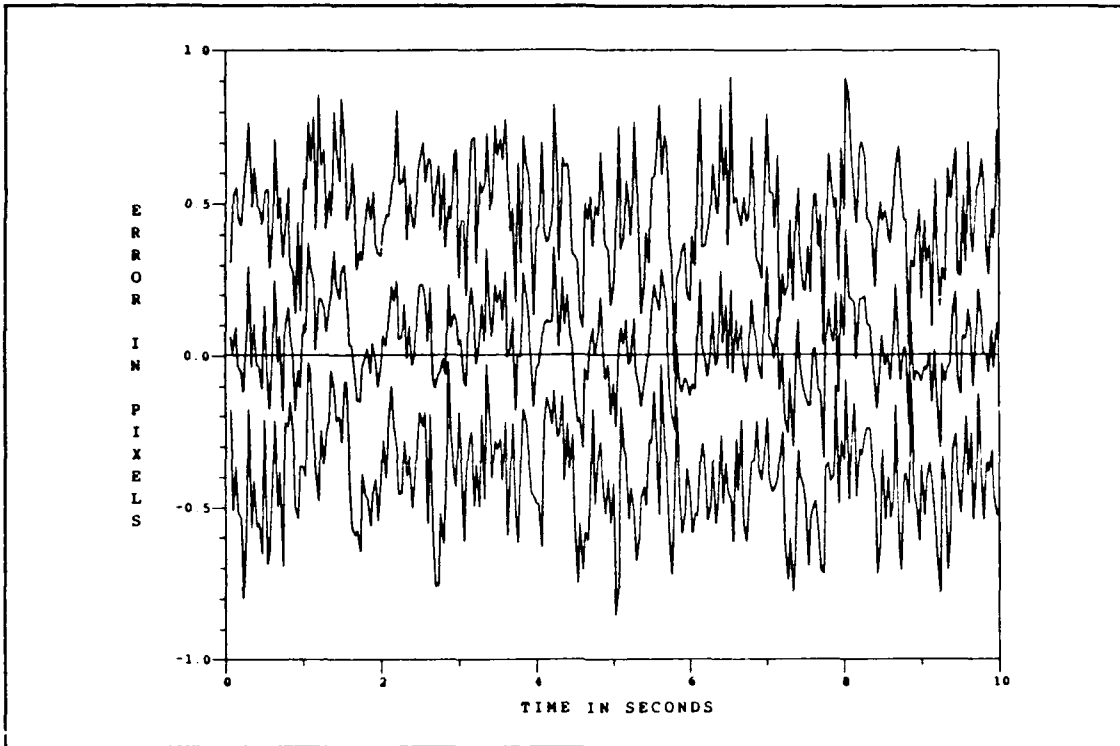


Figure C.13. Six-State Filter Atmospheric Azimuth Error at  $t_i$

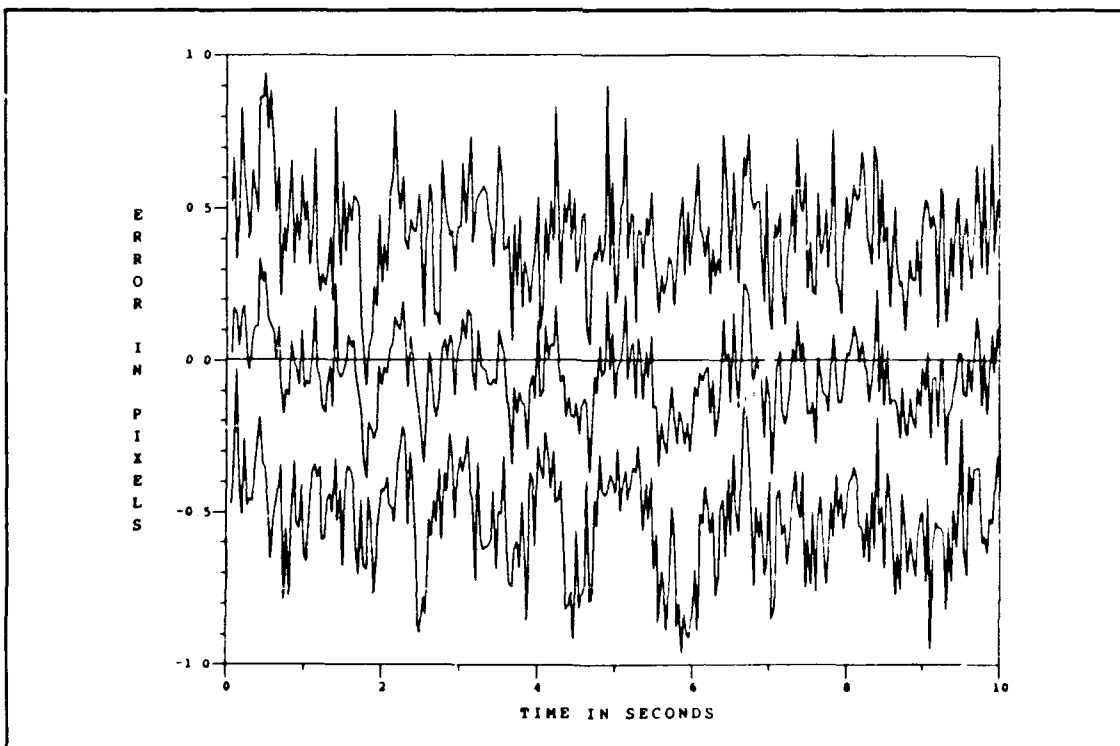


Figure C.14. Six-State Filter Atmospheric Elevation Error at  $t_i$



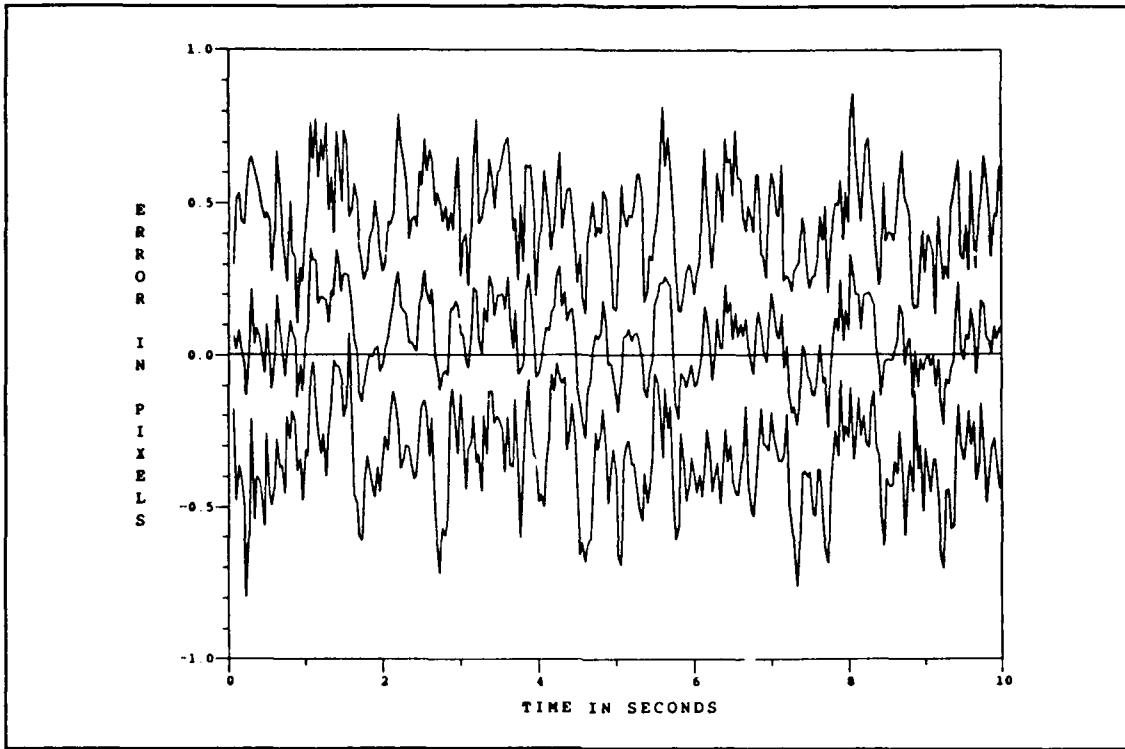


Figure C.15. Six-State Filter Atmospheric Azimuth Error at  $t_i^+$

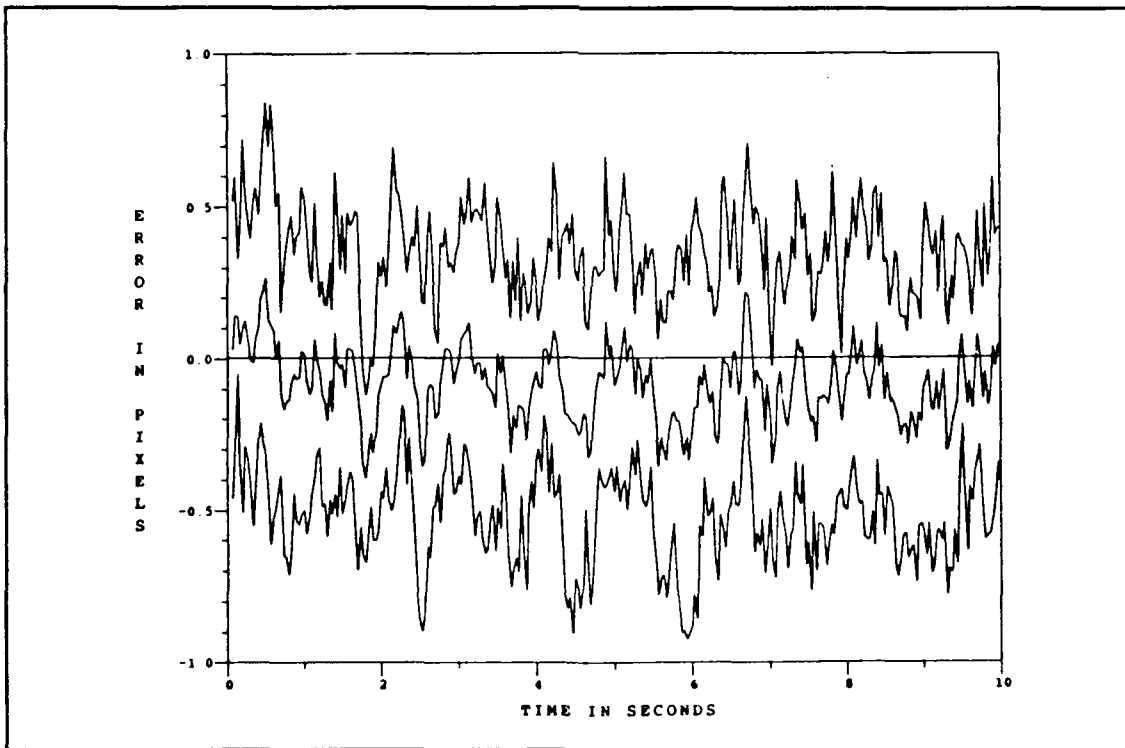


Figure C.16. Six-State Filter Atmospheric Elevation Error at  $t_i^+$

## *Appendix D. Six-State Filter Performance Plots With Plume Pogo*

This appendix contains the six-state (FLIR) filter error plots for the case of including plume pogo of the intensity centroid. The errors are labeled in the azimuth ( $x$ ) and elevation ( $y$ ) directions in the FLIR image plane. The atmospheric data plots are not presented in this appendix, since the plots shown in Appendix C are the same for all configurations of filter testing considered in this thesis; the six-state filter parameters and atmospheric parameters remain the same for all testing. For the discussion pertaining to these plots, refer to Chapter VI, Section 6.4.

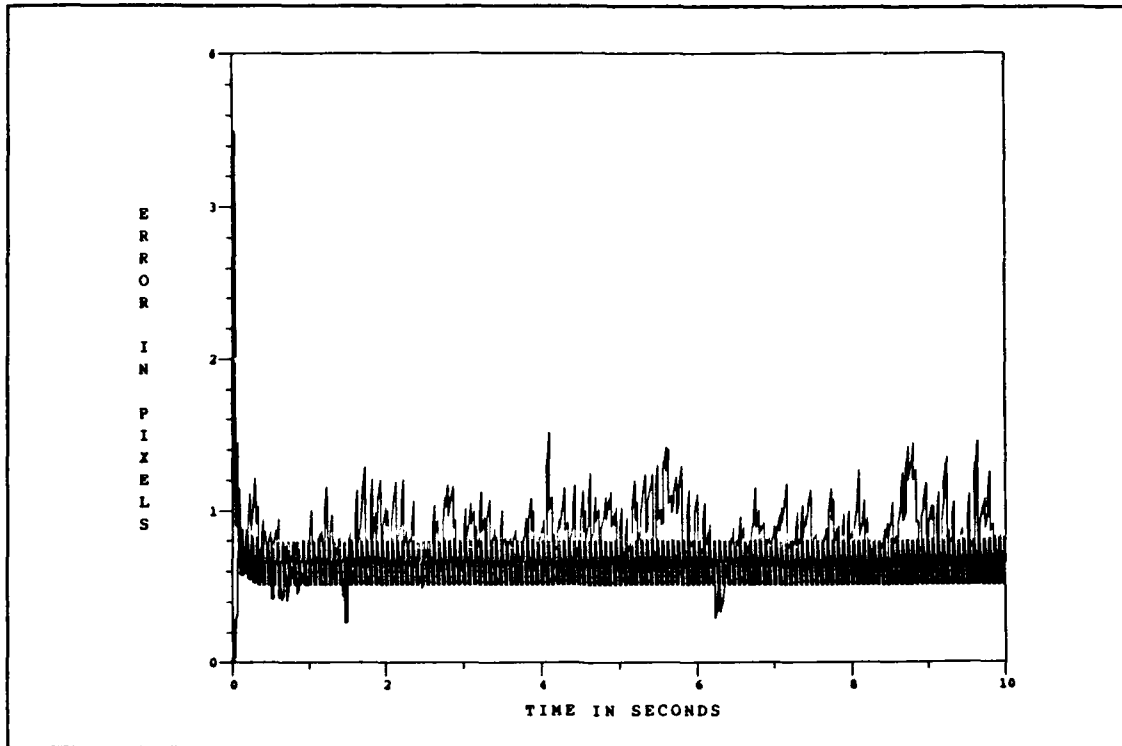


Figure D.1. Six-State Filter vs. Actual rms Target Azimuth Error With Plume Pogo

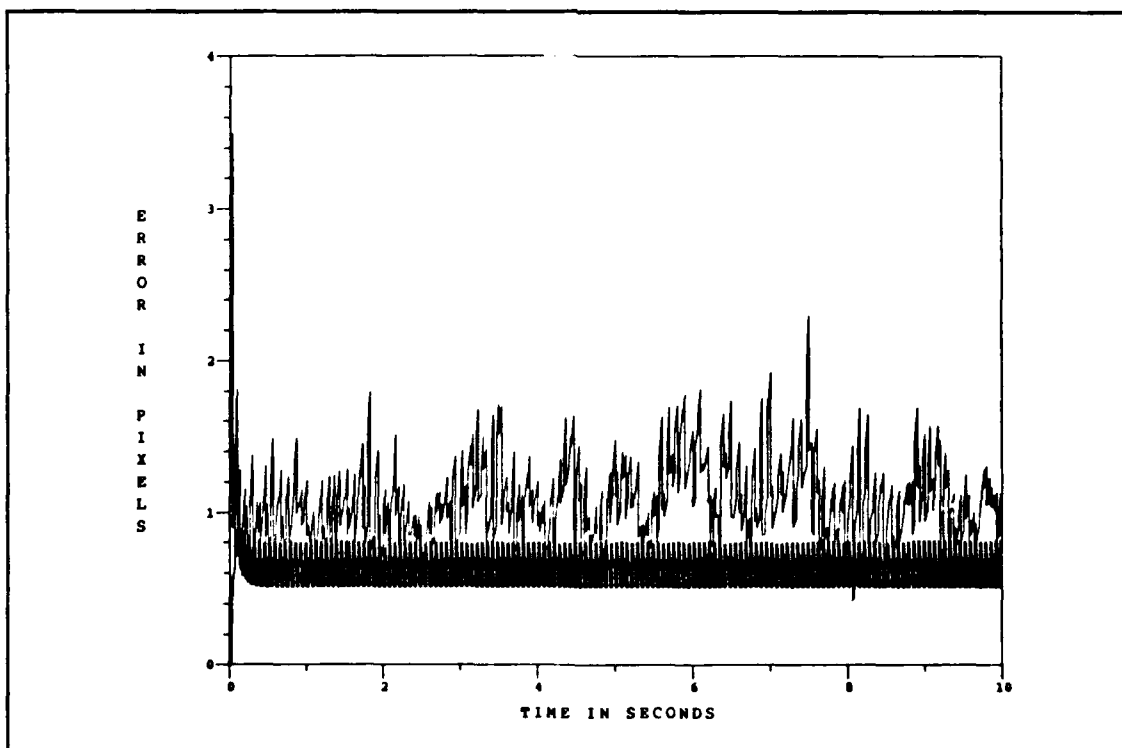


Figure D.2. Six-State Filter vs. Actual rms Target Elevation Error With Plume Pogo

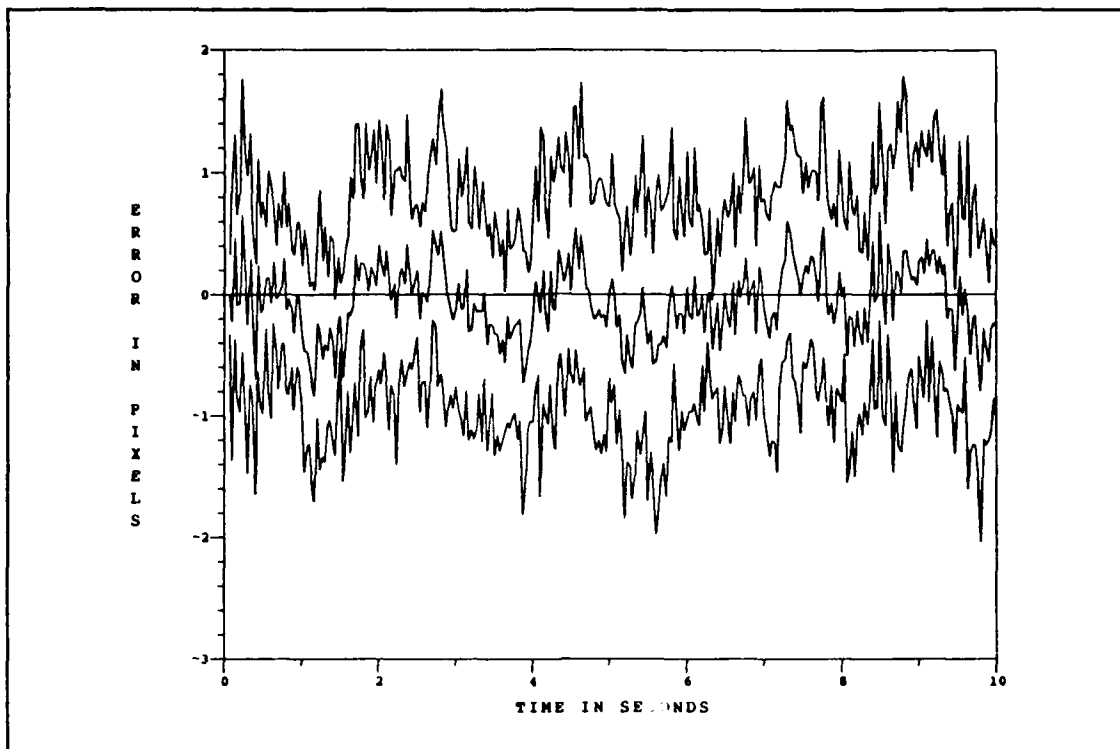


Figure D.3. Six-State Filter Target Azimuth Error at  $t_i^-$  With Plume Pogo

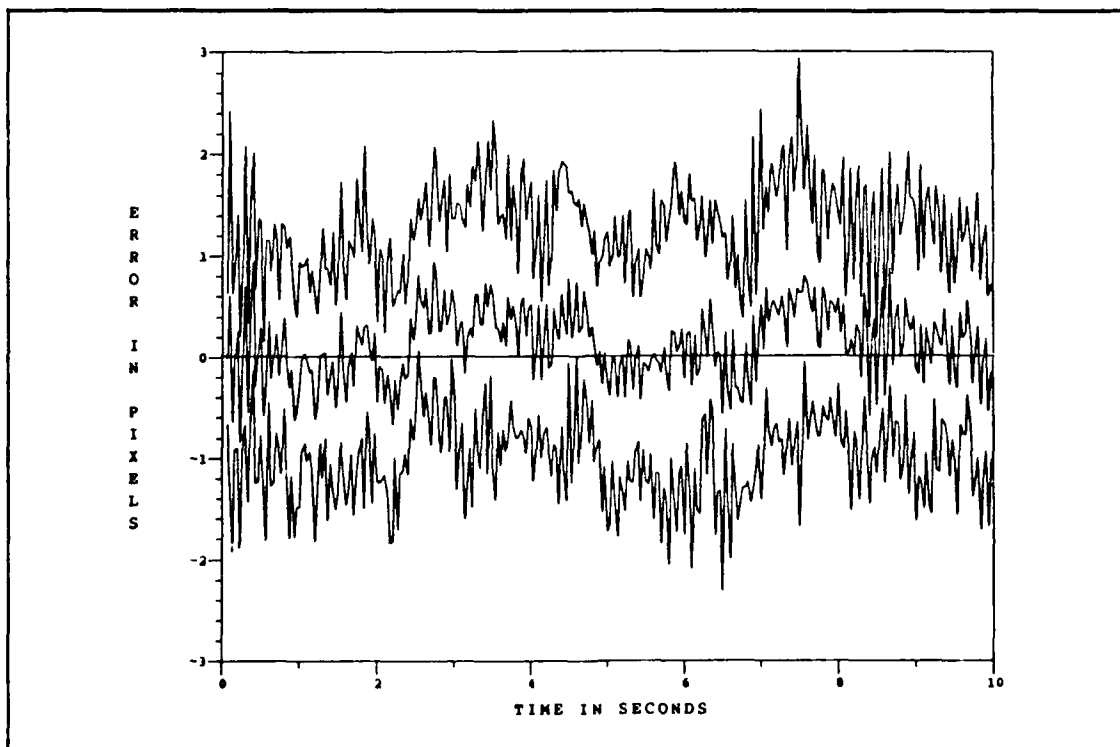


Figure D.4. Six-State Filter Target Elevation Error at  $t_i^-$  With Plume Pogo

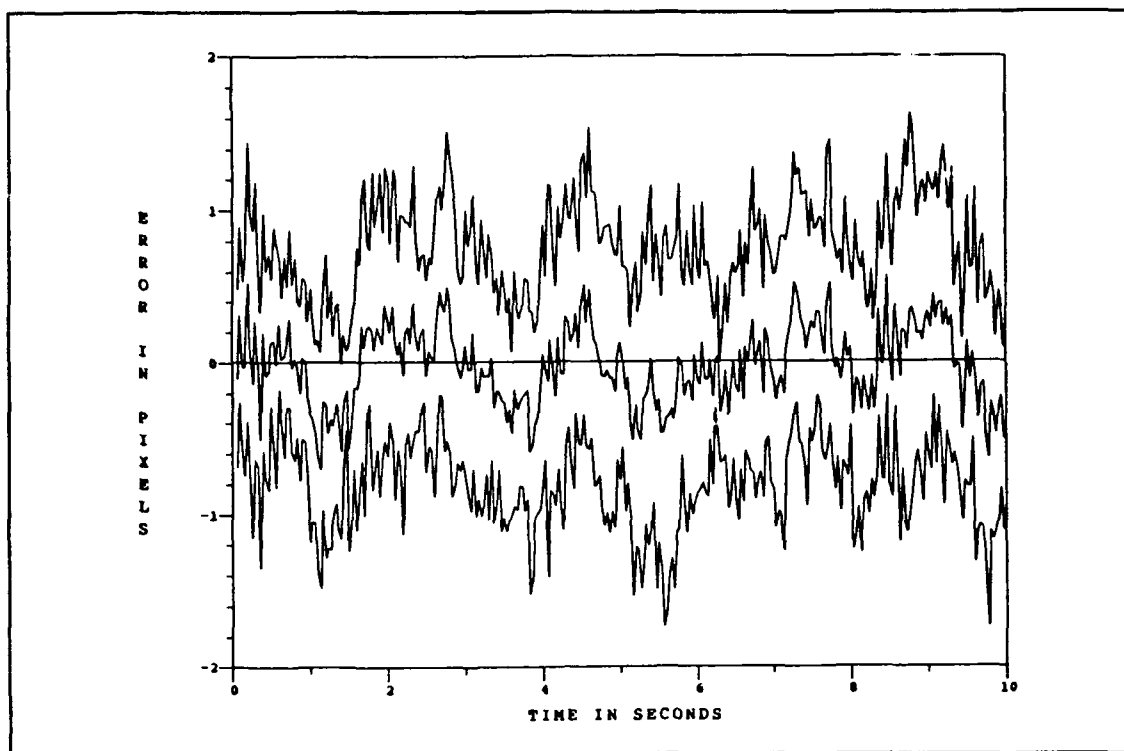


Figure D.5. Six-State Filter Target Azimuth Error at  $t_i +$  With Plume Pogo

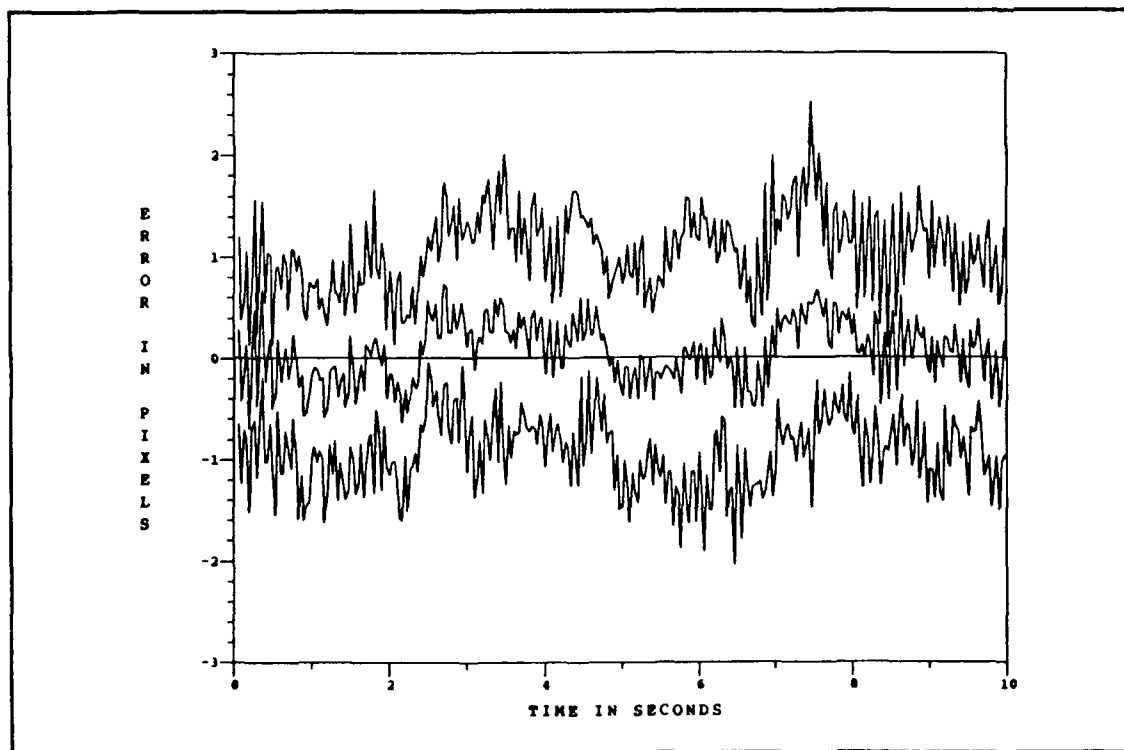


Figure D.6. Six-State Filter Target Elevation Error at  $t_i +$  With Plume Pogo

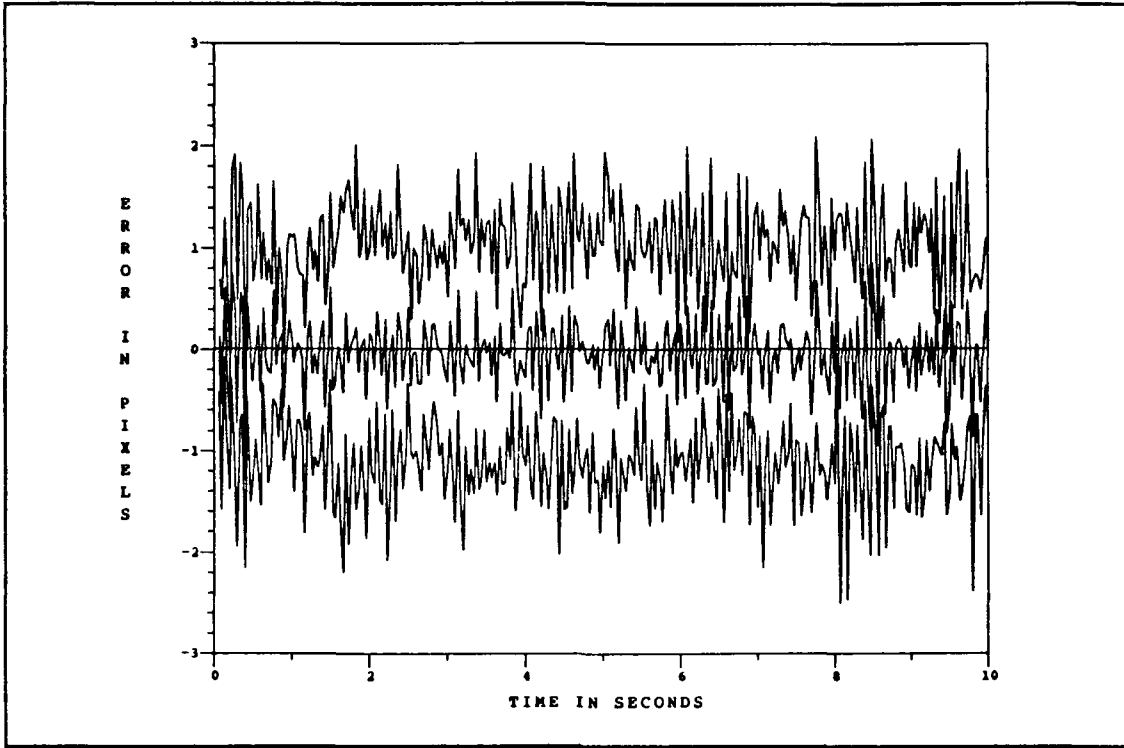


Figure D.7. Six-State Filter Centroid Azimuth Error at  $t_i^-$  With Plume Pogo

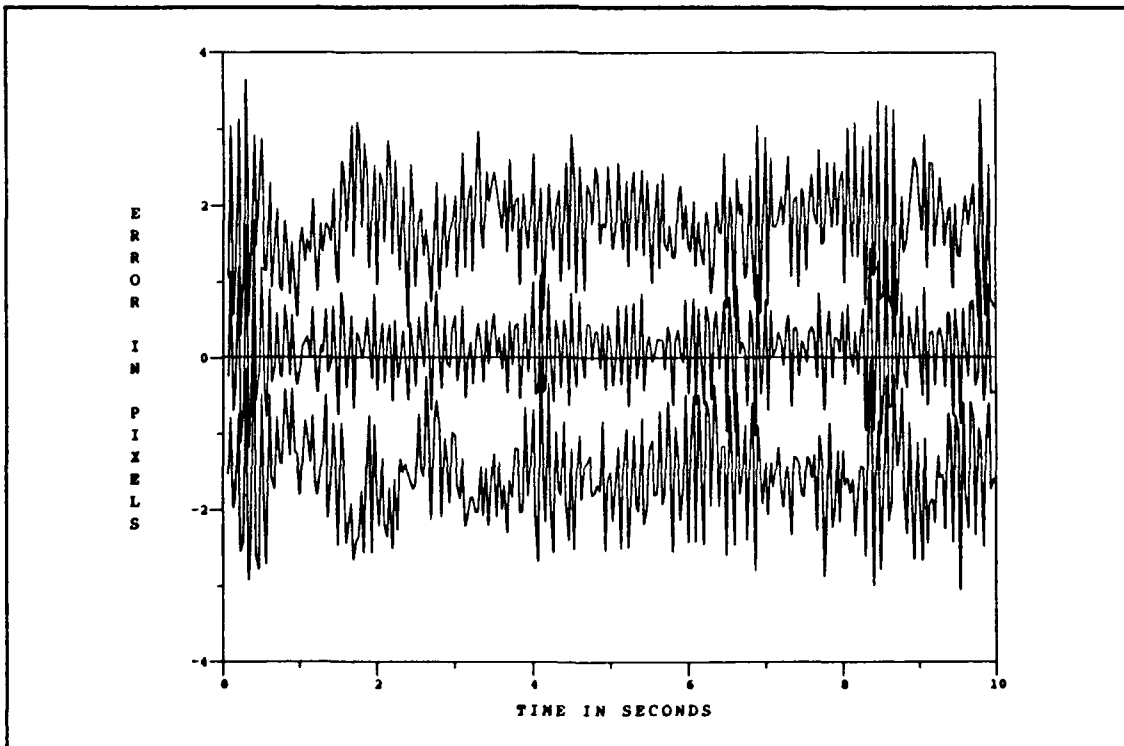


Figure D.8. Six-State Filter Centroid Elevation Error at  $t_i^-$  With Plume Pogo

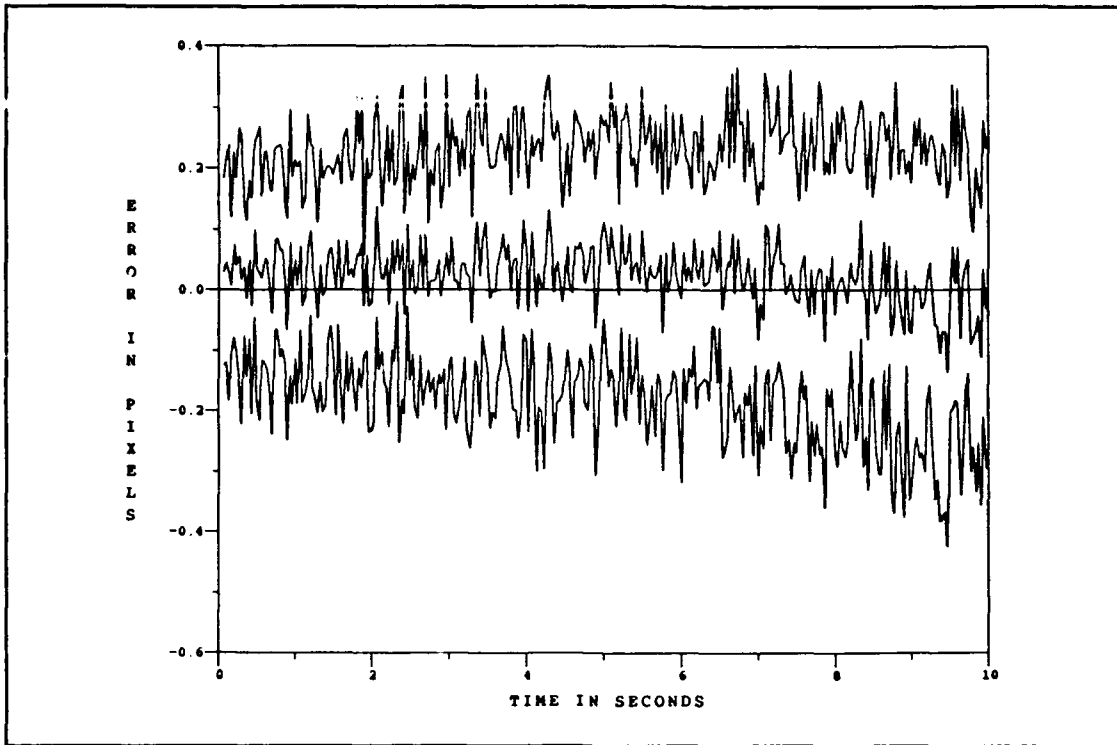


Figure D.9. Six-State Filter Centroid Azimuth Error at  $t_i +$  With Plume Pogo

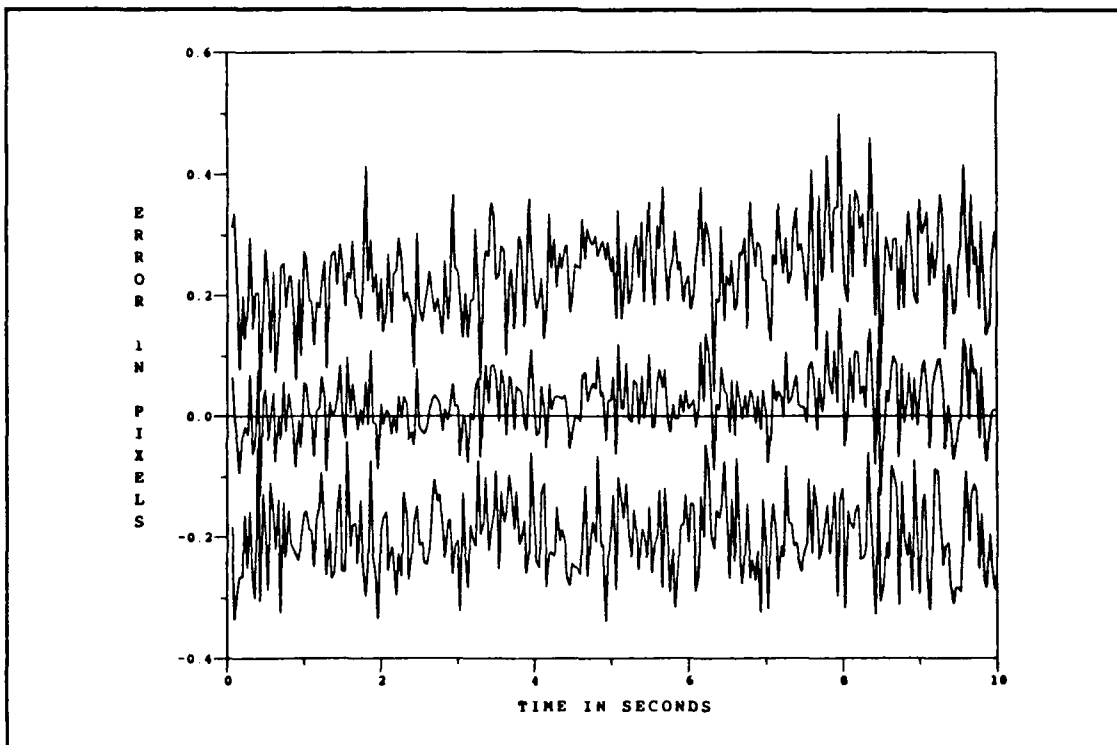


Figure D.10. Six-State Filter Centroid Elevation Error at  $t_i +$  With Plume Pogo

## *Appendix E. One-State Filter Performance Plots Without Low-Energy Laser Sweep and Plume Pogo*

This appendix contains the one-state (center-of-mass) filter error plots for the case of no low-energy laser sweep and with no plume pogo of the intensity centroid. The center-of-mass errors are presented as a magnitude between the true center-of-mass and the filter estimated center-of-mass, the azimuth ( $x$ ) and elevation ( $y$ ) components of the magnitude error, and the along-track and across-track components of the magnitude error. The hardbody binary model is used for the single scan of the low-energy laser (i.e., no sweep), since the hardbody reflectivity model is software configured for a sweep routine; (The hardbody reflectivity model is used for the low-energy laser sweep plots, which are also representative of the hardbody binary plots.) For the discussion pertaining to these plots, refer to Chapter VI, Sections 6.5 and 6.7.



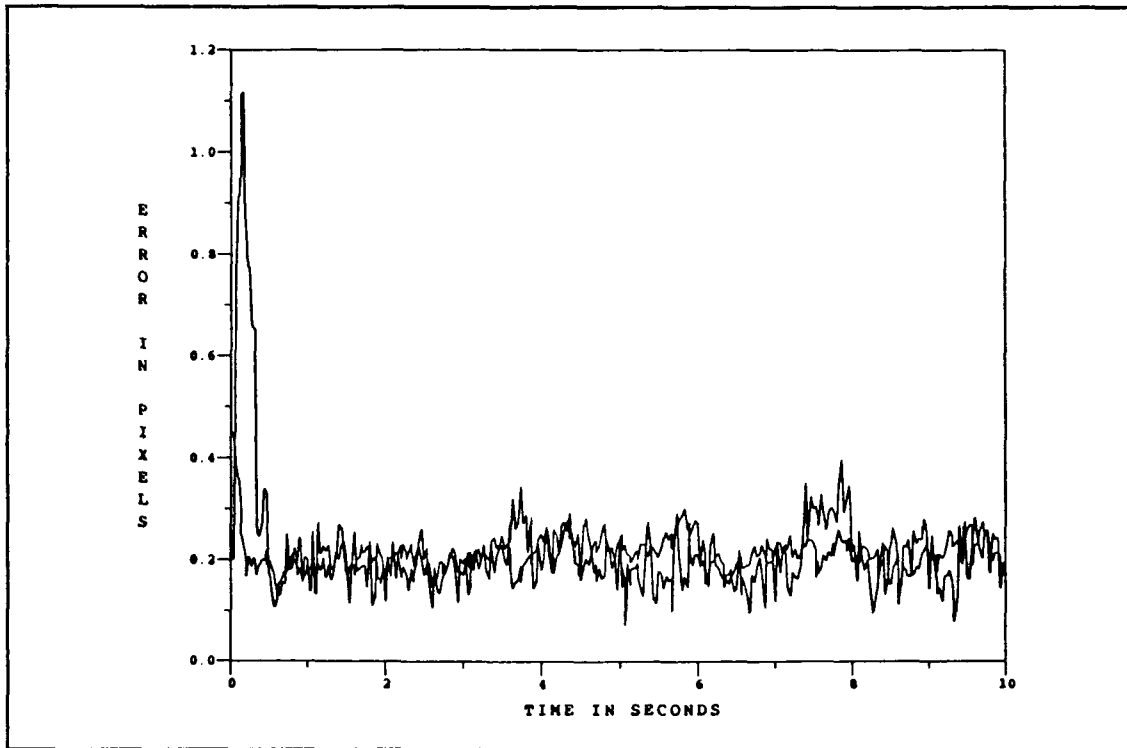


Figure E.1. One-State Filter vs. Actual rms Center-of-Mass Magnitude Error for Binary Model Without Low-Energy Laser Sweep and Plume Pogo

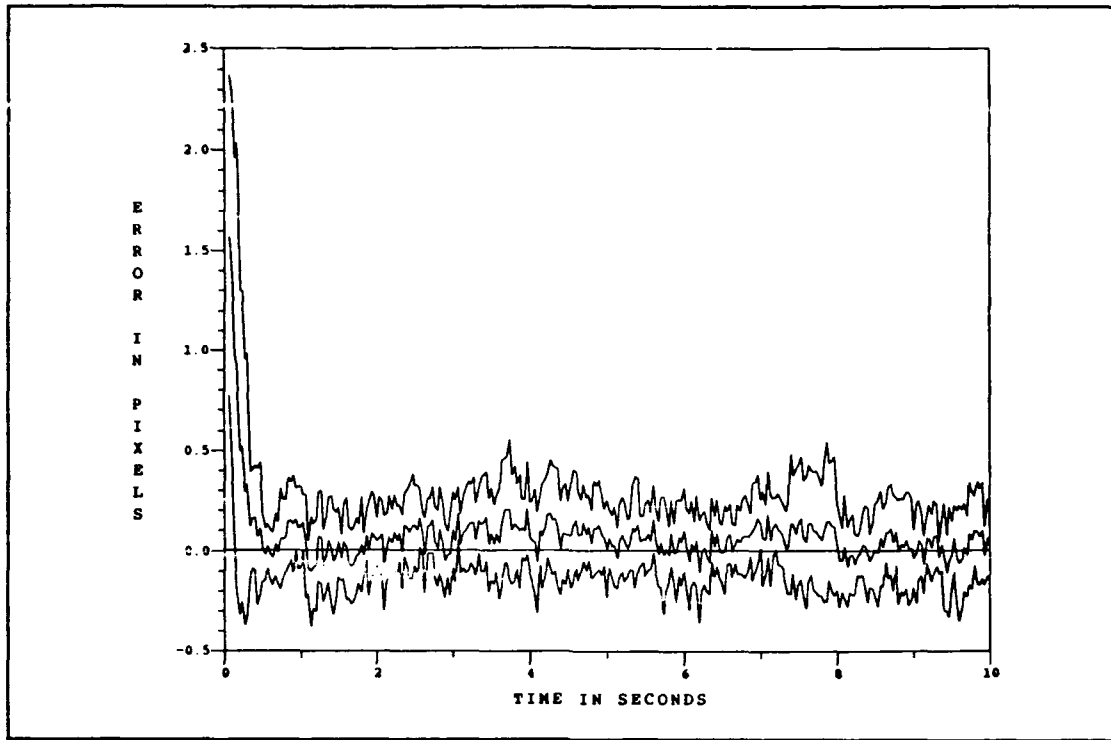


Figure E.2. One-State Filter Center-of-Mass Magnitude Error at  $t_i^-$  for Binary Model Without Low-Energy Laser Sweep and Plume Pogo

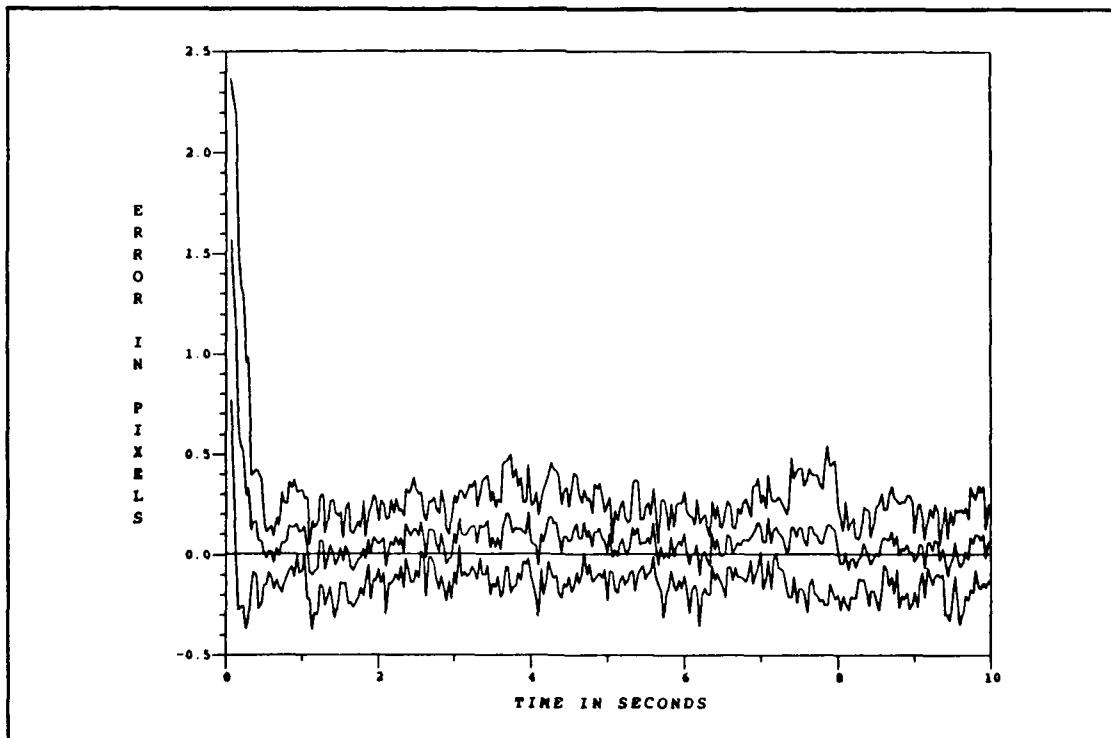


Figure E.3. One-State Filter Center-of-Mass Magnitude Error at  $t_i^+$  for Binary Model Without Low-Energy Laser Sweep and Plume Pogo

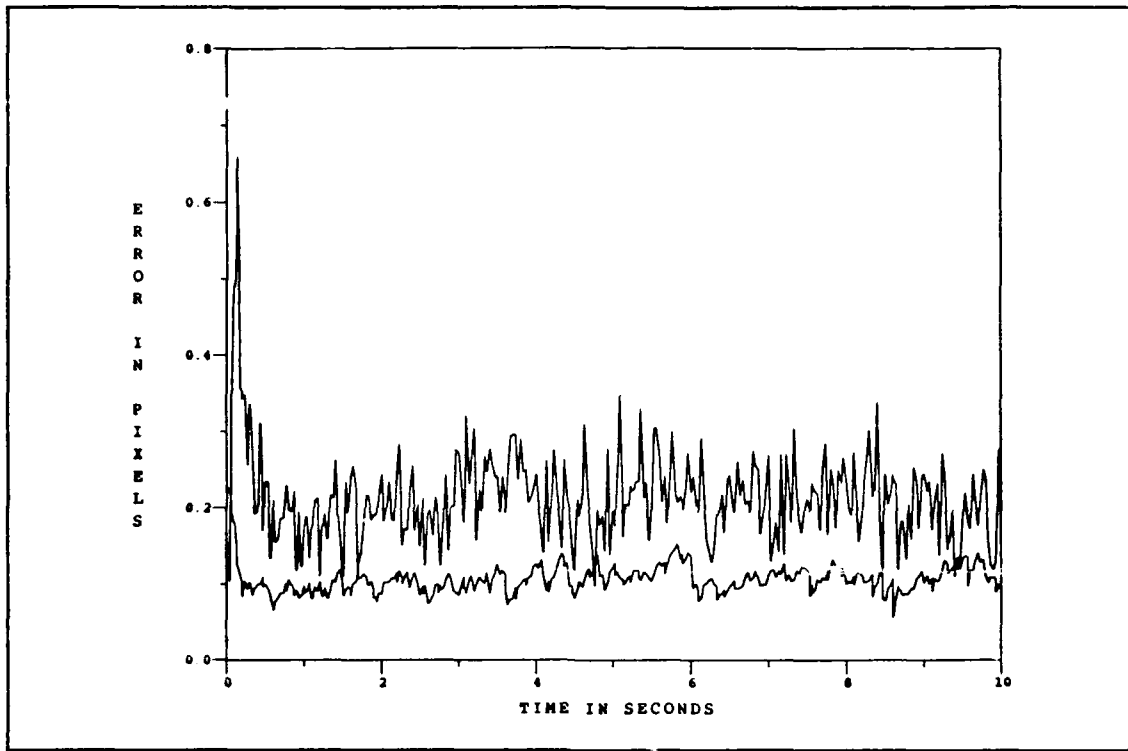


Figure E.4. One-State Filter vs. Actual rms Center-of-Mass Azimuth Error for Binary Model Without Low-Energy Laser Sweep and Plume Pogo

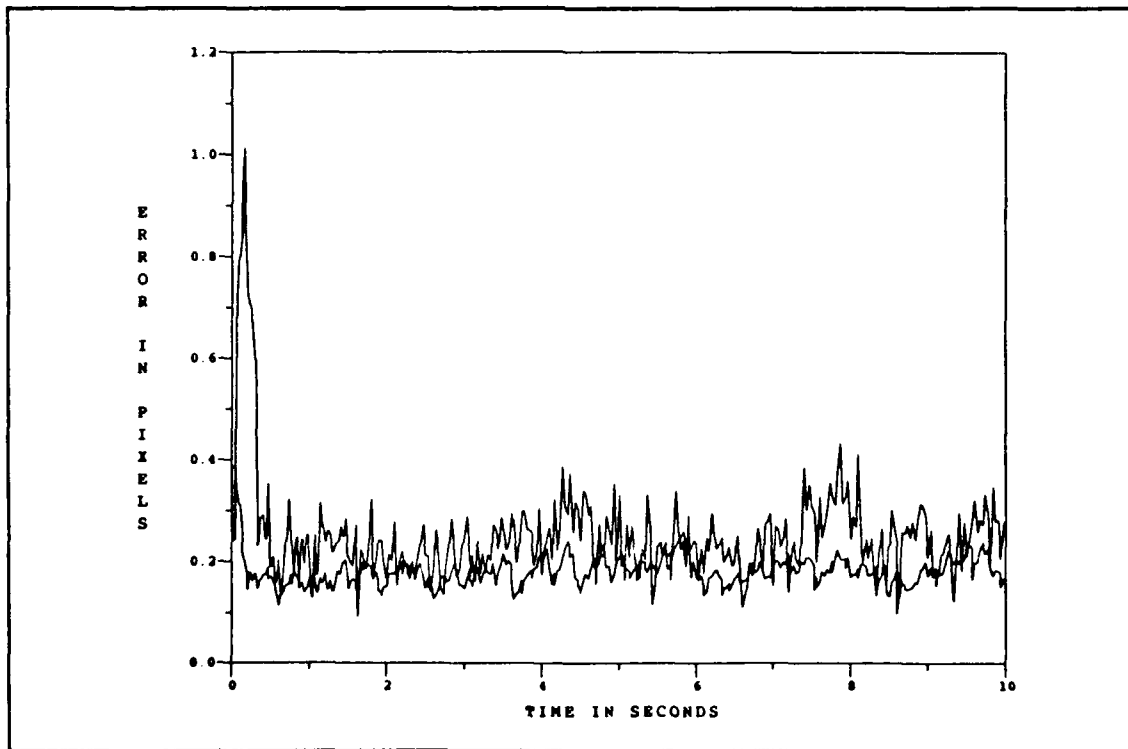


Figure E.5. One-State Filter vs. Actual rms Center-of-Mass Elevation Error for Binary Model Without Low-Energy Laser Sweep and Plume Pogo

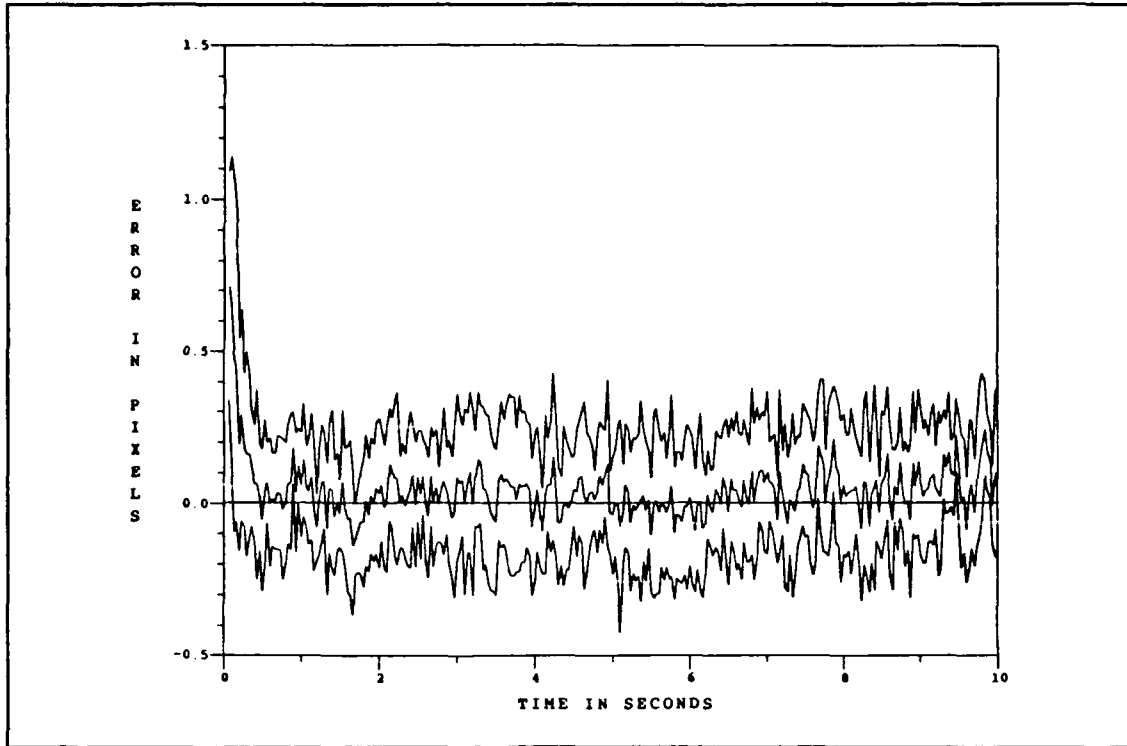


Figure E.6. One-State Filter Center-of-Mass Azimuth Error at  $t_i^-$  for Binary Model Without Low-Energy Laser Sweep and Plume Pogo

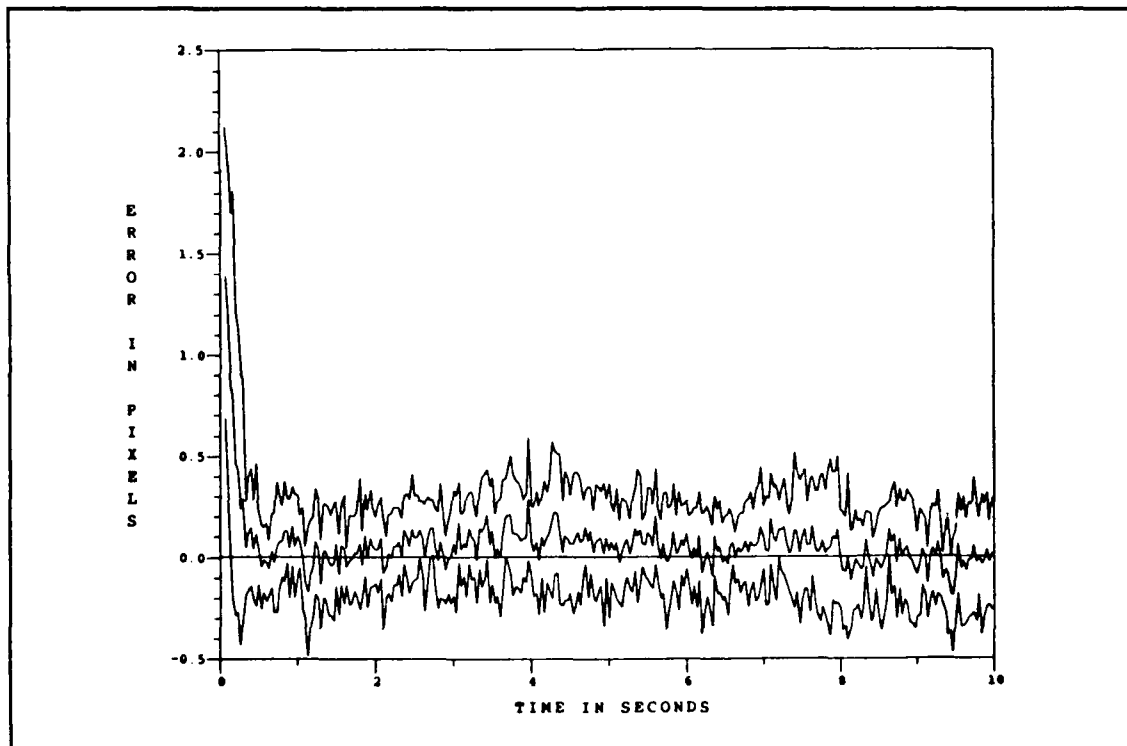


Figure E.7. One-State Filter Center-of-Mass Elevation Error at  $t_i^-$  for Binary Model Without Low-Energy Laser Sweep and Plume Pogo

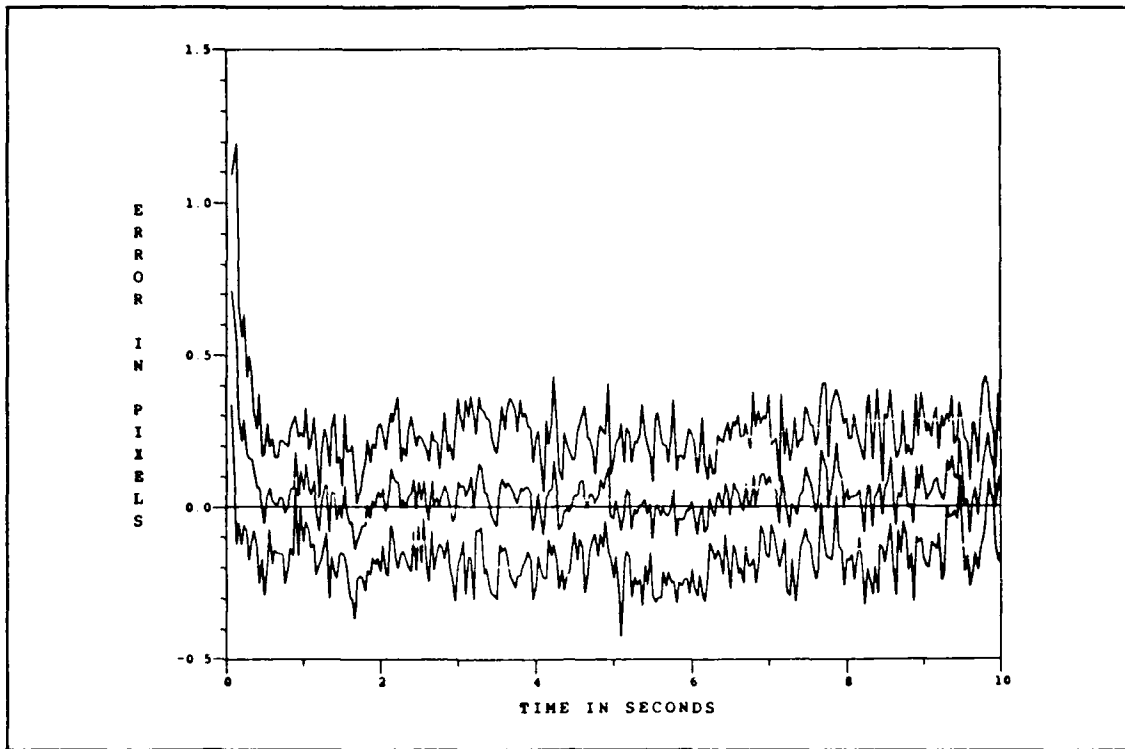


Figure E.8. One-State Filter Center-of-Mass Azimuth Error at  $t_i^+$  for Binary Model Without Low-Energy Laser Sweep and Plume Pogo

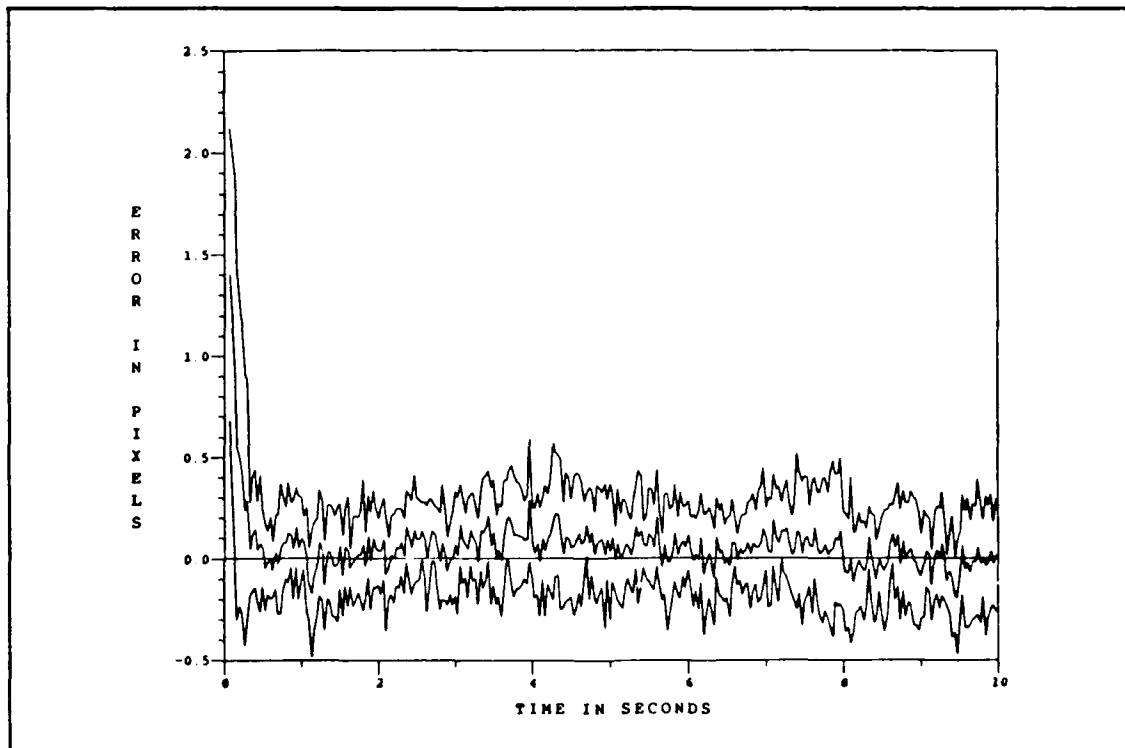


Figure E.9. One-State Filter Center-of-Mass Elevation Error at  $t_i^+$  for Binary Model Without Low-Energy Laser Sweep and Plume Pogo

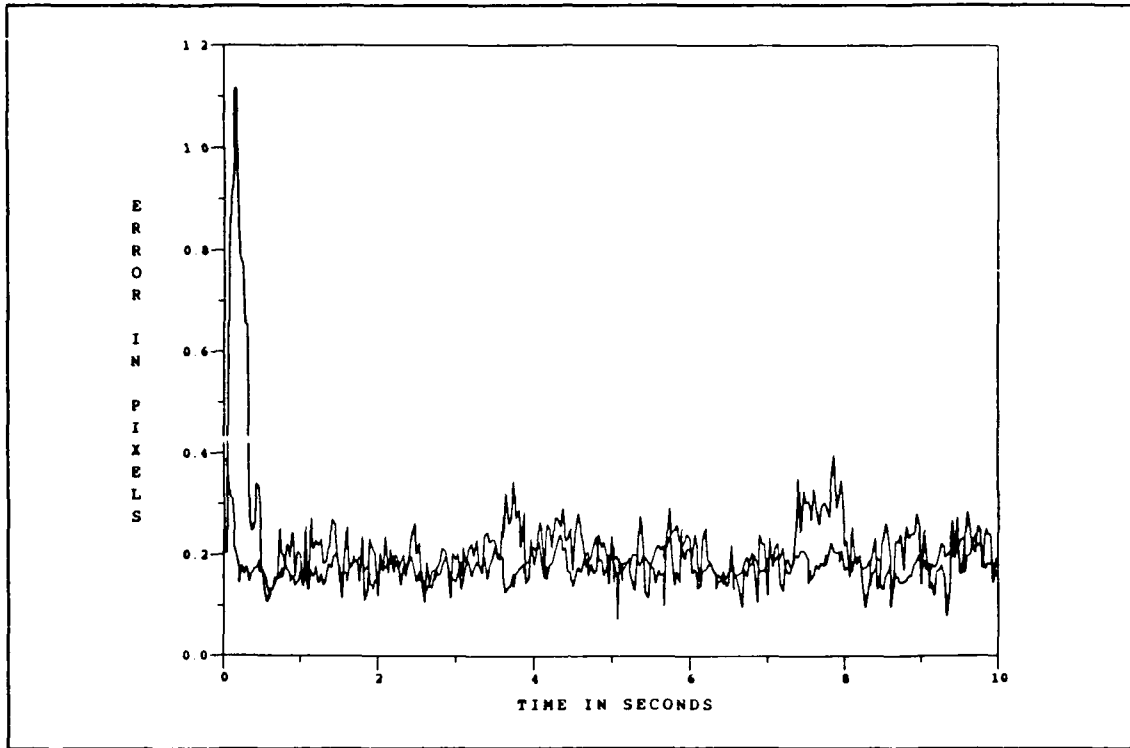


Figure E.10. One-State Filter vs. Actual rms Center-of-Mass Along-Track Error for Binary Model Without Low-Energy Laser Sweep and Plume Pogo

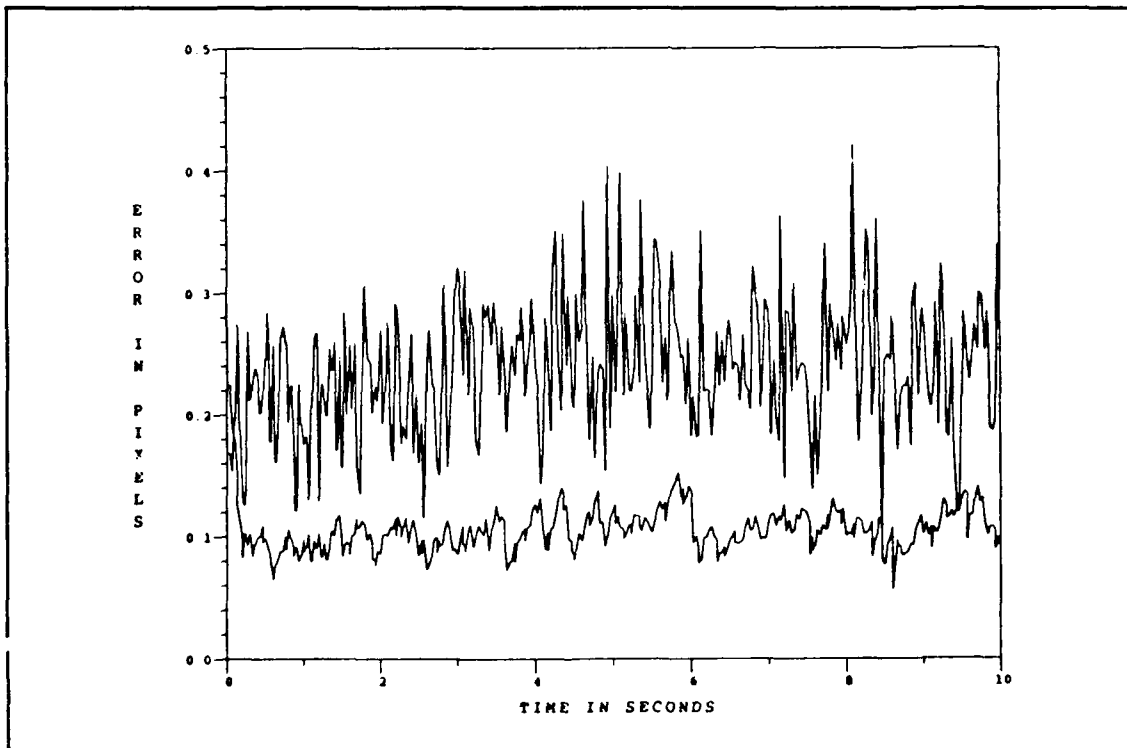


Figure E.11. One-State Filter vs. Actual rms Center-of-Mass Across-Track Error for Binary Model Without Low-Energy Laser Sweep and Plume Pogo

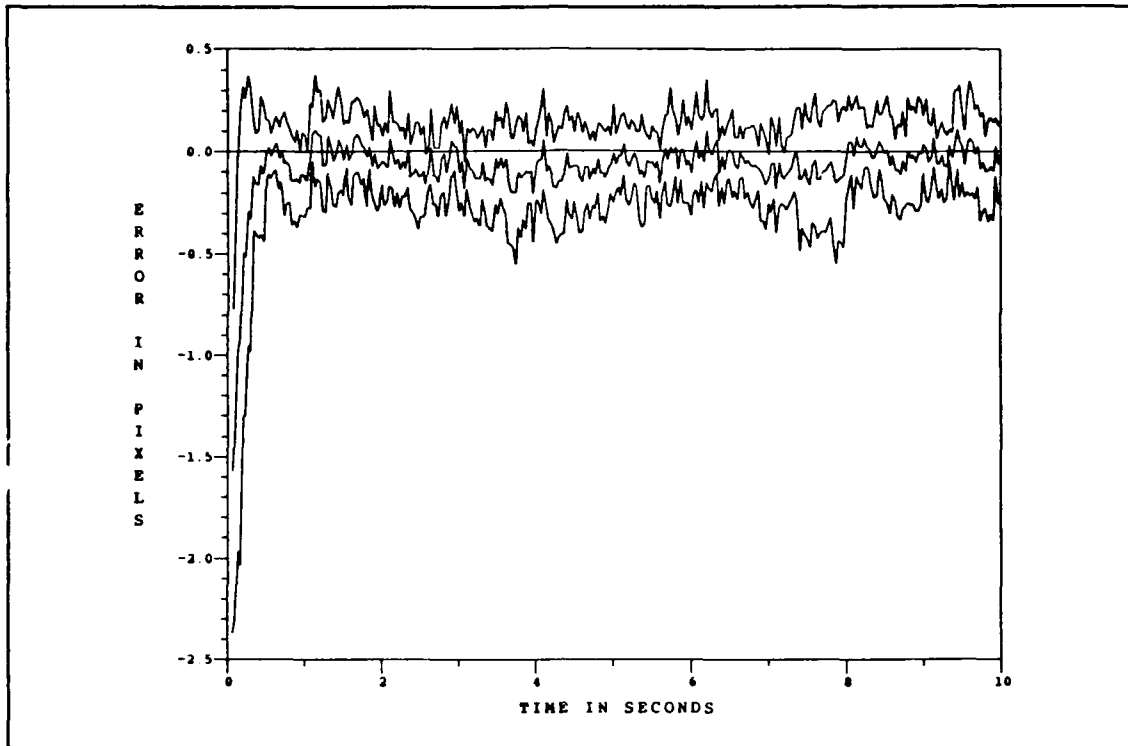


Figure E.12. One-State Filter Center-of-Mass Along-Track Error at  $t_i^-$  for Binary Model Without Low-Energy Laser Sweep and Plume Pogo

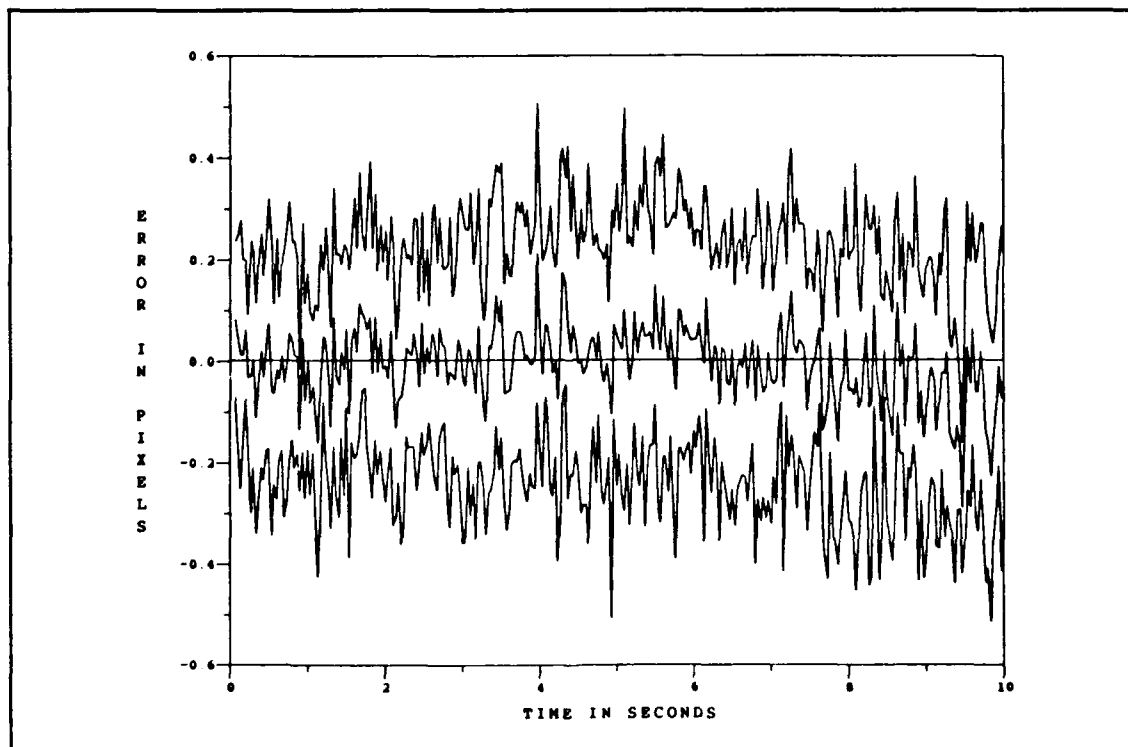


Figure E.13. One-State Filter Center-of-Mass Across-Track Error at  $t_i^-$  for Binary Model Without Low-Energy Laser Sweep and Plume Pogo

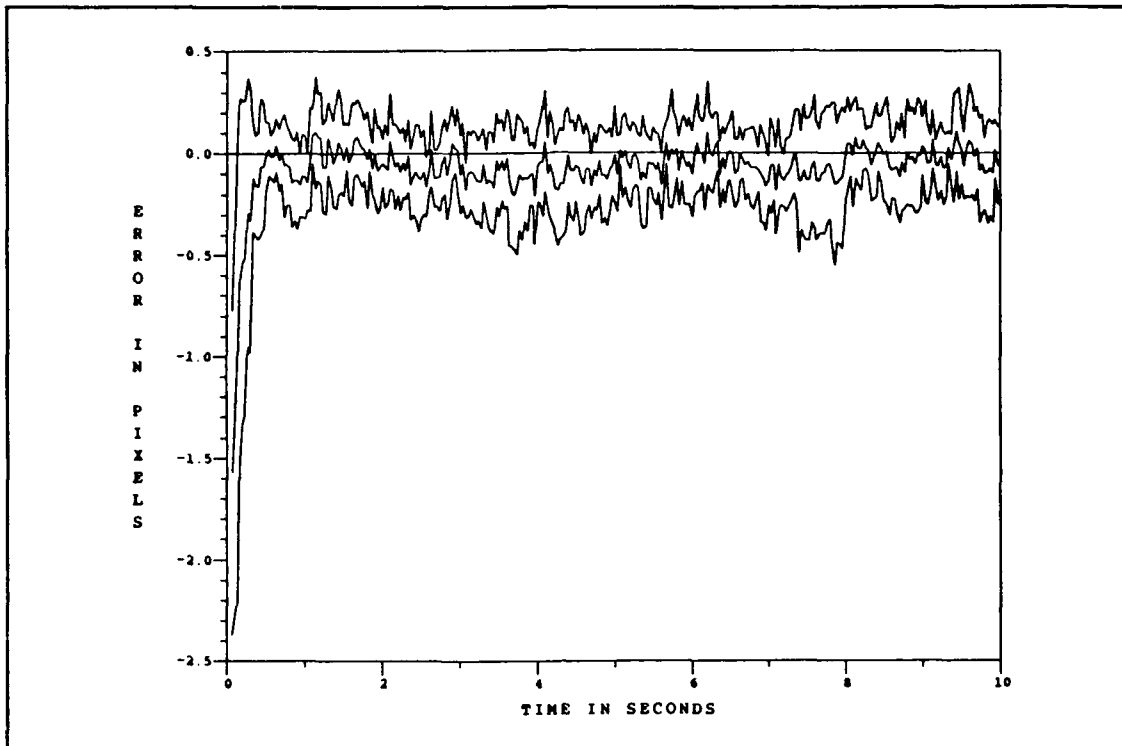


Figure E.14. One-State Filter Center-of-Mass Along-Track Error at  $t_i^+$  for Binary Model Without Low-Energy Laser Sweep and Plume Pogo

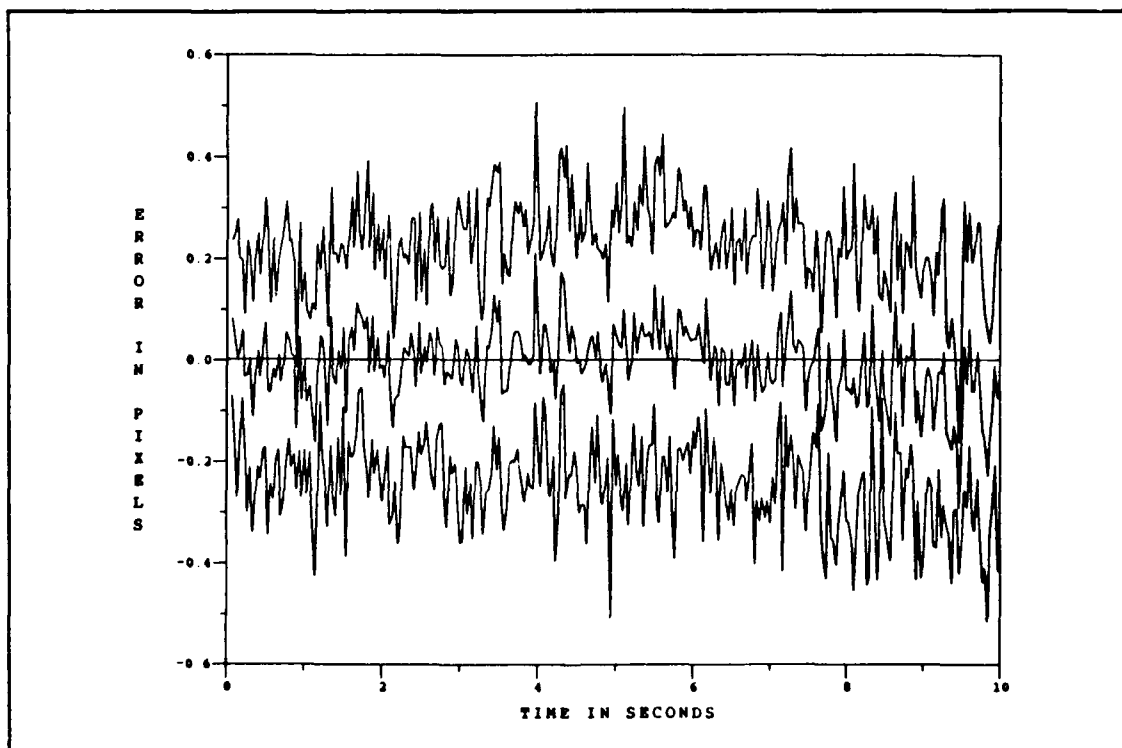


Figure E.15. One-State Filter Center-of-Mass Across-Track Error at  $t_i^+$  for Binary Model Without Low-Energy Laser Sweep and Plume Pogo



## *Appendix F. One-State Filter Performance Plots Without Low-Energy Laser Sweep and With Plume Pogo*

This appendix contains the one-state (center-of-mass) filter error plots for the case of no low-energy laser sweep and with the intensity centroid subjected to plume pogo. The center-of-mass errors are presented as a magnitude between the true center-of-mass and the filter estimated center-of-mass, the azimuth ( $x$ ) and elevation ( $y$ ) components of the magnitude error, and the along-track and across-track components of the magnitude error. The hardbody binary model is used for the single scan of the low-energy laser (i.e., no sweep), since the hardbody reflectivity model is software configured for a sweep routine. (The hardbody reflectivity model is used for the low-energy laser sweep plots, which are also representative of the hardbody binary plots.) For the discussion pertaining to these plots, refer to Chapter VI, Sections 6.5 and 6.7.

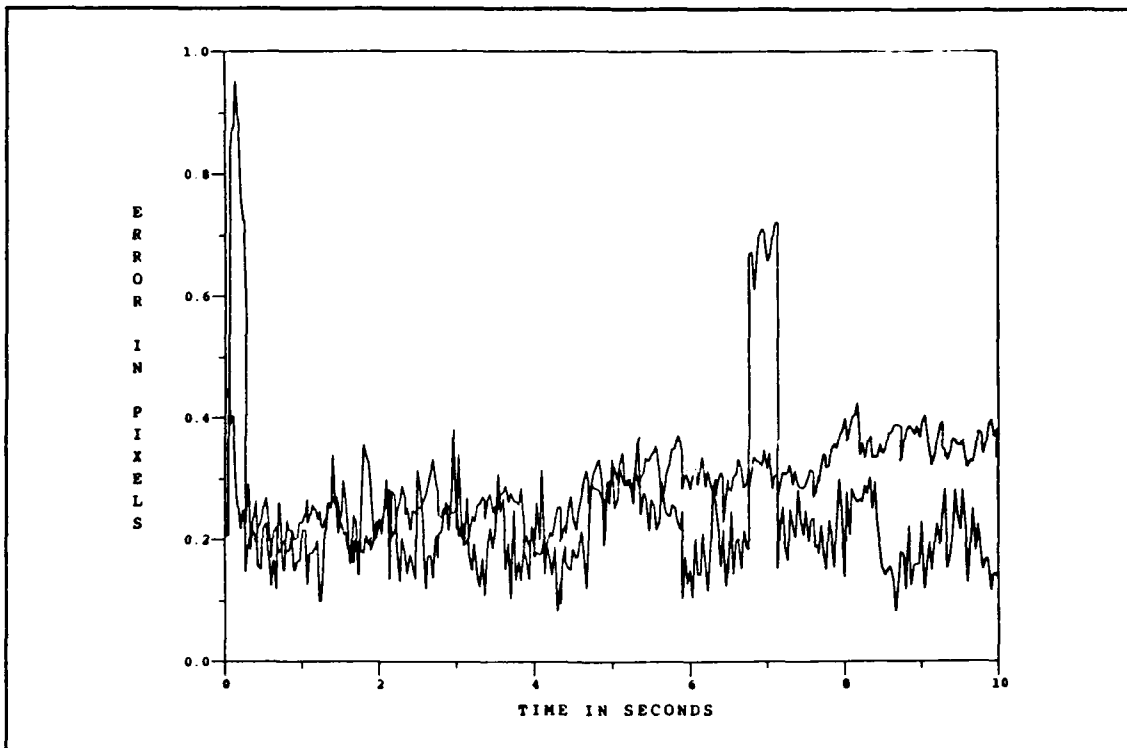


Figure F.1. One-State Filter vs. Actual rms Center-of-Mass Magnitude Error for Binary Model Without Low-Energy Laser Sweep and With Plume Pogo

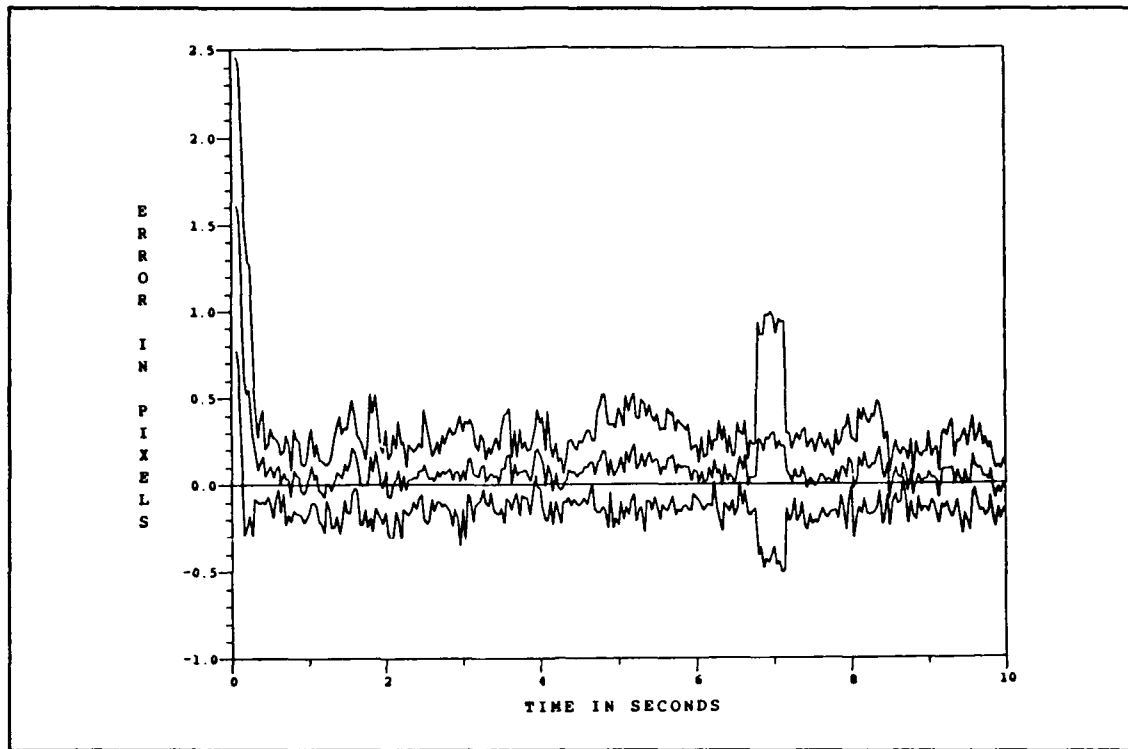


Figure F.2. One-State Filter Center-of-Mass Magnitude Error at  $t_i^-$  for Binary Model Without Low-Energy Laser Sweep and With Plume Pogo

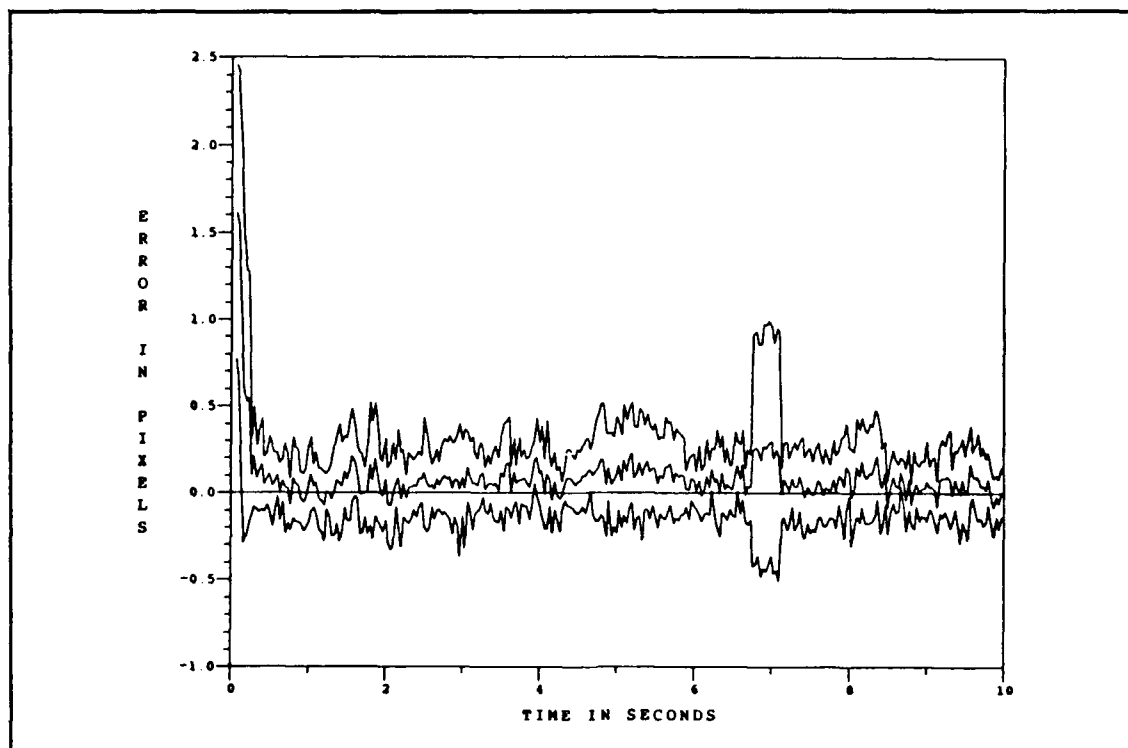


Figure F.3. One-State Filter Center-of-Mass Magnitude Error at  $t_i^+$  for Binary Model Without Low-Energy Laser Sweep and With Plume Pogo

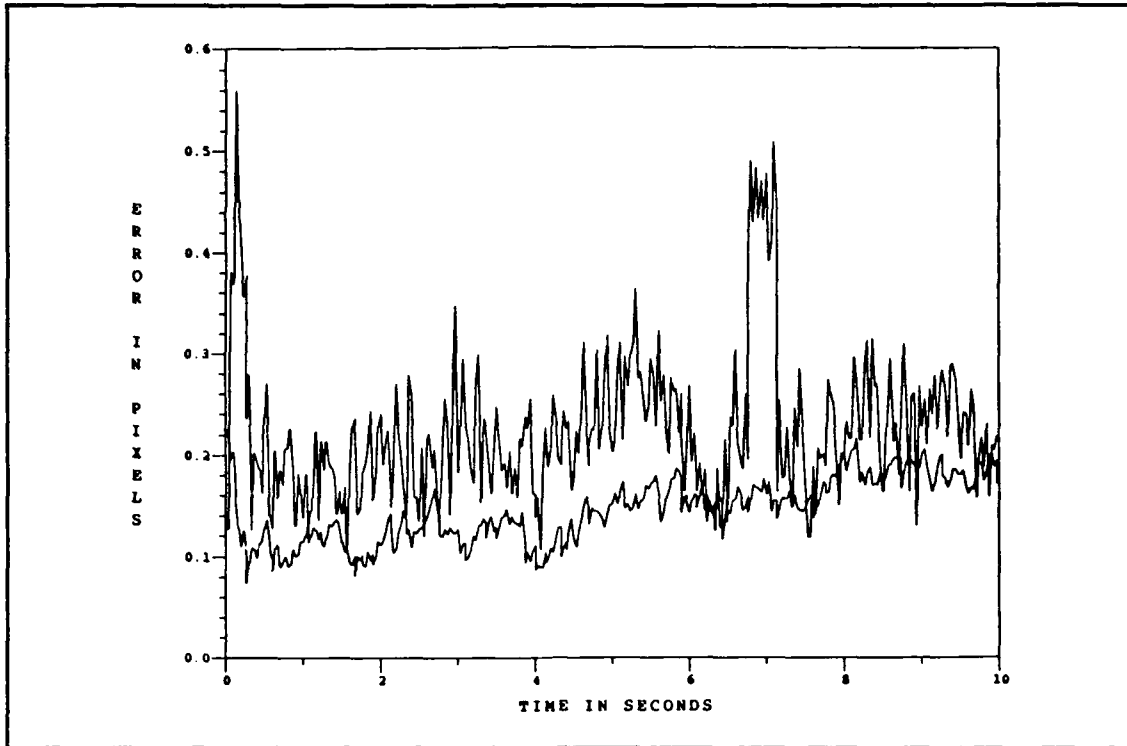


Figure F.4. One-State Filter vs. Actual rms Center-of-Mass Azimuth Error for Binary Model Without Low-Energy Laser Sweep and With Plume Pogo

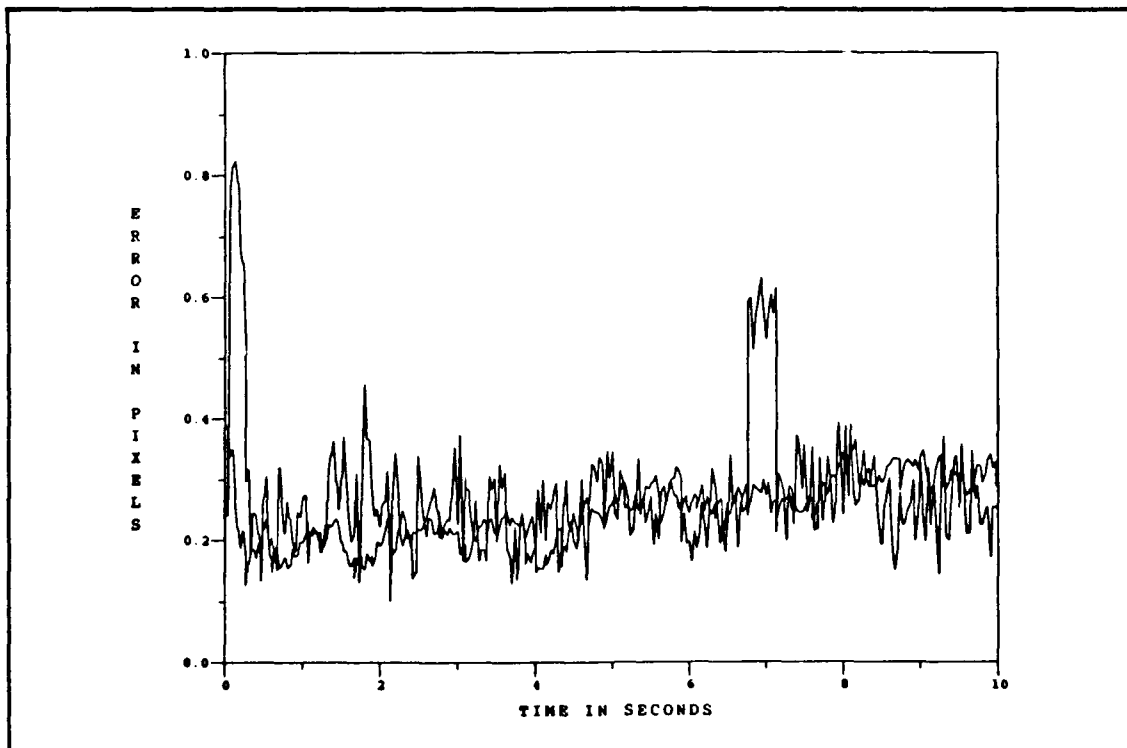


Figure F.5. One-State Filter vs. Actual rms Center-of-Mass Elevation Error for Binary Model Without Low-Energy Laser Sweep and With Plume Pogo

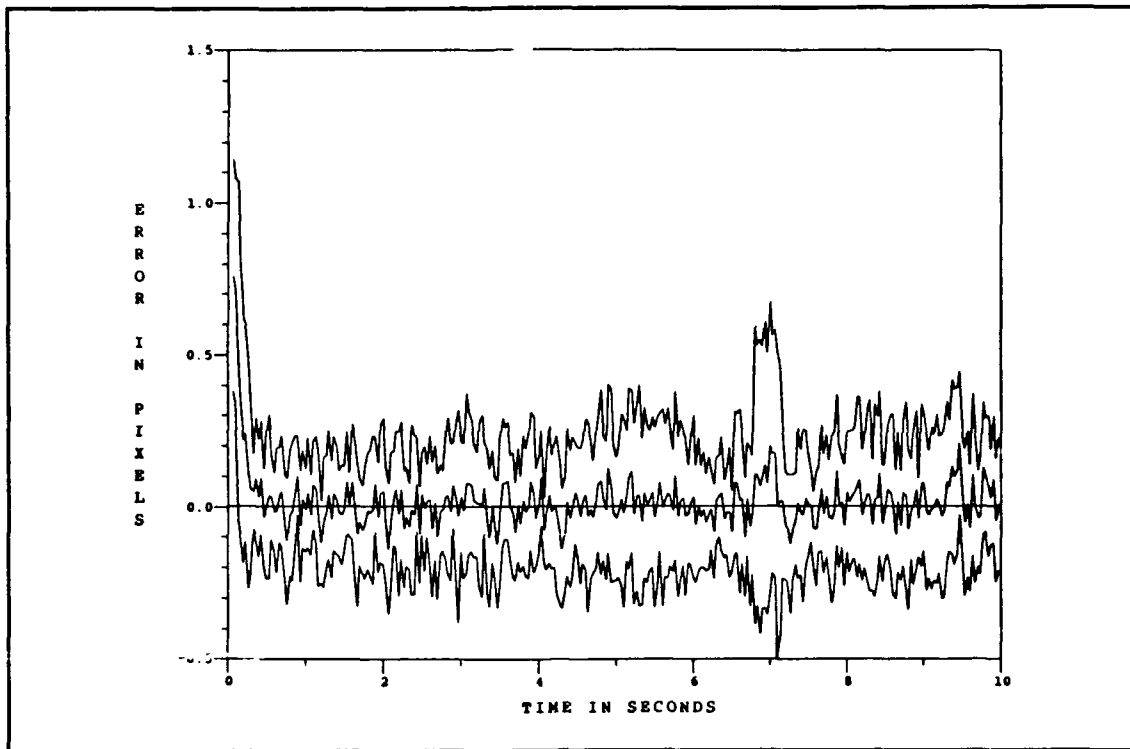


Figure F.6. One-State Filter Center-of-Mass Azimuth Error at  $t_i^-$  for Binary Model Without Low-Energy Laser Sweep and With Plume Pogo

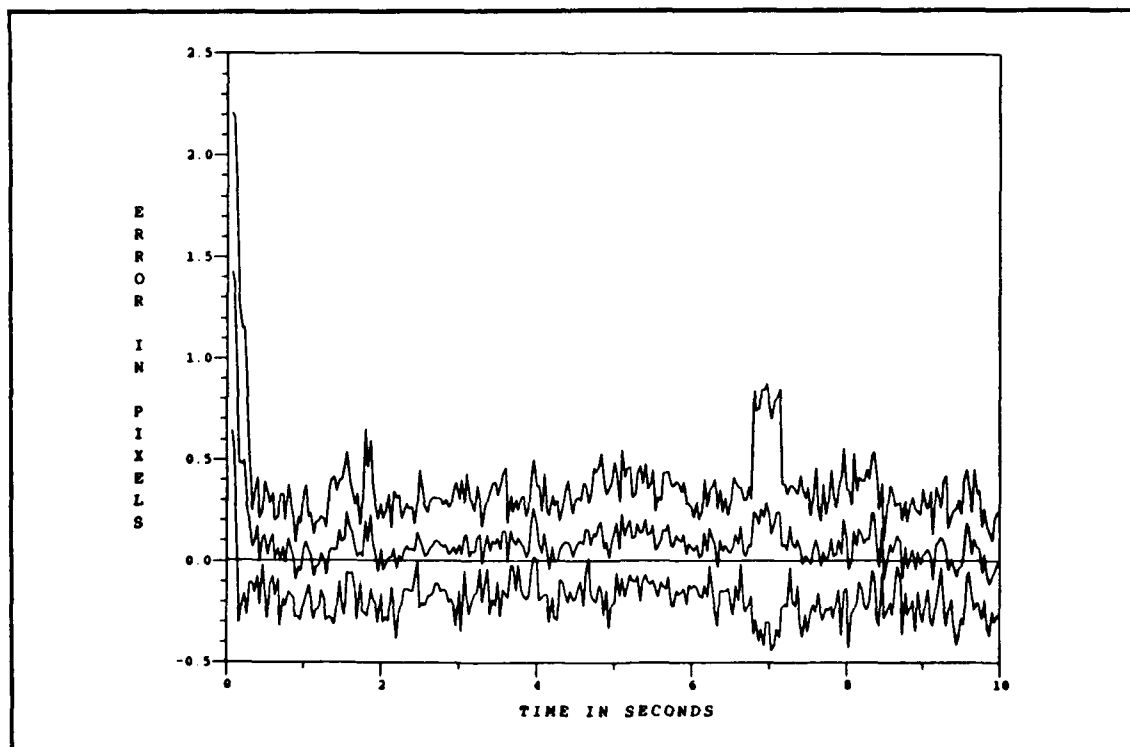


Figure F.7. One-State Filter Center-of-Mass Elevation Error at  $t_i^-$  for Binary Model Without Low-Energy Laser Sweep and With Plume Pogo

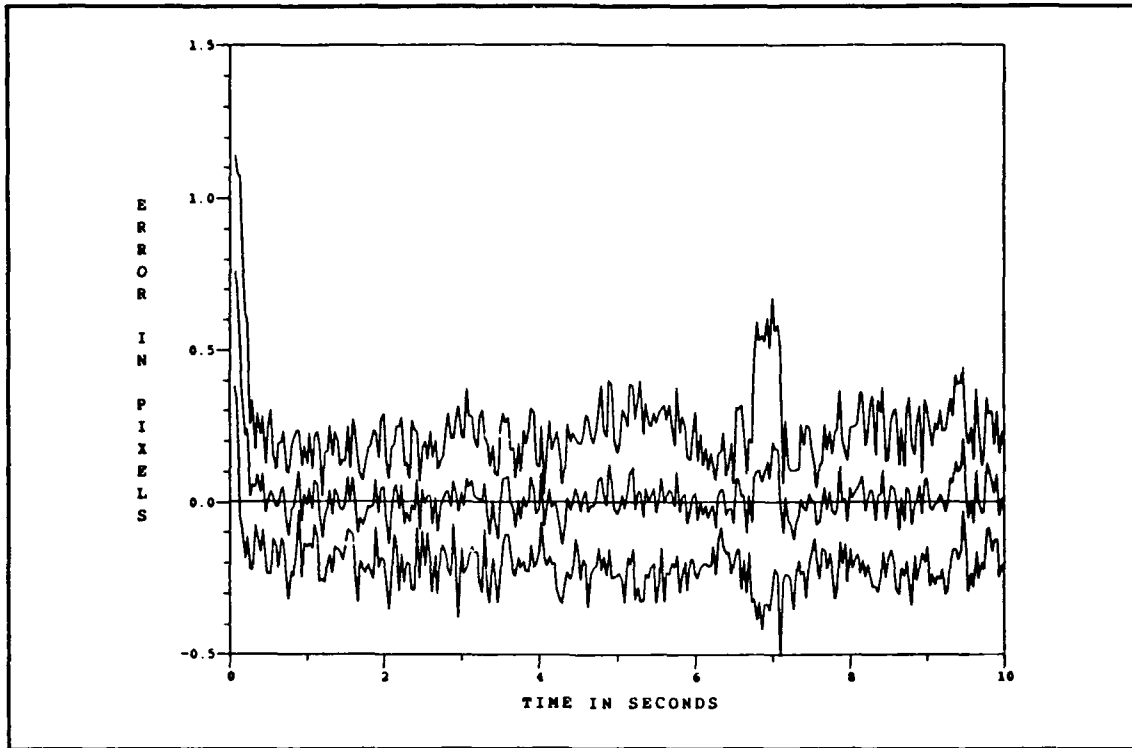


Figure F.8. One-State Filter Center-of-Mass Azimuth Error at  $t_i^+$  for Binary Model Without Low-Energy Laser Sweep and With Plume Pogo

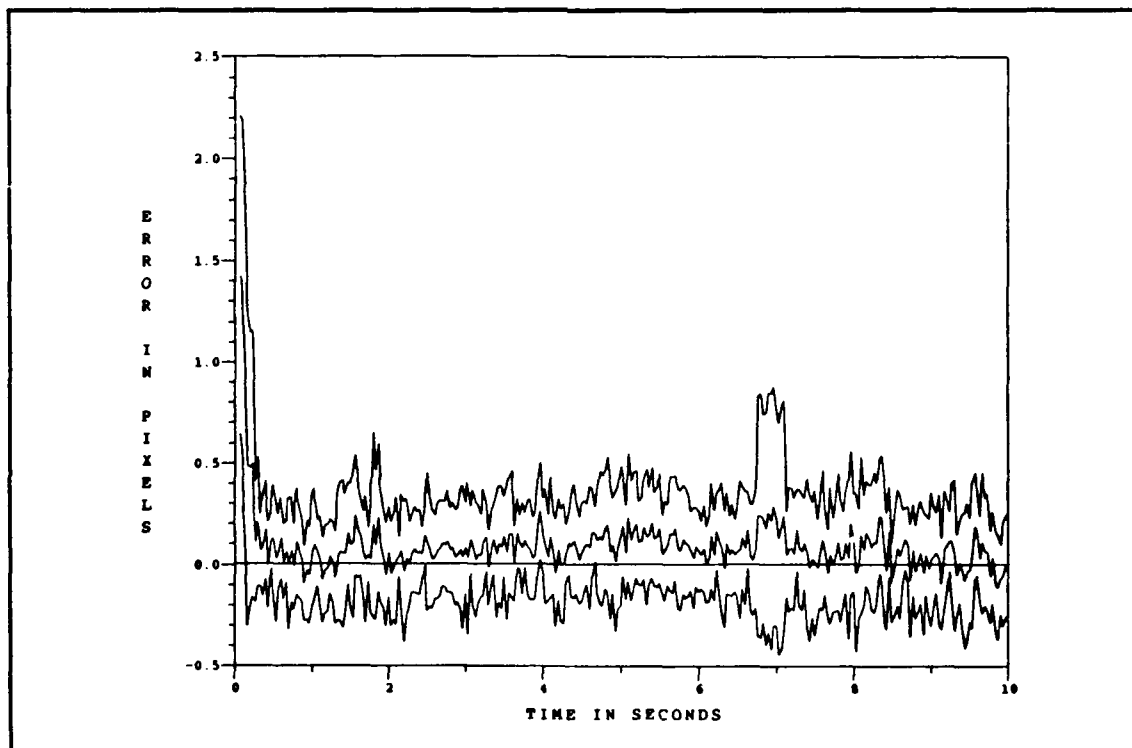


Figure F.9. One-State Filter Center-of-Mass Elevation Error at  $t_i^+$  for Binary Model Without Low-Energy Laser Sweep and With Plume Pogo

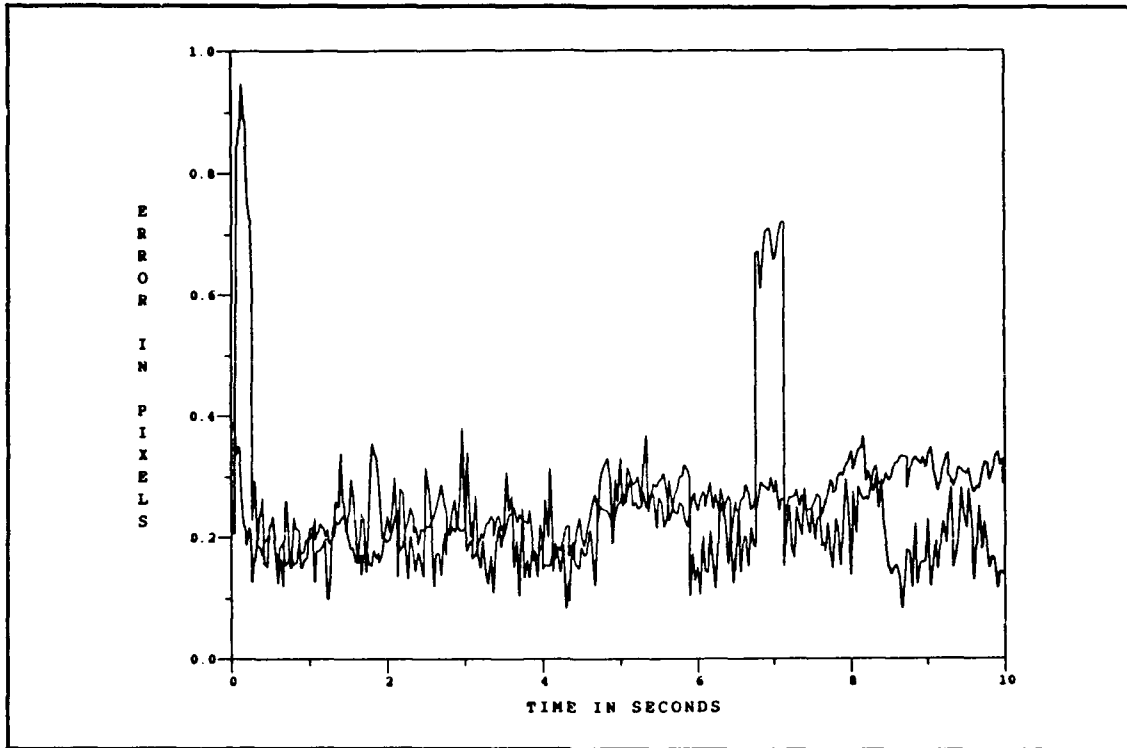


Figure F.10. One-State Filter vs. Actual rms Center-of-Mass Along-Track Error for Binary Model Without Low-Energy Laser Sweep and With Plume Pogo

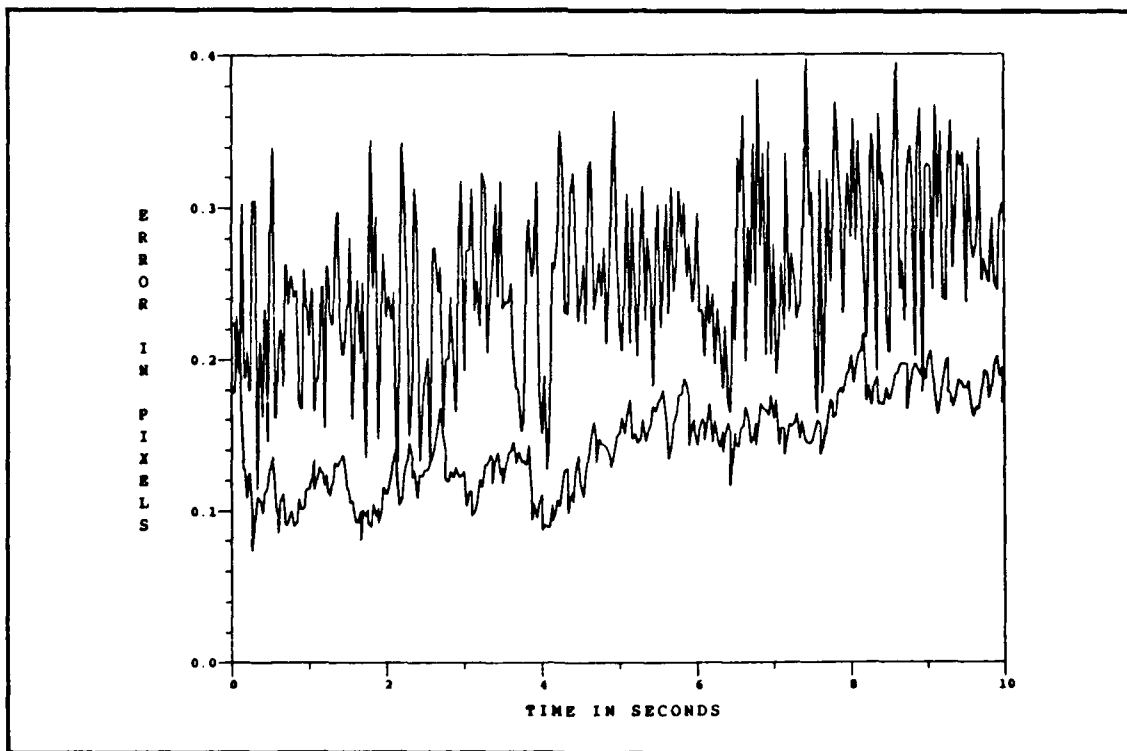


Figure F.11. One-State Filter vs. Actual rms Center-of-Mass Across-Track Error for Binary Model Without Low-Energy Laser Sweep and With Plume Pogo

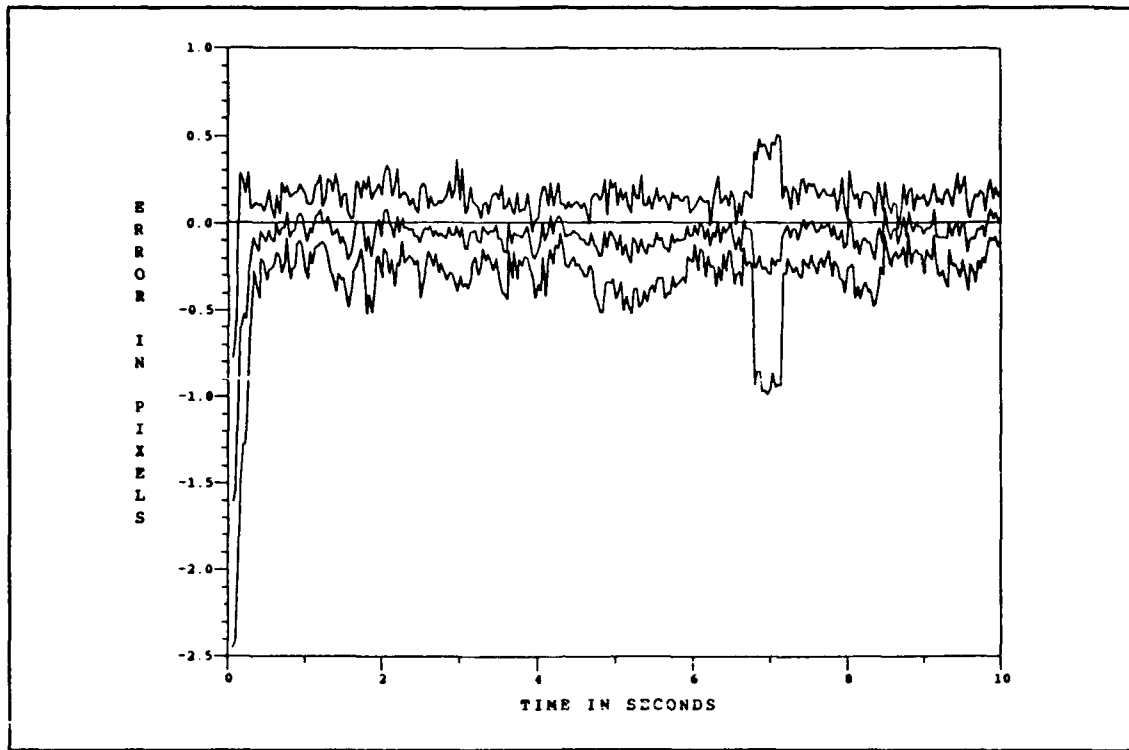


Figure F.12. One-State Filter Center-of-Mass Along-Track Error at  $t_i^-$  for Binary Model Without Low-Energy Laser Sweep and With Plume Pogo

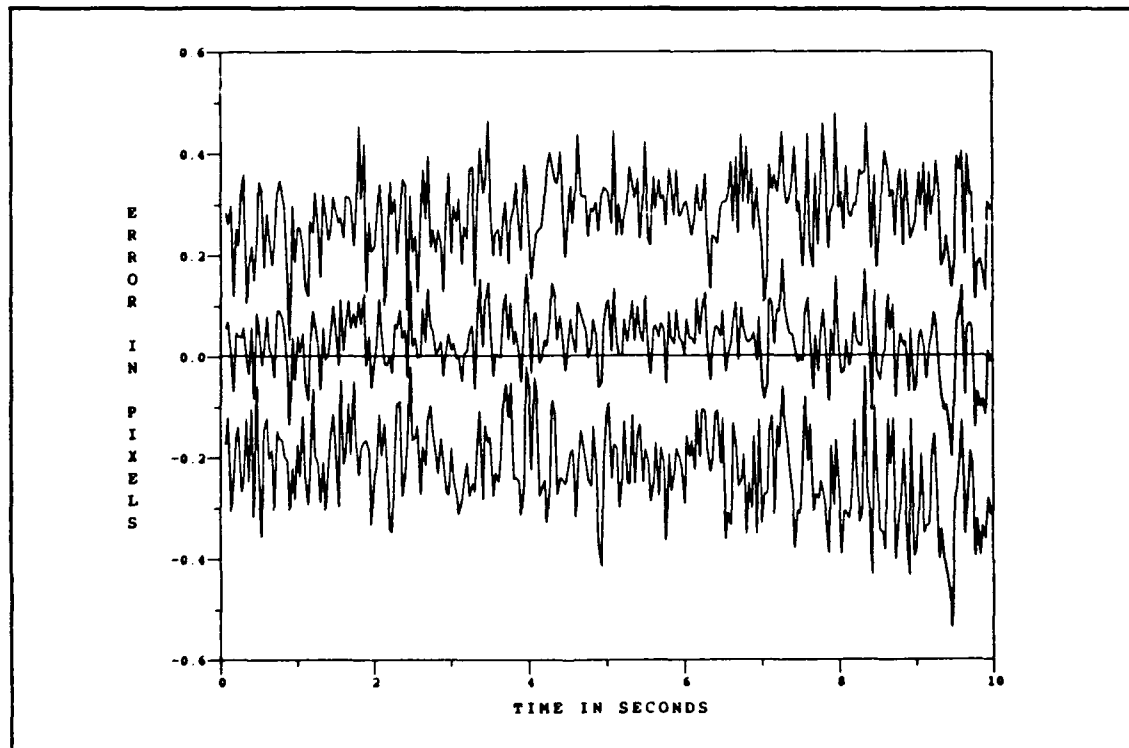


Figure F.13. One-State Filter Center-of-Mass Across-Track Error at  $t_i^-$  for Binary Model Without Low-Energy Laser Sweep and With Plume Pogo



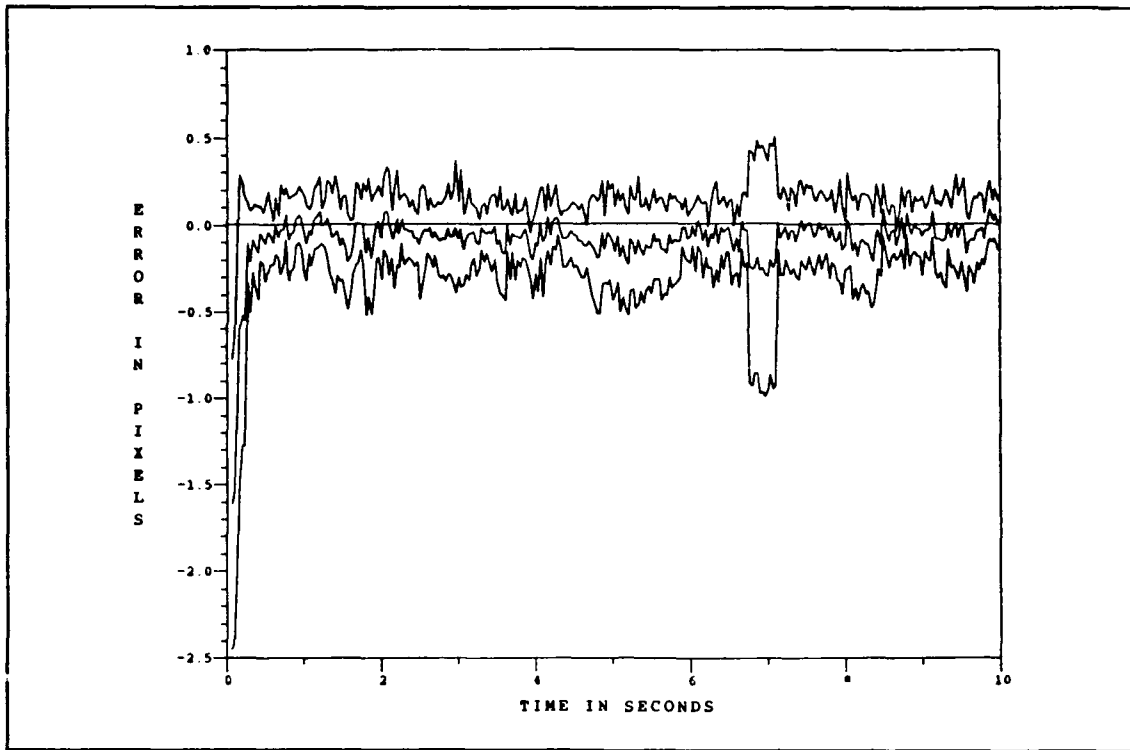


Figure F.14. One-State Filter Center-of-Mass Along-Track Error at  $t_i^+$  for Binary Model Without Low-Energy Laser Sweep and With Plume Pogo

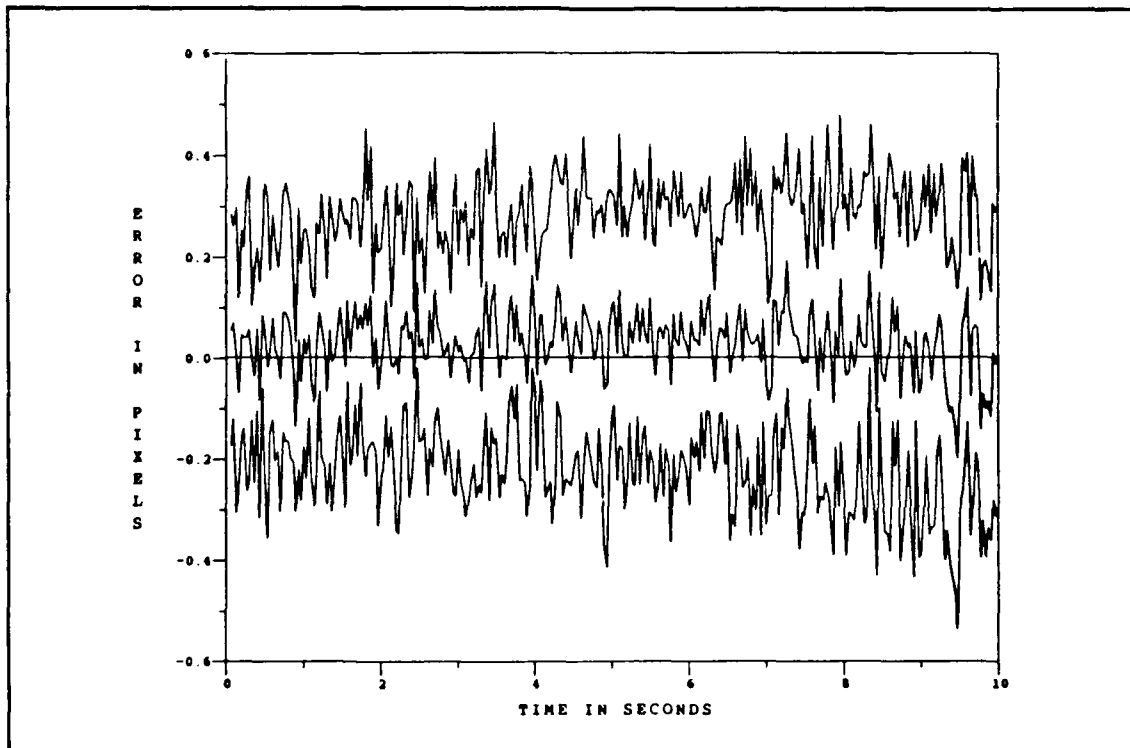


Figure F.15. One-State Filter Center-of-Mass Across-Track Error at  $t_i^+$  for Binary Model Without Low-Energy Laser Sweep and With Plume Pogo

## *Appendix G. One-State Filter Performance Plots With Low-Energy Laser Sweep and Without Plume Pogo*

This appendix contains the one-state (center-of-mass) filter error plots for the case of a low-energy laser sweep and with no plume pogo of the intensity centroid. The center-of-mass errors are presented as a magnitude between the true center-of-mass and the filter estimated center-of-mass, the azimuth ( $x$ ) and elevation ( $y$ ) components of the magnitude error, and the along-track and across-track components of the magnitude error. The hardbody reflectivity model is used for the low-energy laser sweep plots, which are also representative of the hardbody binary plots. (The hardbody binary model is used for the single scan of the low-energy laser (i.e., no sweep), since the hardbody reflectivity model is software configured for a sweep routine.) For the discussion pertaining to these plots, refer to Chapter VI, Sections 6.5 and 6.7.

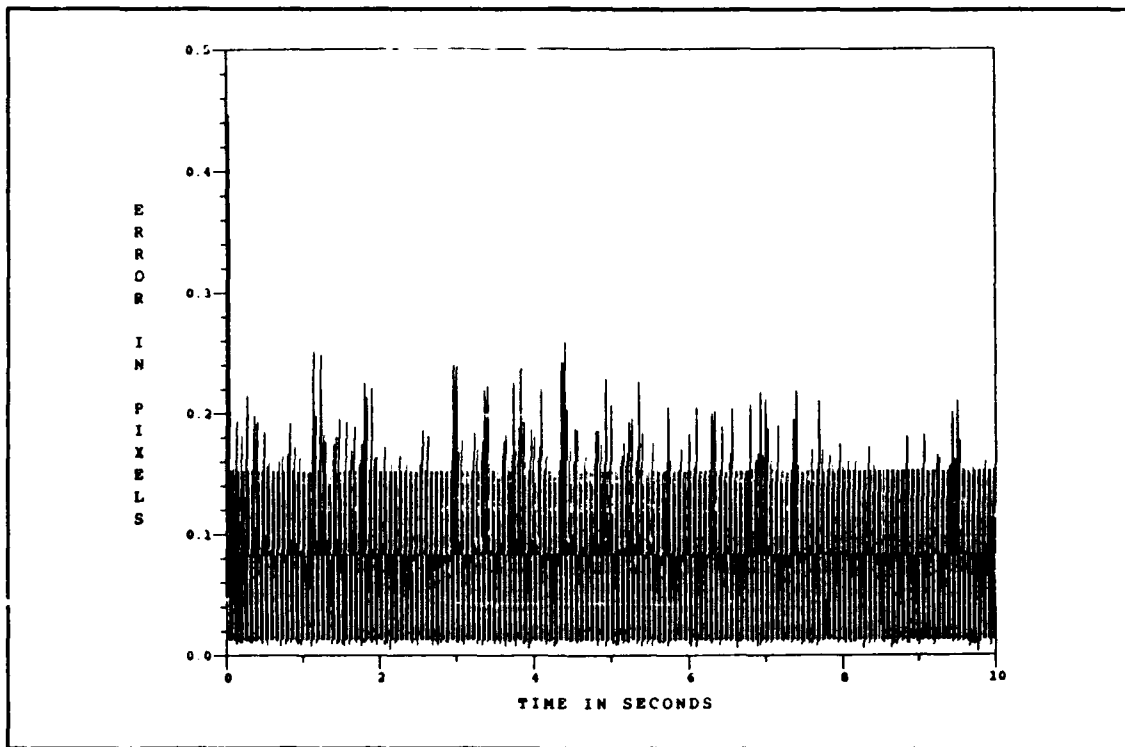


Figure G.1. One-State Filter vs. Actual rms Center-of-Mass Magnitude Error for Reflectivity Model With Low-Energy Laser Sweep and Without Plume Pogo

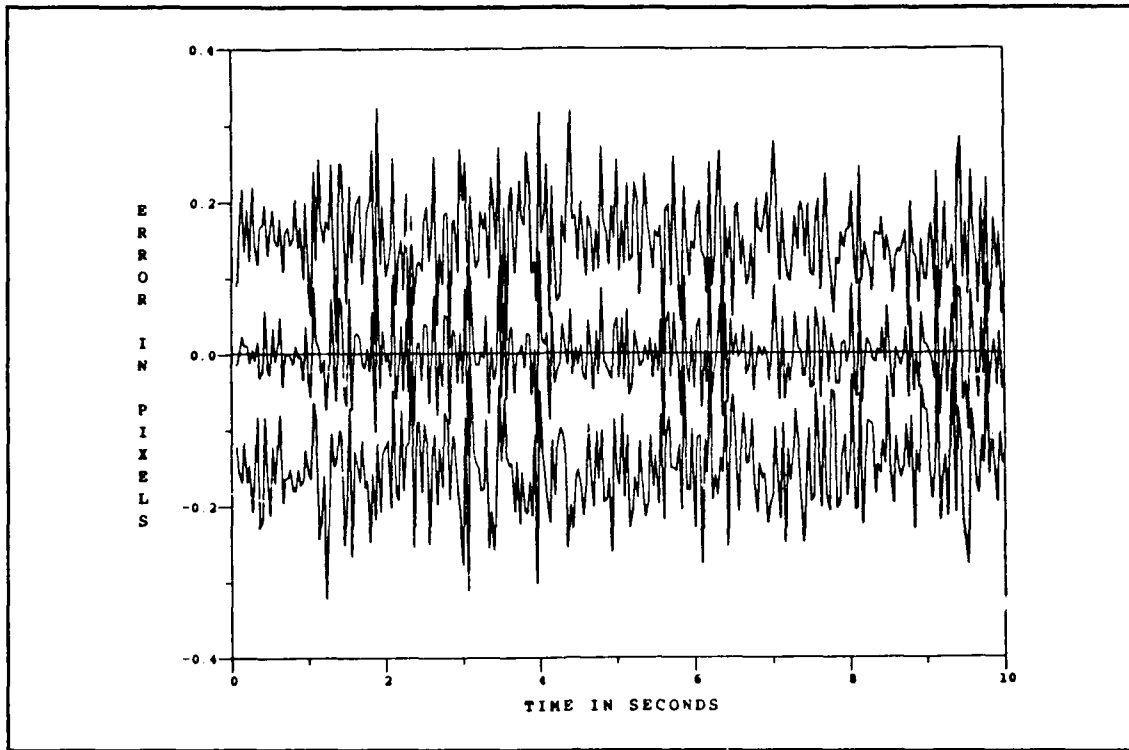


Figure G.2. One-State Filter Center-of-Mass Magnitude Error at  $t_i^-$  for Reflectivity Model With Low-Energy Laser Sweep and Without Plume Pogo

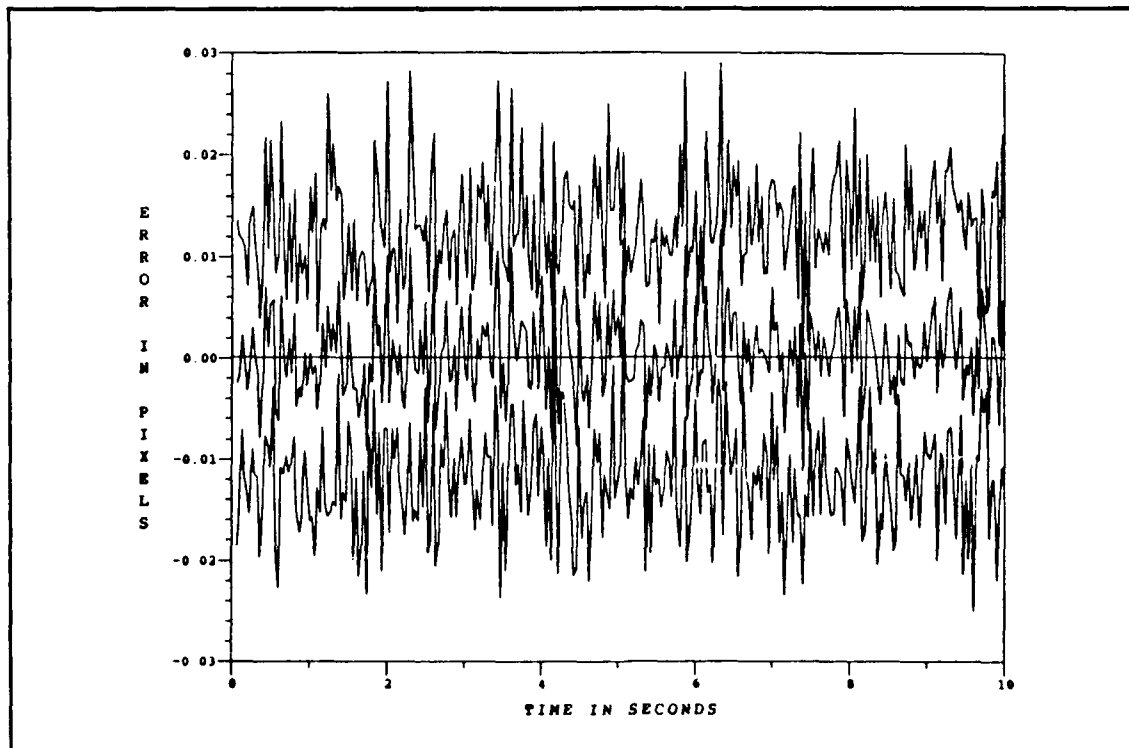


Figure G.3. One-State Filter Center-of-Mass Magnitude Error at  $t_i^+$  for Reflectivity Model With Low-Energy Laser Sweep and Without Plume Pogo

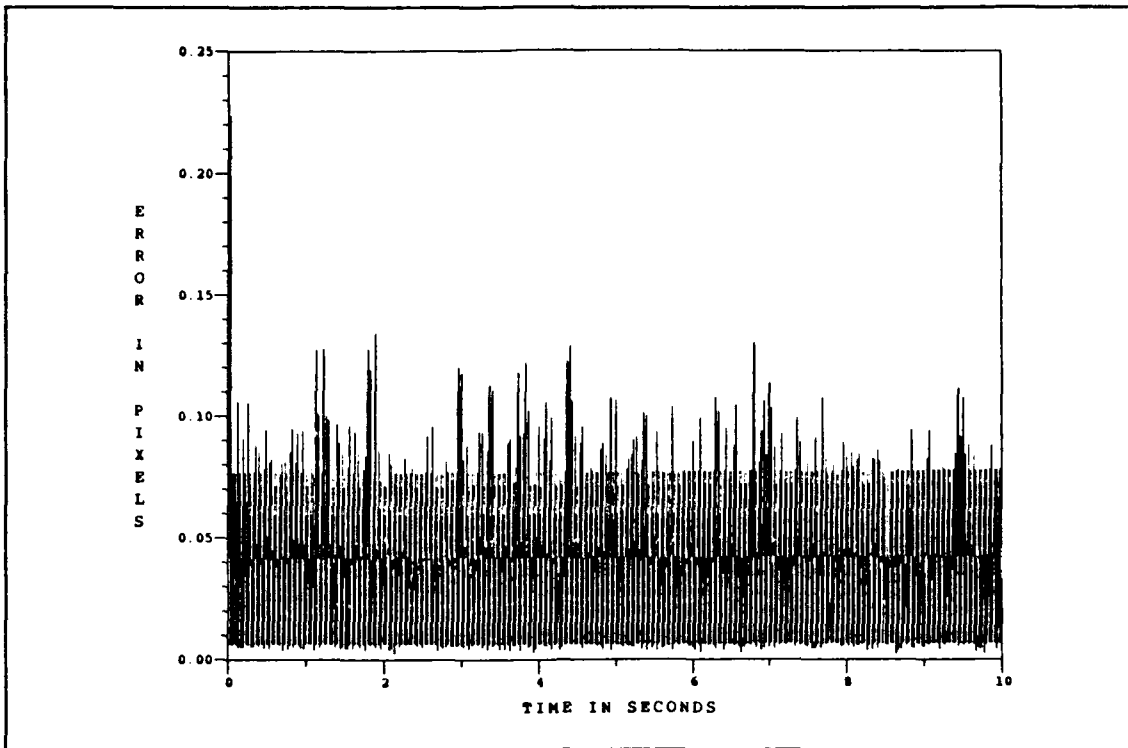


Figure G.4. One-State Filter vs. Actual rms Center-of-Mass Azimuth Error for Reflectivity Model With Low-Energy Laser Sweep and Without Plume Pogo

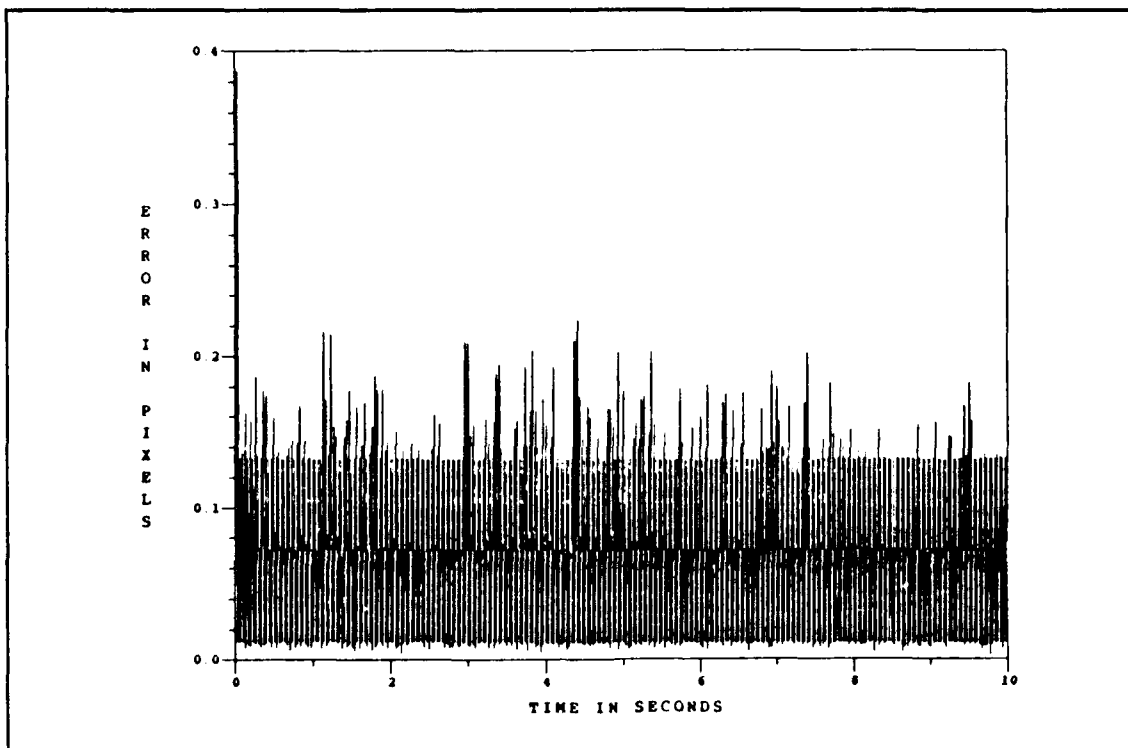


Figure G.5. One-State Filter vs. Actual rms Center-of-Mass Elevation Error for Reflectivity With Low-Energy Laser Sweep and Without Plume Pogo

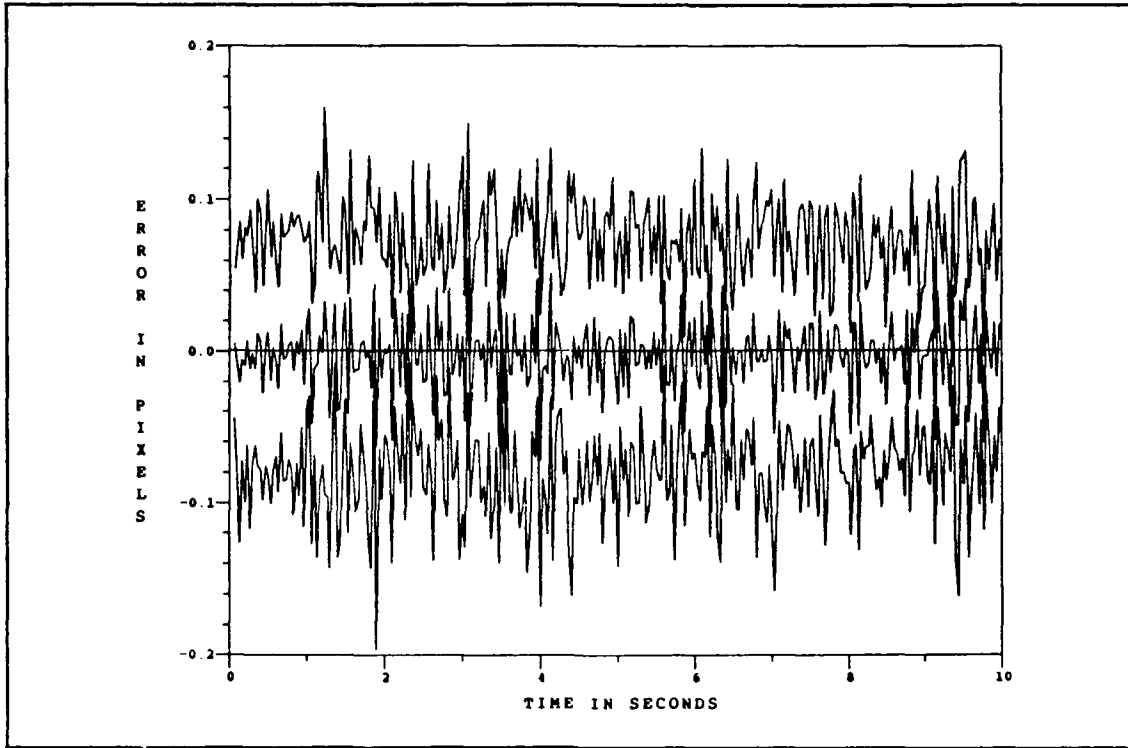


Figure G.6. One-State Filter Center-of-Mass Azimuth Error at  $t_i^-$  for Reflectivity Model With Low-Energy Laser Sweep and Without Plume Pogo

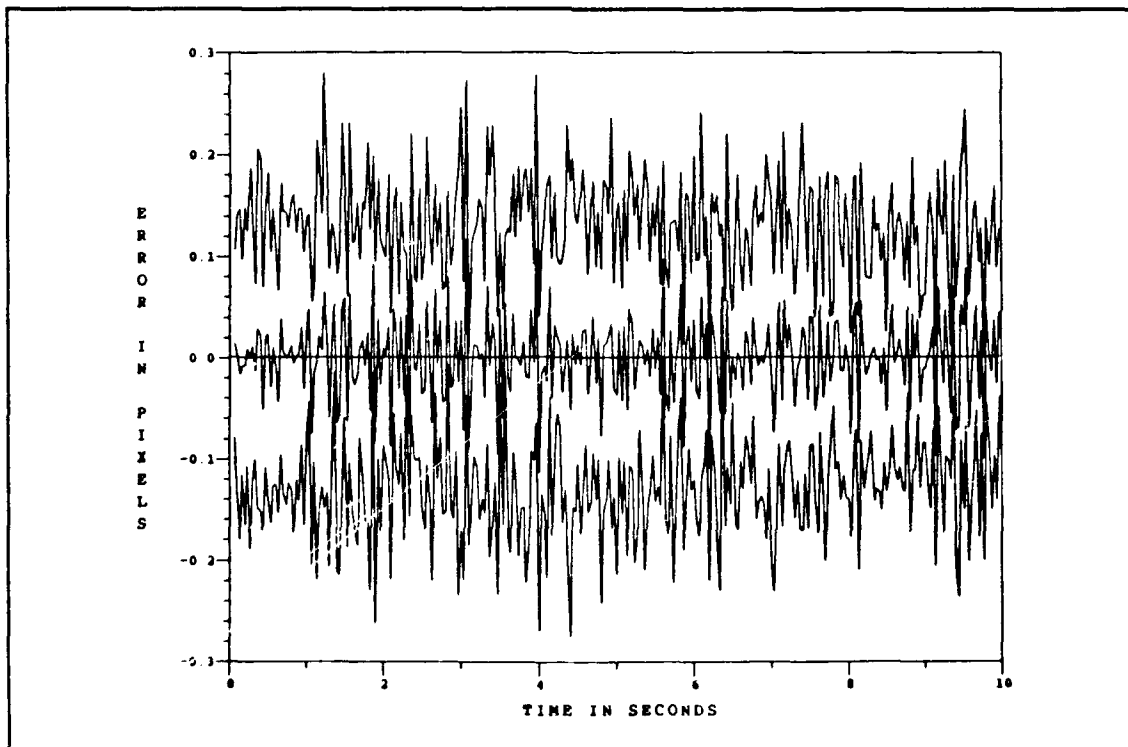


Figure G.7. One-State Filter Center-of-Mass Elevation Error at  $t_i^-$  for Reflectivity Model With Low-Energy Laser Sweep and Without Plume Pogo

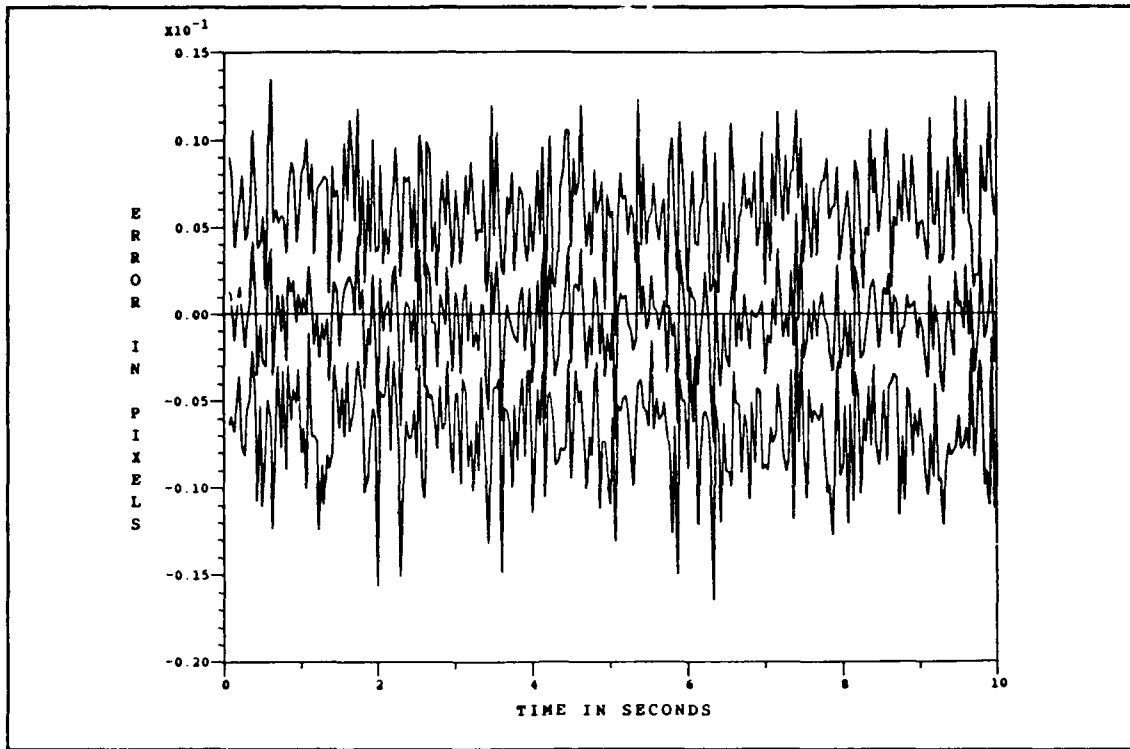


Figure G.8. One-State Filter Center-of-Mass Azimuth Error at  $t_i^+$  for Reflectivity Model With Low-Energy Laser Sweep and Without Plume Pogo

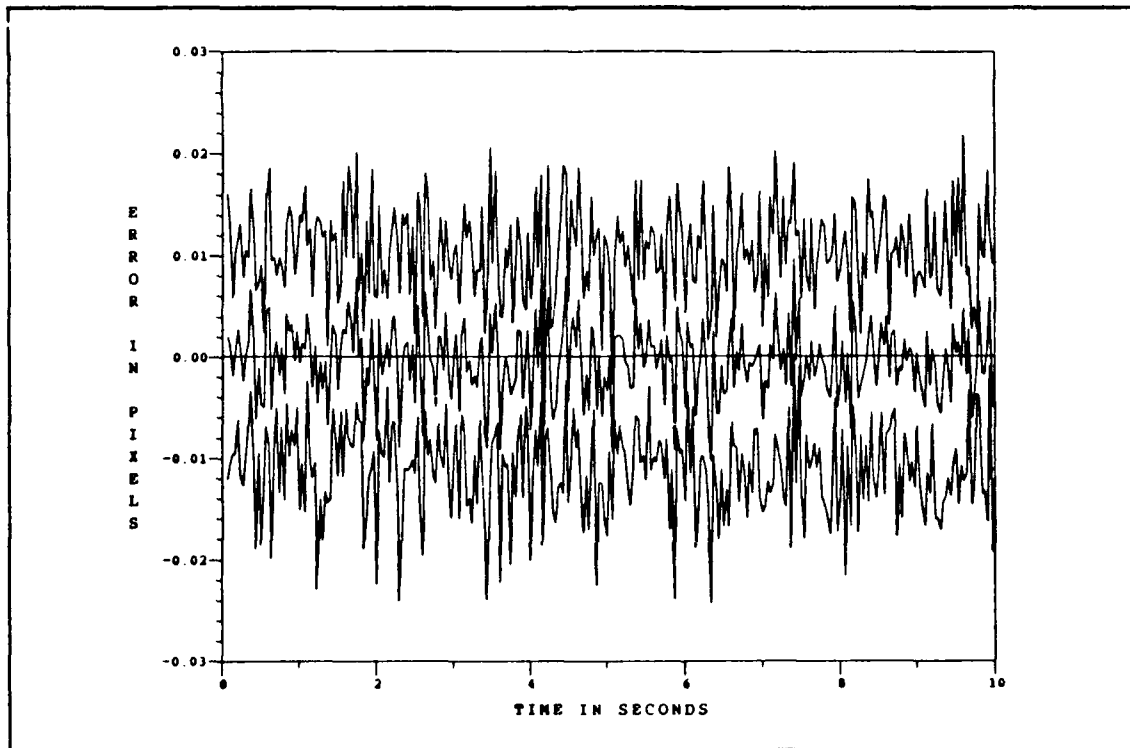


Figure G.9. One-State Filter Center-of-Mass Elevation Error at  $t_i^+$  for Reflectivity Model With Low-Energy Laser Sweep and Without Plume Pogo

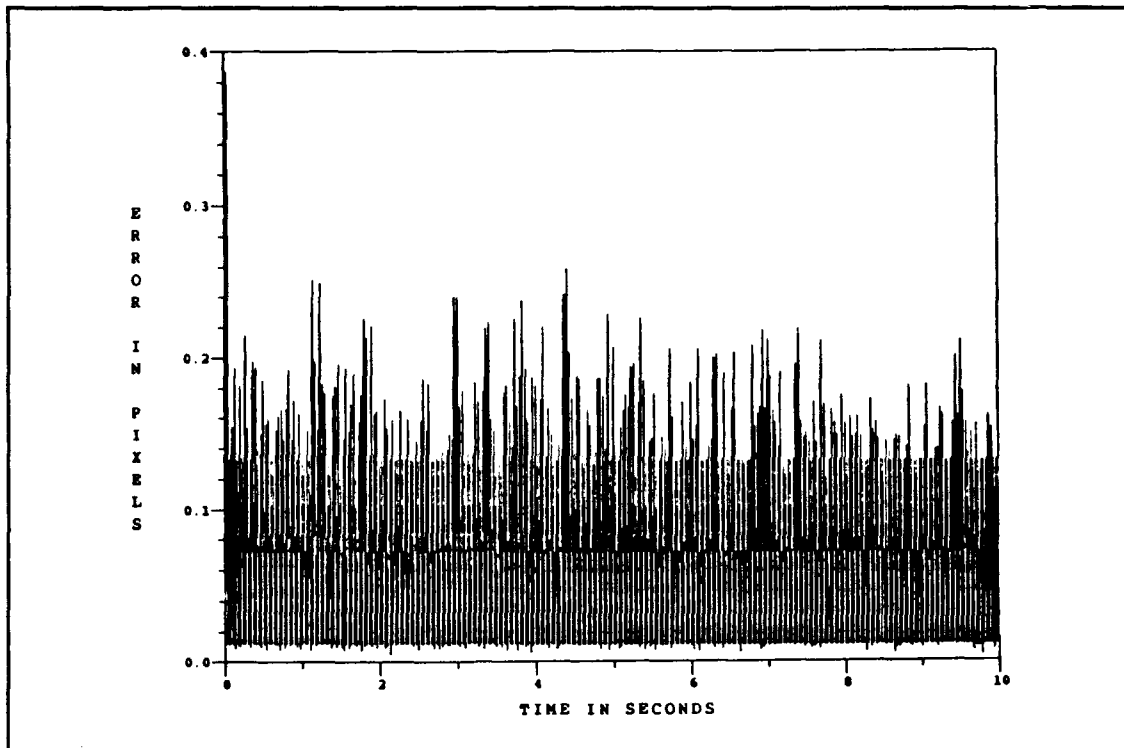


Figure G.10. One-State Filter vs. Actual rms Center-of-Mass Along-Track Error for Reflectivity Model With Low-Energy Laser Sweep and Without Plume Pogo

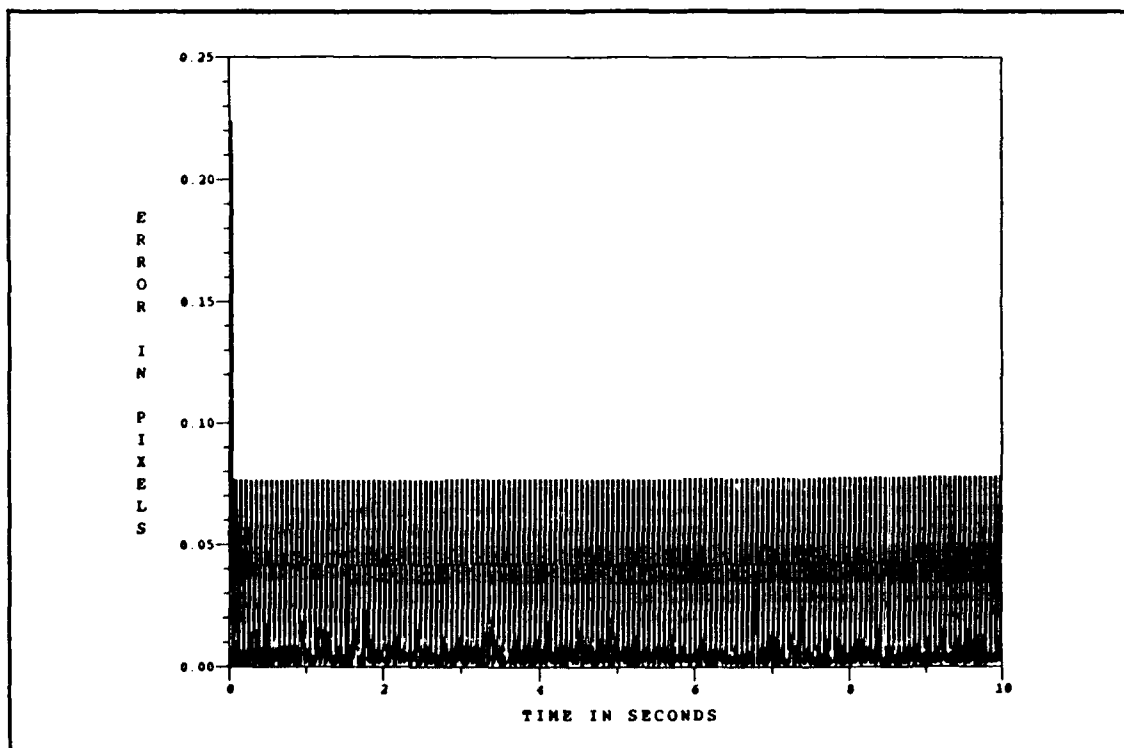


Figure G.11. One-State Filter vs. Actual rms Center-of-Mass Across-Track Error for Reflectivity Model With Low-Energy Laser Sweep and Without Plume Pogo



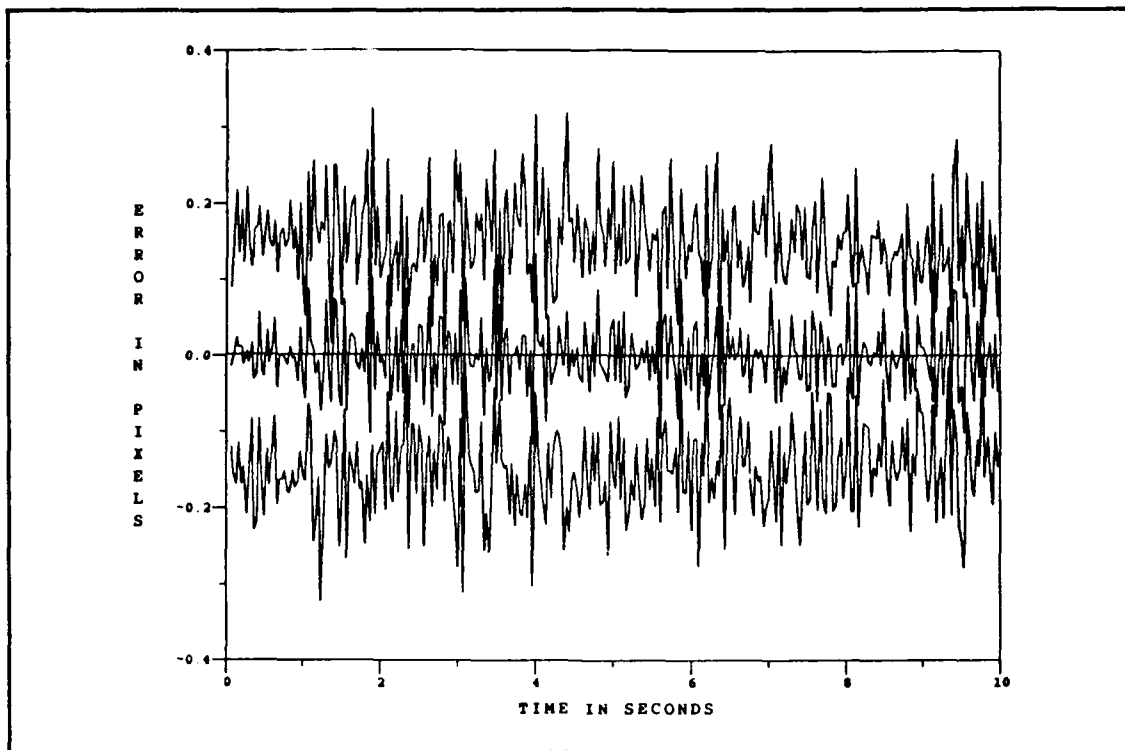


Figure G.12. One-State Filter Center-of-Mass Along-Track Error at  $t_i^-$  for Reflectivity Model With Low-Energy Laser Sweep and Without Plume Pogo

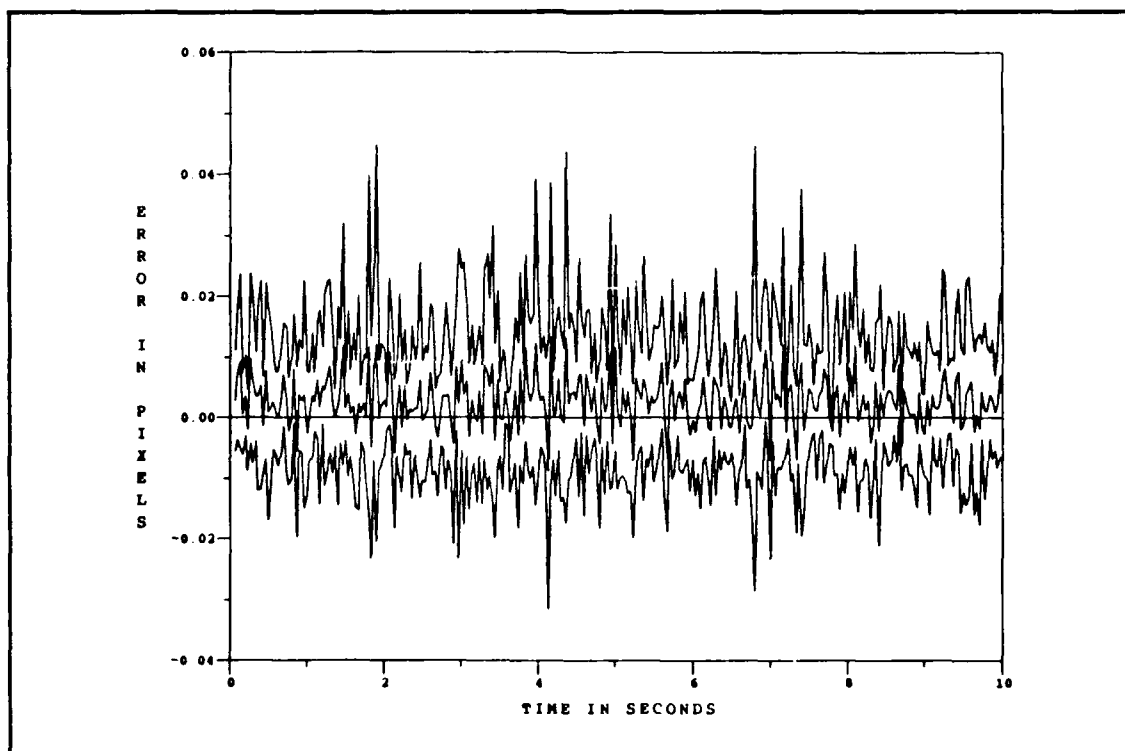


Figure G.13. One-State Filter Center-of-Mass Across-Track Error at  $t_i^-$  for Reflectivity Model With Low-Energy Laser Sweep and Without Plume Pogo

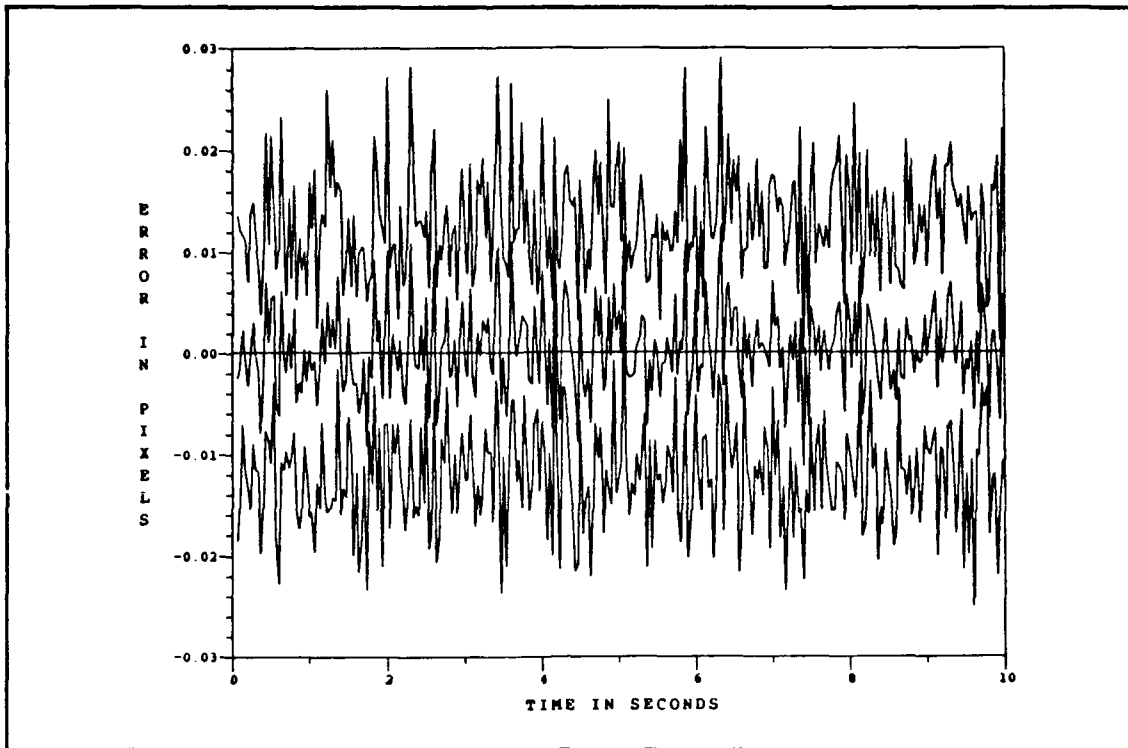


Figure G.14. One-State Filter Center-of-Mass Along-Track Error at  $t_i^+$  for Reflectivity Model With Low-Energy Laser Sweep and Without Plume Pogo

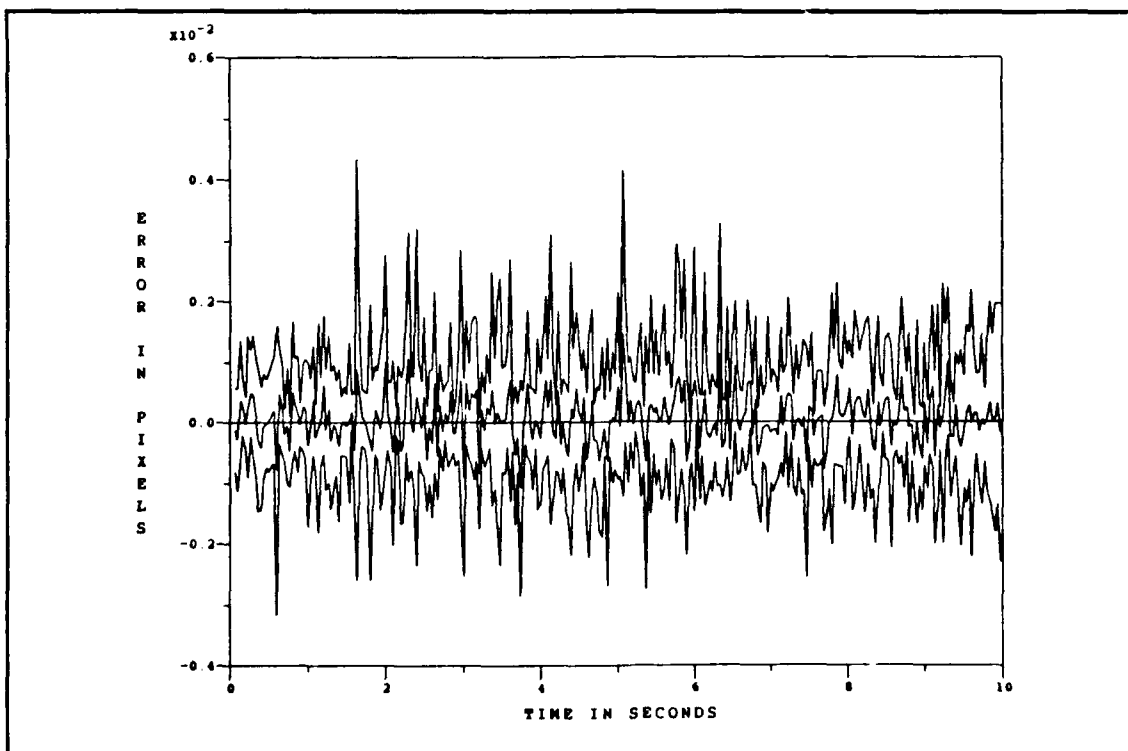


Figure G.15. One-State Filter Center-of-Mass Across-Track Error at  $t_i^+$  for Reflectivity Model With Low-Energy Laser Sweep and Without Plume Pogo

## *Appendix H. One-State Filter Performance Plots With Low-Energy Laser Sweep and Plume Pogo*

This appendix contains the one-state (center-of-mass) filter error plots for the case of a low-energy laser sweep and with the intensity centroid subjected to plume pogo. The center-of-mass errors are presented as a magnitude between the true center-of-mass and the filter estimated center-of-mass, the azimuth ( $x$ ) and elevation ( $y$ ) components of the magnitude error, and the along-track and across-track components of the magnitude error. The hardbody reflectivity model is used for the low-energy laser sweep plots, which are also representative of the hardbody binary plots. (The hardbody binary model is used for the single scan of the low-energy laser (i.e., no sweep), since the hardbody reflectivity model is software configured for a sweep routine.) For the discussion pertaining to these plots, refer to Chapter VI, Sections 6.5 and 6.7.

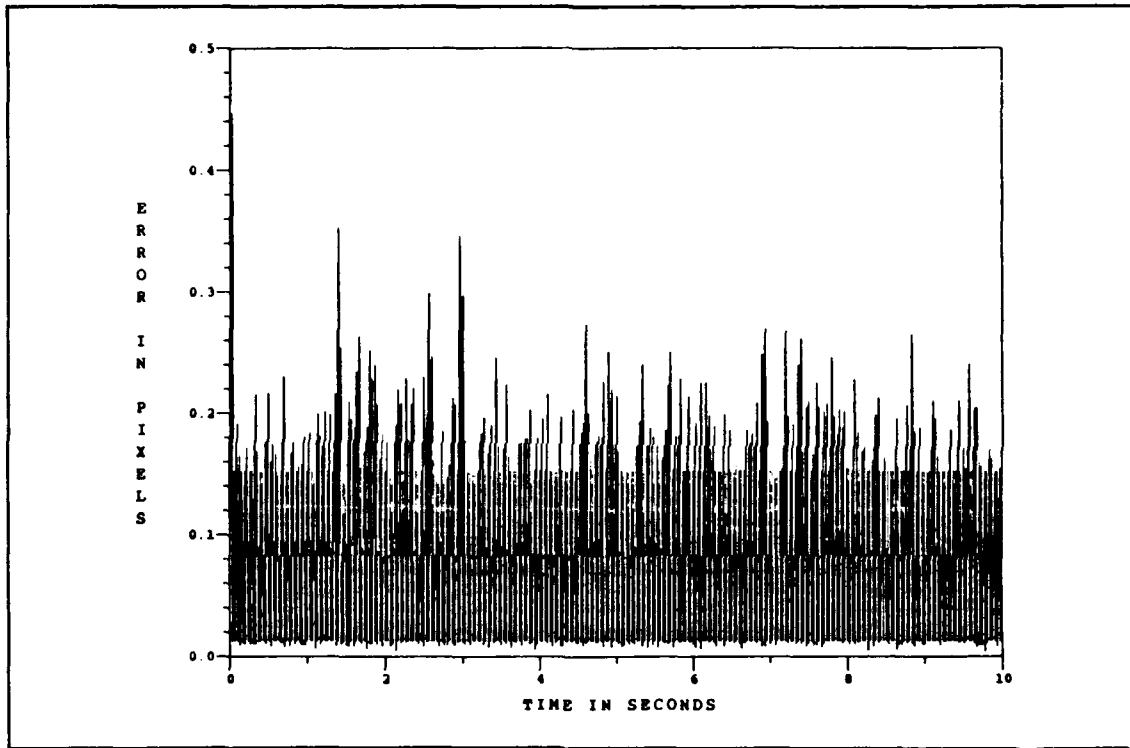


Figure H.1. One-State Filter vs. Actual rms Center-of-Mass Magnitude Error for Reflectivity Model With Low-Energy Laser Sweep and Plume Pogo

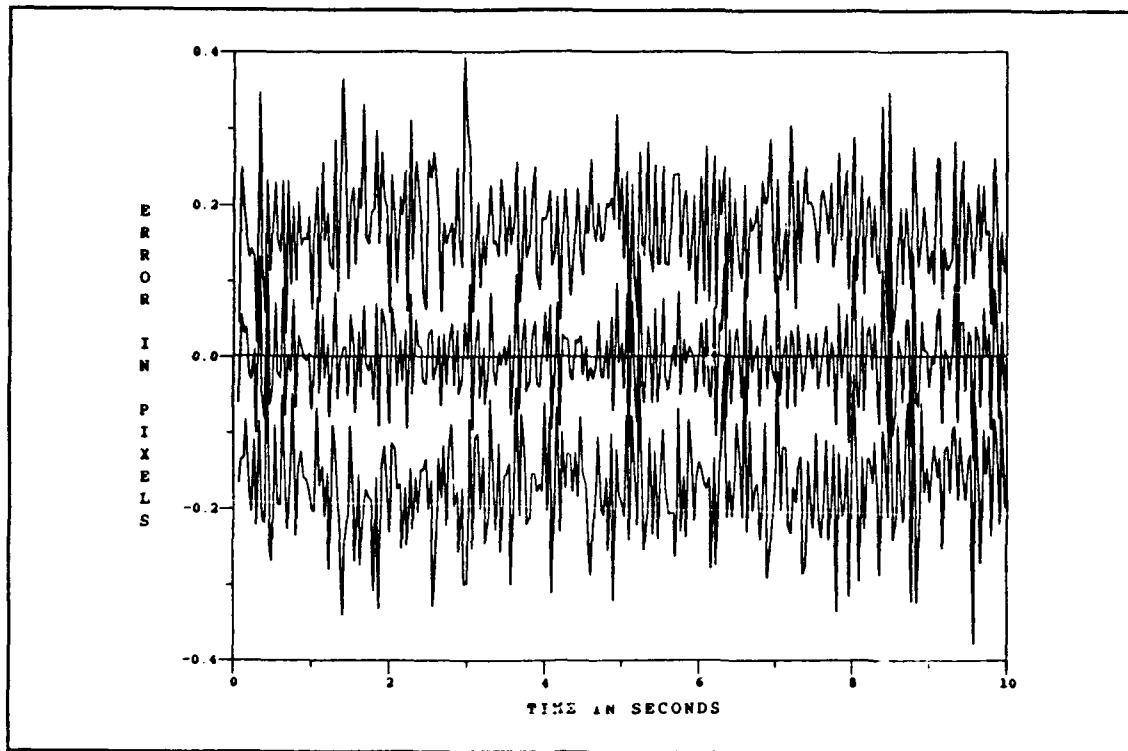


Figure H.2. One-State Filter Center-of-Mass Magnitude Error at  $t_i^-$  for Reflectivity Model With Low-Energy Laser Sweep and Plume Pogo

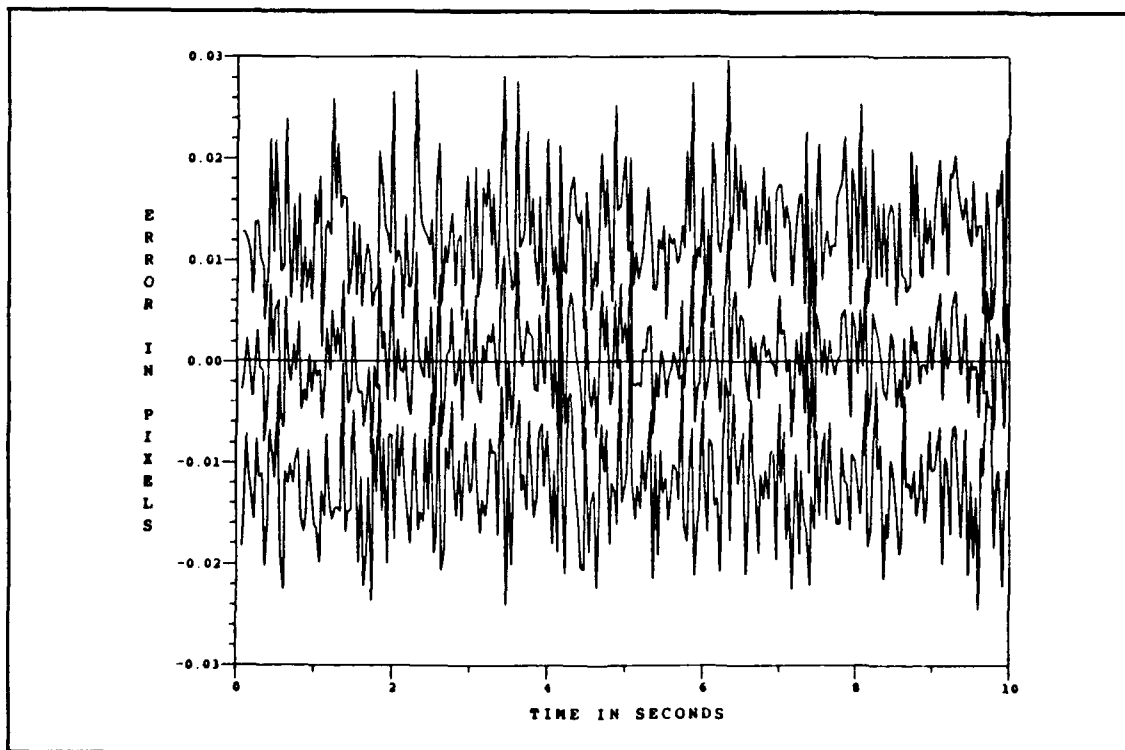


Figure H.3. One-State Filter Center-of-Mass Magnitude Error at  $t_i^+$  for Reflectivity Model With Low-Energy Laser Sweep and Plume Pogo

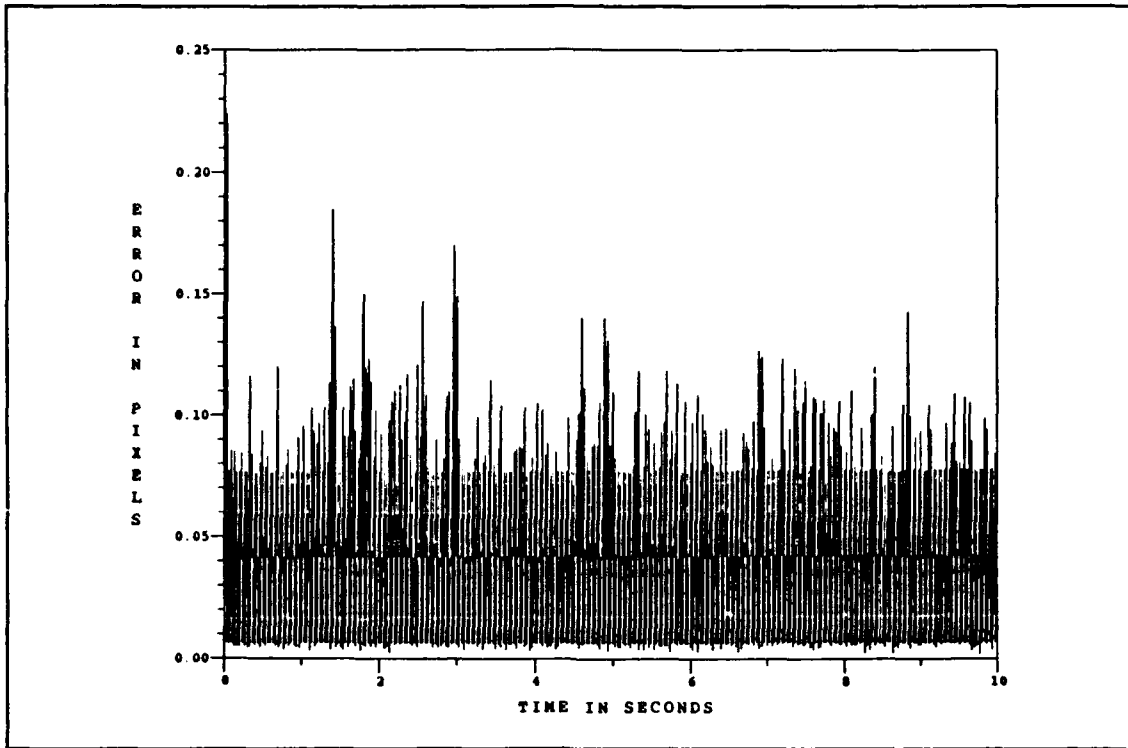


Figure H.4. One-State Filter vs. Actual rms Center-of-Mass Azimuth Error for Reflectivity Model With Low-Energy Laser Sweep and Plume Pogo

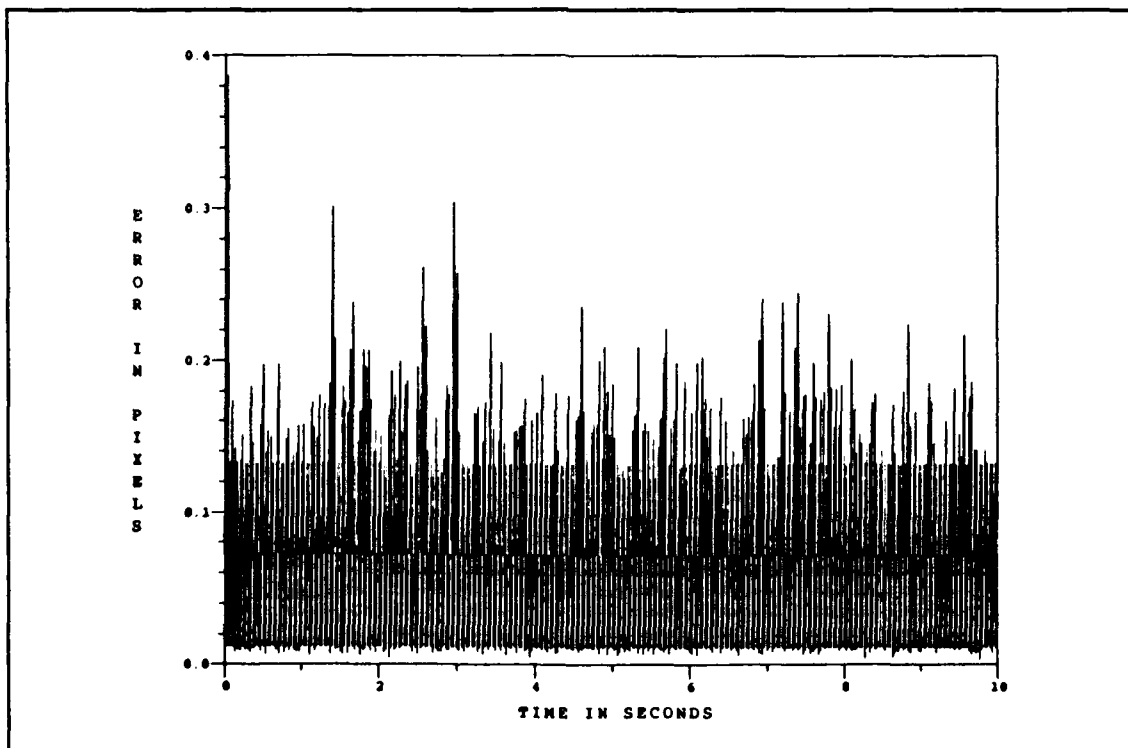


Figure H.5. One-State Filter vs. Actual rms Center-of-Mass Elevation Error for Reflectivity Model With Low-Energy Laser Sweep and Plume Pogo

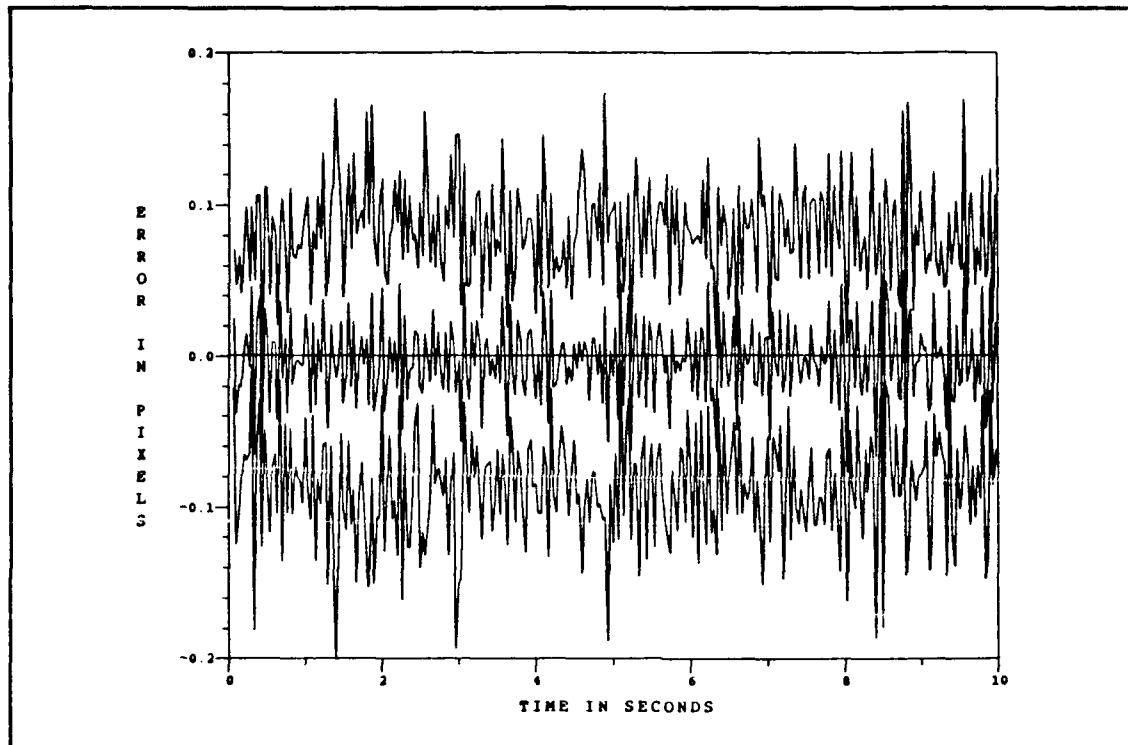


Figure H.6. One-State Filter Center-of-Mass Azimuth Error at  $t_i^-$  for Reflectivity Model With Low-Energy Laser Sweep and Plume Pogo

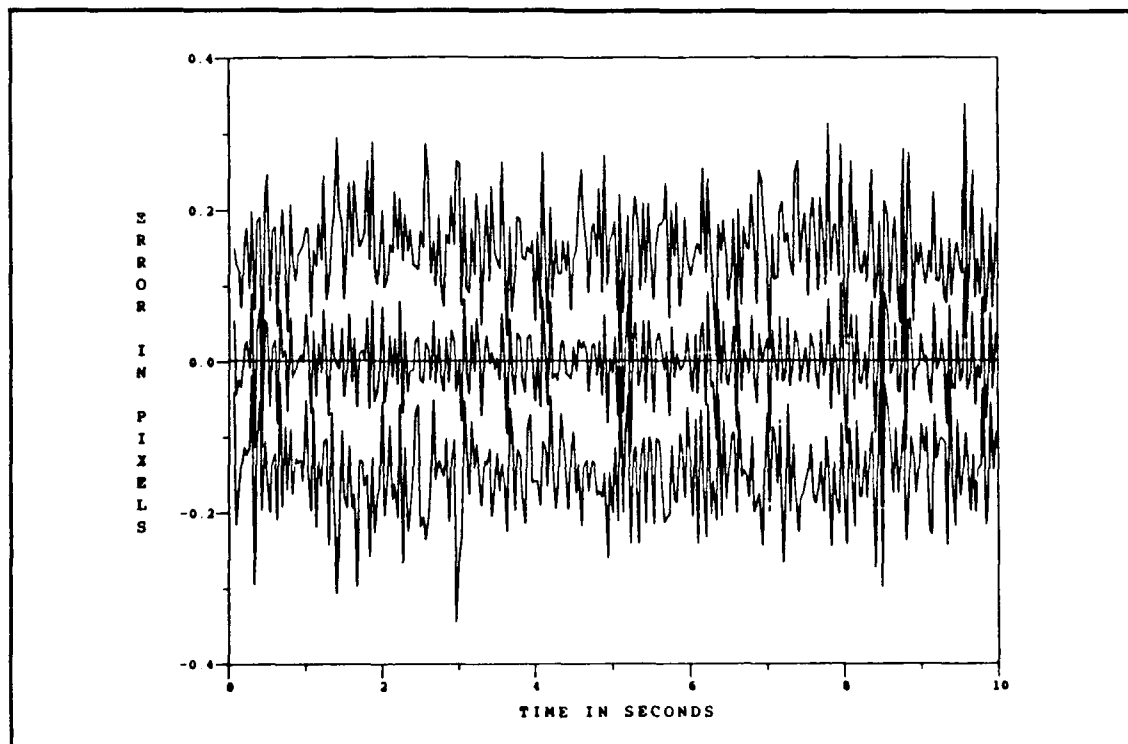


Figure H.7. One-State Filter Center-of-Mass Elevation Error at  $t_i^-$  for Reflectivity Model With Low-Energy Laser Sweep and Plume Pogo

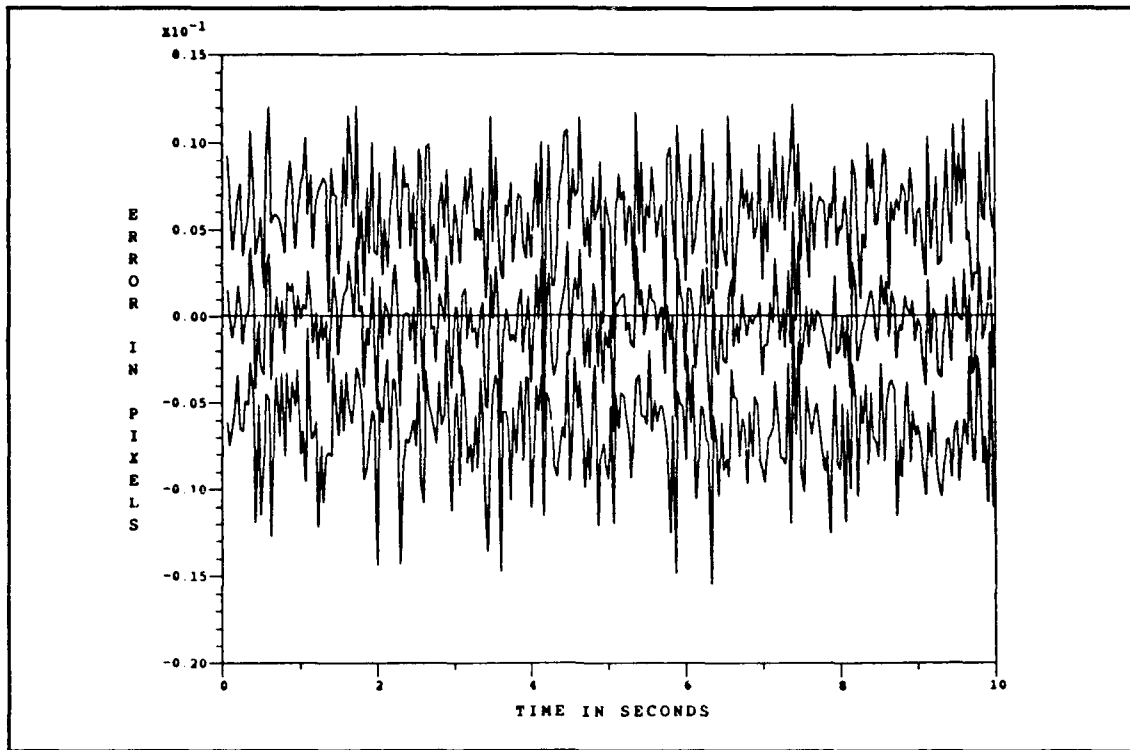


Figure H.8. One-State Filter Center-of-Mass Azimuth Error at  $t_i^+$  for Reflectivity Model With Low-Energy Laser Sweep and Plume Pogo

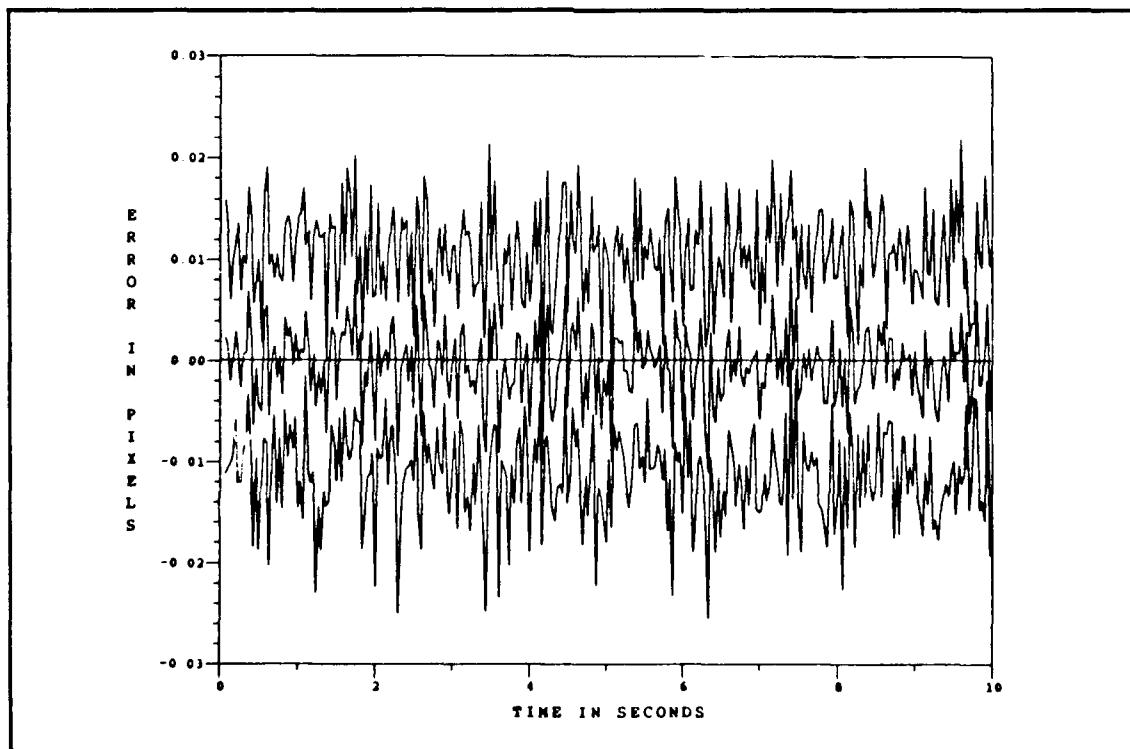


Figure H.9. One-State Filter Center-of-Mass Elevation Error at  $t_i^+$  for Reflectivity Model With Low-Energy Laser Sweep and Plume Pogo



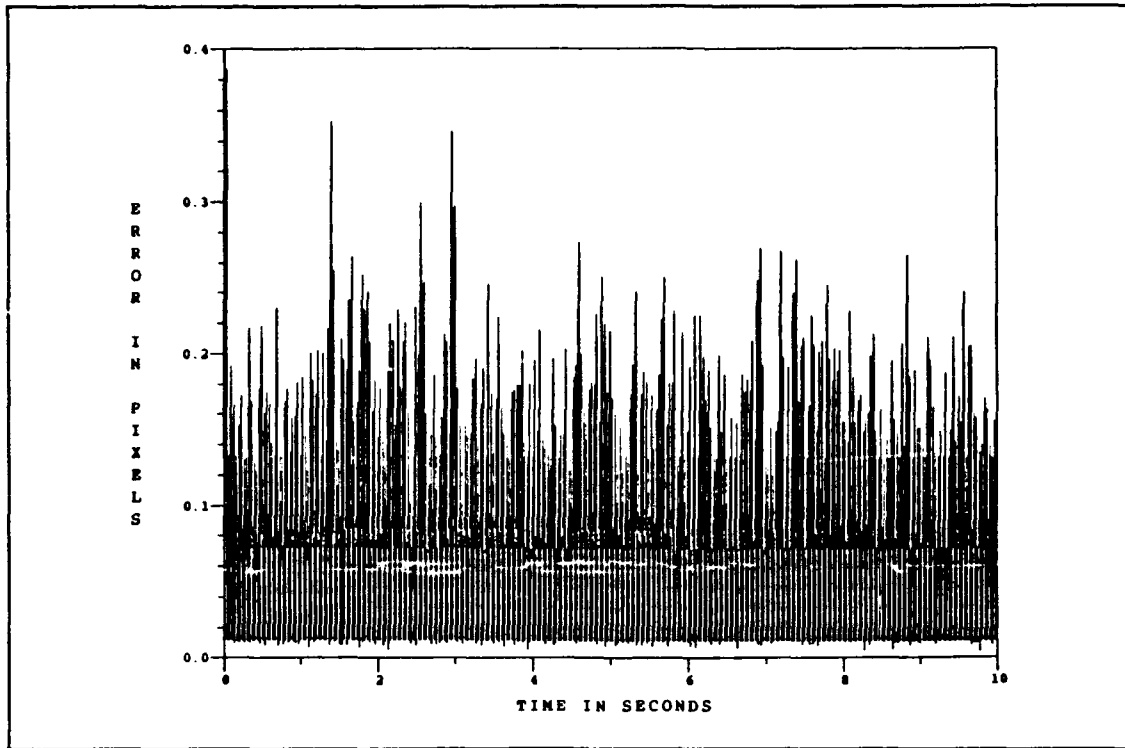


Figure H.10. One-State Filter vs. Actual rms Center-of-Mass Along-Track Error for Reflectivity Model With Low-Energy Laser Sweep and Plume Pogo

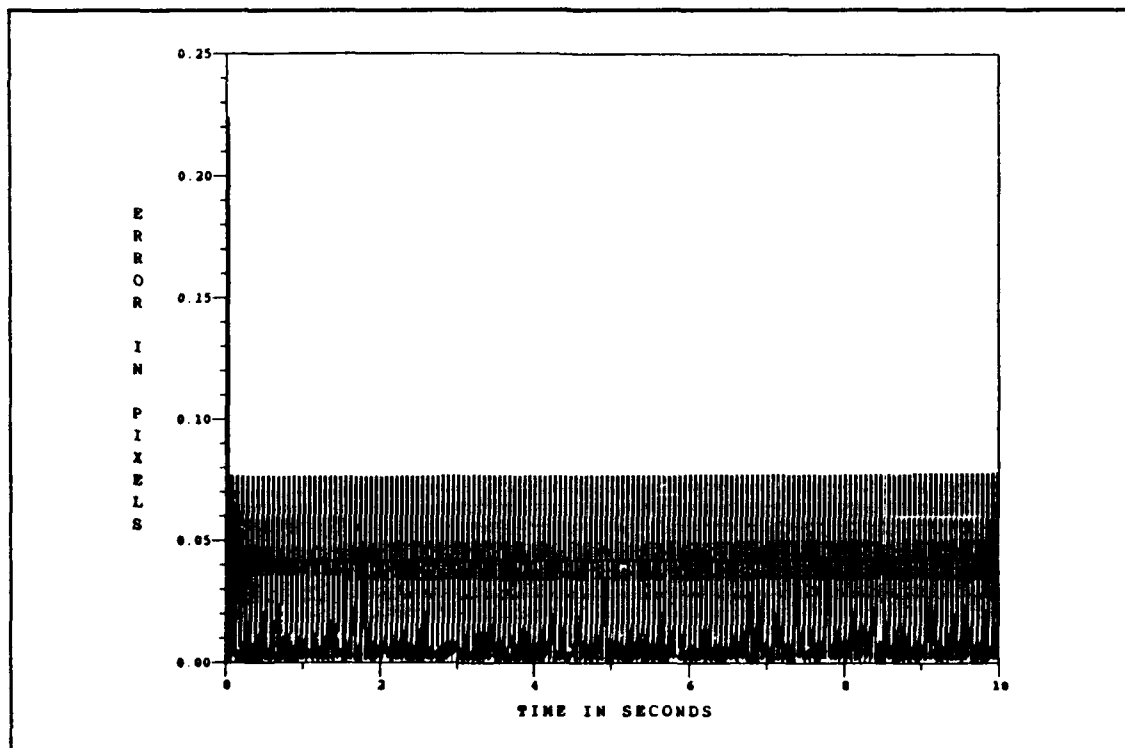


Figure H.11. One-State Filter vs. Actual rms Center-of-Mass Across-Track Error for Reflectivity Model With Low-Energy Laser Sweep and Plume Pogo

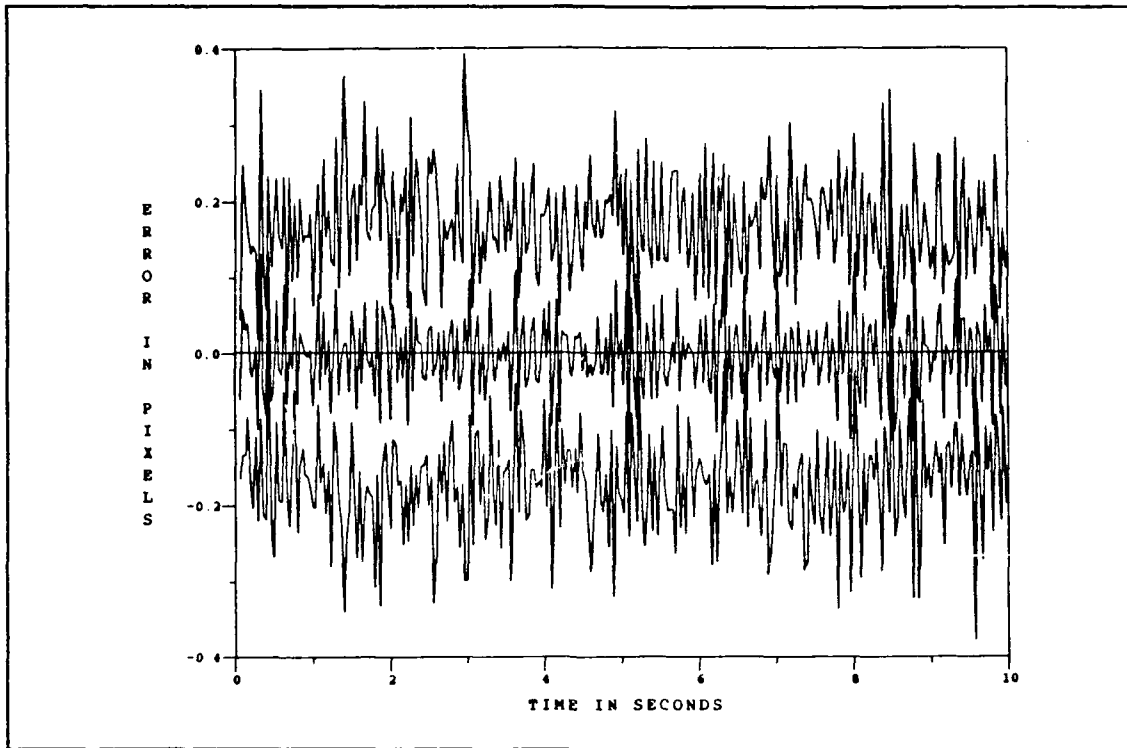


Figure H.12. One-State Filter Center-of-Mass Along-Track Error at  $t_i$  for Reflectivity Model With Low-Energy Laser Sweep and Plume Pogo

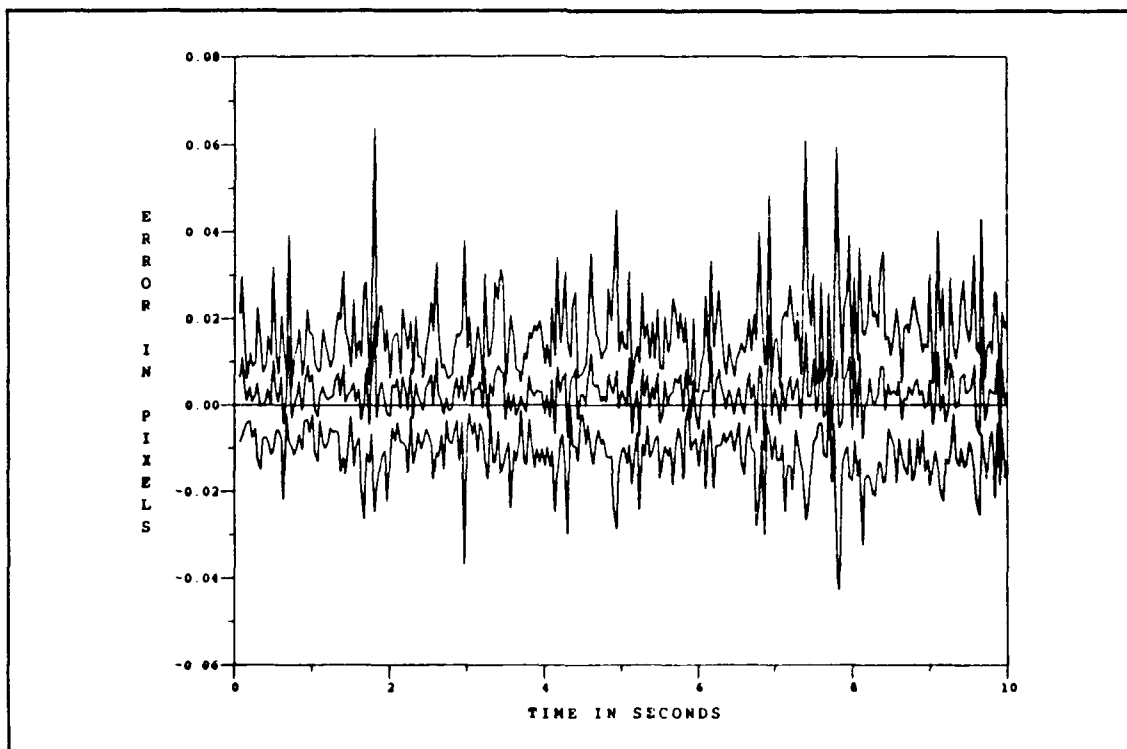


Figure H.13. One-State Filter Center-of-Mass Across-Track Error at  $t_i$  for Reflectivity Model With Low-Energy Laser Sweep and Plume Pogo

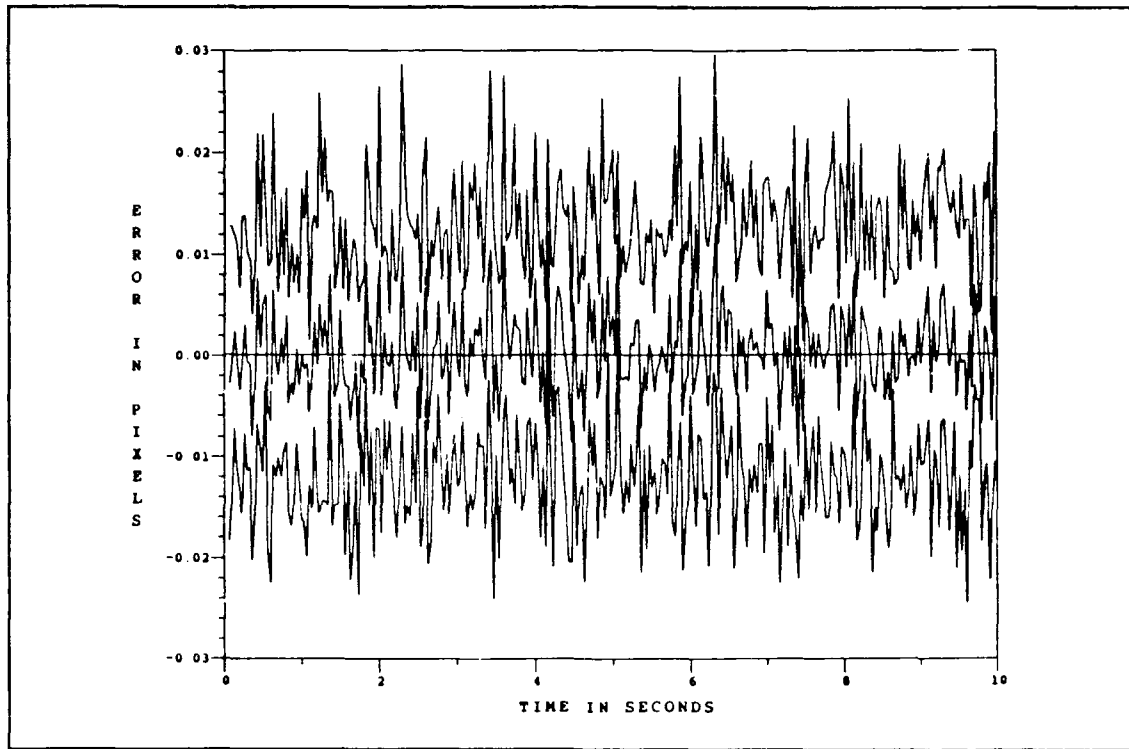


Figure H.14. One-State Filter Center-of-Mass Along-Track Error at  $t_i^+$  for Reflectivity Model With Low-Energy Laser Sweep and Plume Pogo

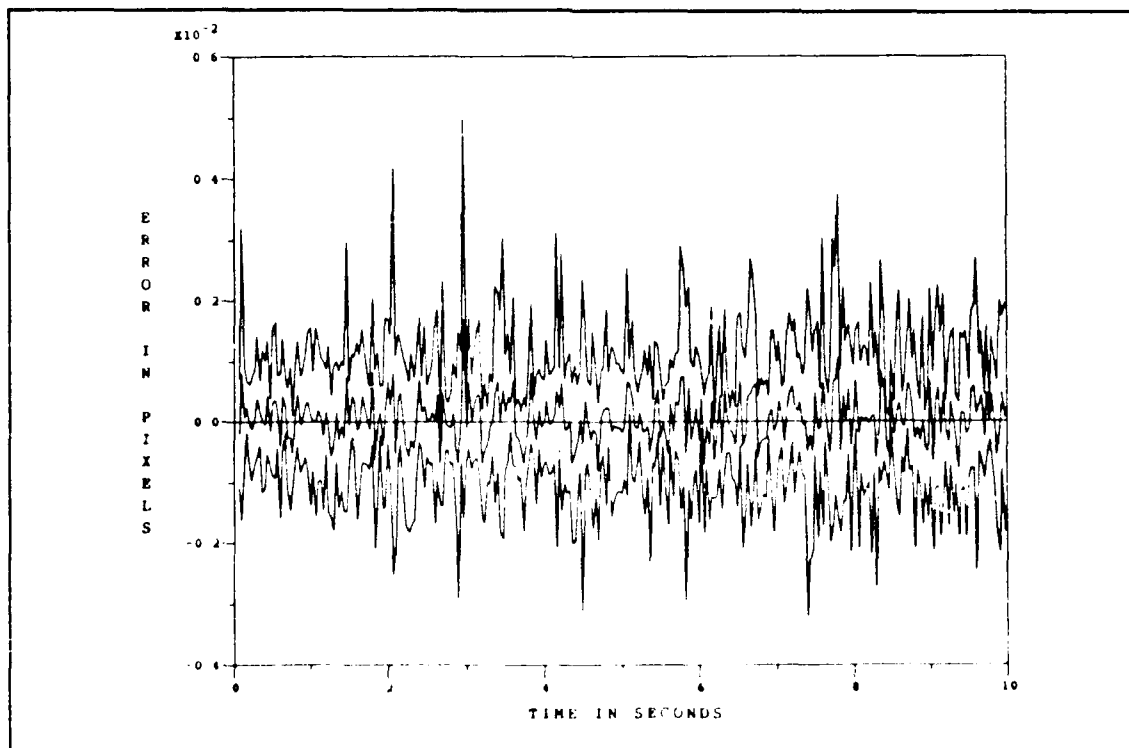


Figure H.15. One-State Filter Center-of-Mass Across-Track Error at  $t_i^+$  for Reflectivity Model With Low-Energy Laser Sweep and Plume Pogo

## *Appendix I. Eight-State Filter Performance Plots Without Low-Energy Laser Sweep and Plume Pogo*

This appendix contains the eight-state (center-of-mass) filter error plots for the case of no low-energy laser sweep and with no plume pogo of the intensity centroid. The center-of-mass errors are presented as the azimuth ( $x$ ) and elevation ( $y$ ) components of the error, and the along-track and across-track components of the error. The hardbody binary model is used for the single scan of the low-energy laser (i.e., no sweep), since the hardbody reflectivity model is software configured for a sweep routine; (The hardbody reflectivity model is used for the low-energy laser sweep plots, which are also representative of the hardbody binary plots.) For the discussion pertaining to these plots, refer to Chapter VI, Sections 6.6 and 6.7.

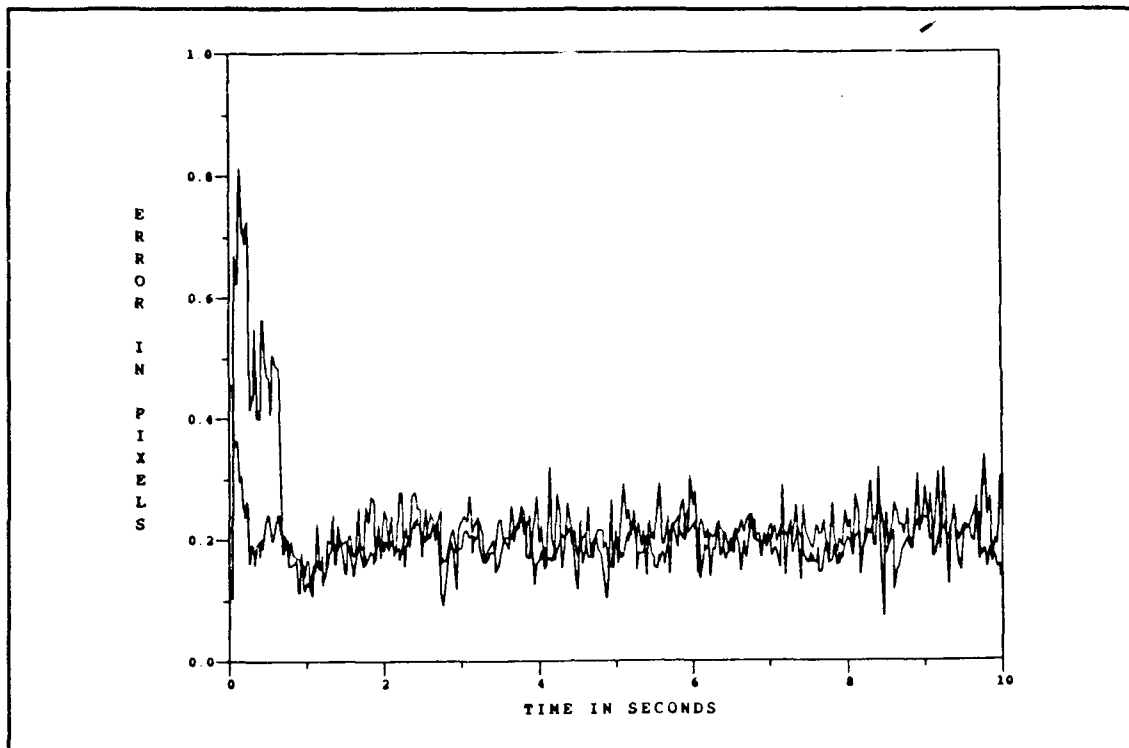


Figure I.1. Eight-State Filter vs. Actual rms Center-of-Mass Azimuth Error for Binary Model Without Low-Energy Laser Sweep and Plume Pogo

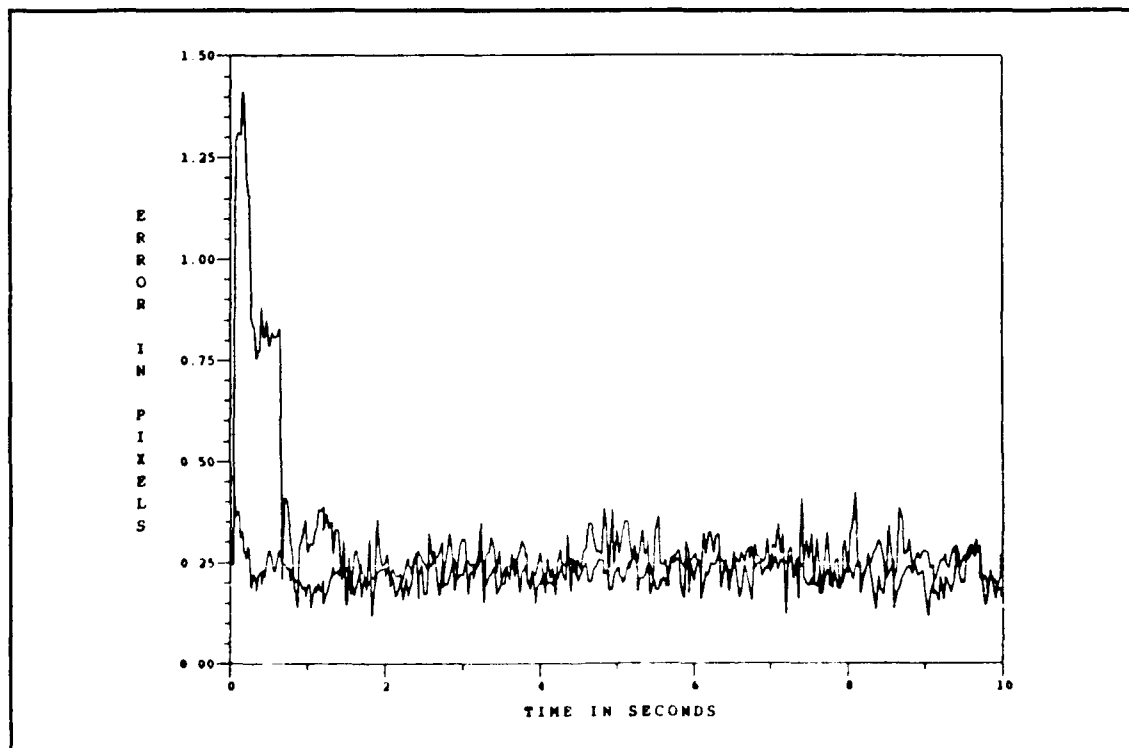


Figure I.2. Eight-State Filter vs. Actual rms Center-of-Mass Elevation Error for Binary Model Without Low-Energy Laser Sweep and Plume Pogo

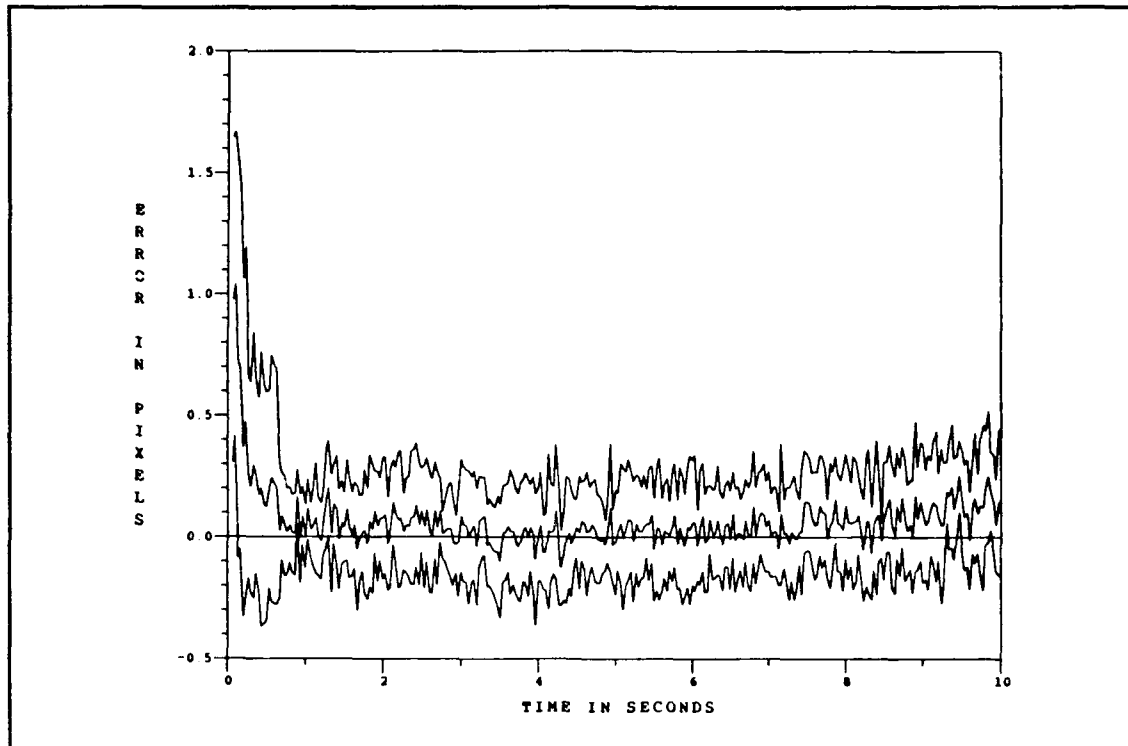


Figure I.3. Eight-State Filter Center-of-Mass Azimuth Error at  $t_i^-$  for Binary Model Without Low-Energy Laser Sweep and Plume Pogo

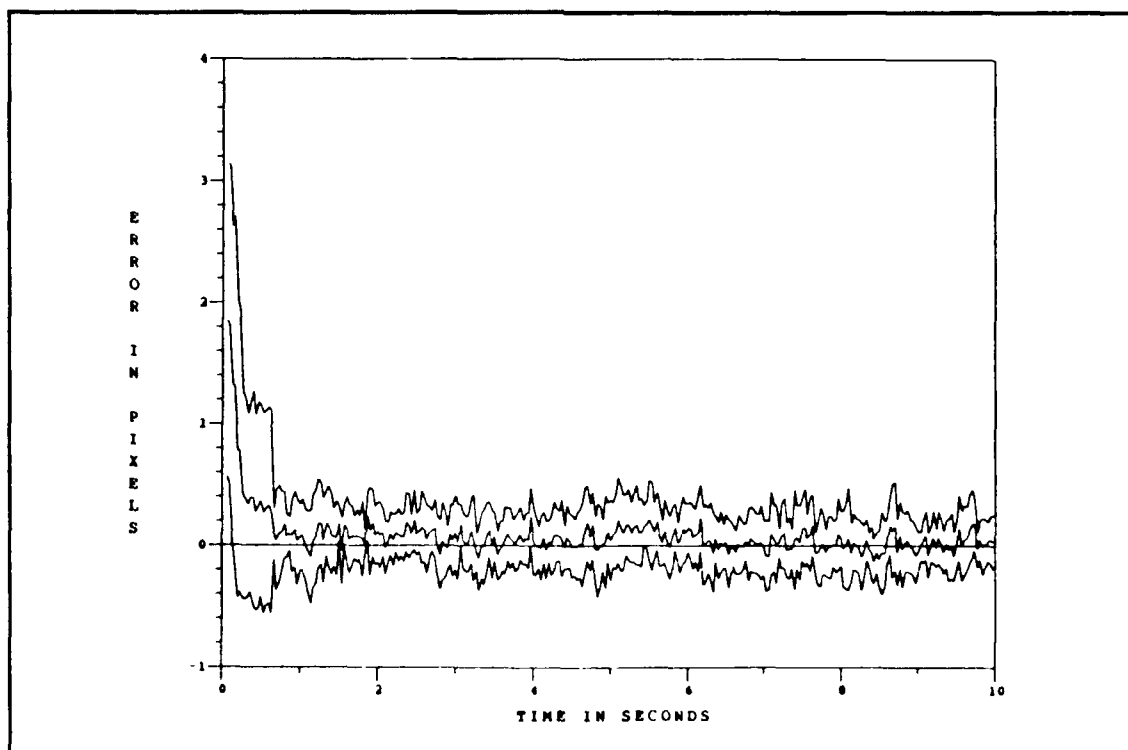


Figure I.4. Eight-State Filter Center-of-Mass Elevation Error at  $t_i^-$  for Binary Model Without Low-Energy Laser Sweep and Plume Pogo

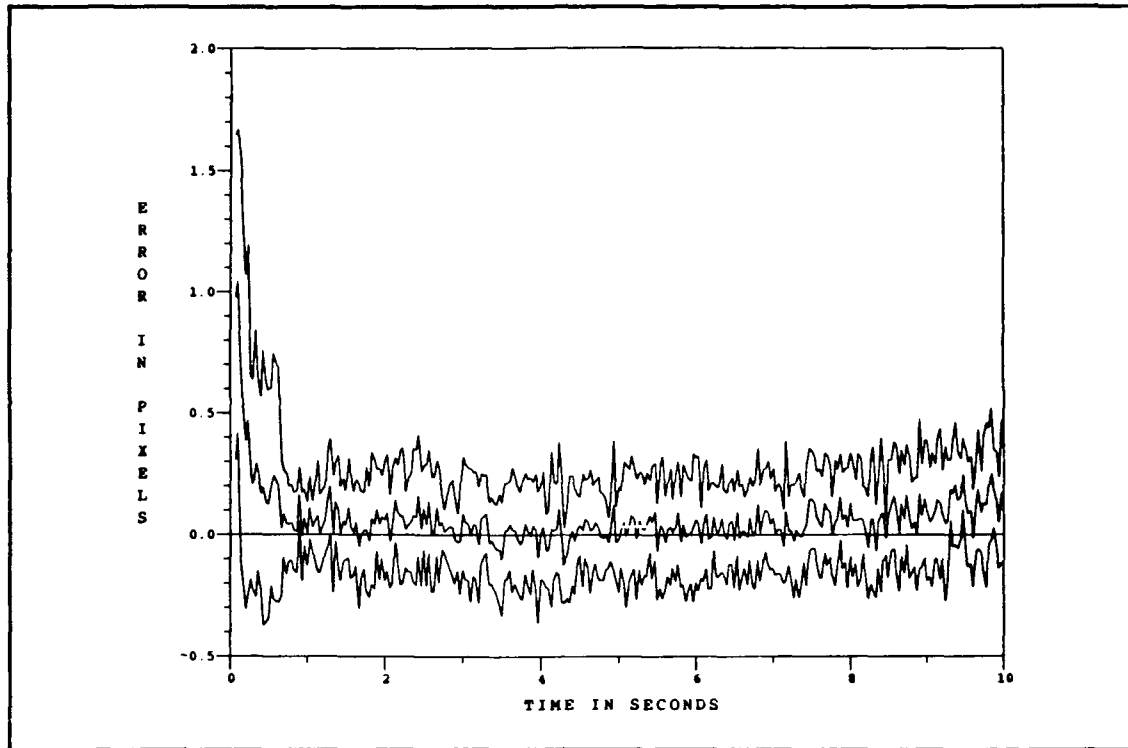


Figure I.5. Eight-State Filter Center-of-Mass Azimuth Error at  $t_i^+$  for Binary Model Without Low-Energy Laser Sweep and Plume Pogo

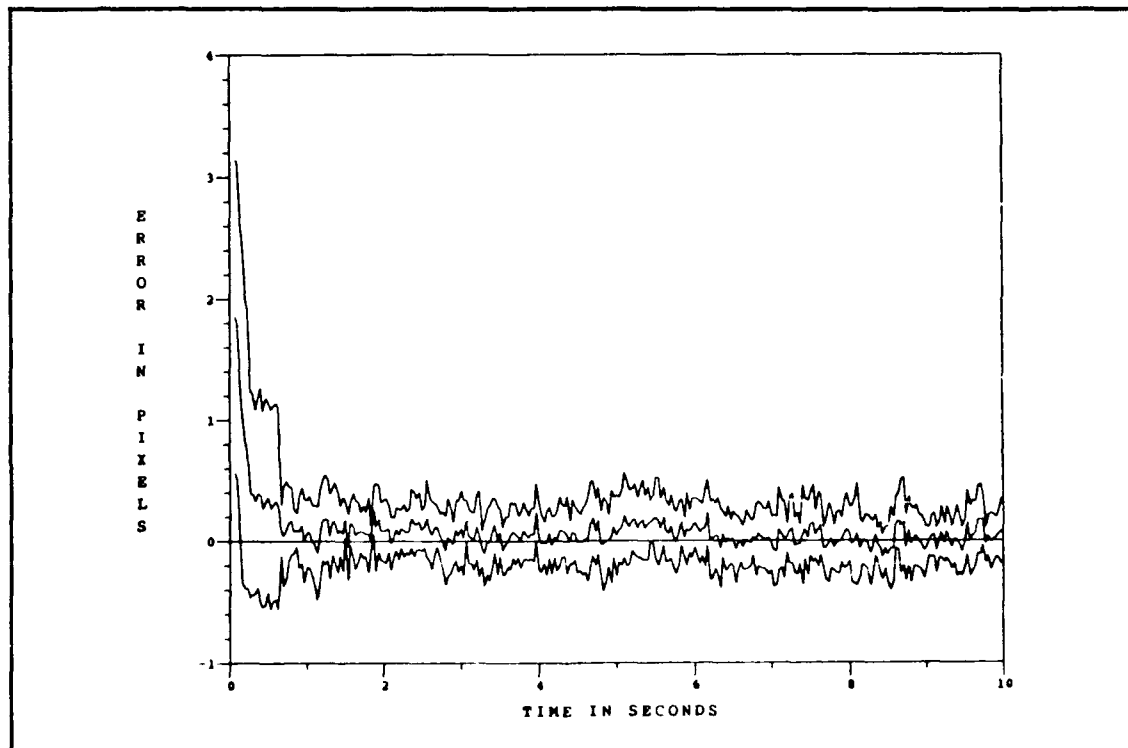


Figure I.6. Eight-State Filter Center-of-Mass Elevation Error at  $t_i^+$  for Binary Model Without Low-Energy Laser Sweep and Plume Pogo

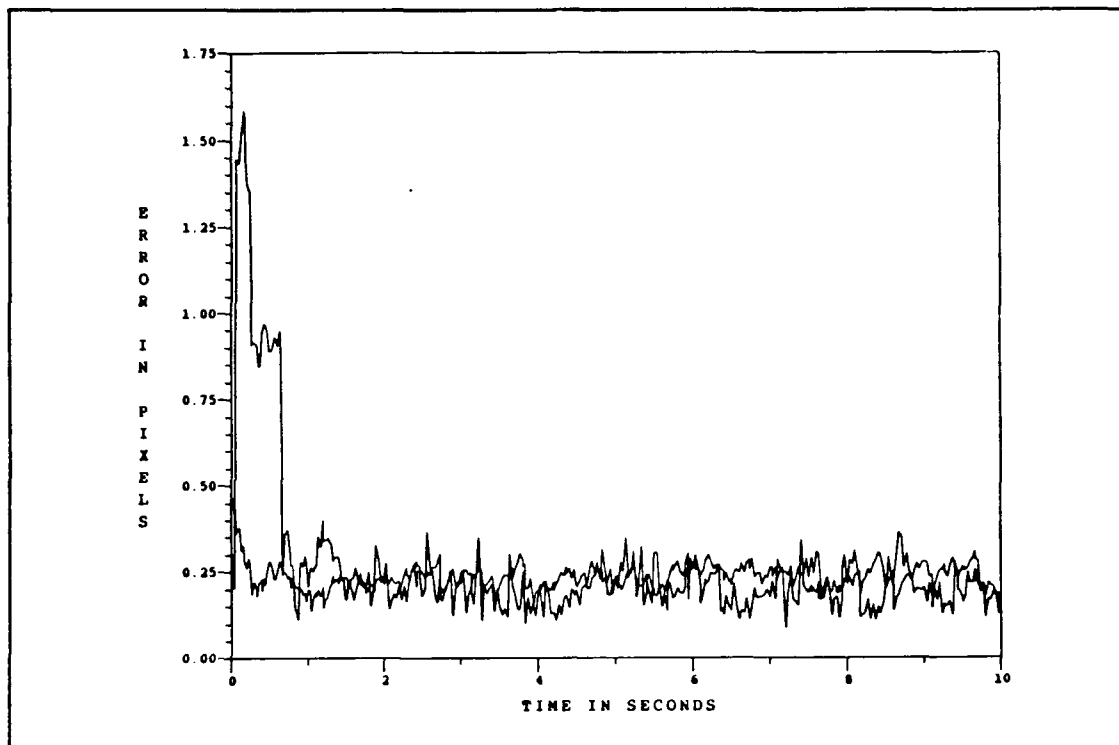


Figure I.7. Eight-State Filter vs. Actual rms Center-of-Mass Along-Track Error for Binary Model Without Low-Energy Laser Sweep and Plume Pogo

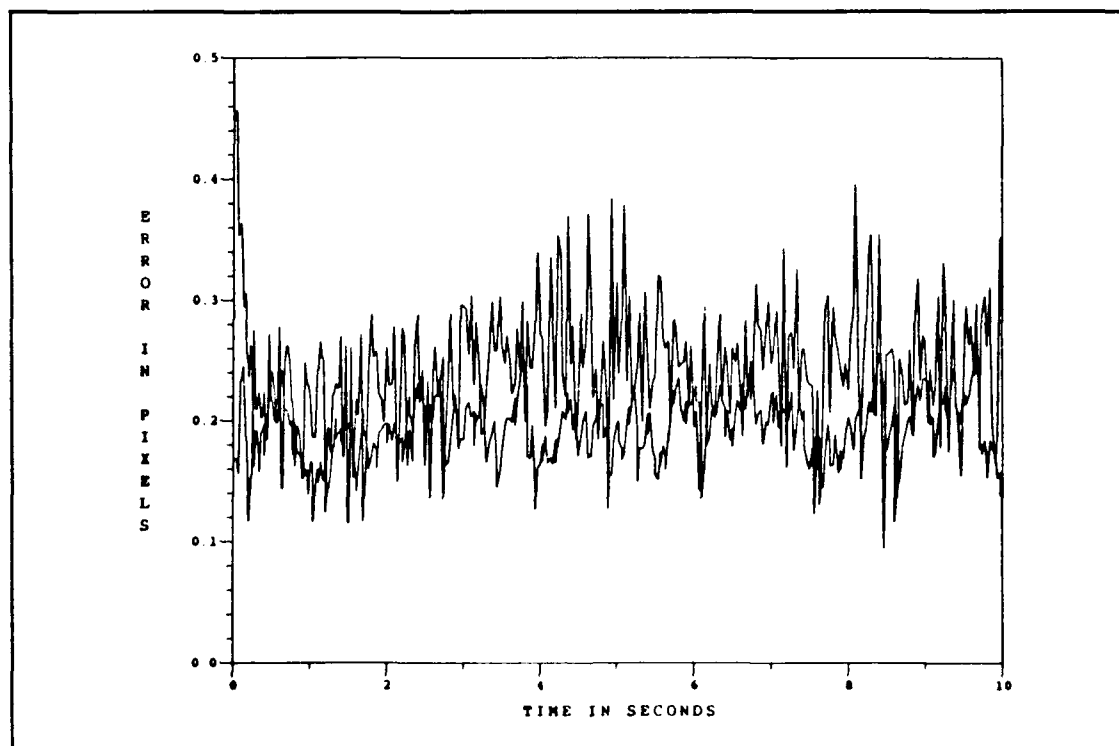


Figure I.8. Eight-State Filter vs. Actual rms Center-of-Mass Across-Track Error for Binary Model Without Low-Energy Laser Sweep and Plume Pogo



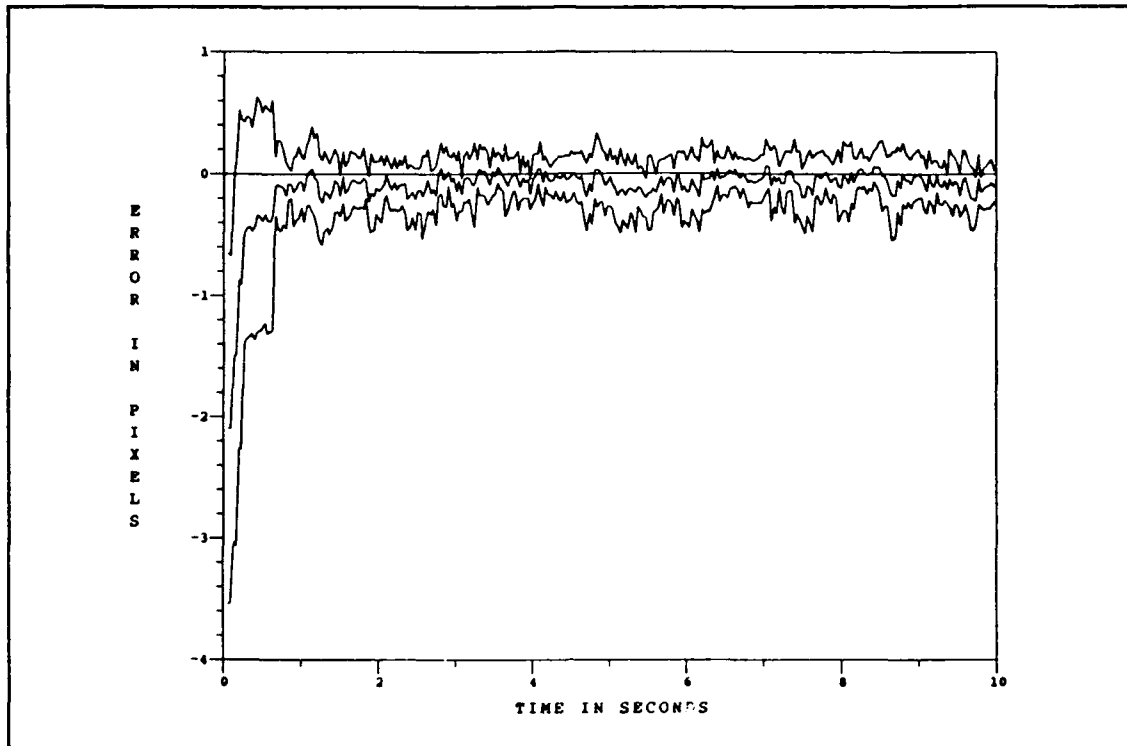


Figure I.9. Eight-State Filter Center-of-Mass Along-Track Error at  $t_i^-$  for Binary Model Without Low-Energy Laser Sweep and Plume Pogo

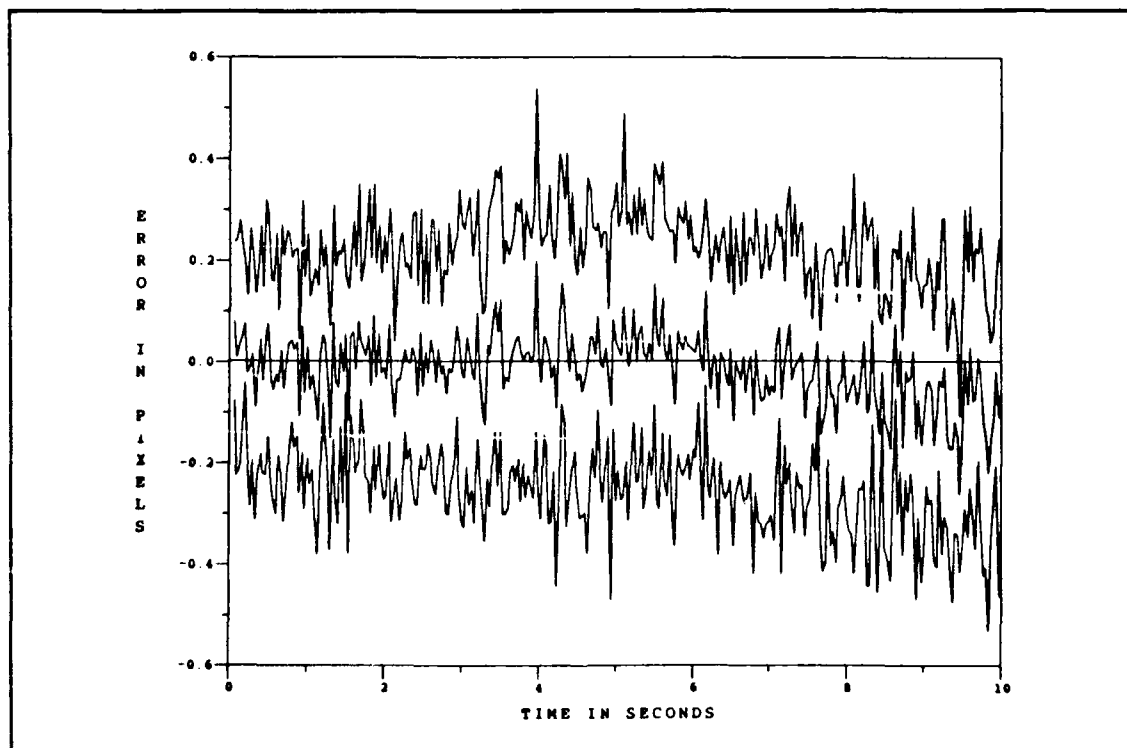


Figure I.10. Eight-State Filter Center-of-Mass Across-Track Error at  $t_i^-$  for Binary Model Without Low-Energy Laser Sweep and Plume Pogo

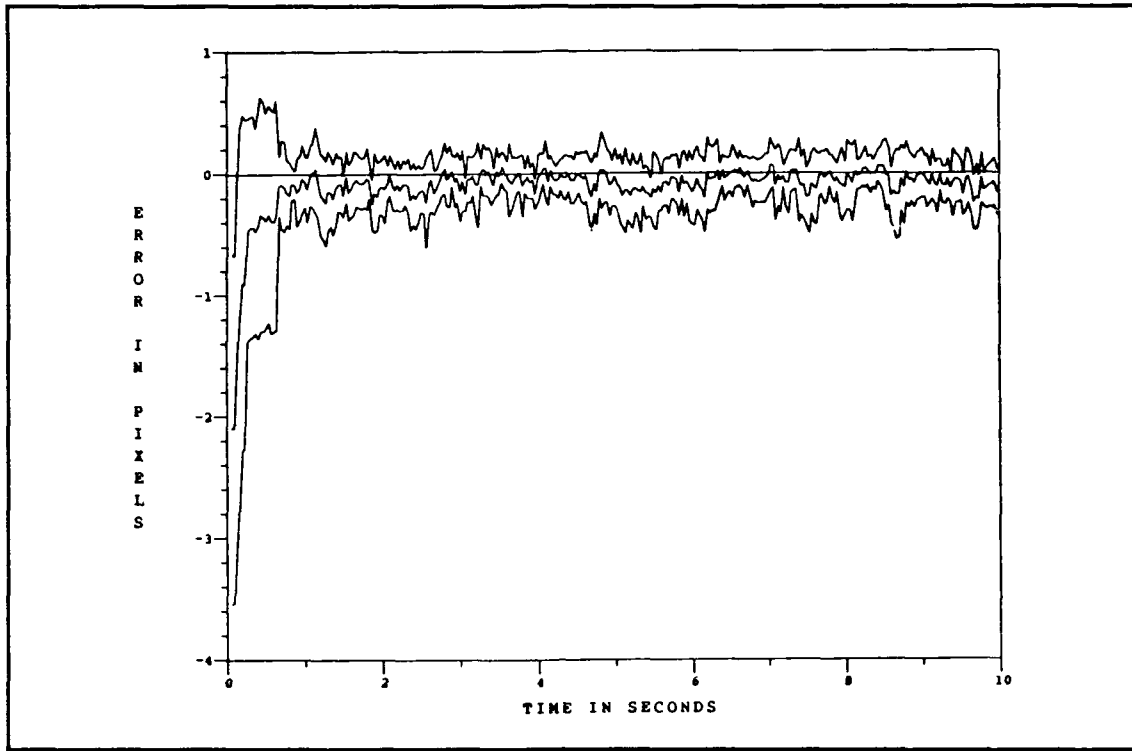


Figure I.11. Eight-State Filter Center-of-Mass Along-Track Error at  $t_i^+$  for Binary Model Without Low-Energy Laser Sweep and Plume Pogo

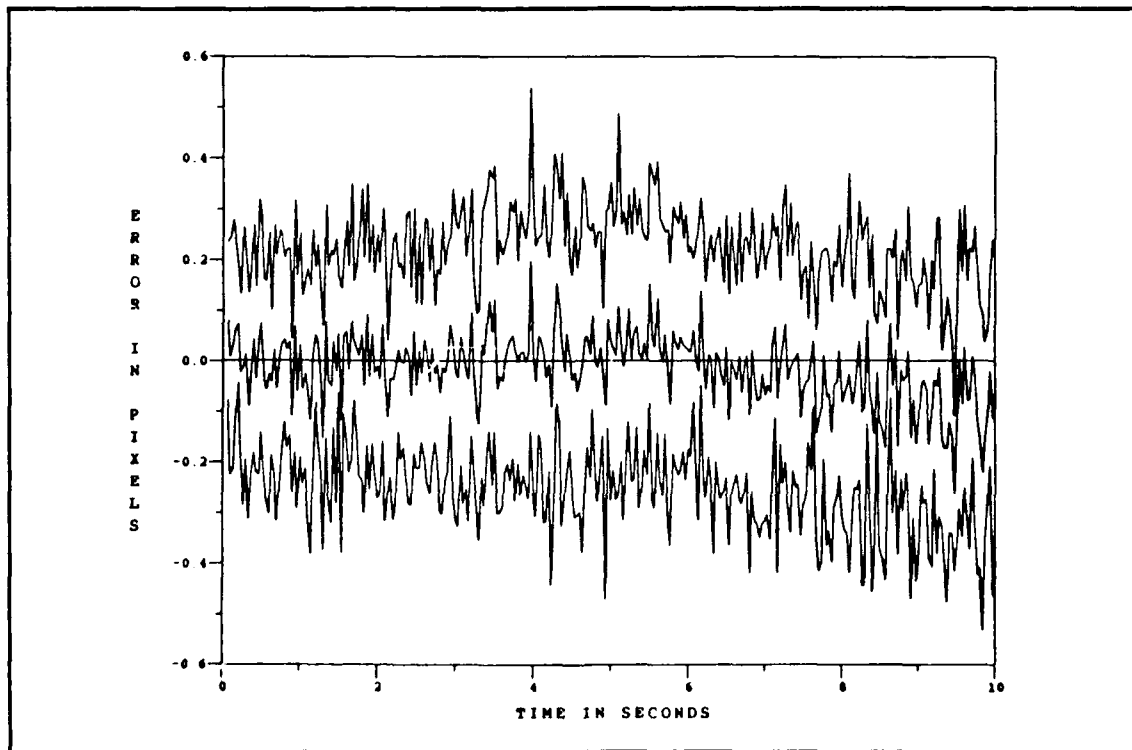


Figure I.12. Eight-State Filter Center-of-Mass Across-Track Error at  $t_i^+$  for Binary Model Without Low-Energy Laser Sweep and Plume Pogo

## *Appendix J. Eight-State Filter Performance Plots Without Low-Energy Laser Sweep and With Plume Pogo*

This appendix contains the eight-state (center-of-mass) filter error plots for the case of no low-energy laser sweep and with the intensity centroid subjected to plume pogo. The center-of-mass errors are presented as the azimuth ( $x$ ) and elevation ( $y$ ) components of the error, and the along-track and across-track components of the error. The hardbody binary model is used for the single scan of the low-energy laser (i.e., no sweep), since the hardbody reflectivity model is software configured for a sweep routine; (The hardbody reflectivity model is used for the low-energy laser sweep plots, which are also representative of the hardbody binary plots.) For the discussion pertaining to these plots, refer to Chapter VI, Sections 6.6 and 6.7.

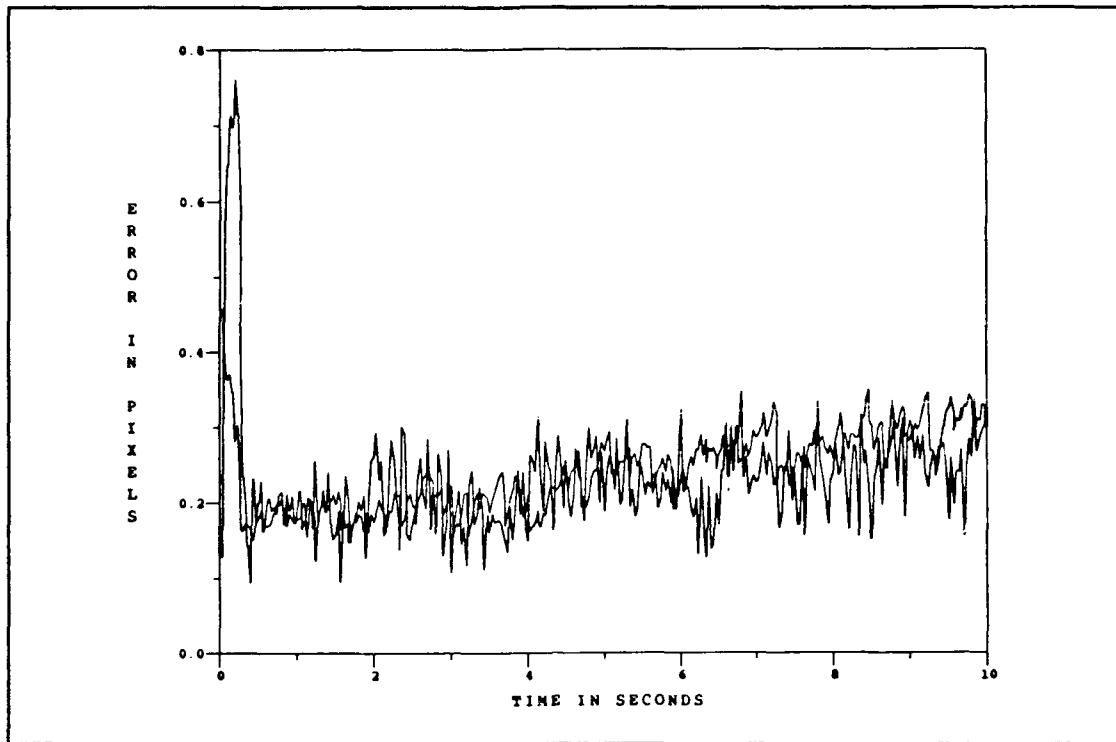


Figure J.1. Eight-State Filter vs. Actual rms Center-of-Mass Azimuth Error for Binary Model Without Low-Energy Laser Sweep and With Plume Pogo

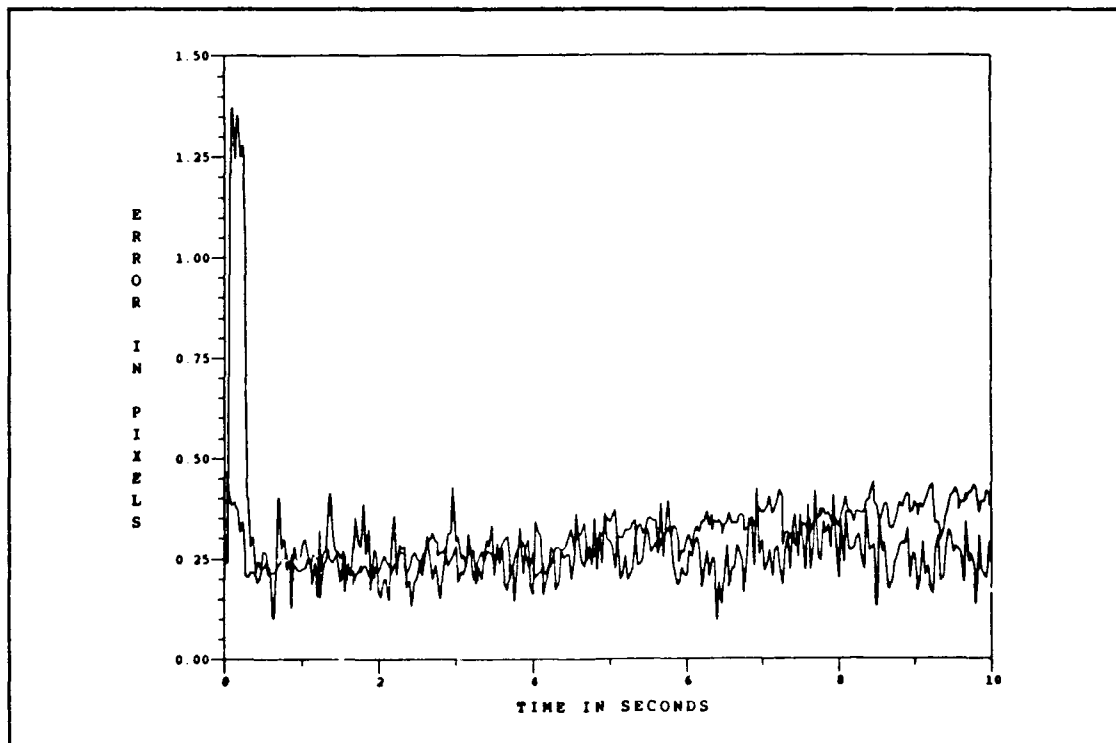


Figure J.2. Eight-State Filter vs. Actual rms Center-of-Mass Elevation Error for Binary Model Without Low-Energy Laser Sweep and With Plume Pogo

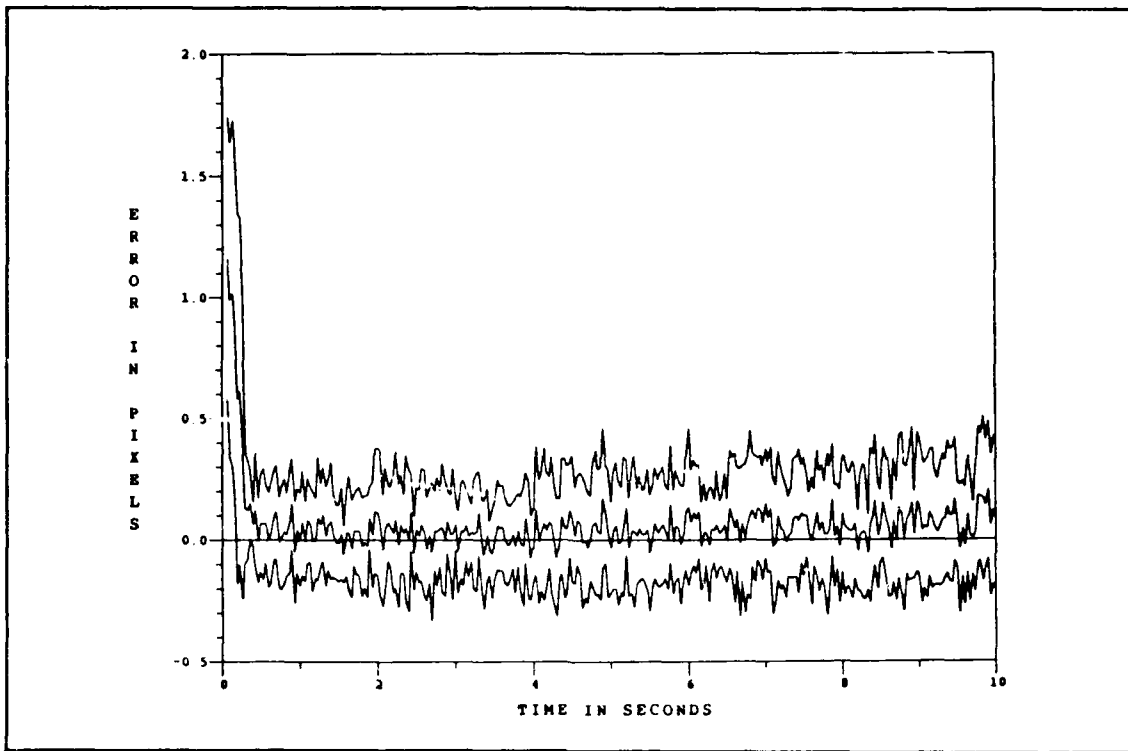


Figure J.3. Eight-State Filter Center-of-Mass Azimuth Error at  $t_i^-$  for Binary Model Without Low-Energy Laser Sweep and With Plume Pogo

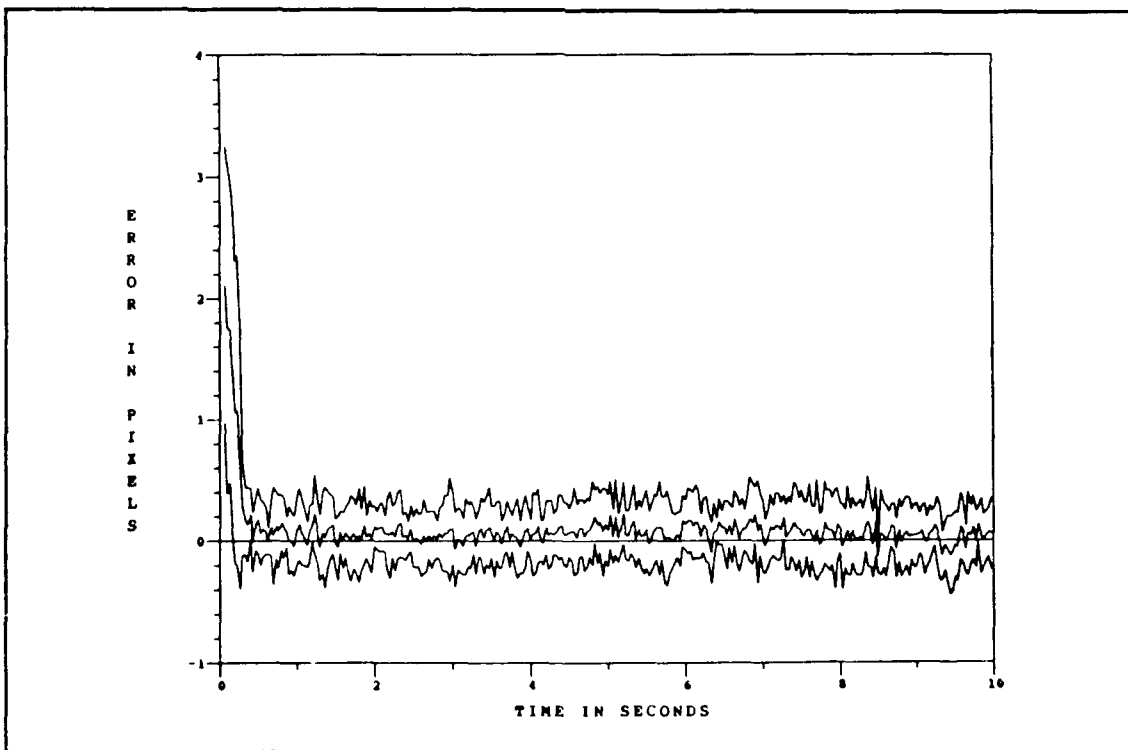


Figure J.4. Eight-State Filter Center-of-Mass Elevation Error at  $t_i^-$  for Binary Model Without Low-Energy Laser Sweep and With Plume Pogo

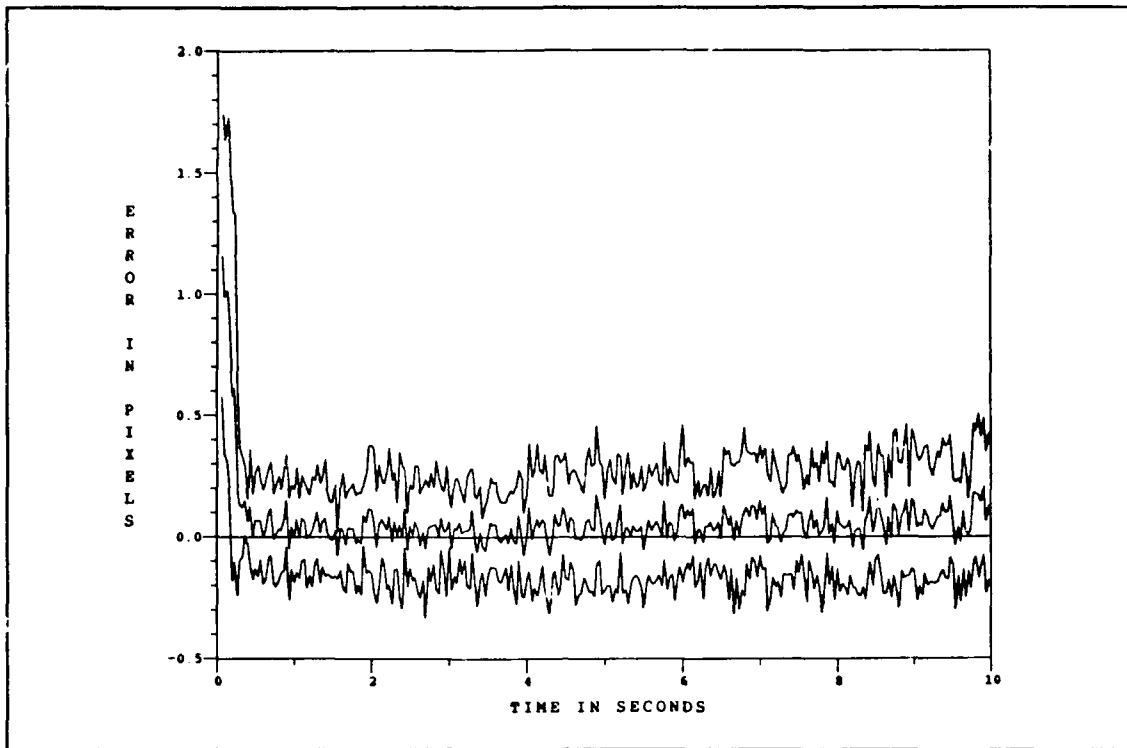


Figure J.5. Eight-State Filter Center-of-Mass Azimuth Error at  $t_i^+$  for Binary Model Without Low-Energy Laser Sweep and With Plume Pogo

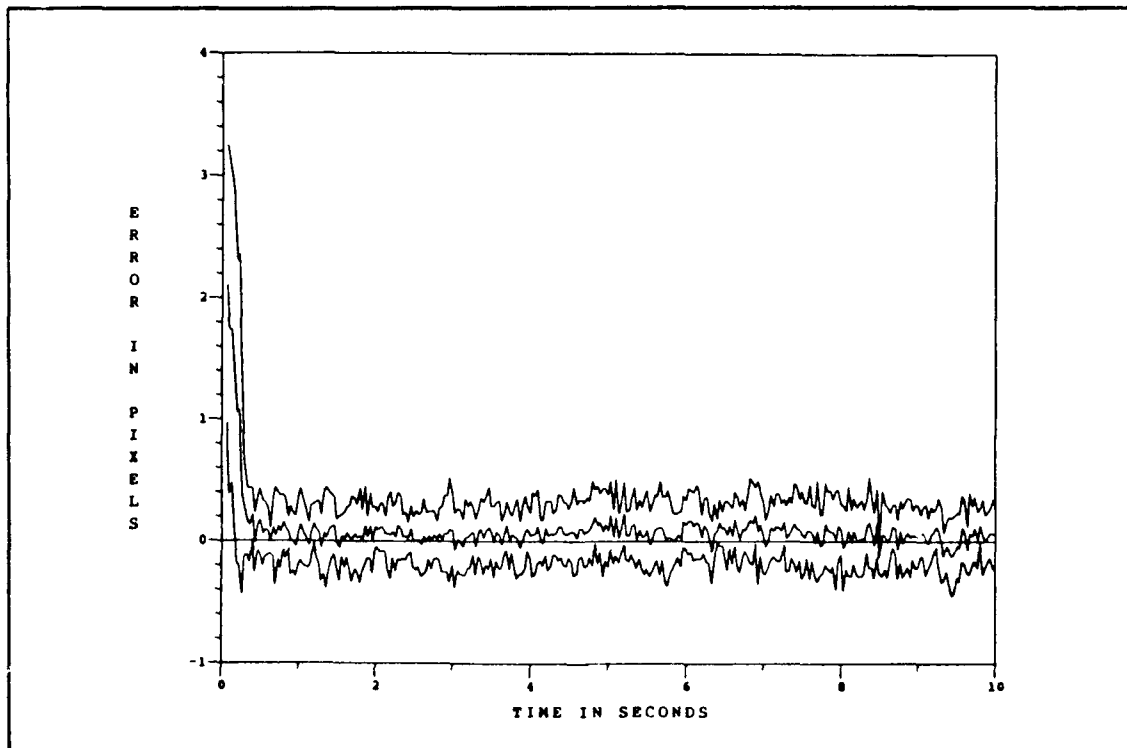


Figure J.6. Eight-State Filter Center-of-Mass Elevation Error at  $t_i^+$  for Binary Model Without Low-Energy Laser Sweep and With Plume Pogo

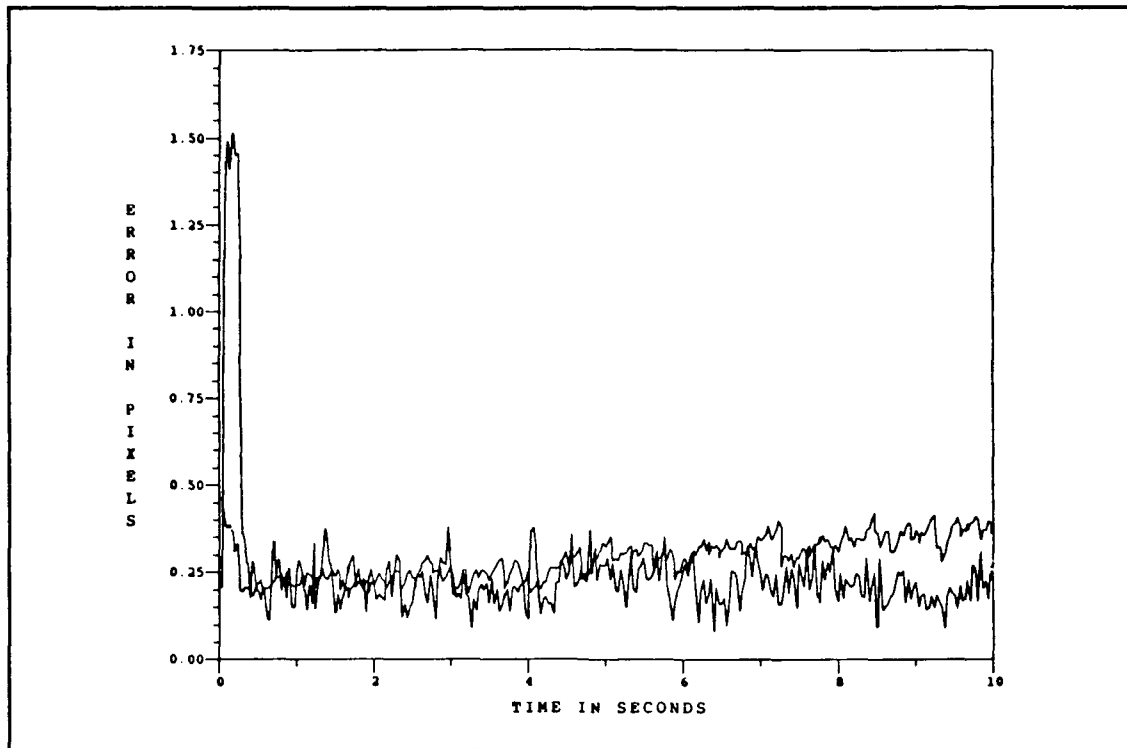


Figure J.7. Eight-State Filter vs. Actual rms Center-of-Mass Along-Track Error for Binary Model Without Low-Energy Laser Sweep and With Plume Pogo

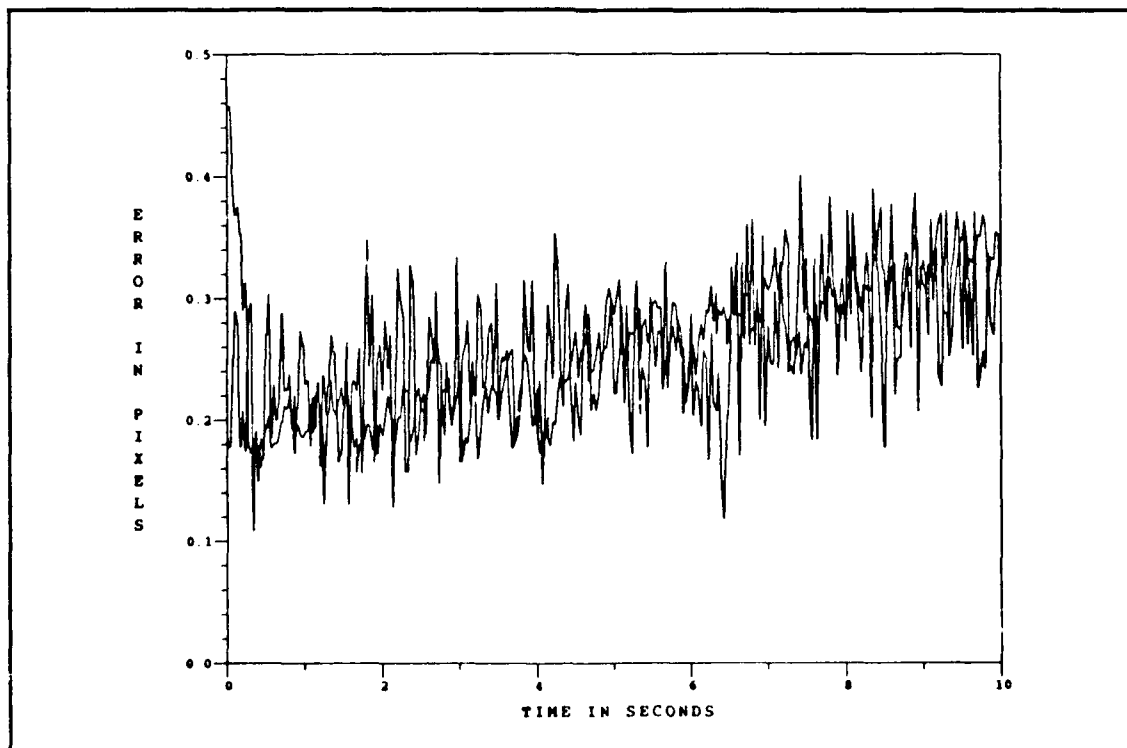


Figure J.8. Eight-State Filter vs. Actual rms Center-of-Mass Across-Track Error for Binary Model Without Low-Energy Laser Sweep and With Plume Pogo

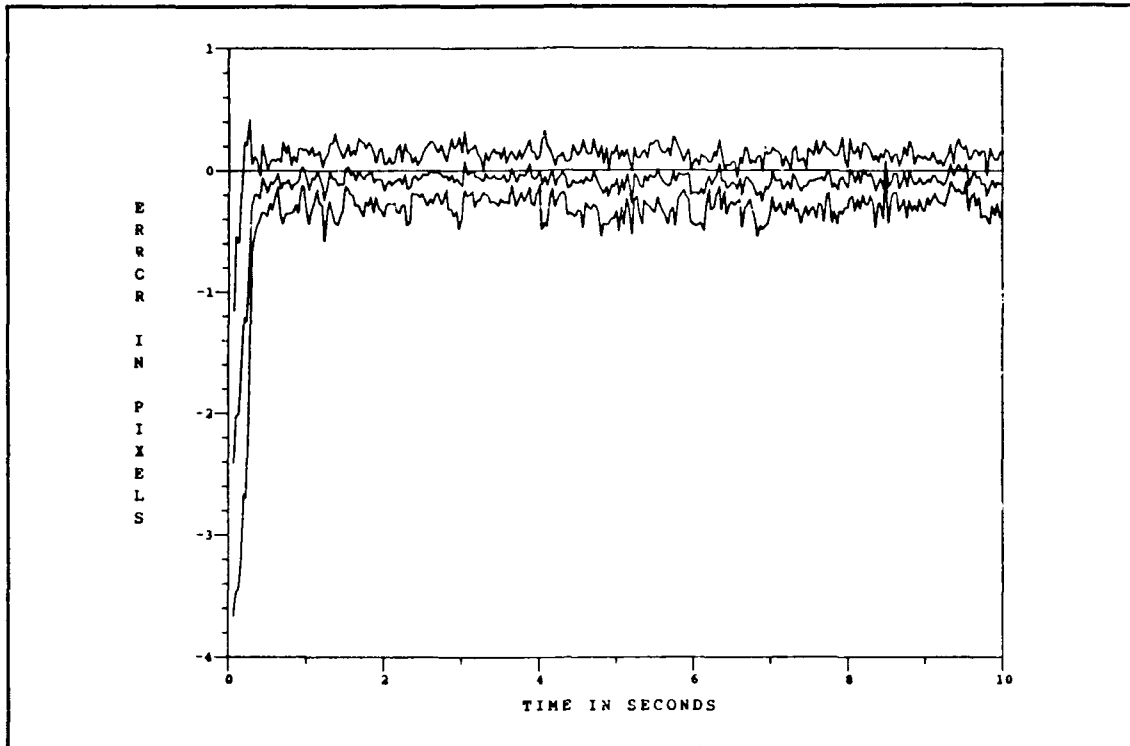


Figure J.9. Eight-State Filter Center-of-Mass Along-Track Error at  $t_i^-$  for Binary Model Without Low-Energy Laser Sweep and With Plume Pogo

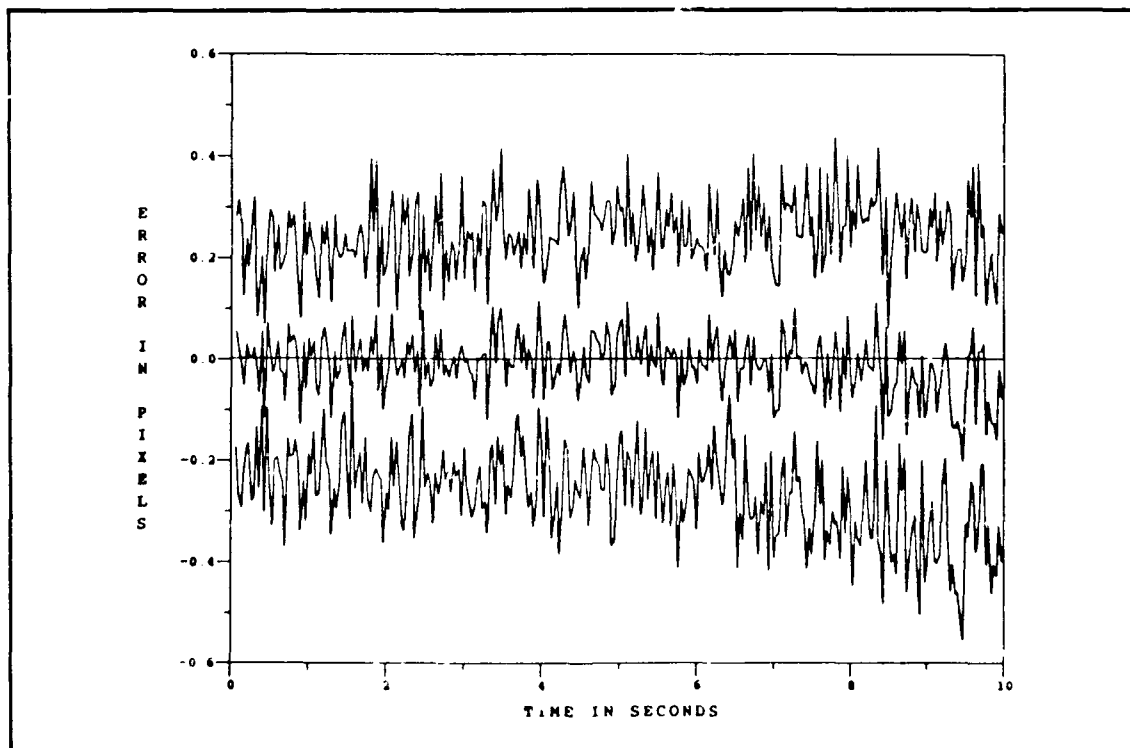


Figure J.10. Eight-State Filter Center-of-Mass Across-Track Error at  $t_i^-$  for Binary Model Without Low-Energy Laser Sweep and With Plume Pogo



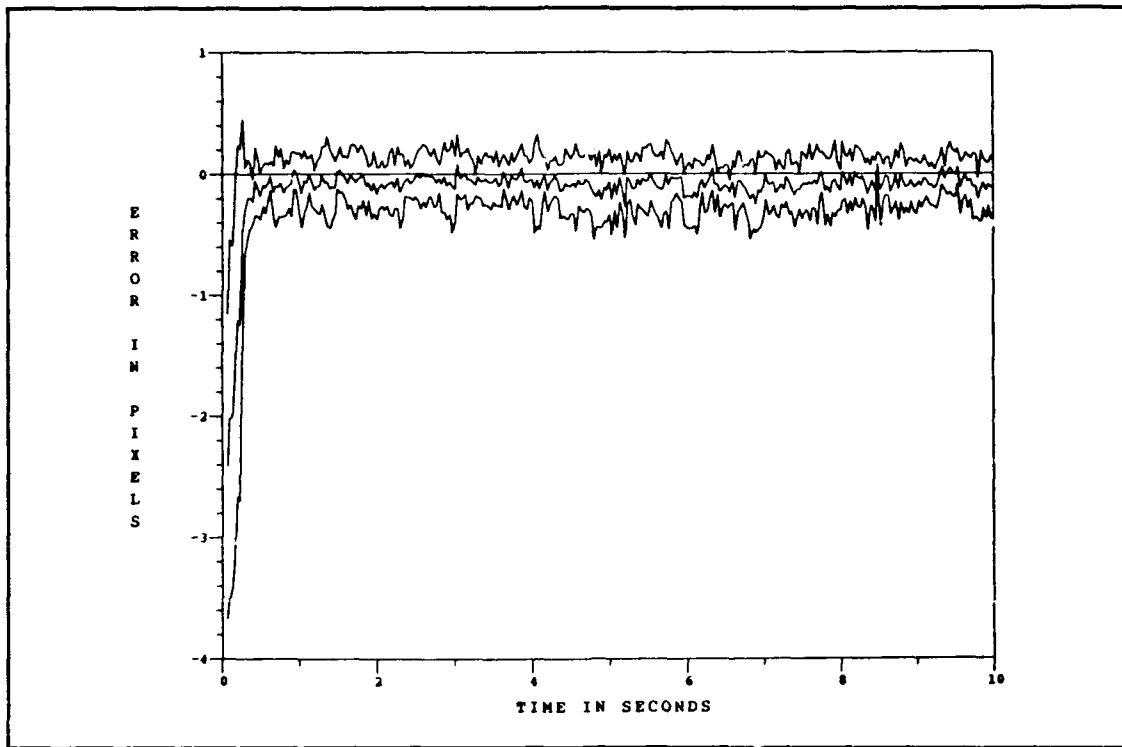


Figure J.11. Eight-State Filter Center-of-Mass Along-Track Error at  $t_i +$  for Binary Model Without Low-Energy Laser Sweep and With Plume Pogo

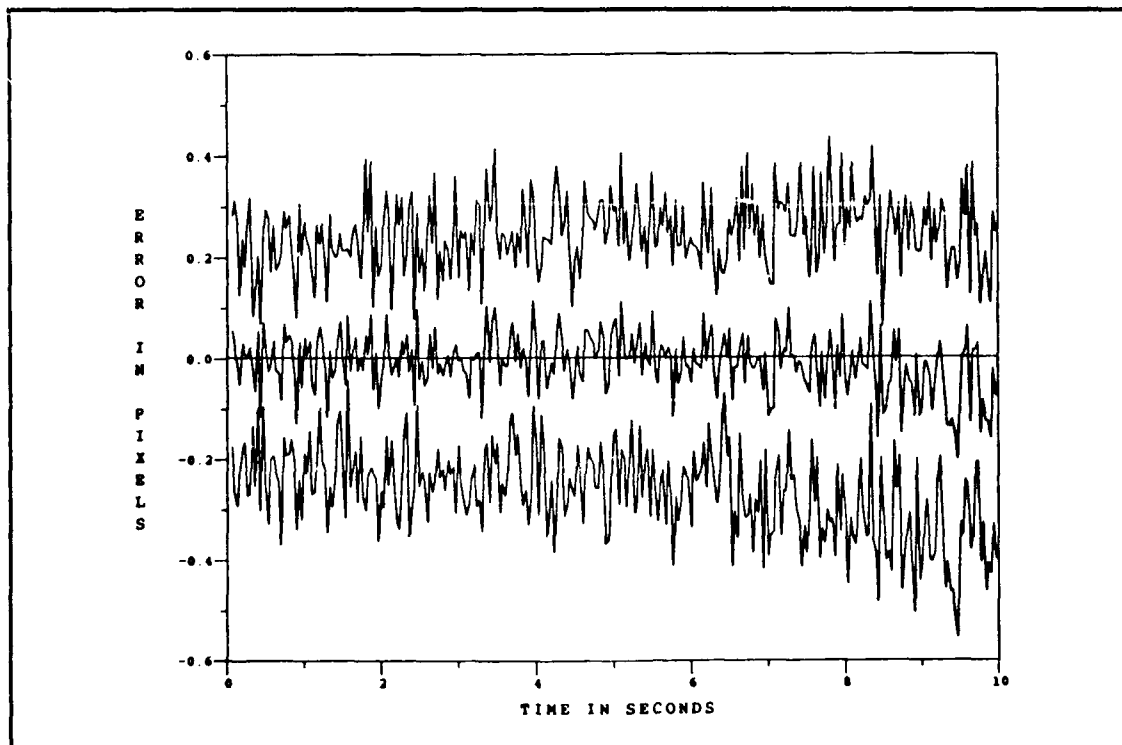


Figure J.12. Eight-State Filter Center-of-Mass Across-Track Error at  $t_i +$  for Binary Model Without Low-Energy Laser Sweep and With Plume Pogo

## *Appendix K. Eight-State Filter Performance Plots With Low-Energy Laser Sweep and Without Plume Pogo*

This appendix contains the eight-state (center-of-mass) filter error plots for the case of a low-energy laser sweep and with no plume pogo of the intensity centroid. The center-of-mass errors are presented as the azimuth ( $x$ ) and elevation ( $y$ ) components of the error, and the along-track and across-track components of the error. The hardbody reflectivity model is used for the low-energy laser sweep plots, which are also representative of the hardbody binary plots. (The hardbody binary model is used for the single scan of the low-energy laser (i.e., no sweep), since the hardbody reflectivity model is software configured for a sweep routine.) For the discussion pertaining to these plots, refer to Chapter VI, Sections 6.6 and 6.7.

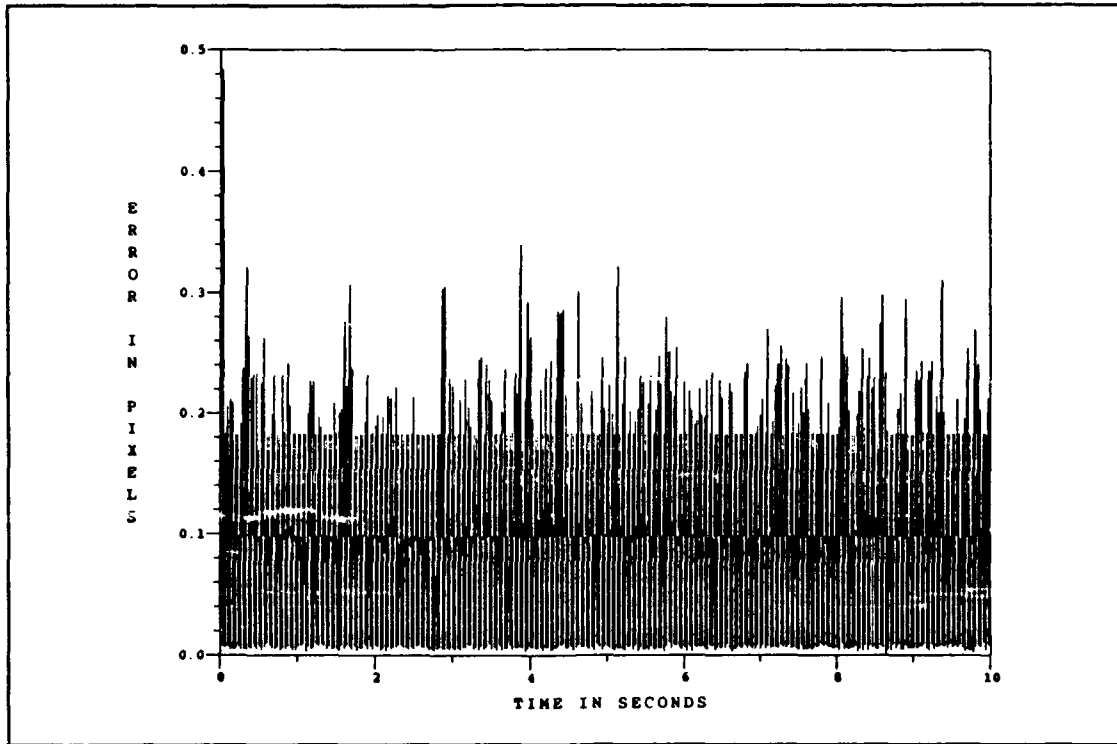


Figure K.1. Eight-State Filter vs. Actual rms Center-of-Mass Azimuth Error for Reflectivity Model With Low-Energy Laser Sweep and Without Plume Pogo

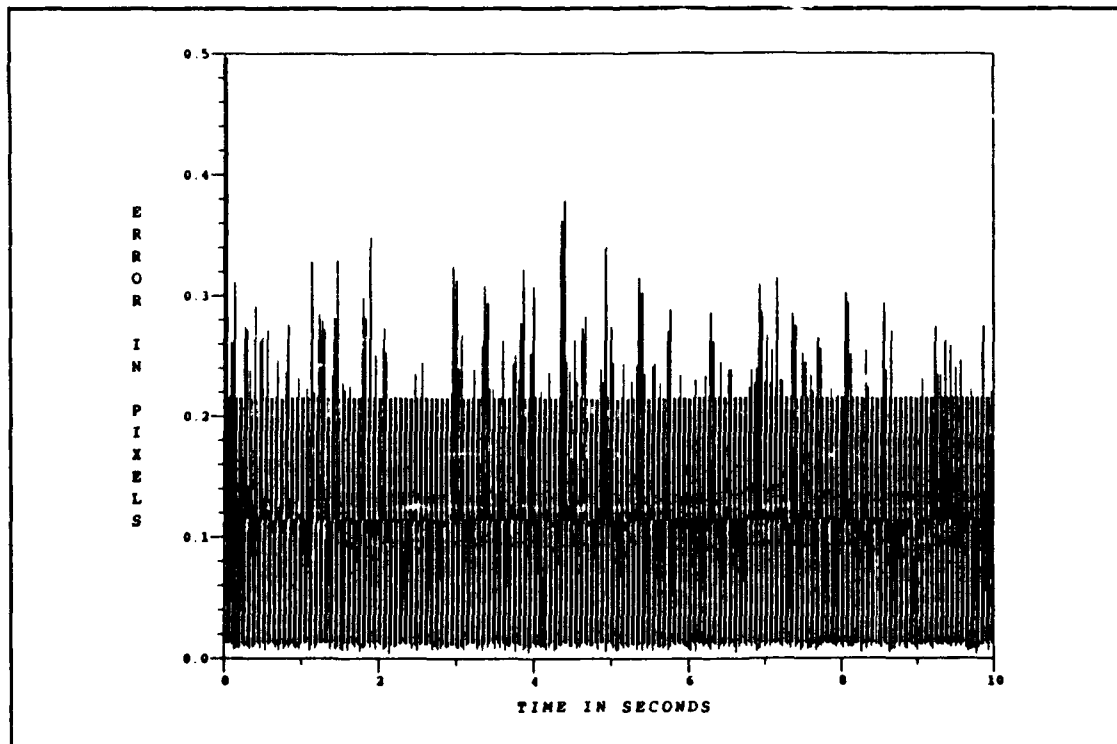


Figure K.2 Eight State Filter vs. Actual rms Center-of-Mass Elevation Error for Reflectivity Model With Low-Energy Laser Sweep and Without Plume Pogo

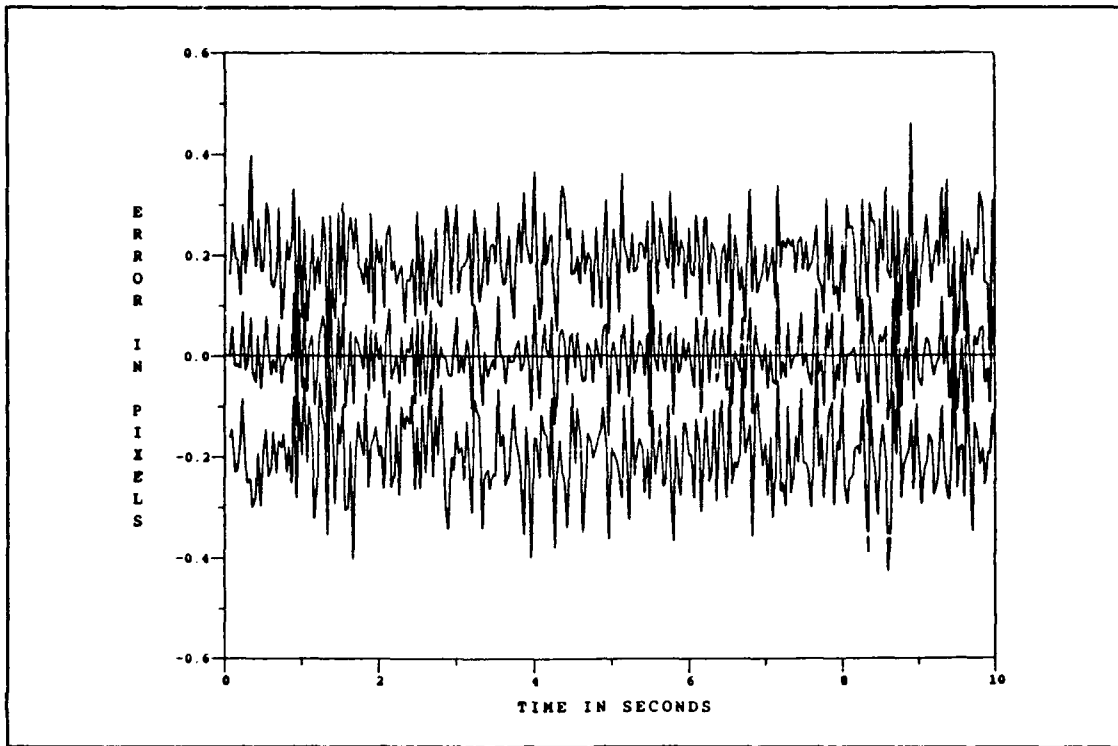


Figure K.3. Eight-State Filter Center-of-Mass Azimuth Error at  $t_i^-$  for Reflectivity Model With Low-Energy Laser Sweep and Without Plume Pogo

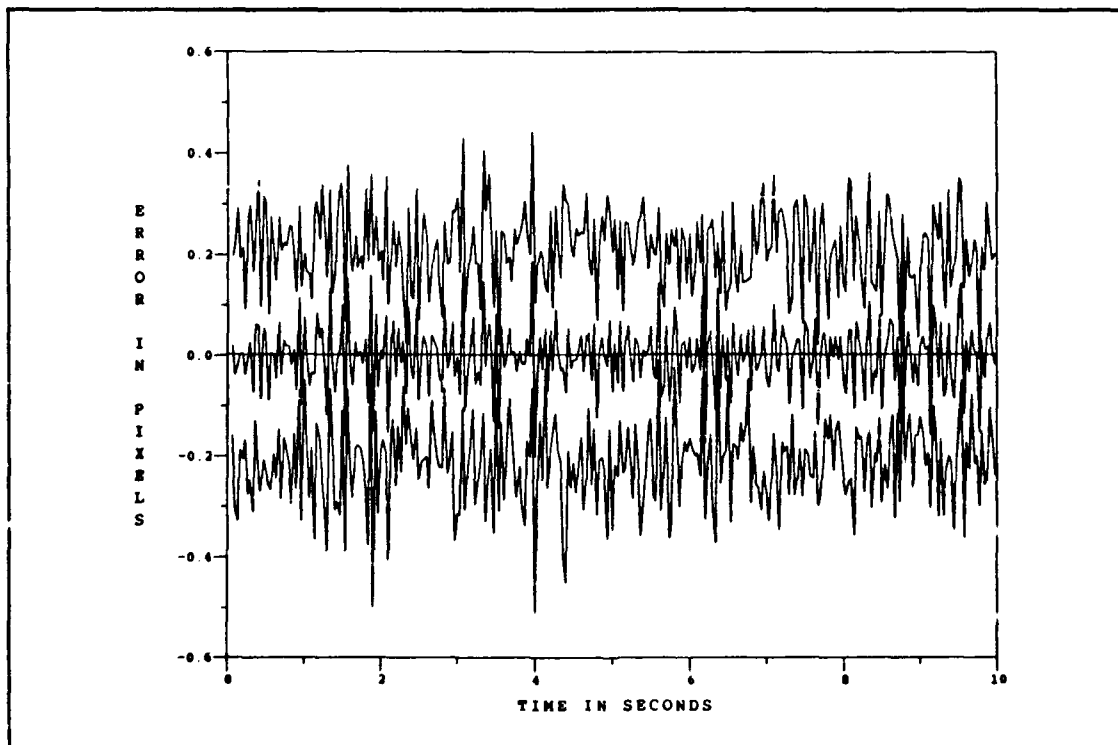


Figure K.4. Eight-State Filter Center-of-Mass Elevation Error at  $t_i^-$  for Reflectivity Model With Low-Energy Laser Sweep and Without Plume Pogo

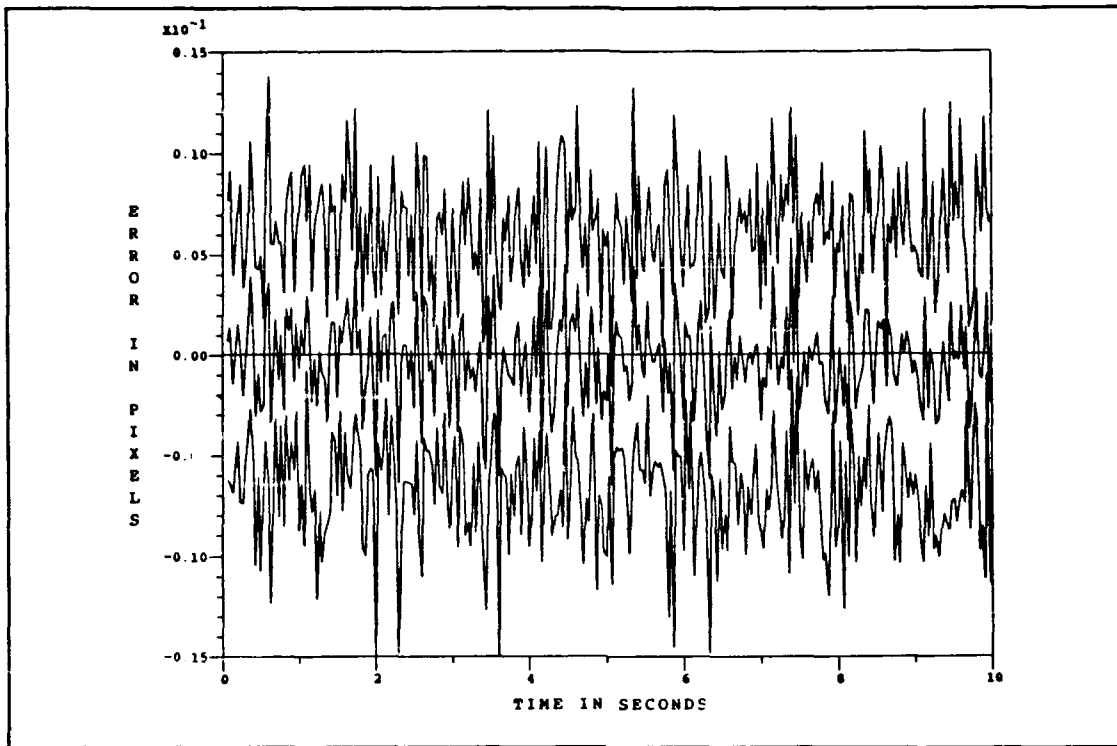


Figure K.5. Eight-State Filter Center-of-Mass Azimuth Error at  $t_i^+$  for Reflectivity Model With Low-Energy Laser Sweep and Without Plume Pogo

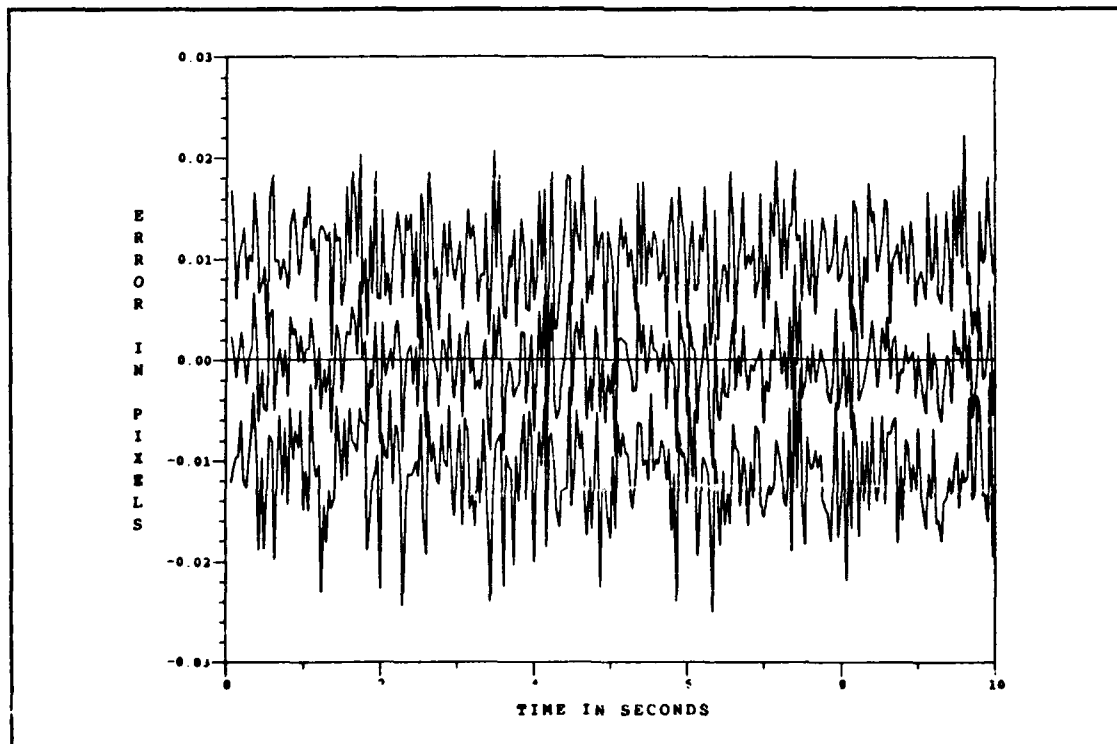


Figure K.6. Eight-State Filter Center-of-Mass Elevation Error at  $t_i^+$  for Reflectivity Model With Low-Energy Laser Sweep and Without Plume Pogo

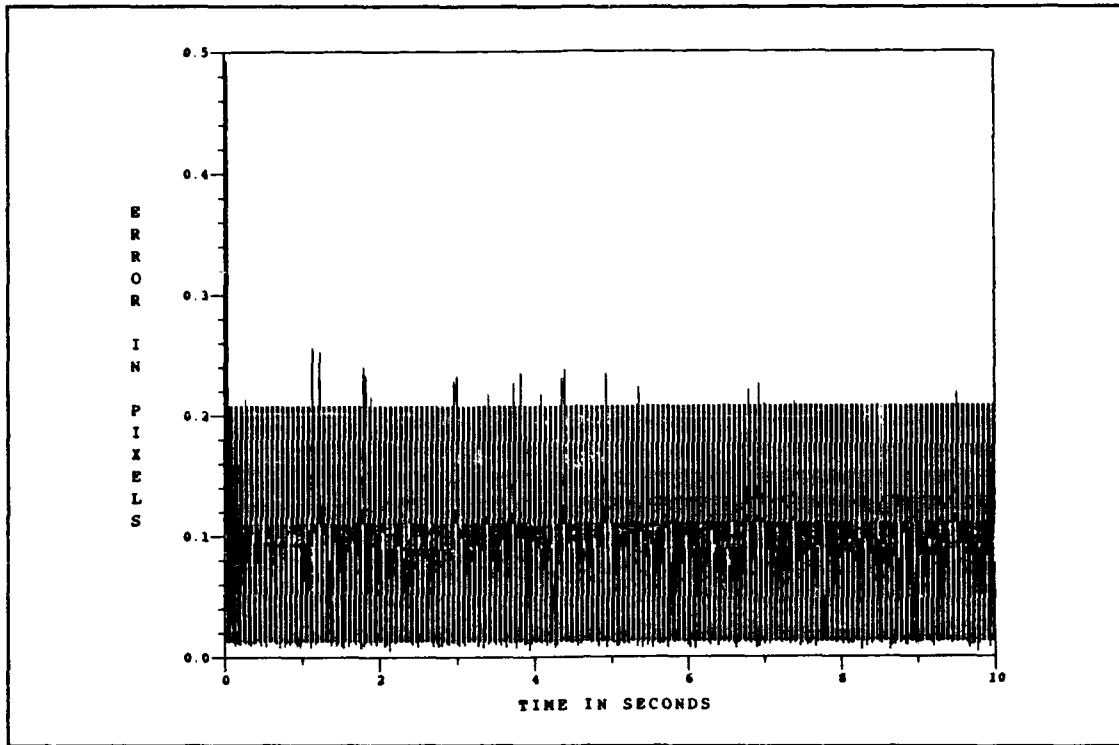


Figure K.7. Eight-State Filter vs. Actual rms Center-of-Mass Along-Track Error for Reflectivity Model With Low-Energy Laser Sweep and Without Plume Pogo

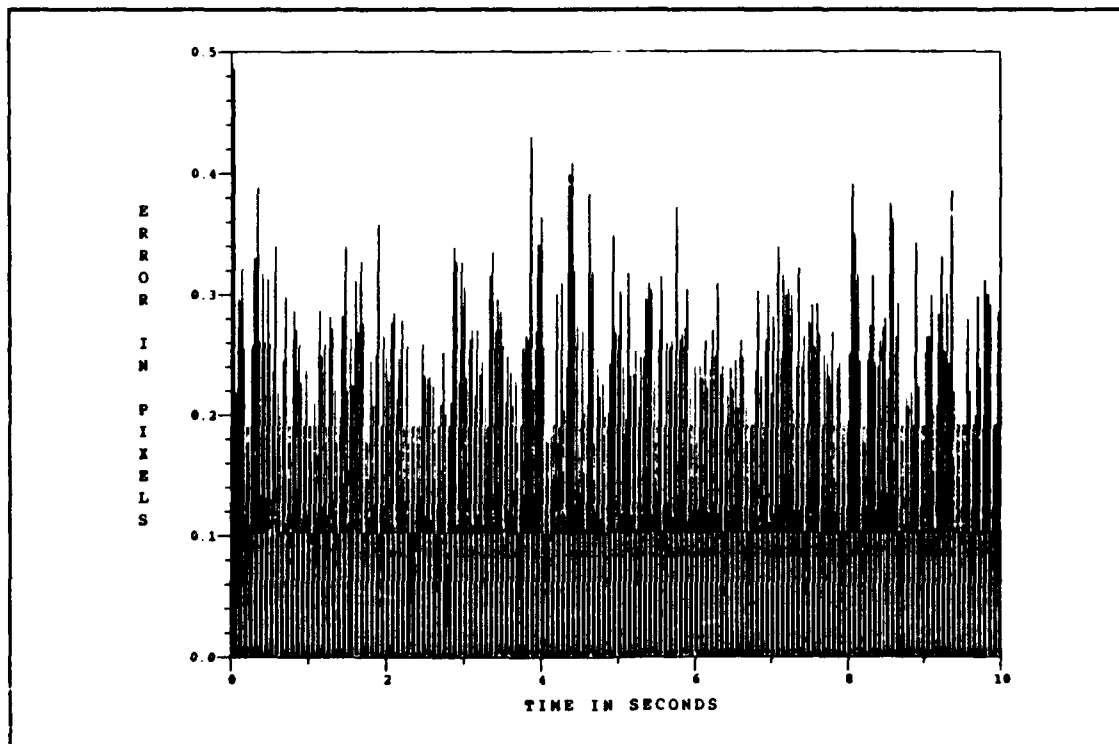


Figure K.8. Eight-State Filter vs. Actual rms Center-of-Mass Across-Track Error for Reflectivity Model With Low-Energy Laser Sweep and Without Plume Pogo

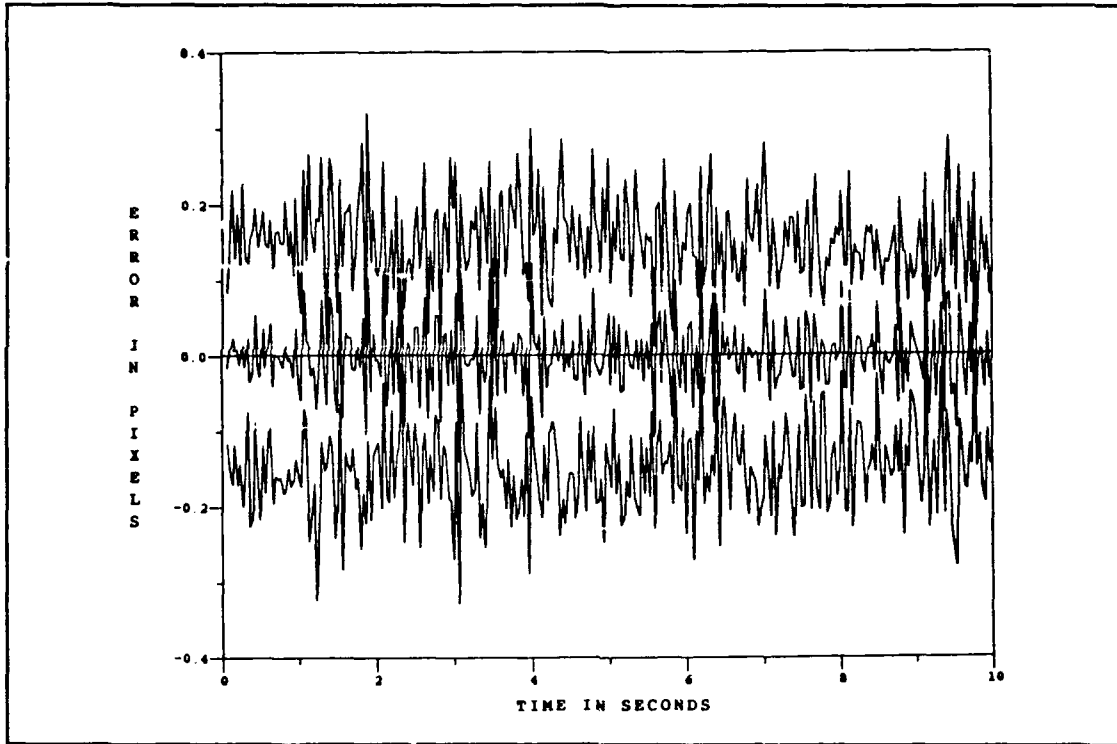


Figure K.9. Eight-State Filter Center-of-Mass Along-Track Error at  $t_i^-$  for Reflectivity Model With Low-Energy Laser Sweep and Without Plume Pogo

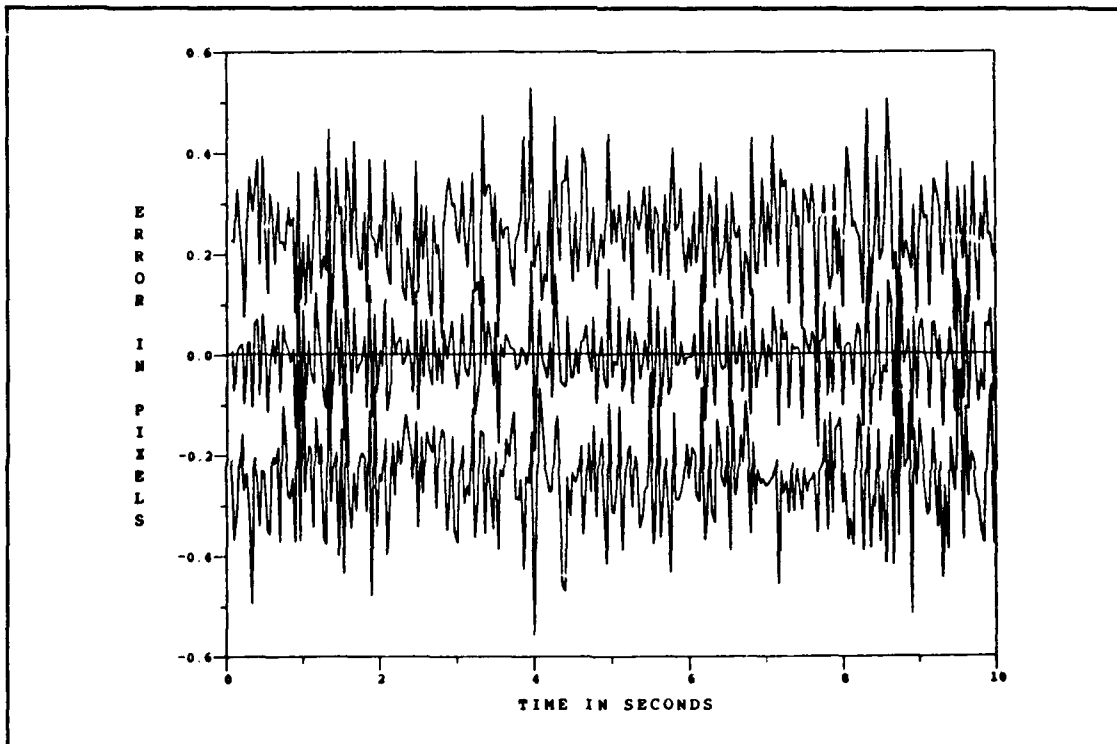


Figure K.10. Eight-State Filter Center-of-Mass Across-Track Error at  $t_i^-$  for Reflectivity Model With Low-Energy Laser Sweep and Without Plume Pogo

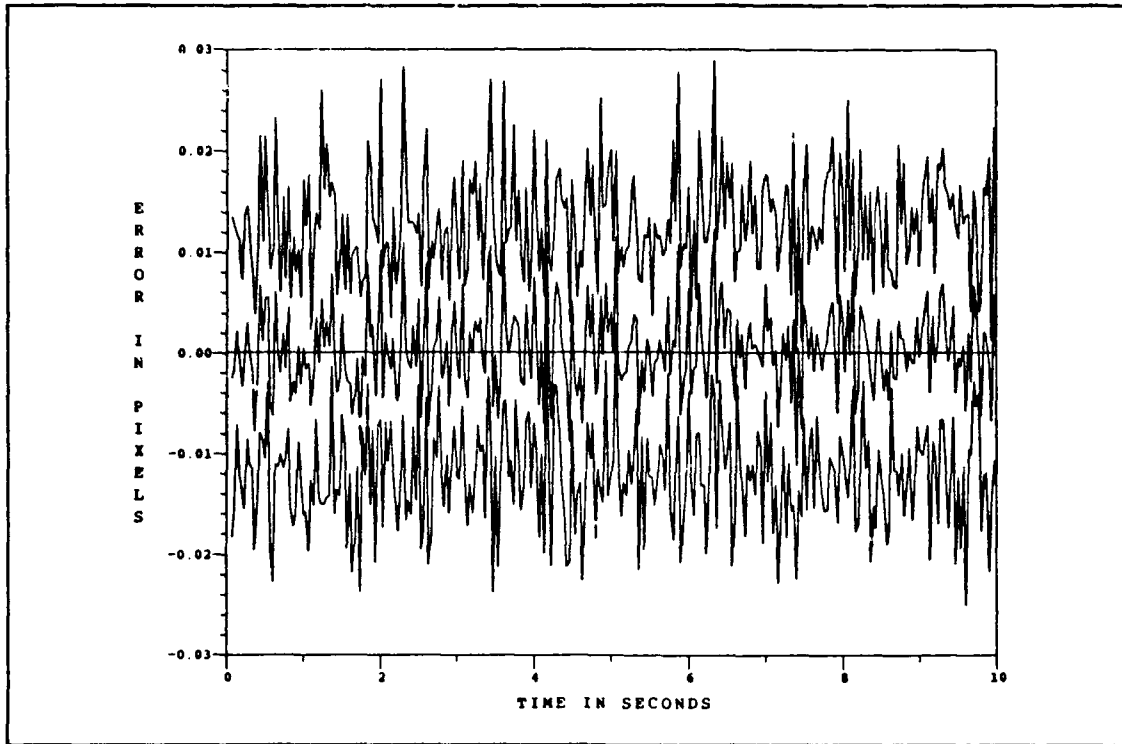


Figure K.11. Eight-State Filter Center-of-Mass Along-Track Error at  $t_i^+$  for Reflectivity Model With Low-Energy Laser Sweep and Without Plume Pogo

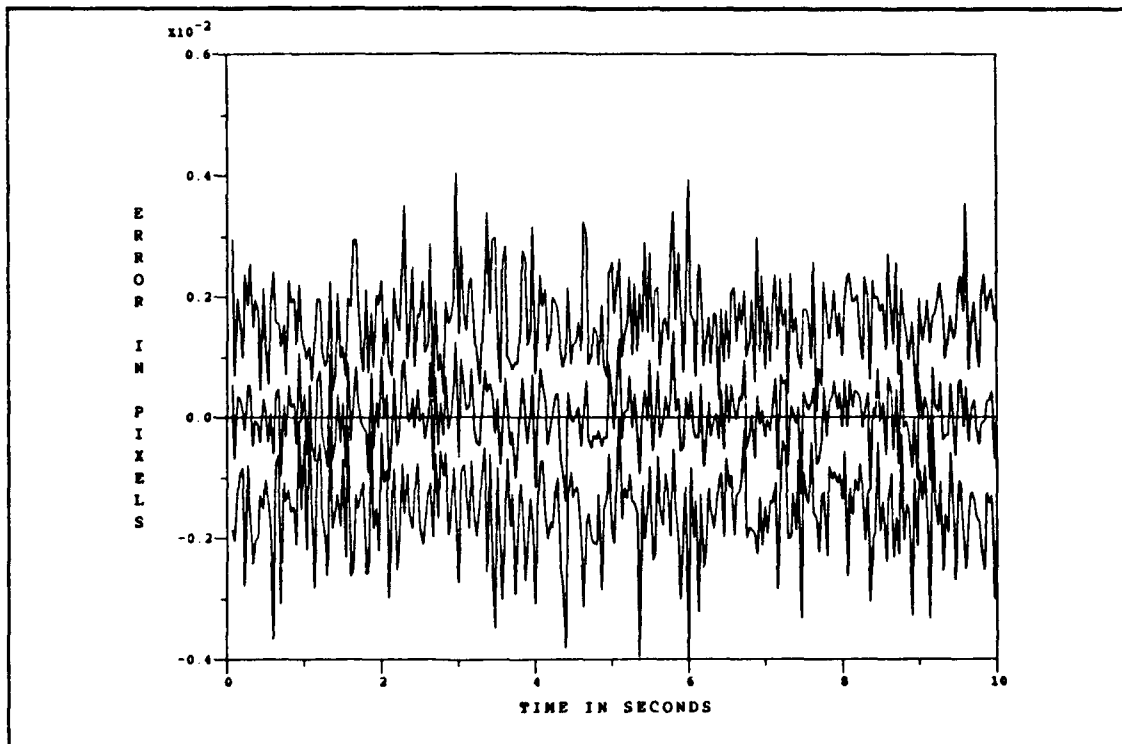


Figure K.12. Eight-State Filter Center-of-Mass Across-Track Error at  $t_i^+$  for Reflectivity Model With Low-Energy Laser Sweep and Without Plume Pogo



## *Appendix L. Eight-State Filter Performance Plots With Low-Energy Laser Sweep and Plume Pogo*

This appendix contains the eight-state (center-of-mass) filter error plots for the case of a low-energy laser sweep and with the intensity centroid subjected to plume pogo. The center-of-mass errors are presented as the azimuth ( $x$ ) and elevation ( $y$ ) components of the error, and the along-track and across-track components of the error. The hardbody reflectivity model is used for the low-energy laser sweep plots, which are also representative of the hardbody binary plots. (The hardbody binary model is used for the single scan of the low-energy laser (i.e., no sweep), since the hardbody reflectivity model is software configured for a sweep routine.) For the discussion pertaining to these plots, refer to Chapter VI, Sections 6.6 and 6.7.

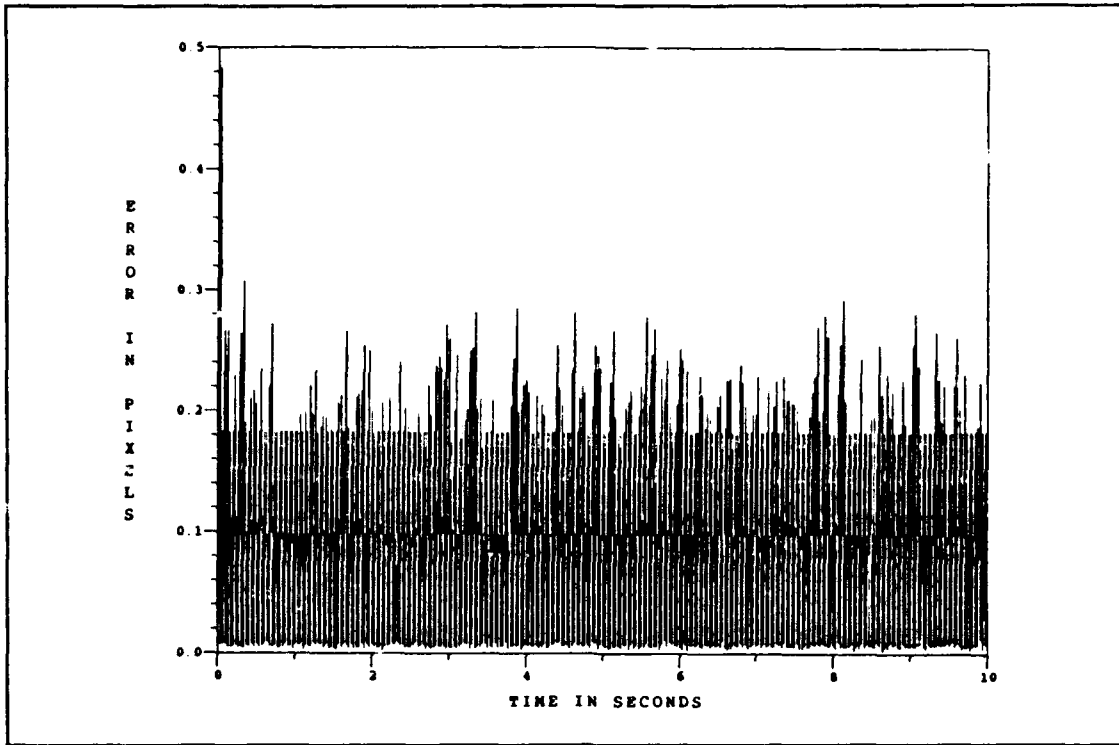


Figure L.1. Eight-State Filter vs. Actual rms Center-of-Mass Azimuth Error for Reflectivity Model With Low-Energy Laser Sweep and Plume Pogo

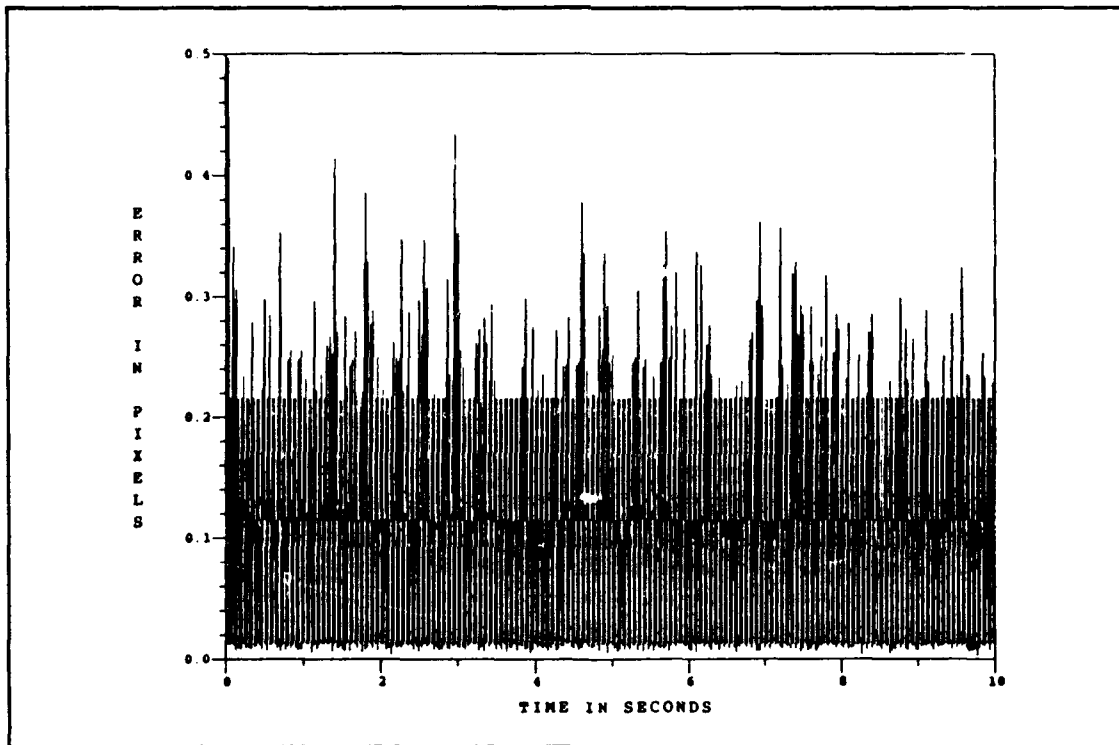


Figure L.2. Eight-State Filter vs. Actual rms Center-of-Mass Elevation Error for Reflectivity Model With Low-Energy Laser Sweep and Plume Pogo

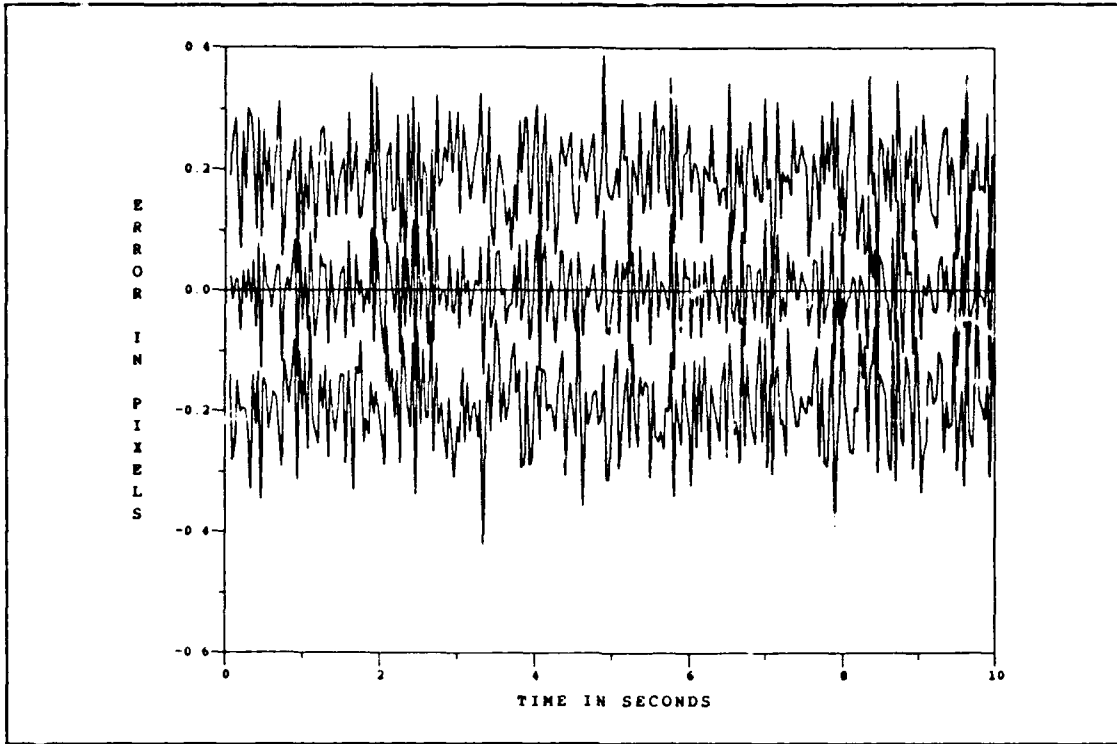


Figure L.3. Eight-State Filter Center-of-Mass Azimuth Error at  $t_i$  for Reflectivity Model With Low-Energy Laser Sweep and Plume Pogo

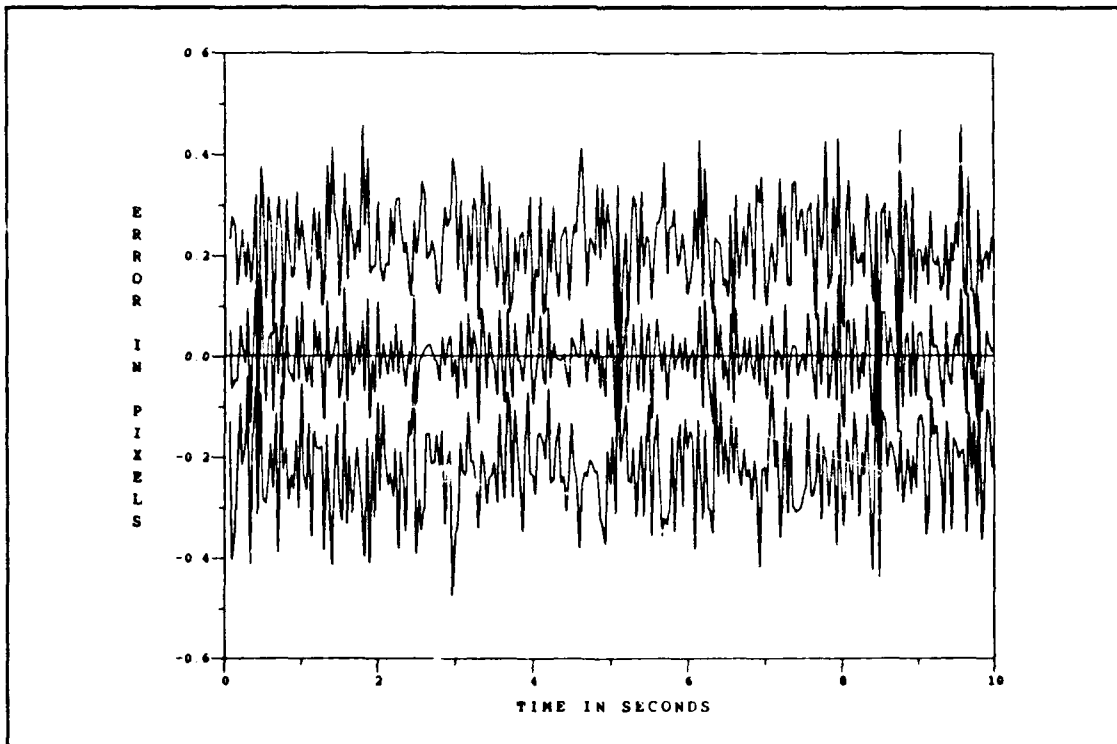


Figure L.4. Eight-State Filter Center-of-Mass Elevation Error at  $t_i$  for Reflectivity Model With Low-Energy Laser Sweep and Plume Pogo

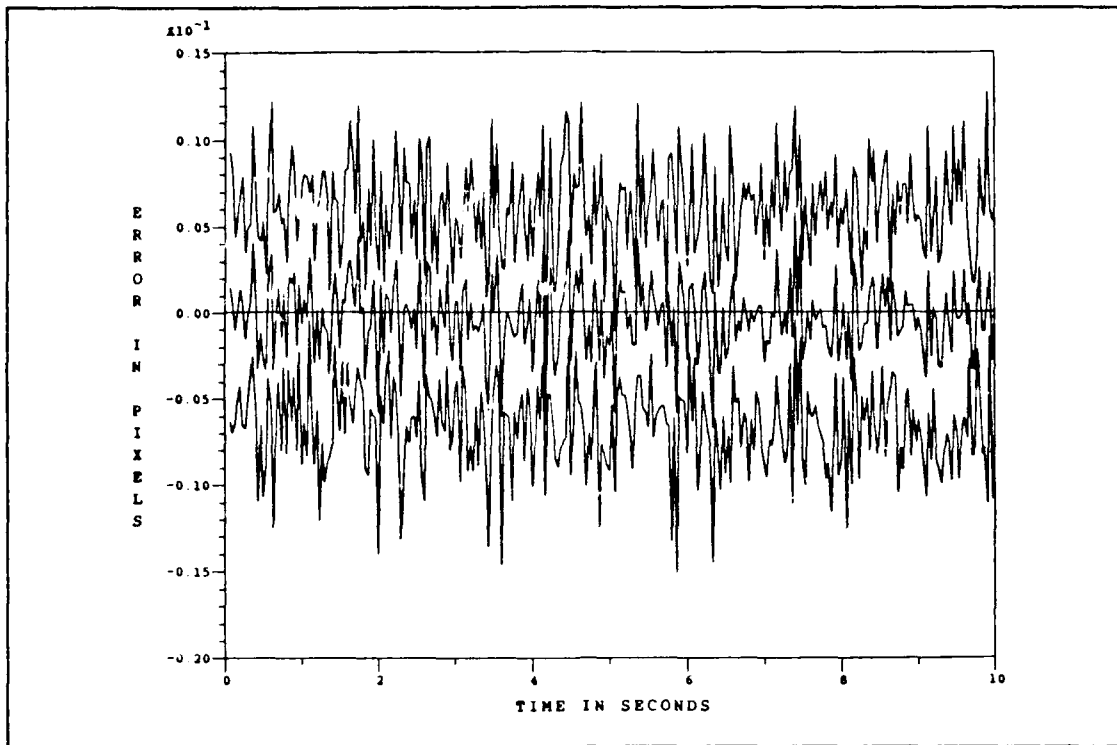


Figure L.5. Eight-State Filter Center-of-Mass Azimuth Error at  $t_i^+$  for Reflectivity Model With Low-Energy Laser Sweep and Plume Pogo

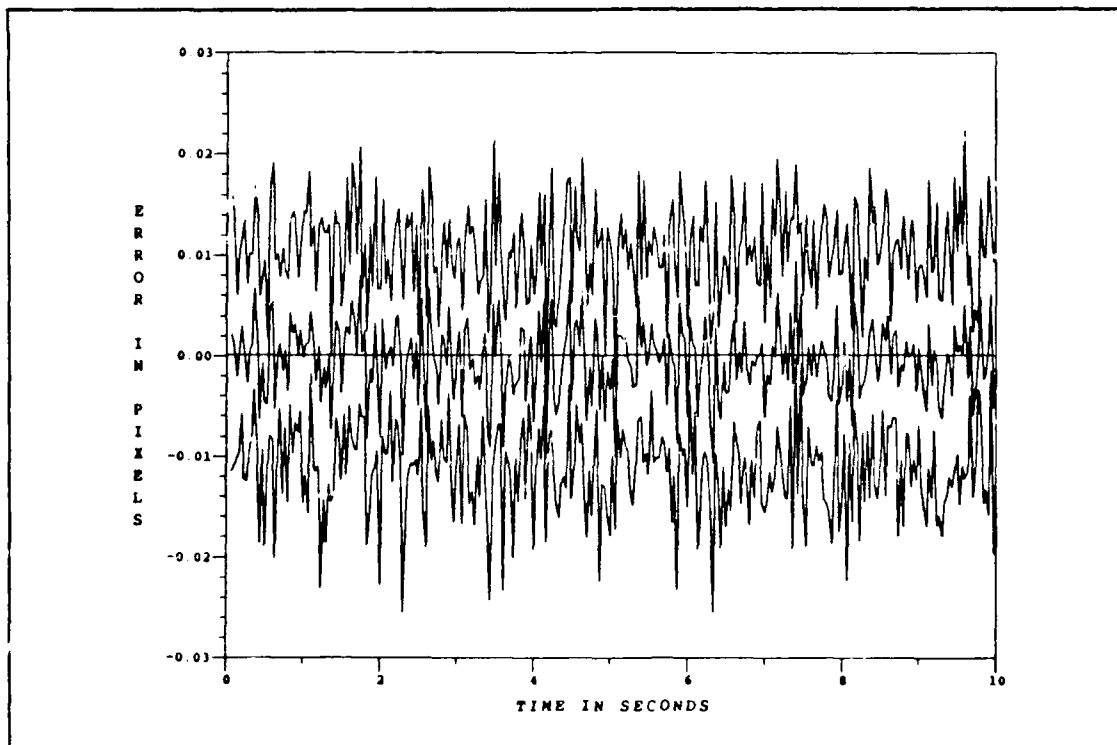


Figure L.6. Eight-State Filter Center-of-Mass Elevation Error at  $t_i^+$  for Reflectivity Model With Low-Energy Laser Sweep and Plume Pogo

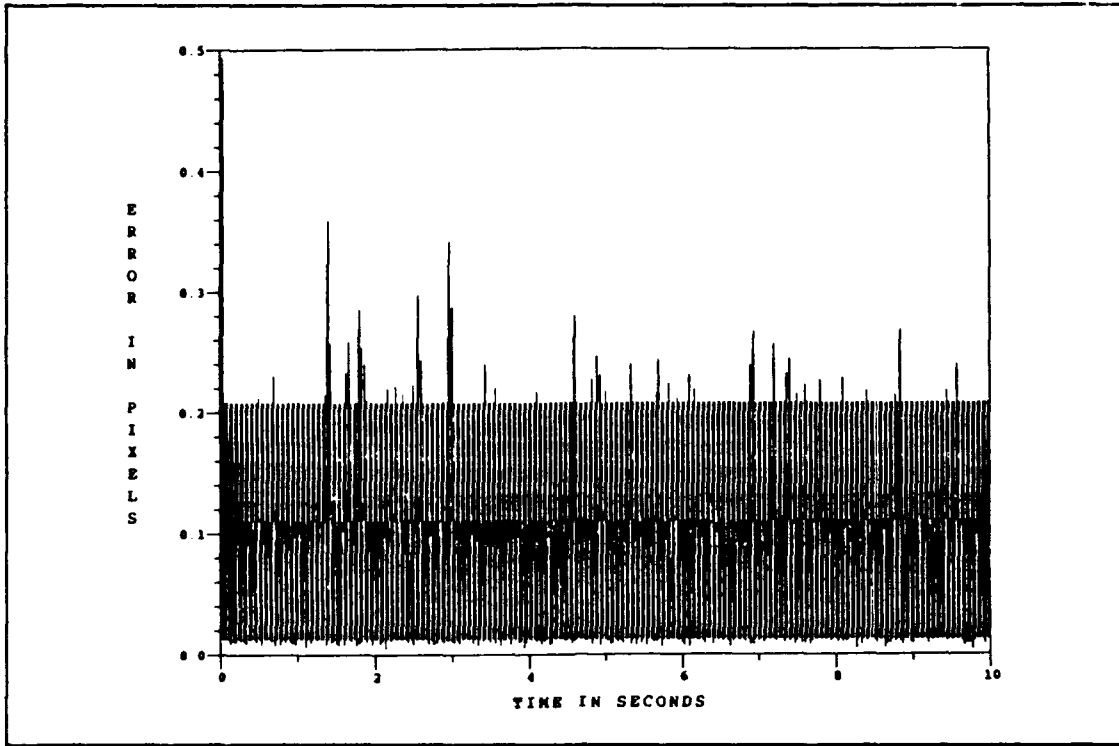


Figure L.7. Eight-State Filter vs. Actual rms Center-of-Mass Along-Track Error for Reflectivity Model With Low-Energy Laser Sweep and Plume Pogo

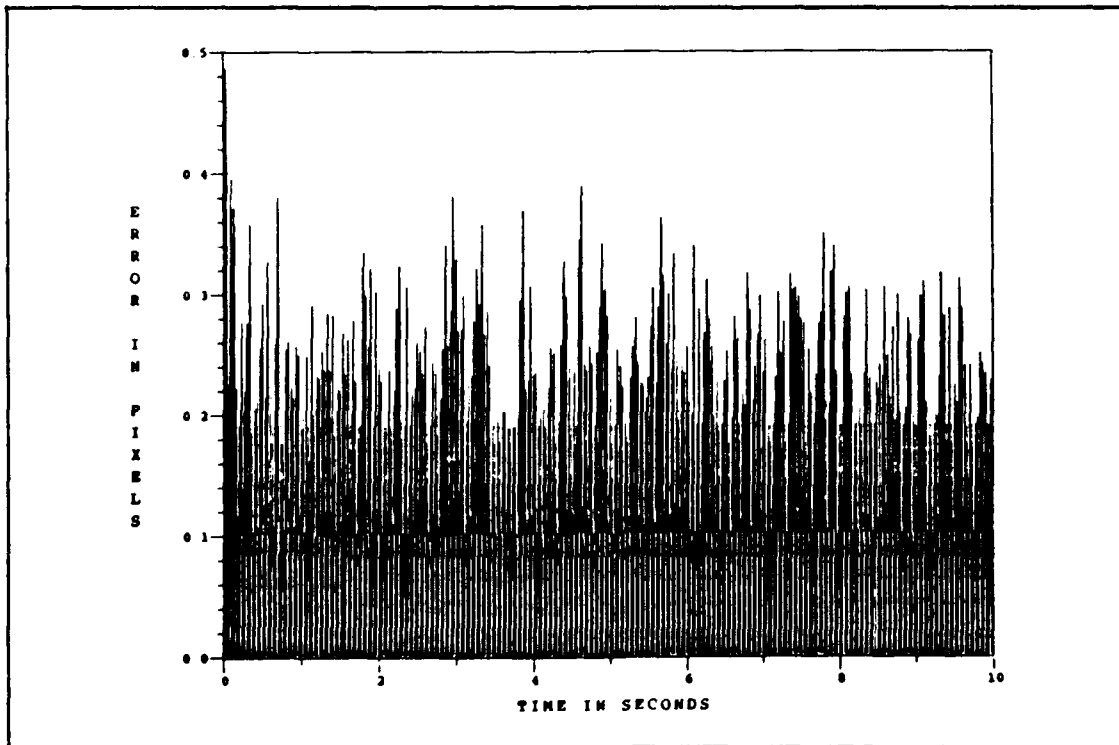


Figure L.8. Eight-State Filter vs. Actual rms Center-of-Mass Across-Track Error for Reflectivity Model With Low-Energy Laser Sweep and Plume Pogo

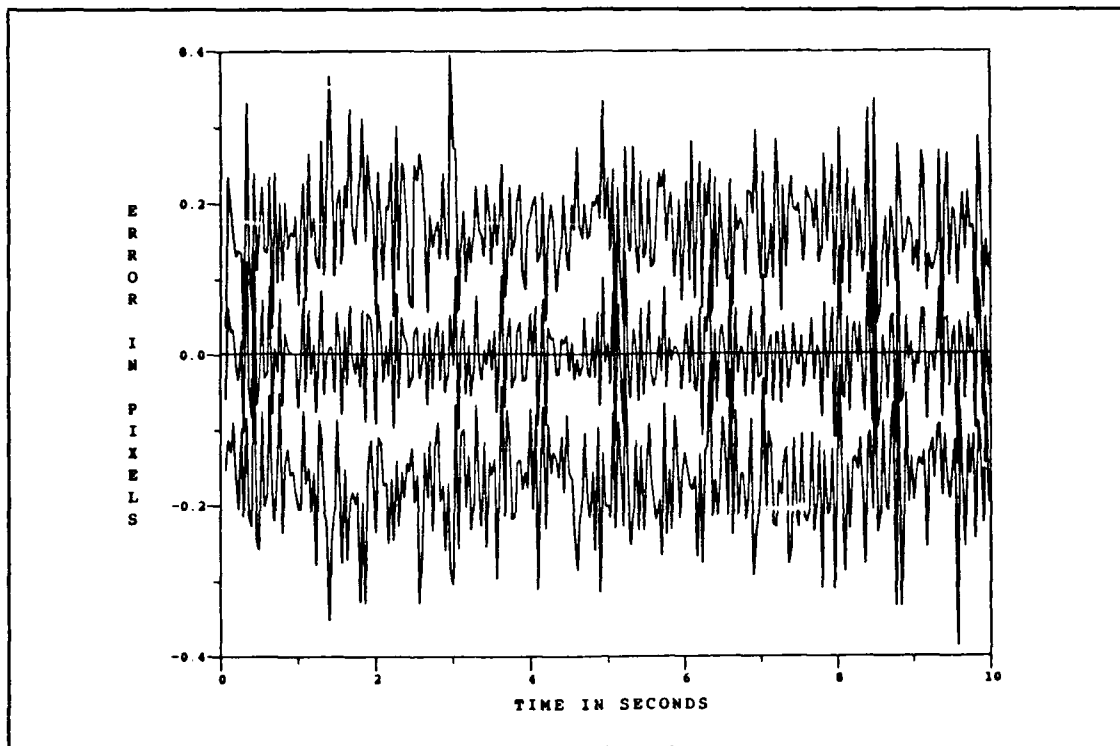


Figure L.9. Eight-State Filter Center-of-Mass Along-Track Error at  $t_i$  for Reflectivity Model With Low-Energy Laser Sweep and Plume Pogo

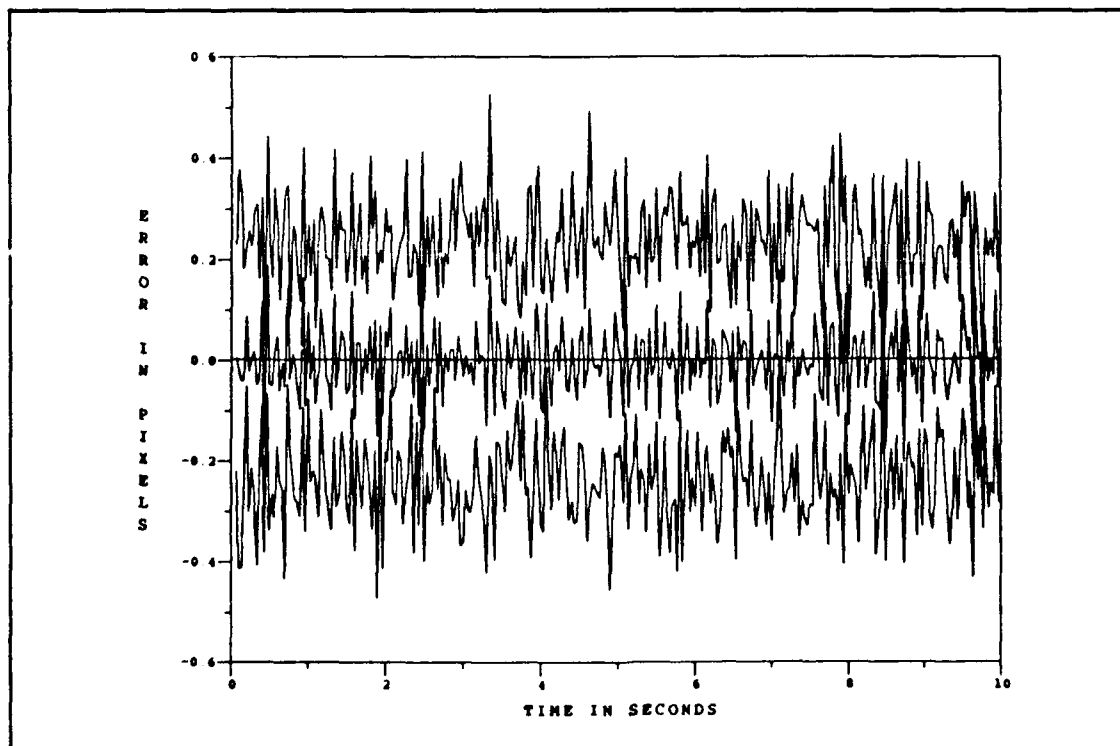


Figure L.10. Eight-State Filter Center-of-Mass Across-Track Error at  $t_i$  for Reflectivity Model With Low-Energy Laser Sweep and Plume Pogo

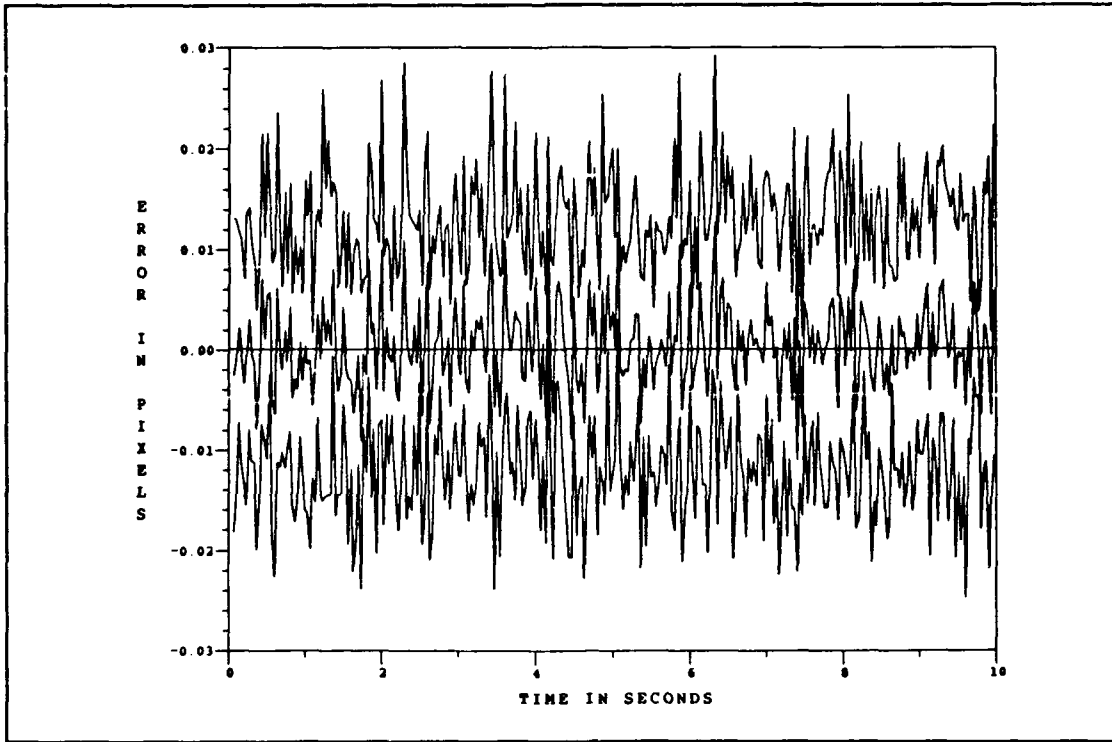


Figure L.11. Eight-State Filter Center-of-Mass Along-Track Error at  $t_i^+$  for Reflectivity Model With Low-Energy Laser Sweep and Plume Pogo

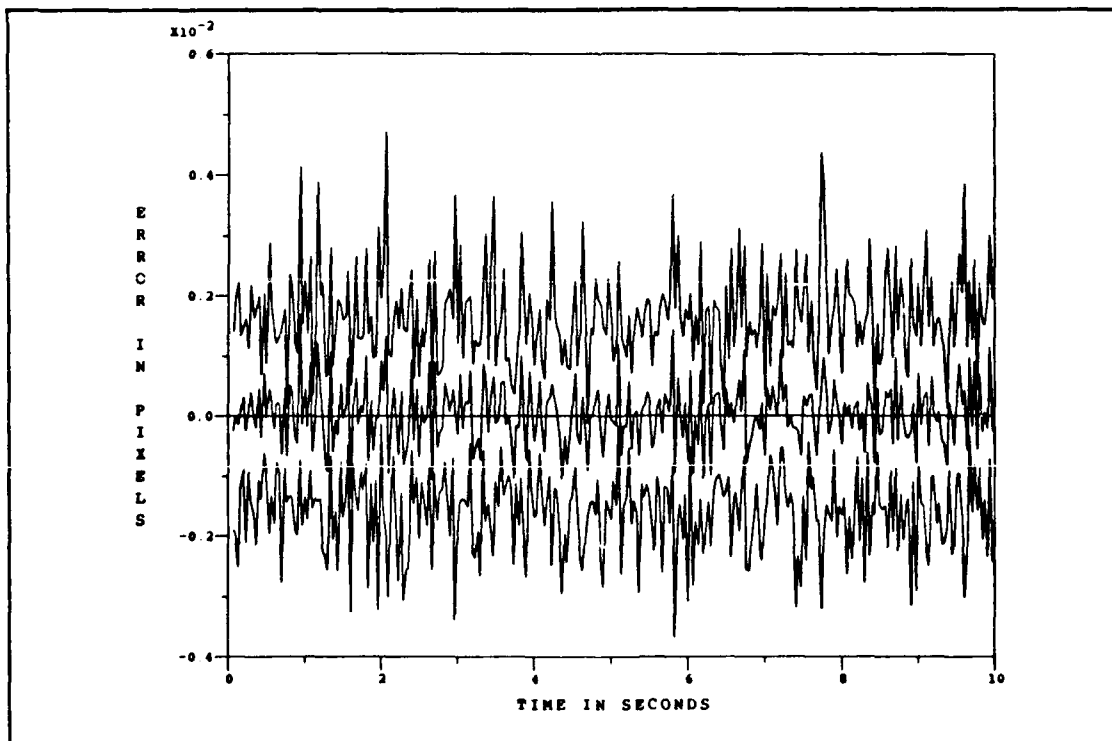


Figure L.12. Eight-State Filter Center-of-Mass Across-Track Error at  $t_i^+$  for Reflectivity Model With Low-Energy Laser Sweep and Plume Pogo

## *Appendix M. Low-Energy Laser Sensor Sensitivity Plots*

This appendix contains the eight-state (center-of-mass) filter error plots from a study of the low-energy laser sensitivity. The study is conducted using the hardbody reflectivity model with a low-energy laser sweep and the intensity centroid subjected to plume pogo. (A comparison can be made with the plots in Appendix L.) The center-of-mass errors are presented as the azimuth ( $x$ ) and elevation ( $y$ ) components of the error, and the along-track and across-track components of the error. For the discussion pertaining to these plots, refer to Chapter VI, Section 6.8.3.



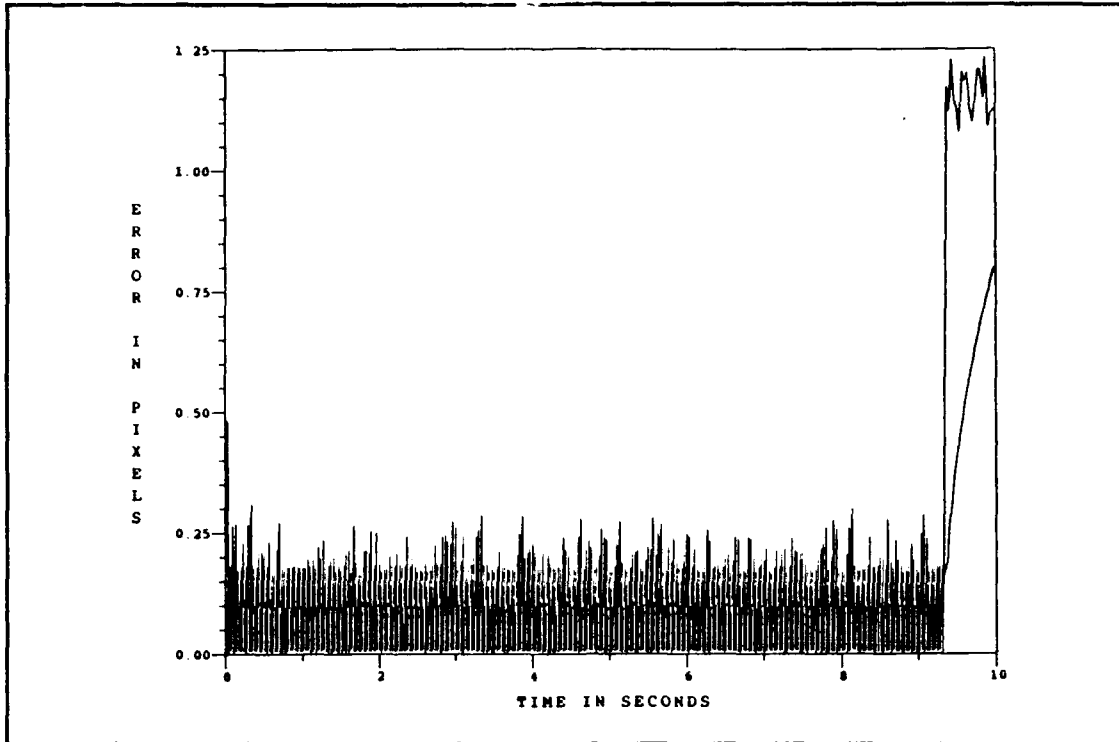


Figure M.1. Study: Eight-State Filter vs. Actual rms Center-of-Mass Azimuth Error for Reflectivity Model With Low-Energy Laser Sweep and Plume Pogo

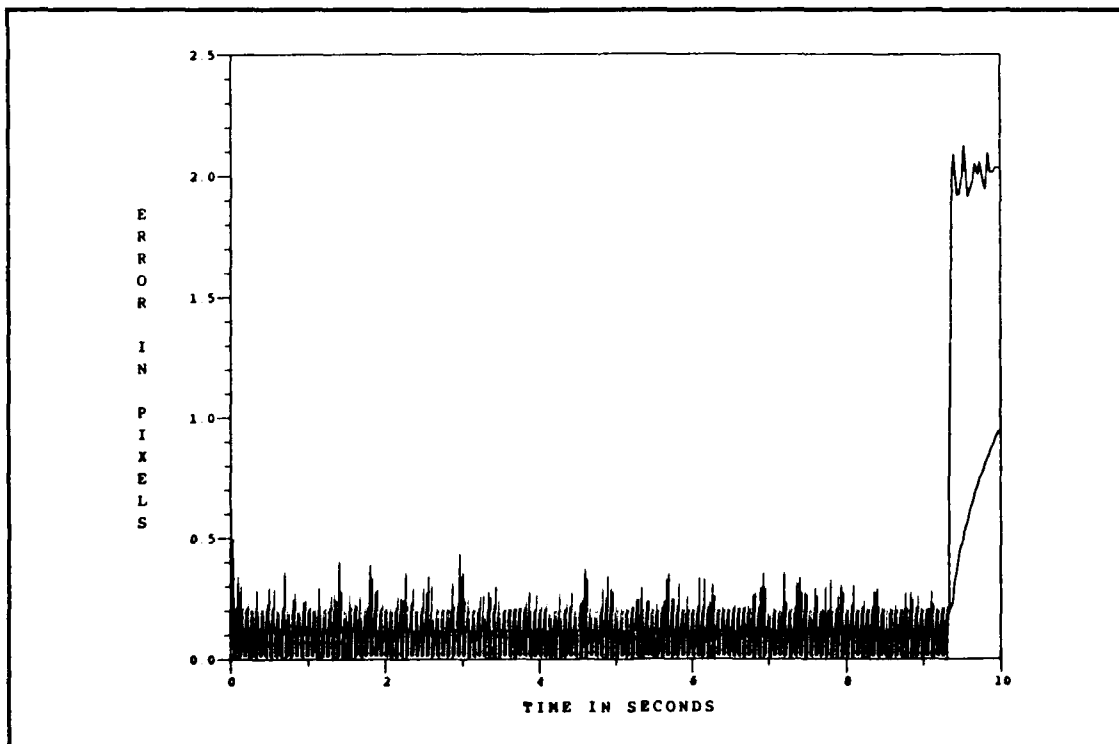


Figure M.2. Study: Eight-State Filter vs. Actual rms Center-of-Mass Elevation Error for Reflectivity Model With Low-Energy Laser Sweep and Plume Pogo

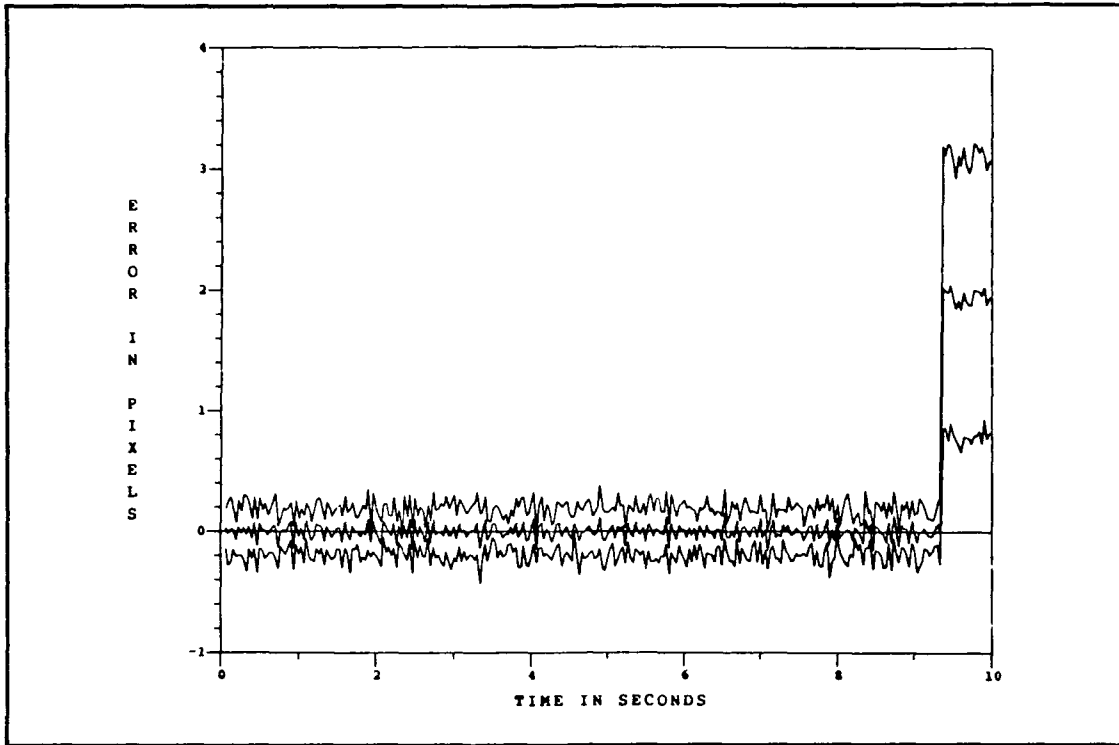


Figure M.3. Study: Eight-State Filter Center-of-Mass Azimuth Error at  $t_i^-$  for Reflectivity Model With Low-Energy Laser Sweep and Plume Pogo

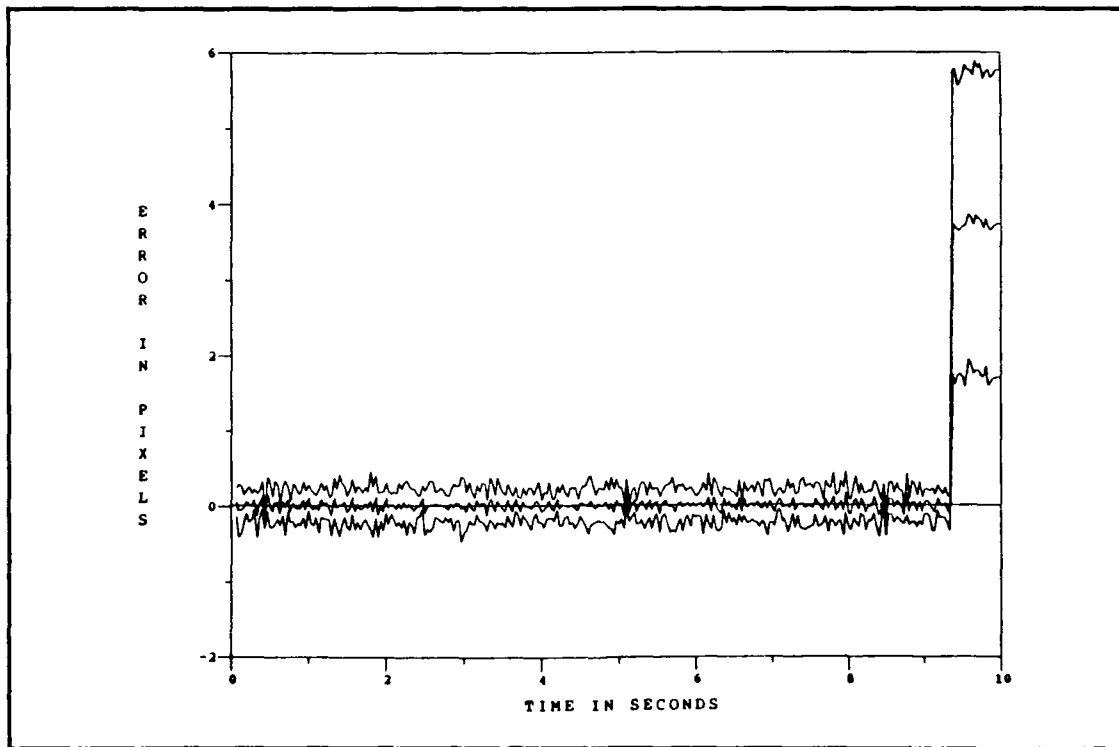


Figure M.4. Study: Eight-State Filter Center-of-Mass Elevation Error at  $t_i^-$  for Reflectivity Model With Low-Energy Laser Sweep and Plume Pogo

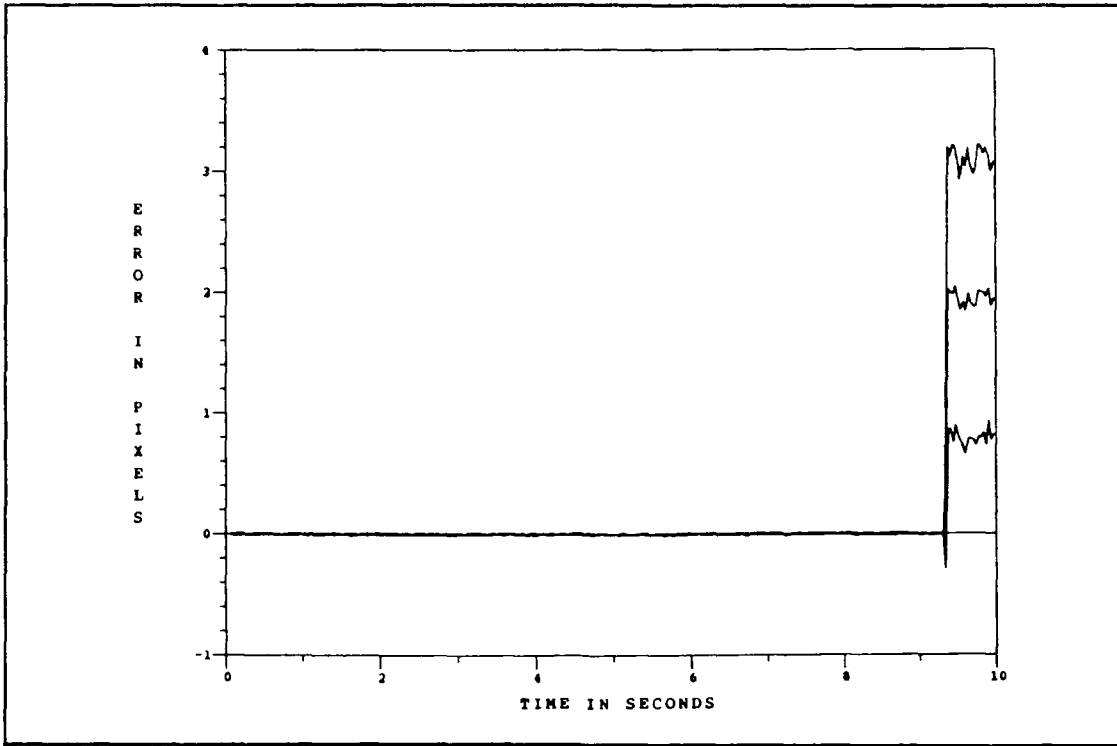


Figure M.5. Study: Eight-State Filter Center-of-Mass Azimuth Error at  $t_i^+$  for Reflectivity Model With Low-Energy Laser Sweep and Plume Pogo

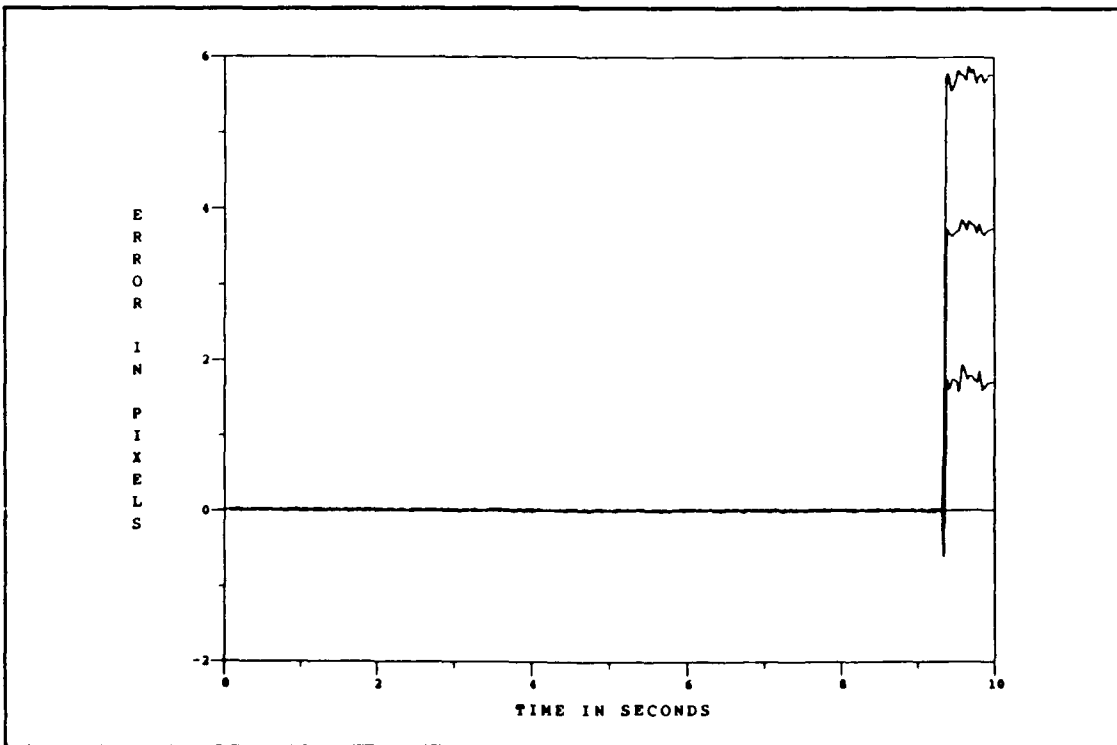


Figure M.6. Study: Eight-State Filter Center-of-Mass Elevation Error at  $t_i^+$  for Reflectivity Model With Low-Energy Laser Sweep and Plume Pogo

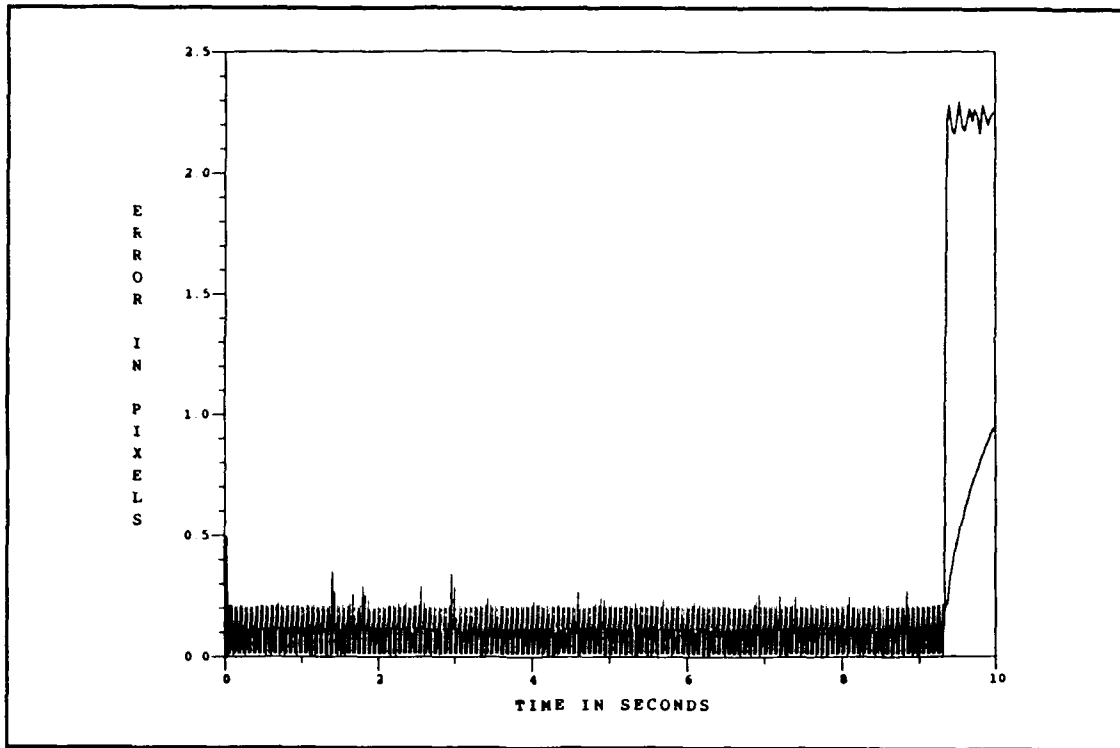


Figure M.7. Study: Eight-State Filter vs. Actual rms Center-of-Mass Along-Track Error for Reflectivity Model With Low-Energy Laser Sweep and Plume Pogo

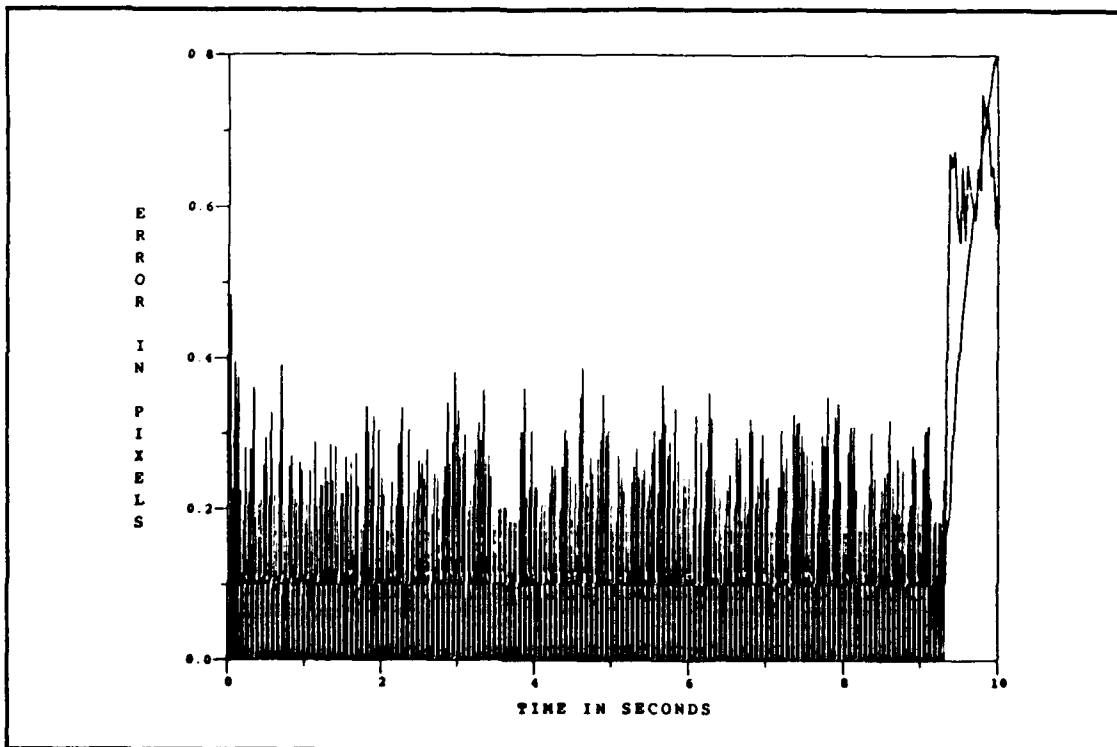


Figure M.8. Study: Eight-State Filter vs. Actual rms Center-of-Mass Across-Track Error for Reflectivity Model With Low-Energy Laser Sweep and Plume Pogo

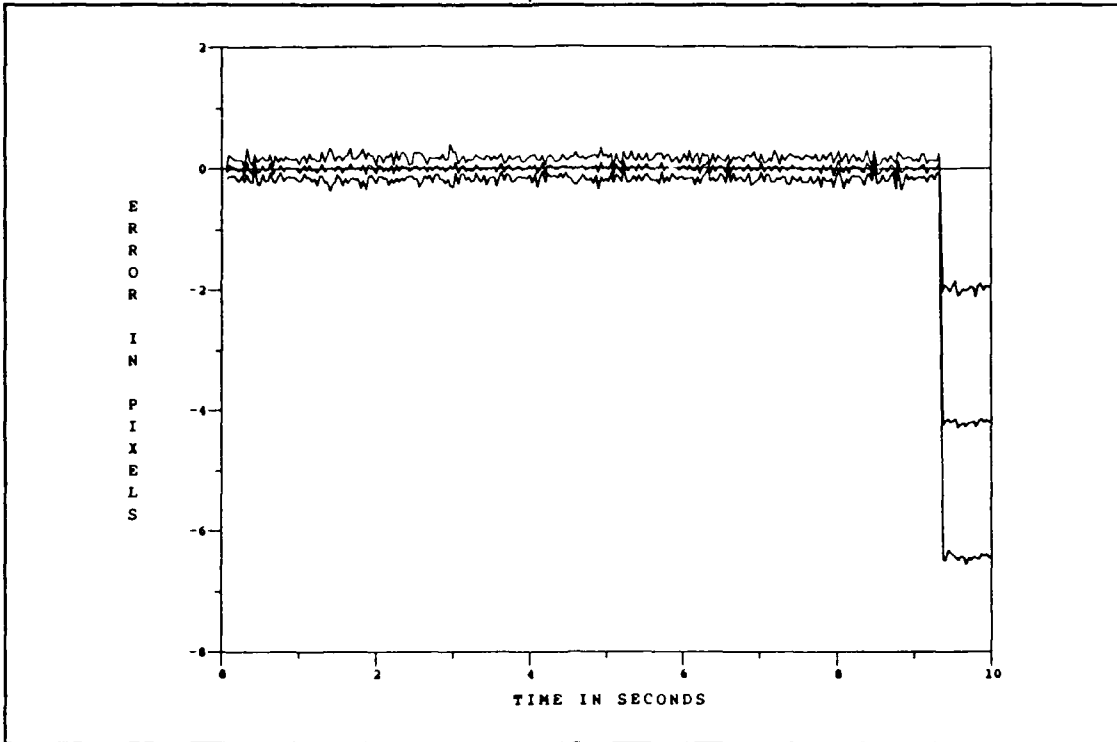


Figure M.9. Study: Eight-State Filter Center-of-Mass Along-Track Error at  $t_i^-$  for Reflectivity Model With Low-Energy Laser Sweep and Plume Pogo

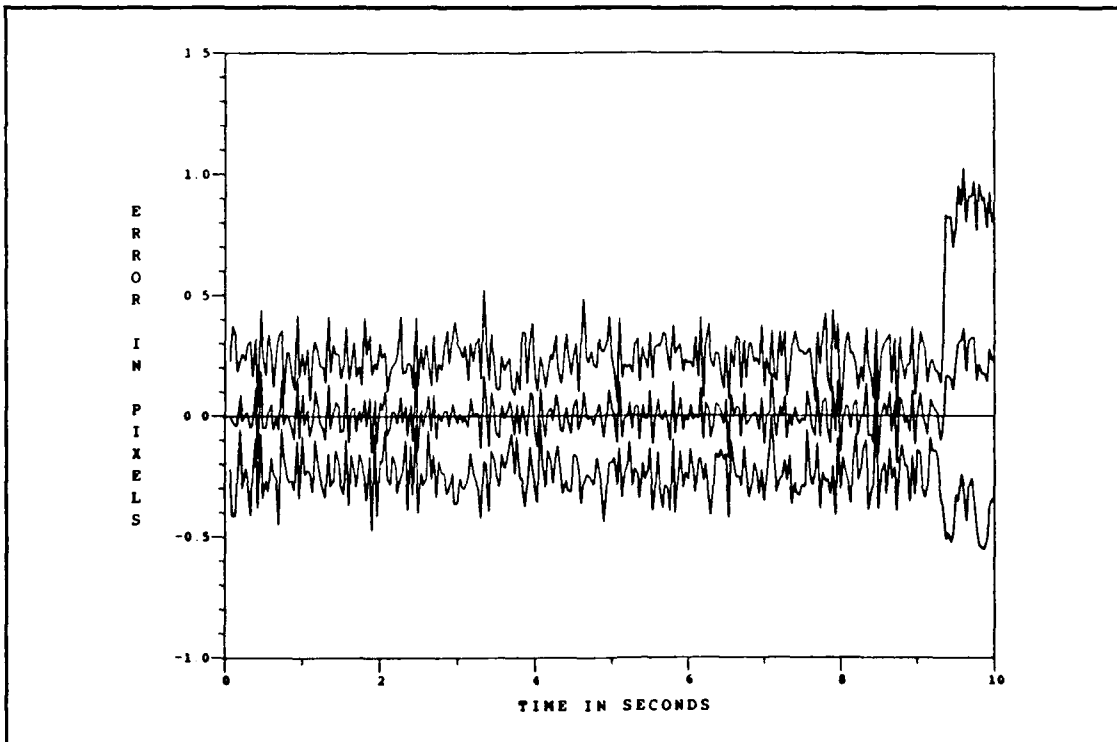


Figure M.10. Study: Eight-State Filter Center-of-Mass Across-Track Error at  $t_i^-$  for Reflectivity Model With Low-Energy Laser Sweep and Plume Pogo

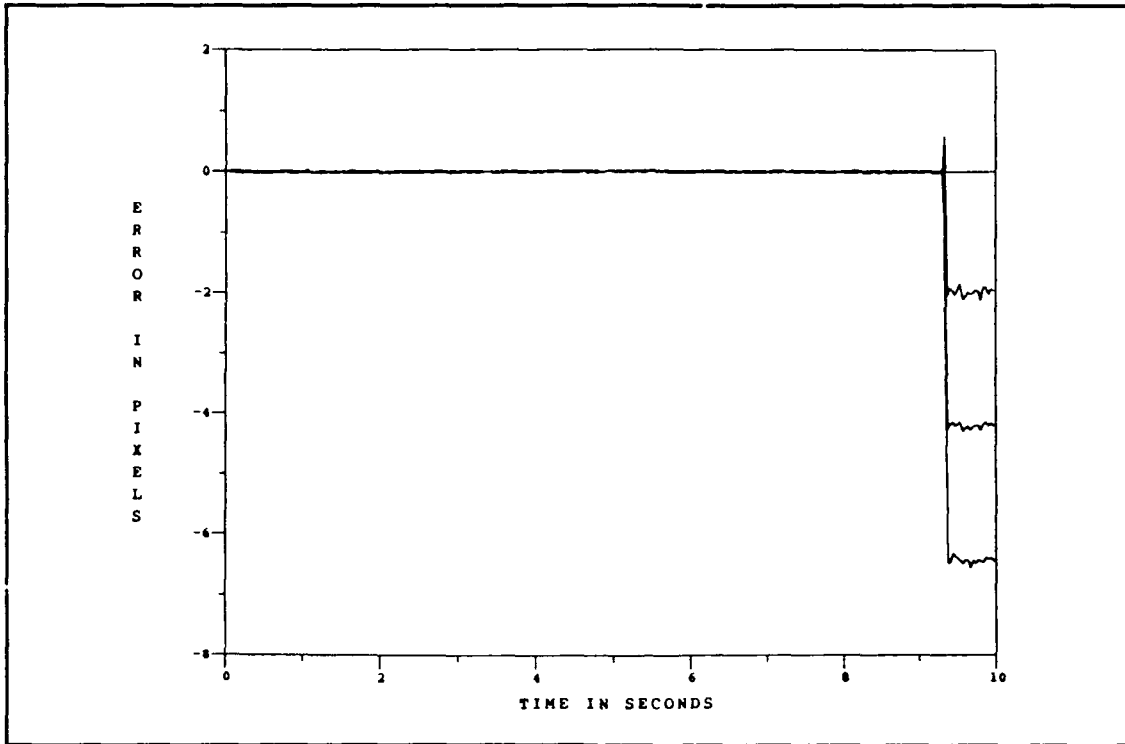


Figure M.11. Study: Eight-State Filter Center-of-Mass Along-Track Error at  $t_i^+$  for Reflectivity Model With Low-Energy Laser Sweep and Plume Pogo

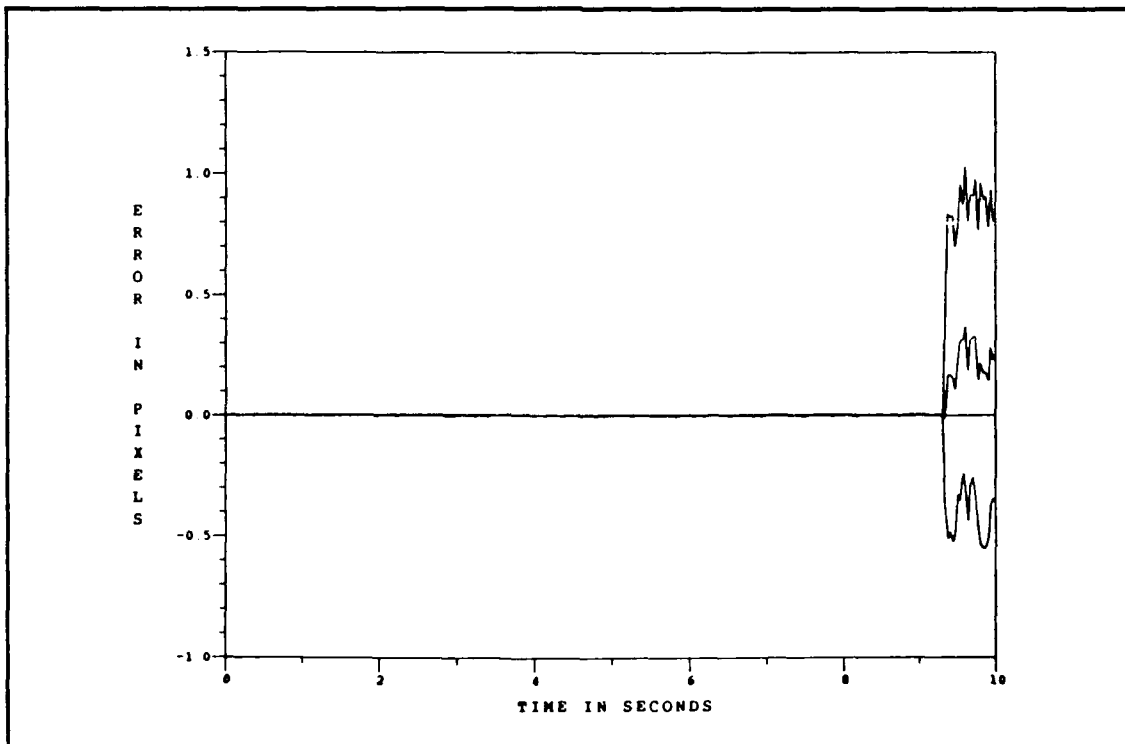


Figure M.12. Study: Eight-State Filter Center-of-Mass Across-Track Error at  $t_i^+$  for Reflectivity Model With Low-Energy Laser Sweep and Plume Pogo

## *Appendix N. Truth Model Atmospheric and Bending/Vibration Plots*

This appendix contains the simulation truth model plots of the atmospheric and bending vibration phenomenon for a study to determine the cause of the "apparent" intensity centroid movement. The plots represent the azimuth ( $x$ ) and elevation ( $y$ ) directions in the FLIR image plane. The atmospheric plots are determined by adding truth model states  $x_3$  and  $x_4$  and truth model states  $x_6$  and  $x_7$  (Chapter IV, Sections 4.3 and 4.3.2). The truth model bending/vibration states plotted are  $x_9$  and  $x_{11}$  (Chapter IV, Sections 4.3 and 4.3.3). For the discussion pertaining to these plots, refer to Chapter VI, Section 6.8.1.

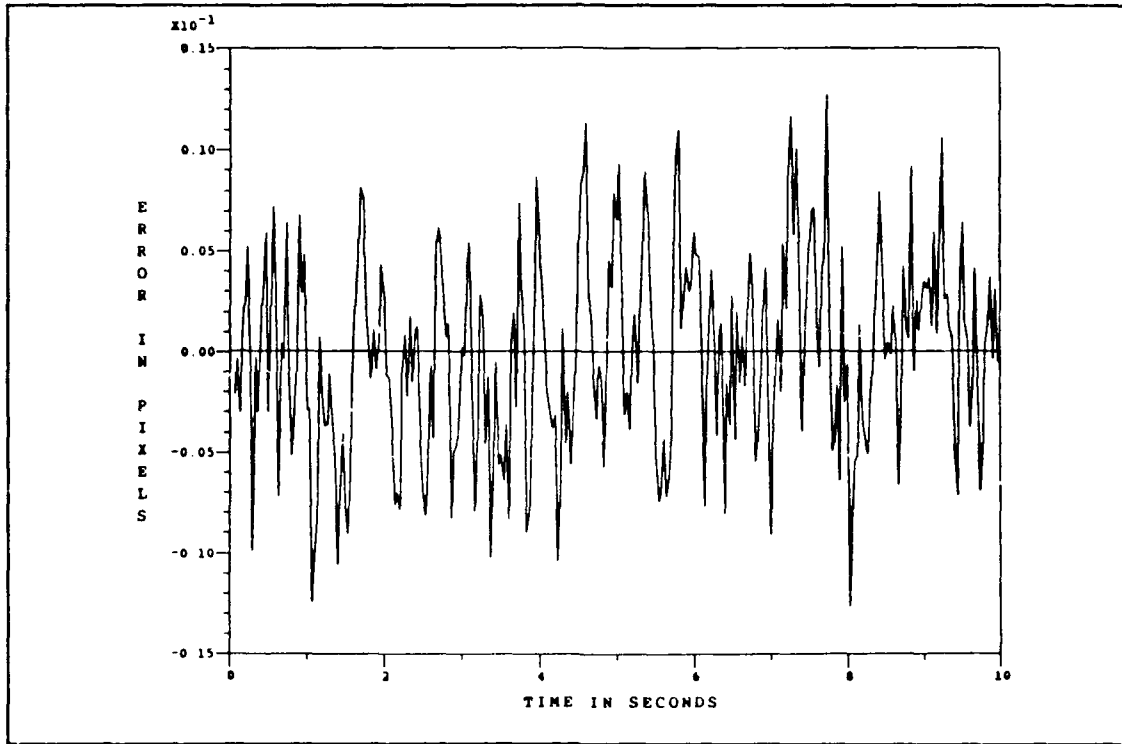


Figure N.1. Truth Model Atmospheric States:  $x_3 + x_4$

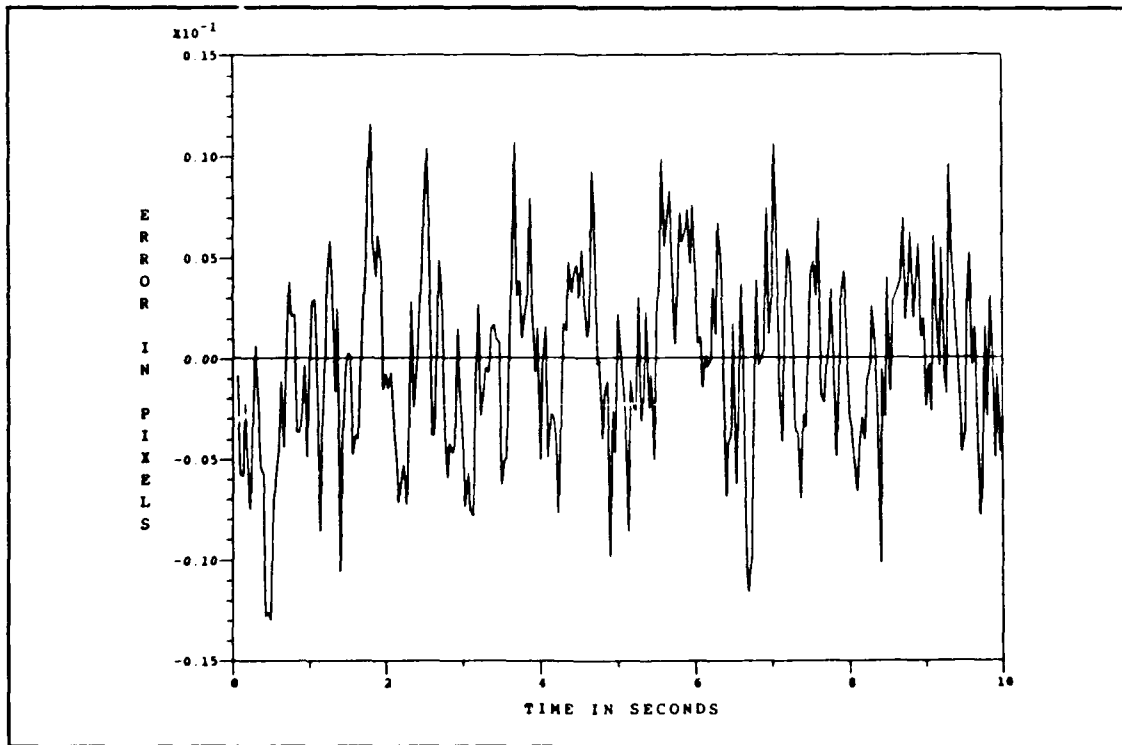


Figure N.2. Truth Model Atmospheric States:  $x_6 + x_7$



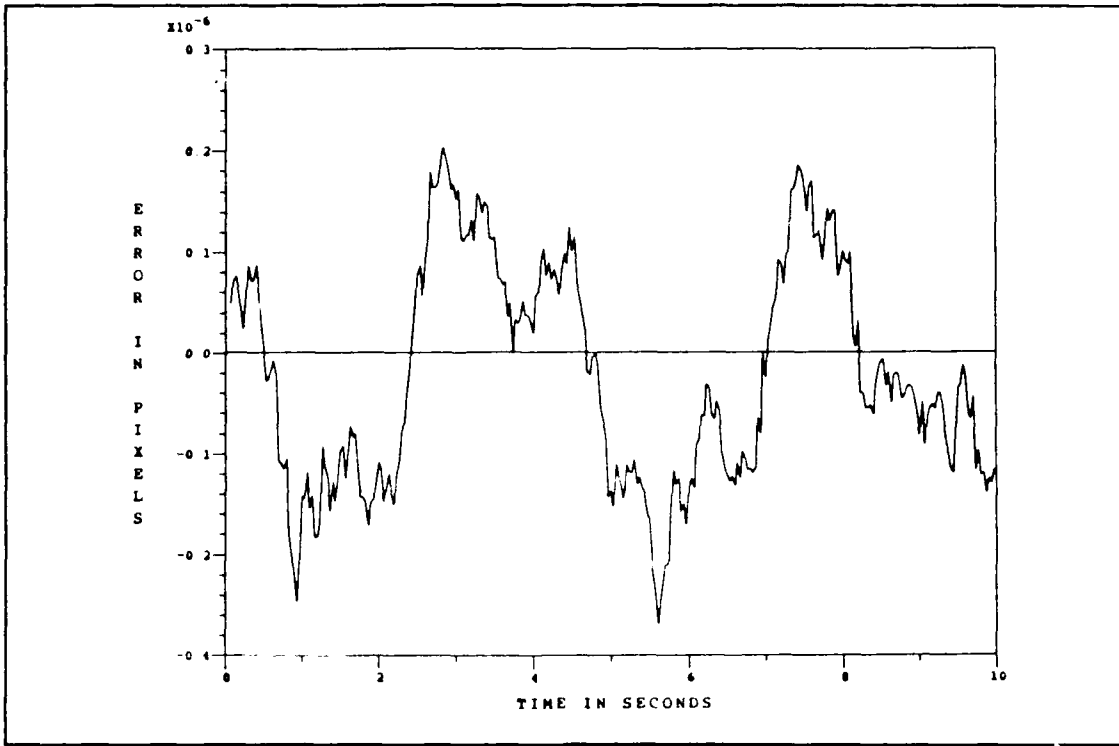


Figure N.3. Truth Model Bending/Vibration State:  $x_0$

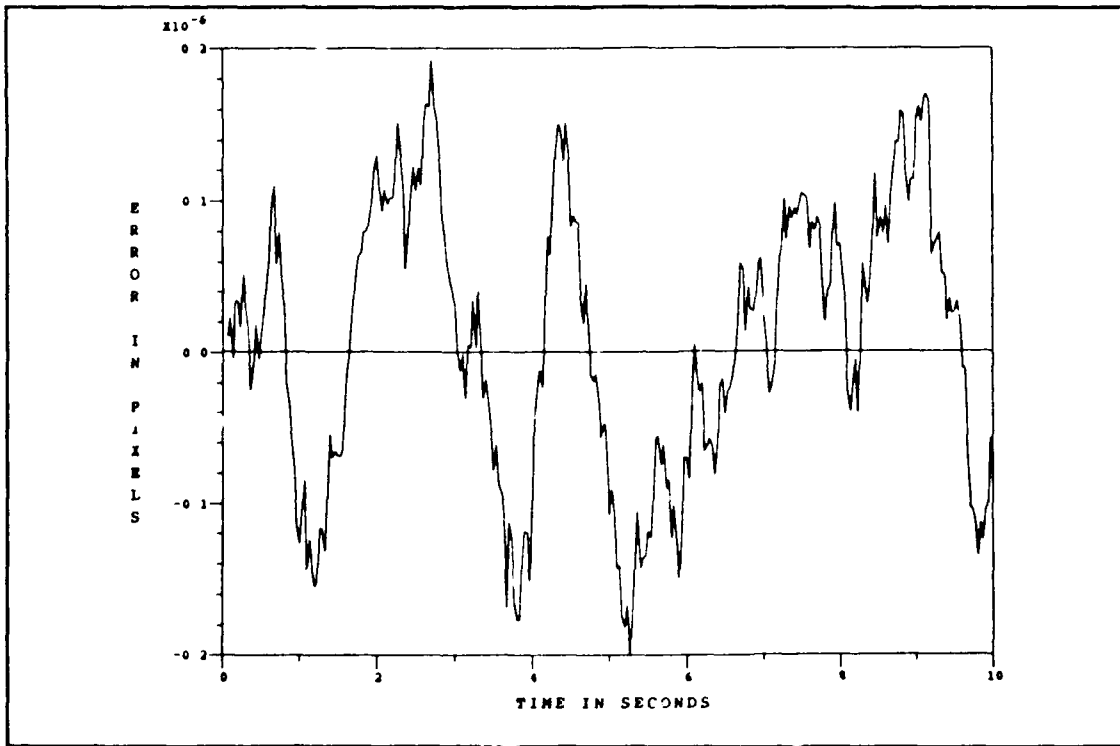


Figure N.4. Truth Model Bending/Vibration State:  $x_{11}$

## Bibliography

1. Brock, L. D. and G. T. Schmidt. "General Questions on Kalman Filtering in Navigation Systems," Theory and Applications of Kalman Filtering, NATO AGARDograph #139, Chapter 10, 205-230, 1970.
2. Eden, Claude W. *Enhanced Tracking of Ballistic Targets Using Forward Looking Infrared Measurements With Active Target Illumination*. MS thesis, AFIT/GE/ENG/89D-11. School of Engineering, Air Force Institute of Technology (AU), Wright-Patterson AFB OH, December 1989.
3. Fairbanks, Ronald R., Capt., Headquarters 6585th Test Group, Holloman AFB, NM. Letter and Unclassified Empirical Radar Information. 19 June 1990.
4. Flynn, P. M. *Alternative Dynamics Models and Multiple Model Filtering for a Short Range Tracker*. MS thesis, AFIT/GE/ENG/81D. School of Engineering, Air Force Institute of Technology (AU), Wright-Patterson AFB OH, December 1981.
5. Hackett, Henry L. *Infrared Radiation*. York, PA: McGraw-Hill Book Company, 1960.
6. Harnly, Douglas A., and Robert L. Jensen. *An Adaptive Distributed-Measurement Extended Kalman Filter for a Short Range Tracker*. MS thesis, AFIT/GA/EE/79-1. School of Engineering, Air Force Institute of Technology (AU), Wright-Patterson AFB OH, December 1979.
7. Kalman, R. E. "A New Approach to Linear Filtering and Prediction Problems," *Journal of Basic Engineering*, Transactions of the American Society of Mechanical Engineers, Vol. 82., 35-45, March 1960.
8. Kalman, R. E. and R. S. Bucy. "New Results in Linear Filtering and Prediction Theory," *Journal of Basic Engineering*, Transactions of the American Society of Mechanical Engineers, Vol. 83., 95-108, March 1961.
9. Kozemchak, Mark R. *Enhanced Image Tracking: Analysis of Two Acceleration Models in Tracking Multiple Hot-Spot Images*. MS thesis, AFIT/GE/ENG/82D. School of Engineering, Air Force Institute of Technology (AU), Wright-Patterson AFB OH, December 1982.
10. Leeney, T. A. *A Multiple Model Adaptive Tracking Algorithm Against Airborne Targets*. MS thesis, AFIT/GE/ENG/87D-37. School of Engineering, Air Force Institute of Technology (AU), Wright-Patterson AFB OH, December 1987.
11. Loving, Phyllis A. *Bayesian vs. MAP Multiple Model Adaptive Estimation for Field of View Expansion in Tracking Airborne Targets*. MS thesis, AFIT/GE/ENG/85M. School of Engineering, Air Force Institute of Technology (AU), Wright-Patterson AFB OH, March 1985.
12. Maybeck, Peter S. *Stochastic Models, Estimation, and Control, Volume I*. New York: Academic Press, 1979.

13. - - - -. *Stochastic Models, Estimation, and Control, Volume II*. New York: Academic Press, 1982.
14. - - - -. "Adaptive Tracking of Maneuvering Targets Based on IR Image Data," *Kalman Filter Integration of Modern Guidance and Navigation Systems*, Proceedings of the North Atlantic Treaty Organization (NATO), AGARD Lecture Series No. 166, 7-1 - 7-18, London, England, 1989.
15. - - - -. Professor of Electrical Engineering. Personal Interviews. Air Force Institute of Technology (AU), School of Engineering, Wright Patterson AFB, OH, January through December 1990.
16. - - - -, D. A. Hamly and R. L. Jensen. "An Adaptive Extended Kalman Filter for Target Image Tracking," *IEEE Transactions on Aerospace and Electronic Systems*, Vol. AES-17, No. 2 173-180, March 1981.
17. - - - - and D. E. Mercier. "A Target Tracker Using Spatially Distributed Infrared Measurements," *IEEE Transactions on Automatic Control*, Vol. AC-25, No. 2, 222-225, April 1980.
18. - - - - and S. K. Rogers. "Adaptive Tracking of Multiple Hot-Spot Target IR Images," *IEEE Transactions on Automatic Control*, Vol. AC-28, No. 10, 937-943, October 1983.
19. - - - - and R. I. Suizu. "Adaptive Tracker Field of View Variation Via Multiple Model Filtering," *IEEE Transactions on Aerospace and Electronic Systems*, Vol. AES-21, No. 4, 529-539, July 1985.
20. - - - - , W. H. Worsley, and P. M. Flynn. "Investigation of Constant Turn-Rate Dynamics Models in Filters for Airborne Vehicle Tracking," Proceedings of the IEEE National Aerospace and Electronics Conference, Dayton, OH, 896-903, May 1982.
21. Mercier, D. E. *An Extended Kalman Filter for Use in a Shared Aperture Medium Range Tracker*. MS thesis, AFIT/GA/EE/78D-3. School of Engineering, Air Force Institute of Technology (AU), Wright-Patterson AFB OH, December 1978.
22. Millner, P. P. *Enhanced Tracking of Airborne Targets Using a Correlator/Kalman Filter*. MS thesis, AFIT/GE/ENG/82M. School of Engineering, Air Force Institute of Technology (AU), Wright-Patterson AFB OH, December 1982.
23. Nawrocki, Paul J. and Robert Papa. *Atmospheric Processes*. New Jersey: Prentice-Hall Inc., 1963.
24. Netzer, Allan S. *Characteristics of Bayesian Multiple Model Adaptive Estimation for Tracking Airborne Targets*. MS thesis, AFIT/GAE/ENG/85D-2. School of Engineering, Air Force Institute of Technology (AU), Wright-Patterson AFB OH, December 1985.
25. Norton, John E. *Multiple Adaptive Tracking of Airborne Targets*. MS thesis, AFIT/GA/ENG/88D-2. School of Engineering, Air Force Institute of Technology (AU), Wright-Patterson AFB OH, December 1988.

26. Rizzo, David R. *Enhanced Tracking of Ballistic Targets Using Forward Looking Infrared Measurements*. MS thesis, AFIT/GE/ENG/89M-7. School of Engineering, Air Force Institute of Technology (AU), Wright-Patterson AFB OH, March 1989.
27. Rogers, Steven K. *Advanced Tracking of Airborne Targets Using Forward Looking Infrared Measurements*. MS thesis, AFIT/GE/ENG/81D. School of Engineering, Air Force Institute of Technology (AU), Wright-Patterson AFB OH, December 1981.
28. Singletery, J. *Adaptive Laser Pointing and Tracking Problem*. MS thesis, AFIT/GEO/EE/ENG/80D-12. School of Engineering, Air Force Institute of Technology (AU), Wright-Patterson AFB OH, December 1980.
29. Suizu, Robert I. *Advanced Tracking of Airborne Targets using Multiple Adaptive Filtering Techniques for Adaptive Field of View Expansion*. MS thesis, AFIT/GE/ENG/83D. School of Engineering, Air Force Institute of Technology (AU), Wright-Patterson AFB OH, December 1983.
30. Tobin, David M. *A Multiple Model Adaptive Tracking Algorithm for a High Energy Laser Weapon System*. MS thesis, AFIT/GE/ENG/86D-37. School of Engineering, Air Force Institute of Technology (AU), Wright-Patterson AFB OH, December 1986.
31. Tobin, David M. and Peter S. Maybeck. "Substantial Enhancements to a Multiple Model Adaptive Estimator for Tracking Image Tracking," *Proceedings of the IEEE Conference on Decision and Control*, Los Angeles, California, 2002-2011, December 1987.

## *Vita*

Captain Roger J. Evans was born on September 16, 1953 in Minneapolis, Minnesota to parents Marcellus and Doris Evans. He graduated from Crosier High School Onamia, Minnesota, in 1971. In September of 1973, he enlisted into the United States Air Force. Following basic military training at Lackland Air Force Base, Texas, he attended the Air Force electronics training school in Biloxi, Mississippi. From August 1974 to August 1980 he was assigned to the 93rd Avionics Maintenance Squadron, Castle Air Force Base, California as a radio technician on B-52 and KC-135 aircraft. In 1980, he was accepted into the Air Force Airman's Education and Commissioning Program (AECP) as an officer candidate. Under the AECP program, he attended Texas A and M University from September 1980 to December 1982, and graduated with a Bachelor of Science degree in Aerospace Engineering. Following graduation from Officer Training School at Lackland Air Force Base, Texas in April 1983, Captain Evans was assigned to the 6595th Aerospace Test Group, Titan Division, Vandenberg Air Force Base, California where he served as a booster and satellite launch controller for DOD space launches until May 1989. In June 1989, Captain Evans was selected to attend the Air Force Institute of Technology to pursue a Master's of Science degree in Electrical Engineering (Guidance and Control).

Permanent address:  
608 Pioneer Dr.  
Santa Maria, CA 93454

# REPORT DOCUMENTATION PAGE

Form Approved  
OMB No. 0704-0188

Public reporting burden for this collection of information is estimated to average 1 hour per response, including the time for reviewing instructions, searching existing data sources, gathering and maintaining the data needed, and completing and reviewing the collection of information. Send comments regarding this burden estimate or any other aspect of this collection of information, including suggestions for reducing this burden, to Washington Headquarters Services, Directorate for Information Operations and Reports, 1215 Jefferson Davis Highway, Suite 1204, Arlington, VA 22202-4302, and to the Office of Management and Budget, Paperwork Reduction Project (0704-0188), Washington, DC 20503.

<b>1. AGENCY USE ONLY (Leave blank)</b>		<b>2. REPORT DATE</b> December 1990	<b>3. REPORT TYPE AND DATES COVERED</b> MS Thesis	
<b>4. TITLE AND SUBTITLE</b> Kalman Filter Tracking of a Reflective Target Using Forward Looking Infrared Measurements and Laser Illumination			<b>5. FUNDING NUMBERS</b>	
<b>6. AUTHOR(S)</b> Roger J. Evans, Capt, USAF				
<b>7. PERFORMING ORGANIZATION NAME(S) AND ADDRESS(ES)</b> Air Force Institute of Technology Wright Patterson AFB, OH 45433-6583			<b>8. PERFORMING ORGANIZATION REPORT NUMBER</b>  90D-20 AFIT/GE/ENG/90-20	
<b>9. SPONSORING/MONITORING AGENCY NAME(S) AND ADDRESS(ES)</b>  Kirtland AFB, NM 87117			<b>10. SPONSORING/MONITORING AGENCY REPORT NUMBER</b>	
<b>11. SUPPLEMENTARY NOTES</b>				
<b>12a. DISTRIBUTION/AVAILABILITY STATEMENT</b>  Approved for Public Release; Distribution Unlimited			<b>12b. DISTRIBUTION CODE</b>	
<b>13. ABSTRACT (Maximum 200 words)</b>  This thesis investigates Kalman filter tracking of a missile hardbody, at a range of 2,000 kilometers, using forward looking infrared (FLIR) measurements and low-energy laser illumination of the missile hardbody. A missile reflectivity model provides realism in the simulation. The tracking scenario uses one filter, provided with FLIR measurements, to estimate the intensity centroid location of the missile's plume. A second, independent, filter estimates the center-of-mass of the missile hardbody. The center-of-mass measurements provided to this filter are computed from information gathered by scanning a low-energy laser along the first filter's estimate of the missile velocity vector. Single scans of the laser produce 20 percent reflection returns, while a sweep (multiple scans) provides a measurement at each sample time. The need for a laser sweep results from inaccurate filter pointing of the FLIR sensor. A comparison between a one-state and two-state filter in estimating the hardbody center-of-mass shows that a one-state estimator performs as well as a two-state filter, with almost no error. The principle error in estimating the missile center-of-mass is along the centerline of the missile, for which the one-state filter is tuned. <span style="float: right;">FS</span>				
<b>14. SUBJECT TERMS</b>  Kalman filter, tracking, plume pogo, ballistic missile, FLIR, laser			<b>15. NUMBER OF PAGES</b> 316	
			<b>16. PRICE CODE</b>	
<b>17. SECURITY CLASSIFICATION OF REPORT</b> Unclassified	<b>18. SECURITY CLASSIFICATION OF THIS PAGE</b> Unclassified	<b>19. SECURITY CLASSIFICATION OF ABSTRACT</b> Unclassified	<b>20. LIMITATION OF ABSTRACT</b> UL	